Magnetic Resonance Studies of Some Silver Halide-Based Model Imaging Systems

by

Myra Toffolon Olm

A Thesis submitted for the Degree of
Doctor of Philosophy
in the
Faculty of Science
at the
University of Leicester

1984

ProQuest LLC
789 East Eisenhower Parkway
P.O. Box 1346
Ann Arbor, MI 48106-1346

Dedicated To my Parents

STATEMENT

The accompanying thesis submitted for the degree of Ph.D. entitled "Magnetic Resonance Studies of Some Silver Halide-Based Model Imaging Systems" is based on work conducted by the author in the Department of Chemistry of the University of Leicester during the period between August 1981 and August 1984. Some of the experimental work described in Chapter 7 was carried out at the University of Paderborn, F. R. G. during the period between May 1983 and July 1983.

All of the work recorded in this thesis is original unless otherwise acknowledged in the text or by reference.

None of the work has been submitted for another degree in this or any other University.

Signed: ...Myra T. Ann... Date: Sept. 3, 1984.

ACKNOWLEDGEMENTS

I am deeply grateful to Eastman Kodak Company, Rochester, N.Y., for providing the leave of absence and the financial support which made this thesis possible. I would like to thank members of the Chemical Physics Laboratory, Rochester and of the Kodak Research Laboratories, Harrow, for many helpful discussions and fruitful collaborations. In particular, I am indebted to Dr. R.S. Eachus for his encouragement and guidance. Sincere thanks are also offered to Prof. J.M. Spaeth, and Dr. J.R. Niklas, and their colleagues at the University of Paderborn for the instruction and hospitality provided during my stay there. Finally, I would like to thank Prof. M.C.R. Symons for his continual help and support.

The experimental expertise provided by Mr. J.A.Brivati and the assistance provided by the technical personnel of the Chemistry Department are gratefully acknowledged. I would especially like to thank Julie Lee, Ann Crane and Vicky Orson-Wright for their patience and expertise in preparing this manuscript.

ABSTRACT

MAGNETIC RESONANCE STUDIES OF SOME SILVER HALIDE-BASED MODEL IMAGING SYSTEMS

Myra Toffolon Olm

Band gap excitation of silver halides produces charge carriers which are subsequently localized at hydrogenic or deep traps. These intrinsic or extrinsic defects control the photographic behaviour of practical silver halide systems. This thesis describes the use of magnetic resonance techniques to study the structure of such traps in model systems.

The lifetime of photoproduced conduction electrons can be greatly extended in silver-halide based materials designed to encourage the partitioning of free electrons and holes. Conduction Electron Spin Resonance was used to study the conduction processes of shallowly trapped and free carriers in several such materials, including Pb^{2+}-doped AgCl, AgBr/AgCl, AgI/AgCl and AgCl/NaCl single crystals and powders. Mechanisms for the extension of the free electron lifetime are proposed, and the temperature and microwave power dependences of the CESR g-value and lineshape are discussed. In addition to studying the band structure and conduction processes as a function of silver concentration and Fermi level in AgCl/NaCl alloys, magnetic resonance studies were used to probe the microcrystalline structure and phase separation processes in these materials.

Transition metal impurities, often associated with lattice defects, act as deep traps in the silver halides. The structure of the metal ion-defect site affects its trap cross-section and lifetime. The enhanced resolution provided by Electron Nuclear Double Resonance techniques was used to determine the structure of Rh^{2+}-silver ion vacancy complexes in Rh^{3+}-doped AgCl and NaCl single crystals and powders. The primary site in AgCl exhibited a static Jahn-Teller distortion at low temperature, which gave way to a two-dimensional and finally to a three-dimensional dynamic distortion as the temperature was raised.

The application of ENDOR to glasses and powders was explored via studies of the DTBN radical in glassy matrices and of γ-irradiated sodium formate and silver:cyclohexene powders. The latter two studies provided, respectively, examples of "single-crystal-like" and "powder-type" ENDOR powder spectra.

CONTENTS

CONTENTS (Continued)

CONTENTS (Continued)

C H A P T E R O N E

THE SOLID STATE CHEMISTRY

AND THE

PHOTOGRAPHIC PROCESS

OF THE

SILVER HALIDES

1.1 INTRODUCTION

The silver halides are the image-recording component of most photographic processes today, and have been so for over one hundred years. Despite their costliness, unparalleled speed and sensitivity has enabled them to retain their pre-eminence. These properties are the result of the silver halides' unique defect structure and electronic behaviour. Much of the latter derives from the position of the silver halides on the boundary between ionic and covalent solids.[1] It is this position that makes the electronic structure of the silver halides of fundamental interest to the solid state chemist. The ionic defect structure and transport mechanisms of the silver halides, which are largely a result of the unusual properties of the silver ion, are also of fundamental interest and have been widely studied. It is of interest to note that the silver halides exhibit a wide range of ionic behaviour, from superconducting silver subfluoride at low temperatures, to α-AgI, which is an ionic superconductor at high temperatures.[2] Thus, the happy situation exists where "not only has solid state physics contributed to the understanding of silver halides but the silver halides have made valuable contributions to solid state physics."[3]

This chapter reviews some aspects of the solid state chemistry of the silver halides, pointing out those properties that result from the borderline nature of their ionicity, as well as those properties that make them such excellent photographic materials. For clarification, a short general description of exiton and polaron models is given before examples specific to the silver halides are discussed. Finally, current views on the photographic process are considered.

1.2 CRYSTAL STRUCTURE

Silver chloride and silver bromide have face-centred cubic structures of the rocksalt type.[4] Lattice constants are listed in Table I. Silver iodide crystallizes from the melt in one of two phases, β-AgI, which has a hexagonal wurtzite type structure and γ-AgI, which has a cubic zincblende structure. A highly conductive high temperature phase, with I^- ions on body-centred cubic sites and Ag^+ ions in interstitial voids, α-AgI, and a high pressure phase with a rocksalt structure, δ-AgI, also exist.[5]

The lattice constants of the alkali halides can be calculated from the hardsphere ionic radii[6] of the constituents, where the assumed ionic radii are consistent for all of the alkali halides; however, lattice constants so calculated for the silver halides are not in good agreement with experiment. This reflects the somewhat covalent nature of bonding in the silver halides.

AgCl and AgBr are completely miscible with a linear change in lattice constant and no change in crystal structure. AgI is soluble to a limited extent in AgBr and less soluble in AgCl.[7]

1.3 IONIC DEFECT STRUCTURE

The silver halides have a Frenkel defect structure on the cation sublattice. The concentration of Frenkel defects is governed by the expression for the rate constant for the reaction $Ag_i^+ + Ag_v^+ \rightarrow Ag_{lattice}^+$, that is:

$$K_F\ (T) = [Ag_i^+]\ [Ag_v^+] \qquad (1)$$

In a pure crystal, the condition for charge neutrality demands that

Table I: Lattice Constants In Some Alkali- And Silver Halides[9]

Lattice	a (Å)	Lattice	a (Å)
NaF	4.62	AgF	4.92
NaCl	5.64	AgCl	5.55
NaBr	5.97	AgBr	5.77

Table II: Energy Gaps At 4.2K In The Silver Halides[2,*]

(eV)

	$L_3' \rightarrow \Gamma_1$	$\Gamma_{25} \rightarrow \Gamma_1'$	$L_3' \rightarrow L_1$	$L_3' \rightarrow L_2'$	$X_5' \rightarrow X_1$	$X_5' \rightarrow X_3$
AgBr	2.69	4.25	5.5	8.02	6.5	10.1
AgCl	3.25	5.10	7.0	8.5	7.5	13.1

Table III: Steepness Parameter For Some Alkali- And Silver Halides[33]

Lattice	σ	Lattice	σ
KCl	0.80	AgCl	0.8
KBr	0.79	AgBr	1.0
KI	0.79		

*Measured from optical absorption spectra of thin films[26,27]

$$N_i = N_v = [K_F]^{\frac{1}{2}} \qquad (2)$$

In a crystal containing multivalent substitutional impurities the condition for charge neutrality becomes:

$$-eN_v + eN_i + e(p-1)N_m = 0 \qquad (3)$$

where p is the charge on the impurity ion m. Thus, with the addition of a divalent cation such as Cd^{2+} or Pb^{2+}, the concentration of interstitial silver ions decreases, and with the addition of a divalent anion, such as S^{2-}, it increases. Because of this effect, the ionic conductivity of even nominally pure cystals is impurity-controlled below room temperature. The temperature dependence of N is given by:

$$N = (NN')^{\frac{1}{2}} e^{-\omega/2kT} \qquad (4)$$

where N and N' are the number of lattice and interstitial positions, and ω is the formation energy of the Frenkel defect pair. At high temperatures, radiotracer techniques have shown that Ag_i^+ moves by an interstitialcy mechanism jumping directly from one interstitial site to another through a (100) plane. At room temperature and below, migration is by a knock-on mechanism, where an interstial ion jumps onto a substitutional site, knocking the substitutional ion into an interstitial position. Ionic motion is frozen out below about 150K. The ionic conductivity is well understood in terms of this mechanism. For a more detailed discussion, including the calculation of mobilities, migration and formation energies of the ionic defects, see references 2 and 8.

There is evidence that a negative space charge layer exists in both AgCl and AgBr, resulting from the difference in the formation energy for interstitial silver ions and silver ion

vacancies at the surface. This results in a surplus of interstitial ions, with the concentration at the surface several orders of magnitude greater than in the bulk. For this same reason, the ionic conductivity of emulsion grains is much larger than that of bulk single crystals.[8]

The fairly high ionic conductivity of the silver halides can be attributed to the low Frenkel defect diffusion energies that result from the reduction of TO phonon frequencies by the quadrupolar deformability of the silver ion (see section 1.4). A similar reduction occurs in the Frenkel defect formation energy and helps explain why Frenkel defects are observed in the silver halides, and Schottky defects in the alkali halides.[9]

1.4 PHONONS

The phonon dispersion curves for AgCl[10] and AgBr[11], measured by inelastic neutron scattering, are shown in Figure 1. These curves, as well as the second-order Raman spectra, are in good agreement with those calculated from a breathing shell model that takes into account the deformability of the silver ion. The deformability, resulting from the filled silver d-shell, accounts for the rather unusual crossing of the LA and TO branches along ⟨111⟩, so that at the L point, the silver ions vibrate in the TO mode and the halide ions in the TA mode.[9]

FIGURE 1

Phonon dispersion curves for (a) AgBr, data from Ref. 11, figure taken from Ref. 3, and (b) AgCl, data from Ref. 20, figure taken from Ref. 2.

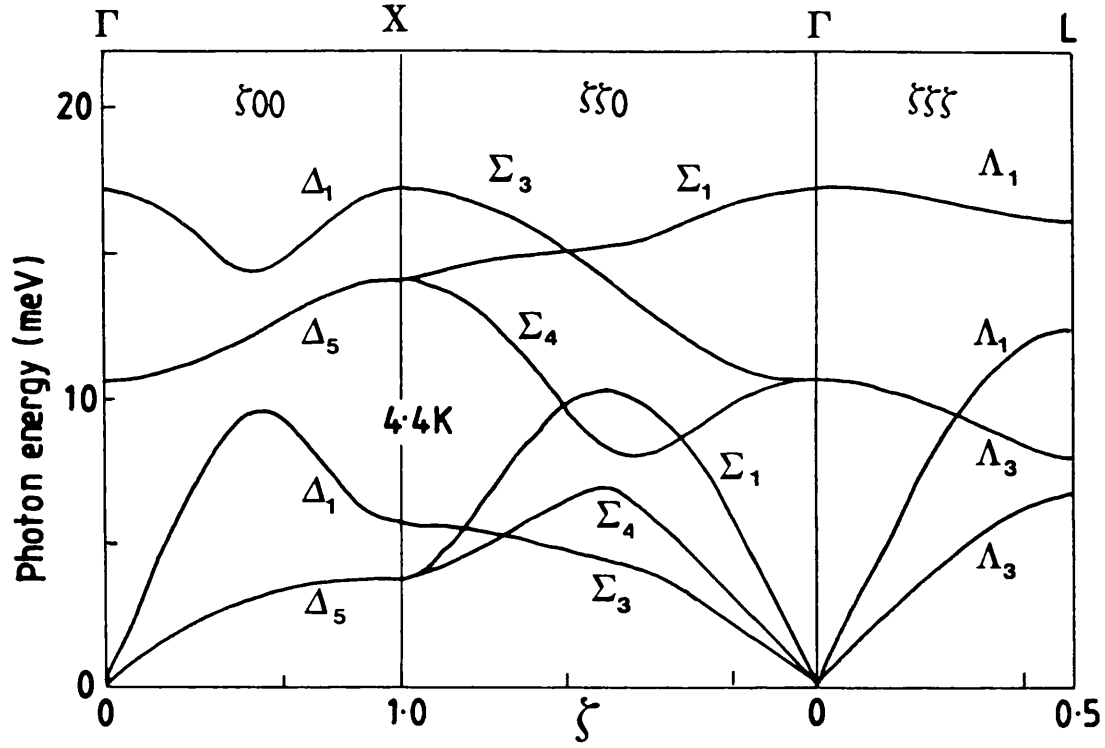

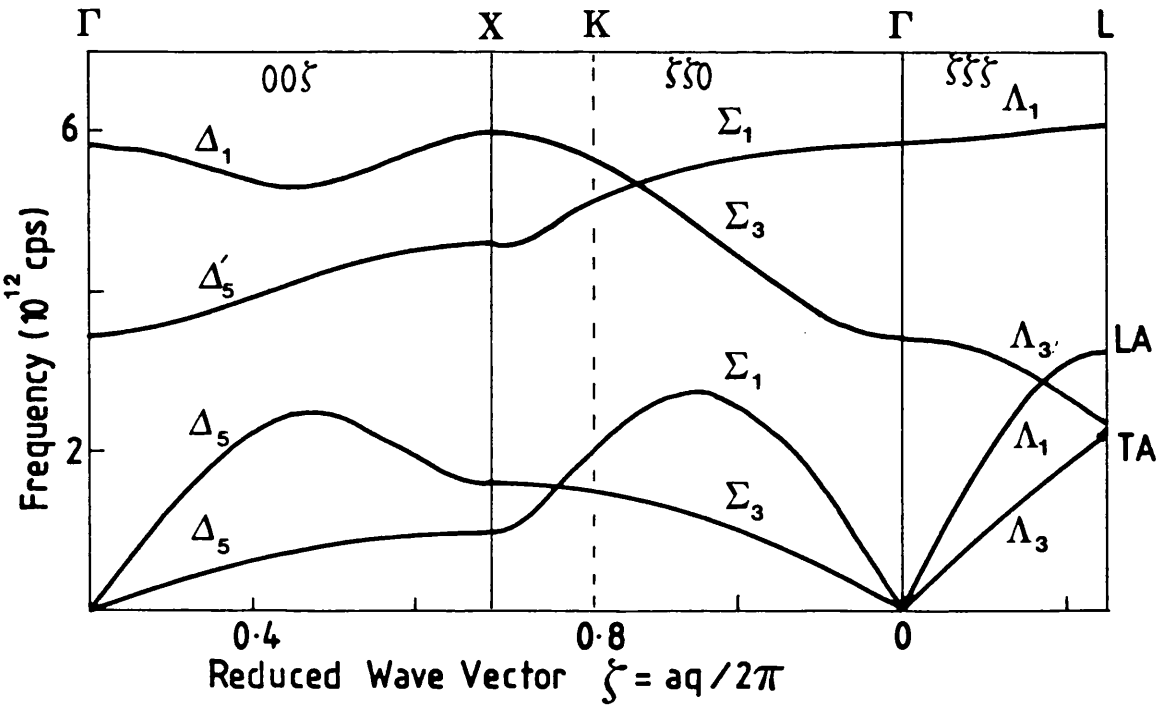

1.5 ELECTRONS AND HOLES

1.5.1 Bare Band Structure

The term "bare band structure" refers to the orbital energies associated with the ground state of the crystal. Polaron effects, which result from the charge polarization produced by an extra hole in the valence band or extra electrons in the conduction band, and exciton interactions, which are a product of the Coulomb attraction between the electron-hole pair produced by photolysis, will be discussed in the following sections.

The valence band structures of AgBr and AgCl were calculated by Bassani, et al., using a tight binding method, and some speculations were made as to the conduction band structure.[12] Some aspects of the latter had been understood from absorption measurements as early as 1951.[13] Complete band structures were calculated by Scop[14] and Fowler[15] using augmented plane wave and mixed-basis methods, respectively. These calculations were in good agreement; however, temperature dependent photoemission studies[16] were consistent with the more qualitative band structures of Bassani, et al. These are shown in Figure 2.

The unique features of the silver halides' band structures are the result of silver 4d-derived levels lying high in the valence band. These hybridize with the levels derived from the valence p orbitals of the halogen and produce a valence band maximum at the L point. The valence band edge is split by spin-orbital coupling, and it has been experimentally confirmed that the highest lying valence band states in AgBr are the $L_{4,5}^{-}$ states.[17] The bottom of the conduction band is derived from Ag 5s states. It is spherical and located at the Γ point, as has been verified by magnetoconductivity experiments.[18]

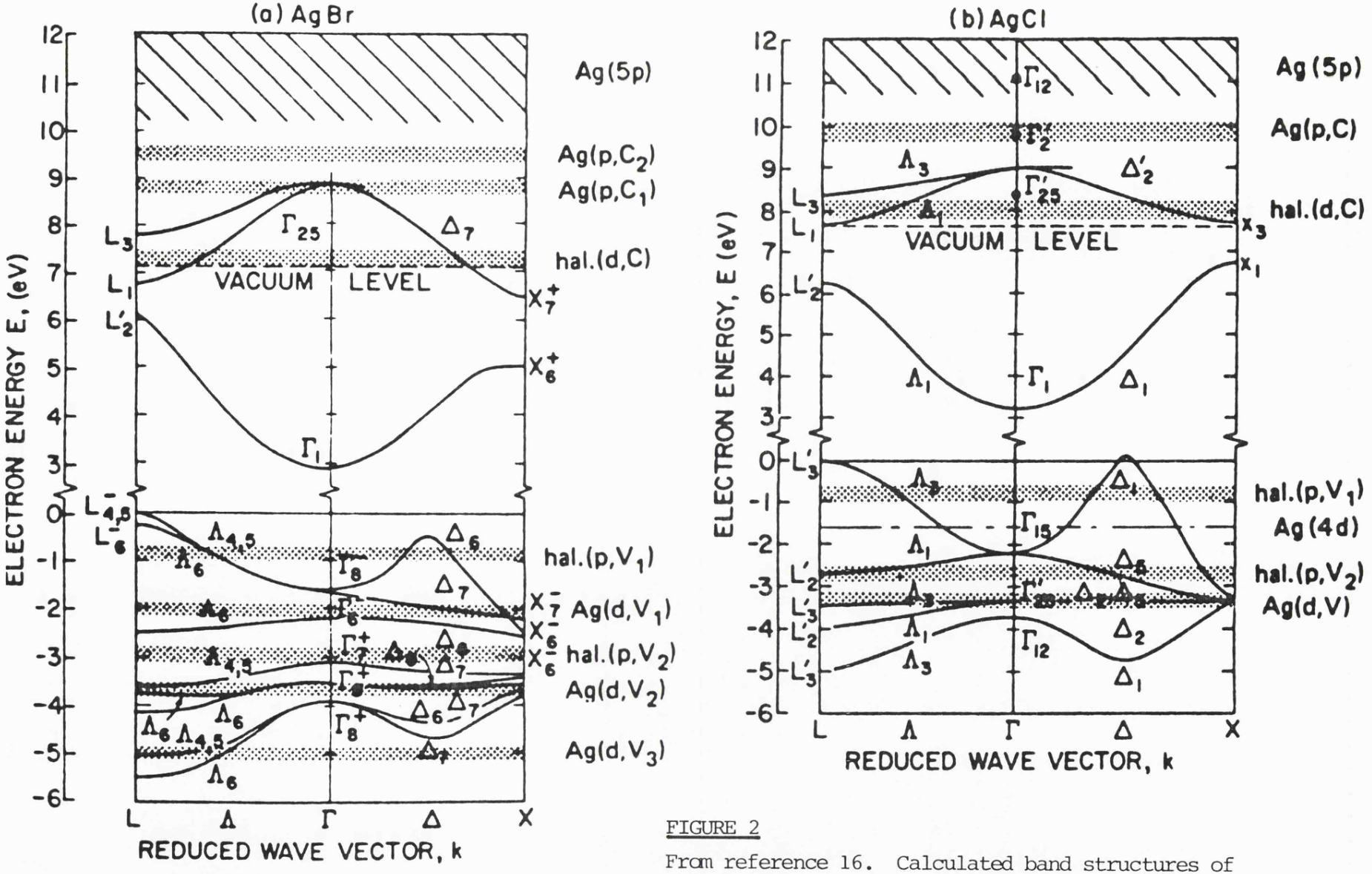

FIGURE 2

From reference 16. Calculated band structures of Bassani et al. for AgBr and AgCl. Shaded areas are the regions of high density-of-states as determined by photoemission spectroscopy (reference 16).

The conduction bands derived from the Ag 5p levels are repelled by the halogen p levels of the valence band and lie higher in energy than the conduction bands derived from the halogen d excited states. As a result of repulsion from the high-lying Ag 4d-derived valence bands, these latter are much higher in energy relative to Γ_1 than corresponding bands in the alkali halides, so that unlike the alkali halides, there is very little amplitude of the lowest conduction band on the halide ion.[19]

Thus, the silver halides are indirect band gap solids. Evidence of this is seen in their absorption spectra, where a long tail extends into the near UV due to the indirect gap transition.[13,20] Temperature dependence studies of the absorption edge show that, as required by momentum conservation, the transition is assisted at helium temperatures by phonons of energy 8.1 and 13.5meV in AgBr[21,22] and 8.0 and 13.0meV in AgCl.[23] The 8 and 13meV phonons correspond to the TO and LA phonons at the L point.[10,11] Thus the valence band maximum is determined experimentally to be at the L point in agreement with band structure calculations. The absorption spectrum of Pure AgBr at 2K is shown in Figure 3. In imperfect crystals impurity scattering relaxes the condition for momentum conservation and a zero phonon indirect transition is allowed. This is observed in Cl^--doped AgBr[3] and in Li^+- and Na^+-doped AgBr.[24]

Direct gap transitions (actually, direct exciton transitions, as discussed below) are also observed in the absorption spectra of the silver halides. The valence band derived from the 4p bromide orbitals is split by spin-orbital coupling (Γ_6^- and Γ_8^- in Figure 2a), and this splitting is observed in the direct optical transition to Γ_1 as shown in Figure 3a. The relative intensities of these two transitions are the

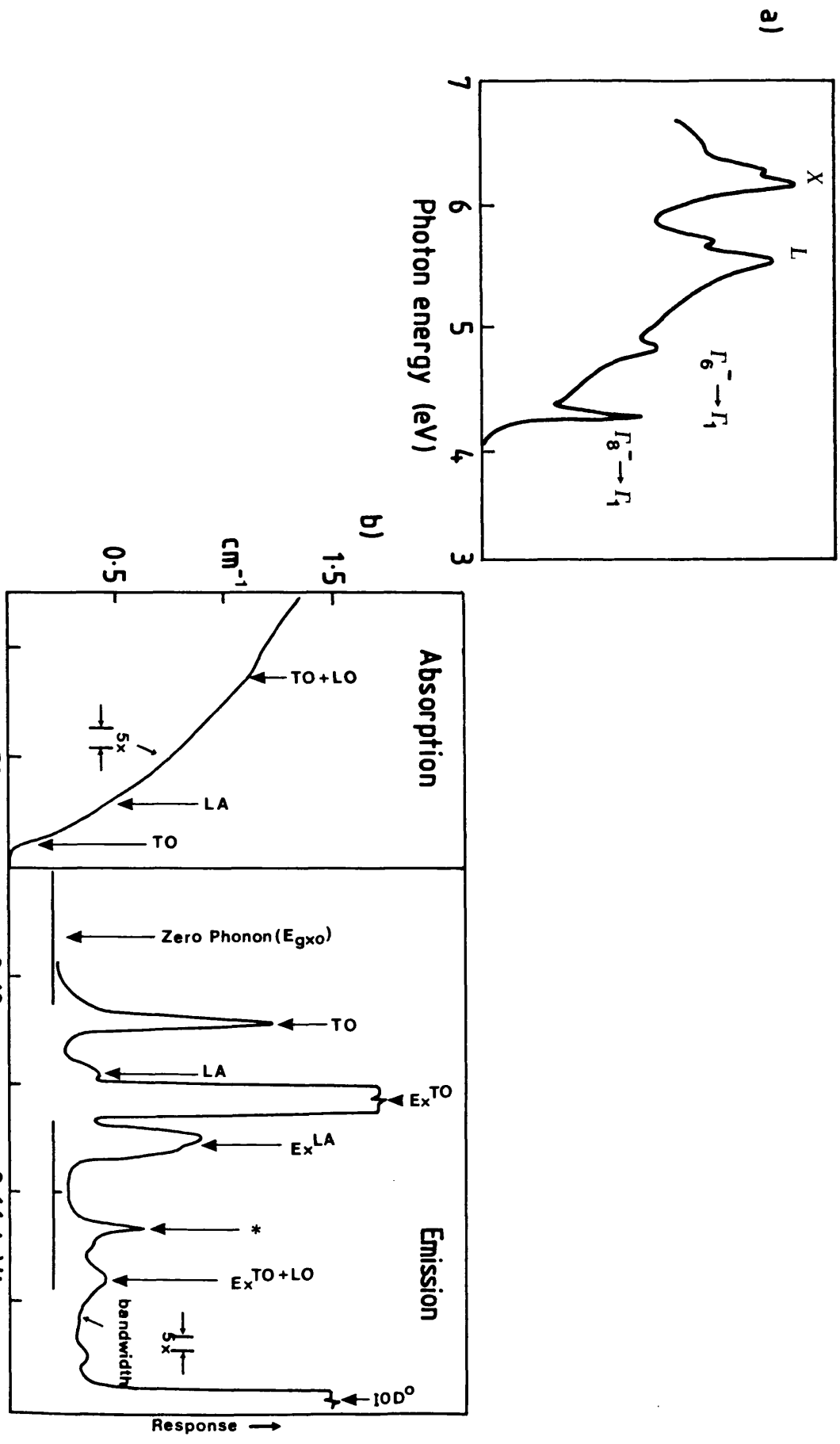
a)
Photon energy (eV)
7
6
5
4
3
X
L
$\Gamma_6^- \rightarrow \Gamma_1$
$\Gamma_8^- \rightarrow \Gamma_1$
b)
cm^{-1}
0·5
1·5
Absorption
TO+LO
5x
LA
TO
2·70
2·68
2·66 (eV)
Zero Phonon (E_{gxo})
TO
LA
Ex^{TO}
Ex^{LA}
*
Ex^{TO+LO}
bandwidth
5x
Emission
I_0D^o
Response

FIGURE 3

a) Extinction coefficient for AgBr at 4.2 K, from reference 2.
b) Absorption and emission spectra of AgBr at 2 K, from reference 3.
c) Emission spectrum of AgBr showing iodide-exciton band (2.5 eV) and "red emission" band (2.14 eV), reproduced by permission of A. P. Marchetti.

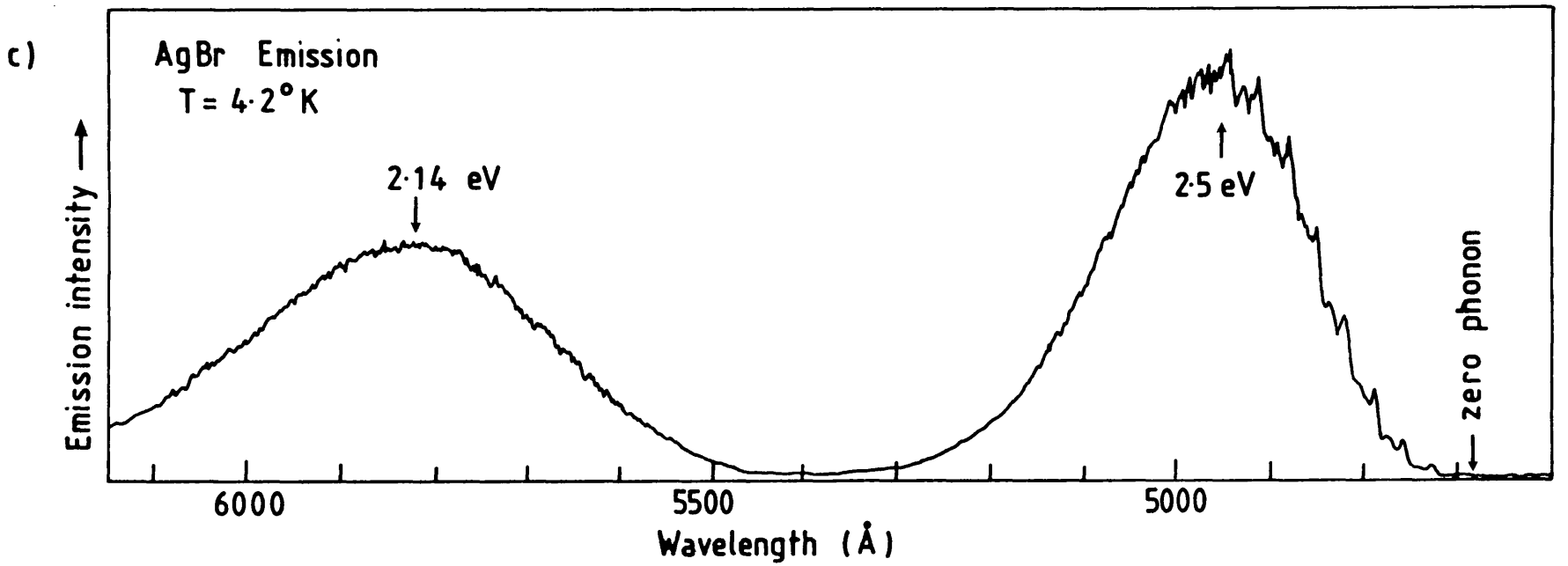

opposite of that observed in the alkali halides and are evidence of a Mott-Wannier exiton (see below).[2,25] Direct transitions at the L and K band edges are also apparent in Figure 3a. Transitions to higher conduction bands have been observed using synchrotron radiation.[26] Experimental band-to-band transition energies are summarized in Table II.

As mentioned above, at low temperatures the absorption edge corresponds to an indirect bandgap transition, and the absorption coefficient is comprised of components arising from the absorption and emission of a single TO phonon. As the temperature is raised different phonon energies become important and various phonon processes merge. Above 100 K however, the absorption edge is no longer determined by single or multi-phonon transitions between band edges; these transitions are broadened by interactions of the electric field arising from the vibrating lattice.[2,28] In this temperature regime, the absorption edge obeys the Urbach rule,[28] which holds for a wide range of solids and was observed in silver halides in 1956:[29]

$$K = K_o \exp[-\sigma(h\omega_o - h\omega) / kT] \qquad (5)$$

K is the absorption coefficient and ω_o is the frequency of the absorption threshold. σ is the steepness parameter and is proportional to the ratio of the exciton band width to the exciton-phonon coupling strength (see next section).[30] Some values of σ in silver and alkali halides are given in Table III. In mixed crystals, $AgCl_{1-x}Br_x$, the absorption edge[31] and σ [26] shift linearly with x.

1.5.2 Excitons and Polarons: General Description

A simple description of the exciton and polaron models that are applicable to the silver halides is given below. These models are discussed in detail in references 34-37.

An exciton is a bound electron-hole pair such as would be produced by band gap irradiation. It is the lowest excited state of the crystal, being lower in energy than the band-to-band transition as a result of the Coulombic attraction of the electron and hole. In the alkali halides the exciton is essentially an atomic excitation localized on a single ion; such a tightly bound state is called a Frenkel exciton. In silver halides the electron and hole may be separated by many lattice spacings. This Mott-Wannier type exciton can be described by a hydrogenic model, where the electron and hole are screened by the dielectric of the crystal, . The lowest energy bound state will have radius, a, and energy, E_{ex}, given by:[98]

$$a = \varepsilon \frac{m}{m^*} a_o \qquad E_{ex} = \frac{m^*}{m} \left(\frac{1}{\varepsilon^2}\right) (13.6)\text{eV} \qquad (6)$$

m^* is the reduced effective mass using the effective valence and conduction band masses ($\frac{1}{m^*} = \frac{1}{m_v} + \frac{1}{m_e}$). **

Excitons are always unstable towards recombination and sometimes unstable towards dissociation into distant electron-hole pairs.

** The effective mass of a carrier, m_e, is reduced from the free electron mass, reflecting change in mobility of the carrier in the crystal lattice relative to vacuum. In the crystal potential, the carrier will accelerate as if it had mass m_e. m_e is inversely proportional to the curvature of the energy band and will be lower at band edges and in wide band solids.[19, 37]

Either type of exciton can move freely throughout the crystal or can become self-trapped if either the electron or hole becomes localized by a lattice distortion. Self-trapping usually occurs at degenerate band edges. Since valence band edges are usually degenerate and holes tend to have larger effective band masses and thus lower mobilities than electrons, self-trapping of excitons is usually the result of hole-trapping.[37]

Whether or not self-trapping occurs depends on the strength of the coupling between the exciton and acoustic phonon modes, which is represented by the coupling constant g. As g increases, the effective mass of the exciton increases discontinuously to an almost infinite value once g becomes larger than a critical value g_c.** This corresponds to changing from an almost free state with small lattice distortion to a self-trapped state with large lattice distortion. The discontinuity in the effective mass is a result of the short range nature of the interaction between exciton and acoustic phonon modes.[35]

An intuitive understanding of the magnitude of g_c can be understood from Figure 4. (Since this discussion is equally applicable to the self-trapping of excitons, holes or electrons,

---

** The effective mass increases by a factor $e^{1/\gamma}$. γ is called the nonadiabaticity parameter and is the ratio of the maximum phonon energy to the electronic bandwidth. It compares the velocity of phonon motion to the velocity of electronic motion. In most ionic crystals and semiconductors it is of the order of 0.01 to 0.1, reflecting the fact that electronic motion is usually much faster than ionic motion. The adiabatic approximation, where γ=0, is assumed in the above discussion. If γ was of the order of 1, as might be the case in molecular crystals, there would be no abrupt change from a free to a trapped state with increasing g.[35]

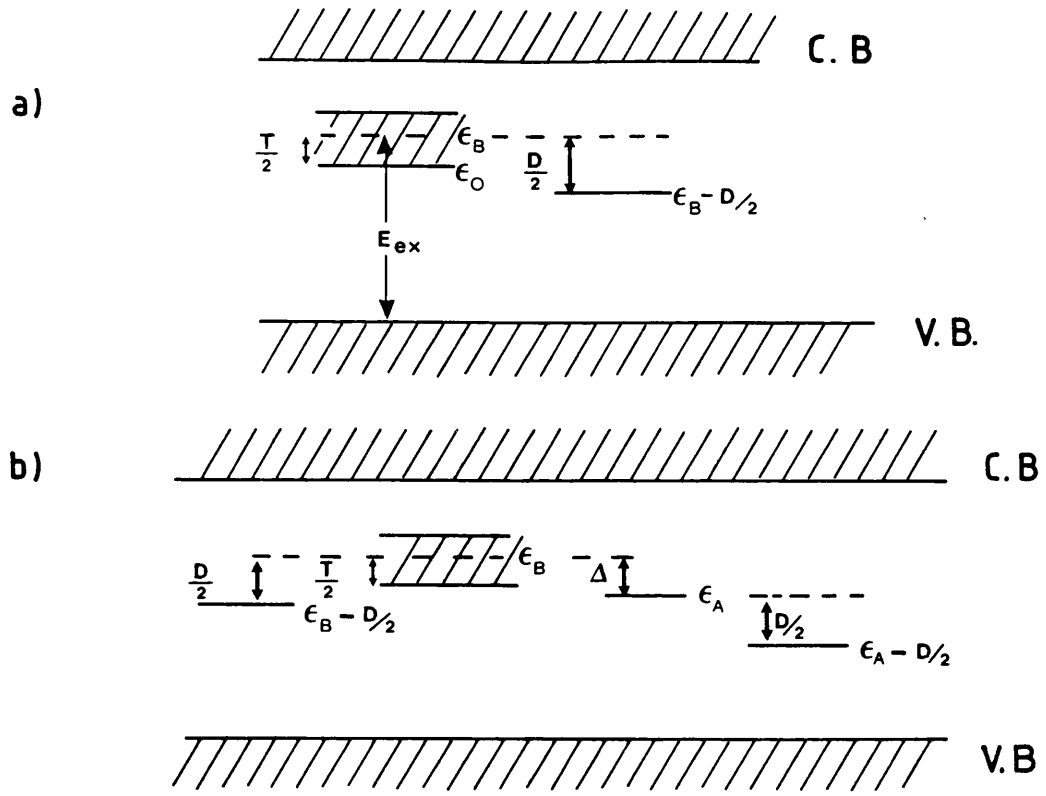

FIGURE 4

Schematic representation of conditions for self-trapping of an electron in:-
a) a pure crystal of B molecules, and
b) a B crystal with A molecule impurities.

for simplicity the self-trapping of electrons is represented here.) In a rigid crystal, the free exciton state will always be stable. The lowest exciton energy will be $\varepsilon_o = \varepsilon_B - {}^{T}/2$ where ε_B is the exciton energy and ${}^{T}/2$ is one-half the exciton band width. In a deformable lattice, self-trapping can occur as a result of the lowering in energy, ${}^{D}/2$, by an asymmetric deformation of the lattice. If ${}^{D}/2 > {}^{T}/2$, then the deformed state will be lower in energy than the lowest free state and self-trapping will occur. ${}^{D}/T$ is simply the coupling constant g, and indeed, in the adiabatic limit, $g_c = 0.9$.[35,36] The optical steepness parameter, σ, mentioned above, is inversely related to g. σ_c is 0.9, and if $\sigma > 0.9$, then the carrier will be self-trapped.[3]

Since self-trapping occurs as the result of a lattice deformation, there will always be a potential energy barrier to self-trapping in a pure crystal.[35]

In a pure crystal three phases are allowed depending on the magnitude of g. These are designated F, F(S) and S(F), corresponding to a stable free state for $g<0.6$, a stable free state and a metastable self-trapped state for $0.6<g<0.9$, and a stable self-trapped state and a metastable free state for $g>0.9$. This is shown schematically in Figure 5a, where the adiabatic potential energy is plotted versus lattice distortion for a series of values of g.[35]

In a mixed crystal a fourth phase is possible where the self-trapped state is stable and no potential energy barrier to self-trapping exists. This would occur at an A impurity site in a B crystal if the attractive potential alone of the impurity A was sufficient to trap a carrier. In Figure 4b, this

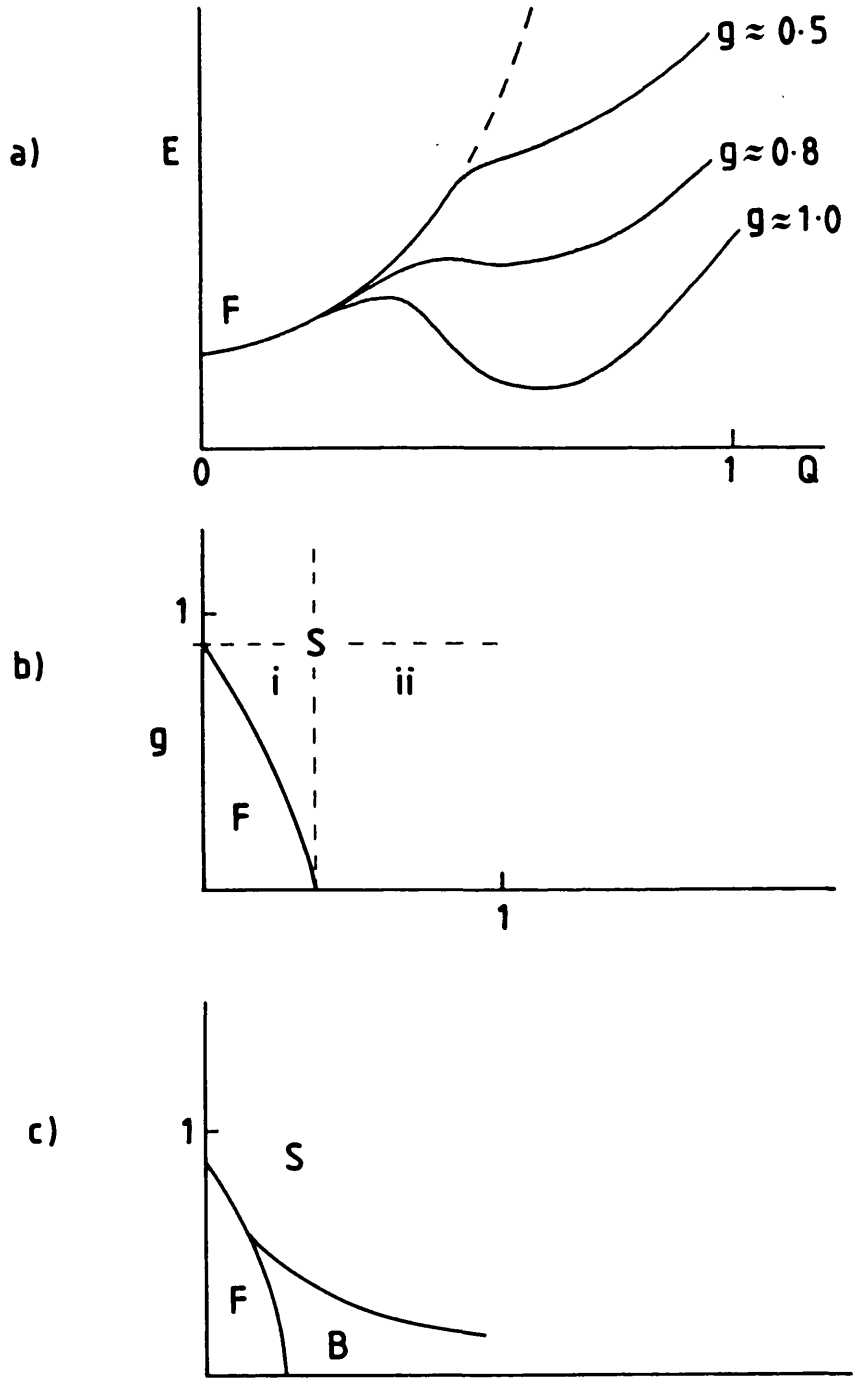

FIGURE 5

Derived from reference 36.

a) Energy versus normalized lattice dilation, Q, as a function of g, for a pure crystal;
b) Phase diagram of free and self-trapped states in a B crystal with A impurity;
c) Phase diagram, including cluster bound state B, for a small A cluster in a B crystal.

corresponds to $\Delta > T/2$, where Δ is the difference between the ε_B and ε_A energy levels. In the adiabatic limit, self-trapping will occur at A in the rigid lattice if $\Delta/T > 0.34$. Self-trapping can also occur through the combined effect of g and Δ/T, as in the region marked i in Figure 5a. Here, neither the impurity potential nor $D/2$ are alone sufficient for trapping to occur at A; but the combination results in self-trapping. In this case, the carrier would not be self-trapped in either pure crystals A or B; this is referred to as "impurity-assisted self-trapping."[36]

In the opposite extreme, when B is an impurity in an A crystal (and $\epsilon_B > \epsilon_A$), self-trapping will occur at A sites if $g > 0.9$, but will not occur at B sites.

For intermediate concentrations of A in B crystals, the coherent potential approximation** has been used to describe optical properties and density-of-states behaviour. This leads to a classification of the energy bands of mixed crystals into two types according to whether the parent bands in the pure solids overlap. Thus, the conduction band in Figure 6 is of the "persistence-type", since the ratio of the difference in parent-band energies to bandwidth, Δ/T, is larger than $\frac{1}{2}$. The valence band in Figure 6 is of the "amalgamation-type". The amalgamation band will always be wider than the component bands and the carriers move fast enough to feel an average potential due to A and B atoms. Thus, amalgamation solids behave to first order like virtual crystals, where the energy spectrum E(k) varies

---

** In the coherent potential approximation, the random binary mixture is treated as a uniform effective medium with "averaged" eigenstates.

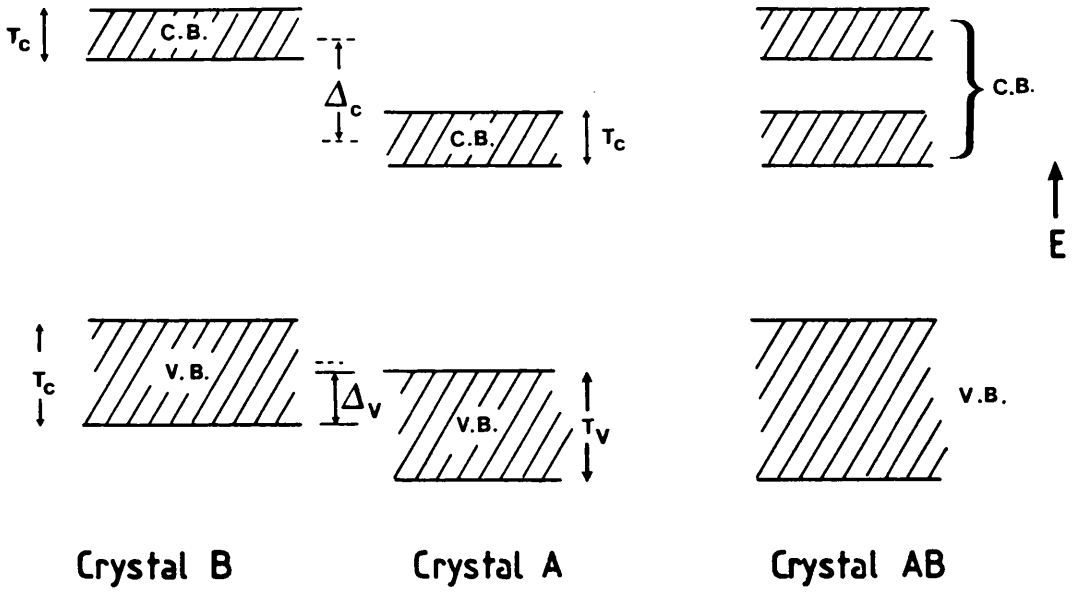

FIGURE 6

Density-of-states in a mixed crystal with a persistence-type conduction band and an amalgamation type valence band.

linearly with concentration.

The coherent potential approximation neglects cluster effects in mixed crystals. Clusters form simply as a result of the disorder of binary mixtures. It becomes possible, in a system with Δ/T such that the exciton would be self-trapped at an A site in the above approximation, for the exciton to be bound to an A cluster but have a wave function that is extended throughout the cluster, that is, to be no longer self-trapped. To see this, consider a mixed crystal with Δ/T in region ii of Figure 5b. Here, the exciton will be trapped in the mixed crystal because of the impurity potential of A, but would be free in an A crystal. As the A cluster increases in size, the electron will always remain bound to the cluster, but once the cluster begins to approximate an A-crystal, the exciton will go from a self-trapped state to a state delocalised over the cluster (B-state). It is possible for the change from an S to a B state to occur discontinuously at a critical size. A representative phase diagram is shown in Figure 5c.

Finally, interactions of carriers with polar modes of the crystal will be considered. If an extra electron is placed in the conduction band of an ionic crystal, it may be energetically favourable for the surrounding ionic charges to be polarized, and for the electron to move throughout the crystal accompanied by this deformation. The electron plus the deformation is called a polaron. The polaron mass will be larger than the band mass. The polaron field results in an essentially Coulombic, long range interaction. Thus, in contrast to exciton interaction with acoustic modes, the effective mass of the polaron increases continuously with increasing coupling constant g. The somewhat localized state of the polaron will always be energetically

favoured relative to the free state.[35] The magnitude of the lattice deformation depends on the coupling constant, and in the extreme case the polaron is localized at a single site and moves from site to site by tunneling at low temperatures and thermal hopping at high temperatures (small polaron).

1.5.3 Excitons in silver halides

i) Intrinsic Excitons

The steepness parameter, σ, is 0.8 for AgCl and 1.0 for AgBr. The critical value of σ is 0.9; thus, one would expect that excitons should be self-trapped in AgCl and free in AgBr. Indeed, this is experimentally observed as discussed below. In mixed crystals $AgCl_{1-x}Br_x$, σ passes through the critical value at $x = 0.5$, and at this concentration an abrupt change from a self-trapped exciton (STE) to a free exciton is observed.

For AgCl, the intrinsic emission band is broad and shows a large Stokes shift, consistent with the decay of a STE (Figure 7b).[24,31,38,39] The size of the Stokes shift indicates that the self-trapping occurs via a fairly large lattice distortion.[2] The STE has also been observed by optically detected magnetic resonance (ODMR) where exchange coupling is sufficient to yield a spectrum characteristic of a triplet state such that the data can be fitted to the Hamiltonian:[40,41]

$$\mathcal{H} = \beta \vec{B}_o \cdot g_e \cdot \vec{\hat{S}} + D\,(\hat{S}_z^2 - 1/3\,S^2) + E(\hat{S}_x^2 - \hat{S}_y^2) \qquad (7)$$

The ODMR spectrum of the STE is shown in Figure 8 and the magnetic resonance parameters are listed in Table IV. The ODMR lines are 50 G wide and no hyperfine coupling is detected. The g-values are in agreement with the equations:[42]

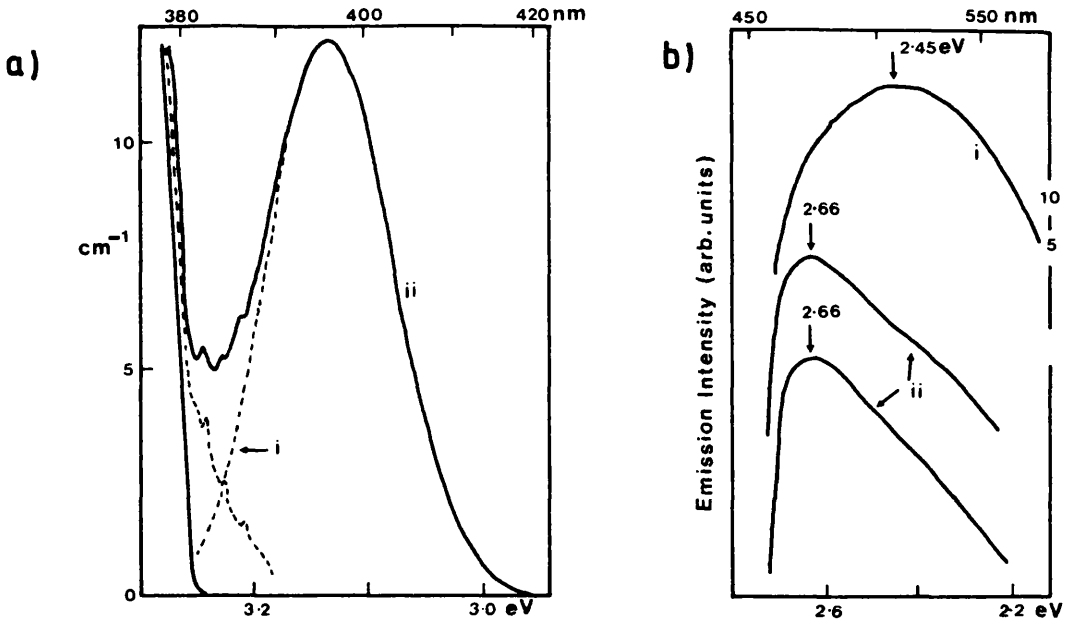

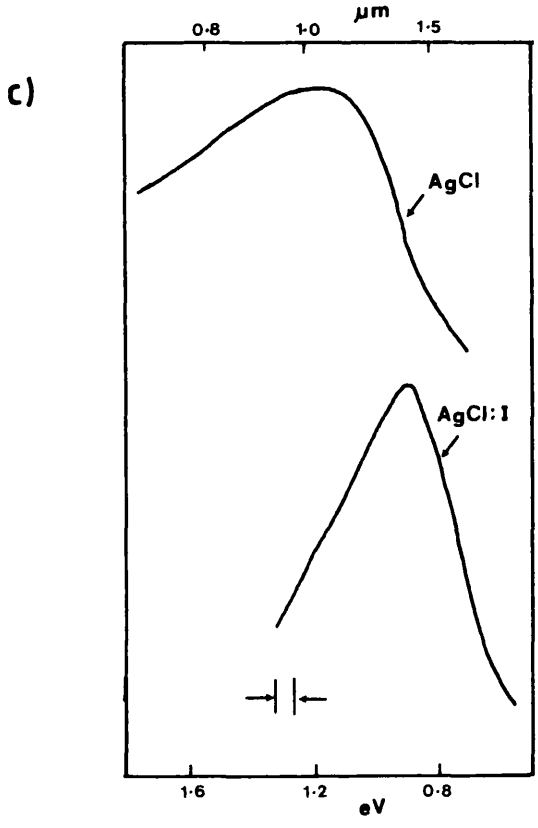

FIGURE 7

a) Absorption and
b) emission spectra of AgCl (i) and I/AgCl (ii), from reference 38.
c) Transient absorption spectra of trapped holes in AgCl at 2 K, from reference 3.

FIGURE 8

ODMR spectra of AgCl and AgBr.
a) and c) from Ref. 63.
b) from Ref. 47.
d) from Ref. 56.

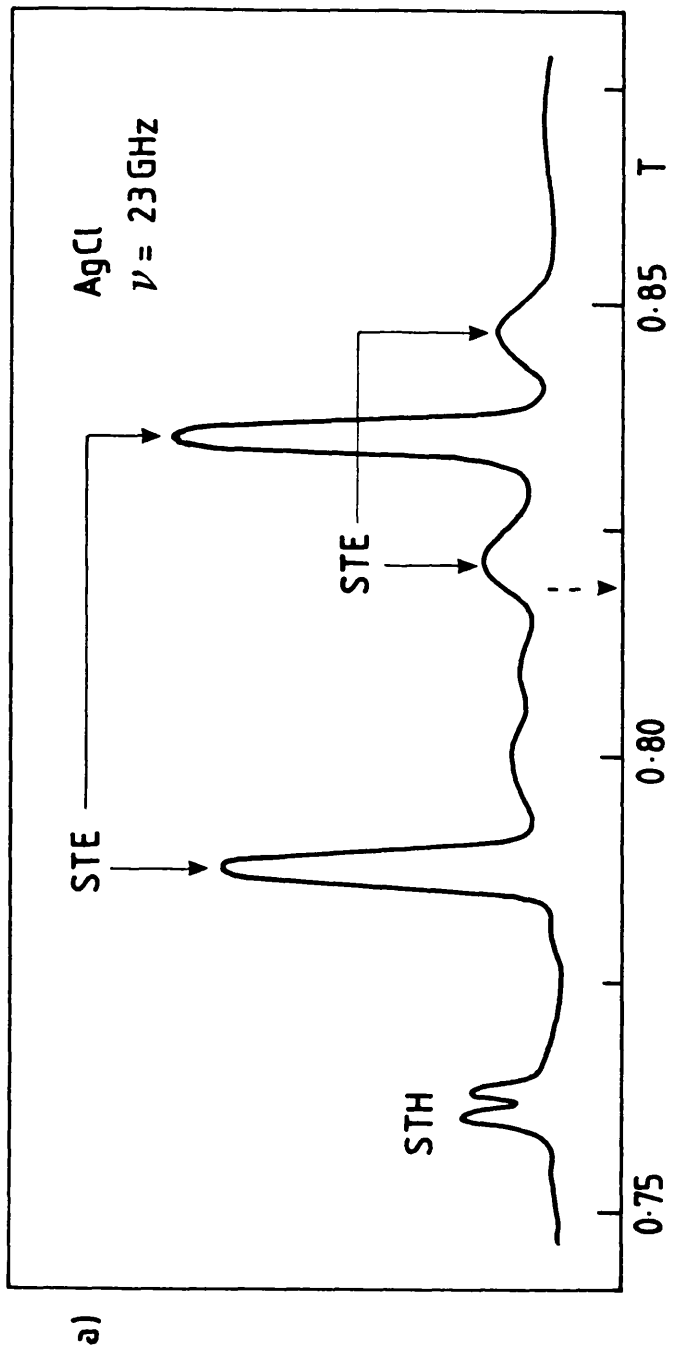

b)

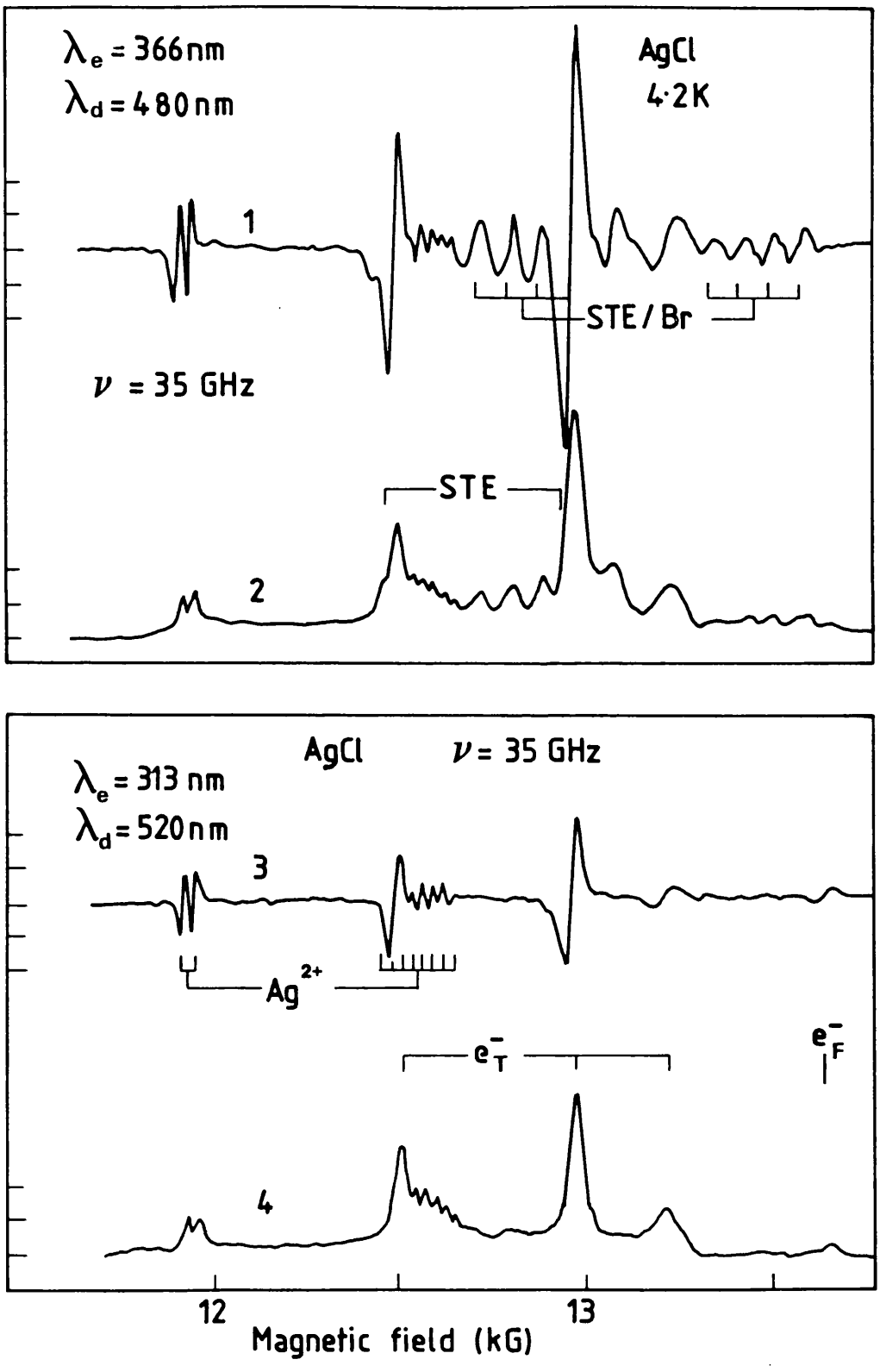
λe = 366nm
λd = 480nm
AgCl
4·2K
1
STE / Br
ν = 35 GHz
STE
2
AgCl
ν = 35 GHz
λe = 313 nm
λd = 520nm
3
Ag2+
e⁻T
e⁻F
4
12
13
Magnetic field (kG)

c)

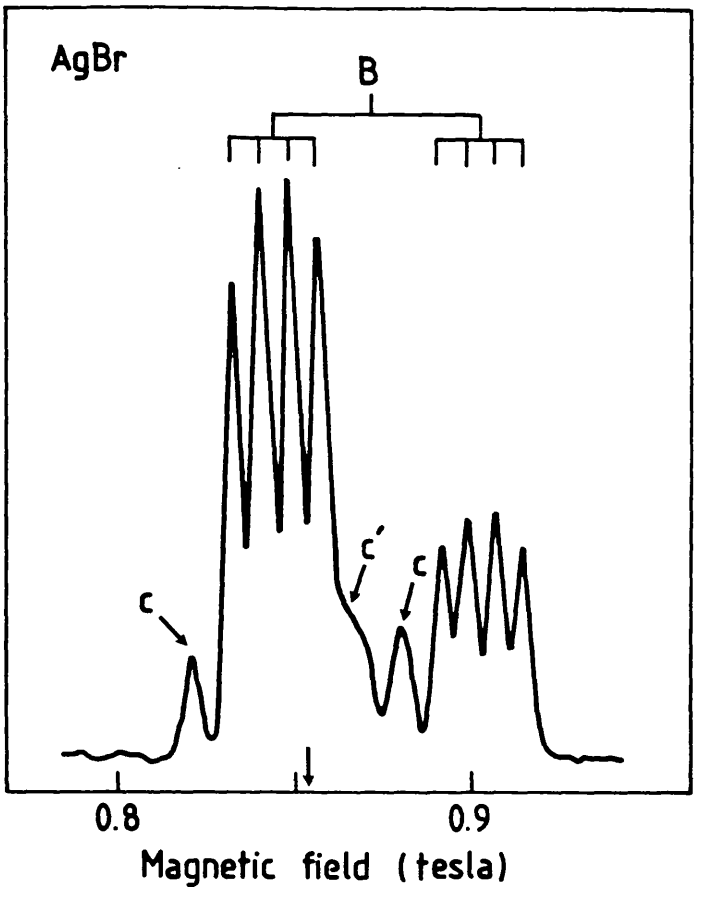
AgBr
B
c
c'
c
0.8
0.9
Magnetic field (tesla)

d)

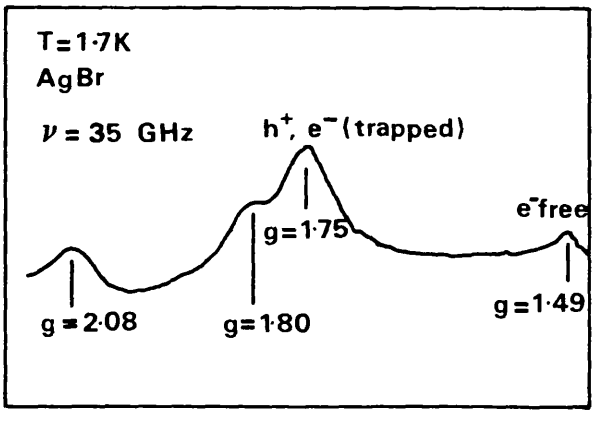
T=1·7K
AgBr
ν = 35 GHz
h+, e− (trapped)
e− free
g=1·75
g=2·08
g=1·80
g=1·49

$$g_{\parallel}^{STE} = \frac{(g_{\parallel}^{STH} + g_e^{free})}{2} \qquad (8)$$

$$g_{\perp}^{STE} = \frac{(g_{\perp}^{STH} + g_e^{free})}{2}$$

These observations are consistent with the electron being in a diffuse orbit around the self-trapped hole (STH), and with the Mott-Wannier exciton model. The singlet-triplet splitting parameter, δ, is estimated to be small, also consistent with the model of a weakly bound exciton.[41]

It should be noted that ODMR and luminescence decay measurements indicate that the intrinsic broad emission band in AgCl also has a long lived component due to the recombination of distant electrons with the STH.[41,43,32] This implies that even at 1.7 K the excitons produced by UV irradiation decay efficiently to unbound electron-hole pairs.

The indirect exciton transition in AgBr is observed in low temperature optical absorption measurements as described in section 1.5.3, as well as in the lumimescence spectrum (Figure 3). The decay of the free exciton is assisted by TA and LO phonons, with the emission bands separated for the corresponding absorption bands by twice the phonon frequency.[38] No Stokes energy shift is observed for the exciton transistion, which suggests that the exciton is free. This is further supported by the temperature dependence of the luminescence data.[3] The binding energy of the free exciton is estimated to be 20 m.eV[46] and the radius, ~26 Å (Table V).

In mixed crystals, $AgCl_{1-x}Br_x$, when $x \lesssim 0.3$, the self-trapped excitons $(AgCl_5Br)^{5-}$ and $(AgBr_6)^{5-}$ have been detected.[42] The magnetic resonance parameters are listed in Table IV.

Table IV: Magnetic Resonance Parameters For Intrinsic Centers In Silver Halides

Species	System	Parameters	Method	Ref.
Self-trapped excitons				
$(AgCl_6)^{5-}$	AgCl	$g_{ll} = 2.021$, $g_{\perp} = 1.968$, $D = 241.7$	ODMR	40,41
$(AgCl_5Br)^{5-}$	Br/AgCl	$g_{ll} = 1.956$, $g_{\perp} = 1.987$ $D = 300G$ $A_{ll}^{Br} = 80G$	ODMR	41
$(AgCl_5Br)^{5-}$	Br/AgCl	$g_x = 1.952$, $g_y = 1.971$* $g_z = 2.007$ $D = -29.4G$, $E = 9.8G$ $A_x^{Br} = 82G$	ODMR	42
Iodine-bound exciton				
	I/AgBr	$g_e^{free} = 1.54$ $g_h = .8$	Zeeman eff. on lum.	46
Intrinsic Defects				
trapped e^-	AgCl	$g_{ll} = 2.051$, $g_{\perp} = 1.941$ $g_{iso} = 1.978$	ODMR	41
		$g_{iso} = 1.975$	ESR, 1.5K	45
trapped e^-	AgBr	$g_{iso} = 1.80$	ODMR	56
trapped h^+	AgBr	$g_{iso} = 1.75$	ODMR	56
trapped h^+ ass.w/I^-	I/AgBr	$g_{iso} = 1.67$	ODMR	61
surface sites	AgCl and AgBr	$g_{iso} = 2.0036$ $g_{iso} = 1.975$ $g_{iso} = 1.93$	ESR	62

*g_z is along the J-T distortion axis, g_x is along the Ag-Br axis.

Table IV: Magnetic Resonance Parameters For Intrinsic Centers In Silver Halides (Cont.)

Species	System	Parameters	Method	Ref.
Nearly free electrons				
	$Br^-/AgCl$	$g_{iso} = 1.8775$	ESR	94
	$Pb^{2+}/AgCl$	$g_{iso} = 1.882$	ESR	94
	AgCl	$g_{iso} = 1.881$	ODMR	41
	AgCl	$g_{iso} = 1.88$	ESR(2K)	45
	AgCl	$g_{iso} = 1.9 \pm .2$	magneto-absorption	95
	AgCl	$g_{iso} = 1.87 \pm .05$	magneto-absorption	96
	$AgCl_{1-x}Br_x$	$g_{iso} = (1.49 - 1.88)x + 1.88$	ODMR	63
	$Pb^{2+}/AgBr$	$g_{iso} = 1.491$	ESR	45
	AgBr	$g_{iso} = 1.49_3$	ODMR	56
	$I^-/AgBr$	$g_{iso} = 1.46$	ODMR	61
Nearly free holes				
	AgBr	$g_{iso} = 2.08$	ODMR	56
	AgBr	$g_{\parallel} = 2.61$ $g_{\perp} = 0$	Raman	17
	AgBr	$g_{\parallel} = 2.5 \pm .3$	magneto-absorption	95
	AgBr	$g_{\parallel} = 0.98 \pm .3$	magneto-absorption	96
Self-trapped holes				
$(AgCl_6)^{4-}$ $\lvert x^2 - y^2 \rangle$	$AgCl_{1-x}Br$ x=0-0.001	$g_{\parallel} = 2.146$, $g_{\perp} = 2.037$ A = 28G B= 4G $A'_{\parallel}(Cl) = 26G$	ESR	48
$(AgCl_5Br)^{4-}$ $\lvert x^2 - y^2 \rangle$	x=.001-.05	$g_x = 2.024$, $g_y = 2.051$ $g_z = 2.133$ A = 25G B = 5G $A'_x(Cl) = 21G$, $A'_x(Br) = 146G$	ESR	49

Table IV: Magnetic Resonance Parameters For Intrinsic Centers In Silver Halides (Cont.)

Species	System	Parameters	Method	Ref.
$(AgCl_4Br_2)^{4-}$	x=.02-.05	$g_{\parallel} = 2.003$, $g_{\perp} = 2.114$	ESR	48
$\|3z^2 - r^2\rangle$		$A = 26G$ $B = -6G$		
		$A'_{\parallel}(Br) = 124G$		
$(AgCl_4Br_2)^{4-}$	x=.02-.05	$g_{\parallel} = 2.112$, $g_{\perp} = 2.004$	ESR	50
$\|x^2 - y^2\rangle$		$A = 23G$ $B = 6G$		
		$A'_{x,y}(Cl) = 20G$, $A'_{x,y}(Br) = 142G$		
$(AgCl_2Br_4)^{4-}$	x=.05-.15	$g_{\parallel} = 2.108$, $g_{\perp} = 2.044$	ESR	50
$\|x^2 - y^2\rangle$		$A = 23G$ $B = 6G$		
		$A'_{\parallel}(Br) = 123G$		
$(AgBr_6)^{4-}$	x=.15-.53	$g_{\parallel} = 2.078$, $g_{\perp} = 2.065$	ESR	50
$\|x^2 - y^2\rangle$		$A'_{\parallel}(Br) = 108G$		

Silver centers (latent image)	System g_{iso}	Parameters ΔH(MHz)	Method	Ref.
AgBr	2.0035	62	ESR	62
Ir^{3+}/AgBr	2.0291	42	ESR	62
Pb^{2+}/AgBr	2.0291	40	ESR	62
Ir^{3+}/AgCl	2.0154	86	ESR	62
AgCl	2.0051	70	ESR	62

There are two interpretations given of the data for the $(AgCl_5Br)^{5-}$ exciton. The second interpretation by Yamaga and Hayes[42] assumes that lines C and C' in Figure 8b are part of the $(AgCl_5Br)^{5-}$ spectrum, arising from those complexes oriented with $\vec{B}_o$ along the z and y axes. This interpretation fits the previously unexplained zerofield ODMR measurements.[41] In earlier experiments, C' and C had not been observed, resulting in the first set of parameters for $(AgCl_5Br)^{5-}$ listed in Table IV.[40,41]

Although no hyperfine structure is observed for the exciton $(AgBr_6)^{5-}$, its g-values are consistent with those measured for the corresponding STH in mixed crystals,[48-53] and with eqn. 8. As x increases, the number of bromide ligands in the self-trapped exciton increases. For $0.3 \lesssim x \lesssim 0.53$, apparently all of the self-trapped excitons are of the form $(AgBr_6)^{5-}$, however, at x = 0.53 only 2.2% of the silver sites are surrounded by six bromide ligands. It is clear that the STE tunnels to these deeper traps and a tunneling length of $3.5a_o$ has been calculated from the exciton intensity ratios. a_o is the nn distance.[54]

Close to the critical concentration in mixed crystals the luminescence spectrum consists of a broad band at 4850 Å due to STE, and a broad band at 4500 Å assigned to free excitons. As the critical concentration is approached the STE band disappears, and characteristic phonon structure of the free exciton begins to appear on the side of the broad free exciton band. With further increases in x the broad band disappears.[32] It has been suggested that the broad free exciton band arises from the B-state of a AgBr cluster.[54] A Monte Carlo calculation using the calculated tunneling length of $3.5a_o$ and fitting the curve of the relative amounts of free and STE versus concentration, found that the transition from self-trapped to bound state for

a cluster $(AgBr_6)_n$ occurs at n = 2.[54]

ii) Extrinsic Excitons

The recombination efficiency of the free exciton in AgBr is not very high and even in nominally pure AgBr the emission spectrum is dominated by the decay of the iodine-bound exciton at 2.5 eV.[44] The zero phonon band of this emission is noted in Figure 3b. Multiphonon assisted transitions involving up to 10 phonons are also observed (Figure 3c). The maximum of the iodine-associated absorption is above the exciton indirect gap. This suggests that the free exciton is more stable than the unrelaxed impurity-bound exciton and, thus, that the impurity potential alone is insufficient to bind the exciton. Exciton localization at iodine is an example of impurity-assisted self-trapping.[3] The localization energy of the iodine bound exciton is 43 meV,[44] the binding energy 26 meV,[46] and the estimated radius, 26 Å[46] (Table V, Figure 9). The electron is sufficiently loosely bound to approximate a free electron and a g_e value of 1.54 has been obtained from the Zeeman splitting of the zero phonon luminescence band (Table IV).[46] No ODMR resonances associated with the iodine-bound exciton have been observed. As the iodide concentration in AgBr is increased, a luminescence at 2.4 eV appears which is assigned to bound exciton decay at iodine pairs. The pair localization energy is 100 - 150 meV.[44]

In AgCl, as the iodide concentration is increased, a broad band at 2.66 eV grows in, attributed to the decay of an iodide-bound exciton.[39] The presence of both the extrinsic and intrinsic emission bands in similar proportions differs from AgBr, where in even nominally pure samples the extrinsic luminescence dominates the emission spectrum. This can be attributed to the

FIGURE 9

Representation of Binding Energies (d_1, d_2, c_1) and localization energies ($a_1 + a_2$, $b_1 + b_2$) for excitons and shallow electron traps.

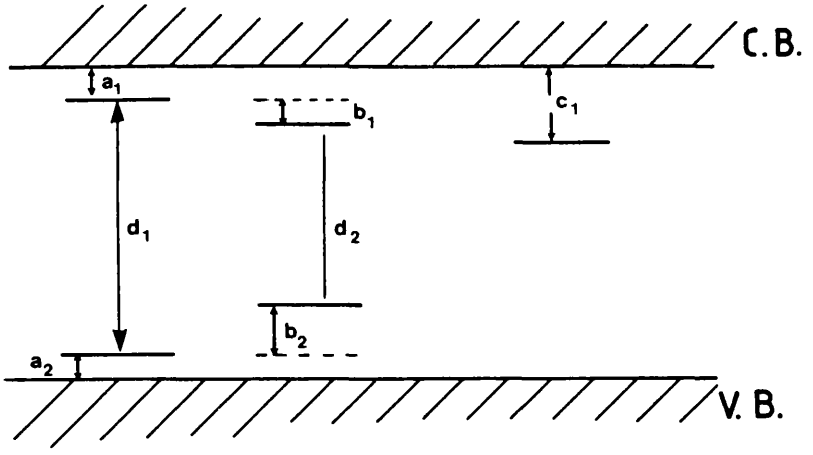

TABLE V

Binding Energies and Radii for Excitons and Localized Carriers in Silver Halides

	meV	Reference
Localization energy of I^--bound exciton-AgBr ($b_1 + b_2 \simeq b_2$)	43	44
Localization energy of I^--pair bound exciton-AgBr	100-150	44
Binding energy of I^--bound exciton-AgBr (d_2)	26	46
Binding energy of free exciton-AgBr (d_1)	20	46
Localization energy of shallow-bound extrinsic exciton-AgBr	6-7	3
Binding energy of shallow trapped e^- - AgCl	30	38
unrelaxed - AgBr	20	38
relaxed - AgBr	100-200	65
Radius of I^--bound exciton -AgBr	20 Å	47
Radius of free exciton	26 Å	47
Binding energy of e^- in shallow trap + Ag^+_i (AgBr)	300-400	65
Localization energy of hole at vacancy (AgBr)	~380	3

fact that the exciton in AgBr is free. The absorption spectrum of I^--doped AgCl can be resolved into a broad Gaussion line due to the iodine bound exciton and some fine structure on the absorption edge more characteristic of a free exciton. This is not understood and it is suggested that it might arise from free exciton decay at some other valence band edge.[39]

There are several unexplained features of the AgBr luminescence spectrum. The first of these is the "red emission", a broad band at 2.14 eV (Figure 3c).[24,31] This becomes more pronounced in alkali-doped AgBr and in samples doped with divalent cations such as Cd^{2+}. On the basis of experiments outlined below, Kanzaki has proposed that it arises from recombination of the distant electron-hole pairs, the electrons localized at interstitial silver ions and the holes at silver ion vacancies.[3] This would be consistent with the enhancement observed on addition of Cd^{2+} which would increase the silver ion vacancy concentration. The decay of this emission resolves into three components with lifetimes of 32μs, 180μs and 866μs.[55] The lifetimes of the latter two components are long enough to allow ODMR measurements. Signals from the free electrons, free holes, and electrons and holes trapped at intrinsic sites have been observed, suggesting that the red emission includes components from the radiative recombination of all of these species.[56] It has also been suggested that some of these resonances might be due to carrier recombination at small silver specks.[56]

The other puzzling feature of the AgBr luminescence spectrum are labelled EX and * in Figure 3b. The latter band is not phonon assisted and increases dramatically with the addition of alkali ions.[24] The EX transitions are phonon assisted and are associated with excitons shallowly localized

at extrinsic sites (localization energy ≈ 6 meV). These bands increase with the addition of divalent cations.[3]

1.5.4 Polarons in silver halides

The behaviour of charge carriers in the silver halides can be understood in terms of weak and intermediate polaron theory.[57,58] Measured values of microscopic mobility (from Hall mobility measurements) are given in Table VI. At room temperature, the microscopic mobility is determined by scattering from LO phonons. The mobility increases with decreasing temperature to a limiting value determined by impurity scattering and interaction with acoustic phonons.[2] The temperature dependence of the microscopic hole mobility in AgBr is much steeper than might be expected by polaron theory; however, Toyozawa and Sumi have shown that this is the result of the presence of a metastable self-trapped hole state.[59]

The electron mobility in AgBr and AgCl, and the hole mobility in AgBr, are sufficiently high to allow cyclotron resonance measurements. These measurements confirm that in AgBr, even at liquid helium temperatures, the hole is not self-trapped.[60] The cyclotron resonance lines are asymmetric, reflecting the nonparabolic nature of the polaron bands which is a result of the interaction between the carriers and LO phonons. The hole polaron band is the more nonparabolic.[60] The polaron masses and electronic band masses are given in Table VII. The cyclotron resonance lineshapes suggest that holes interact with acoustic phonons while electrons are scattered by neutral impurities.

The drift mobility of carriers, which reflects the effects of shallow traps, is very sample dependent and usually less

Table VI: Mobilities And Lifetimes For Electrons And Holes In AgBr At Room Temperature[2]

	Hall mobility (cm^2/V-sec)	Drift mobility (cm^2/V-sec)	Lifetime (μsec)
Large Crystals			
electrons	60	60	0.01-10
holes	1.7	1.1	0.01-10
Emulsion Grains			
electrons		0.2	3
holes		0.001	15

Table VII: Polarons And Band Masses In AgBr And AgCl

	Polaron mass m_p/m	Band mass m^*/m	Ref.
AgBr			
Electrons	$0.289 \pm .01$	0.2	60
Holes	$1.71 \pm .06$	1.25	60
	$0.79 \pm .01$	0.52	
AgCl			
Electrons	$0.43 \pm .02$		97

than the microscopic mobility. As seen from Table VI, in emulsion grains,** the drift mobility is $\sim 1/300$ of that in large single crystals. This is thought to be the result of the much higher interstitial silver ion concentration in small grains. If, as discussed below, the shallow traps are interstitial silver ions, then the ratio of the drift and microscopic mobilities suggests a trap depth of 0.05eV.[2] The drift mobility of holes in emulsion grains is $\sim 1/1000$ of that in single crystals. This probably reflects the greater depth of the "shallow hole traps".

Conduction electron processes in powders and emulsion grains can be conveniently monitored by microwave photoconductivity.[64] In AgBr microcrystals at room temperature, three lifetime components are detected in the decay of the microwave photoconductivity signal. The two short components are on the order of 0.1 and 10 nsec;[65] processes giving rise to these components are discussed further below. The longer component has a lifetime of $\sim$0.1 μsec which corresponds to that calculated from photoconductivity transit time and field decay measurements. These lifetimes are very dependent on sample purity and morphology, but some representative values are given in Table VI.

The g-values of free carriers are summarized in Table IV. These have been measured by magnetic-optical methods, ODMR and electron spin resonance (ESR). In general, the conduction electron is too short-lived (10 μsec) for detection by conventional ESR techniques, although a signal has been reported in

---

** A photographic emulsion consists of small crystallites, 1 micron in diameter, suspended in gelatin.

pure AgCl and AgBr at 1.5K.[45] The electron lifetime can be extended sufficiently for observation at higher temperatures by the addition of certain impurities.[94] The reasons for the lifetime extension are discussed further in Chapter 5.

The ODMR spectra of free electrons in AgBr and AgCl are shown in Figure 8. All of the ODMR resonances in these spectra, excluding those from the two self-trapped exciton species, result from electron-hole pairs with small exchange coupling. The spectra of such pairs show features characteristic of both the electron and the hole and each can be fit to the Hamiltonian:

$$\mathcal{H} = \beta \vec{B}_o \cdot g_e \cdot \vec{S} + \vec{I} \cdot \vec{\vec{A}} \cdot \vec{S} \qquad (9)$$

Free hole resonances in AgBr have not been observed by ESR. The g-values for holes, calculated from magnetoabsorption and resonance Raman scattering experiments vary widely (Table IV). The latter are perhaps more reliable since the magneto-absorption curves for indirect gap materials show only slight kinks which are difficult to fit accurately to the appropriate Hamiltonian. The calculated values of $g^h_{\parallel} = 2.61$ and $g^h_{\perp} = 0$ reflect the anisotropic hole mass.[17] The ODMR resonance assigned to free holes is isotropic with a g-value of 2.08.[56] The isotropic nature of the resonance does not rule out this assignment, (i.e. g_e for Ge is isotropic); however, there is no strong evidence for associating the resonance with a free carrier.

As described above, the STH is stable in AgCl. A small barrier to self-trapping, ~1.7 meV, has been observed.[66] The STH is only stable in pure AgCl below ~2K, but can be readily observed at higher temperatures by the addition of an electron trap, according to the mechanism:

$$h\nu \rightarrow h^+ + e^-$$

$$e^- + M^{n+} \rightarrow M^{n-1} \qquad Ag^+ + h^+ \rightarrow STH \qquad (10)$$

The hole complex is Jahn-Teller distorted with an $|x^2 - y^2\rangle$ ground state. Hyperfine couplings to silver and four chlorines are observed (Table IV).[48]

A number of interesting points have come out of the elaborate ESR studies of the STH $(AgCl_{6-x}Br_x)^{4-}$ in $AgCl_{1-i}Br_i$ (i = 0- 0.3) mixed crystals by Yamaga and coworkers.[48-53] In addition to $(AgCl_6)^{4-}$ and $(AgBr_6)^{4-}$, the following species have been identified:

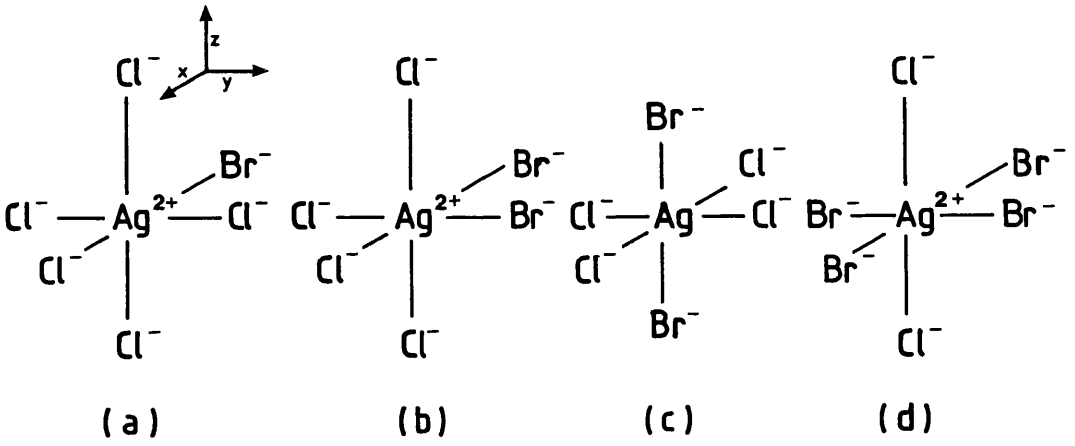

All of the STH species are Jahn-Teller distorted along the z-axis, with an $|x^2 - y^2\rangle$ ground state, except $(AgCl_4Br_2)^{4-}$ (c) which is in the $|3z^2 - r^2\rangle$ configuration. These configurations maximize the hole density on the Br^- ligands, which are less electronegative than the Cl^- ligands. Thus, for the complex $(AgCl_5Br)^{4-}$, the total spin density on the bromide ligand is 21.6% with 12.4% on each of the three in-plane Cl^- ligands. The electronegativity difference is also reflected in the

stability of the hole complexes towards thermal decay, which increases with the addition of bromide ligands. As the bromide content of the mixed crystal increases, the hole complexes become less stable as the barrier between the free and self-trapped state is lowered. This decrease in localization energy is corroborated by transient absorption measurements of the hole complexes.[3] As the temperature is raised, the hole species decays by downward hopping to more stable impurity hole traps. The decay rate is consistent with the theory of the hopping motion of small polarons assisted by LO phonons.[67] As observed for self-trapped excitons in mixed crystals, the intensity ratios of the various hole signals are consistent with a tunneling length of 2.5 lattice spacings before permanent self-trapping occurs.

1.5.5 Localized electrons and holes in silver halides

The luminescence decay of the silver halides can be resolved into a prompt and a delayed component. The prompt component is attributed to exciton decay, and the long component to the radiative recombination of distant electron-hole pairs.[3,38] No Coulomb contribution to the delayed emission is observed. Thus, the electrons are localized and the resulting site is neutral.[3] Decay kinetics suggest that an exponential distribution of trap depths exist.[2] Further evidence of the existence of shallow electron traps is seen in field decay measurements[2] and in the low microscopic mobility of the electron.

The transient IR absorption spectrum of shallow traps was first recorded by Brandt and Brown during UV irradiation. These studies were extended by Kanzaki and coworkers using the more sensitive modulation techniques of conductivity and luminescence

enhancement.[69,38,3] In these techniques, applied during UV irradiation, infrared radiation is used to depopulate the shallow electron centres to give an enhancement of the conductivity and of the luminescence intensity. At low temperatures in silver halides, the conductivity enhancement technique is sensitive to electron processes and the luminescence technique is sensitive to both electron and hole processes. The luminescence technique will tend to be sensitive to electrons localized close to trapped holes.[3]

The conductivity modulation spectrum of shallow electron traps in AgBr is shown in Figure 10a. It is the same as the transient absorption spectrum observed by Brandt and Brown and confirms that the localized carriers are electrons.[3] The decay of the localized electrons by tunneling recombination is assisted by phonons of energy ~17 meV. The luminescence modulation spectrum is slightly shifted from the conductivity spectrum because the former principally detects electrons localized in the vicinity of the bound hole. Binding energies of 30 meV in AgBr and 20 meV in AgCl are measured.[38] These energies are close to the binding energy of the free exciton and support the model of an electron in a hydrogenic orbital.

It has been proposed that the electrons are shallowly trapped at interstitial silver ions based on the fact that the absorption intensity increases with the addition of divalent anions.[70,3] An alternative proposal is that the shallow traps are charged surface kink sites.[13] In AgBr, with the addition of divalent cations, the intrinsic absorption disappears and a new absorption assigned to electrons shallowly trapped at divalent cation sites grows in (Figure 10c). The energy shifts of the new bands are proportional to the second ionization

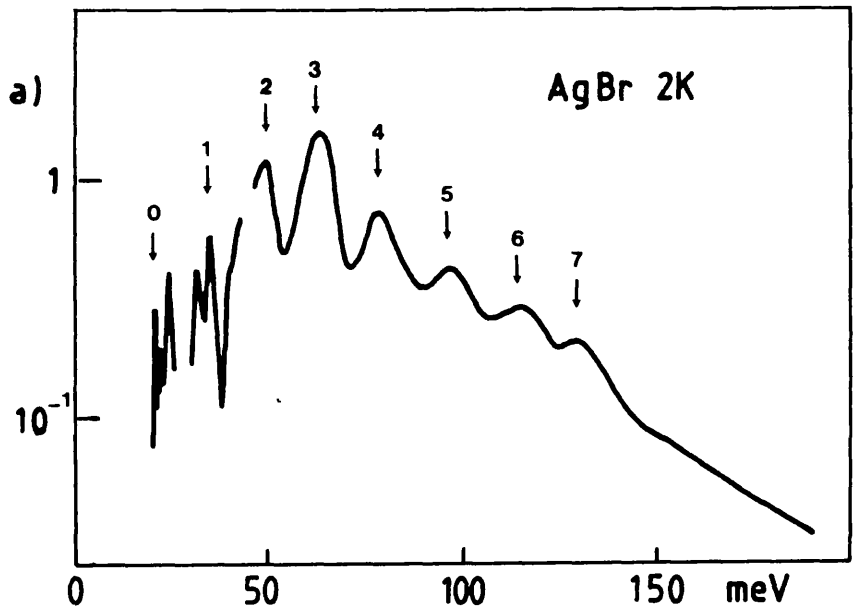

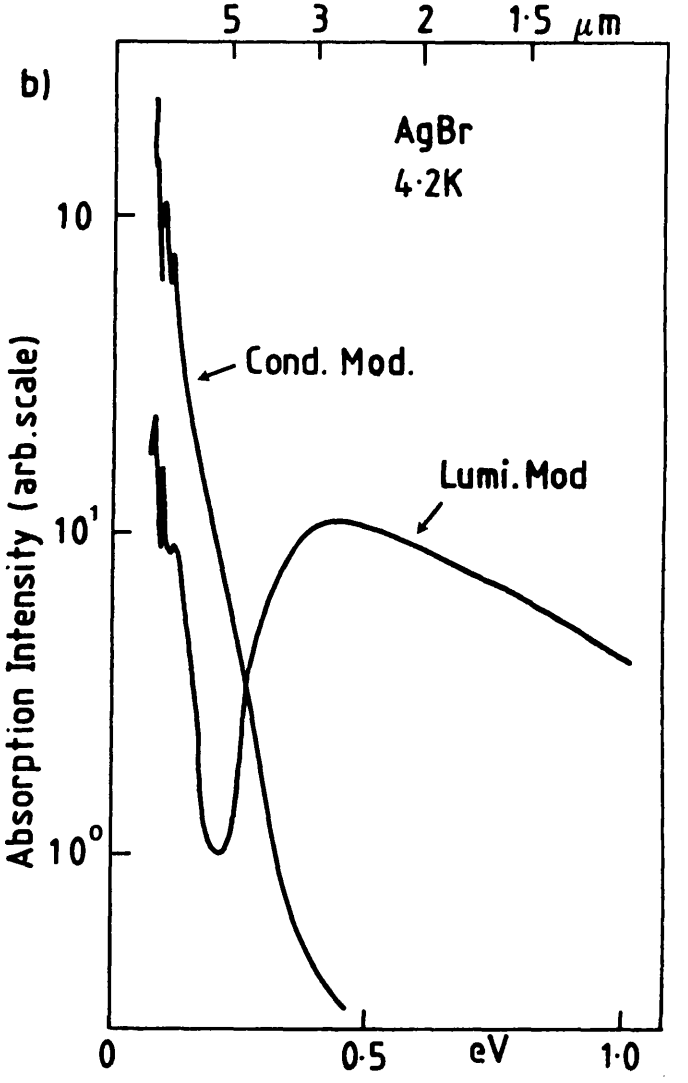

FIGURE 10

AgBr transient absorption spectra from ref. 3: a) Conductivity modulation, b) Conductivity and luminescence modulation, c) Zero phonon line shift due to additives, d) Conductivity modulation spectra at various temperatures. [Solid lines are during irradiation, dotted lines after irradiation.]

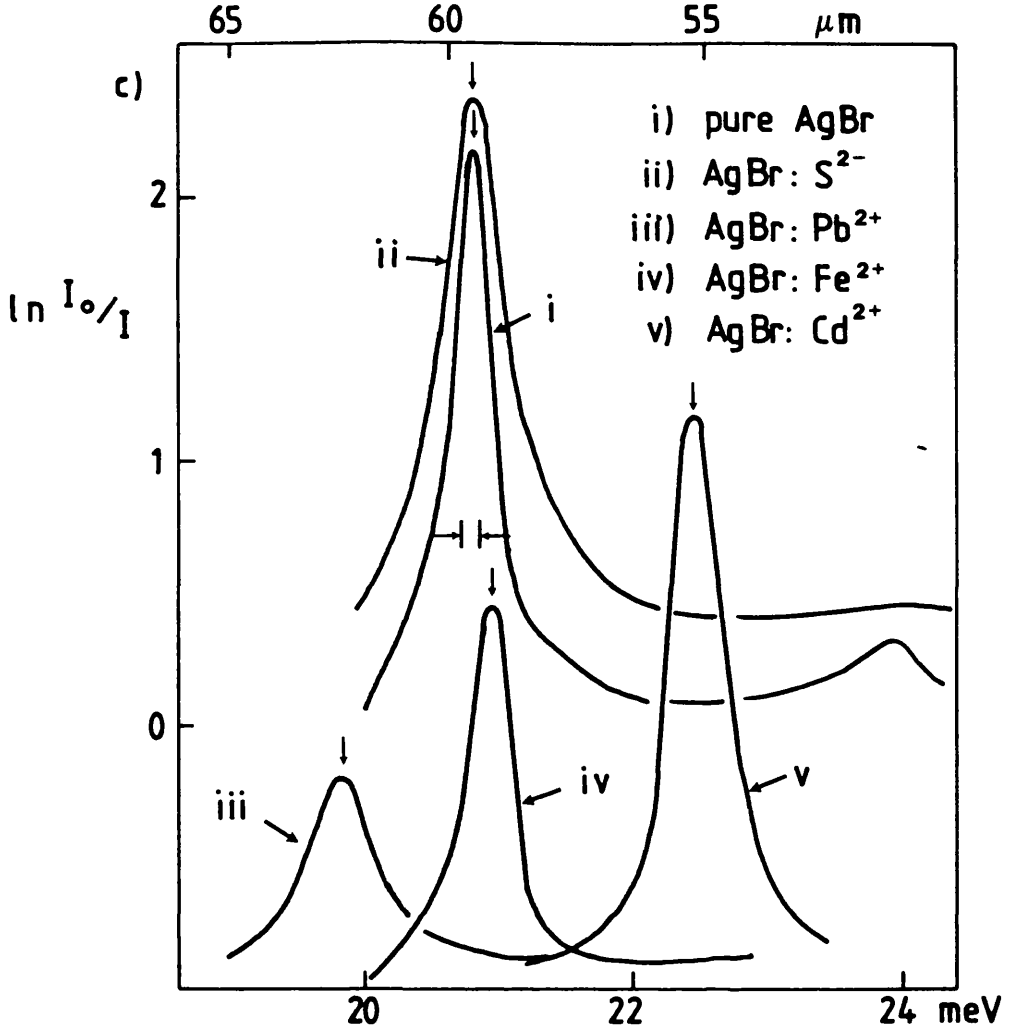
65
60
55
μm
c)
i) pure AgBr
ii) AgBr: S2-
iii) AgBr: Pb2+
iv) AgBr: Fe2+
v) AgBr: Cd2+
ln I0/I
2
1
0
ii
i
iii
iv
v
20
22
24 meV

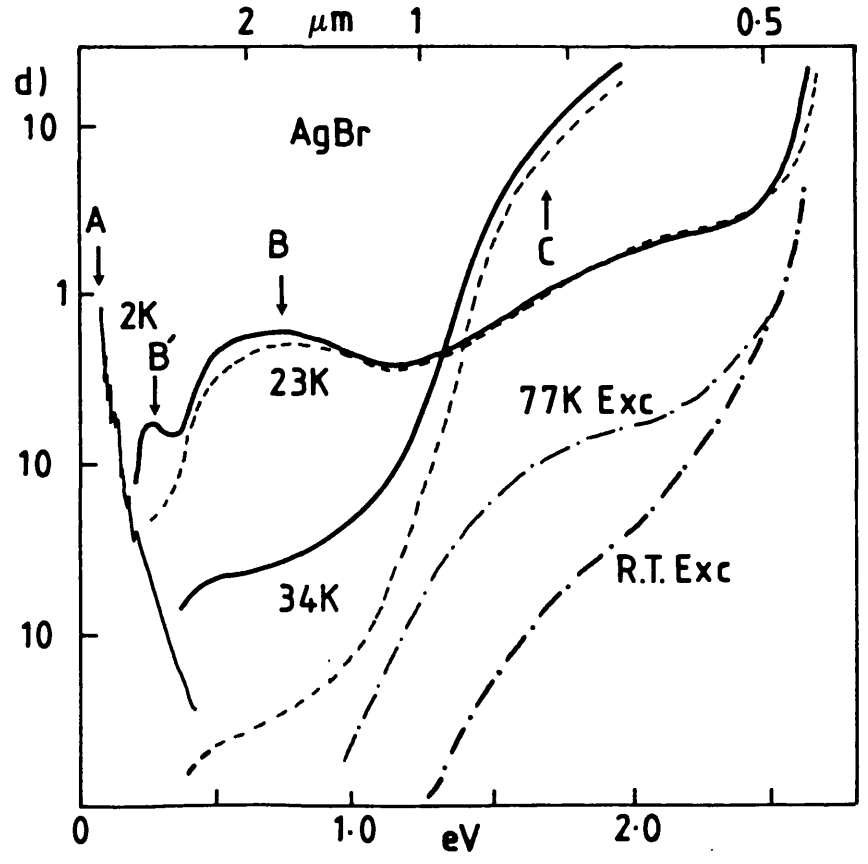
2 μm 1
0·5
d)
AgBr
10
1
10
10
A
B
C
2K
B'
23K
34K
77K Exc
R.T. Exc
0
1·0
eV
2·0

potential of the divalent cation. Similar results are observed in AgCl, but here the intrinsic sites do not disappear completely upon addition of the cations. It is suggested that this observation implies the production of Frenkel defects during UV irradiation.[3] The activation energies for the decays of these various centers are on the order of ~10meV, except for the intrinsic center in AgCl, which decays with an activation energy of~1 meV. The lifetimes of the shallow traps at 2K are of the order of 10 to 1000 sec.[70]

At higher temperatures, during and after UV excitation, conductivity modulation experiments detect several stable, higher energy bands due to deep electron traps (Figure 10d).[3] In AgBr, bands B at 0.3 eV and 0.75 eV are produced by irradiation at~20K and band C, at~1.6 eV, by irradiation above ~70K. The low energy absorption threshold of band C is consistent with that expected for the excitation of electrons from silver metal to silver halide conduction band and with the onset of red light bleaching of the latent image in photographic film.[3] Kanzaki has proposed that band B is due to the sub-latent image and C to the silver latent image.[3]

The microwave photoconductivity decay data, mentioned above of Deri, et.al.[65] supports an alternative scheme. This is that the short lifetime component is due to the decay of the shallow electron traps and the intermediate state to decay of a relaxed state of the traps where the relaxation is a thermally activated lattice distortion. It is then speculated that bands B might be due to the relaxed electron trap. The depth of the relaxed state is~100-200 MeV. The lifetime of the long decay of the microwave photoconductivity correlates well with those given in Table VI. In a wide range of samples, these lifetimes

are very close to those measured by ionic conductivity for the decay of Frenkel defects.[71] Thus, the long decay seems to be due to the neutralization of shallow electron traps by a mobile silver ion. The depth of the resulting state is 300-400 meV.[65]

The luminescence modulation transition absorption spectrum of AgBr reveals a broad band at 0.38 eV not observed by conductivity modulation (Figure 10b). As this transition energy is consistent with that of a hole in a Coulomb field, the 0.38 eV band has been assigned to a holes bound to vacancies (Table V). Thus, one of the processes contributing to the red emission in AgBr could be the radiative recombination of shallow-trapped electrons and shallow-trapped holes.[3]

The transient absorption spectrum of the STH in AgCl agrees well with the static absorption spectrum for doped AgCl, (Figure 7c).[38] A more deeply localized STH with an associated vacancy, the absorption of which increases with the addition of divalent cations, is also observed.[70] Evidence also exists for the presence of an iodine-bound hole in AgCl (Figure 7c).[3]

ODMR measurements have observed resonances in AgBr[56] and in AgCl[4] attributed to intrinsic electron and hole traps (Figures 8b and 8d). The assignments were made on the basis of doping experiments. The g-values are given in Table IV. The isotropic electron-trapped species in AgCl has also been observed by conventional ESR at 2K.[45] Three isotropic stable resonances, at 2.0036, 1.975 and 1.93 have been detected by ESR in unexposed and exposed AgCl and AgBr emulsion grains.[62] On the basis of doping and washing experiments and responses to atmospheric conditions, it has been determined that the resonances result from unidentified surface sites. No hyperfine structure was observed on any of these ODMR or ESR

resonances, which makes more definite identification difficult.

Recently, Eachus et al. have observed an ESR signal in pure and doped AgCl and AgBr emulsions which has been assigned to silver latent image centers on the basis of correlated ESR and photographic experiments.[62] The signal consists of a single isotropic line whose g-value is independent of exposure levels but depends to some extent on the matrix (Table IV). No precursor to the signal is observed. Work is in progress to relate the observed magnetic resonance parameters to particle size.

ESR spectroscopy has been very successful in deducing the electronic and defect structure as well as the photobehaviour of a large number of deep electron and hole traps associated with transition metal impurities in silver halides. Representative examples of such studies are given in references 72-73. Transition metal "dopants" are used to control the photographic properties of emulsion systems, as discussed in the next section.

1.6 THE PHOTOGRAPHIC PROCESS

A photographic emulsion consists of a suspension of silver halide microcrystals, approximately 0.2-1 micron in diameter, suspended in gelatin. The technology exists to prepare monodispersed grains with well defined crystallographic faces. Following chemical sensitization, to increase the photoefficiency of the grain, and dye sensitization, exposure to visible light produces several small silver specks per exposed grain, called the latent image. During development, the latent image catalyzes the reduction of the entire grain, resulting in an amplification factor of 10^8 - 10^9. The latent image forming mechanism is only briefly reviewed below. A

comprehensive treatment of this and all other aspects of the photographic process can be found in reference 5.

The efficiency of the silver halides as recording media depends on the quantum yield of silver. This depends in turn on the quantum efficiency of the initial photoevent, the production of conduction band electrons and valence band holes, and then on the efficiency of the silver speck formation. The initial quantum efficiency was shown to be quite high by W. Lehfeldt[74] and has been measured as 0.6 - 0.75 in AgCl single crystals.[75] Measurements on emulsions have found the overall efficiency for silver production to be close to 1. However, high exposure levels and efficient growth processes could mask inefficiencies early in the nucleation process.[76]

The practical efficiency of the photographic process also depends on the "concentration effect", that is, the formation of only one or two latent image centers per grain, and on the size of the developable latent image. In addition, the latent image must be induced to form on the grain surface where it is most accessible to developers. The latent image forms preferentially at internal sites in grains with internal disorder. In perfect grains, the latent image tends to form at the surface and this tendency is encouraged by "chemical sensitization."[5]

It is usually assumed that the latent image is composed of a range of particle sizes. The minimum size that will catalyze development (without high "fog" levels, resulting from unexposed grains) has been estimated at 3 - 5 silver atoms, assuming no preexisting silver centers are present. This is based on a large body of photographic evidence.[76] There is also considerable photographic evidence that a stable but undevelopable sublatent image occurs, that is, that the

latent image formation process consists of a nucleation and a growth stage.[78] Based on the comparison of theoretical and experimental low intensity reciprocity failure curves,** it is estimated that the sublatent image contains two silver atoms. Measurements and calculations of the minimum developable size of bare nuclei are consistent with these size estimates.[79,80] Hamilton and Logel found that four silver atoms or two gold atoms on an inert substrate were just developable.[79]

The involvement of both electrons and interstitial silver ions in the latent image forming process was shown by a series of experiments in which pulsed electric fields and light flashes were applied to emulsions in varying sequences and time separations. The crystallites were then developed only partially and the distribution of latent image centers examined.[81,82,83] Such experiments also showed that light-formed silver particles in silver halides act as electron traps.[81]

The most widely accepted theory of latent image formation is based on a theory proposed by Gurney and Mott.[84] In this scheme, the photoelectron is trapped at a shallow electron trap which then traps an interstitial silver ion to form a silver atom. Following these initial trapping events, the latent image is formed by a series of alternating electronic and ionic steps involving the capture of an electron or an interstitial silver ion, until a silver speck is produced of

---

** High and low reciprocity failure refers to the fall-off in developed silver density observed at high and low intensity exposures.

a size that is both stable and developable.

The nature of the primary shallow electron trap is unknown, and the assumptions one makes about its nature affect the details of the subsequent latent image forming mechanism. For instance, the assumption of the Gurney-Mott mechanism leads to the sequence of events shown in Figure 11a. If the initial electron trap has a Coulombic charge of +1 relative to the lattice, then after trapping an electron it is neutral, and in subsequent trapping events the charge alternates between neutral and +1.

Mitchell[85] has proposed that the primary electron trap is associated with an interstitial silver ion, so that the initial step forms a silver atom which then attracts an interstitial silver ion (Figure 11b). Thus, the site charge alternates between a negative and a positive charge in subsequent steps.

Hamilton[76] suggested that the initial trapping event occurs at a physical defect site, such as a silver ion surface kink or jog in an edge dislocation, which has a Coulombic charge of $^{+e}/_{2}$ relative to the lattice. The charge on the site would then alternate between $^{+e}/_{2}$ and $^{-e}/_{2}$ as shown in Figure 11c.

Molecular orbital calculations for a model of 12 AgBr units and a silver aggregate forming at the surface suggests that the favoured trapping site will be a defect with positive charge, that even-sized silver atoms do not trap electrons, and that latent image stability increases with size.[86] An alternative growth mechanism based on these points was proposed (Figure 11d).

A number of other latent image forming mechanisms,

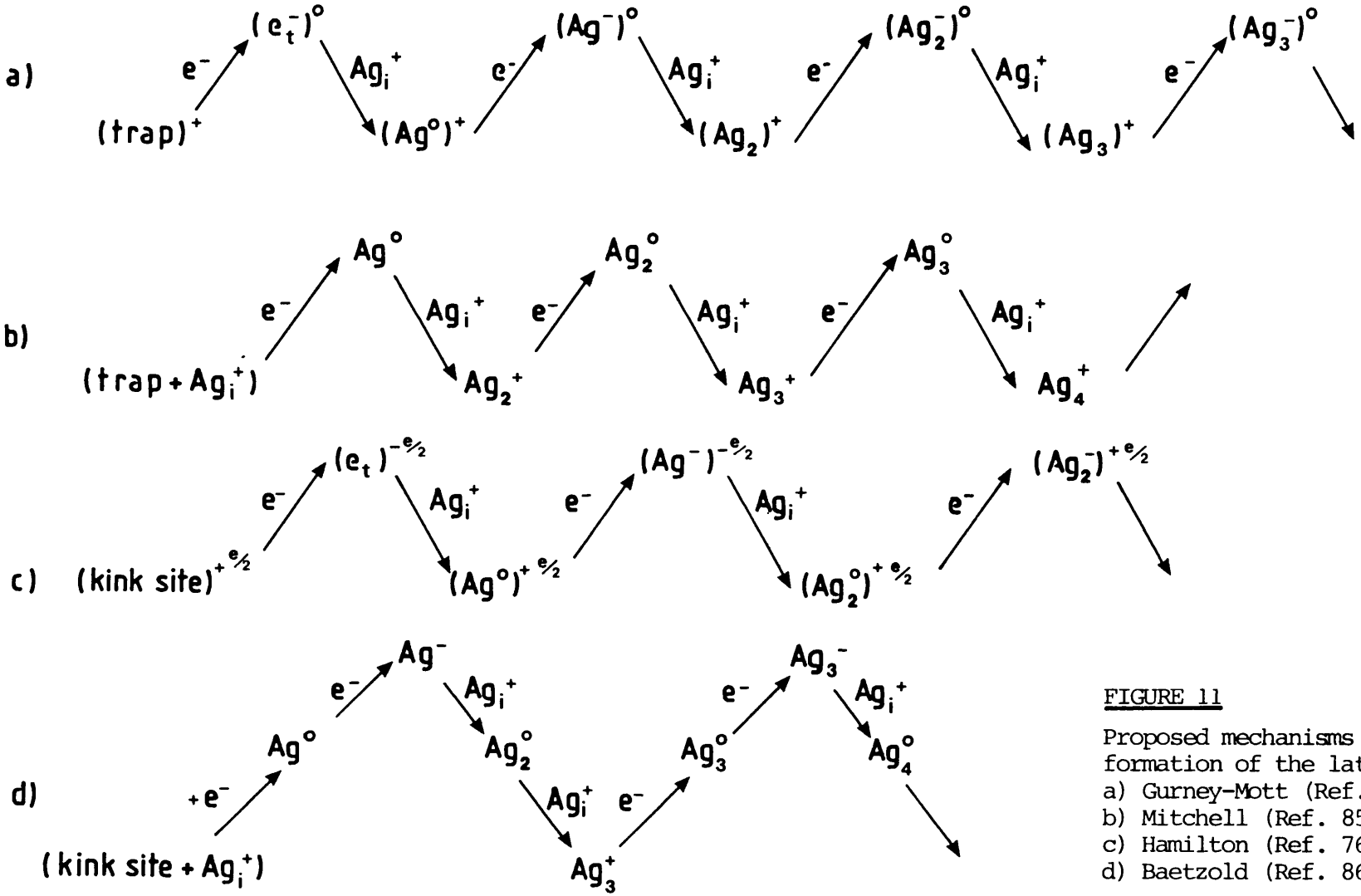

FIGURE 11

Proposed mechanisms for the formation of the latent image:
a) Gurney-Mott (Ref. 84);
b) Mitchell (Ref. 85);
c) Hamilton (Ref. 76);
d) Baetzold (Ref. 86).

differing more radically from those described above have been proposed.

Malinowski[87] suggests that the initial formation of silver atoms occurs via the Gurney-Mott mechanism but that aggregation occurs by diffusion of silver atoms. He points out that evidence suggesting that silver atoms are unstable can be explained if the silver atoms are mobile, and that the experiments supporting the electron trapping behaviour of small silver particles can equally well support electron trapping at structural defects resulting from the presence of the silver particles.

Matajec and Moisar[88] propose that during long exposures the latent image forms via the stepwise mechanism described above, but that during short flash exposures, a high concentration of electrons are produced, causing a "supersaturation" of electrons and the spontaneous separation of a silver phase.

Galashin[89] and Chibsov[90] carry this approach further. They suggest that chemical sensitization of an emulsion produces a supersaturated solution of silver centers in the silver halide grain. On exposure the photoelectrons raise the Fermi level and lower the barrier for the formation of a silver phase. It is suggested that the sublatent image contains approximately 22 atoms, and the latent image 68-680 atoms depending on exposure level.

For a critical analysis of these various mechanisms, see reference 76.

Figure 12 represents the initial events in the latent image forming mechanism in a way that emphasizes possible loss processes.[76] Direct recombination of photocarriers is forbidden, but can occur between localized and free carriers. Some of the efficiency of the latent image forming process can

FIGURE 12

Schematic representation of the initial events in the formation of the latent image (reference 76).

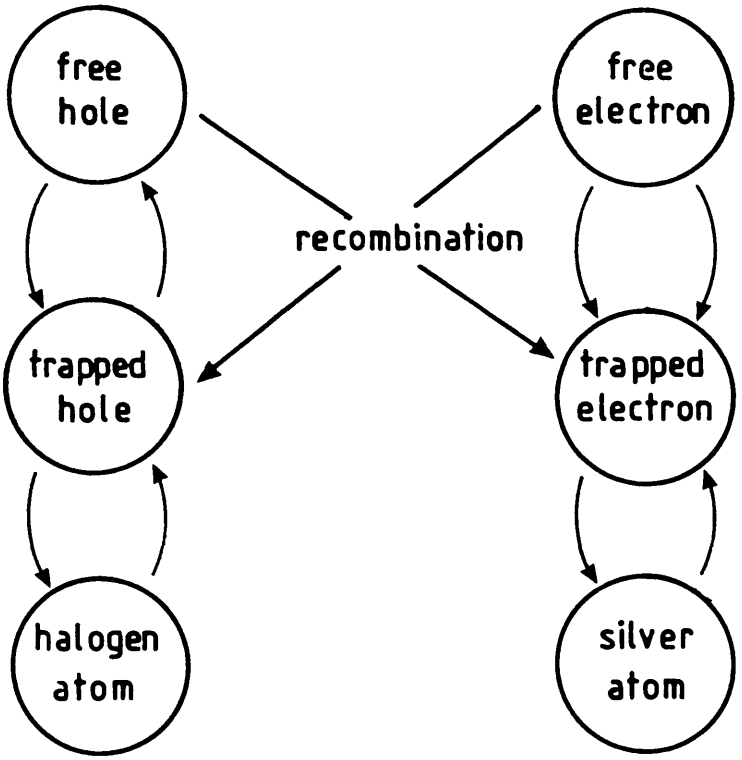

be attributed to the carrier separation that results from the negative surface charge and the resulting space charge layer. Other loss processes include thermal regression of the pre-latent image clusters and hole attack on the latent image. The high efficiency of the silver halides indicates that a parallel mechanism for hole removal exists. One proposal is that the hole is localized at a silver ion vacancy forming a neutral species which diffuses to the surface.[91] The desorption of halogen molecules from the surface of silver halides during exposure has been detected.[92] The diffusion time is consistent with the diffusion of a neutral species. Hole removal can also occur as a result of deep trapping by extrinsic impurities.[93] It is clear from Figure 12 that the photographic properties of an emulsion can be controlled by doping with transition metal impurities.

1.7 SUMMARY

In conclusion, the highest quantum efficiency of the photographic process in the silver halides can be attributed to the following unique combination of solid state properties:

1. An indirect bandgap which results in a long absorption tail into the near uv and a low probability of carrier recombination.
2. A high efficiency for the decay of excitons into free carriers at room temperature.
3. Intrinsic shallow electron and hole traps which localize carriers and contribute to low recombination inefficiencies.
4. A negative surface charge and resulting space charge also contribute to carrier separation.
5. Large differences in electron and hole masses and mobilities.

6. A Frenkel defect structure with low defect formation energy and high defect mobility.

REFERENCES

1. J.C. Phillips, Physics Today 23, 23 (1970).

2. F.C. Brown in Treatise on Solid State Chemistry, Vol.4, Reactivity of Solids, ed. N.B. Hannay (Plenum Press, New York, 1976).

3. H. Kanzaki, Phot. Sci. and Eng. 24, 219 (1980).

4. R.B. Wilsey, Phil. Mag. 42, 262 (1921); ibid. 46, 487 (1923).

5. J. Pouradier, R. Pailliotet and C.R. Berry in The Theory of the Photographic Process, 4th ed., ed. T.H. James (Macmillan, New York, 1977) p 2.

6. L. Pauling, The Nature of the Chemical Bond, 3rd ed. (Cornell Univ. Press, Ithaca, New York, 1960) p 514.

7. H. Chateau, M.C. Moncet and J. Pouradier in Wissenschaftliche Photographie, eds. W. Eichler, H. Frieser and O. Helwich. (Verlag Dr., Darmstedt, 1958) p 16.

8. B.E. Bayer and J.F. Hamilton, J. Opt. Soc. Am. 55, 439 (1965); ibid. 55, 528 (1965).

9. K. Fischer, H. Bilz, R. Haberkorn and W. Weber, phys. stat. sol. (b) 54, 285 (1972).

10. P.R. Vijayaraghavan, R.M. Nicklow, H.G. Smith and M.K. Wilkinson, Phys. Rev. B 1, 4819 (1970).

11. Y. Fujii, S. Hoshino, S. Sakuragi, H. Kanzaki, J.W. Lynch and G. Shirane, Phys. Rev. B 15, 358 (1977).

12. F. Bassani, R.S. Knox and W.B. Fowler, Phys. Rev. 137, A1217 (1965).

13. F. Seitz, Rev. Mod. Phys. 23, 328 (1951).

14. P.M. Scop, Phys. Rev. 139, A934 (1965).

15. W.B. Fowler, phys. stat. sol. (b) 52, 591 (1972).

16. R.S. Bauer and W.E. Spicer, Phys. Rev. B 14, 4539 (1976).

17. H. Stolz, W. Wassmuth, W. Von der Osten and Ch. Uihlein, J. Phys. C: Sol. St. Phys. 16, 955 (1983).

18. H.H. Tippins and F.C. Brown, Bull Am. Phys. Soc. II 7, 221 (1963).

19. R.S. Knox and K.J. Teegarden in Physics of Color Centers, ed. W.B. Fowler (Academic Press, New York, 1968) p 25.

20. F.C. Brown, T. Masumi and H.H. Tippins, J. Phys. Chem. Solids 22, 101 (1961).

21. G. Ascarelli, Phys. Rev. 179, 797 (1969).

22. G. Ascarelli and J.E. Baxter, Sol. St. Comm. 10, 315 (1972).

23. B.L. Joesten and F.C. Brown, Phys. Rev. 148, 919 (1966).

24. H. Kanzaki and S. Sakuragi, J. Phys. Soc. Jpn. 29, 936 (1970).

25. Y. Onodera and Y. Toyozawa, J. Phys. Soc. Jpn. 22, 833 (1967).

26. N.J. Carrera and F.C. Brown, Phys. Rev. B 4, 3651 (1971).

27. J.J. White, J. Opt. Soc. Am. 62, 212 (1972); J.J. White and S.W. Straley, J. Opt. Soc. Am. 58, 759 (1968).

28. F. Urbach, Phys. Rev. 92, 1324 (1953).

29. F. Moser and F. Urbach, Phys. Rev. 102, 1519 (1956).

30. K. Cho and Y. Toyozawa, J. Phys. Soc. Jpn. 30, 1555 (1971); H. Sumi and Y. Toyozawa, J. Phys. Soc. Jpn. 31, 342 (1971).

31. H. Kanzaki and S. Sakuragi, J. Phys. Soc. 29, 924 (1970).

32. H. Kanzaki, S. Sakuragi and S. Sakamoto, Sol. St. Comm. 9, 999 (1971).

33. R.S. Knox in Solid State Physics, Supp. 5, eds. F. Seitz D. Turnbull (Academic Press, New York, 1963) p 155.

34. Polarons and Excitons, eds. C.G. Kaper and G.D. Whitfield (Oliver-Boyd, Edinburgh, 1963).

35. Y. Toyozawa, in reference 34, p 211.

36. Y. Shinozuka and Y. Toyozawa, J. Phys. Soc. Jpn. 46, 505 (1979).

37. C. Kittel, Introduction to Solid State Physics, 5th ed. (John Wiley and Sons, New York, 1976).

38. H. Kanzaki and S. Sakuragi, Phot. Sci. and Eng. 17, 69 (1973).

39. H. Kanzaki, T. Hattori and S. Sakuragi, Proc. 3rd Int. Conf. on Photoconductivity 1969 (J. Phys. Chem. Sol., Suppl. 1972) p 165.

40. W. Hayes, I.B. Owen and P.S. Walker, J. Phys. C: Sol. St. Phys. 10, 1751 (1977).

41. A.P. Marchetti and D.S. Tinti, Phys. Rev. B 24, 7361 (1981).

42. M. Yamaga and W. Hayes, J. Phys. C: Sol. St. Phys. 15, L1215 (1982).

43. C.L. Marquardt, R.T. Williams and M.N. Kabler, Solid St. Comm. 9, 2285 (1971).

44. H. Kanzaki and S. Sakuragi, J. Phys. Soc. Jpn. 27, 109 (1969).

45. R.S. Eachus, unpublished results.

46. W. Czaja and A. Baldereschi, J. Phys. C: Solid St. Phys. 12, 405 (1979).

47. A.P. Marchetti and D.S.Tinti, Phys. Lett. 69A, 353 (1979).

48. M. Yamaga, M. Fukui, Y. Hayashi, H. Yoshioka, J. Phys. Soc. Jpn. 42, 1067 (1977).

49. M. Yamaga, Y. Hayashi and H. Yoshioka, J. Phys. Soc. Jpn. 44, 154 (1978).

50. M. Yamaga and H. Yoshioka, J. Phys. Soc. Jpn. 46, 1538 (1979).

51. M. Yamaga, Y. Hayashi and H. Yoshioka, J. Phys. Soc. Jpn. 47, 677 (1979).

52. M. Yamaga and H. Yoshioka, J. Phys. Soc. Jpn. 44, 1901 (1978).

53. M. Yamaga, Y. Hayashi, M. Fukui, and H. Yoshioka, J. Phys. Soc. Jpn. 44, 471 (1978).

54. M. Yamaga, N. Sugimoto and H. Yoshioka, J. Phys. Soc. Jpn. 52, 3637 (1983).

55. M. Scozzafava, M.E. Long and A.P. Marchetti, unpublished results (1979).

56. A.P. Marchetti, J. Phys. C: Solid St. Phys. 14, 961 (1981).

57. F.C. Brown in Point Defects in Solids eds. J.H. Crawford and L.M. Slifkin (Plenum Press, New York, 1972) p 491.

58. P.G. Harper, J.W. Hodby and R.F. Stradling, Rep. Progr. Phys. 36, 1 (1973).

59. Y. Toyozawa and A. Sumi, Proc. 12th Inter. Conf. on Physics in Semiconductors, ed. B.G. Teubner, (Stuttgart 1974) p 179.

60. H. Tamura and T. Masumi, Solid St. Comm. 12, 1183 (1973).

61. A.P. Marchetti and M.S. Burberry, Phys. Rev. B 28, 2130 (1983).

62. R.S. Eachus in The Physics of Latent Image Formation in Silver Halides ed. W. Czaja (World Scientific Pub. Co., Singapore, 1984).

63. W. Hayes, Semicond. and Insul. 5, 533 (1983).

64. R.J. Deri and J.P. Spoonhower, Phys. Rev. B 25, 2821 (1982).

65. R.J. Deri, J.P. Spoonhower and J.F. Hamilton, Conf. on Defects in Insulating Crystals, Salt Lake City, August, 1984.

66. E. Laredo, L.G. Rowan and L. Slifkin, Phys. Rev. Lett. 47, 384 (1981).

67. D. Emin, Adv. Phys. 24, 305 (1975); Phys. Rev. B 4, 3639 (1971).

68. R.C. Brandt and F.C. Brown, Phys. Rev. 181, 1241 (1969).

69. H. Kanzaki and S. Sakuragi, Solid St. Comm. 9, 1667 (1971).

70. H. Kanzaki, Semicond. Insulators 3, 285 (1978).

71. Reference 5, p 118

72. D.A. Corrigan, R.S Eachus and M.T. Olm, J. Chem. Phys. 70, 5676 (1979).

73. R.S. Eachus, R.E. Graves and M.T. Olm, phys. stat. sol. (a), 57, 429 (1980).

74. W. Lehfeldt in Electronic Processes in Ionic Crystals, N.F. Mott and R.W. Gurney (Clarendon Press, Oxford, 1960).

75. R.S. Van Heyningen and F.C. Brown, Phys. Rev. 111, 462 (1958).

76. J.F. Hamilton in reference 5, p 111.

77. P.C. Burton and W.F. Berg, Photogr. J. 86B, 2 (1946). P.C. Burton, Photogr. J., 8613, 62 (1946). W.F. Berg and P.C. Burton, Photogr. J., 88B, 84 (1948). P.C. Burton, Photogr. J., 88B 13, 123 (1948).

78. L. Silberstein, J. Opt. Soc. Am. 29, 432 (1939). E. Katz, J. Chem. Phys. 17, 1132 (1949). J.H. Webb, J. Opt. Soc. Am. 40, 3, 197 (1950).

79. J.F. Hamilton and P.C. Logel, Photogr. Sci. Eng. 18, 507 (1974).

80. I. Konstantinov and J. Malinowski, J. Photogr. Sci. 23, 1 (1975).

81. J.R. Haynes and W. Shockley, Phys. Rev. 82, 935 (1951).

82. J.F. Hamilton and L.E. Brady, J. Appl. Phys. 30, 1893, 1902 (1959).

83. E. Klein and R. Matajec, Z. Elecktrochem. 63, 883 (1959).

84. R.W. Gurney and N.F. Mott, Proc. R. Soc. (London) A164, 151 (1938).

85. J.W. Mitchell, J. Photog. Sci. 5, 49 (1957).

86. R.C. Baetzold, J. Solid St. Chem. 6, 352 (1973); Photog. Sci. Eng. 17, 78 (1973).

87. J. Malinowski, Photogr. Sci. Eng. 18, 363 (1974).

88. R. Matajec and E. Mosiar, Photogr. Sci. Eng. 2, 133 (1968); E. Mosiar, J. Photog. Sci. 13, 46 (1965).

89. References 232-236 in reference 76.

90. References 41, 42, 237, 238, 240 in reference 76.

91. J. Malinowski, Photog. Sci. Eng. 18, 363 (1974).

92. H. Kanzaki and T. Mori, Phys. Rev. B 29, 3573 (1984).

93. A. Buroff and J. Malinowski, phys. stat. sol. 26, 267 (1968).

94. R.S. Eachus, R.E. Graves and M.T. Olm, phys. stat. sol. b 88, 705 (1978).

95. M. Matsushita, J. Phys. Soc. Jpn. 35, 1688 (1973).

96. S. Kurita and K. Kobayashi, J. Phys. Soc. Jpn. 44, 1583 (1978).

97. H. Tamura and T. Masumi, J. Phys. Soc. Jpn. 30, 897 (1971).

98. N.W. Ashcroft and N.D. Mermin, Solid State Physics (Saunders College, Philadelphia, 1981).

C H A P T E R T W O

THE THEORY OF THE

CONDUCTION ELECTRON SPIN RESONANCE SIGNAL

IN SEMICONDUCTORS

CHAPTER 2

The Theory Of The Conduction Electron Spin Resonance Signal In Semiconductors

The characteristics of the conduction electron spin resonance (CESR) signal are quite different from those of localized electrons. There are also differences between CESR in metals and in semiconductors, arising principally from the lower free electron concentration in the latter. In this chapter those properties which are relevant to conduction processes in the silver halides are discussed. Some of these properties are elucidated by a brief discussion of CESR in the well-studied system, phosphorous-doped silicon.

2.1 The g-value

For a free electron, the g-value, the ratio of the spin magnetic moment to the spin angular momentum, has a value of $g_e = 2.00232$. If the electron is placed in an isolated atom, the departure of g from the free spin value is a result of the spin-orbit interaction, that is, the interaction of the electron spin with the magnetic field induced by the motion of other electrons. For an electron in a solid, the spin-orbit interaction is not much altered from the free atom since it occurs deep in the ion core. Thus, the g-shift (from g_e) of a conduction electron in a solid is expected to be of the same order of magnitude as in the free atom. A slightly larger g-shift is expected because the electron wavefunction is normalized to the unit cell, rather than over all space. This effectively increases the electron density at the ion cores.[1]

In a solid, however, an additional contribution to the g-shift can result from the extended orbital motion of the electron throughout the lattice. The electron moves in a Bloch wavefunction which is spread over many unit cells. Thus, the spin angular momentum has an additional component arising from the orbital motion of the electron as it diffuses through the lattice. Both the spin-orbit interaction and the "diffusive" orbital momentum are reflected in the g-shift of the conduction electron, and the latter accounts for the huge g-shifts of 50 - 200 observed in InSb[2] and Bi.[3]

The calculations of g-values for conduction electrons are complicated by two factors. First, because the wavefunctions of the electrons extend throughout the lattice, they are greatly affected by the magnetic field and perturbation methods cannot be used to calculate energy levels and ultimately the g-value. Second, the conduction electrons occupy a quasicontinuous band of states, where each state has a unique energy characterized by its k-vector. Each of these levels is split into a Kramers doublet by the magnetic field. The splitting is related to g, as for a paramagnetic atom, by

$$h\nu = g\mu_B H \qquad (1)$$

where μ_B is the Bohr magneton. However, the splitting is not necessarily the same for each doublet and a range of g-values may be obtained. These must be calculated and averaged to give the g-value that would be observed under the conditions of motional narrowing.

The expression for the g-shift of a conduction electron is often of the form:

$$\Delta g \propto \left(\frac{\lambda}{E_k - E_{k'}}\right) \cdot \left(\frac{m_e}{m^*}\right) \cdot g_e \qquad (2)$$

The first term in brackets also appears in the expression of the g-shift of an electron localized in an atom. It is a measure of how effectively the spin-orbit interaction, represented by λ, the spin-orbit coupling constant, mixes the groundstate of the electron, k, with the state at energy $E_{k'}$. The effective mass of the conduction electron, m^*, is included in eqn 2 because it is related to the "diffusive" orbital moment of the electron, $\mu \approx {}^{e}/_{2m^*c}$.[1] Since the effective mass is determined by the curvature of the energy band, ${}^{1}/_{m^*} = \left({}^{1}/_{\hbar^2}\right) d^2\epsilon/dk^2$, it is easy to see why Δg can be dependent on k. It is also clear that the g-shift will have a different behaviour above the Fermi, or degeneracy temperature, where the conduction electrons are nondegenerate and are described by Boltzmann statistics, than below the degeneracy temperature, where the electrons are degenerate and are described by Fermi-Dirac statistics. The degeneracy temperature is proportional to the Fermi level or to the concentration of conduction electrons. The dependence of the g-shift on the effective mass means that conduction electron spin resonance studies can be used to determine band parameters in much the same way as cyclotron resonance studies. Indeed, under certain conditions pure cyclotron resonance transitions, and mixed cyclotron-spin resonance transitions can be detected in the conduction electron spin resonance experiment.[1]

The g-shift has different characteristics depending on whether it arises from electrons in degenerate or nondegenerate energy bands. For electrons in a nondegenerate band, the

g-shift is zero if the spin-orbit interaction is negligible, as is evident from eqn 2. For electrons at a degenerate band edge, such as the valence band in silicon, a nonzero g-shift can result even when the spin-orbit interaction is "quenched", due to the diffusive orbital motion of the electron. The magnitude of such a g-shift is determined solely by the band parameters.[1,4]

Different approaches to the g-shift must also be taken according to whether the conduction electrons have kinetic energies large or small compared to the spin-orbit interaction energy. This is demonstrated in Figure 1. The g-shift is generally determined by interactions with the spin-orbit split valence band edges and the filled levels just below these bands. If an electron is in a state E_2, it will be affected by the spin-orbit interactions to a much lower degree than an electron in E_1. The condition of large kinetic energy relative to the spin-orbit interaction usually applies in metals and this case has been treated by Elliott.[5] Due to the cancellation of the effective mass from the numerator and denominator of the g-shift, a particularly simple relation for Δg holds:[1]

$$\Delta g \propto \frac{\lambda}{\Delta E} \qquad (3)$$

Thus, in general, g-shifts for conduction electrons are smaller in metals than in semiconductors. The special case of carriers in narrow band gap solids has been treated by Zawadzki.[6]

The high concentration of electrons in metals also means that a large range of g-values are obtained. Thus, the requirement of motional narrowing is more critical to the

observation of CESR in metals than in semiconductors. It has been suggested that a breakdown in motional narrowing occurs at low temperatures in aluminium and accounts for the observed linewidth.[7] This fits the experimental observation that the linewidth was independent of temperature, as might be expected when impurity scattering becomes important, but that it was also independent of sample purity.[8] The spread in g-values that can be obtained is quite large. For a conduction electron with kinetic energy large compared to the spin-orbit coupling in a nondegenerate conduction band, the maximum spread of g-values is $2\Delta g_{max}$ where Δg_{max} is the g-shift of the highest energy electrons, those at the Fermi surface.[7] A symptom of the breakdown of motional narrowing is that $T_1 \neq T_2$.

Finally, as a result of the high concentration of free electrons in metals, the degeneracy temperature is very high, and under most experimental conditions the electrons obey Fermi-Dirac statistics.

The treatment of the g-shift discussed below was developed by Luttinger and Kohn,[9] and Roth[10] for application in Si and Ge and by Cohen and Blount[3] for Bi. The general treatment has been summarized by Yafet.[1]

Although the magnetic field greatly perturbs the energy levels of the Bloch wavefunctions, they remain clustered in bands. The calculation of the energy levels and of g involves obtaining an effective Hamiltonian for which interactions between bands have been "decoupled." When only a small portion of the Brillouin zone is occupied, that is, when the number of conduction electrons is small, a perturbation calculation in powers of k can be applied. The Hamiltonian that is obtained

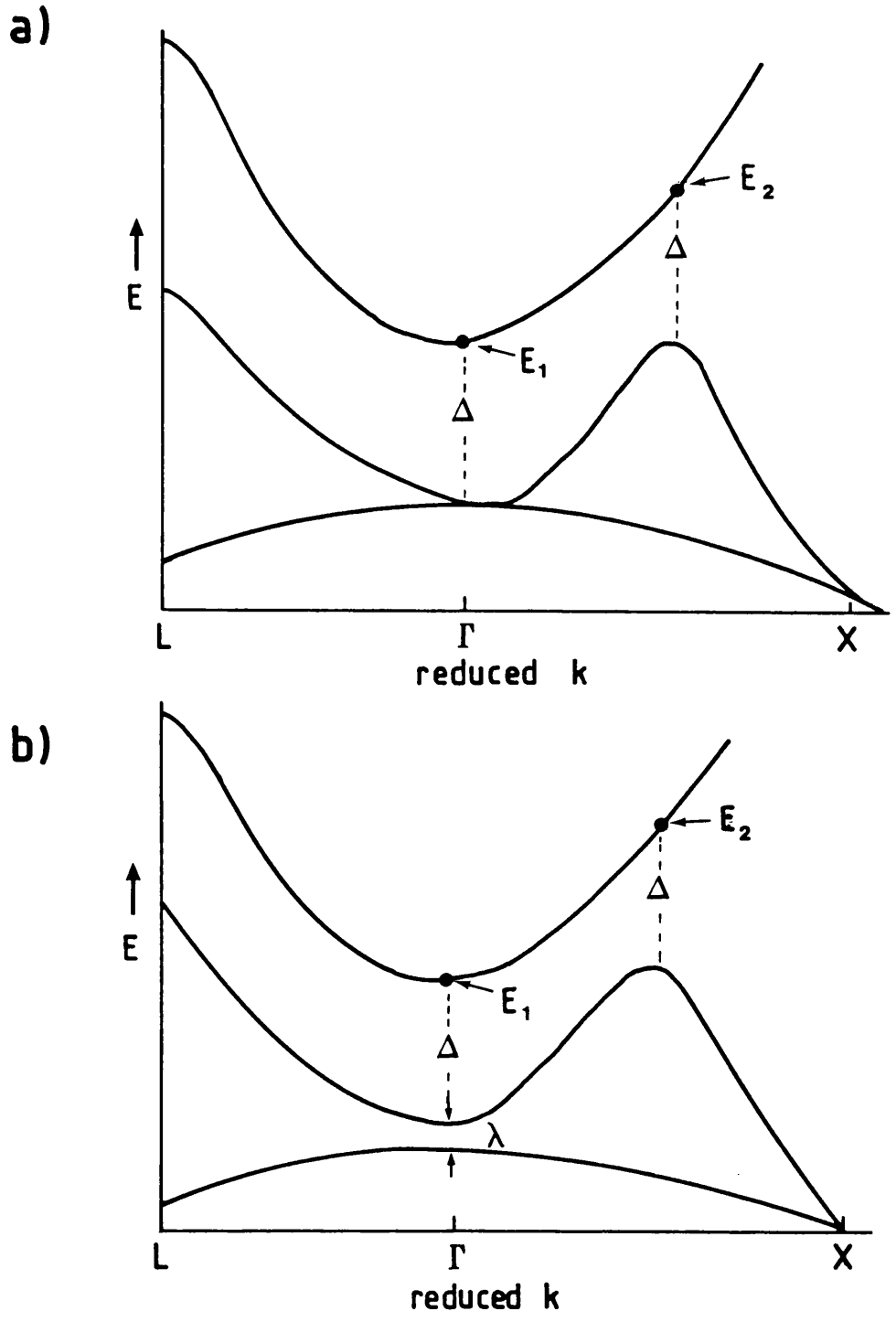

FIGURE 1

Schematic representation of a silver halide-like band structure calculated without (a) and with (b) the spin-orbit interaction. It can be seen that the spin-orbit interaction has a smaller effect on the band structure and thus on Δg for an electron at E_2 compared to an electron at E_1.

is to first order the effective mass Hamiltonian:

$$\mathcal{H}\psi = \left(\frac{\hbar^2}{2m^*}\right) \cdot \nabla^2 \psi = E\psi \qquad (4)$$

The use of an effective mass for the conduction electron takes into account the periodic potential of the lattice. For a conduction electron at the minimum of a spherical, nondegenerate conduction band edge at k = 0, as found in the silver halides, the g-value is then given by [10,11]

$$\frac{g}{g_e} - 1 = \frac{1}{im_e} \sum_{k'} \frac{\langle k_o | p_x | k' \rangle \langle k' | p_y | k_o \rangle - \langle k_o | p_y | k' \rangle \langle k' | p_x | k_o \rangle}{E_{k_o} - E_{k'}} \qquad (5)$$

E_{k_o} is the energy at the conduction band minimum. p_x and p_y are the components of the angular momentum operator coupling the edge of the conduction band with state k'. The summation is over all bands close enough and with the correct symmetry to be coupled with the conduction band minimum. In AgBr and AgCl the conduction band edge transforms as the representation Γ_1. The only nearby bands of appropriate symmetry are from the valence band at Γ which is split by the spin-orbit interaction into a fourfold degenerate Γ_8^- state and a doubly degenerate Γ_6^- state. (See Figure 1.2.) If only coupling to these states in considered, the g-shift for a conduction electron in AgCl or AgBr is given by:[11]

$$\Delta g = (g_e - g) = \frac{\lambda}{3E_G + 2\lambda} \left(\frac{m_e}{m^*} - 1\right) g_e \qquad (6)$$

E_G is the direct energy gap between the conduction band minimum

and the valence band, and λ is the spin-orbit splitting of the valence band at Γ.

The calculated and measured g-values of conduction electrons in AgBr and AgCl are listed in Table I. Experimental values for E_G in AgBr and AgCl and for λ in AgBr were taken from Chapter 1. A theoretical estimate of λ in AgCl was used.[12] The experimental polaron masses (Table VII, Chapter 1) were used for m^*. As might be expected intuitively, both the calculated and measured g-shifts for AgBr are larger than those for AgCl. The rather poor agreement between measured and calculated g-values is probably the result of ignoring spin-orbit couplings to other bands. The two band model also failed to give good values for g-shifts of conduction electrons in Si and interactions where deep lying 2p levels had to be taken into account.[13] Similarly, in the silver halides, interactions with deep level p- and d- states are probably important. The discrepancy cannot be attributed to the binding of the electrons to shallow traps.[14] As discussed below, this should result in a smaller g-shift than predicted by eqn. 6.

The spin properties of electrons bound to shallow traps in semiconductors can also be treated by the effective mass approximation. Thus, the effective mass Hamiltonian for electrons bound to donor sites is [9]

$$\mathcal{H}\phi = \left[-\frac{\hbar^2}{2m^*} \nabla^2 + U \right] \phi = E\phi \qquad (7)$$

U is the potential due to the impurity ion, screened by the lattice dielectric constant ($= e^2/\epsilon r$). The solutions are of the form

Table I: Calculated and Experimental g-values in AgCl and AgBr

	g (calculated)	g (experimental)*
AgCl	1.980	$1.8785 \pm .0003$
AgBr	1.800	$1.4870 \pm .0005$

* Chapter 4

Table II: The g-values of Donor Electrons and Conduction Electrons in Silicon*

Impurity Ion	Ionization Energy (eV)	g-value
$Sb^{121,123}$	0.043	1.99858
P^{31}	0.045	1.99850
$As^{75,76}$	0.054	1.99837
Bi^{209}	0.071	2.00025
e^-_{CB}	-	1.99875

g_{iso} (calculated) = 1.9990

* from reference 16

$$\phi = F(r)\ \psi(k_o, r) \tag{8}$$

where $\psi(k_o, r)$ is the Bloch wavefunction at k_o. For an isotropic effective mass, such as occurs at the spherical conduction band minimum in AgCl and AgBr, F(r) is just the wavefunction for the hydrogen atom, with the electron mass replaced by the effective mass, and e^2 replaced by e^2/ϵ. Thus, the lowest energy state has an orbital radius and ionization energy given by:

$$a_o = a_H \left(\frac{E_o}{(m^*/m_e)} \right) \tag{9}$$

$$E_o = \frac{(m^*/m_e)}{\epsilon^2} \times 13.5 \text{ eV}$$

a_H is the Bohr radius. Equations 7-9 can only be used if a_o is large relative to the lattice spacing. Equation 9 implies that the donor electron behaves like a Bloch electron if observed over small distances. Over larger distances, its orbit is modulated by the wavefunction F(r) (Figure 2).[9] If m^* is anisotropic, as in Si and Ge, F(r) takes on a somewhat modified form. In the case of extreme anisotropy, when $\frac{m_\parallel}{m_\perp} \approx \infty$ or 0, the wavefunction looks like a pancake, extended in the plane of smallest effective mass.

Thus, in the effective mass approximation, the properties of the donor electron are entirely dependent on the host lattice, and are only affected by the donor ion via a Coulombic interaction. The g-value of the donor electron is not affected by the spin-orbit coupling constant or the ionization energy of the impurity ion, and is the same as a "free" electron at the bottom of the conduction band.

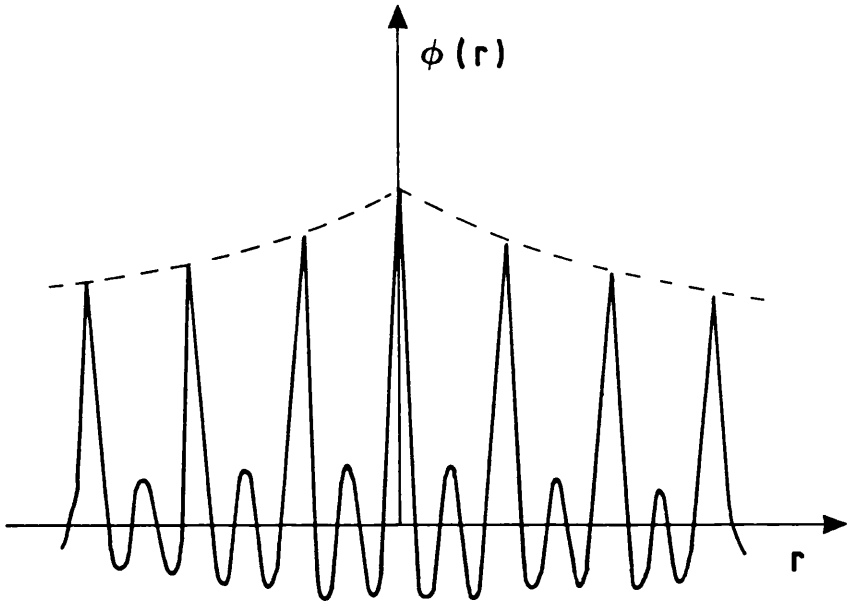

FIGURE 2

Schematic representation of the donor wavefunction in the effective mass approximation (from reference 15).

The measured ionization energies and g-values for a series of donors in silicon are listed in Table II along with those calculated from the effective mass approximation. It can be seen that, to a large extent, the approximation holds, and the ionization energies and g-shifts are fairly independent of the donor nucleus. These change by a factor of ~2 from Sb to As, while the spin-orbit coupling constant changes by a factor of more than 10. The deviations that are observed are a result of the breakdown of the wavefunction F(r) in the neighbourhood of the donor impurity. The effective mass approximation underestimates the donor electron density at the nucleus. The ionization energies calculated for the excited p states, which have a larger radius and very little density at the donor ion, are in excellent agreement with experiment.[9] It can be seen from Table II that the larger the ionization energy, the larger the deviation of the observed g-value from the calculated value. This is because the effective mass approximation is not applicable to deep traps. As the trap depth deepens, the g-shift should become closer to that observed for the free impurity atom. This appears to be the case for Bi in Si (Table II).

The temperature, microwave power and donor concentration dependences of the g-shift are relevant to the studies of doped silver halides discussed in Chapter 4. Thus, the trends observed in P/Si are presented here. The phenomena of impurity band conduction and the metallic-nonmetallic transition are discussed only simplistically. More elaborate treatments can be found in references 17 - 19.

Phosphorous-doped silicon samples can be divided into metallic and nonmetallic regimes according to the temperature dependence of the electrical resistivity.[20] In heavily doped

samples ($N_D \gtrsim 3 \times 10^{18}$ electrons cm^{-3}) the resistivity decreases with T, as phonon scattering is reduced, to a finite value at $T \approx 0$ K, determined by impurity scattering.[20] This behaviour is characteristic of a metal.[18] At lower donor concentrations the samples are nonmetallic, and the resistivity increases to an infinite value as T is lowered. In the metallic sample, donor ions are close enough for their wavefunctions to overlap and form an impurity band of states, just below the conduction band. At sufficiently high concentrations, this merges with the bottom of the conduction band. Conduction is metallic in this continuum of states. In nonmetallic samples, conduction can occur by two parallel mechanisms: thermal excitation of localized electrons above a "mobility edge" and variable-range hopping from one impurity to another. Both processes are decreased as the temperature is lowered and more carriers become localized.[19,21]

In nonmetallic samples, at donor concentrations less than $\sim 7 \times 10^{16}$ cm^{-3}, the esr spectrum at low temperature consists of a doublet centered at g = 1.98850.[22] The splitting is due to the hyperfine interaction with the P impurity. The lines are inhomogenously broadened by hyperfine interactions with Si^{29} nuclei.[23] As the donor concentration is increased, additional hyperfine lines are detected due to exchange coupling between pairs of P nuclei.[24] As the donor concentration is increased still further, the two-nuclei cluster lines broaden into a single central line. Temperature dependent lineshape studies suggest that, at its onset, the broad central line results from exchange interactions between isolated impurities and 2-nuclei clusters.[25,26] A radius of 17.2 Å for the donor electron has been calculated by fitting the lineshape to

calculated values of the exchange coupling constant.[27] On the basis of Monte Carlo cluster calculations, it appears that spin exchange begins at impurity separations 1.5 times greater than those required for metallic conduction.[28] Finally, at donor concentrations of $\sim 1 \times 10^{18}$ cm^{-3}, a motionally narrowed line, indicative of complete spin delocalization, is observed at low temperature.[29] This occurs at a lower concentration than that required for metallic conduction. The discrepancy has been attributed to the effects of electron correlation.[30] The g-value for the delocalized electrons was $1.99875 \pm .0001$;[31] in close agreement with the value of 1.9990, calculated as described above.[13] The impurity band of states merges with the bottom of the conduction band at a donor concentration of approximately 2×10^{19} electrons/cm^3.[33] There is no abrupt change in g-value at this point. Thus, as the effective mass approximation predicts, the donor impurity band is very similar to the bottom of the conduction band. However, at donor concentration greater than $\sim 2 \times 10^{19}$ cm^{-3}, the g-shift increases linearly with increasing concentration.[32] This can be understood qualitatively as resulting from the increase in energy (and k-vector) of the conduction electrons. At a donor concentration of $10^{20} cm^{-3}$, an electron at the top of the Fermi level will have an energy ~ 0.07 eV above the conduction band minimum.[32] On the basis of eqn. 2, this would result in a decreased g-shift; however, such arguments neglect the changes that result from mixing of band edges at k-values away from $k = 0$.

At donor concentrations greater than 2×10^{19} cm^{-3}, and at temperatures above the degeneracy temperature, the g-shift also increases with increasing temperature.[32] This shift can also

be attributed to an increase in energy of the conduction electrons, in this case, as a result of thermal excitation.

At donor concentrations less than 2×10^{19} cm^{-3}, the g-shift of the delocalized electrons is essentially independent of temperature and concentration.[34] At temperatures lower than ~2 K in nonmetallic samples, an apparent g-shift was observed which has been attributed to the presence of an "internal" field. This is thought to support the suggestion that at low temperatures the spins are localized, forming an amorphous antiferromagnet.[41]

Finally, it should be noted that although the effective mass and g-tensor are anisotropic in Si, under normal experimental conditions, only an isotropic conduction g-value, at $g = \frac{1}{3}(g_{\parallel} + 2 g_{\perp})$ is measured. This is a result of the high symmetry of the silicon structure. The conduction band minimum occurs away from the middle of the Brillouin zone, approximately 85% of the way to the zone boundary along (100).[16] As a result, there are six equivalent energy minima and six ellipsoidal Fermi surfaces, one along each (100) vector. Unless the crystal is uniaxially stressed,[22] the energy minima are equally populated. Thus, the difference between the transverse and longitudinal orbital motions of the electron, and its effect on the g-value averages to zero. In a crystal with lower symmetry, such as graphite, g-anisotropies are apparent in unstressed crystals.[35]

2.2 Relaxation Times

An electron spin resonance signal can be characterized by two relaxation times. T_1 is the longitudinal relaxation time and is the time in which the spin system loses $1/e$ of the

component of the magnetisation which is parallel to the magnetic field:

$$\frac{dM_z}{dt} = \frac{M_z - M_z^0}{T_1} \qquad (10)$$

The magnetic energy is lost via interactions of the spin system with the surroundings; T_1 is also called the spin-lattice relaxation time. The lattice interactions which can affect T_1 are those that produce a modulating magnetic field transverse to M_z:

$$\frac{1}{T_1} \propto (\delta H_x^2 + \delta H_y^2) \qquad (11)$$

T_1 can be measured directly by pulse methods or indirectly by a saturation method. The saturation method, which was used for the work described in Chapter 4, extracts T_1 from the microwave power dependence of the ESR signal intensity. As described by Poole,[36] T_1 can be derived most simply from the relationship:

$$T_1 \propto \frac{(4.920 \times 10^{-8})\ \Delta H_{pp}^0}{H_1^2\ g} \quad \text{(sec)} \qquad (12)$$

ΔH_{pp}^0 is the peak-to peak linewidth in gauss measured at low power. H_1^2 is the field at the sample corresponding to that microwave power where the maximum ESR signal intensity was obtained. H_1^2 is related to the microwave power by the relationship

$$P = K H_1^2 \qquad (13)$$

where K, the cavity calibration factor, is of the order of 1. K can be calculated from measurements of T_1 for a standard sample with a known relaxation time, such as DPPH. Assuming K = 1, H_1^2 in equation (12) is the microwave power in watts.

T_2 is the transverse relaxation time and characterises the return of the x and y components of the magnetisation to zero. It is a measure of the dephasing of the spin components in the plane perpindicular to M_z by fluctuations of transverse local magneic fields in that plane, as well as by fluctuations of fields parallel to M_z:

$$\frac{1}{T_2} \propto \frac{1}{2}(\delta H_x^2 + \delta H_y^2) + \delta H_z^2 \qquad (14)$$

Thus, the transverse relaxation rate is the sum of one-half the longitudinal relaxation rate and of a second component. Equation (14) can be rewritten:

$$\frac{1}{T_2} = \frac{1}{2T_1} + \frac{1}{T_2^*} \qquad (15)$$

T_2^* is the spin-spin relaxation time and is a measure of the effectiveness of spin-spin interactions in dephasing the M_x and M_y components of the magnetisation. For localised spins in most solids, $T_1 \gg T_2$, so that $1/T_2 \approx 1/T_2^*$. A homogenously broadened line usually has a Lorentzian line shape. For such a line, the transverse relaxation can be obtained directly from the linewidth measured at nonsaturating powers:[36]

$$T_2 = \frac{(1.3131 \times 10^{-7})}{g\,\Delta H_{pp}} \qquad (16)$$

A line that is inhomogenously broadened, generally has a Gaussian lineshape and the linewidth bears no relation to the

T_2 of the individual spin packets which make up the line. Inhomogenous broadening is the result of unresolved hyperfine structure, fine structure or dipolar coupling between unlike spins. However, it has been shown that in some cases T_1 and T_2 can be extracted for an inhomogenously broadened line using the saturation method applied at low powers.[36,37]

Most theoretical treatments of relaxation times of conduction electrons have been applied to T_1. However, as measurements of T_2 are more readily available, one must consider the relationship between T_1 and T_2. It has been shown that if the correlation time of the conduction electron is short compared to the Larmor precession time, the view of the lattice from the rotating frame and the laboratory frame are the same. Thus, δH_x, δH_y and δH_z are independent of the direction of M_z and for isotropic solids such as the silver halides, $T_1 = T_2$. This equality holds for conditions of motional narrowing and an isotropic lattice.[1] It is because of the rapid motion of the electron that spin-spin interactions are not important and $\delta H_z^2 = \frac{1}{2}(\delta H_x^2 + \delta H_y^2)$.[39]

The spin-lattice relaxation rate for conduction electrons is made up of several components:

$$\frac{1}{T_1} = \frac{1}{T_{phonon}} + \frac{1}{T_{s.c.}} + \frac{1}{T_{imp}} + \frac{1}{T_{surf.}} + \frac{1}{T_{hyp}} \qquad (17)$$

The T_{phonon} relaxation process results from phonon modulation of the spin-orbit interaction. It is the dominant relaxation pathway at high temperatures and becomes negligible at low temperatures.[1] The $1/T_{s.c.}$ term, the spin current relaxation rate, arises from the diffusive orbital motion of the electron beyond the unit cell and, because of the long-range nature of

this interaction, it has a Tlog T temperature dependence.[1] It will be dominated by the spin-orbit interaction at all but the lowest temperatures. The last three terms, arise from impurity scattering, surface scattering and the nuclear hyperfine interaction and generally only become important at low temperatures. Furthermore, it is expected that the hyperfine interaction relaxation rate will only be significant at low temperatures in very pure samples.[1]

Yafet[1] has calculated $^1/T_{phonon}$ for conduction electrons in a semiconductor with the conduction band minimum at k = 0 or at $K_n/2$, where K_n is a reciprocal lattice vector:

$$\frac{1}{T_{phonon}} = \frac{8}{\pi^{3/2}\hbar} \frac{A^2}{\rho u^2} \left[\frac{2 m^* K_B T}{h^2} \right]^{7/2} \qquad (18)$$

ρ is the density; u is the velocity of sound. A is approximately given by:

$$A \approx C \Delta g \quad (\hbar/m E_G) \qquad (19)$$

where C is the deformation potential. Equation 9 can be rewritten in terms of the reciprocal scattering time τ:

$$\frac{1}{\tau} = \frac{2}{\pi^{3/2}\hbar} \frac{C^2}{\rho u^2} \left[\frac{2 m^* K_B T}{\hbar} \right]^{3/2} \qquad (20)$$

$$\frac{1}{T_{phonon}} \approx \frac{1}{\tau} \left(\Delta g \frac{m^*}{m_e} \right)^2 \cdot \left(\frac{K_B T}{E_G} \right)^2 \qquad (21)$$

τ can be replaced by $(m^*\mu/_e)$, where μ is the electron mobility. The dependence of $^1/T_{phonon}$ on the term $(\Delta g \frac{m^*}{m_e})$ is not surprising since the spin-orbit interaction is involved in both the g-shift and the relaxation process. Equation (21) only considers a spin-orbit interaction between

two bands. It was also derived assuming that the conduction electrons obey Boltzmann statistics. For a semimetal, T in equation (21) becomes the degeneracy temperature. Equation (21) is applicable to the silver halides; thus the CESR linewidth is expected to have a $T^{7/2}$ temperature dependence above the degeneracy temperature, and to have a temperature dependence which is the inverse of that of the mobility below the degeneracy temperature.

For a semiconductor with a conduction band minimum which is not at k = 0, such as Si, equation 18 is replaced by:[1]

$$\frac{1}{\tau_{phonon}} \approx \frac{2}{\pi^{3/2}\hbar} \cdot \frac{C^2 a^2 \Delta g^2}{\rho u^2} \cdot \left[\frac{2m^* K_B T}{\hbar^2}\right]^{5/2} \qquad (22)$$

where a is a length approximately equal to the lattice constant.

For "free electrons" metals, such as the alkalis a rather simpler temperature relationship for $\frac{1}{\tau_{phonon}}$ holds:[5]

$$\frac{1}{\tau_{phonon}} \propto \frac{\Delta g^2}{\tau_R} \qquad (23)$$

τ_R is the reciprocal of the resistive scattering time. Thus, $\frac{1}{\tau_{phonon}}$ is proportional to T at temperatures above the Debye temperature and to $\sim T^3$ at lower temperatures.

Elliott estimated that for a semiconductor, the relaxation rate as a result of impurity scattering is approximately:[5]

$$\frac{1}{\tau_{imp}} \approx \frac{\Delta g^2 R^2 k_{av}^2}{\tau_R} \qquad (24)$$

R is of the order of the atomic radius, and k_{av} is the average k-vector of the conduction electrons. Assuming that each

impurity donates one electron, below the degeneracy temperature $1/T_{imp}$ is given by:

$$\frac{1}{T_{imp}} \approx \frac{\Delta g^2 \, C^{2/3}}{\tau_R} \qquad (25)$$

and above the degeneracy temperature by:

$$\frac{1}{T_{imp}} \approx \left[\frac{2 m K_B T \Delta g^2 \, R^2}{\hbar^2}\right] \cdot \frac{1}{\tau_R} \qquad (26)$$

C is the concentration of impurity ions. Thus, the impurity scattering rate is expected to have the same temperature dependence as the inverse of the mobility at high temperatures. At lower temperatures, the impurity relaxation rate will be proportional to T/μ.

The relaxation rate that results from surface collisions has been calculated by Kawabata:[40]

$$\frac{1}{T_{surf.}} \approx \varepsilon (\Delta g)^2 \, V_{F/d} \qquad (27)$$

V_F is the Fermi velocity. ε is a numerical factor of the order of one which is determined by the specific characteristics of the spin-orbit interaction. Equation 27 does not consider the effect of the environment on surface relaxation. The surface relaxation rate is expected to be important in the silver halide samples discussed in Chapter 4. Assuming a modest conduction electron concentration of 1×10^{17} electrons cm^{-3} and an approximate particle diameter of 4 microns, a surface relaxation rate of $\cdot 5 \times 10^{-8}$ sec^{-1} is calculated.

The relaxation behaviour of conduction electrons in phosphorous-doped silicon (P:Si) is now briefly considered. In the metallic regime, at donor concentrations greater than $\sim 2 \times 10^{19}$ cm^{-3}, the CESR linewidth was proportional to $C^{2/3}$, as predicted by equation 25.[32] In both metallic and non-metallic samples the linewidth decreased with temperature.[32,34] Below 77 K, this decrease was found to be consistent with the dominance of the impurity scattering mechanism described by equation 25.[32] At higher temperatures, after subtracting the impurity scattering contribution to the linewidth, the linewidth had a $T^{5/2}$ temperature dependence, as predicted by equation 22 for phonon scattering.[16] Below ~10 K, in non-metallic samples, the linewidth began to increase with decreasing temperature.[34,41] This has been attributed to incomplete motional narrowing. Consistent with this interpretation, no minimum in the temperature dependence of the linewidth was observed for samples in the metallic regime.[34] At low concentrations, motional narrowing is either the result of thermally activated hopping of electrons between donor sites, or of exchange interactions between localised donor electrons. It is not known to what extent each of these mechanisms contributes to the observed line broadening. It is thought that the amorphous antiferromagnetic character of the exchange interaction might be important in explaining the temperature dependence of the linewidth.[41] It is not known whether the line is homogeneously or inhomogeneously broadened in this regime.[41] The minimum linewidth was observed at $\sim 3 \times 10^{18}$ donors/cm^3, the concentration associated with the metal-non-metal transition.[29,32]

Relaxation processes of localised electrons in P:Si have been extensively studied[46] and will not be discussed here.

2.3 Relative Paramagnetic Susceptibilities

The amplitude of the ESR line is proportional to the paramagnetic susceptibility of the sample. While absolute susceptibility measurements are very difficult to perform, measurements of relative susceptibility as a function of temperature can yield a great deal of information about the conduction mechanisms which occur in a sample.

Ideally, in a sample which can be defined as metallic, the paramagnetic susceptibility is expected to exhibit Pauli-type behaviour. That is, below the degeneracy temperature, T_F, the susceptibility should be independent of temperature and is given by:[18,42]

$$\chi = \frac{N}{V} \cdot \left\{ \frac{(g_e \mu_B)^2}{3} \right\} \cdot \frac{J(J+1)}{K\ T_F} \qquad (28)$$

where N/V is the electron concentration and J is the spin angular momentum. This temperature independence is a result of the Pauli exclusion principle which has a greater effect than thermal disorder on whether or not the spins align with the magnetic field.[42] Above the degeneracy temperature, where the electrons obey Boltzmann statistics, the degeneracy of the electron gas is temperature dependent and the susceptibility has a Curie-type behaviour, decreasing with increasing temperature.[42] The Curie susceptibility is given by equation 28 except that T_F is replaced by the absolute temperature T.[42,18] Curie susceptibility behaviour is also characteristic of localised spins.

In heavily doped P:Si ($n \geq 4 \times 10^{19}$ cm^{-3}), a Pauli type susceptibility was observed. The signal intensity was essentially independent of temperature up to $\sim$100 K,[34,43] and then

decreased with increasing temperature once the degeneracy temperature had been reached.[44] In very lightly doped samples where no exchange interactions occurred between localised donors, the susceptibility increased with decreasing temperature, in good agreement with the Curie law.[33] At concentrations on the "just-insulating" side of the metal-non-metal transition, at temperatures below 10 K, the observed deviations from the Curie law have been attributed to antiferromagnetic exchange interactions between randomly distributed localised spins.[41] As the concentration is increased, the susceptibility appears to have both Pauli and Curie components.[34] This has also been explained as resulting from electron correlation effects.[18] An alternative explanation is that localised and non-localised spins co-exist and both contribute to the susceptibility in the intermediate regime.[34,45]

2.4 The Dysonian Lineshape

As mentioned above, the CESR signal intensity is proportional to the paramagnetic susceptibility of the sample. This is changed in a resonant way when unpaired spins absorb power from the microwave electromagnetic field and "align" with the static field. The interaction of the spins with the microwave field is, of course, dependent on how the electromagnetic wave propagates in the sample. This, in turn, is dependent on the dielectric properties and conductivity of the sample. In high dielectric materials, the wave is attenuated as it propagates through the sample; in highly conductive media, the wave is attenuated and also changes phase as it propagates. The classical skin depth, δ, is that distance over which the microwave field is attenuated to 1/e of its amplitude at the sample surface:

$$\delta = \left(\frac{c^2}{2\pi\omega\sigma}\right)^{\frac{1}{2}} \qquad (29)$$

σ is the conductivity and ω is the angular microwave frequency. Thus, as a result of the propagation properties of the microwave field and of the detection techniques normally used for ESR, the resonance signals of spins in highly conductive media are characterized by a "Dysonian" lineshape under certain conditions. An example of a Dysonian line is shown in Figure 3.

The theory treating the Dysonian lineshape was first developed by Dyson for application to CESR signals in "infinite" metal slabs,[47] with H_o normal to the surface. His treatment was verified experimentally by Feher and Kip.[48] Since then, Dyson's theory has been extended to samples of arbitrary thickness and conductivity,[49,50] in the "anomalous skin effect" region,[48,51,52] with an arbitrary orientation of H_o and of the microwave field[50,52,53] and to small spherical semiconductor[54] and metal[55] particles. The subject has been reviewed by Khabibullin and E. G. Kharakhash'yan[56] and more recently by Poole.[36] The qualitative results are unchanged from those expected by Dyson. In this section, the necessary background for extracting the g-value and T_2 from a Dysonian CESR line in a semiconductor crystal is presented, based on the treatment by Pifer and Magno.[50] The extension to small spherical particles is not necessary since the conductivities of all of the systems discussed in this thesis were too low for Dyson lineshapes to be observed in powder samples.

The resonant change in the imaginary part of the magnetic susceptibility results in a change in the Q of the cavity and an absorption signal. The change in the real part of the susceptibility results in a shift of the cavity's resonance frequency and a dispersion signal. Both changes affect the microwave power which is reflected back to the detector. The absorption and dispersion signals are related by the Kramers-Kronig

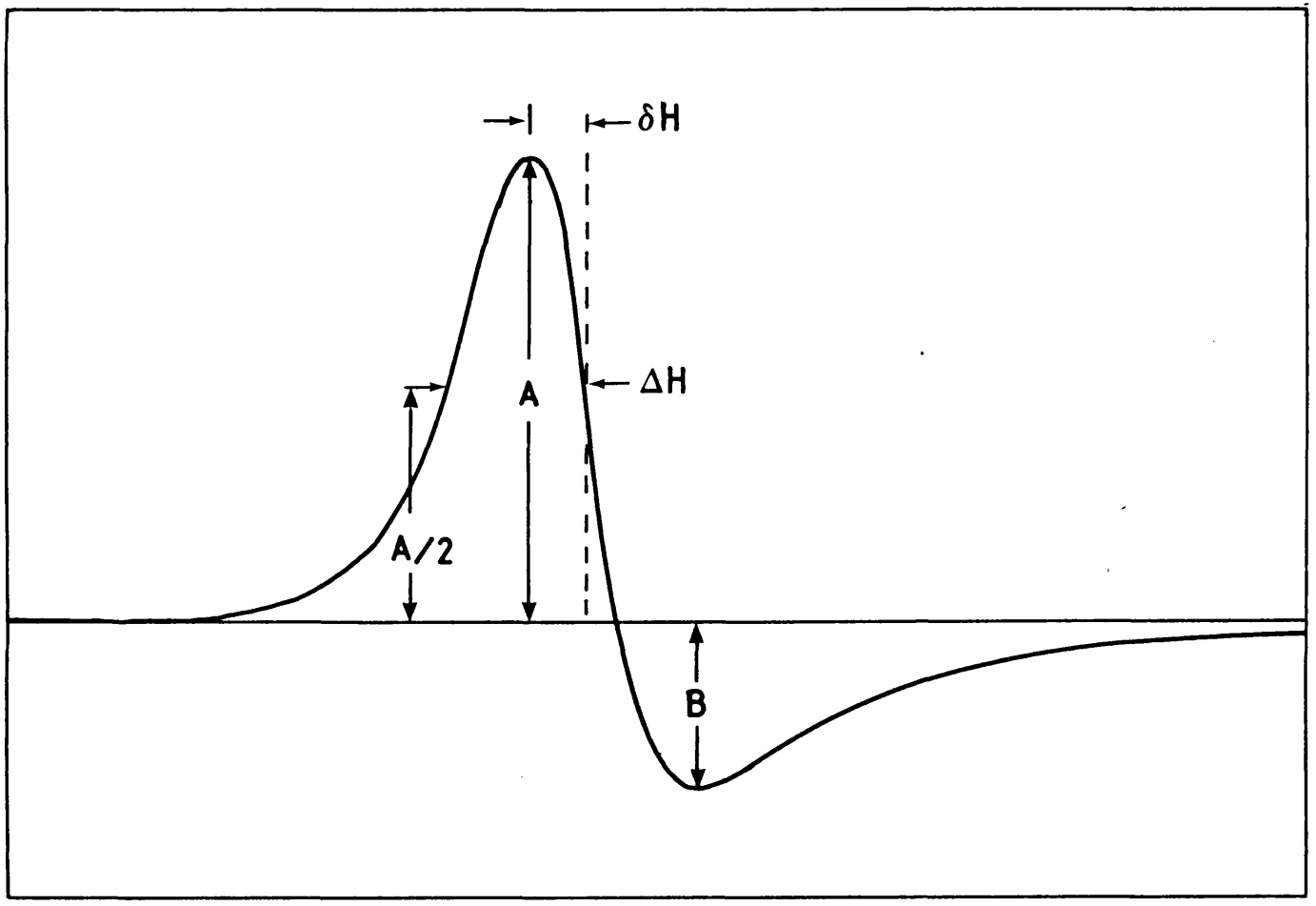

FIGURE 3

Example of a first derivative Dysonian lineshape.

relations, which ensure that the measurement of either quantity uniquely defines the power absorbed.[37] For the measurements described in this thesis, the two were separated by a lock-in detection system which automatically tuned the klystron frequency to the cavity frequency. Thus, with the phase of the lock-in detector appropriately adjusted, only changes in power absorption due to Q shifts were detected. The phase of the microwave field changes as it propagates in a conductive sample; thus, if the lock-in detector phase is adjusted so as to compensate for frequency changes at the surface of the sample, it will not null out frequency change due resonances occurring in the bulk. A mixture of absorption and dispersion signals will be obtained. This effect occurs for both mobile and localized spins. An additional consideration for mobile spins results from the fact that the spin memory of the electron is usually longer than its resistive scattering time. Thus, the magnetization carried around by the electron can be carried past the skin depth. Thus, there exist in the sample an electromagnetic wave which is strongly attenuated over the distance δ, and a less intense wave which is weakly attenuated over the distance travelled in time T_2.[51] For localized paramagnetic moments distributed uniformly throughout the skin depth, the asymmetry ratio, A/B, for a Lorentzian line is 2.7 and for a Gaussian line is 2.0.[48] As one might expect, the linewidth is proportional to $1/T_2$, just as when δ is much greater than the sample dimensions. The situation is less clear for mobile spins. For mobile carriers, the linewidth and intensity of the ESR signal are affected by the fact that the carrier moves through the skin depth and so experiences a continuum of frequencies. If an electron moves through the skin depth in time T_D, it experiences a band of frequencies of width $1/T_D$. One might expect therefore that the line

observed would have width $1/T_D$. Indeed, an extremely weak line of width $1/T_D$ is sometimes observed; however, superimposed on this is a line of width $1/T_2$ (Figure 3.8). The reason for this can be understood by noting that as long as the time the electron takes to move across the skin depth is longer than T_2, it will experience a series of pulses of microwave radiation as it moves in and out of the skin depth. The interval between pulses varies from 0 to T_2. The electron moves randomly in the skin depth and experiences a different phase history during each pulse. The CESR spectrum which results is the sum of all the pulses each electron experiences and is an interference pattern spread over width $1/T_D$. However, each time the electron returns to the surface it experiences the same phase, and thus part of the pulse always adds constructively to give a strong central line of width $1/T_2$.[47] Dyson showed that for a sample with dimensions less than one-quarter of the skin depth, the CESR line is Lorentzian in shape. If $d > 4\delta$, then the lineshape is a complicated function of T_2, T_D, δ and d. Through δ, the lineshape depends on the carrier mobility and concentration. Thus, for instance, the asymmetry ratio A/B increases as the sample conductivity increases (Figure 4a). In order to extract the true g-value and T_2 from the CESR line, the ratios d/δ and T_2/T_D must be known. If the sample is not that well-characterized, these ratios can be obtained from the measured ratio A/B by changing d/δ (by varying the sample thickness or conductivity) determining the maximum value of A/B, and fitting this to a curve such as that shown in Figure 4a. This determines the ratio T_2/T_D and relates A/B uniquely to d/δ. T_2 and the g-value can then be determined from curves such as those in Figures 4b and 4c.

The lineshape equations used to calculate the curves in Figure 4 must be altered if the experimental conditions are such that the skin depth

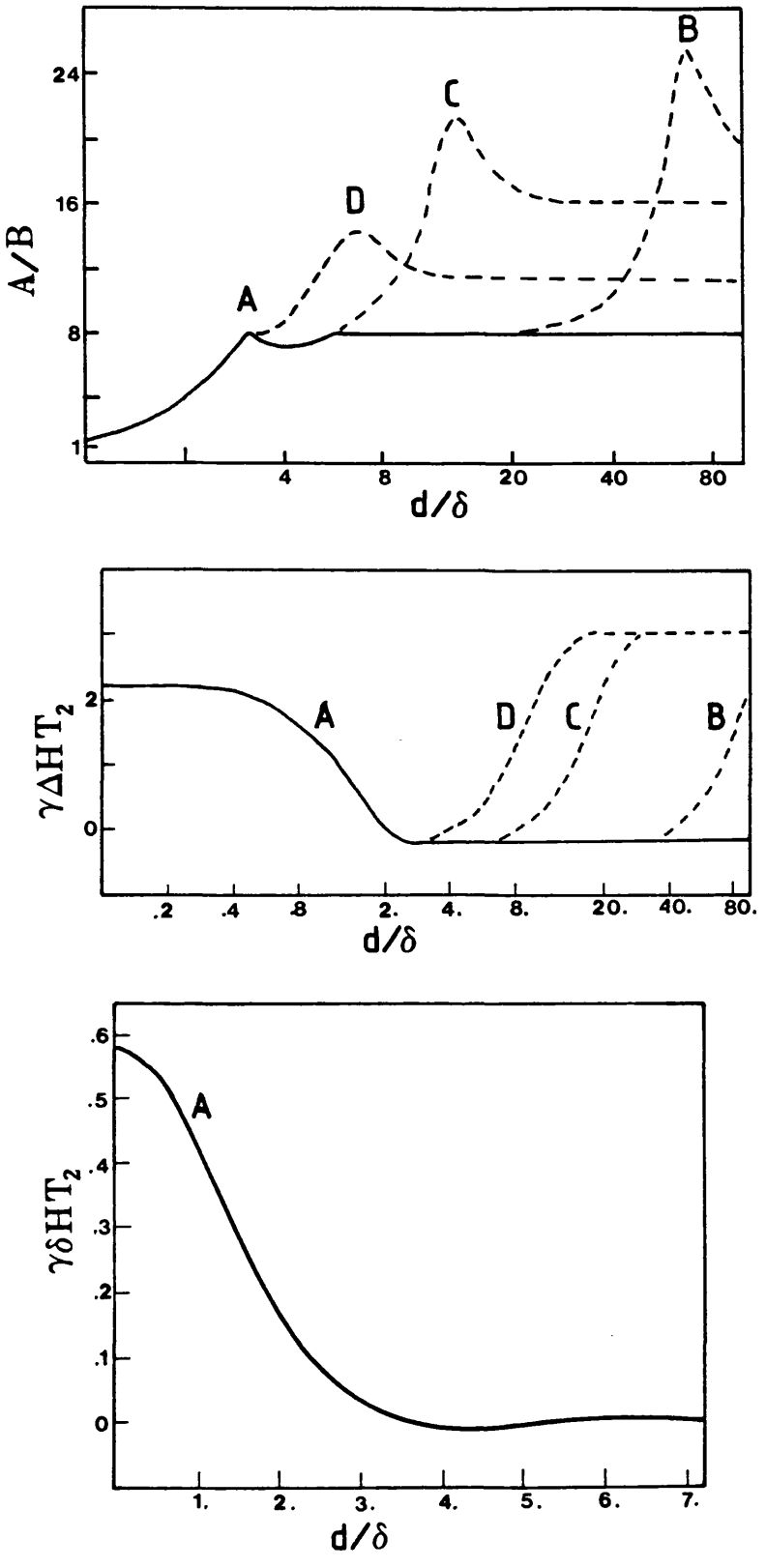

FIGURE 4

Parameters characterizing a Dysonian first derivative CESR line as a function of d/δ and T_2/T_D, calculated assuming H_1 impinges on one side of the sample. For curves marked A, B, C and D, T_2/T_D equals ∞, 50, 10 and 5 respectively. (a) A/B vs d/δ, (b) ΔHT_2 vs d/δ and (c) shift of peak from true g-value vs d/δ. After reference 50.

is controlled by the anomalous skin effect. In this region the skin depth is comparable or less than the mean free path of the electron. In general, the ratio A/B for a given d/δ and T_2/T_D is reduced from the value expected when the classical skin effect holds.

REFERENCES

1. Y. Yafet, Solid State Physics 14, 1 (1963).
2. R. A. Isaacson, Phys. Rev. 169, 312 (1968).
3. R. H. Cohen and E. I. Blount, Phil. Mag. 5, 115 (1960).
4. L. M. Roth, B. Lax and S. Zwerdling, Phys. Rev. 114, 90 (1959).
5. R. J. Elliott, Phys. Rev. 96, 266 (1954).
6. W. Zawadzki in New Developments in Semiconductors ed. P. R. Wallace (Holland Nordhoff Int., 1973) p.441.
7. R. Dupree and B. W. Holland, Phys. Stat. Sol. 24, 275 (1967).
8. S. Schultz, G. Dunifer and C. Latham, Phys. Letters (Netherlands) 23, 292 (1966).
9. W. Kohn and J. M. Luttinger, Phys. Rev. 98, 915 (1955).
10. L. M. Roth, Phys. Rev. 118, 1534 (1960).
11. M. Yamaga, N. Sugimoto and H. Yoshioka, J. Phys. Soc. Jpn. 52, 3637 (1983).
12. P. M. Scop, Phys. Rev. 139, A934 (1965).
13. L. Liu, Phys. Rev. 126, 1317 (1962).
14. C. Weisbach and C. Hermann, Phys. Rev. B15, 816 (1977).
15. W. Kohn, Solid State Physics 5, 258 (1957).
16. G. Lancaster, Electron Spin Resonance in Semiconductors (Hilger & Watts, Ltd., London, 1966).
17. N. F. Mott and W. D. Twose, Adv. Phys. 10, 107 (1961).
18. P. P. Edwards and M. J. Sienko, Int. Rev. Phys. Chem. 3, 83 (1983).
19. N. F. Mott and E. A. Davis, Electronic Processes in Non-Crystalline Materials, 2nd. ed. (Clarendon Press, Oxford, 1979).
20. W. Sasaki, Phil. Mag. B 42, 725 (1980).
21. H. Kamimura and N. F. Mott, J. Phys. Soc. Jpn. 40, 1351 (1976).
22. D. K. Wilson and G. Feher, Phys. Rev. 124, 1068 (1961).
23. R. C. Fletcher, W. A. Yager, G. L. Pearson and F. R. Merrit, Phys. Rev. 95, 944 (1954).
24. C. P. Slichter, Phys. Rev. 99, 479 (1955).
25. M. Rosso, J. Phys. Soc. Jpn. 38, 780 (1975).
26. Y. Toyoda, N. Kishimoto, K. Murakami and K. Morigaki, J. Phys. Soc. Jpn. 43, 114 (1977).
27. P. R. Cullis and J. R. Marko, Phys. Rev. B 1, 632 (1970).
28. D. F. Holcomb and J. J. Rehr, Phys. Rev. 183, 773 (1969).
29. S. Maekawa and N. Kinoshita, J. Phys. Soc. Jpn. 20, 1447 (1965).
30. D. F. Holcomb in The Metal Non-metal Transition in Disordered Systems eds. L. R. Friedman and D. P. Tunstall (Edinburgh Univ., 1978) p.251.

31. G. Feher, Phys. Rev. 114, 1219 (1959).

32. J. D. Quirt and J. R. Marko, Phys. Rev. B 5, 1716 (1972).

33. D. F. Holcomb and M. N. Alexander, Rev. Mod. Phys. 40, 815 (1968); M. N. Alexander and D. F. Holcomb, Solid State Commun. 6, 355 (1968).

34. J. D. Quirt and J. R. Marko, Phys. Rev. B 7, 3842 (1973).

35. G. Wagoner, Phys. Rev. 118, 647 (1960).

36. C. P. Poole, Jr., Electron Spin Resonance: A Comprehensive Treatise on Experimental Techniques, 2nd. ed. (John Wiley & Sons, New York, 1983).

37. S. Hasegawa and S. Yazaki, Thin Solid Films 55, 15 (1978).

38. D. Pines and C. P. Slichter, Phys. Rev. 100, 1014 (1955).

39. A. W. Overhauser, Phys. Rev. 89, 689 (1953).

40. A. Kawabata, J. Phys. Soc. Jpn. 29, 902 (1970).

41. C. T. Murayama, W. G. Clark and J. Sanny, Phys. Rev. B 29, 6063 (1984).

42. N. W. Ashcroft and N. D. Mermin, Solid State Physics (Holt-Saunders International Ed., Tokyo, 1981).

43. H. Ue and S. Maekawa, Phys. Rev. 3, 4232 (1971).

44. A. M. Portis, A. F. Kip and C. Kittel, Phys. Rev. 90, 988 (1953).

45. W. Sasaki, Phil. Mag. B 42, 725 (1980).

46. G. Feher and E. A. Gere, Phys. Rev. 114, 1245 (1959).

47. F. J. Dyson, Phys. Rev. 98, 349 (1955).

48. G. Feher and A. F. Kip, Phys. Rev. 98, 337 (1955).

49. H. Kodera, J. Phys. Soc. Jpn. 28, 89 (1970).

50. J. H. Pifer and R. Magno, Phys. Rev. B 3 (1971).

51. M. Ya. Azbel', V. I. Gerasimenko and I. M. Lifshitz, Sov. Phys. - JETP 5, 986 (1957); 35, 691 (1958).

52. M. Lampe and P. M. Platzman, Phys. Rev. 150, 340 (1966).

53. M. B. Walker, Can. J. Phys. 48, 111 (1970).

54. J. E. Sansonetti, D. P. Mullin, J. R. Dixon and J. K. Furdyna, J. Appl. Phys. 50, 5431 (1979).

55. R. H. Webb, Phys. Rev. 158, 225 (1967).

56. B. M. Khabibullin and E. G. Kharakash'yan, Sov. Phys. - Usp. 16, 806 (1974).

C H A P T E R T H R E E

AN ESR STUDY OF AgCl/NaCl BINARY MIXTURES

3.1 INTRODUCTION

The electronic properties of binary mixtures are topics of current interest with practical applications in the fields of catalysis and semiconducting devices. As discussed in Chapter 1, many of these properties can be understood by classifying binary mixtures as amalgamation or persistence-type solids. While this approach is useful in explaining overall properties, such as optical spectra and density - of-states behaviour, it neglects cluster effects.

Clusters form simply as the result of the disorder of the binary mixture. Electrons, holes and/or excitons can be confined to such clusters or extended throughout the mixture. If confined to the cluster, they can be either bound or free (extending over the entire cluster). The relative stability of the two states is expected to depend on cluster size and geometry.[2] If the nature of the binary mixture is such that the clusters are metallic, or can be made so (i.e. by irradiation of a photoconductor), then the electronic and magnetic properties of the clusters will also depend on their size and geometry.[3] This dependence results from the fact that for sufficiently small sizes (the "quantum size regime"), conduction levels are discrete, with spacings greater than kT or $h\upsilon$. Thus, for example, in this size regime the conduction electron spin resonance (CESR) g-value is size dependent. Despite an interest in cluster properties, arising in part from applications in the fields of catalysis and photographic science, there remains a paucity of theoretical descriptions, which is compounded by the difficulty of preparing well-characterized, monodisperse clusters for experimental studies. In addition, matrix and surface effects, which are expected to be significant,

have tended to be minimized in theoretical treatments, and in experimental studies, which are often carried out in rare gas matrices.

Cluster properties are of interest in the field of photographic science because the photographic latent image is thought to be a small silver cluster of three to five atoms, usually located near the silver halide grain surface. Based upon optical and ESR measurements for silver atoms in rare gas matrices, latent image particles containing five atoms or less should be molecular rather than metallic in nature.[4,5] Both ESR and UV-visible spectroscopy have been used to detect such species in silver halides but to no avail.[5,6] Matrix interference effects might account for the failure of optical methods to detect the silver cluster. One reason proposed for the failure of ESR to detect any molecular silver species is that the ESR spectra are inhomogenously broadened beyond detection. The abundance of magnetic nuclei and the delocalized nature of wavefunctions in the covalent silver halides would contribute to this problem. However, molecular silver species (Ag^{o} and Ag_2^{+})[7,8] have been observed after γ-irradiation in the more ionic alkali halides doped with impurity levels of silver ($<3\%$).

AgCl/NaCl binary mixtures are known to form solid solutions from 0 to 100 mole % silver (% Ag).[6] These mixtures, of covalent AgCl, a relatively wide band solid with an indirect band gap, and ionic NaCl, a narrow band solid with a direct band gap, might be expected to exhibit some unusual electronic behaviour. In an earlier note, the results of an ESR study of γ-irradiated AgCl/NaCl mixed powders were reported.[7] The distinctive feature observed after γ-irradiation of some

of these samples, (exact conditions are given below), was a long-lived structureless ESR signal. In the present chapter, this is assigned to mobile electrons in a AgCl-like impurity band. The extremely long free electron lifetime, relative to that in pure AgCl, is explained in terms of the inability of the conduction electron to move into the NaCl-rich regions of the grain, where Ag^{2+} centres are localized. The localization of the conduction electron to certain areas of the grain, as well as the photo-behaviour of these systems, can be understood on the basis of a persistence-type mixture. With the work described below, it was hoped to produce silver atom clusters in γ-irradiated samples either by annealing to cause atom aggregation or by increasing the silver concentration so that silver ions were in close enough proximity for silver clusters to be formed during the initial irradiation event. Also, by increasing the silver levels, the effects of matrix interactions on the properties of molecular atom clusters could be studied. Unfortunately, no molecular silver metal aggregates could be detected. However, CESR signals from free electrons in small AgCl clusters, where the clusters were in the quantum size regime were observed. Thus, the AgCl/NaCl system offers the opportunity to study the properties of metallic (AgCl) clusters as a function of matrix polarizability.

Finally, lineshape studies of the CESR line suggest that the system might be useful in studying the metal-insulator transition in semiconductors, since the conduction electron concentration can be varied without changing the disorder of the system. (For a comprehensive review of this problem, see reference 8.)

The electronic properties of the AgCl/NaCl binary mixtures

depend in a complicated way on the method of preparation and age of the sample. This chapter outlines this dependence and the general electronic behaviour as determined by ESR spectroscopy.

3.2 EXPERIMENTAL

The NaCl used for preparation of these samples was recrystallized twice from doubly-distilled 6M hydrochloric acid. AgCl was prepared by dissolving high-purity Ag shot (Alfa Products, m6N) in doubly-distilled nitric acid to give $AgNO_3$, which was then added to doubly-distilled HCl. The precipitate was washed well with distilled H_2O and dried. These compounds were melted together in appropriate proportions at a temperature approximately 50 C above the melting point of each mixture in a Cl_2 atmosphere, quenched in liquid nitrogen and ground with a pestle and mortar. Single crystals, grown in Cl_2 by the Bridgman technique, were cooled over a period of 6 to 12 hours to minimize strains and were then cleaved. Crystals with Ag concentrations as high as 60% cleaved easily and powders were not noticeably plastic until the silver concentration reached about 70%, when they were ground under liquid nitrogen.

Crystals were transparent immediately after growth. Spark source mass spectrometry showed that the metal impurity concentration in the interior of the boule was about five times higher than in the exterior, 10ppm of Fe being the highest impurity level. For a crystal containing nominally 56% Ag, silver analysis (X-ray fluorescence spectroscopy) showed that the concentration at the core was 61% and at the edge, 55%. Generally, the Ag concentrations quoted correspond to the nominal amount of silver added.

Samples were γ-irradiated with a ^{60}Co Vickrad source with a dose rate of about 1 Mrad h^{-1}. UV exposures were carried out with 150W or 500W high-pressure mercury lamps using either broad band irradiation or selected wavelengths from a grating monochromator. Unless otherwise noted, all of the exposures were made at 77 K.

ESR measurements were made on a Varian E-109 Spectrometer at 77 K. Helium measurements were carried out using an ESR-9 Oxford Instruments Cryostat. The high conductivity and dielectric properties of some of the samples required the use of a slide screw tuner for tuning the spectrometer. Care was taken to ensure that this did not affect lineshape measurements.

3.3 RESULTS

γ-Irradiation of these solids produced free electrons and holes. These carriers were eventually trapped to give a number of species that could be observed by ESR spectroscopy. The species produced by irradiation not only depended on the sample composition, but also on its age and morphology, on irradiation time, and on the wavelength of radiation used. Figure 1 shows the ESR spectra of the species that will be discussed below. The signal referred to generally as the CESR signal in Figure 1 was actually one of four different types of CESR signals, as shown in Figures 4, 6, 7 and 8, depending on the experimental conditions used. Those powder samples which had been quenched from the melt, and immediately γ-irradiated at 77 K for 30 minutes and observed by ESR, will be discussed first.

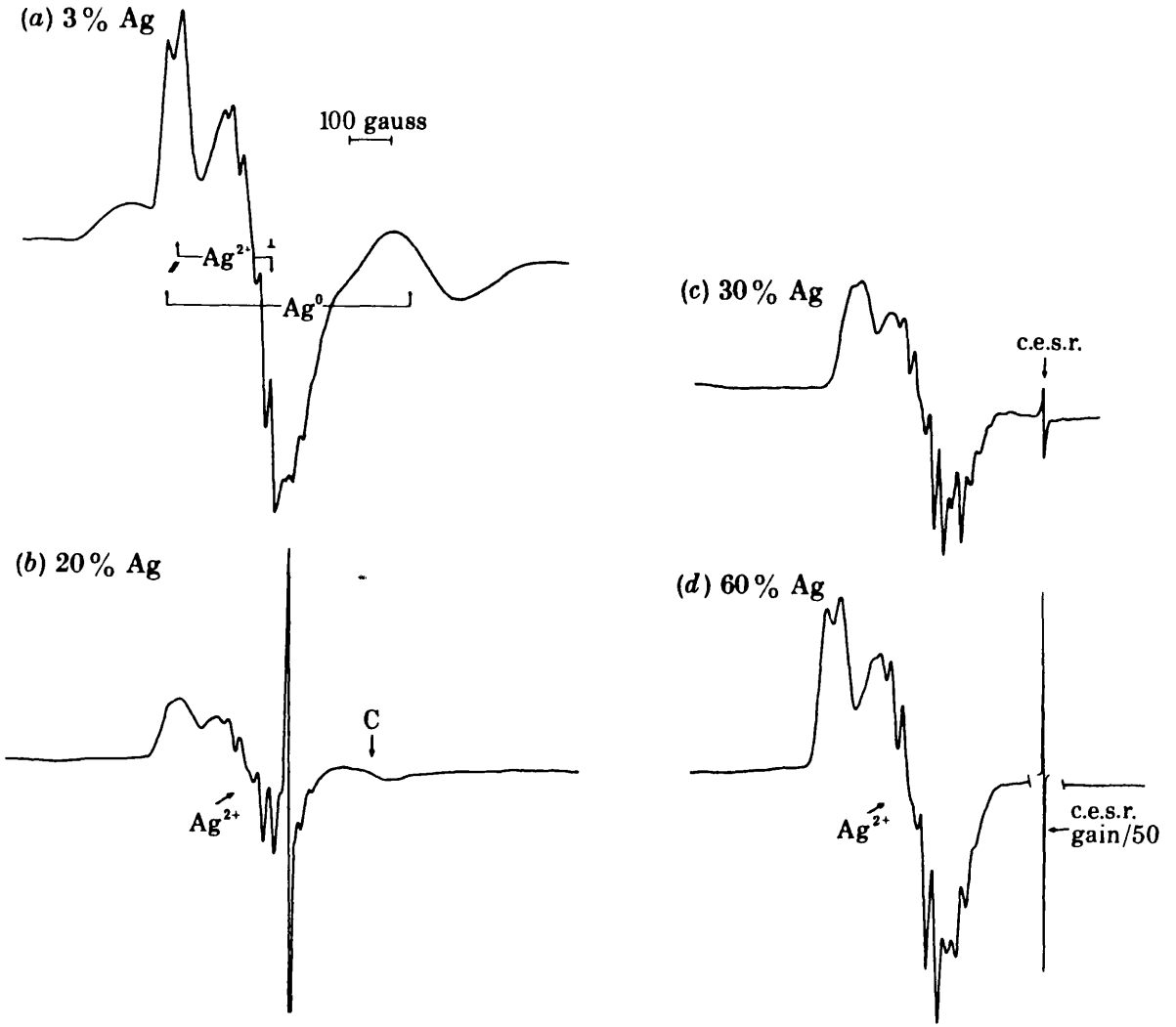

FIGURE 1. First derivative X-band e.s.r. spectrum at 77 K, after exposure to ^{60}Co γ-rays at 77 K, of a (*a*) 3 %, (*b*) 20 %, (*c*) 30 % and (*d*) 60 % Ag–NaCl powder. These show features assigned to Ag^{2+}, Ag^0 and conduction electron centres. (1 gauss = 10^{-4} T.)

3.3.1 Effects of % Ag

Impurity levels of Ag in NaCl (<3% Ag) have been well studied previously.[9,10,11] Consistent with these studies, it was observed that γ-irradiation produced the intrinsic trapped hole or V_K centre (Cl_2^-), Ag^{2+} and a single trapped electron state, Ag^0. At sufficiently low concentrations, only the V_K centre and Ag^0 were produced with subsequent annealing causing the decay of the V_K centre and the appearance of Ag^{2+}. Due to the large magnetic moment of sodium, chlorine superhyperfine structure on the Ag^o lines was not well-resolved[10], and the chlorine hyperfine lines broadened beyond resolution as the silver level increased.

In the concentration range from 3 to 10% Ag, Ag^o and Ag^{2+} were the only trapped electron and trapped hole species observed. A typical spectrum is shown in Figure 1a.

As the silver concentration was raised to 30%, Ag^o and Ag^{2+} were still observed; but, in addition, a broad, asymmetric line (C) appeared, at slightly lower field than the $m_I=\frac{1}{2}$ line for Ag^o. Its intensity increased relative to Ag^o as % Ag increased (Figures 1b and 2). It was most pronounced at high powers and at low temperatures and is shown particularly clearly in Figures 3 and 9. On annealing to 200 K, line C decayed simultaneously with the Ag^{2+} signal, presumably by a recombination process, implying that species C is an electron-rich centre.

Between 30 and 50% Ag, Ag^{2+} was still the only trapped hole species observed, Ag^o was no longer present, and a third electron-rich centre in addition to line C was detected. This is assigned below to conduction electrons in a AgCl-like impurity band and will be referred to as the CESR signal.

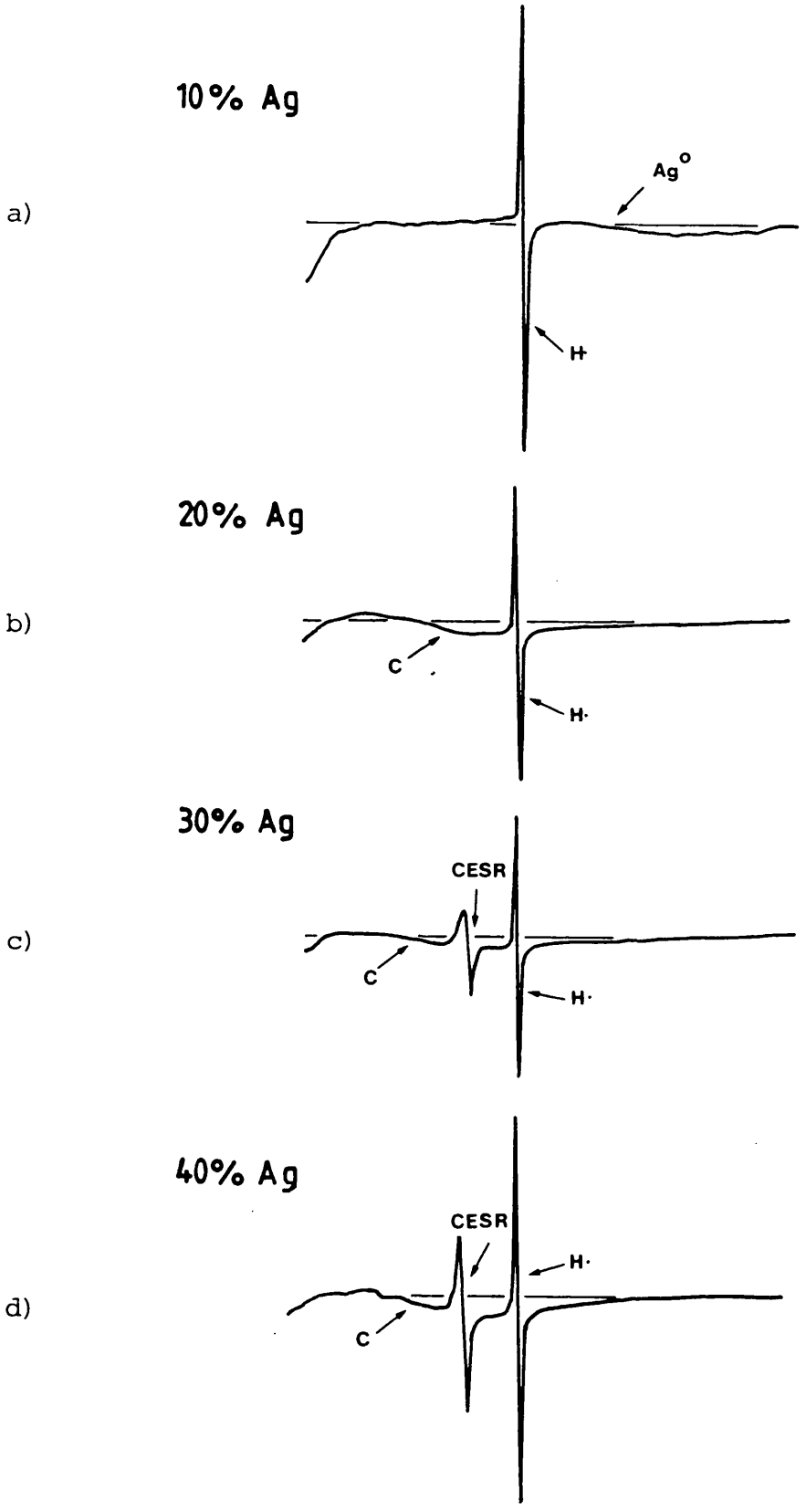

FIGURE 2

Line C in γ-irradiated a) 10%, b) 20%, c) 30% and d) 40% Ag/NaCl powders at 77 K. In c) and d) the narrow CESR line is apparent. [The hydrogen atom line, in the glass, is included as a reference.]

Typical spectra are shown in Figures 1c and 3.

The CESR line was narrow, but had an asymmetric shape, as shown in Figure 4. The g-values were measured at the crossover point and were constant throughout the concentration range within experimental error at $g = 1.8882 \pm .0010$. The linewidth and asymmetry (A/B) were also constant within experimental limits of $4.2 \pm .7$ gauss and $.64 \pm .12$ (see Chapter 4). The intensity of line C decreased relative to the CESR line as % Ag increased.

Above 50% Ag, line C was no longer observed and the CESR signal was the only electron-rich species present (Figure 1d). Ag^{2+} was still the only detectable hole-trapped species produced.

Above 90% Ag, no stable trapped electron or trapped hole species were produced by γ-irradiation at 77 K.

Signals with distinct hyperfine components attributable to molecular silver aggregates were not observed in either fresh or aged samples, even at high Ag^{+} concentrations and after a variety of exposure and annealing treatments. Some samples darkened after irradiation at 77 K and annealing to room temperature, or after exposure to room light for extended periods at ambient temperature. In these samples, a line at 2.011 was observed at temperatures less than 77 K (Figure 3). This g-value is within the range of values observed for small silver aggregates in other systems,[12,13] but further work is necessary before an assignment to inadvertent impurities can be ruled out. In addition, an asymmetric, narrow line was observed in some samples at g=1.96. Its intensity was initially weak but increased dramatically after long exposures (8 hours)

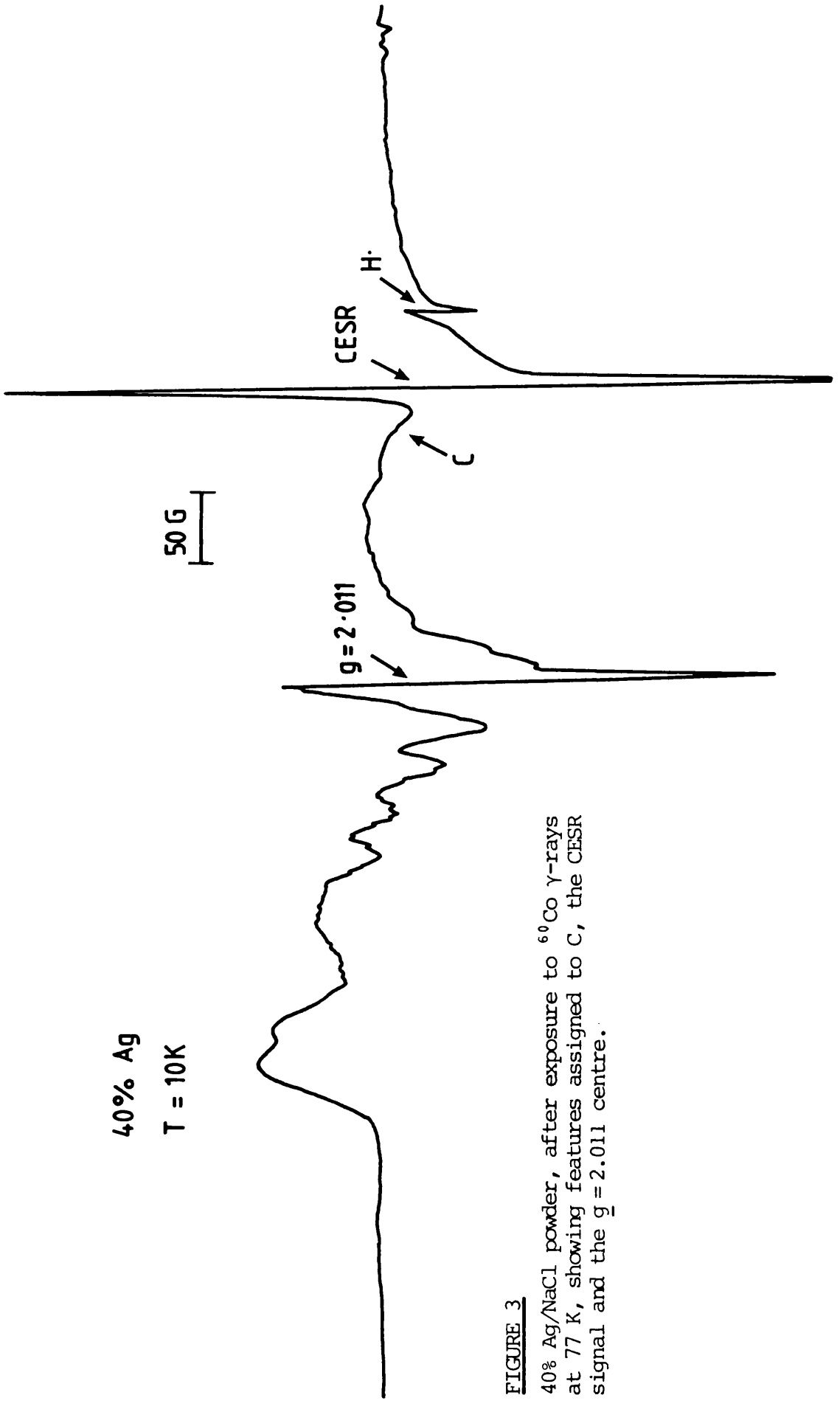

FIGURE 3

40% Ag/NaCl powder, after exposure to ^{60}Co γ-rays at 77 K, showing features assigned to C, the CESR signal and the $\underline{g} = 2.011$ centre.

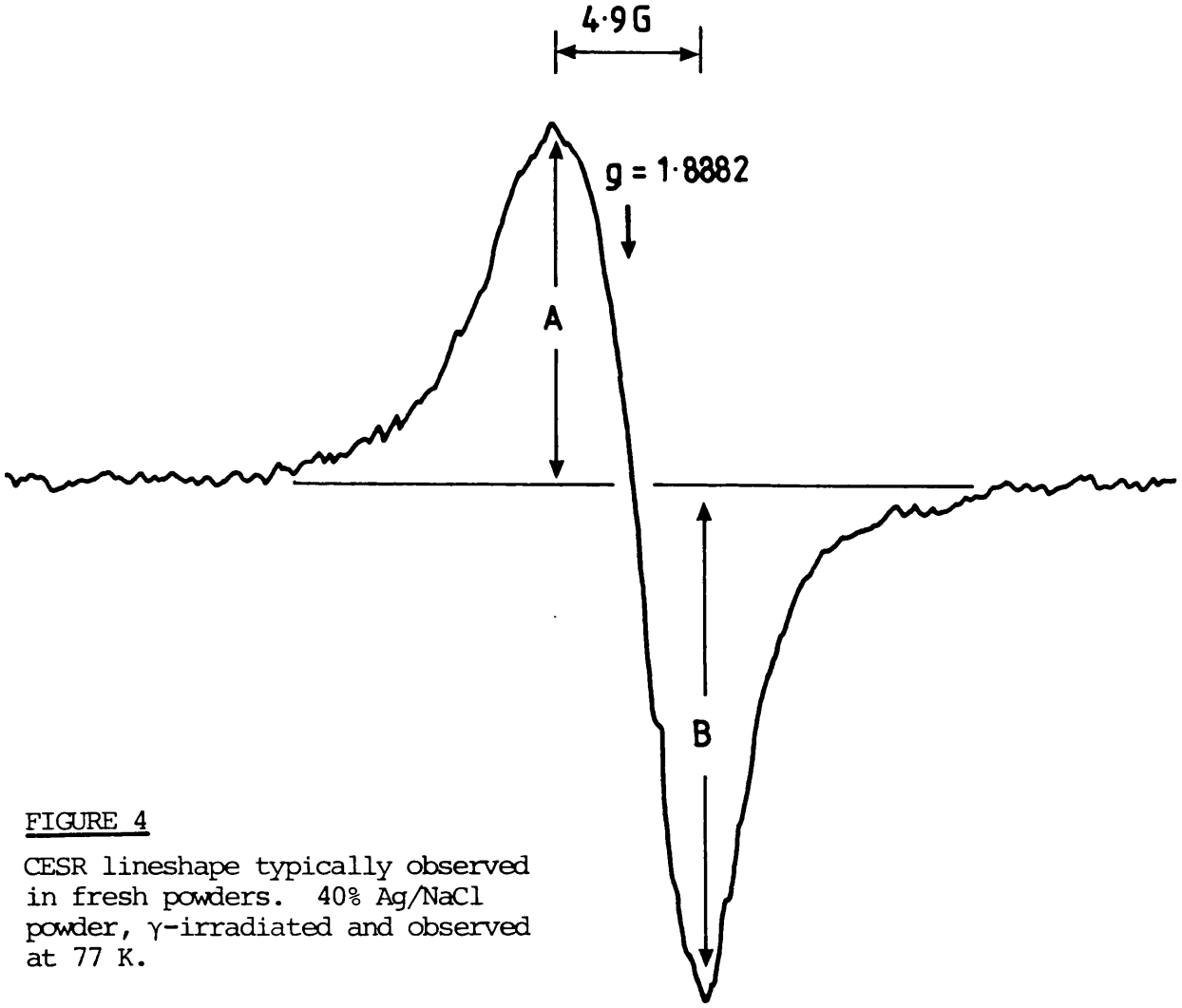

FIGURE 4

CESR lineshape typically observed in fresh powders. 40% Ag/NaCl powder, γ-irradiated and observed at 77 K.

at 77 K. The g-value is close to that of a signal observed in electrolytically coloured KCl heavily doped with Pb^+, Tl^+ or Ag^+, which was assigned to electrons in the KCl conduction band.[14] The lineshape was unusual, with A/B less than 1, but again, the assignment of this line is outside the scope of the present work.

Table 1 lists the ESR parameters measured for Ag^{2+} as a function of silver concentration. One can see that as the Ag^+ concentration increased, $g_{||}$ for Ag^{2+} decreased monotonically from the value measured for holes trapped at isolated silver impurity levels in NaCl to that measured for the self-trapped hole in pure AgCl. As the Ag^+ concentration increased, $A_{||}$ also decreased, to a value less than that measured in pure AgCl. Analysis of the Ag^{2+} parameters was complicated by the very broad lines in the parallel region which we feel arise from the presence of a range of Ag^{2+} species (Figure 5).

When warmed to 180 K, Ag^{2+} and the electron-rich centres (Ag^o, C and the CESR species) decayed simultaneously. These decays were associated with a strong luminescence.

3.3.2 Effects Of Ageing

NaCl and AgCl form solid solutions above about 170 C. Below that temperature, there is a miscibility gap between 20% and 85% Ag.[15] The quenching procedure that was adopted had been shown to freeze-in the temperature equilibrium situation; but, at silver concentrations between 20% and 85%, separation into 20% and 85% Ag phases is expected to occur over a period of weeks at room temperature.[15]

The effects of ageing on the CESR line were very complicated and varied throughout the silver concentration range.

TABLE I

ESR Parameters for Ag^{2+} in Fresh Powders

	g-tensor[e]		A-tensor[d]		A'-tensor[d]	
% Ag	$g_{\parallel}$	$g_{\perp}$	$A_{\parallel}$	$A_{\perp}$	$A'_{\perp}$	Reference
<2	2.198 ± .001	2.041 ± .001	39 ± 2	31 ± 2	32.5 ± 1	b
10	2.178 ± .003	~2.038	25 ± 3	~25	-	a,b
20	2.180 ± .003	~2.037	25 ± 3	~24	-	a,b
30	2.176 ± .003	~2.038	23 ± 3	~25	-	a,b
	2.156 ± .005	-	30 ± 3	-	-	a,c
40	2.162 ± .003	~2.037	24 ± 3	~24	-	a,b
50	2.159 ± .004	~2.038	20 ± 4	-	-	a,b
100	2.145 ± .003	2.038 ± .003	31 ± 1	23 ± 3	26.6 ± 2	29

a This reference

b Produced by γ-irradiation

c Produced by UV-irradiation

d ($x10^{-4}cm^{-1}$)

e It is not meant to imply that each of the different g-tensors refers to a specific Ag^{2+} species. Rather, these are the best values measured from ESR spectra, which probably result from a range of different Ag^{2+} species.

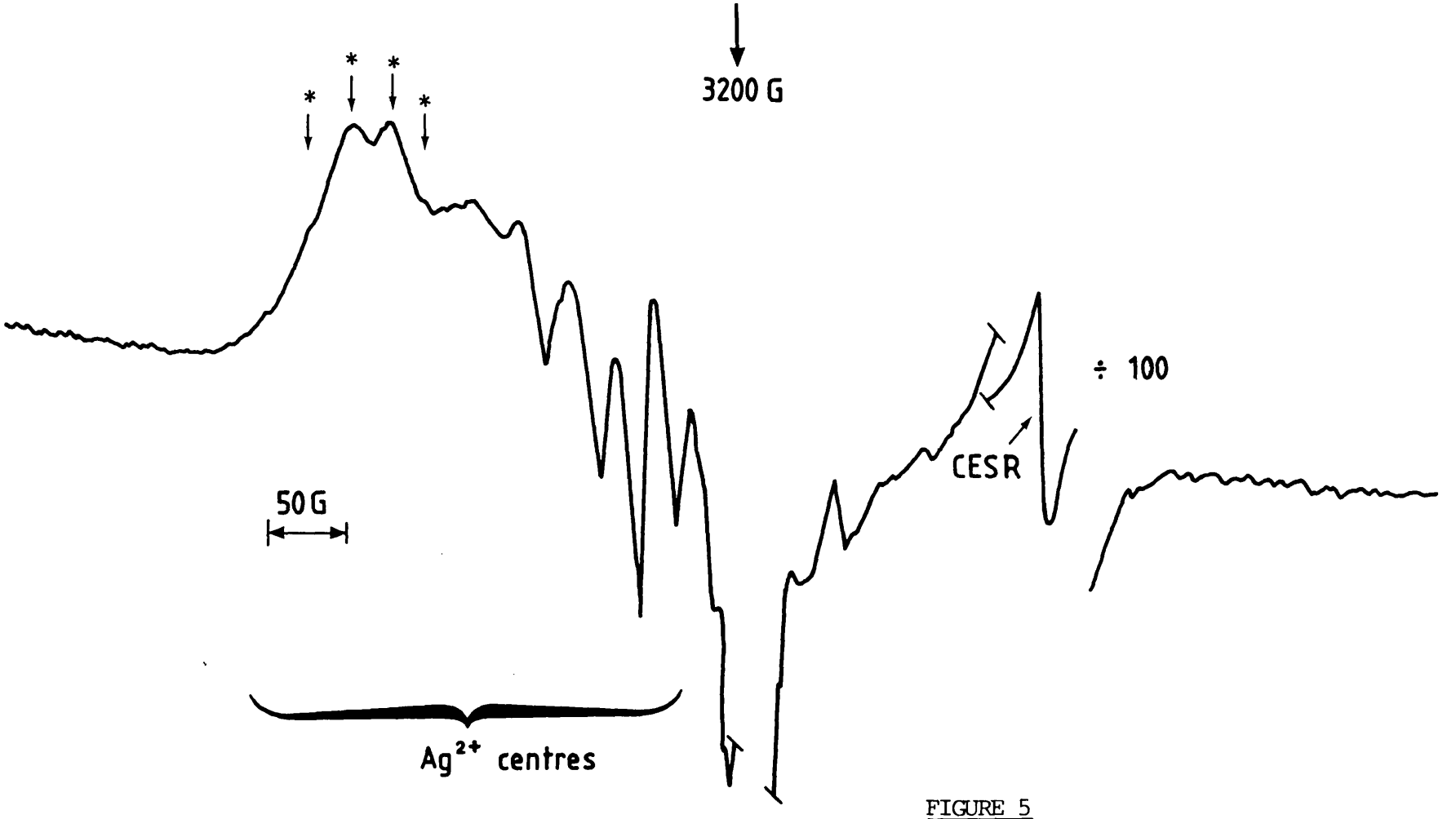

FIGURE 5

40% Ag/NaCl powder, after exposure to ^{60}Co γ-rays at 77 K, showing features assigned to a range of Ag^{2+} centres.

The line became more Lorentzian, with a g-value shift to 1.890, several days after quenching. The g-shift probably reflects the lineshape change rather than a real g-shift. In older samples, however, a real g-shift was observed, with the CESR line moving from 1.888 to about 1.886 (see Figure 6). The line at highest field tended to be narrower, with ΔH_{pp} between 4 and 9 gauss, while the low-field line had a linewidth of 1 to 3 gauss. The presence of the two lines was often better revealed after annealing, which resulted in the partial decay of the CESR signals. Also, in the older samples, the Ag^{2+} and symmetric CESR signals were much stronger than the signals observed in fresh samples. After ageing, the CESR line could be produced at lower Ag concentrations, eventually becoming observable in powder samples containing as little as 10 to 20% silver.

In 5 and 10% Ag single crystals, Ag^{o}, Ag^{2+} and a very weak CESR signal were observed immediately after growth and exposure to radiation. Thus, it would appear that single crystals are already "aged" as grown, and that the highest temperature metastable state could not be completely frozen into single crystals as a result of the method of crystal growth. As a crystal is lowered through the Bridgman furnace, the portion of the crystal that has just solidified remains at a high temperature while the rest of the crystal growth is completed; this encourages ionic diffusion and phase separation. After growth, the crystal is highly strained and cannot be quenched in liquid nitrogen without shattering. It must be cooled slowly to allow these strains to anneal out. Crystals were initially clear but became cloudy with time. Ageing

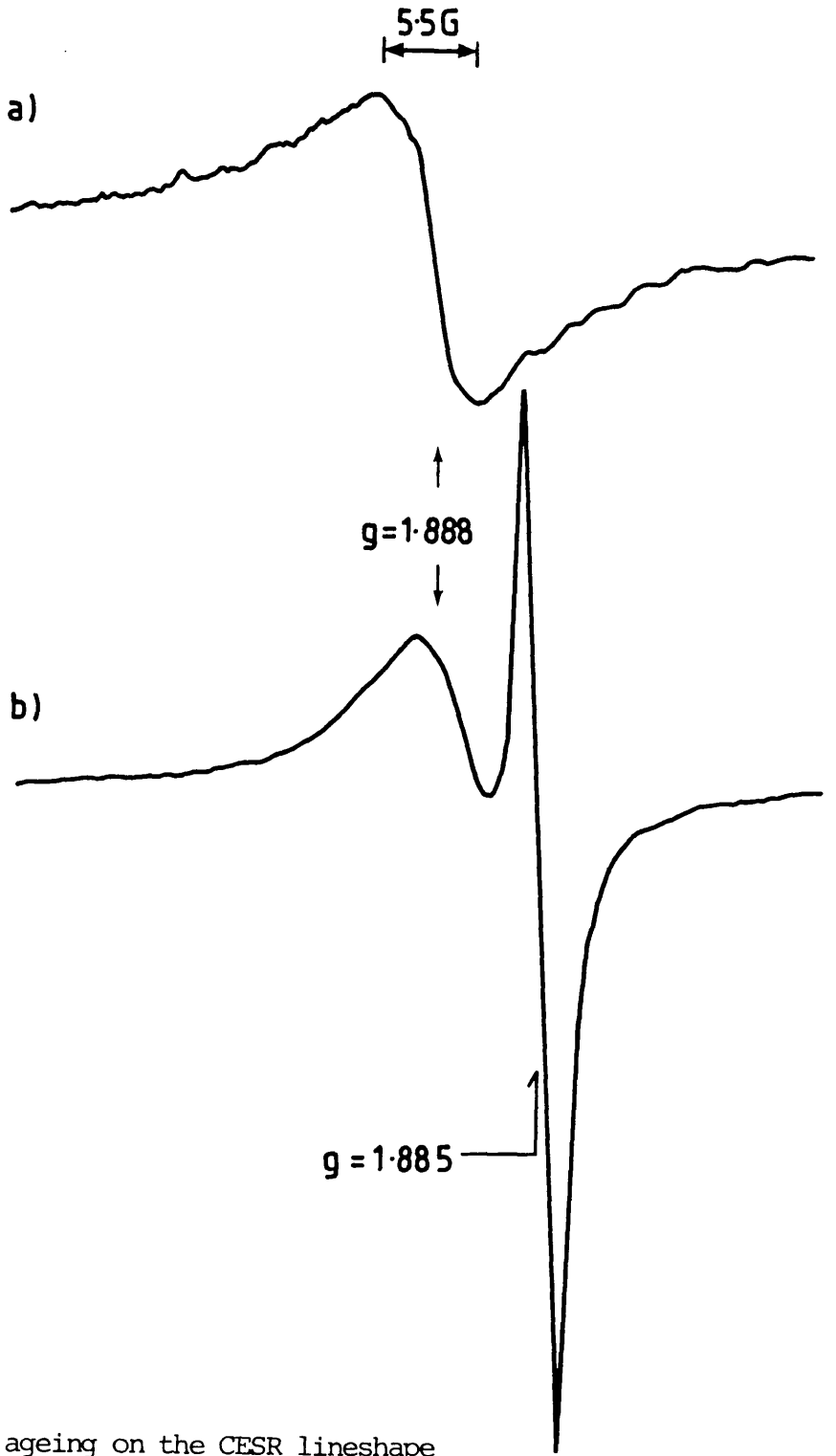

FIGURE 6

Effect of ageing on the CESR lineshape for a 40% Ag/NaCl powder a) fresh sample, b) after 48 hours.

occurred more rapidly in powders than in single crystals.

Ageing affected the Ag^{2+} ESR parameters as shown in Table II. The $g_{\|}$ and $A_{\|}$ values of Ag^{2+} moved towards those measured for disperse Ag^{2+} centres in NaCl. However, this reversion never went to completion, indicating the continuing presence of neighbouring silver ions even in well-aged samples. It is interesting to note that in older samples with both "fresh" and "aged" Ag^{2+} species present, the "fresh" Ag^{2+} species decayed first.

3.3.3 CESR Lineshape

As mentioned, the CESR line became more Lorentzian in older samples. In addition to depending on the age of the sample, the CESR lineshape was dependent on radiation dosage, or more generally, on the conduction electron concentration. At the electron concentrations produced by low irradiation levels (<1 minute), or produced by annealing above 180 K after irradiation, a narrow, asymmetric line was observed, which became less asymmetric and Gaussian at higher electron levels (Figure 7). This effect was more pronounced in older samples. The electrons giving rise to the asymmetric line had a much longer lifetime than those giving rise to the less asymmetric and nearly Gaussian lines.

In 50 and 60% Ag crystals, at low electron concentrations, the CESR signal had a nearly Lorentzian lineshape which became Dysonian at higher electron levels (Figure 8). The line aysmmetry, A/B increased as the sample was irradiated further. This is expected since A/B will increase as T_2/T_D increases. (T_D is the time for the electron to diffuse across the skin

TABLE II

ESR Parameters of Ag^{2+} as a Function of Sample Age

% Ag	$g_{\|\|}$	$A_{\|\|}$ [a,b]	Age
10	2.178	25	fresh
	2.186	30	2 days
	2.191	29	1 week
20	2.180	25	fresh
	2.189	25	2 days
	2.191	29	1 week
	2.194	32	1 year
40	2.162	24	fresh
	2.183	27	1 day
	2.190	36	2 days
	2.192	36	7 weeks

a $(\times 10^{-4}\ cm^{-1})$

b ± 3

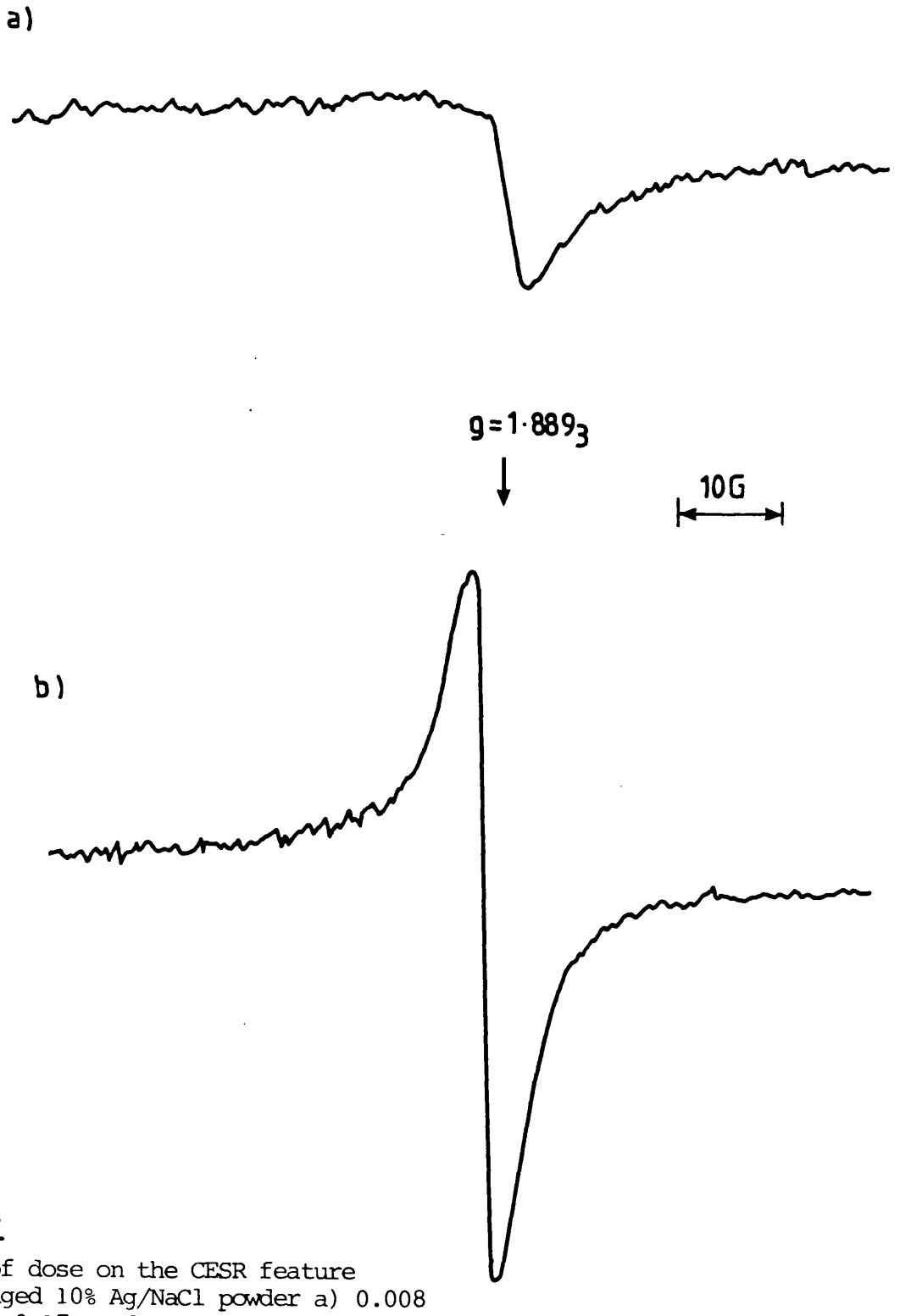

FIGURE 7

Effect of dose on the CESR feature for an aged 10% Ag/NaCl powder a) 0.008 Mrad, b) 0.17 Mrad.

depth. It will decrease as the electron concentration and thus the sample conductivity increase, causing the skin depth to decrease). If the samples were irradiated still further, their conductivity increased to such an extent that the Q of the ESR cavity was dramatically reduced by the introduction of the sample, and no CESR signal was observed. This was presumably due to the loss in sensitivity due to both the reduced Q and reduced skin depth. At high electron concentrations, the crystals were bronze coloured. If a thick and a thin crystal were irradiated for equal amounts of time, the onset of the Dysonian lineshape was observed first in the thicker crystal. This demonstrates that in these samples, the conduction electron sampled the entire crystal and was not confined to small clusters of any type dispersed in the crystal. If a crystal with a Dysonian CESR line was crushed at 77 K, the line became nearly Lorentzian in shape. The CESR g-value in single crystals was measured as shown in Figure 8. This is not the true g-value. The experimental g-value varied from 1.890 to 1.883. In older samples the CESR lines tended to be narrower and appeared at higher field. The CESR lineshape is discussed in more detail in chapter 4.

The CESR lines were often narrower in single crystals than in powders. This might arise from fewer strains or more advanced ageing in the melt-grown, uncrushed crystals.

X-ray powder diffraction measurements confirmed that the fresh powders used in this study were homogeneous. Previous X-ray diffraction studies indicated that clear single crystals grown as described above were single phase.[15] Thus, it was assumed that the fresh single crystals used in this study were equally homogeneous. It should be noted that X-ray

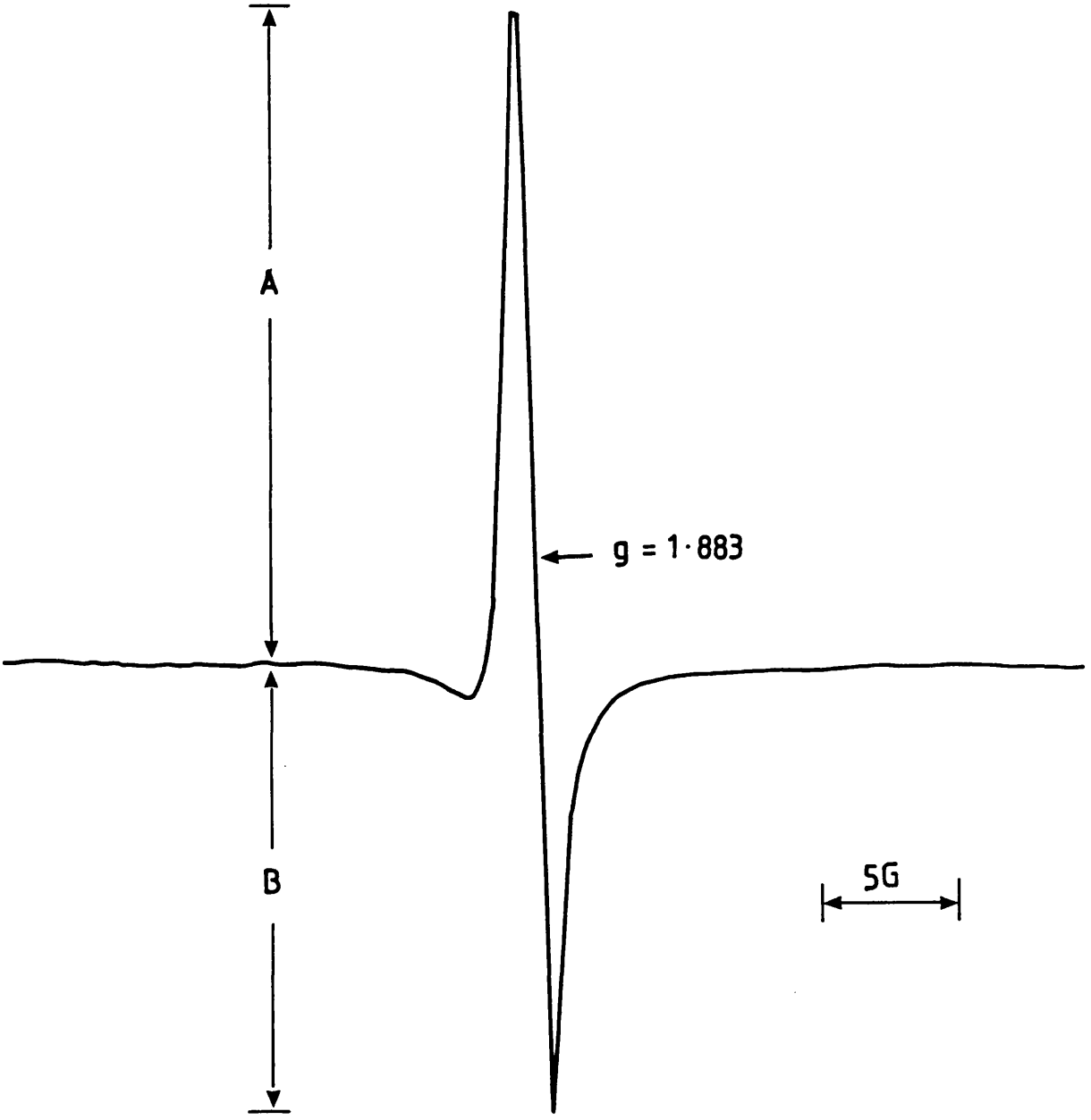

FIGURE 8

Dysonian CESR line in a 50% Ag/NaCl single crystal, after a 30-minute exposure to ^{60}Co γ-rays at 77 K. [The wings are part of the Dysonian lineshape.]

diffraction measurements yield an "averaged" lattice constant and will not distinguish clusters smaller than 100 lattice units.

3.3.4 Photochemistry

Ag^{2+} and signal C could be produced in fresh samples by UV exposure below 77 K, with a wavelength sensitivity tail extending to about 375 nm (Figure 9). During UV exposure, an intense blue emission was observed. The signals were much weaker than those produced by γ-irradiation. Also, the Ag^{2+} species was different from those species produced by γ-irradiation. Its ESR parameters are given in Table I, and are identical with those measured for pure AgCl. The UV-produced Ag^{2+} species begin to dynamically Jahn-Teller distort at about 50 K, which is $\sim$100 K lower than the γ-produced species. Finally, both Ag^{2+} and signal C were less stable than in γ-irradiated samples, decaying at about 70 K.

3.4 DISCUSSION

The CESR lines observed in fresh and aged samples with g-values between 1.883 and 1.890 are assigned to mobile carriers for the following reasons. The Dysonian lines and skin depth effects observed in 50 and 60% Ag crystals are uniquely characteristic of mobile carrier resonances. The nearly Lorentzian lineshapes of the signals observed at $g = 1.890$ and 1.886 in aged powder samples are consistent with an assignment to motionally narrowed resonances from mobile carriers. The narrow asymmetric lines at 1.888 in fresh powders are assigned to mobile carriers because of their proximity to those observed in single crystals and aged

powder samples. The origin of the asymmetric lineshape is discussed below. These assignments are supported by the fact that the microwave cavity Q and frequency were significantly changed by the introduction of all of the above irradiated samples (see Chapter 4).

Furthermore, the CESR signals are due to mobile electrons, not holes, since the mobility of holes in these solids is expected to be too low to give rise to a mobile carrier resonance.[16] Also, localized holes (Ag^{2+}) were present throughout the silver concentration range and they decayed simultaneously with the CESR resonances. This presumably occured via a recombination process, presumably that responsible for the observed blue luminescence.

The CESR g-values were close to those observed for AgCl conduction band electrons in Br^--doped AgCl powders (g=1.8775) and for electrons in shallow impurity bands in Pb^{2+}- and Cd^{2+}-doped AgCl (g=1.8815).[17] They were too high a field to arise from sodium or silver metal clusters or colloids.[12,18] Likewise, the resonances were too far removed from free spin to be assigned to electrons in a NaCl-like conduction band. Conduction band electrons have been observed in KCl samples with high F-centre and heavy metal dopant concentrations (.2%) at g=1.952 - 1.954.[14] One would not expect NaCl conduction band electrons to give rise to a significantly larger shift from free spin. Therefore, the observed g-values of 1.890 - 1.883 in these systems implies that the electron is in a AgCl-like conduction band or impurity band with no substantial NaCl character.

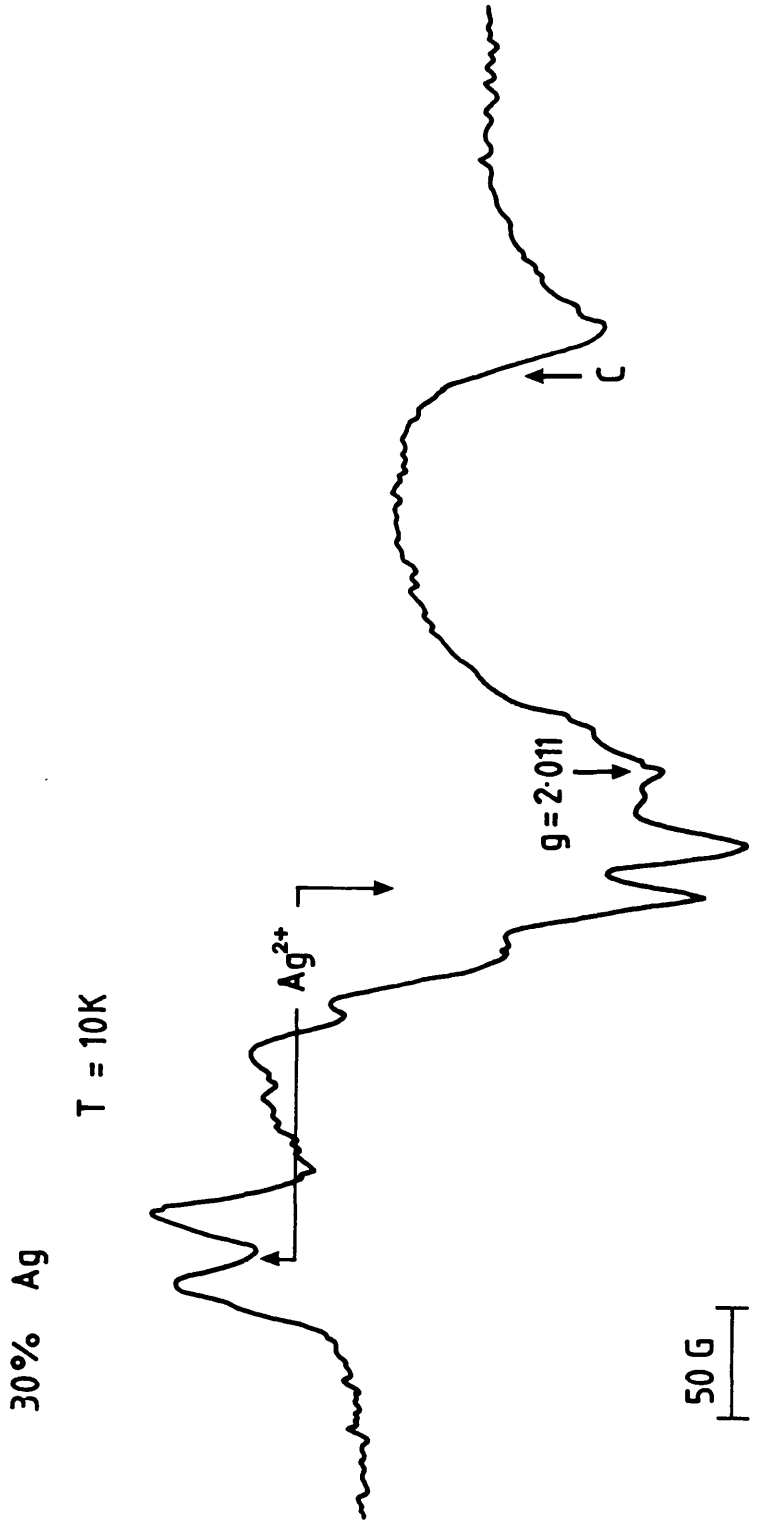

FIGURE 9

ESR spectrum obtained for a 30% Ag/NaCl powder after exposure to 350 nm light at at 20 K.

The broad, asymmetric ESR line, C, was assigned to electron-rich centres since it decayed concomitantly with the Ag^{2+} signals. The lineshape and width are similar to those observed for the CESR of small particles of aluminium,[19] silver[12] and magnesium.[20] It has been shown that such asymmetric lines could occur as a result of the g-value dependence of particle size and a Gaussian distribution of sizes.[12] Since line C is so close to the CESR signals assigned above, it can be assigned to free or nearly free electrons in small AgCl clusters with the asymmetric lineshape resulting from a distribution of cluster sizes. A cluster is defined as a section of lattice where adjacent cations are silver ions. Such clusters arise from the statistical disorder of the alloy and their existence does not imply that the alloy is inhomogeneous. As the silver concentration is increased, the clusters grow in size until at a critical concentration, an interconnecting network, or "percolated cluster" is formed. This concentration, c_p, the percolation threshold, depends on the crystal structure and has been calculated to be 29% for a simple cubic lattice.[21] The cation sub-lattice in AgCl/NaCl mixtures is simple cubic. Thus, the appearance of the CESR line at 30% Ag corresponds with the onset of percolated AgCl clusters. Its growth at the expense of line C supports the assignment of C to conduction electrons in isolated AgCl clusters. The simultaneous presence of isolated and percolated clusters has been observed before in emission studies of TlCl/TlBr mixtures.[2,22]

It was difficult to obtain accurate values for $g_{\|}$ and $A_{\|}$ for the Ag^{2+} species produced by γ-irradiation, since several Ag^{2+} species were present. However, it is obvious

that the "average" $g_{||}$ and $A_{||}$ values shifted from those measured in pure NaCl towards those measured in pure AgCl. Only a small part of the g-shift can be attributed to the decrease in lattice constant which occurs as [Ag] is increased, since only a small $g_{||}$-shift for Ag^{2+} was observed for comparable lattice constant changes in the alkali halides.[23] The rest of the change in $g_{||}$ and $A_{||}$ can probably be attributed to an increase in the covalency of the matrix.[24]

The Ag^{2+} species produced by γ-irradiation were not located in the AgCl clusters mentioned above, since their ESR parameters indicate the presence of some neighbouring Na ions. Hole trapping most probably occurred at isolated Ag ions in NaCl-rich clusters. These clusters would become smaller and the distance from the isolated Ag^{+} to surrounding AgCl clusters would decrease as % Ag increased. This is reflected in the ESR parameter trends. Also, since there would be a distribution of NaCl cluster sizes, one would expect a range of Ag^{2+} species to be produced, as was observed.

The Ag^{2+} species produced by UV exposure were in AgCl clusters since the ESR parameters were close to those observed for $(AgCl_6)^{4-}$ in AgCl.

The two different types of Ag^{2+} species produced by γ-and UV-irradiation suggests a localization of excitations. This, as well as the existence of a AgCl-like conduction band, strongly indicates that these alloys have a persistence-type band structure. Thus, γ-irradiation produces holes in a NaCl-like valence band which in real space is located in NaCl clusters. Hole mobility is low, and holes are trapped at isolated Ag ions in these clusters. Conduction electrons in

a NaCl-like conduction band have a higher mobility and migrate into the lower energy AgCl-like conduction band (see Figure 10). Physically, these electrons are in AgCl clusters or percolated clusters. Thus, the physical separation of charge carriers would account for the exceptional electron lifetime observed in these solids. UV excitation produces holes and electrons in a AgCl-like valence band and conduction band. This excitation occurs in the AgCl clusters or extended clusters, and the increased likelihood of recombination is reflected by the greatly reduced quantum efficiency which is observed, and by the fact that only those electrons localized in clusters are long-lived enough to be detected. Optical absorption and emission studies are required in order to elucidate the band structure of these materials; however, these alloys do not appear to behave as perfect crystals. This contradicts an earlier study by Kanzaki on Li/AgBr.[25]

The asymmetric lineshape of the CESR line observed at $g = 1.888$ in fresh powders is not well understood. The degree of asymmetry was quite variable from sample to sample. It cannot be due to the distribution of powder grain sizes, since the grains were several orders of magnitude larger than the quantum size regime. It does not simply arise from the presence of background signal C, since lines in 80% Ag powders, where signal C was negligible, were as asymmetric as those in 10% powders. The asymmetry might arise from overlapping lines with small g-value differences due to subtle differences in percolated cluster geometries and dimensionality. Since there can only be one infinite percolated AgCl cluster per grain,[21] these lines would originate from different grains. Some mechanism must be proposed to explain the disappearance

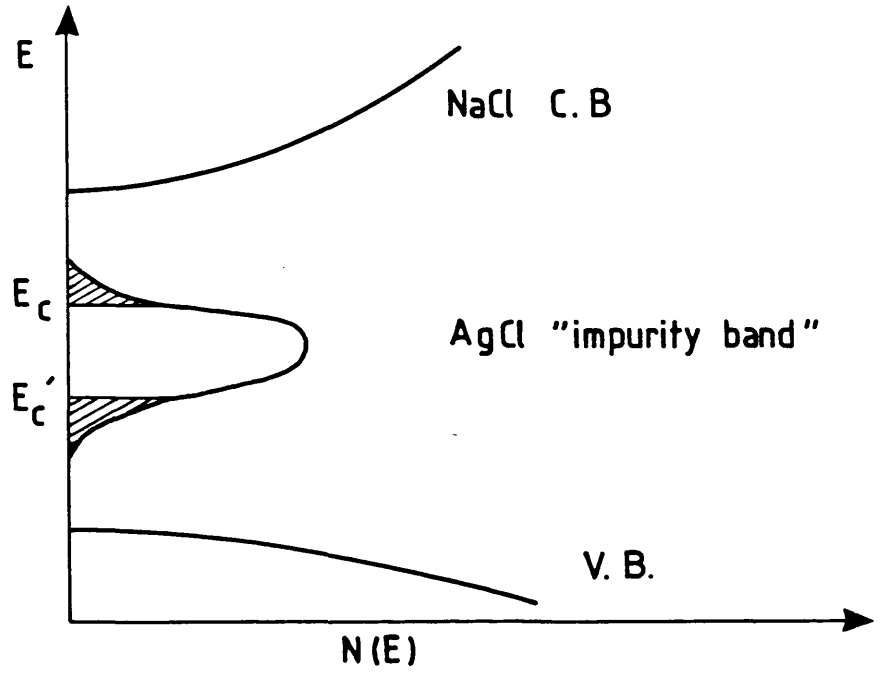

FIGURE 10

Schematic diagram of the band structure for Ag/NaCl binary mixtures.

of these differences as the CESR line became Lorentzian with time. A similar asymmetric CESR lineshape has been observed in Pb-doped AgCl powders.[17] This problem is discussed in more detail in Chapter 4.

On ageing, the CESR g-value shifted from 1.888 to 1.886, closer to that observed in pure AgCl. Only in very old, or heat-treated samples was a separate AgCl phase, with a CESR line at g= 1.877, detected. It is thought that this g-shift reflects a decrease in matrix effects on the AgCl extended cluster. This change parallels the shift in Ag^{2+} parameters towards those measured at impurity silver levels in NaCl. Thus, with time, the AgCl and NaCl clusters and percolated clusters grew in size and became less inter-mixed. This resulted in increased charge carrier separation, as in a heterojunction system, which was reflected in the much greater quantum yield of Ag^{2+} and CESR signals in older samples. These ageing effects may represent incipient phase separation into 20% and 85% Ag phases. However, ageing effects (shift in Ag^{2+} parameters, appearance of CESR line) were also observed at silver concentrations less than 20%, outside the miscibility gap, where this phase separation is not expected to occur.

It is interesting to note that while γ-irradiation produces stable Ag^{2+} centres in AgCl/KCl mixtures, no long-lived conduction electron was observed in either powders or "single crystal" mixtures. AgCl and KCl do not form solid solutions. However, one might expect the heterojunction system that is formed to allow charge separation in the same way as the aged AgCl/NaCl samples.

The relative stability of bound and free electron states in a cluster is expected to depend on cluster size and geometry (Chapter 1).[2] The lineshape and g-value of signal C indicate that the electron is free or nearly free, bound to shallow traps, in the silver chloride clusters.

ENDOR measurements might be able to determine if the Ag atoms observed at 10-30% Ag levels are localized in AgCl clusters, and possibly the size and geometry of such clusters. Future work might also correlate the distribution of cluster sizes expected for a given Ag concentration and the position and shape of line C.

The CESR signal from percolated clusters was narrow and asymmetric at low electron concentration (Figure 7). Once again, a distribution of g-values from various "cluster" sizes is invoked to explain this asymmetry; however, in this case, the "clusters" are not envisaged as electrons localized in physically separate clusters, but to electrons confined to potential wells in the percolated AgCl cluster. Such localization (Anderson localization) can occur if the ratio of the fluctuation in the depths of the crystalline potential wells (V_o), which results from the disorder of the alloy, to the conduction bandwidth, B, is less than ~ 2[26] and has been observed in doped semiconductors.[27] Even if the criterion for Anderson localization is not met, localization of wavefunctions can also occur in band tails (Figure 10). Then, a critical energy, E_c', exists below which wavefunctions will be localized.[28] The disorder responsible for the localization is assumed to arise from variations in the Coulomb potentials of the silver and sodium ions. The band tails might also be considered to result from band bending at the interface of

NaCl-rich and AgCl-rich phases. This view is supported by the fact that the asymmetry of the CESR line at low concentrations was especially pronounced in older samples. Whether the electrons are localized in bandtails or are Anderson localized, the localized wavefunctions are generally considered to be atomic. In this case, the asymmetric CESR line observed at low electron levels is interpreted as arising from a distribution of motionally narrowed CESR lines which implies that the "localized" wavefunction extends over sufficient atoms to give rise to motional narrowing. This might occur for electrons localized in hydrogenic orbitals at various shallow traps. The radius of such orbitals is expected to be between twenty and thirty ångströms in silver chloride. Further lineshape studies and DC conductivity measurements are necessary to confirm this interpretation.

We have not been able to detect molecular silver atom clusters characterized by distinct hyperfine features in these systems. The presence of such clusters in small concentrations in the samples with less than 30% Ag might be easily masked by the Ag^{2+} spectrum and the broad Ag^{o} lines. Unfortunately, at low Ag concentrations ($<3\%$), where spectral resolution is better, Ag atoms are apparently too widely separated, and the Ag^{+} mobility too low for aggregation to occur. The low Ag^{+} mobility results from the Schottky defect structure of the NaCl host. The 2.011 line, tentatively assigned to "metallic" Ag atom clusters, was only observed at silver concentrations greater than about 30%, where Ag^{+} mobility might be expected to be higher.

3.5 CONCLUSIONS

The events leading to the formation of stable conduction electron systems in NaCl/AgCl crystals can be summarized as follows. Initial electron loss on irradiation results in the formation of Cl_2^- (V_K) or Ag^{2+} centres, the former being favoured in Na^+-rich systems and the latter in Ag^+-rich systems. The V_K centres are relatively mobile and react to give Ag^{2+} on annealing[9]

$$Cl_2^- + Ag^+ \Rightarrow 2Cl^- + Ag^{2+}$$

It is stressed that the Ag^{2+} centre is better represented as $(AgCl_6)^{4-}$, the hole being stabilized by partial delocalization onto four of the Cl^- ligands.

The ejected electron is trapped at isolated Ag^+ ions to give Ag^o. "Isolated" refers to Ag^+ centres in a NaCl environment. As the concentration of Ag^+ increases, there may be a tendancy for Ag^o to move towards neighbouring Ag^+ ions to give isolated $(Ag\text{-}Ag)^+$ centres. It has already been established that such centres, as well as Ag_3^{2+} and Ag_4^{3+}, are readily formed by Ag^o in other media.[28] Some ESR evidence for $(Ag\text{-}Ag)^+$ units has been obtained for dilute KCl/AgCl crystals,[11] but no clear evidence for such entities was obtained in the present work. Indeed, instead of moving towards Ag^o clusters, there is a tendency for electrons to accumulate in a AgCl-like conduction band.

Initially, broad conduction electron signals are detected co-existing with Ag^o signals. These are due to electrons confined to small AgCl clusters, whilst the Ag^o and Ag^{2+} centres are formed by silver in NaCl environments. As the Ag^+

concentration increases, so these clusters grow and eventually combine, at the percolation limit, to give large AgCl domains which extend effectively throughout the whole volume of the crystal. In this model, the conduction electron is unable to penetrate to some of the Ag^{2+} ions in the NaCl-like zones because the AgCl-like conduction band is well below the NaCl-like conduction band, and, it seems, tunnelling through this barrier to the isolated Ag^{2+} ions is unfavourable. Thus, charge carrier separation, and the resulting decrease in recombination inefficiencies, account for the remarkably long free electron lifetime observed in these systems.

In the AgCl-rich systems, a reverse clustering is envisaged in which there are NaCl clusters contained within an AgCl enviroment. These still contain isolated Ag^{+} ions which can form trapped Ag^{2+} centres. Evidently, under these circumstances, electrons ejected in such zones move down into AgCl-like bands before they can become trapped to give Ag^{o} in the NaCl regions. Any Ag^{2+} ions formed in the AgCl region will be transient since the back reaction with electrons to give Ag^{+} ions (with emission of blue light) is very favourable. Thus, the most stable Ag^{2+} species produced by γ-irradiation were located in NaCl clusters. Their ESR parameters reflected the increasing covalency of the lattice as the Ag concentration was increased and the NaCl clusters decreased in size. In contrast, UV exposure produced Ag^{2+} in AgCl clusters. This difference, along with the observation of conduction electrons in a AgCl-like impurity band, indicates that the AgCl/NaCl mixtures cannot be treated as perfect crystals. On this basis, it is suggested that these solids have persistence-type structures.

The g-value of 1.890 - 1.888 for the CESR signal arising from percolated AgCl clusters was larger than that measured for CESR in AgCl. The CESR line shifted to 1.886 with ageing. Correlated X-ray diffraction and ESR studies would determine the structural change responsible for this shift. Such studies could also provide additional information on impurity band CESR and on surface and matrix effects on the CESR g-value of clusters. Lineshape studies of the CESR signal suggest that at low electron concentrations electronic wavefunctions are localized. However, this localization appears to extend over sufficient lattice sites to cause motional narrowing of the ESR resonances.

REFERENCES

1. G. Mason, Phys. Rev. B 27, 748 (1983).
2. Y. Shinozuka & Y. Toyozawa, J. Phys. Soc. Jap. 46, 505 (1979)
3. J. Buttet, R. Car & C.W. Myles, Phys. Rev. 26, 2414 (1982).
4. G.A. Ozin, J.A.C.S.102, 3301 (1981).
5. J.A. Howard, R. Sutcliffe and B. Mile, to be published (1984).
6. S.F. Zemczuzny, Z. Anorg. Chem. 153, 47 (1926).
7. D.R. Brown & M.C.R. Symons, Chem. Phys. Lett. 39, 69 (1976).
8. N.F. Mott & E.A. Davis, Electronic Processes in Non-crystalline Materials (Oxford, Clarendon Press, 1979).
9. C.T. Delbecq, W. Hayes, M.C. O'Brien & P.H. Yuster, Proc. Roy. Soc. A 271, 243 (1963).
10. G.E. Homberg, W.P. Unruh & R.J. Friauf, Phys. Rev. B 13, 983 (1976).
11. R.A. Zhitnikov, P.G. Baranov & N.I. Mel'nikov, Phys. Stat. Sol. (B) 59, K111 (1973).
12. A. Chatelain, J.-L. Millet & R. Monot, J. Appl. Phys. 47, 3670 (1976).
13. S.C. Jain, N.D. Arora & T.R. Reddy, Phys. Lett. 54A, 53 (1975).
14. A. Hausmann, Solid State Comm. 5, 945 (1967).
15. R.J. Stokes & C.H. Li, Acta Meta. 10, 535 (1962).
16. L.M. Kellog, Phot. Sci. Eng. 18, 378 (1974).
17. R.S Eachus, R.E. Graves & M.T. Olm, Phys. Stat. Sol. (B) 88, 705 (1978).
18. D.M. Lindsay & D.R. Herschbach, Mol. Phys. 32, 1199 (1976).
19. J.-L. Millet & R. Monot In Magn. Reson. Related Phemomn., Proc. Congr. AMPERE, 18th 1974, ed. P.S. Allen E.R. Andrew & C.A. Bates (North-Holland, 1975) p. 319.
20. J.-L. Millet & R. Monot, Solid State Comm. 43, 217 (1982).
21. V.K.S. Shante & S. Kirkpatrick, Adv. Phys. 20, 325 (1971).

22. K. Takahei & K. Kobayashi, J. Phys. Soc. Jap. 44, 1850 (1978).

23. J. Sierro, J. Phys. Chem. Solids 28, 417 (1967).

24. M.C.R. Symons & M.T. Olm, 1982 unpublished results.

25. H. Kanzaki & S. Sakuragi, J. Phys. Soc. Jap. 29, 937-945 (1970).

26. P.W. Anderson, Phys. Rev. 102, 1008 (1958).

27. J. Doehler, Phys. Rev. 12, 2917-2913 (1975).

28. N.F. Mott, Adv. Phys. 13, 325 (1966).

29. C.L. Marquardt, R.T. Williams & M.N. Kabler, Solid State Comm. 9, 2285 (1971).

C H A P T E R F O U R

THE ANALYSIS OF

CESR LINESHAPES AND g-VALUES

IN

SOME SILVER HALIDE-BASED SYSTEMS

CHAPTER 4

The Analysis of CESR Lineshapes and g-values in Some Silver Halide-Based Systems

4.1 Introduction

As described in Chapter 2, the temperature dependence of the paramagnetic susceptibility can be used to characterize a material as a metal or a non-metal and to distinguish between shallowly trapped or mobile carriers. Characteristics of the sample, such as compositional homogeneity, structural uniformity and powder grain size, as well as details of its conduction processes can sometimes be deduced from the temperature dependences of T_1 and T_2 and from the shape and g-value of the CESR line.

Such information is of use in evaluating and improving the efficiency of practical silver halide photographic systems in which CESR signals have been observed. These include Pb^{2+}- and Cd^{2+}-doped AgCl[1] and AgBr[2] powders Br^--doped AgCl powders and single crystals.[1]

In this chapter, lineshape studies of the CESR signal in 40% Ag/NaCl powders and single crystals are described. These studies expand the picture of the AgCl/NaCl binary mixtures presented in the last chapter. It is of interest to compare these with the results of lineshape analyses of CESR signals in the doped AgCl systems studied. These include Pb^{2+}-doped, Br^--doped and I^--doped AgCl powders as well as two-phase AgCl/AgClI powders. The observation of a CESR signal in the latter two systems is reported here for the first time.

Conduction electrons, produced by photolysis, in pure silver halides have lifetimes too short to allow their detection by ESR. With a modulation frequency of 100 KHz, an ESR spectrometer is limited to the detection of species with lifetimes greater than 100 μsec. At 90 K,

microwave photoconductivity and photodielectric measurements† indicate that the conduction electron has a fast component of less than 7 μsec.[3] For longer times, the conduction electron is equilibrated with electrons in shallow intrinsic traps, and both decay over a time of ~40 μsec.[3] One might expect, however, that shallowly trapped electrons could be observed, since at 1.5 K these have a lifetime on the order of 2 sec,[4] and a concentration in pure samples $(\sim 10^{17})^3$ sufficient for detection by ESR. Indeed, at 1.5 K, a CESR signal has been detected in pure AgCl[2] which could be attributed to shallowly trapped electrons.

CESR signals from either shallowly localized or conduction electrons have been observed at higher temperatures only in doped silver halide samples. The CESR signal which was observed in Pb^{2+}- and Cd^{2+}-doped AgCl powders following band gap exposure was indefinitely stable up to ~120 K and was observed in powders doped with as little as 0.1 mppm (2×10^{15} ions/cm^3) of the divalent cation.[1] The g-value of 1.88 was the same as that measured in pure AgCl at low temperatures, within experimental error. A narrow line at 1.88 was also observed in ODMR studies of pure AgCl, arising from the recombination of free or nearly free electron with localized holes.[7]

For exposures below 30 K, both the CESR signal and the self-trapped hole were detected. The self-trapped hole decayed above 30 K; deeper

---

† Microwave photoconductivity and microwave photodielectric experiments consist of measuring, respectively, the sample-dependent Q and frequency changes in a microwave cavity, which are induced by light. The Q change results from a change in the conductivity of the sample which to first order results from free electrons.[5] Holes are not expected to have sufficiently high mobilities to respond to the 10 GHz frequency of the microwave field.[6] The frequency shift arises from changes in the dielectric constant of the sample which to first order results from the polarization of shallowly trapped electrons.[5] Microwave techniques are very sensitive and particularly well suited to the study of silver halides and of powdered samples since the need for contact electrodes is eliminated.

hole-trapped species were not detected following this decay. Above 120 K, both the CESR signal and the microwave photoconductivity signal decayed at the same rate. The decay was comprised of a fast and a slow component with identical activation energies but different frequency factors. Below 140 K, the activation energy was 0.050 eV and above 140 K it was 0.36 eV.[8] The sign and magnitude of the microwave photodielectric shift, -1 MHz, implied that the shift resulted from the polarization of shallowly trapped electrons.[8] The shift decayed at the same rate as the long decay component of the CESR and photoconductivity signal. The effects just described were also obtained in AgCl powders "washed" with Pb^{2+} or Cd^{2+}. No CESR signals were observed in doped single crystals.

On the basis of the above data, the following model was proposed. The microwave and CESR signals were associated with a surface or subsurface impurity band of divalent cations.[1] Pb^{2+} and Cd^{2+} are known to diffuse readily in the silver halide lattice ultimately segregating at grain boundaries.[9] For dopant levels of ~5 mppm (4×10^{15} ions/cm^3), surface levels of 10^2-10^4 mppm (8×10^{17}-10^{20} ions/cm^3) may be reached.[10] The longer electron lifetime was attributed to the lower electron mobility in the impurity band and a partitioning of photoelectrons to the grain surface and photoholes to the grain interior. The high temperature activation energy was close to that for the diffusion of an interstitial silver ion.[11] Thus, the high temperature decay was associated with the trapping of electrons at interstitial silver ions. This was consistent with the observed build-up of the Ag_n° CESR signal concomitant with the decay of the Pb^{2+}-associated CESR signal.[1] It was also consistent with the photographic observation that Pb^{2+} sites "locate" the latent image.[12] The change in the 0.36 eV activation

energy below 140 K reflected the freezing of ionic motion at low temperatures. Furthermore, it was proposed that the trap depth of the latent image speck was deepened by the presence of a nearby Pb^{2+} site. This proposal is supported by the observation that Pb^{2+}-doping reduces the dispersity of the latent image on the surface.[13]

The origin of the fast and the slow decay components in AgCl might be the same as for the fast and slow decay components of the microwave photoconductivity signal in AgBr. In AgBr, as in AgCl, the long decay had an activation energy close to that for interstitial silver ion motion.[14] As in AgCl, the activation energy for the long decay decreased below a critical temperature, in this case, 90 K. Unlike AgCl, the fast decay had an activation energy different from the long decay, of 0.024 eV. The conduction process which was associated with the fast decay was the dominant conduction mechanism above 165° K. It was proposed that the microwave photoconductivity signal could be attributed to two types of mobile electrons: electrons in the conduction band and electrons in an impurity band, possibly moving by a hopping mechanism. The decay of the conduction electrons into a Pb^{2+}-associated impurity band .024 eV below the conduction band edge gave rise to the short decay component of the photoconductivity signal. Above 90 K, electrons decayed from the impurity band by trapping at interstitial silver ions. Below 90 K, the impurity band electrons decayed by hopping to trapping sites with an activation energy of .010-.060 eV. The latter two decay processes gave rise to the slow component of the photoconductivity decay. The photodielectric shift was associated with the impurity band electrons. These apparently stayed trapped long enough to contribute to the sample polarization.[14] Thus, it is likely that the fast and slow decay components of the CESR signal in Pb^{2+}-doped AgCl also arise from

conduction band and impurity band electrons, respectively. It was the purpose of the study described below to determine if the temperature dependence of the CESR lineshape was consistent with this assignment. Attempts were also made to explain the g-value temperature dependence and the asymmetric shape of CESR line.

In order to better define the terms "conduction electron" and "impurity band electron", which have been used rather loosely up to now, and to provide a model against which to evaluate the results of this study, it is useful to review that model which has been applied to P:Si.[15,16] As described in Chapter 2, one expects that as the impurity concentration is raised, eventually the impurity wavefunctions will overlap sufficiently for metallic conduction to occur. Considering this in more detail, at low concentrations, phosphorous ions are well separated and each "extra" electron is localized on its atom. As the phosphorous atoms become more closely spaced, their ground state wavefunctions overlap forming an "impurity valence band". If the semiconductor is uncompensated, this valence band is full so that no impurity conduction in the impurity valence band occurs. In addition, of course, an "impurity conduction band" forms from the $^{\text{doubly occupied}}_{\wedge}$ levels of the phosphorous atoms. The excitation of an electron to the impurity conduction band is analogous to placing a second electron on a phosphorous atom. For well separated atoms, the energy required for this, corresponding to the "impurity band gap", is (I-A) where I is the ionization energy of the isolated P atom and A is the electron affinity. Because the excited state orbitals are more extended, the upper band forms before the lower band. As the phosphorous atoms become more closely spaced, the impurity band gap decreases. The semiconductor does not become metallic when the impurity valence band and impurity conduction band

merge. This is because states in the band tails are localized due to the disorder of the semiconductor. Rather, the system becomes metallic when the Fermi level crosses a mobility edge E_c, above which electron states are non-localized (Figure 1). This crossing of the mobility edge as a result of a band structure change is referred to as a Mott transition. If the Fermi level is raised to cross the mobility edge by injecting electrons, the metal-insulator transition is referred to as an Anderson transition. The upper and lower impurity bands are referred to as the upper and lower Hubbard bands, separated by the Hubbard gap. In P:Si, the upper Hubbard band forms at a phosphorous concentration of 3×10^{15} ions/cm^3.[17] At concentrations lower than this, the P^- ions are well separated and the extra electron is bound to the atom with an energy of .0017 eV. At this concentration, P° states are .04 eV below the conduction band edge. After the formation of the upper Hubbard band, the binding energy of the lowest energy P^- states increases to .008 eV. This energy corresponds to the depth below the conduction band edge of electrons localized in band tails of the upper Hubbard band.[17] At a donor concentration of 1×10^{17} ions/cm^3, the lower Hubbard band forms. As the donor concentration is increased still further, the upper and lower Hubbard bands merge, and at a concentration of 3×10^{18} ions/cm^3 a Mott transition occurs. The upper Hubbard band merges with the conduction band edge at $\sim 3 \times 10^{19}$ ions/cm^3.[15]

If the semiconductor is "compensated", containing shallow hole traps which can accept electrons from the filled lower Hubbard band, then hopping conduction can occur in the lower Hubbard band.[15,16] This is a thermally activated rather than a tunnelling process as a result of the local fields of the acceptor ions and the random distribution of the impurity ions. The activation energy, ε_3, corresponds to an average of

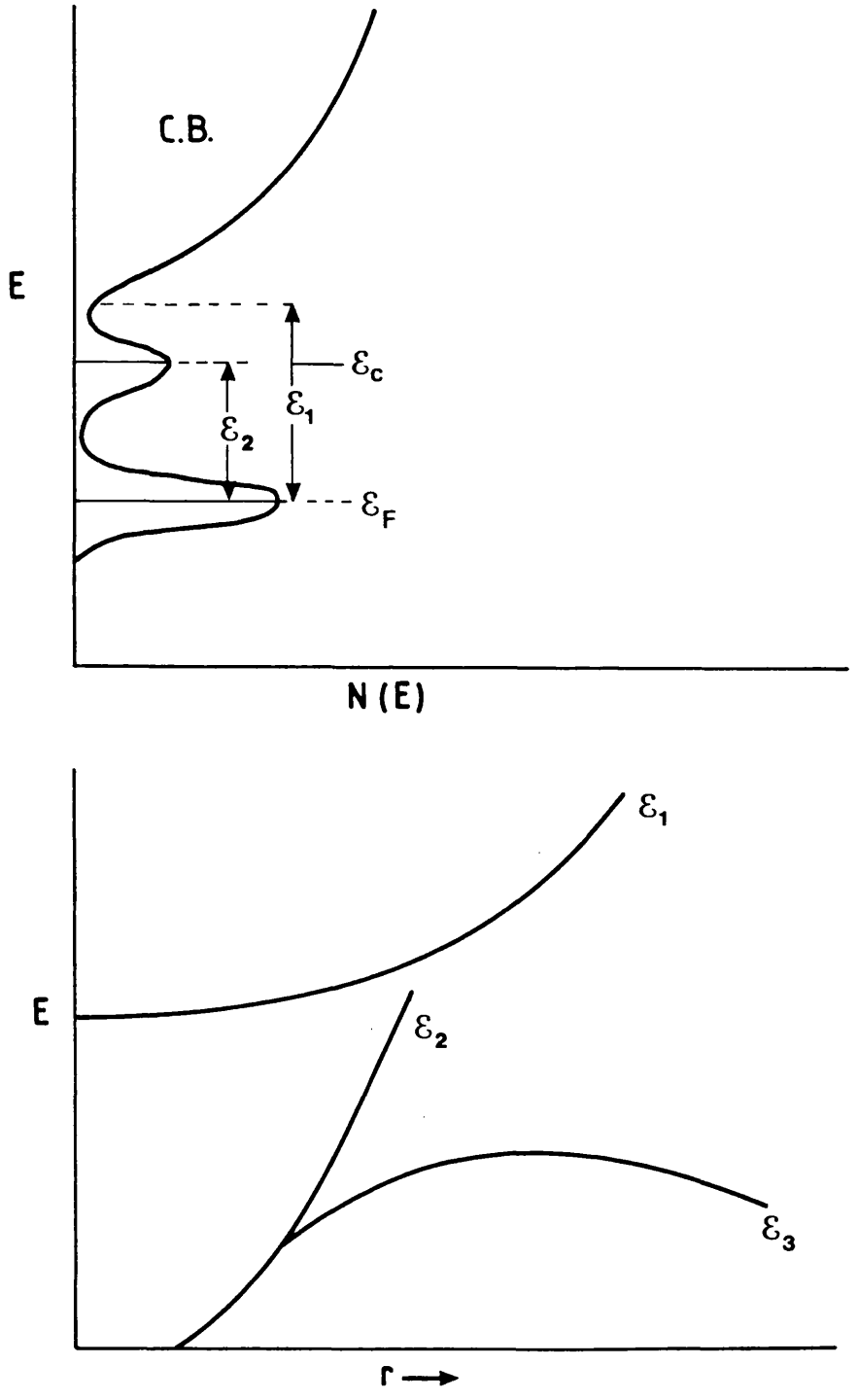

FIGURE 1

a) Density of states diagram for a compensated, insulating p-type semiconductor showing the upper and lower Hubbard bands.
b) Schematic representation of the variation of the activation energies ε_1, ε_2 and ε_3 with r, the distance between donors. After reference 19.

the difference in potentials between impurity sites. At high concentrations where overlap in the lower Hubbard band is strong, ε_3 goes to zero in compensated semiconductors. In compensated, insulating, semiconductors, conduction can occur either by excitation of electrons to the mobility edge where either hopping conduction or a band process can take place, or by ionization of the donor and excitation of the electron into the conduction band where a band process takes place. The activation energy for the first process is ε_2 and for the second process ε_1. These two activation energies differ the most near a Mott transition (Figure 1b).

Thus, Pb^{2+}-doped AgCl is analogous to heavily compensated P:Si. On exposure, it may be possible to raise the Fermi level high enough for an Anderson metal-insulator transition to occur. If the Pb^{2+} ions are close enough for a Mott transition to take place, and if the Fermi level can be raised past the mobility edge, the sample will be metallic at all temperatures. Impurity conduction might be expected to occur in the lower Hubbard band. The activation energy for this would be ε_3 or ε_1 depending on the separation of the Pb^{2+} sites. The model described above can probably also be applied to pure AgCl since the concentration of intrinsic shallow traps is fairly high.

4.2 Experimental

Pure silver halide powders were prepared by adding 1M solutions of silver nitrate and the appropriate potassium halide salt, at a rate of ~10 mℓ/min, to an equal volume of water with stirring. All of the solutions were acidified (pH ≈ 4) and kept at ~70°C. The fine powder that was produced was then washed with water and reagent grade acetone and dried under vacuum in a dark oven at 50°C. Distilled, deionized water, with a resistivity of 10 mega ohm-cm was used for all of the preparations

which were carried out in acid-etched glassware.

All of the sample preparation and handling procedures were carried out under dim red light (Wratten 1A filter). Electron micrographs of powders previously prepared by this technique have shown that the grains are "clumped" with very irregular shapes and "diameters" ranging between 2 and 4 microns.

The $AgNO_3$ salts used in the above preparation were either prepared from 6N Ag shot (Alfa Products) dissolved in triply distilled HNO_3, or from reagent grade $AgNO_3$ recrystallized three times from triply distilled HNO_3. The latter method has been shown to decrease to the total impurity content from .35 weight ppm to .05 ppm.[20] High purity potassium halide salts were used (Alfa Products, "Ultrapure", 5N and "Purex" 7N) for the silver halide precipitations without further purification. The dopant salts $Cd(NO_3)_2$ and $Pb(NO_3)_2$ were recrystallized twice and added to the silver nitrate solution at levels ranging from 2-50 mppm ($2\text{-}100 \times 10^{16}$ ions/cm^3).

The Br^--doped AgCl single crystals were grown under chlorine by the standard Bridgman technique, the materials being held in HF-etched quartz tubes.

Silver chloride emulsions doped with 3% and 6% iodide were supplied by Dr. M. Ledger, Kodak Ltd. (Harrow). The iodide salt was added at points 50% and 67% into the precipitation process, resulting in grains having a pure AgCl core and an external sheath consisting of a 6% and 11% AgI/AgCl phase, respectively. The addition of iodide resulted in grains which were irregular spheroids, with an approximate diameter of .6 microns, instead of the usual well-defined cubic AgCl morphology.

The iodide-doped emulsions were "degelled" in order to increase the density of silver halide grains in the sample and, thereby, to optimise

the concentration of photoactive sample in the ESR cavity and to improve the ease of handling. Degelling consisted of heating the emulsion to 40°C at which point it began to flow, adding an equal volume of distilled water, centrifuging the sample and, finally, decanting the gelatin-containing liquid. Distilled water was added to the centrifugate which was then stirred and recentrifuged. The process was repeated a third time after which the compacted material was washed with acetone and air-dried at room temperature. The grains of AgCl produced by this treatment retained a thin sheath of gelatin, but they packed well into an ESR tube.

The degelled emulsions were transferred to ESR tubes and cooled to 77 K in the dark and measurements were then made in subdued lighting. Thus, the samples were not exposed to actinic light at room temperature. Controlled irradiations were made at low temperatures in the ESR cavity using a 200W high pressure mercury arc lamp whose output was attenuated with an IR and red light blocking filter, and either a 325 or 400 nm band pass filter.

The AgCl/NaCl samples discussed below were prepared and γ-irradiated in the manner described in Chapter 3.

ESR measurements were carried out on a standard Varian E109 spectrometer. Measurements below 77 K employed an Oxford Instruments ESR-9 cryostat.

CESR signals were not detected in all of the doped AgCl powders or in any of the AgCl single crystals prepared for this study. This lack of sample reproducibility is attributed to the inadvertent incorporation of transition metal impurity ions. Cu^{2+} was detected by ESR in some of the powder samples at the sub-part-per-million level. In melt-grown single crystals, Mn^{2+} and Fe^{3+} were the predominant transition metal

impurities and were present at the ppm level. They were probably present as aggregates in the precursor powder samples and were dispersed during crystal growth to be included as isolated, substitutional ions. All of these impurities act as deep electron traps or recombination centers.[21] Their presence would be expected to shorten the lifetime of free or shallowly trapped electrons.

4.3 Results

4.3.1 Pb^{2+}-doped AgCl powders and two-phase AgCl/AgClI emulsions

Following the exposure of the Pb^{2+}-doped silver chloride powders to band gap irradiation ($\lambda \leq 325$ nm) below 140 K, a single, narrow ESR line was observed which is shown below to have a behaviour consistent with the earlier assignment to mobile electrons.[1] The photoproduced hole was self-trapped as $(AgCl_6)^{4-}$ and detectable by ESR below 30 K (Figure 2). This signal decayed irreversibly at temperatures above 30 K through a process in which the hole was initially detrapped and subsequently localised at other deep intrinsic or extrinsic defect sites. The existence of "ESR silent" hole traps has been noted previously.[21]

The CESR line had a Lorentzian lineshape at low power levels which became increasingly asymmetric as the power was raised to saturating levels (Figure 3). The asymmetry ratio, A/B, decreased with power to a minimum value which was obtained when the signal was well-saturated. The CESR line in 40% Ag/NaCl samples had a similar behaviour which is shown in Figure 12. For the Pb^{2+}/AgCl powders, the high field lobe of the asymmetric line was broadest. Each lobe of the asymmetric line could still be fitted to a Lorentzian lineshape. The CESR line also became increasingly asymmetric if the power was kept constant and the temperature was raised (Figure 4).

Although the height of the CESR line increased as the temperature was

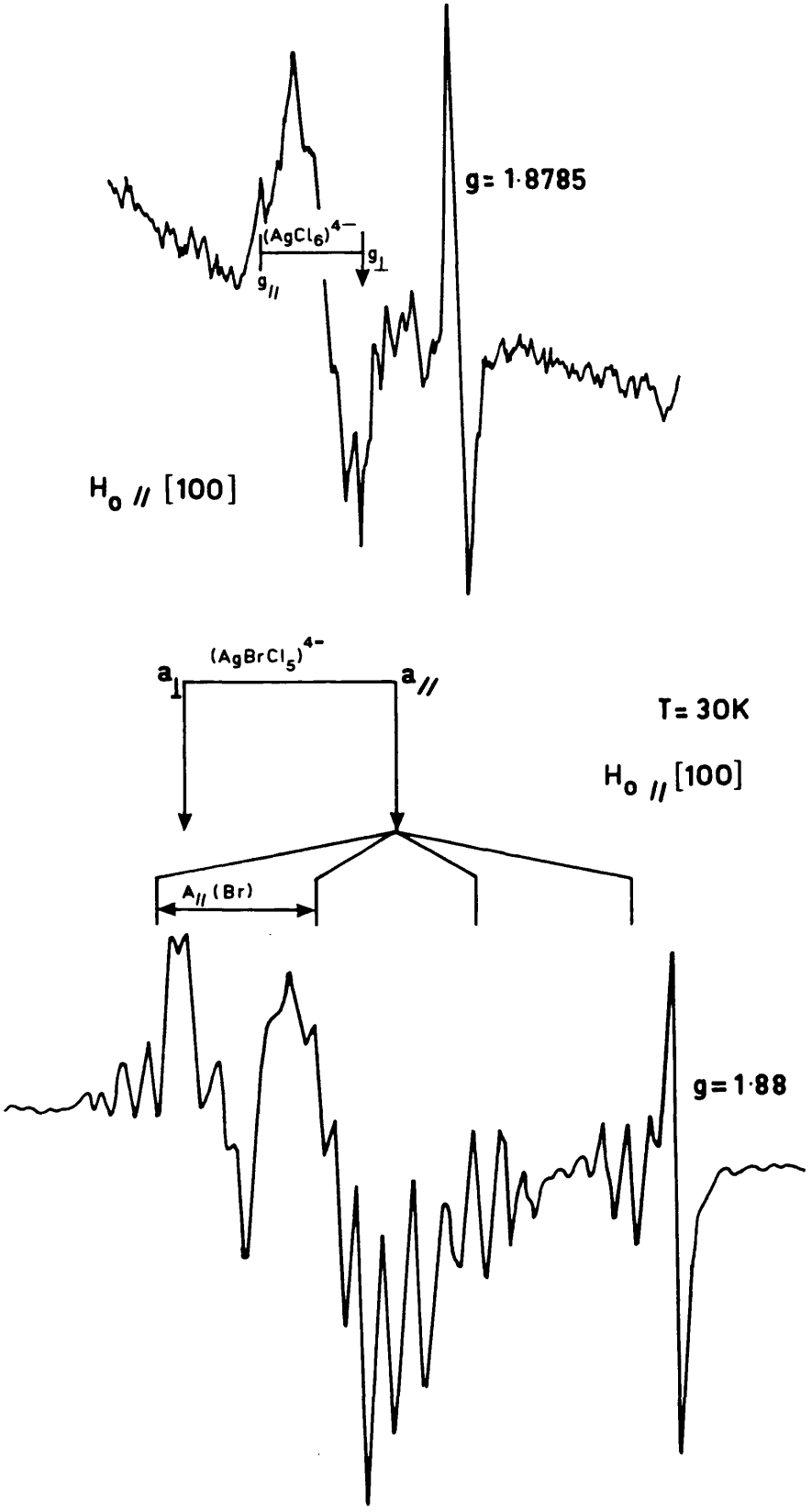

FIGURE 2

An X-band ESR spectrum of (a) a AgCl powder containing 1.7×10^{16} ions/cm^3 of Pb^{2+} after band gap excitation at 30 K, (b) a AgCl powder containing 5×10^{18} ions/cm^3 of Br^- ions during band gap excitation at 30 K [from reference 1].

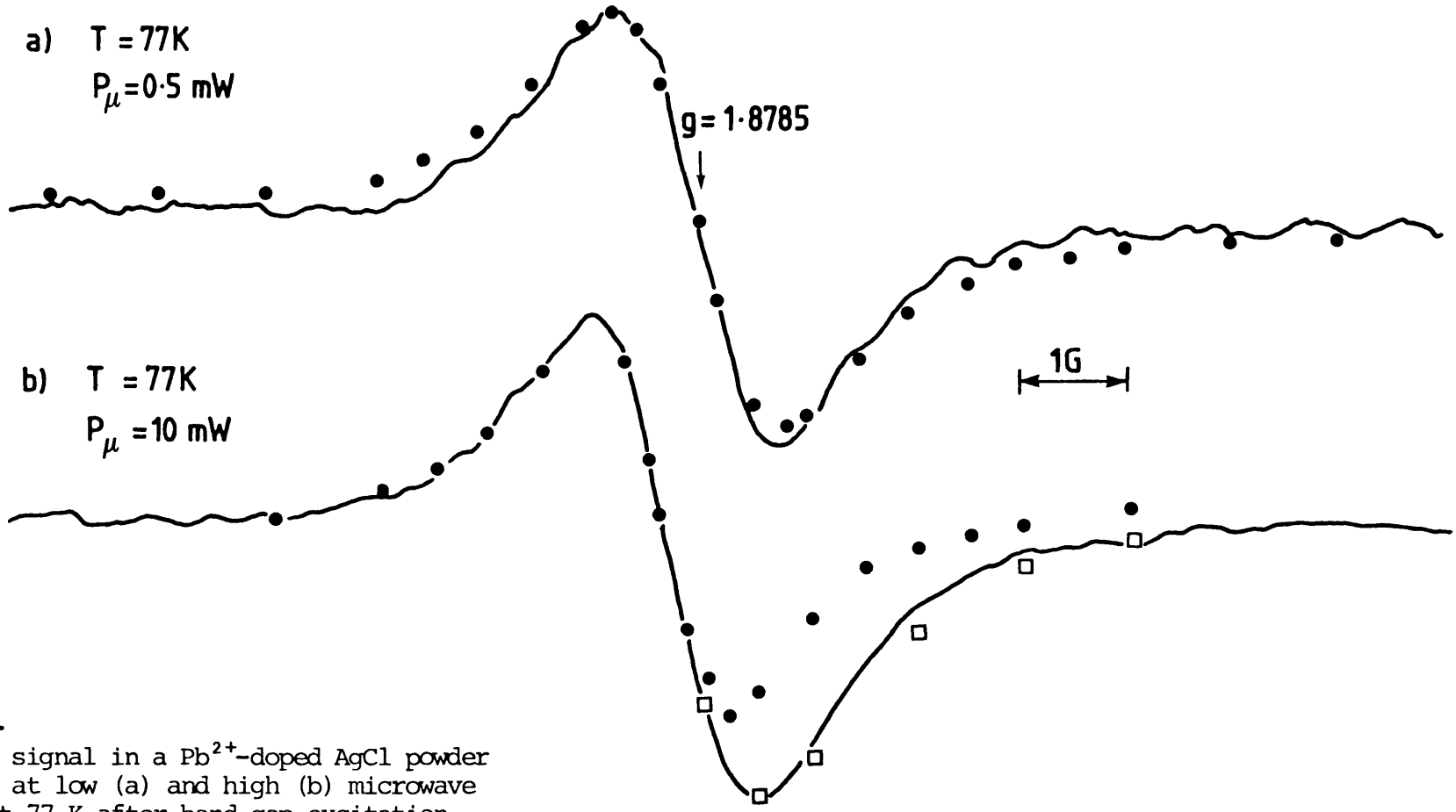

FIGURE 3

The CESR signal in a Pb^{2+}-doped AgCl powder measured at low (a) and high (b) microwave powers at 77 K after band gap excitation. [The dots and squares represent a Lorentzian lineshape fitted to the positive and negative lobes respectively.]

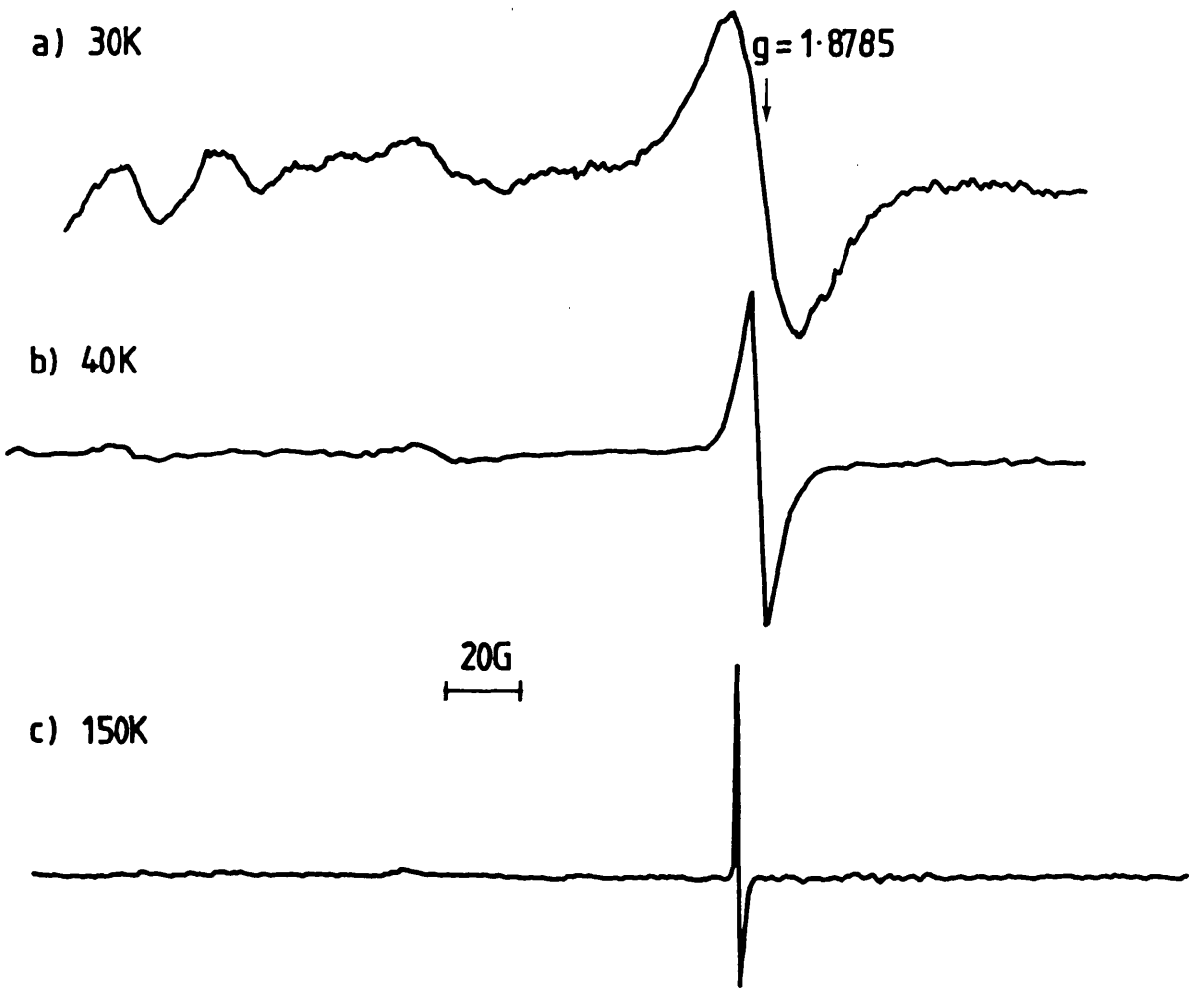

FIGURE 4

X-band ESR spectra obtained from a powder of AgCl containing 1.7×10^{16} ions/cm^3 of Pb^{2+}. Exposures to 350 nm radiation were made at a) 30 K, b) 40 K and c) 150 K.

raised between 10 and 77 K, this was the result of line narrowing and masked a decrease in the paramagnetic susceptibility. The relative paramagnetic susceptibility, χ, was calculated from the derivative peak height, y'_m, and the peak-to-peak linewidth, ΔH_{pp}, according to the relationship:[22]

$$\chi = \frac{2\pi}{3} y'_m (\Delta H_{pp})^2 \qquad \ldots\ (1)$$

The temperature dependence of $1/\chi$ below 77 K is shown in Figure 5. The susceptibility continued to decrease with increasing temperature above 77 K until the CESR signal decayed irreversibly. Below 30 K the linewidth was very large so that the measurement of χ was not possible.

The spin-lattice relaxation time, T_1, was calculated from power saturation studies at 77 K, performed according to the method described by Poole[22] (Figure 6). The spin-lattice relaxation times measured by the saturation method and the spin-spin relaxation times calculated from the CESR linewidth are collated in Table I for all the systems studied. At 77 K, T_1 was $(5 \pm 4) \times 10^{-6}$ sec. It was assumed that the cavity calibration factor, K, was unity (equation 2.13). This assumption is expected to affect the value of T_1 by less than a factor of 2. The Lorentzian lineshape suggests that the CESR line was homogeneously broadened and so it is valid to extract the spin-spin relaxation time from ΔH_{pp}. T_2 at 77 K, corresponding to a linewidth of 1.43 gauss, was $(5 \pm 1) \times 10^{-8}$ sec. The discrepancy between T_1 and T_2 is outside the limits of error for the measurements. The temperature dependence of T_2 is shown in Figure 7. The linewidth was approximately independent of temperature above 60 K, and then increased rapidly as the temperature was lowered.

The g-value of the CESR line in Pb^{2+}-doped AgCl powders was 1.8785 ± 0.0002, measured at non-saturating power levels. The line shifted to

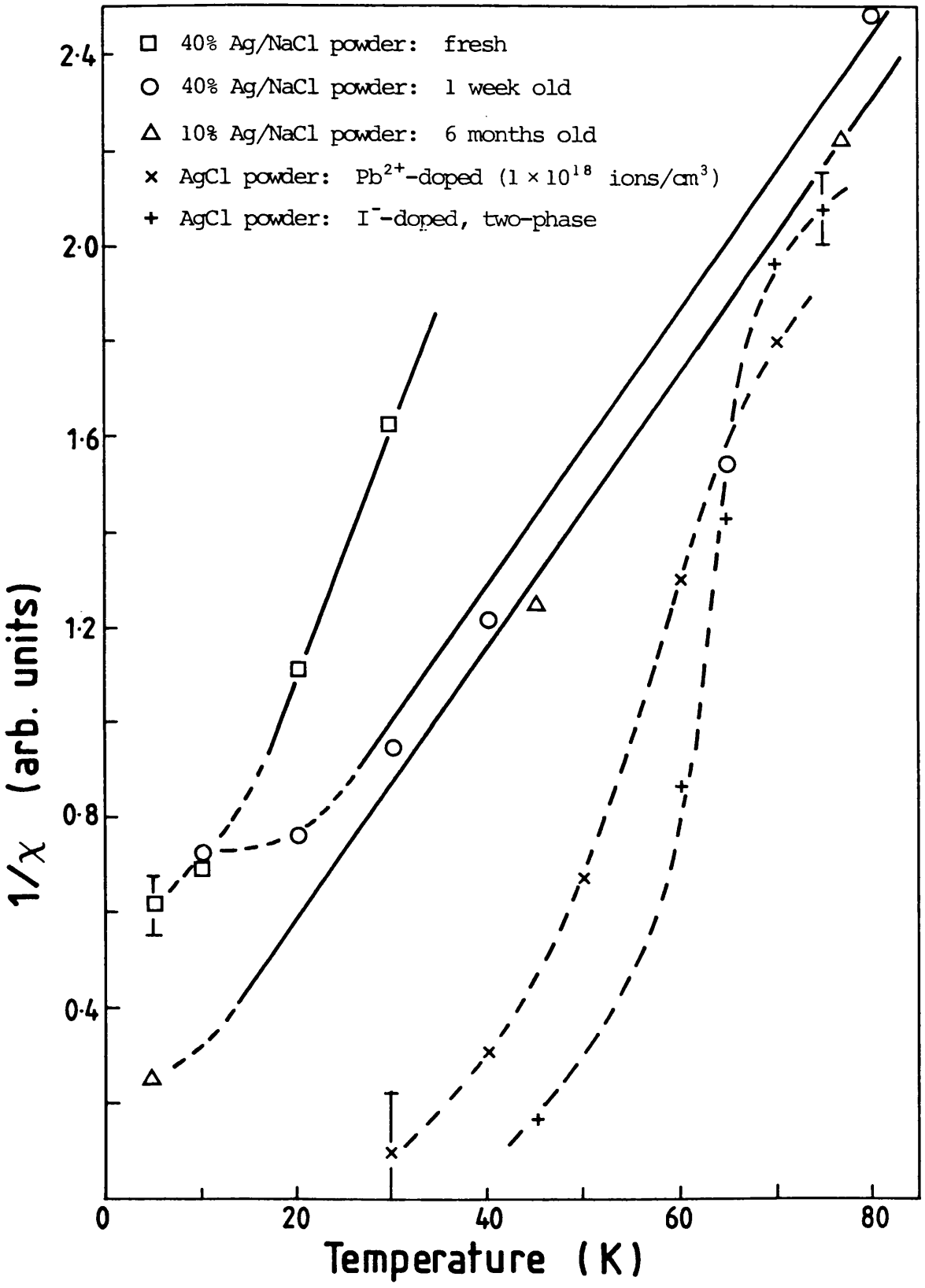

FIGURE 5

The temperature dependence of the inverse relative paramagnetic susceptibility (1/χ) of the CESR signal for several systems. The solid lines depict Curie law behaviour. The dashed lines are a guide for the eye. The 10% Ag/NaCl powder is included for comparison.

TABLE I

Relaxation Times for the CESR Line in Various Powders

	T_1 (sec)		T_2 (sec)		
Temperature:	45 K	77 K	4 K	45 K	77 K
System					
Pb^{2+}/AgCl (1×10^{18} ions/cm^3)		$(5 \pm 4) \times 10^{-6}$			$(5 \pm 1) \times 10^{-8}$
AgClI/AgCl					
light on	$(8 \pm 7) \times 10^{-7}$			$(5 \pm .5) \times 10^{-8}$	$(1 \pm .5) \times 10^{-7}$
light off	$(4 \pm 4) \times 10^{-7}$				
40% AgCl/NaCl - fresh		$(2.3 \pm 1.5) \times 10^{-6}$	$(1 \pm .3) \times 10^{-8}$	$(1.4 \pm .3) \times 10^{-8}$	$(1.5 \pm .3) \times 10^{-8}$

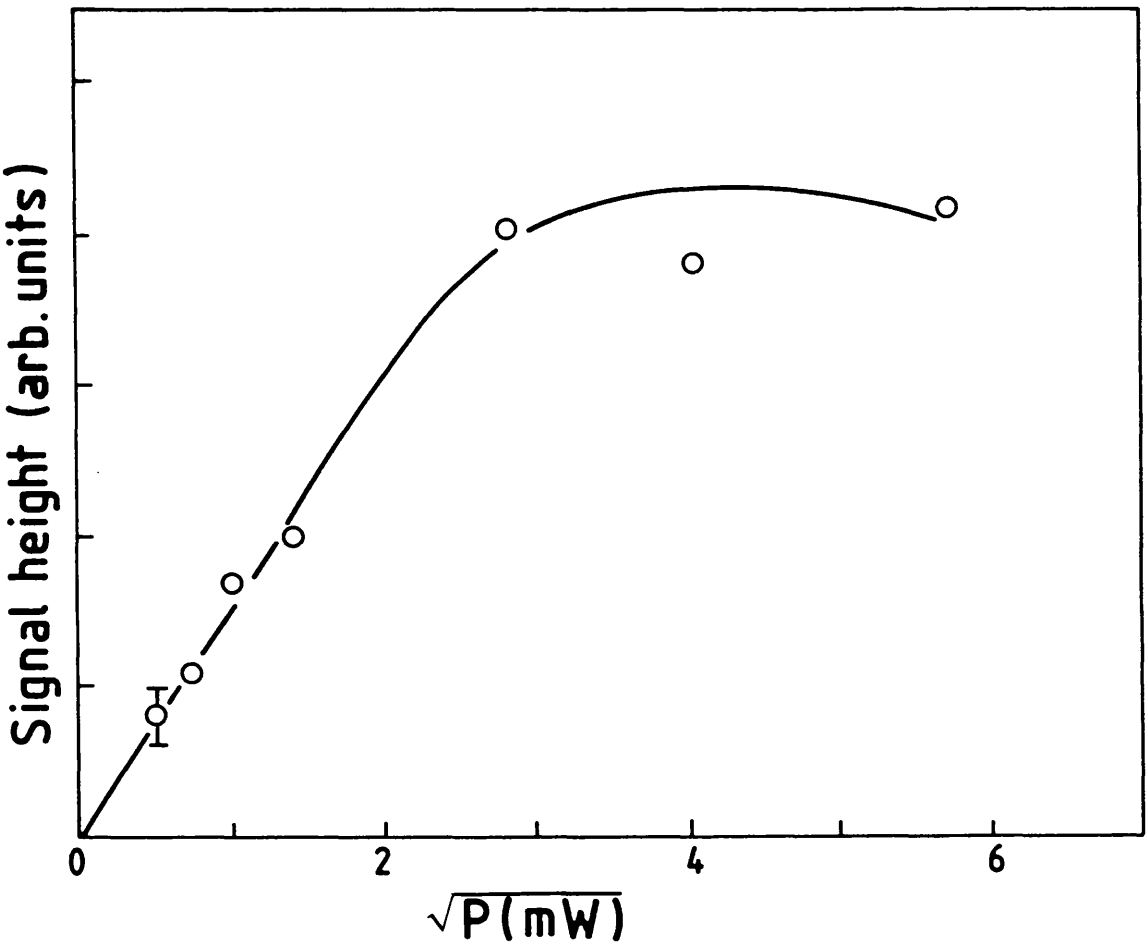

FIGURE 6

The power saturation behaviour of the CESR signal in a Pb^{2+}-doped AgCl powder (1×10^{18} ions/cm^3) at 77 K.

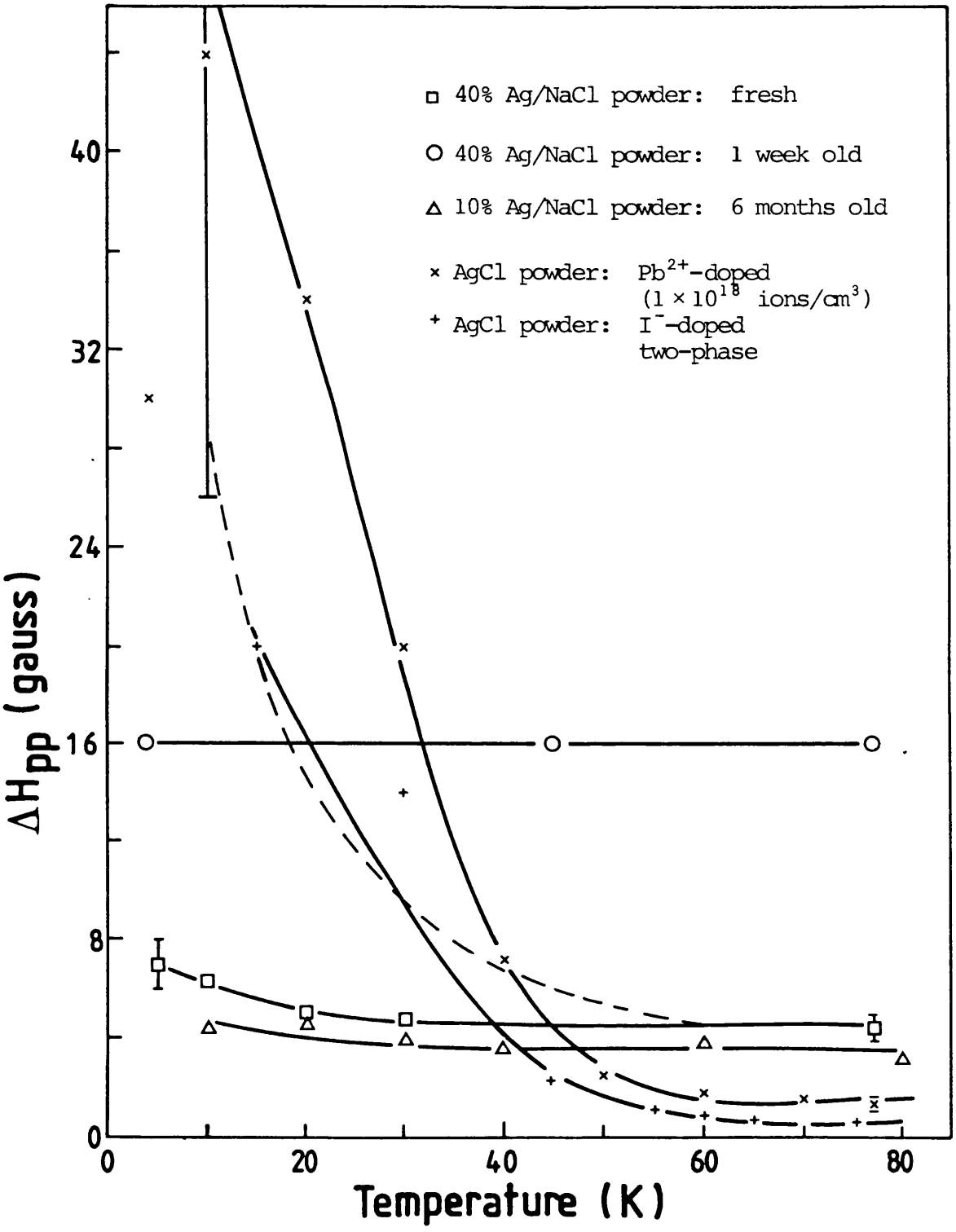

FIGURE 7

The CESR linewidth as a function of temperature. The solid lines are a guide for the eye. The dashed line is an example of a 1/T temperature dependence.

lower field with increasing microwave power, in the manner shown later in Figure 11 for 40% AgCl/NaCl powders. Within experimental error, g was found to be independent of temperature below 77 K. It did not shift during band gap exposure. In agreement with the more complete measurements described in reference 1, the g-value did not depend on Pb^{2+} concentration. In this study, careful g-value measurements were not made above 77 K; however, the earlier study reported that the CESR line shifted to lower field as the temperature was raised above about 100 K.[1]

The results obtained from the degelled I/AgCl emulsion with a 6% iodide phase were identical to those obtained from the emulsion containing an 11% phase. A CESR signal was observed at $g = 1.8785 \pm 0.0003$ following band gap irradiation. The signal was less stable then in the Pb^{2+}/AgCl system and began to decay at about 80 K. The line was approximately Lorentzian at low power levels (Figure 8b). It became asymmetric with increasing power (Figure 12), and the high field lobe was the broadest. As in the Pb^{2+}-doped powders, the CESR line shifted to lower field at high power levels (Figure 11). The temperature dependence of the paramagnetic susceptibility was very similar to that observed for Pb^{2+}-doped powders and is shown in Figure 5. The linewidth at 77 K was 0.70 gauss which corresponds to a T_2 of $(1 \pm .5) \times 10^{-7}$ sec. T_1, measured by the saturation method at 45 K, was $(8 \pm 7) \times 10^{-7}$ sec; T_2 at 45 K was $(5 \pm 0.5) \times 10^{-8}$ sec. Thus, T_1 and T_2 were not equal.

An additional narrow line was observed in the two-phase AgCl/AgClI emulsions following band gap excitation. This was much weaker than the CESR line and had a g-value of 1.8934 (Figure 8a). Its linewidth and temperature behaviour have not yet been thoroughly studied.

For the systems reported here, the CESR signal intensity reached a

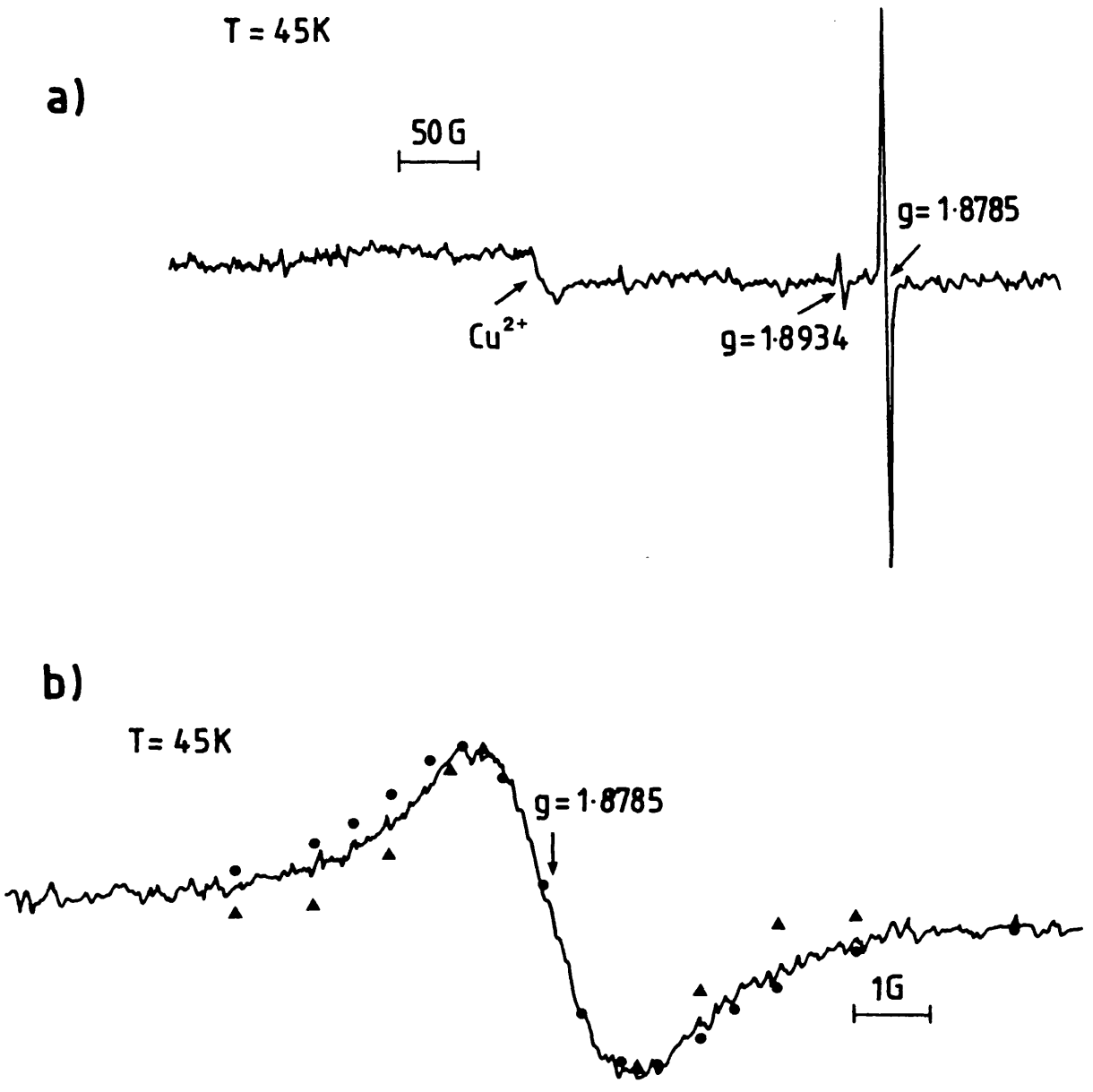

FIGURE 8

a) X-band ESR spectrum of a 3% I^- two-phase AgCl/AgClI degelled emulsion at 45 K after band gap excitation.
b) g = 1.8785 CESR line fitted to a Lorentzian (•) and a Gaussian (▲) lineshape.

maximum after several seconds of band gap exposure. Most of the measurements were made during irradiation. It was assumed that this resulted in a steady state population of conduction band electrons. Band gap irradiation did not affect the g-value of the CESR line. Likewise, at low power levels and at temperatures at which the CESR line was stable, band gap irradiation did not affect the CESR lineshape or intensity. However, at higher power levels, the linewidth increased and saturation was reached at slightly lower power levels with the light on (Figure 9). T_1, measured with the light off at 45 K in the iodide-doped emulsions, was $(4 \pm 4) \times 10^{-7}$ sec. These changes were small and did not affect the overall trend of the results reported here. Unless otherwise noted, all data reported here were measured during irradiation.

Although the CESR line did not change, a reversible shift of the cavity resonance frequency of +0.8 MHz was observed when the light was turned on. The AFC (automatic frequency control) lock stabilized essentially instantaneously when the light was turned on or off. This is in contrast to some samples studied previously.[2] In these samples measurements could not be made during irradiation because light so badly detuned the instrument. When the light was turned off the cavity frequency and Q reached equilibrium on a time scale of tens of seconds.

Qualitatively, the same results were observed in Pb^{2+}-doped AgBr powders as in AgCl. A g-value of $1.4870 \pm .0002$ was measured at low powers. The linewidth at 77 K was 0.7 gauss.

4.3.2 One-phase I^--doped and Br^--doped powders

No CESR signals were observed in the AgCl powders uniformly doped with iodide at 3 and 6% dopant levels. In the 1.2% I^--doped AgCl powder a weak single line was observed at $g = 1.8693$ following band gap exposure

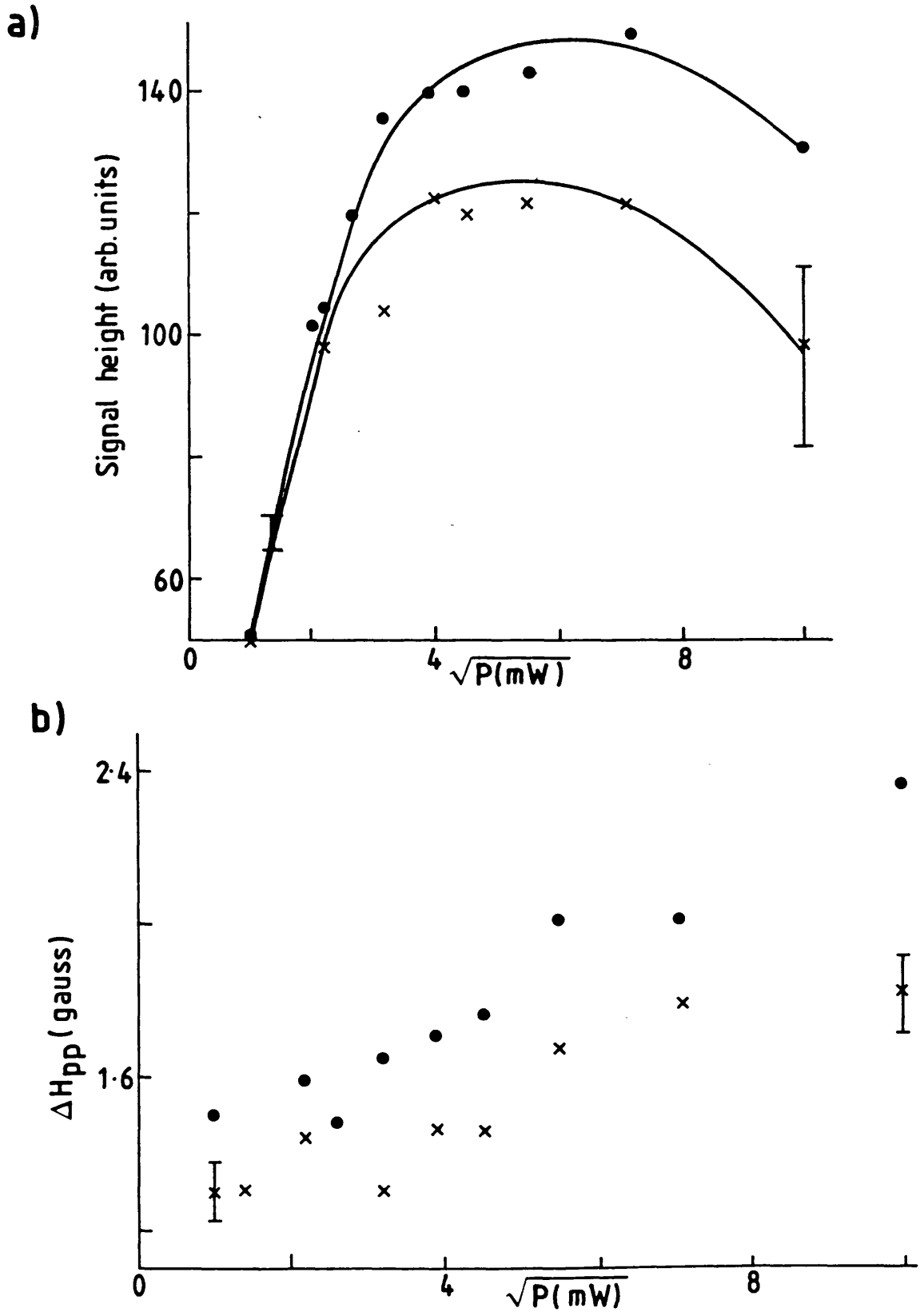

FIGURE 9

Signal height (a) and linewidth (b) of the CESR line as a function of microwave power in a 3% I^-, two-phase AgCl/AgClI degelled emulsion. [The dots and x's represent data measured at 45 K with the light on and off respectively.]

at low temperatures. The signal decayed irreversibly above 30 K. The signal was too weak for lineshape studies but had a linewidth less than one-half that of Pb^{2+}-doped AgCl powders and two phase I^-/AgCl emulsions at comparable temperatures.

No CESR signals were observed in Br^--doped AgCl powders at Br^- concentrations of 5% or greater. In the 1% Br^--doped AgCl sample a weak signal at $g = 1.878$ was observed at temperatures less than 30 K. The $(AgCl_5Br)^{4-}$ species was too broad to be detected. Once again, the line was too weak to permit lineshape analysis.

4.3.3 40% AgCl/NaCl powders

This concentration of silver was chosen as a representative example of the AgCl/NaCl mixed system. Variations within the system as a function of concentration have not yet been investigated.

The powders discussed here were γ-irradiated 30 minutes at 77 K. Thus, the asymmetric CESR line observed at low power levels and assigned to localized electrons (Chapter 3) is not discussed here.

The behaviour of the 40% AgCl/NaCl powder differed markedly from the systems just discussed in a number of aspects. The first of these was the CESR lineshape. The CESR line, which was observed after 30' γ-irradiation was asymmetric even at low power levels. In a fresh powder, the asymmetry ratio was 0.66. This falls within the error limits of the fairly constant A/B ratio of 0.64 ± 0.07, measured in fresh AgCl/NaCl powders over the concentration range of 30% to 80% (Table II). Each lobe could be fitted to a Gaussian lineshape (Figure 10a). In contrast to the asymmetric CESR line in the Pb^{2+}- and I^--doped powders, the linewidth was symmetric about the crossover point. As before, A/B decreased with increasing power. A minimum was reached at approximately that power where saturation of the line began to level off (Figures 12 and 13).

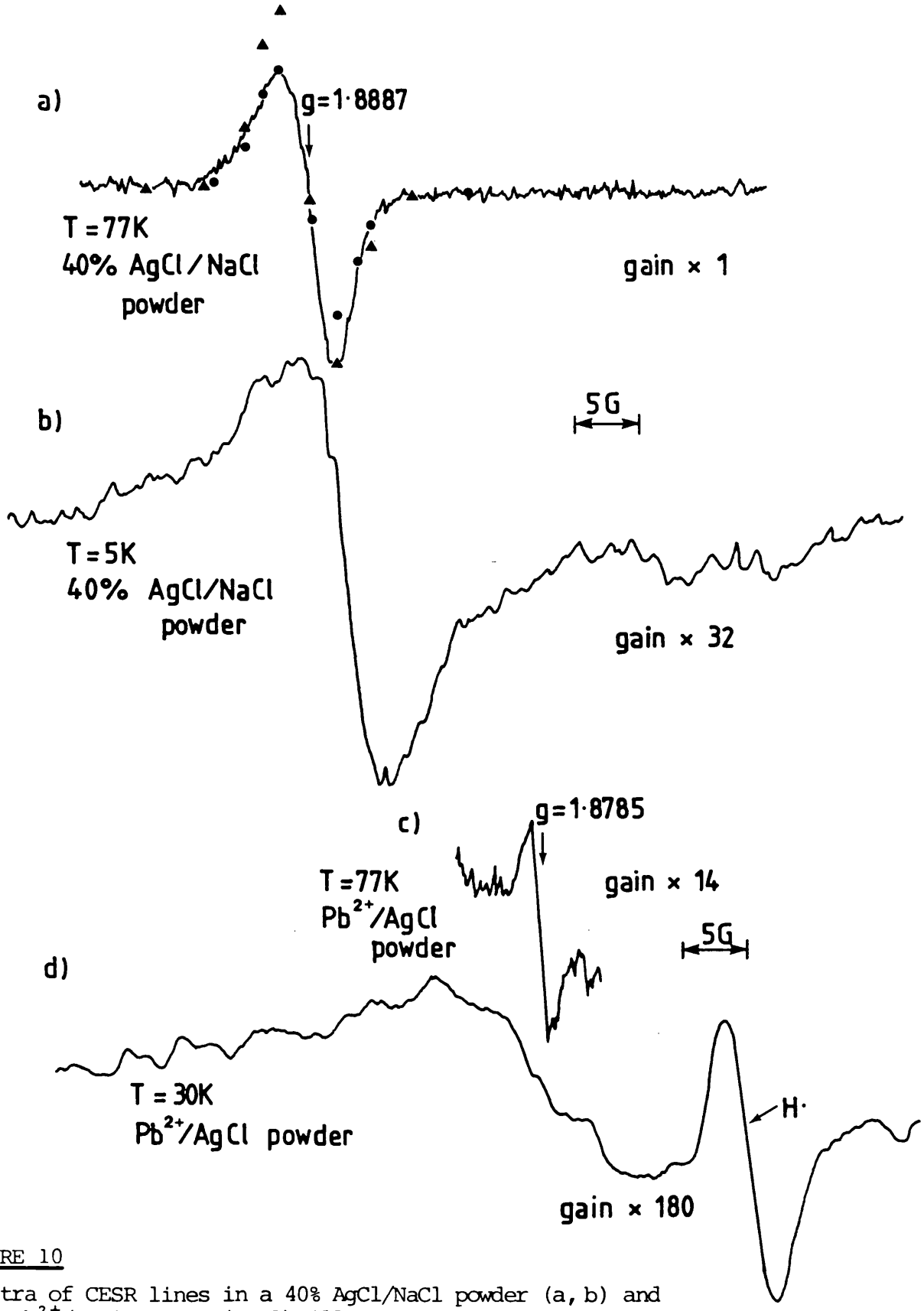

FIGURE 10

Spectra of CESR lines in a 40% AgCl/NaCl powder (a, b) and in a Pb^{2+}/AgCl powder (c, d) illustrating the increase in linewidth with decreasing temperature. [The dots and triangles in (a) are the calculated points of a Gaussian line, fitted to the positive and negative lobes respectively.]

FIGURE 11

The g-value of the CESR line in a 40% Ag/NaCl fresh powder as a function of microwave power. The g-value was measured at the crossover point (•) and midpoint (×) of the CESR line.

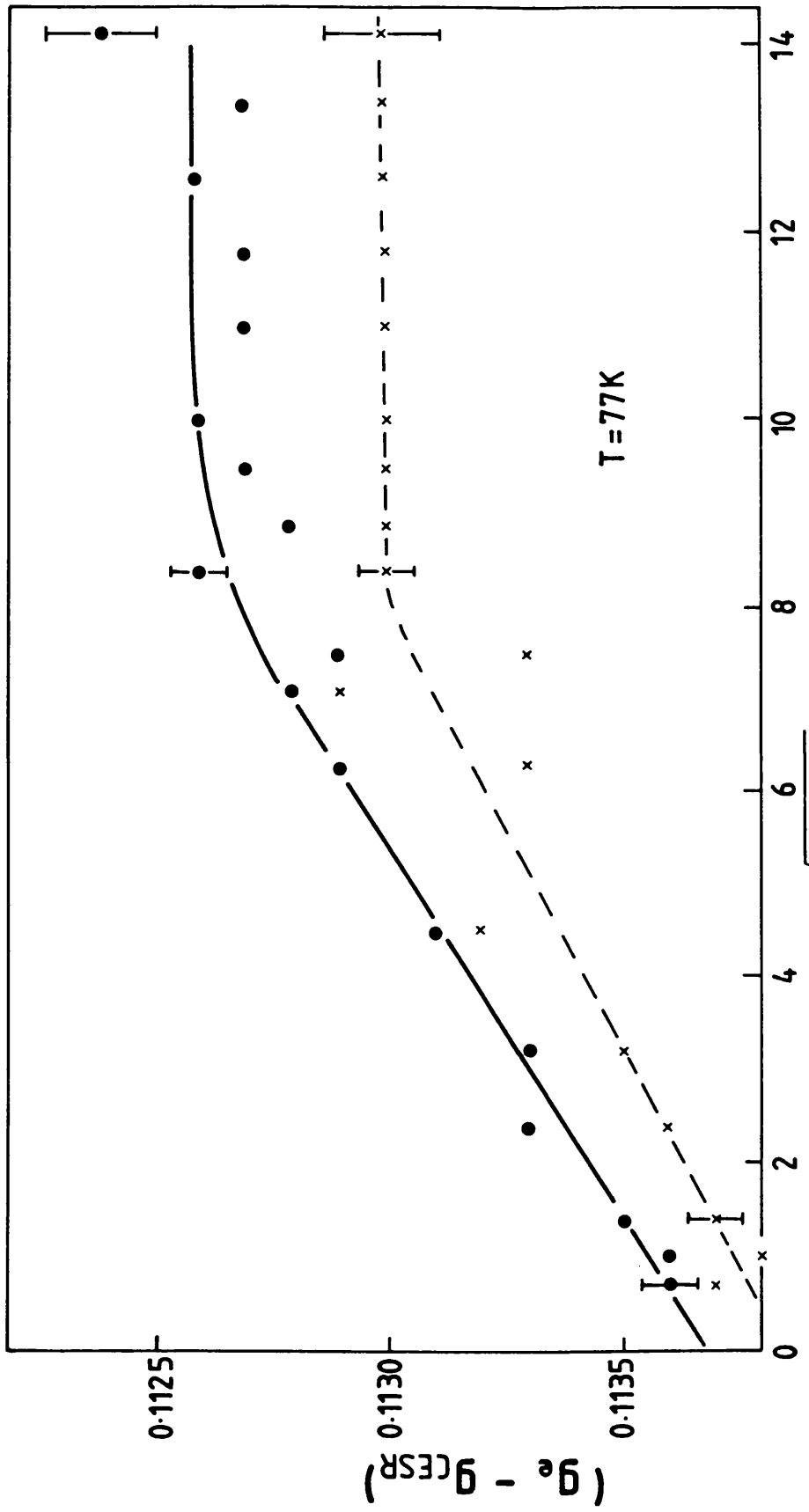

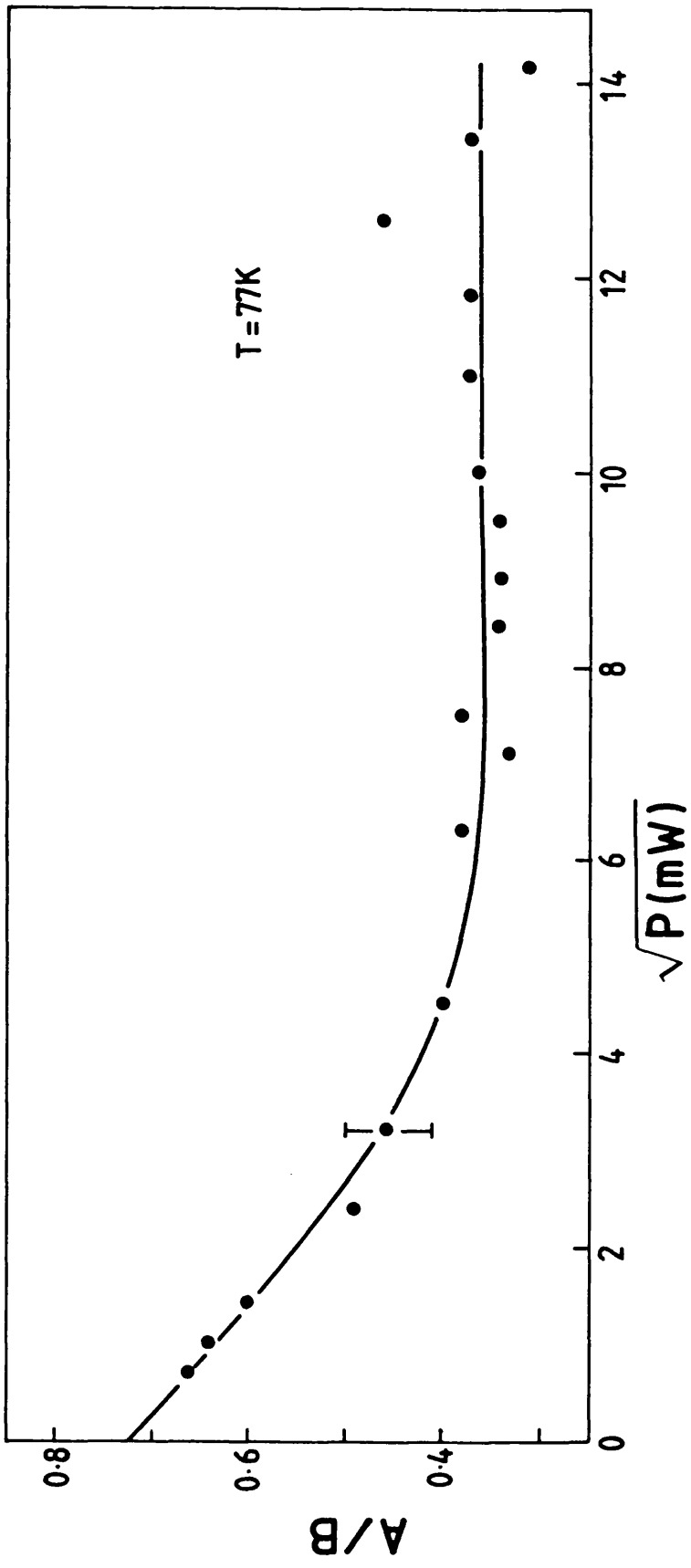

FIGURE 12

The asymmetry ratio A/B of the CESR line in a fresh 40% Ag/NaCl powder as a function of microwave power.

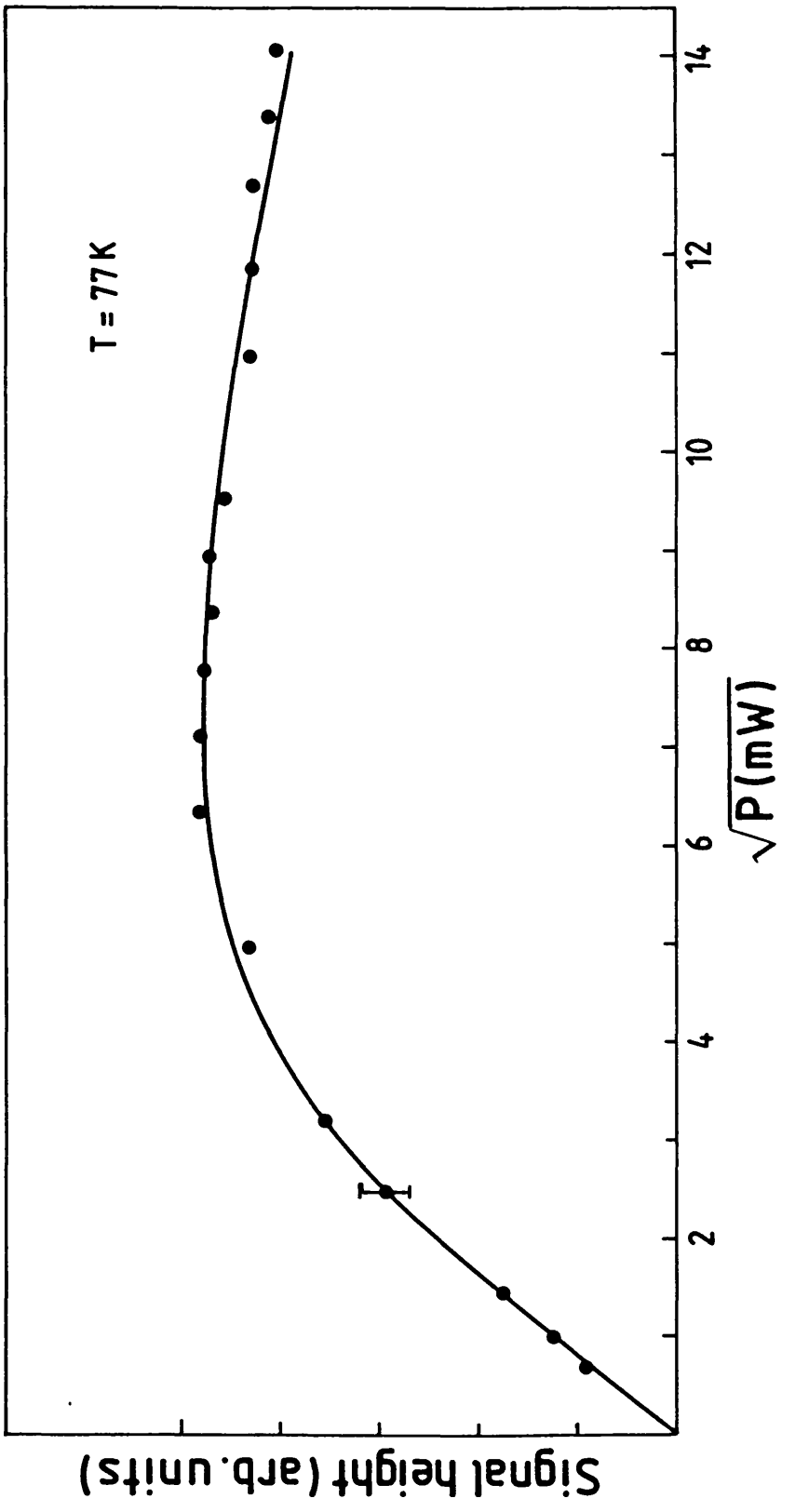

FIGURE 13

The power saturation behaviour of the CESR signal in a fresh 40% AgCl/NaCl powder at 77 K.

The CESR line was broader than those described above, with a linewidth at 77 K of 4.5 gauss. The linewidth was independent of temperature down to 20 K where it began to broaden slightly with decreasing temperature (Figure 7). The contrast with the temperature dependence of the Pb^{2+}/AgCl CESR line is emphasized by Figure 10.

The temperature dependence of the relative paramagnetic susceptibility was also qualitatively different from the Pb^{2+}/AgCl or two-phase AgCl/AgClI emulsion. This is shown in Figure 5. The relative paramagnetic susceptibility was inversely proportional to temperature, decreasing with increasing temperature up to 160 K, where the signal decayed irreversibly.

The g-value of the CESR line was 1.8887 ± .0002 for the 40% AgCl/NaCl powders on which lineshape measurements were made. The error limits refer to variations from the average of g-values measured for different 40% AgCl/NaCl powders which were prepared from the same 40% mixture of AgCl and NaCl, but quenched from the melt, ground up, γ-irradiated and measured at different times. The error includes the errors incurred in the g-value measurement as well as those which might have resulted from differences between the samples. Typical variations in the ESR parameters of the CESR line for 40% AgCl/NaCl powders prepared from the same batch material are shown in Table II. ESR parameters measured for the CESR line in different 40% AgCl/NaCl batches are also listed in Table II, showing that the variation in g rises to ± .0005 between batches. The ESR parameters for the CESR line for a series of 30%-80% AgCl/NaCl powders are included in Table II. The average g-value over the entire concentration range was 1.8882 ± .0010. There seems to be a trend to lower g-values at high silver concentrations but a larger series of measurements are needed before it is possible to tell if this trend

TABLE II

Linewidths, g-values and A/B of the CESR Line in Fresh AgCl/NaCl Powders

ESR Parameters for:

same Ag% and same material batch †,*			same Ag% and different batches *			different Ag% *			
g	ΔH_{pp} (G)	A/B	g	ΔH_{pp} (G)	A/B	% Ag	g	ΔH_{pp} (G)	A/B
1.8881	3.8	.72	1.8892	4.9	.66	30	1.8883	4.3	.55
1.8881	3.5	.84	1.8882	3.6	.75	40	1.8892	4.9	.66
1.8884	3.6	.64	1.8887	4.5	.63	50	1.8884	4.3	.54
						60	1.8876	3.9	.77
1.8882 ± .0002	3.6 ± .2	.75 ± .10	1.8887 ± .0005	4.3 ± .6	.68 ± .05	70	1.8881	4.0	.69
						80	1.8878	3.6	.64
							1.8882 ± .0010	4.2 ± .7	.64 ± .12

† For these measurements, the same 40% Ag/NaCl source mixture was used but for each measurement a new sample was quenched, ground-up and irradiated.

* Irradiation time = 30 minutes.

is outside experimental error.

The variation in g-value within each 40% AgCl/NaCl batch was approximately the same as the variations in g-value measured for each of the AgCl systems discussed above and thus, most probably arises from measurement errors. The same trends in g-value with power and temperature were observed as were described above. The g-value increased with power to a maximum value which was attained after the saturating power was reached. The g-value shift does not seem to be the result of a lineshape change since both the crossover and midpoint of the line shifted with power (Figure 11). A small variation was observed in g with changing temperature. The g-value shifted from 1.8869 at 20 K or below to 1.8887 at 77 K. The g-value continued to shift to higher values with increasing temperature until the CESR line decayed irreversibly at ~160 K.

Following the formation of the CESR signal, a -3 MHz shift of the resonance frequency of the filled cavity was measured.

γ-Irradiated 40% Ag/NaCl single crystals were bronze coloured. A Dysonian lineshape was observed in those samples which had been irradiated long enough for the skin depth to exceed the sample dimensions. The ratio A/B increased with irradiation time until the sample was so lossy that measurements could not be made. A/B was fairly independent of temperature above 77 K. Below 77 K,A/B approached unity with decreasing temperature. At present, the 40% Ag/NaCl system is not well characterized; the conductivity T_2 and T_D as a function of temperature are unknown. Thus, in order to determine T_2/T_D and d/δ for lineshape analysis, as described in Chapter 2, attempts were made to measure $(A/B)_{max}$. The maximum value of A/B which could be observed was ~7. This is less than $(A/B)_{max}$ for $T_2/T_D = \infty$ and large d/δ, (see Figure 2.4),

which made a quantitative analysis impossible. As for powder samples, in certain crystals several CESR lines were detected. The linewidths varied with the age and thermal history of the sample but tended to be much smaller than in the powders. The narrowest lines detected were .1-.2 gauss wide.

As mentioned in Chapter 3, the g-value and linewidth of the CESR line produced after γ-irradiation were strongly dependent on the age of the sample. Over the period of 1-7 days, the CESR signal broadened in the wings, becoming more Lorentzian in character and the overall linewidth increased. After annealing to a temperature which allowed the decay of some of the CESR signal intensity, up to three CESR lines could be resolved, depending on the sample. In a given sample, the linewidth of each CESR line was directly proportional to $(\Delta g)^2$, as shown in Figure 14. Over longer periods of time, the linewidth narrowed again and only a single, nearly Lorentzian line at $g \approx 1.886$ was observed. This behaviour was qualitatively the same for 30% Ag/NaCl to 80% Ag/NaCl powders.

4.4 Discussion

4.4.1 Pb^{2+}-doped AgCl powders and two-phase AgCl/AgClI emulsions

The observation of a Lorentzian lineshape at low powers in both of these systems suggests that the CESR line was homogeneously broadened. Thus, the CESR line most likely arises from a single type of mobile electron and T_2 can be extracted from the linewidth. Since $T_1 \neq T_2$, the variation of linewidth with temperature cannot be understood in terms of the spin-lattice relaxation methods discussed in Chapter 2. The inequality of T_1 and T_2 points to a breakdown in motional narrowing. The AgCl lattice is isotropic so the inequality of the longitudinal and transverse relaxation times is not a result of low crystal symmetry.

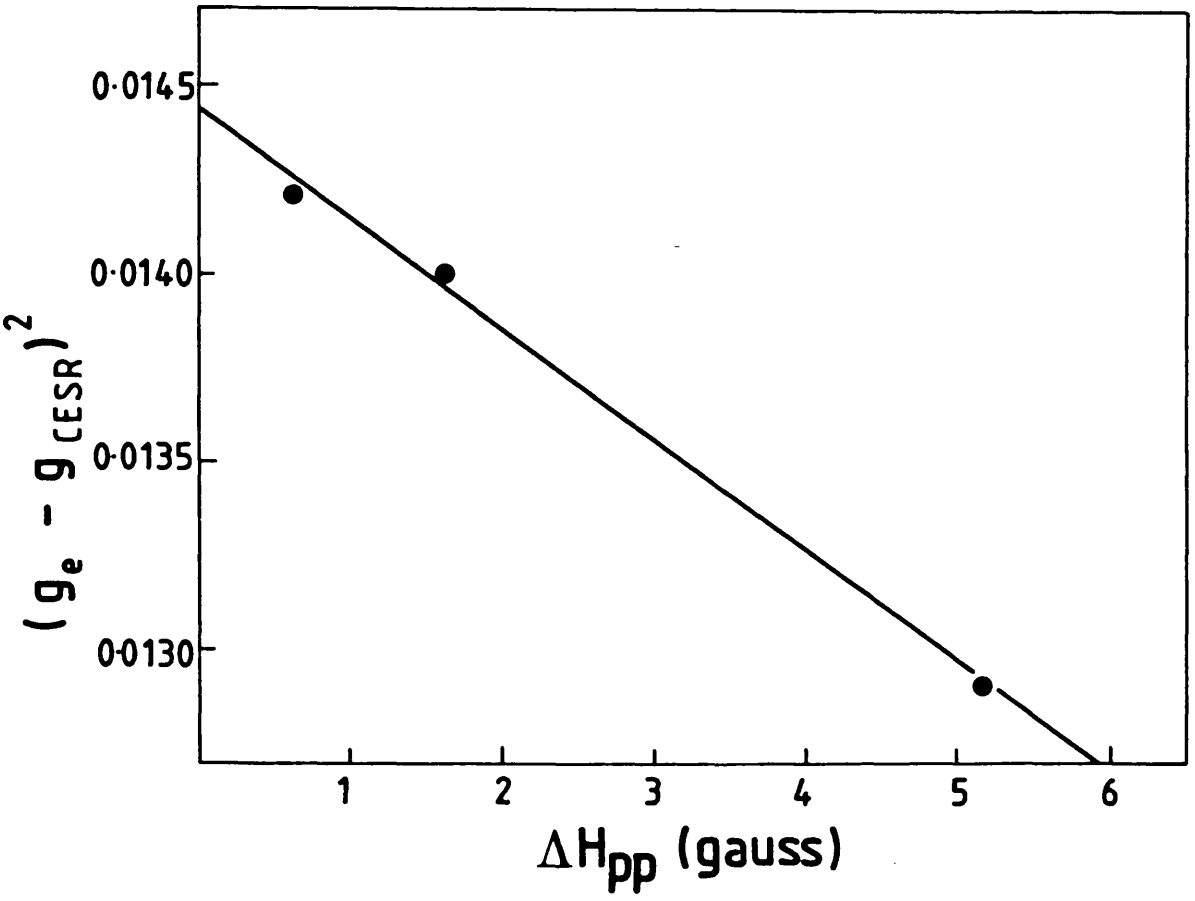

FIGURE 14

Plot of Δg^2 vs ΔH_{pp} for the CESR lines in a 1 day old 40% Ag/NaCl powder. T = 77 K.

Rather, the motion of the electron is not sufficiently rapid to average out spin-spin interactions.[23]

Since T_1 was much greater than T_2 at 45 K and 77 K (Table I), the CESR linewidth for both the Pb^{2+}-doped powders and I^--doped emulsions was determined entirely by T_2^*, the spin-spin relaxation time. One might speculate that the relevant spin-spin interactions will be those that most often give rise to homogeneous broadening for localized spins in solids, namely, electron spin - electron spin dipolar interactions, and electron spin - nuclear spin dipolar interactions.[24] It has been estimated that at electron concentrations of 2×10^{18} cm^{-3} in P:Si that the former interactions are negligible and it is likely that the same is true of the systems under consideration here.[25,26] The spin-spin interactions are therefore assumed to arise from the fluctuating anisotropic hyperfine fields experienced by the mobile electron. Since $T_1 \gg T_2$, and thus $\omega_o \tau \gg 1$, the longitudinal relaxation rate is given by:[22]

$$\frac{1}{T_2} \approx \gamma^2 \langle H_z^2 \rangle \tau_c = \frac{1}{T_2^*} \qquad \ldots. (2)$$

where γ is the electronic gyromagnetic ratio; ω_o is the Larmor precession frequency and τ_c is the correlation time of the mobile electron. This is inversely proportional to the mobility of the electron. Thus, as the mobility of the electron decreases, the linewidth increases, eventually reaching a maximum determined by the homogeneous line broadening interactions of a localized spin in the solid.[27] If inhomogeneous hyperfine broadening occurs for the localized spin, then this will become a source of broadening for the CESR line as motional narrowing breaks down:[26]

$$(\Delta H_{pp})_{inhomogeneous} \propto \tau_c \qquad \ldots. (3)$$

For conduction electrons in the silver halides, the mobility increases with decreasing temperature, as phonon scattering is reduced, and then

levels off at a maximum determined by sample purity.[28] In nominally pure samples this maximum occurs around 40 K.[28] Thus, if the CESR line were due to conduction electrons on the metallic side of the metal-insulator transition in either the conduction band or an impurity band, according to equations 2 and 3 the linewidth would decrease with temperature to a minimum value and then remain constant. This case, then, does not pertain. The narrow CESR line observed at high temperatures must arise from electrons excited from shallow traps or the lower Hubbard band to levels above the mobility edge. This process is thermally activated and the mobility is trap limited, increasing with temperature until at a sufficiently high temperature it is determined by the mobility at the mobility edge. This temperature is ~60 K for the Pb^{2+}-doped and two-phase I^--doped systems. If the impurity ions are close enough for the system to be near a Mott-type transition, then the mobility at the mobility edge should <u>increase</u> with decreasing temperature.[29,30] This occurs when $\varepsilon_2 < \varepsilon_1$ (Figure 1b). When $\varepsilon_2 \approx \varepsilon_1$, so that thermal excitation places the electron in the conduction band, then the mobility is that of the conduction band. In this case it is independent of temperature as a result of impurity scattering. The mobility is apparently too low to average out spin-spin interactions and $T_1 \gg T_2$. Below 60 K, the CESR line broadened as the mobility decreased and motional narrowing became less complete. Also, at some temperature below 60 K the spins may become localized and the line broadening could occur via incomplete exchange narrowing between localized spins. This would occur according to the relation[31]

$$\Delta H_{\frac{1}{2}} \approx \omega_a^2 \, (\gamma_e \, \omega_e)^{-1} \qquad \ldots\ (4)$$

where ω_a is the frequency of the interaction that must be narrowed, and ω_e is a temperature dependent exchange frequency. Either or both of

these mechanisms have been suggested to account for the observed line broadening in insulating P:Si.[26,32] Broadening occurred below 10-20 K, at the lower temperature in more heavily doped samples.[32]

Thus, in these Pb^{2+}-doped powders as well as in the two-phase emulsions, the linewidth behaviour indicated that it is not possible to raise the Fermi level high enough by injection of photoelectrons, for an Anderson-type metal-insulator transition to occur. Most likely, the level of stable photoelectrons is limited by the concentration of hole traps or shallow electron traps. In addition, the mobility temperature dependence deduced from the linewidth suggests that $\varepsilon_2 \approx \varepsilon_1$ and thus, that impurity levels were not closely enough spaced for a Mott-type transition to occur.

The suggestion that $\varepsilon_2 \approx \varepsilon_1$ leads to a paradox. If electrons are excited above a mobility edge in impurity-associated upper Hubbard band (Figure 1) then the extended electron lifetime can be attributed to the fact that this band is localized in space at impurity (or defect) levels. If, however, the electron is excited directly from the lower Hubbard band into the conduction band, it should be able to move freely through the grain and recombine at trapped hole sites. Thus, one must postulate that the mobility is very low because of impurity scattering, so that the electron does not sample the entire grain, or that there is a potential barrier between the impurity-rich and "pure" regions of the grain. The latter suggestion seems more reasonable.

The temperature dependence of the paramagnetic susceptibility was roughly similar for Pb^{2+}-doped powders and I^--doped emulsions. Below 80 K, $1/\chi$ approximately varied as T^4, becoming less dependent on temperature above 80 K and below 40 K. This temperature dependence is much greater than that expected for localized spins or for either a

non-degenerate[33] or degenerate electron gas.[34] It is also greater than the decrease in susceptibility that might be expected for an array of antiferromagnets which become non-aligned above the Neel temperature.[15] The temperature dependence differs radically from that observed in either insulating or metallic P:Si.[26,32,35] At present no explanation can be put forward. A better understanding of the behaviour might be obtained by extrapolating quantitative susceptibility measurements to low and to high temperatures.

The magnitude and direction of the frequency shift of the cavity resonance which was observed upon turning off the UV lamp were consistent with the decay of free conduction electrons.[5] Since the CESR signal did not change in intensity when the light was turned on or off at low microwave powers it can be concluded that these free electrons did not contribute to the CESR resonance. The lifetimes of the electrons were apparently too short to be detected in the ESR experiment. The free electrons shortened both T_1 and T_2 in the iodide-doped emulsions at 45 K. A similar effect by photoelectrons has been observed for localized spins in P:Si.[36] Thus, this suggests that at 45 K the spins contributing to the CESR signal were localized to some extent. It would be useful to extrapolate these measurements above 60 K where the lineshape studies indicated that the electrons were thermally excited above a mobility edge. Electron-electron interactions are expected to be less important for such free electrons.

Thus, above ~60 K, it is suggested that the CESR line results from electrons excited from shallow traps. Below that temperature, the electrons move by thermally activated hopping and the mobility decreases with temperature so that line broadening interactions are no longer broadened out and/or the electrons become localized and exchange

broadening becomes important. In the Pb^{2+}-doped powders, the shallow traps are the Pb^{2+} surface states discussed in the Introduction. In the iodide-doped emulsions it is suggested that the traps are either intrinsic traps or are structural defects introduced by iodide-doping. Iodide-doping is thought to result in high internal disorder.[37] Localization might also occur at the interface of the two phases as the result of Schottky barrier formation or high defect densities. If intrinsic sites are responsible for the lifetime extension then it must be proposed that these are physically separated from the photoholes, since no lifetime extension is observed in pure samples. It is reasonable to propose that hole trapping occurs in the iodide-doped phase.[31] The CESR g-value indicates that the mobile electron is confined to the pure AgCl phase.

The existence of impurity conduction in the lower Hubbard band, in addition to the thermally activated conduction band process, was postulated in the Introduction. This model explained the microwave photoconductivity and photodielectric data as well as the two component decay of the CESR signal. The long decays of the CESR line and the microwave photoconductivity signal as well as the photodielectric shift were attributed to shallowly trapped electrons in the lower Hubbard band. One would expect such electrons to have a lower mobility and possibly a different g-value from conduction band electrons. Such differences were not discernible in the linewidth and lineshape studies of the CESR line. In addition, there was no evidence of shallowly trapped electrons above 60 K. It is possible that such centres would give rise to a very broad undetectable resonance signal, as at temperatures less than 20 K. This, however, contradicts the suggestion that such centres are responsible for the long decay component of the

CESR line. Further correlated microwave and ESR studies are required to clarify this situation.

In Pb^{2+}-doped AgBr powders, pre-exposure by sub-band gap light enhanced the microwave photoconductive response observed on subsequent band gap exposure.[39] The effects of sub-band gap radiation indicated the presence that a Pb-associated trap ~0.5 eV below the conduction band edge. It was suggested that this might be associated with bulk or interstitial Pb^{2+} ions, or with spin orbit split 6p Pb^{2+} levels.[39] Alternatively, these deep levels might correspond to the lower Hubbard band, i.e. filled Pb^{2+} traps. Then, the observed conductivity would occur in the upper Hubbard band, associated with Pb° states, with localization occurring in band tails. It would be interesting to determine the effects of sub-band gap light in Pb^{2+}-doped AgCl in order to test this hypothesis.

The second narrow line observed in the iodide-doped emulsion cannot be assigned on the basis of existing data. The g-value suggests localization at a deeper "shallow" trap where spin-orbit interactions with the donor ion more important than for the major CESR line. However, it does not seem likely that any iodide-associated defects would act as an electron trap.

4.4.2 One-phase I^--doped and Br^--doped powders

One question raised by the Pb^{2+}-doped and I^--doped, two-phase systems is whether the shallow traps provided by impurities must be physically separated from the region of the grain where hold trapping occurs in order for the lifetime of the electron lifetime to be extended. The extended electron lifetime might result solely from a lower mobility of the electron in the impurity band which reduces the likelihood of the electron reaching a recombination centre. The failure to observe a CESR

signal in AgCl powders uniformly doped with 3% and 6% iodide indicates that some degree of phase separation is necessary.

At present there is insufficient data to determine whether the CESR signals observed in powders doped uniformly with low levels of Br^- or I^- are due to localized or free electrons. The reduced linewidth at low temperatures compared to the Pb^{2+}-doped and two-phase systems could result from a greater separation of localized electrons which would reduce exchange broadening. This would be consistent with the weak signal intensity observed and the expectation that the electrons giving rise to the CESR signal are distributed uniformly throughout the grain. The reduced linewidth might also result from a free conduction electron which would give rise to a narrower CESR line through motional narrowing. The extended electron lifetime might arise from the charge separation resulting from electrons localized at intrinsic shallow traps and holes localized at widely separated Br^- or I^--associated traps. Holes trapped at Ag^+ ions associated with bromide are more stable than the self-trapped hole in AgCl.[40] The latter are not stable above 2 K in pure AgCl while the bromide-associated holes were stable up to ~60 K. Thus, the decay of the CESR signal at ~30 K would be associated with the thermalization of the shallowly trapped electrons followed by recombination at trapped holes. If the CESR signal results from free electrons then one must postulate a small capture cross-section of iodide- and bromide-associated holes for electrons. The CESR line seemed rather broad for a conduction electron and on the basis of the present data it seems more plausible that the CESR line arises from shallowly trapped electrons. This model explains the decrease in the stability of the CESR signal with increasing Br^- or I^- concentration since the electron and hole trapped species are only spatially separated at low concentrations.

If this model holds, it implies that the broad linewidth observed for Pb^{2+}-doped and two-phase I^--doped powders at temperatures less than 30 K must result in part from exchange interactions, since at equivalent temperatures widely separated, localized electrons in one-phase I^- and Br^--doped powders gave rise to narrower lines. Concurrent ESR and microwave photoconductivity measurements would help to clarify the situation. It would also be useful to compare the lifetimes of localized electrons as measured by transient absorption spectroscopy in pure AgCl and Br^--doped AgCl.[4] Further lineshape studies comparing relaxation mechanisms in Br^--doped AgCl powders and single crystals would be interesting and would be facilitated by improved sample purity.

4.4.3 40% AgCl/NaCl powders

It is tempting to use the observation of a Dysonian line with $A/B > 2.7$ in 40% AgCl/NaCl single crystals as justification for assigning the CESR line in 40% AgCl/NaCl powders and single crystals to delocalized electrons. However, in powders and at low electron concentrations in crystals, the CESR line was not perfectly Lorentzian suggesting that a number of components contributed to the Dysonian line. For some distributions of g-values (but not for a Lorentzian or Gaussian distribution) this can result in a Dysonian lineshape with $A/B > 2.7$ for localized spins.[41] Thus, the strongest evidence for the delocalization of spins in these samples is the disappearance of the broad line C and the appearance of a narrow CESR line, presumably as the result of motional narrowing, at a silver concentration corresponding to the percolation threshold, and the dependence of the observation of a Dysonian lineshape on the size of the crystal.

The temperature dependences of the CESR linewidth and intensity were

analysed to see if they were consistent with this picture and to determine if localization of spins occurred at low temperature. For this analysis it is helpful to make a rough estimate of the electron concentration in the samples used. For a .02 cm thick crystal the onset of the Dysonian lineshape at 77 K was observed after 5 minutes of γ-irradiation. Thus, at this electron concentration the skin depth was 0.005 cm and corresponding to a conductivity of approximately 100 $(\text{ohm-cm})^{-1}$. Assuming the electron mobility is the same as in pure AgCl this corresponds to an electron level of $\sim 3.5 \times 10^{18}$ cm^{-3}. The signal intensity increased linearly with irradiation time up to 30', so in the powders studied here the electron concentration could be as high as 2×10^{19} cm^{-3}. It is also useful to calculate the degeneracy temperature according to the equation[42]

$$T_F = \frac{\hbar^2}{2m} (3\pi^2 n)^{2/3} \frac{1}{k_B} \qquad \ldots\ (5)$$

An electron concentration of 1×10^{17} cm^{-3} corresponds to a degeneracy temperature of 10 K; an electron concentration of 2×10^{19} results in a degeneracy temperature near room temperature.

The CESR line in powders was asymmetric ($A/B < 1$) and approximately Gaussian. The origin of the asymmetry is discussed further below; the Gaussian lineshape indicates that the line was inhomogeneously broadened. If the CESR line arises from free electrons, which, as discussed above, is a reasonable assumption at 77 K, then it is unlikely to be broadened by hyperfine interactions. Rather, it must be broadened by a distribution of g-values. The linewidth of the inhomogeneously broadened line with "relaxation time" T_2' can be related to the true linewidth and relaxation time:[22]

$$\Delta H_{pp}' = \left(\frac{T_2}{T_2'}\right) \Delta H_{pp} \qquad \ldots\ (6)$$

Thus, the temperature dependence of $\Delta H'_{pp}$ gives a qualitative indication of the temperature dependence of T_2. T_2' was independent of temperature down to 20 K, below which some line broadening was observed. If T_2 is governed by spin-spin interactions, as for the Pb-doped powders, then the model proposed for Pb-doped powders applies here, with the critical temperature for the onset of hyperfine or exchange broadening interactions being 10 K rather than 60 K.

T_1 was measured at low powers by the saturation method described by Poole.[22] This has been shown to be valid for inhomogeneously broadened lines where $\Delta H' \gg \Delta H$.[43] Assuming that this condition holds, at 77 K, T_1 was 1×10^{-7} sec. If $T_1 = T_2$, this yields a linewidth of 0.35 gauss and the assumption that $\Delta H'_{pp}$ (= 4.5 gauss) $\gg \Delta H_{pp}$ would probably just be valid. If spin-spin interactions are important, $T_1 > T_2$ and the assumption is probably not valid.

If T_1 does equal T_2 then, of the spin-lattice relaxation mechanisms discussed in Chapter 2, only impurity scattering (equation 2.25) and surface scattering (equation 2.27) result in a temperature independent linewidth. This is consistent with the fact that the linewidth calculated assuming that phonon scattering is the dominant relaxation pathway at 77 K, and using parameters for AgCl, is 50 times less than the measured linewidth. The linewidths calculated assuming that surface scattering is the dominant relaxation mechanism overestimate both the measured linewidth and the proposed "true" linewidth of 0.35 gauss. For a particle diameter of 1-2 microns with $n = 2 \times 10^{19}$ cm^{-3}, a linewidth of 16-32 gauss is calculated. This reduces to 2-3 gauss if $n = 1 \times 10^{17}$ cm^{-3}.

The fact that the g-shifts observed in older samples fitted the proportionality $1/\Delta g^2 \propto \Delta H$ implies that impurity scattering was the dominant relaxation mechanism. As discussed in Chapter 2, ordinarily

$\Delta g^2 \propto \Delta H$. The observed dependence can be understood if the change is attributed to the separation of an increasingly AgCl-like phase. Thus, the g-value moved to high fields, toward the pure AgCl g-value, and the linewidth decreased as the AgCl phase became more pure.

Thus, the true linewidth was less than ΔH_{pp} and was broadened by impurity scattering. The differing components giving rise to the line-with width ΔH_{pp} probably arose from slight compositional and structural differences between grains of the percolated AgCl cluster. This view is supported by the fact that much narrower lines, of approximately the same linewidth as the estimated "true" linewidth for powders, were observed in single crystals. It has been suggested that only one percolated cluster 1 per grain exists,[44] so the Gaussian lineshape cannot be attributed to the existence of inequivalent clusters in the same grain. With time, the intergrain differences decreased as the system phase-separated, approaching an equilibrium composition. With fewer different components, the CESR line became more Lorentzian. The g-value changes are consistent with the formation of a NaCl-rich phase and the AgCl-rich phase. Eventually the meta-stable solid solution is expected to separate into two stable phases of 15% Ag/NaCl and 85% Ag/NaCl.[45] The former phase is below the percolation threshold, thus, in the oldest samples only a single CESR line was observed, presumably from the 85% Ag/NaCl phase. The intermediate phases in the ageing process would be expected to vary according to the composition and thermal history of the sample, as was observed.

As described in Chapter 3, the 40% Ag/NaCl single crystals were already "aged" when freshly grown. The CESR line was more nearly Lorentzian than in fresh powders but, in some cases, could still be resolved into several components. The failure to fit the observed line

to a Dysonian lineshape, as described in Chapter 2, is thus attributed to the existence of a number of phases in the crystal and several overlapping CESR lines.

Below 20 K, the CESR line begin to broaden with decreasing temperature. As in the Pb^{2+}-doped AgCl system this is probably due to incomplete averaging of hyperfine interactions by an electron hopping between shallowly trapped sites, or due to increasing exchange interactions between localized electrons. Thus, below 20 K it would appear that these systems are non-metallic. The lower temperature required for electron localization suggests that the band tails or traps in which electrons are localized are shallower than in the Pb^{2+}-doped system. The linewidth seems to become temperature independent down to at least 4 K with age (Figure 7). This might indicate that with time, the electron concentration can be increased sufficiently for an Anderson transition to occur. It would be useful to expand these studies to include linewidth measurements as a function of sample age and irradiation time.

The temperature dependence of the relative paramagnetic susceptibility approximately obeyed a Curie law, down to ~15 K. This indicates that the moments giving rise to the CESR line were either localized or part of a non-degenerate electron gas with the degeneracy temperature less ~15 K. The data outlined above indicates that the spins were not localized.

A concentration of $\sim 2 \times 10^{17}$ cm^{-3} spins is required for a degeneracy temperature of 15 K, which is 100-1000 times less than the concentration estimated from skin depth calculations. Concurrent ESR and DC conductivity measurements on both fresh and completely phase-separated samples as a function of irradiation time are necessary to resolve this

discrepancy.

The magnitude and sign of the frequency shift of the cavity resonance was consistent with it resulting from shallowly trapped species.[5] It should be noted, however, that the magnitude of the shift from a few localized spins might overwhelm the small shift in the opposite direction due to free carriers. Thus, electrons in band tails, which give rise to the weak, asymmetric line at low electron levels, described in Chapter 3, might dominate the photodielectric shift, while only those free electrons near the Fermi level contributed to the CESR line.

4.4.4 G-values and lineshapes

The observation of a CESR g-value of 1.8785 ± .0002 in both Pb^{2+}-doped and two-phase I^--doped AgCl powders is consistent with the mechanisms for conduction proposed for these systems. If $\varepsilon_1 \approx \varepsilon_2$ in the Pb^{2+}-doped powders, then, above 60 K, electrons are thermally excited above a mobility edge in the conduction band rather than in the upper Hubbard band and should have the same properties as electrons which are excited from intrinsic traps into the conduction band in the two-phase I^--doped powders. However, the observation of identical g-values in the two systems does not prove that the 1.8785 value is characteristic of the bottom of the conduction band, since a g-value arising from shallowly localized electrons or electrons in the upper Hubbard band can be extremely close to that of the conduction band.

The 1.8693 g-value measured in the 1.2% one-phase I^--doped AgCl probably reflects the influence of iodide on the AgCl band structure. Using 1.8785 as the AgCl conduction band g-value and extrapolating to 100% cubic AgI, a g-value of 1.11 is calculated. This is in line with the larger spin orbit coupling effect of iodide and the g-value shift of ~1.49 observed for pure AgBr. Similarly, the g-value of 1.8887 ± .0005

observed for 40% Ag/NaCl powders reflects the influence of sodium ions on the persistence-type AgCl conduction and valence band structure.

The g-value shift of the CESR line at high microwave power levels could result from two mechanisms. The electron spins may be polarized at high power levels leading to an induced polarization field H_p and a higher effective g-value. The magnitude of the observed g-shifts would be consistent with the fact that H_p is an induced field of 1-2 gauss. Such an effect has been observed in Li colloids.[46] The g-value shift might also arise from microwave heating of the free electrons and the subsequent population of higher energy levels in the conduction. This mechanism is supported by the observed g-shifts with temperature in the Pb^{2+}-doped AgCl and 40% Ag/NaCl systems. It is also consistent with the g-shift to lower field with higher electron concentrations observed in all AgCl/NaCl powders.

The decrease of the asymmetry ratio A/B from one at high power levels can also be attributed to microwave heating and the excitation of conduction electrons to higher energy levels. In order for an asymmetric line to be observed, motional narrowing must be incomplete. In addition, the g-shift must be related to the linewidth. As discussed in Chapter 2, since both these quantities depend on the spin-orbit coupling operator, they should be interdependent.

The observation of an asymmetric CESR line even at low power levels in AgCl/NaCl powders can be attributed to the higher electron concentrations in these samples. As a result, a greater fraction of the conduction band is populated and incomplete motional narrowing leads to an asymmetric line. However, at least some of the asymmetric character is probably due to intergrain structural differences as described above, since the asymmetric lineshape was different from that observed in doped

AgCl powders.

4.5 Conclusions

Conduction electron spin resonance was observed for the first time in two-phase iodide-doped AgCl powders. Above 60 K, the CESR signal was attributed to electrons in the conduction band, thermally excited from intrinsic shallow traps. The extended free electron lifetime was attributed to separation of the electrons and holes. Holes were trapped in the iodide-rich phase. The much lower stability of nearly free electrons in one-phase iodide-doped AgCl powders indicated that electron/hole separation is required for an extended electron lifetime.

In Pb^{2+}-doped AgCl powders, the CESR signal above 60 K was also attributed to conduction band electrons. In both Pb^{2+}-doped AgCl and two-phase I^--doped AgCl, motional narrowing was incomplete and line broadening occurred via impurity scattering.

An unusual, strongly temperature dependent, paramagnetic susceptibility was observed which is presently not understood. The linewidth temperature dependence indicated that the systems studied were insulators, with localization occurring at low temperatures. The Fermi level was apparently limited by the concentration of shallow electron and/or hole traps and an Anderson transition did not take place. In addition, the systems did not seem to be close to a Mott transition.

The CESR studies of the Pb^{2+}-doped AgCl powders provided no evidence for the presence of a second type of conduction occurring in the lower Hubbard band, although this does not rule out such a process. Also, shallowly trapped species which would rise to a microwave photodielectric shift were not detected. Thus, further correlated ESR and microwave photoconductivity and photodielectric measurements are called for to

determine if several types of mobile electrons contribute to the CESR signal.

The CESR signal which was observed in one-phase I^--doped AgCl powders was assigned to localized electrons shallowly trapped at intrinsic sites. At low I^- levels these were physically separated from holes trapped at iodide. A similar mechanism was proposed to account for the CESR signal observed in Br^--doped AgCl powders. Again, correlated ESR and microwave studies would help prove or disprove this model. Such studies would be facilitated by the use of samples of higher purity than used in the studies just described.

It was suggested that the g-value characteristic of the bottom of the conduction band in AgCl is $1.8785 \pm .0002$. More complete studies of lightly-doped Br^-/AgCl and I^-/AgCl systems would also help in confirming this suggestion.

The CESR line in fresh 40% AgCl/NaCl powders was inhomogeneously broadened possibly as a result of intergrain structural differences. Spin relaxation occurred via impurity scattering. Most evidence points to the signal arising from free electrons above 20 K. Below 20 K, localization may occur. Thus, after 30' γ-irradiation in fresh powders, an Anderson transition did not occur, although there is some evidence that older samples were metallic after the same irradiation time. The temperature dependence of the paramagnetic susceptibility indicated that the electron gas was non-degenerate, which contradicts rough estimates of the degeneracy temperature. Further ESR studies as a function of irradiation time and of sample age as well as conductivity measurements would help resolve these questions.

The dependence of the CESR g-value on microwave power and on temperature was attributed to thermal excitation of conduction band

electrons to higher energy levels. The resulting range of g-values and incomplete motional narrowing contributed to the dependence of the CESR lineshape on microwave power, temperature and electron concentration (Ag/NaCl powders).

REFERENCES

1. R. S. Eachus, R. E. Graves and M. T. Olm, phys. stat. sol. b 88, 705 (1978).
2. R. S. Eachus and M. T. Olm, unpublished results.
3. R. J. Deri and J. P. Spoonhower, Phys. Rev. B 25, 2821 (1982).
4. H. Kanzaki, Semicond. Insulators 3, 285 (1978).
5. J. P. Spoonhower, Phot. Sci. and Eng. 24, 130 (1980).
6. L. M. Kellogg, Phot. Sci. and Eng. 18, 378 (1974).
7. A. P. Marchetti and D. S. Tinti, Phys. Rev. B 24, 7361 (1981).
8. R. S. Eachus and J. P. Spoonhower, Phot. Sci. and Eng. 26, 20 (1982).
9. A. P. Batra and L. M. Slifkin, J. Phys. C 8, 2911 (1975).
10. M. E. Van Hulle and W. Maenhout-Van der Vorst, phys. stat. sol. a 39, 253 (1977).
11. P. Muller, phys. stat. sol. 12, 775 (1965).
12. W. West and V. I. Saunders, J. Phys. Chem. 63, 45 (1959); V. Platikanova and V. Starbova, Phot. Sci. Eng. 22, 6 (1978).
13. V. Platikanova and J. Malinowski, Zh. Nauchn. Prikl. Fotogr. Kinematogr. 17, 281 (1972).
14. R. J. Deri, Ch. Haynam and J. P. Spoonhower, phys. stat. sol. b 109, 645 (1982).
15. N. F. Mott, Metal-Insulator Transitions (Taylor & Francis, London, 1974).
16. N. F. Mott and E. A. Davis, Electronic Processes in Non-crystalline Materials, 2nd. ed. (Clarendon Press, Oxford, 1979).
17. P. Norton, Phys. Rev. Lett. 37, 164 (1976).
18. A. Miller and E. Abrahams, Phys. Rev. 120, 745 (1960).
19. E. A. Davis and W. D. Compton, Phys. Rev. A 140, 2183 (1965).
20. G. D. McDugle, private communication, Kodak Research Laboratories, Rochester, N.Y.
21. R. S. Eachus, R. E. Graves and M. T. Olm, J. Chem. Phys. 69, 4580 (1978); R. S. Eachus and R. E. Graves, J. Chem. Phys. 65, 5445 (1976).
22. C. P. Poole, Jr., Electron Spin Resonance: A Comprehensive Treatise on Experimental Techniques, 2nd. ed. (John Wiley & Sons, New York, 1983).
23. A. W. Overhauser, Phys. Rev. 89, 689 (1953).
24. J. E. Wertz and J. R. Bolton, Electron Spin Resonance: Elementary Theory and Practical Applications (McGraw-Hill, New York, 1972).
25. K. Andres, R. N. Bhatt, P. Goalwin, T. M. Rice and R. E. Walstedt, Phys. Rev. B 24, 244 (1981).

26. C. T. Murayama, W. G. Clark and J. Sanny, Phys. Rev. B 29, 6063 (1984).

27. See reference 22, p.579.

28. F. C. Brown in Polarons and Excitons, eds. C. G. Kuper and G. D. Whitfield, (Oliver & Boyd, Edinburgh, 1963) p.341.

29. Reference 16, p.219.

30. H. Kamimura and N. F. Mott, J. Phys. Soc. Jpn. 40, 1351 (1976).

31. A. Abragam, The Principles of Nuclear Magnetism (Oxford, London, 1961) pp.435-441.

32. J. D. Quirt and J. R. Marko, Phys. Rev. B 7, 3842 (1973).

33. A. M. Portis, A. F. Kip and C. Kittel, Phys. Rev. 90, 988 (1953).

34. P. P. Edwards and M. J. Sienko, Int. Rev. Phys. Chem. 3, 83 (1983).

35. J. D. Quirt and J. R. Marko, Phys. Rev. B 5, 1716 (1972).

36. G. Feher and E. A. Gere, Phys. Rev. 114, 1245 (1959).

37. M. Ledger, personal communication.

38. A. P. Marchetti and D. S. Tinti, Phys. Lett. 69A, 353 (1979); A. P. Marchetti and M. S. Burberry, Phys. Rev. B 28, 2130 (1983).

39. J. Phys. D: Appl. Phys. 15, 1071 (1982).

40. M. Yamaga and H. Yoshioka, J. Phys. Soc. Jpn. 46, 1538 (1979).

41. W. M. Walsh, Jr., J. P. Remeika and L. W. Rupp, Jr., Phys. Rev. 152, 223 (1966).

42. C. Kittel, Introduction to Solid State Physics, 5th. ed. (John Wiley & Sons, New York, 1976) p.162.

43. S. Hasegawa and S. Yazaki, Thin Solid Films 55, 15 (1978).

44. V. K. S. Shante and S. Kirkpatrick, Adv. Phys. 20, 325 (1971).

45. R. J. Stokes and C. H. Li, Acta metall. 10, 535 (1962).

46. G. Feher and R. A. Isaacson, J. Magn. Res. 7, 111 (1972).

C H A P T E R F I V E

THE INTERPRETATION

OF

ENDOR SPECTRA

CHAPTER FIVE

The Interpretation of ENDOR Spectra

5.1 Introduction

This chapter is meant to provide a practical understanding of the mechanisms that give rise to an ENDOR spectrum, the theory necessary for its interpretation, and the information that can be gained therefrom. A complete mathematical treatment of the spin Hamiltonian appropriate to the ENDOR experiment can be found in references 1 and 2 and the references therein. In the following discussion, a familiarity with the techniques and the theory of ESR spectroscopy is assumed, and for a thorough discussion of these topics the reader is directed to references 2-5. For the most part, the discussion of the theory of ENDOR is based on the treatment presented by Seidel.[1] Some aspects of the ENDOR spectrum will depend on the experimental setup used and on the relative amplitudes of the various spin relaxation rates in the system. For a complete review of such effects see references 6 and 7. The experimental details of the ENDOR experiment are discussed in Chapter 6.

The ENDOR experiment is ultimately an NMR experiment. Briefly, it consists of the application of a static magnetic field, B_o, to a sample that is simultaneously irradiated with saturating microwave and radiofrequency fields. B_o removes the degeneracy of the electronic and nuclear spin levels, and is chosen to fulfill the ESR resonance condition, $h\upsilon = g_e \mu_B B_o$ for a particular electronic Zeeman transition. The static magnetic field and the microwave frequency are not swept during the ENDOR experiment. The microwave field, $H_1 \cos\omega_1 t$, induces the chosen ESR absorption. The population of the electronic spin levels connected by the saturating microwave field tend

to be equalized by the field so that the intensity of the ESR absorption can be used to detect the NMR transitions. These are induced by sweeping the saturating radiofrequency field, $H_2 \cos\omega_2 t$, and tend to desaturate the electronic transition. The details of the various ENDOR mechansims are described in section 5.2.

The experimental data that are most often derived from ENDOR measurements are hyperfine and quadrupole splittings. Quadrupole transitions are not allowed in the ESR experiment. The data that can be derived from quadrupole splittings are discussed in the last section of this chapter. Hyperfine splittings can, of course, also be derived from ESR spectroscopy, and the analysis of hyperfine data is discussed in references 3 and 4. In ENDOR one can unequivocally determine the nucleus giving rise to the hyperfine splitting. However, the greatest advantage of the ENDOR experiment over ESR is its increased resolution. It is often said that the ENDOR experiment combines the sensitivity of ESR with the resolution of NMR. Although the ENDOR signal intensity is never as high as the ESR signal intensity, it is of the same order of magnitude, which, because of the larger energy term in the Boltzmann factor, is larger than the corresponding NMR signal by approximately the factor $\exp(g_e \mu_B B_o / kT)$. For an isotropic system, such as a liquid, the resolution of an ESR experiment is defined by the spectral density or number of lines per gauss. This is given by:[6]

$$\text{ESR spectral density} = \prod_{k=1}^{K} \left[\frac{(2N_k I_k + 1)}{\sum_{k=1}^{K} 2 A_k N_k I_k} \right] \qquad (1)$$

where there are N nuclei k with hyperfine splitting A_k and nuclear spin I_k. In ENDOR, as in NMR, to first order each different kind of nucleus gives rise to a pair of resonance lines so that the spectral density is given by

$$\text{ENDOR spectral density} = \frac{2K}{A_{max}} \qquad (2)$$

The ESR spectral density increases much more rapidly with K than the ENDOR spectral density. An example of the increase in resolution is shown in Figure 1.

Because of the increased resolution and the smaller linewidths of an ENDOR spectrum, it is possible to resolve hyperfine splittings that are not detectable in inhomogenously broadened ESR lines. A solid state ESR spectrum may consist of overlapping spectra from a number of different orientations of the paramagnetic complex with respect to the static magnetic field B_o. The ENDOR spectrum is often simpler being due only to those few orientations giving rise to the saturated ESR line.

It should perhaps be noted that because ENDOR spectroscopy allows small hyperfine constants to be determined with great accuracy, ENDOR can be used for position mapping of nuclei.[14] In this application, small hyperfine splittings due entirely to dipolar coupling of the unpaired electron with distant nuclei are used to calculate the distance to such nuclei according to the relationship:

$$r(\text{cm}) = \left[\frac{1.39962\,(3\cos^2\theta - 1)\,(g_e)_\theta\, g_N\, \beta_N\,(\text{erg G}^{-1})}{A_{//}\,(\text{MHz})}\right]^{1/3}$$

where θ is the angle between the z-axis and $\vec{B_o}$.

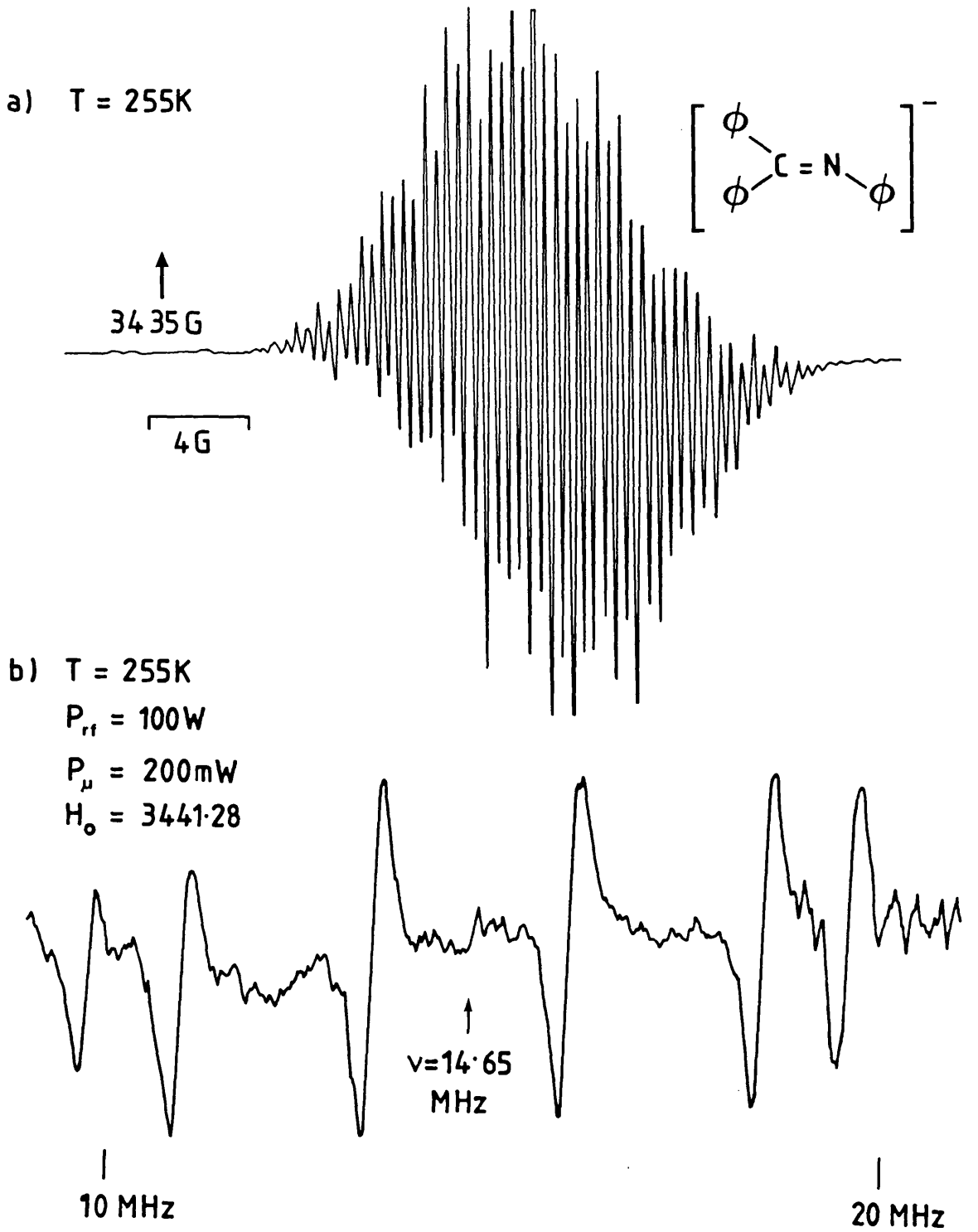

FIGURE 1

A comparison of solution ESR (a) and ENDOR (b) spectra of the N-phenyl benzophenone imine radical anion, above a K/Na alloy suspension in THF, showing the increased spectral resolution of ENDOR. The ENDOR spectrum was measured using 12.5 KHz FM rf modulation with a 50 KHz modulation depth.

5.2 ENDOR Mechanisms

A number of mechanisms can give rise to an ENDOR response. A four level system ($m_S = \frac{1}{2}, m_I = \frac{1}{2}$), with an isotropic g-tensor and hyperfine interaction, will be used to illustrate the different ENDOR mechanisms. The effective spin Hamiltonian for this system can be written as

$$\underset{\wedge}{\mathcal{H}} = \mu_B \vec{B}_0 g_e \underset{\wedge}{\vec{S}} + a \underset{\wedge}{\vec{I}} \underset{\wedge}{\vec{S}} - \mu_N \vec{B}_0 g_N \underset{\wedge}{\vec{I}} \tag{3}$$

g_e and g_N are the electronic and nuclear g-factors; μ_B is the Bohr magneton and μ_N is the nuclear magneton. The first and third terms are the electronic and nuclear Zeeman interactions respectively, and the second term describes the hyperfine interaction of the electronic and nuclear spin in the applied static field, B_o. The exact eigenvalues are given by[2]

$$\begin{aligned} E_1 &= -\tfrac{1}{2}[a^2 + (g_e \mu_B + g_N \mu_N)^2 B_0^2]^{\frac{1}{2}} - a/4 \\ E_2 &= -\tfrac{1}{2}[(g_e \mu_B - g_N \mu_N) B_0] + a/4 \\ E_3 &= +\tfrac{1}{2}[a^2 + (g_e \mu_B + g_N \mu_N)^2 B_0^2]^{\frac{1}{2}} - a/4 \\ E_4 &= +\tfrac{1}{2}[(g_e \mu_B - g_N \mu_N) B_0] + a/4 \end{aligned} \tag{4}$$

In the high field approximation, where $|(g_e \mu_B + g \mu_N) B_o| \gg |a|$, E_1 and E_3 are given to second and first order by[2]

$$\begin{aligned} E_1 &= -a/4 - \tfrac{1}{2}(g_e \mu_B + g_N \mu_N) B_0 \left[1 + \frac{a^2}{2(g_e \mu_B + g_N \mu_N)^2 B_0^2}\right] \\ &\approx -a/4 - \tfrac{1}{2}(g_e \mu_B + g_N \mu_N) B_0 \\ E_3 &= -a/4 + \tfrac{1}{2}(g_e \mu_B + g_N \mu_N) B_0 \left[1 + \frac{a^2}{2(g_e \mu_B + g_N \mu_N)^2 B_0^2}\right] \\ &\approx -a/4 + \tfrac{1}{2}(g_e \mu_B + g_N \mu_N) B_0 \end{aligned} \tag{5}$$

The energy levels in the high field approximation are shown as a function of magnetic field in Figure 2a. The high field approximation applies under most conditions for the ESR experiment, and the first order eigenvalues are usually sufficient

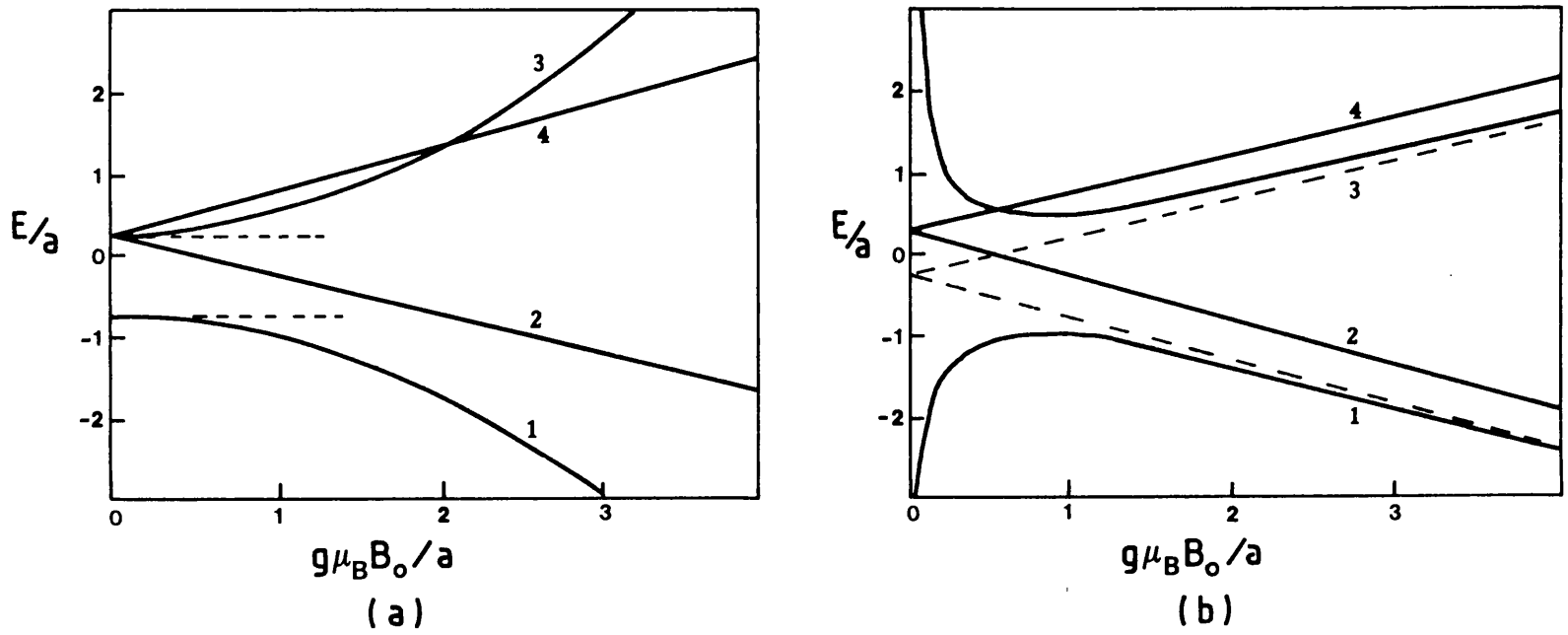

FIGURE 2

(a) Low field approximation of eigenvalues in equation 4 to first (----) and second (——) order.
(b) High field approximation of eigenvalues in equation 4 to first (----) and second (——) order.
From reference 2.

to explain the observed ESR spectrum.

In the low field limit, where $|a| \gg |(g_e\mu_B + g_N\mu_N)B_o|$, E_1 and E_3 become[2]

$$E_1 = -a/4 - a/2\left[1 + \frac{(g_e\mu_B + g_N\mu_N)B_o^2}{2a^2}\right] \approx -\frac{3a}{4}$$

$$E_3 = -a/4 + a/2\left[1 + \frac{(g_e\mu_B + g_N\mu_N)B_o^2}{2a^2}\right] \approx \frac{a}{4} \qquad \ldots\ (6)$$

This approximation is illustrated in Figure 2b.

The energy level diagram for the first order solution of the Hamiltonian in Eqn. 3, in the high field approximation, is shown in Figure 3a. The allowed ESR transitions are between levels 1 and 4, and 2 and 3, and the allowed NMR transitions are between 1 and 2, and 3 and 4. The possible relaxation pathways for a four level system are shown in Figure 3b. T_{1e} and T_{1n} are the electron and nuclear spin relaxation times. T_{x1} and T_{x2} are the cross relaxation times. An alternative method of representing the relaxation pathways between spin levels, as an electric circuit, is shown in Figure 3c. T_i now correspond to resistances between points 1 through 4. For the ENDOR mechanism which is operative in most systems studied, the T_{1e} mechanism, results from an effective increase in the relaxation rate between the two levels connected by the saturating microwave field, following the application of the saturating radiofrequency field. There are two types of T_{1e} ENDOR mechanisms. These are the transient ENDOR and stationery ENDOR mechanisms. Which one is operative is dependant on the relative ratios of the relaxation times T_i.

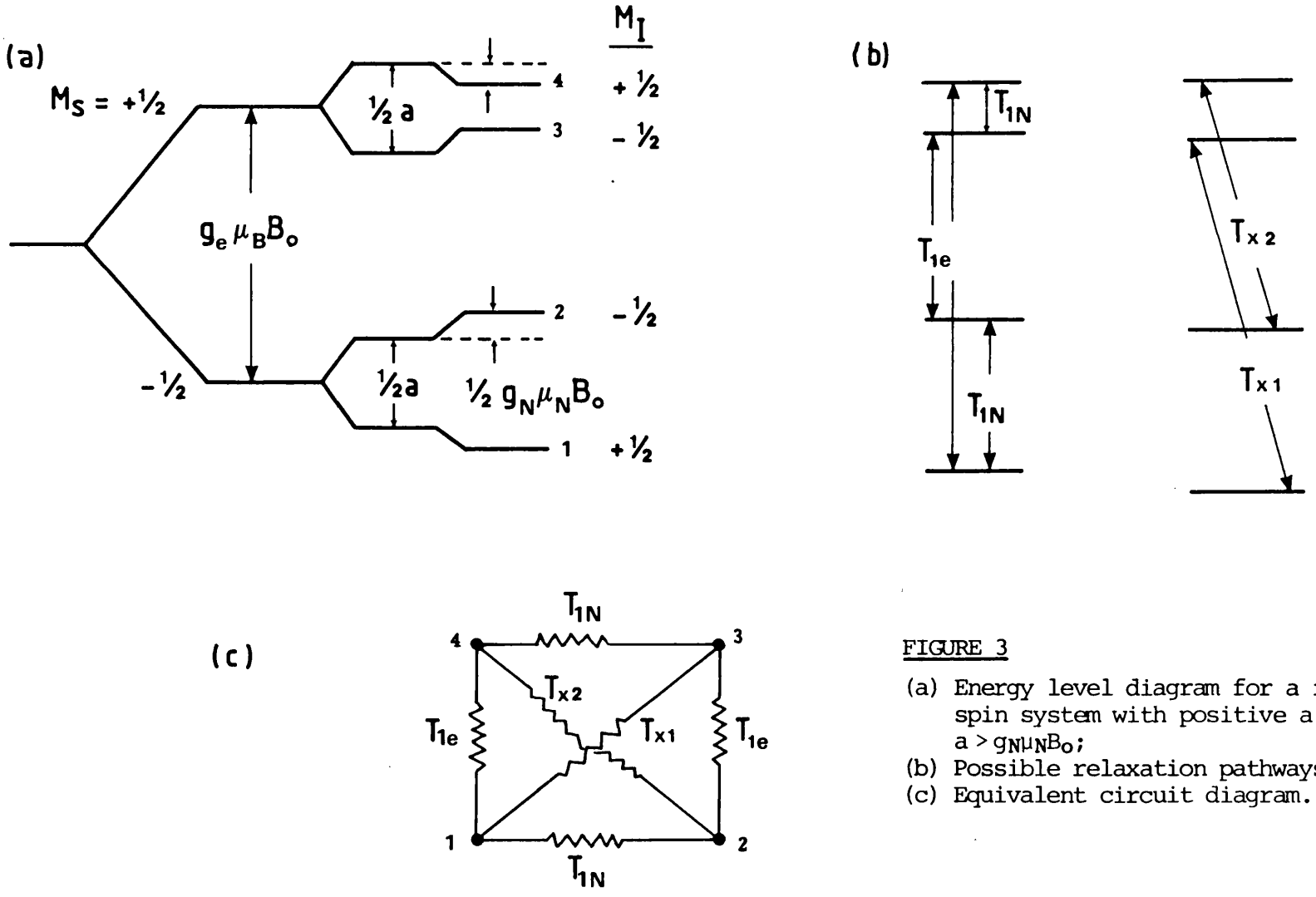

FIGURE 3

(a) Energy level diagram for a four level spin system with positive a and $a > g_N \mu_N B_o$;
(b) Possible relaxation pathways;
(c) Equivalent circuit diagram.

For the transient ENDOR mechanism, T_{1e} must be longer than the instrument response time, and all the other relaxation times must be long enough to be considered infinite. Given these conditions, the spin populations of levels 1-4 before application of either microwave or radiofrequency fields are shown in Figure 4a, the upper electronic levels being lower in population by the Boltzmann factor, which is approximately $1 - (g_e \mu_B B_o/kT)$. The last term of this approximation will be labelled ϵ. Upon application of a nonsaturating microwave field, spins will be pumped from level 1 to level 4, and an ESR response will be observed; however the steady state populations of levels 1 and 4 will not change, as T_{1e} is sufficient to maintain the Boltzmann distribution. In order to saturate the electronic transition, a microwave field must fulfill the condition:

$$\nu_e H_1 \geq (T_{1e}\ T_{2e})^{-\frac{1}{2}} \tag{7}$$

where $\nu_e = g_e \mu_B B_o/h$ and T_{2e} is the spin-spin relaxation time. Application of such a field between levels 1 and 4 will equalize their spin populations, so that an ESR response is no longer observed (Figure 4b). If a radio frequency field which is strong enough to compete with the microwave field and relevant relaxation mechanisms, that is:

$$\nu_N H_2 \approx \nu_e H_1 \geq (T_{1e}\ T_{2e})^{-\frac{1}{2}} \tag{8}$$

is then applied between levels 3 and 4, level 3 will be depopulated and an ESR transition can once more occur, (Figure 4c). This will be a transient ESR response, only detectable if T_{1e} is longer than the instrument response time. Eventually the populations of levels 1,3 and 4 will be equalized so that no

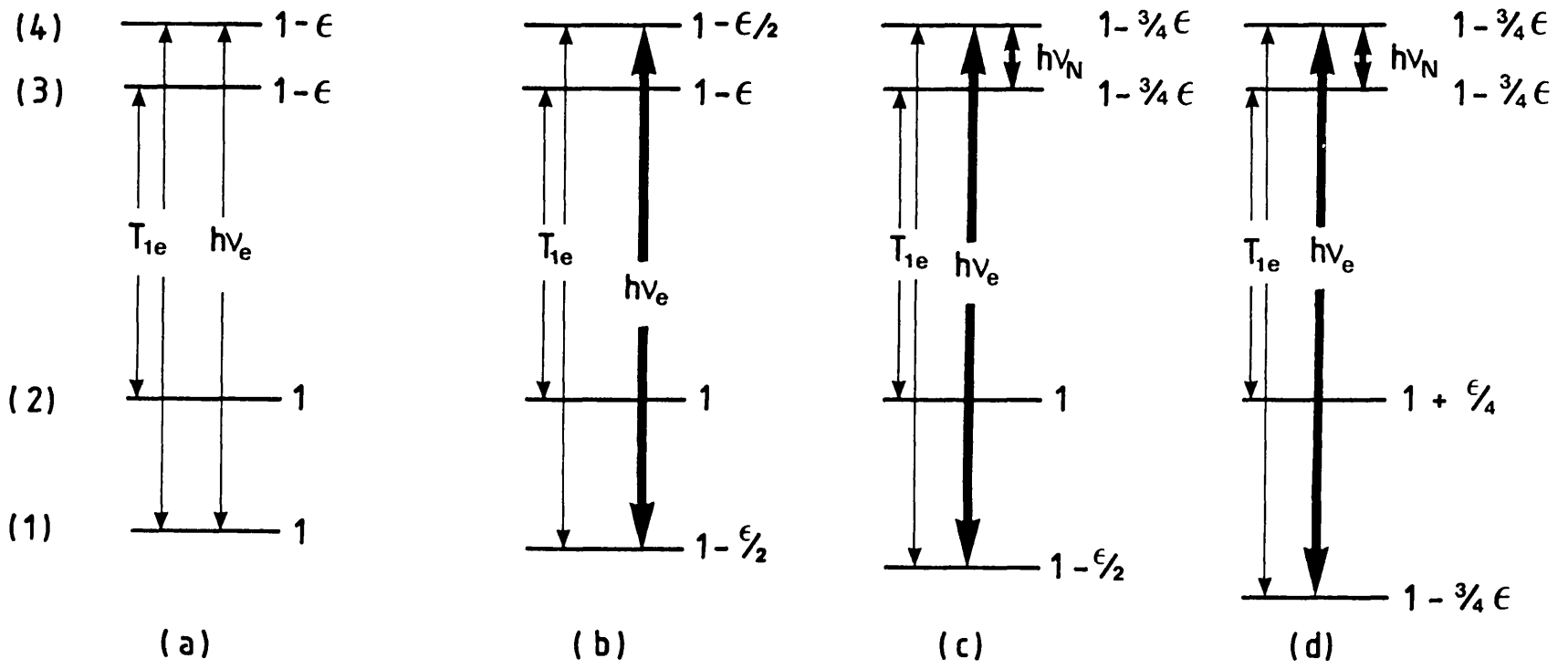

FIGURE 4

Transient ENDOR mechanism: Spin populations of a four level system, (a) in the presence of a non-saturating microwave field, (b) in the presence of a saturating microwave field, (c) immediately following the application of a strong radio-frequency field and (d) the steady state population.

ESR absorption is possible, (Figure 4d). The application of the rf field can be thought of as decreasing the relaxation time T_{1e} so that the 1-4 transition is desaturated.

The conditions of a long T_{1e} and other relaxation times which are infinite are fulfilled in only a few systems at very low temperatures. It is the steady state ENDOR mechanism which accounts for the success of the ENDOR experiment in a wide range of materials. The steady state ENDOR response results from the fact that a saturating rf field increases the relaxation rate between the levels connected by the saturating microwave field and thus desaturates the ESR transition. As an example, consider a solid with weak coupling between the spin system and the lattice such that $T_{x1} \sim T_{1N} < T_{1e}$. T_{x2}, which involves the selection rule $\Delta(m_s + m_I) = 2$ is usually very long, especially for isotropic and axial symmetries,[6] and is ignored here. Then, before application of the rf field, the total relaxation rate between levels 1 and 4 is given by the reciprocal of the "resistance" of the circuit connecting these levels, (Figure 3c). Assuming $T_{1e} = T_{1N} = 1$, this is

$$W_1 = 1/T_{1e} + 1/T_{1N} + T_{1e} + T_{1N} + 1/(T_{1N} + T_{x1})$$
$$= 1 + 1/3 + 0 = 1.33$$

The application of a saturating rf field between levels 3 and 4 is equivalent to replacing the T_{1N} resistor with a short, increasing the relaxation rate to

$$W_2 = 1 + \tfrac{1}{2} + 0 = 1.50$$

Thus, the ESR signal is enhanced by a factor of $1.50/1.33 = 1.12$. This is the ENDOR response. An ENDOR response is also obtained if the NMR transition 1-2 is stimulated. Thus, a pair of ENDOR lines is observed, corresponding to saturation of the 1-2 and 3-4 NMR transitions. The relative amplitudes of the

two ENDOR lines and the ENDOR enhancement factors depend on the relative values of the T_i relaxation times. Values, under various relaxation conditions, are given in Table I. Clearly, "percent enhancement studies", as well as ENDOR linewidth studies, can provide information about the magnitudes of the T_i relaxation times of a system.[7] The intensities of ENDOR lines are discussed further in Chapter 6 and in references 6 and 7.

A number of less common mechanisms have been reported and these are described in reference 6. One of these, which has some relevance to the studies described in this thesis, is the "line-shift" mechanism.

If the saturated electron spin system polarizes the nuclear spins of surrounding nuclei through a contact interaction, then the induced polarization creates a new effective field which adds to the applied static field. The ESR line will therefore shift slightly from its nonsaturated position. An NMR transition depolarizes the nuclei and causes a return of the ESR line to its nonsaturated position. If the signal intensity at a particular field value is monitored during these events, then the ESR signal intensity at that point will change when the sweeping rf field reaches an NMR transition frequency. This is shown in Figure 5 for the conduction electron spin resonance signal in Li colloids. An NMR transition will occur at the nuclear frequencies of the nuclei which are in contact with the electron spin system.

Table 1: ENDOR Enhancements and Relative Transition Intensities

Relaxation Conditions	$h\nu_N^+ / h\nu_N^-$	Enhancement Factor (%)
$T_{1e} = T_{1N} \ll T_{x1}$	1	12
$10T_{1e} = T_{1N} \ll T_{x1}$	1	4
$T_{1e} < T_{1N} \ll T_{x1}$	1	<12
$T_{1e} = T_{x1} \gg T_{1N}$	∞	100
$10T_{1e} = T_{x1} \ll T_{1N}$	∞	10
$T_{1e} < T_{x1} \ll T_{1N}$	∞	<100
$T_{1e} = T_{1N} = T_{x1}$	4	36
$T_{1e} = T_{1N} = T_{x1} = T_{x2}$	1	29
$T_{2e} \ll T_{1e} < T_{x1} < T_{1N}$	-	0

From reference 6, p 21.

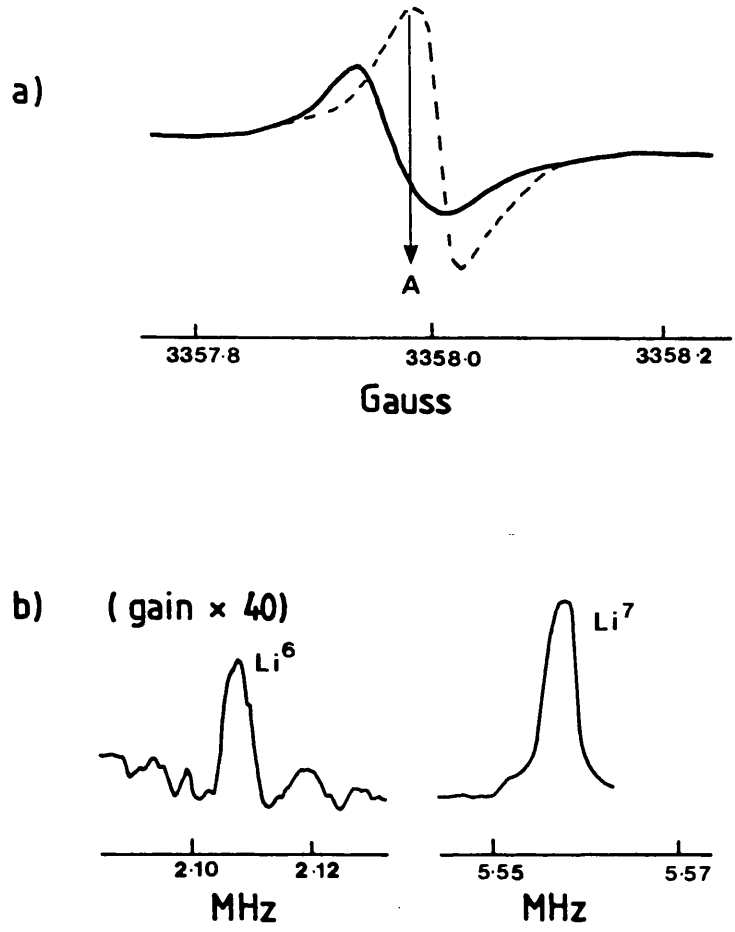

FIGURE 5

The line-shift ENDOR mechanism:
(a) ESR spectrum of conduction electrons in colloidal Li at saturating (——) and non-saturating (----) microwave powers. Point A is the optimum position for observing ENDOR.
(b) ENDOR spectrum from conduction electrons in colloidal Li. From reference 6.

5.3 The ENDOR Transition Frequencies

5.3.1 The General Hamiltonian

For a multilevel system, made up of a central nucleus and a number of ligand nuclei, the general spin Hamiltonian, describing the interaction of the total electronic spin $\vec{S}$ and (N+1) nuclei with nonzero nuclear spin with the magnetic field $\vec{B}_o$, can be written as:[1]

$$\begin{aligned}\hat{\mathcal{H}} = {} & \mu_B \vec{B}_0 g_e \vec{S} + (\vec{S} \tilde{A}_\alpha \vec{I}_\alpha - g_{N_\alpha} \mu_{N_\alpha} \vec{B}_0 \vec{I}_\alpha + \vec{I}_\alpha \tilde{Q}_\alpha \vec{I}_\alpha) \\ & + \sum_{\beta=1}^{N} (\vec{S} \tilde{A}_\beta \vec{I}_\beta - g_{N_\beta} \mu_{N_\beta} \vec{B}_0 \vec{I}_\beta + \vec{I}_\beta \tilde{Q}_\beta \vec{I}_\beta)\end{aligned} \tag{9}$$

α refers to the central ion and β to the ligand nuclei. No spin-spin term has been included in eqn 9. The 4^{th} and 7^{th} terms describe the quadrupole interaction of the i^{th} nucleus with the electric field gradient at that nucleus.

The hyperfine and quadrupole tensors can be expressed in the following convenient forms. The hyperfine tensor is the sum of an isotropic portion, a, the Fermi contact term and an anisotropic portion, $\tilde{B}$:

$$\begin{aligned}\tilde{A} &= a + \tilde{B} \\ a &= \frac{2}{3} \mu_o g_e \mu_B g_N \mu_N |\psi(o)|^2 \\ B &= \frac{\mu_o}{4\pi} g_e \mu_B g_N \mu_N \int \left(\frac{3}{r^5} x_i x_k - \frac{1}{r} \delta_{ik}\right) |\psi(r)|^2 \, dV\end{aligned} \tag{10}$$

x_i and x_k are Cartesian coordinates. Along principle axes, the tensor $\tilde{B}$ has the form

$$\tilde{B} = \begin{bmatrix} -b + b' & & \\ & -b - b' & \\ & & 2b \end{bmatrix} \tag{11}$$

where $b' = 0$ for axial symmetry. The quadrupole interaction tensor, $\tilde{Q}$, has components given by

$$Q_{ik} = \left[\frac{eQ}{2I(I-1)}\right]\left[\frac{\partial^2 V}{\partial x_i \partial x_k}\right] \qquad i,k = x,y,z \qquad (12)$$

Q is the nuclear electric quadrupole constant of the nucleus under consideration and $\frac{\partial^2 V}{\partial x_i \partial x}$ is the crystalline electric field gradient at that nucleus. For the principal axes system, $Q_{ik} = 0$ when $i = k$, and

$$Q_{ii} = \left[eQ/2I(2I-1)\right]\left[\partial^2 V/\partial x_i^{\,2}\right] \qquad i = x,y,z \qquad (13)$$

$\partial^2 V/\partial x_i^{\,2}$ is the electric field gradient along the i^{th} axis. Thus, the quadrupole interaction tensor becomes

$$Q = \begin{bmatrix} -q - q' & & \\ & -q + q' & \\ & & 2q \end{bmatrix} \qquad (14)$$

q' (or sometimes q'/q) is called the asymmetry parameter, η, and is zero for axial symmetry. The quadrupole Hamiltonian can then be written

$$\begin{aligned} \underset{\wedge}{\mathcal{H}} &= \vec{\underset{\wedge}{I}}\,\tilde{Q}\,\vec{\underset{\wedge}{I}} \\ &= Q_{xx} I_x^2 + Q_{yy} I_y^2 + Q_{zz} I_z^2 \\ &= q\,[3\vec{\underset{\wedge}{I}}_z^2 - \vec{\underset{\wedge}{I}}(\vec{\underset{\wedge}{I}}+1) + q'(\vec{\underset{\wedge}{I}}_x^2 - \vec{\underset{\wedge}{I}}_y^2)] \end{aligned} \qquad (15)$$

where $q = \frac{eQ}{4I(2I-1)}\left(\frac{\partial^2 V}{\partial z^2}\right) = Q_{zz}/2$

and $q' = \frac{eQ}{4I(2I-1)}\left(\frac{\partial^2 V}{\partial x^2} - \frac{\partial^2 V}{\partial y^2}\right)$

Q_{ii} are the principal values of the quadrupole tensor.

5.3.2 The First Order ENDOR Spectra

The Hamiltonian in eqn 9 can be considered as the sum of an electronic Hamiltonian, which includes the first term and any fine structure term, and a nuclear Hamiltonian, made up of the remaining terms:

$$\hat{\mathcal{H}} = \hat{\mathcal{H}}_e + \hat{\mathcal{H}}_N \tag{16}$$

The electronic Zeeman interaction is much larger than any of the other terms, and to first order the ENDOR transitions can be calculated by considering only the nuclear Hamiltonian.

For the moment, however, consider the first order solution to the complete Hamiltonian in eqn 3 for a single nucleus with nuclear spin I. If $I = \frac{1}{2}$, then there will be no quadropole interaction and the first order eigenvalues are those given in eqns 5 which can be rewritten as

$$E = (g_\theta \mu_B B_0) m_S + [A_\theta m_S m_I - (g_N \mu_N B_0) m_I] \tag{17}$$

where $g_\theta^2 = g_{xx}^2 \ell_{xx}^2 + g_{yy}^2 \ell_{yy}^2 + g_{zz}^2 \ell_{zz}^2$

and $A_\theta^2 = A_{x'x'}^2 \ell_{x'x'}^2 + A_{y'y'}^2 \ell_{y'y'}^2 + A_{z'z'}^2 \ell_{z'z'}^2$

l_{ii} and $l_{i'i'}$ are the direction cosines relating the magnetic field direction with the principal g- and A- directions respectively. The selection rules and transition energies for the ESR and ENDOR experiments are:

$$\begin{aligned} &\Delta m_S = \pm 1;\ \Delta m_I = 0 \quad \Delta E_{ESR} = \left| g_\theta \mu_B B_0 + \sum_{i=-1}^{+I} A_\theta m_i \right| \\ &\Delta m_S = 0;\ \Delta m_I = \pm 1 \quad \Delta E_{ENDOR} = \left| A_\theta m_S - g_N \mu_N B_0 \right| \end{aligned} \tag{18}$$

Thus, two lines are observed, at the frequencies given by:

$$\upsilon(\pm) = \left| (A_\theta/h) m_s - \upsilon_N \right| \tag{19}$$

υ_N is the nuclear frequency of the nucleus in question. $\upsilon(\pm)$ refers to the $m = \pm \frac{1}{2}$ transitions. The pair of lines are centred at $(A/h)/2 \pm \upsilon_N$ if $(A/h)/2 > \upsilon_N$, and at $\upsilon_N \pm (A/h)/2$ if $\upsilon_N > (A/h)/2$. This is shown in Figure 6. For a nucleus with $I > \frac{1}{2}$, a quadrupolar interaction can occur. The first order energy levels are given by:[1]

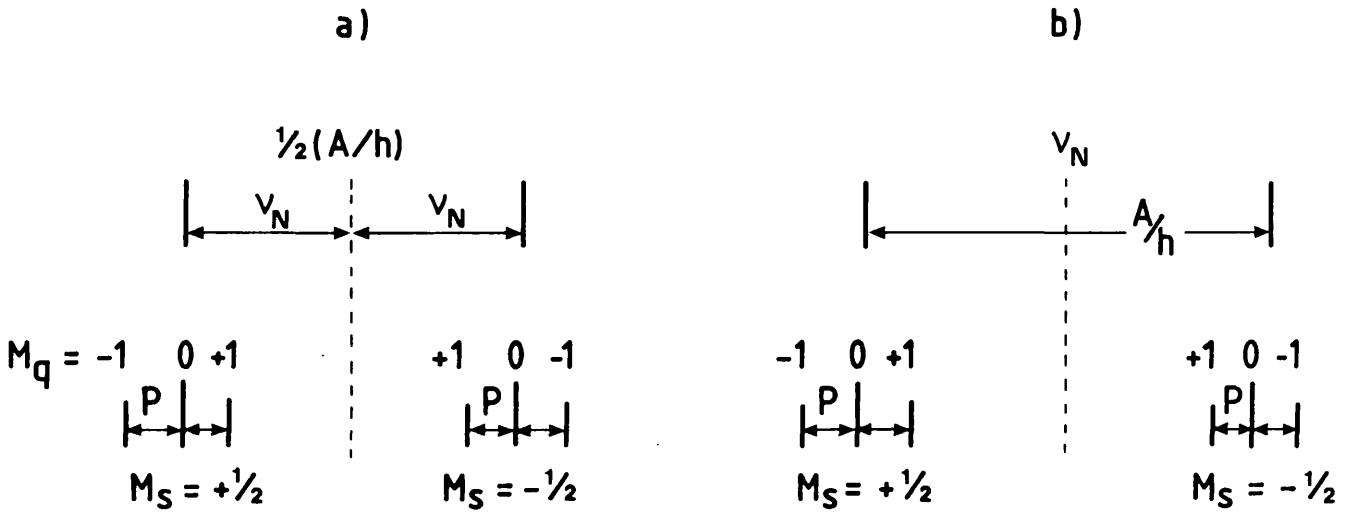

FIGURE 6

First order ENDOR transition frequencies with and without a quadrupole interaction, for a nucleus with $I = 3/2$, $A > 0$, $P > 0$ and (a) $(A/h)/2 > \nu_N$ and (b) $\nu_N > (A/h)/2$.

$$E = g_\theta \mu_B B_0 m_S - g_N \mu_N B_0 m_I + A_\theta m_S m_I + \tfrac{1}{2}[m_I^2 - \tfrac{1}{3} I(I+1)]P_\theta \qquad (20)$$

where $P_\theta = 3(Q_{x''x''} \ell_{x''x''} + Q_{y''y''} \ell_{y''y''} + Q_{z''z''} \ell_{z''z''})$

$= 3[q(3\cos^2\theta'' - 1) + q' \sin^2\theta'' \cos^2\theta'']$

$l_{i''} l_{i'}$ are the direction cosines relating the principal axes of the quadrupolar tensor to the magnetic field direction, and φ'' and θ'' are the corresponding polar angles. Selection rules forbid the observation of quadrupole transitions in the ESR experiment, and to first order the ESR transitions are not affected. The ENDOR transition energies are now given by:[1]

$$\Delta E_{ENDOR} = |A_\theta m_S - g_N \mu_N B_0 + m_q P_\theta| \qquad (21)$$

where $m_q = \dfrac{m_I + m_{I'}}{2}$

Equation (19) becomes

$$\nu(\pm) = \left|\left(\frac{A_\theta}{h}\right) m_S - \nu_N + \left(\frac{P_\theta}{h}\right) m_q\right| \qquad (22)$$

and 2(2I) lines are observed.

For a nucleus with I = 3/2, m_q can equal +1,0 or -1. Thus, each of the two ENDOR lines given by equation 19 is split into three by the quadrupole interacion (Figure 6).

The maximum number of quadrupole transitions allowed is 2I for each m_s component, but not all of these are necessarily observed. The m_I components of the saturated ESR transition determine which quadrupole transitions are observed. If I=3/2, then a resolved ESR spectrum will consist of four lines. If the m_I = -3/2 transition is saturated, only the two m_q = -1 ENDOR lines will be observed.

For K <u>different</u> nuclei with nonzero spin I, there will be $\prod_{k=1}^{K} (2I_k + 1)$ ESR lines observed at energies given by

$$\Delta E_{ESR} = \left|g_\theta \mu_B B_0 + \sum_{k=1}^{K} \sum_{m_{i_k} = -I}^{I} A_{\theta_k} m_{i_k}\right| \qquad (23)$$

However, only a single pair of ENDOR lines (each of which may be split into 2I quadrupole lines) is observed for each different kind of nucleus, and the transition energies can be calculated to second order by considering the solution to the complete Hamiltonian for each nucleus independantly.

For N equivalent nuclei, (2NI + 1) ESR lines are observed at transition energies given by

$$\Delta E_{ESR} = \left| g_\theta \mu_B B_0 + \sum_{m_i=-I_T}^{I_T} A_\theta m_i \right| \qquad (24)$$

where I_T is the total nuclear spin for the system. To first order, only two ENDOR lines at frequencies given by equation 19 (or 2(2I) lines at frequencies given by equation 22, if there is a quadrupole interaction) are observed. To second order, these lines are split by an indirect nuclear-nuclear spin coupling as described in the next section.

As an example, consider the paramagnetic transition metal complex, $(RhCl_6)^{4-}$, which is tetragonally elongated so that the single unpaired electron interacts with two equivalent chloride ligands (I = 3/2). The ENDOR study of such a complex will be discussed in later chapters. The first order transition energies are shown in Figure 7, and the ESR spectrum with B_o parallel to the symmetry axis is shown in Figure 8. The corresponding ENDOR spectrum of the two axial Cl^- ligands is shown in Figure 9. The ENDOR spectrum in Figure 9b exhibits all of the allowed quadrupole transitions, and was obtained while saturating the m_I= 0 ESR line. The spectrum in Figure 9 b was obtained while saturating the m_I= -3(high field) ESR line. Thus, only the m_q= -1 ENDOR transitions are present. The quadrupole splitting measured with $\vec{B}_o$ along the z-axis is 6q and with $\vec{B}_o$ perpendicular to the z-axis is 3q, in accordance with eqn 20.

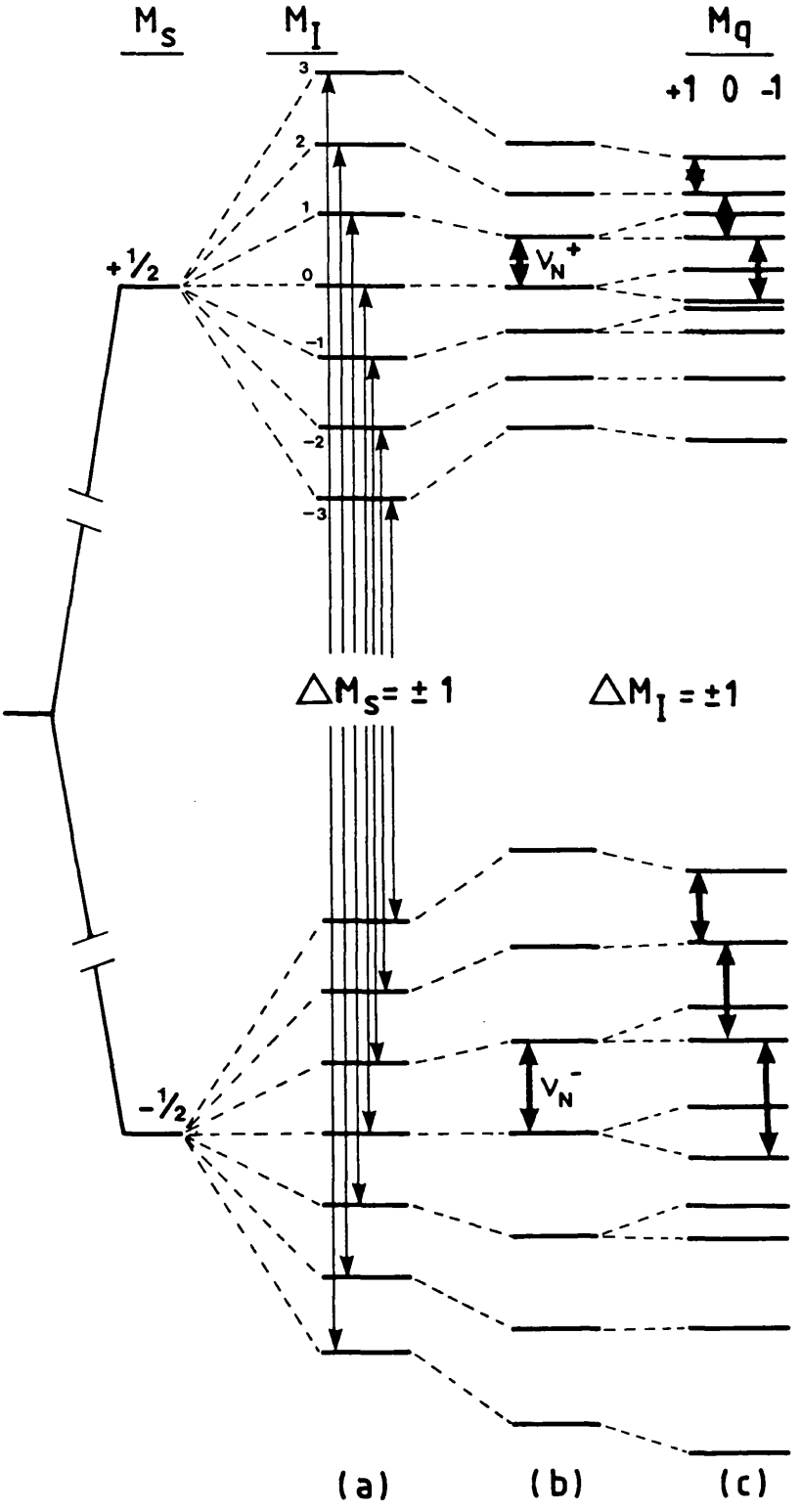

FIGURE 7

Energy level diagram for $(RhCl_6)^{2-}$, showing an interaction with two equivalent Cl^- ligands, assuming A, q > 0. ESR transitions (a), and ENDOR transitions with (c) and without (b) a quadrupole interaction are shown.

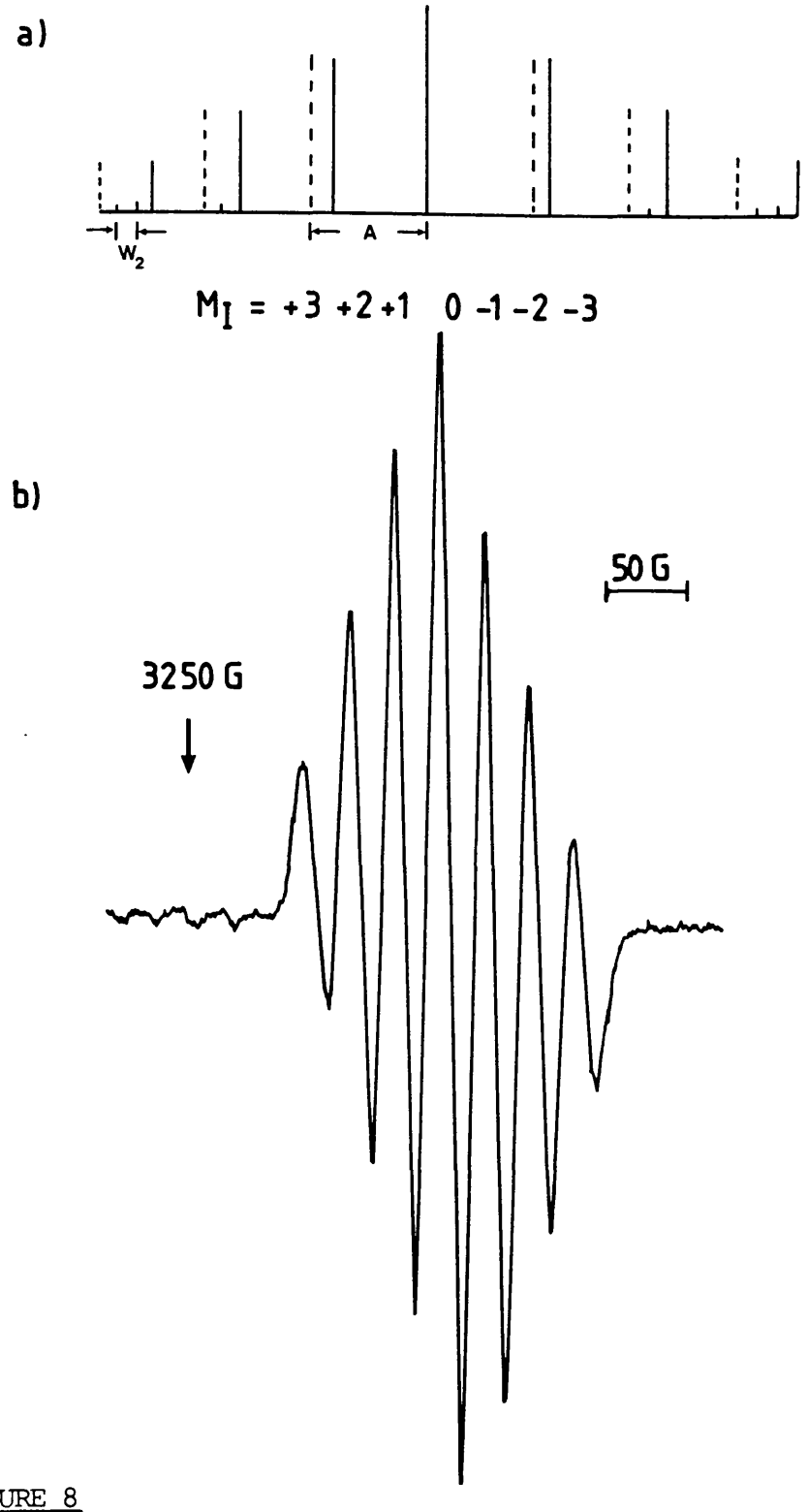

FIGURE 8

(a) First (----) and second (——) order ESR transitions for two equivalent nuclei with $I = 3/2$. The second order correction term, W_2, is exaggerated.
(b) ESR spectrum of the $(RhCl_6)^{4-}$ complex in AgCl with $B_o \parallel Z$, showing the hyperfine interaction with the two equivalent axial Cl^- ligands. $A > 0$.

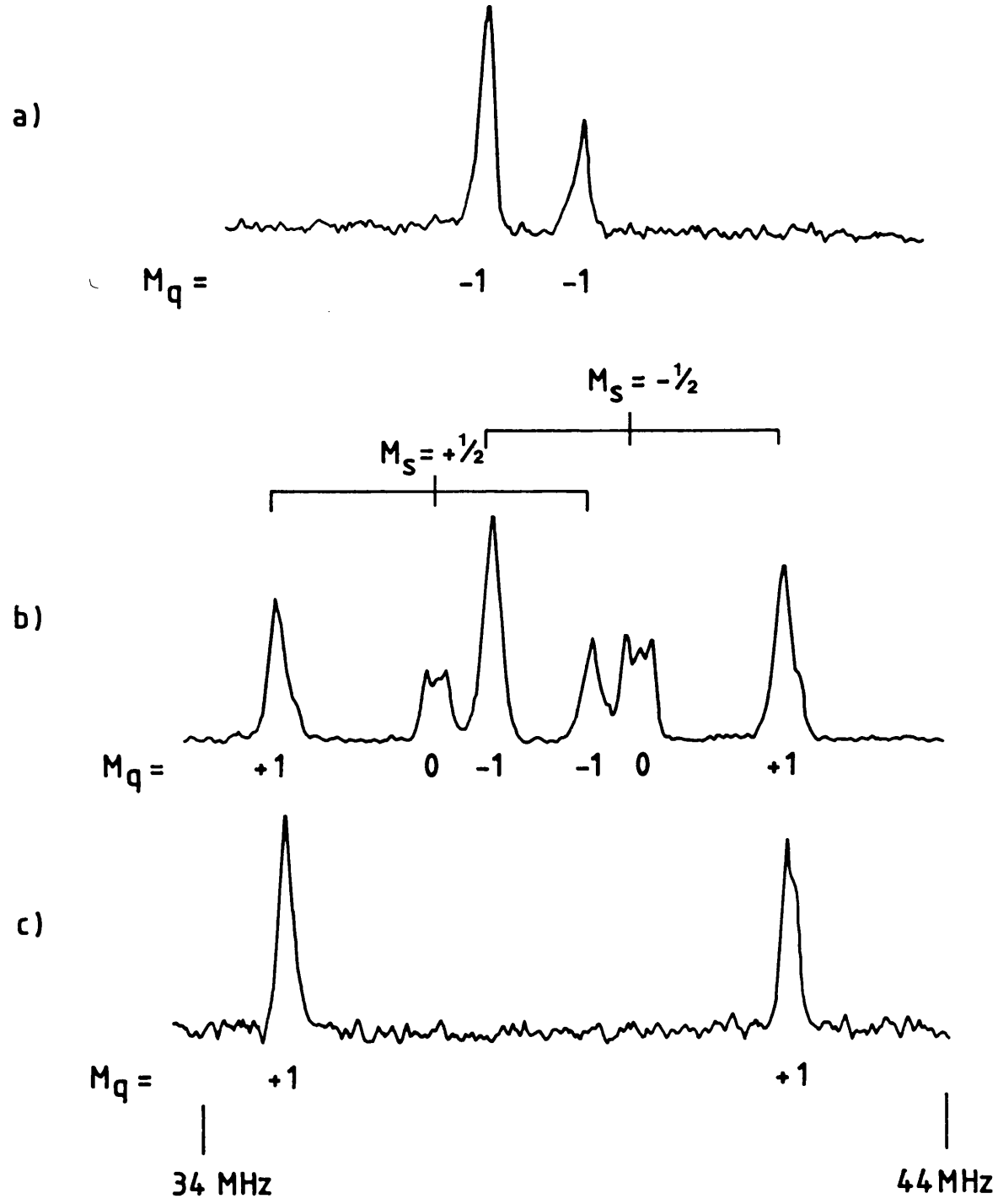

FIGURE 9

The ENDOR spectra from the 2 axial $^{35}Cl^-$ ligands of $(RhCl_6)^{4-}$/AgCl with B_o 11 Z, measured while saturating the (a) $M_I = -3$, (b) $M_I = 0$ and (c) $M_I = +3$ ESR lines shown in Figure 8.

5.3.3 Second Order Effects

For large hyperfine interactions, the high field approximation breaks down (Figure 2). Then, to second order, the eigenvalues for the general Hamiltonian in eqn. 9, for an electron interacting with a single nucleus of spin I and an isotropic hyperfine coupling, are[1]

$$E = g_\theta \mu_B B_0 m_S + a m_I m_S + m_S W_2 [I(I+1) - m_I(m_I \pm 1)] - g_N \mu_N B_0 m_I \qquad (25)$$

This is sometimes referred to as the Breit-Rabi correction.[13] For $m_s = \frac{1}{2}$, and $m_I = \frac{1}{2}$, eqn 25 corresponds to the energy levels given by eqn 5. The ESR lines will be shifted at large A, and the ENDOR lines will be shifted and will be split if $I > \frac{1}{2}$. The transition energies are[1]

$$\Delta E_{ESR} = g_\theta \mu_B B_0 + a m_I + W_2 [I(I+1) - m_I^2] - g_N \mu_N B_0 m_I$$
$$\Delta E(\pm)_{ENDOR} = a/2 - W_2 (m_q \pm \tfrac{1}{2}) \mp g_N \mu_N B_0 \qquad (26)$$

W_2 is given by $a^2/2g_\theta \mu_B B_o$. The second order ESR transitions are shown schematically in Figure 8a for a large positive hyperfine interaction with two equivalent nuclei of spin 3/2. The second order ENDOR transition frequencies, for a single nucleus of spin $\frac{1}{2}$, are shown is Figure 10a, and for a single nucleus with spin 3/2 and no quadrupole splitting, in Figure 10b.

For an anisotropic hyperfine interaction "a" in eqns 25 and 26, is replaced by "A_θ", and the third term in eqn 25 is replaced by[1]

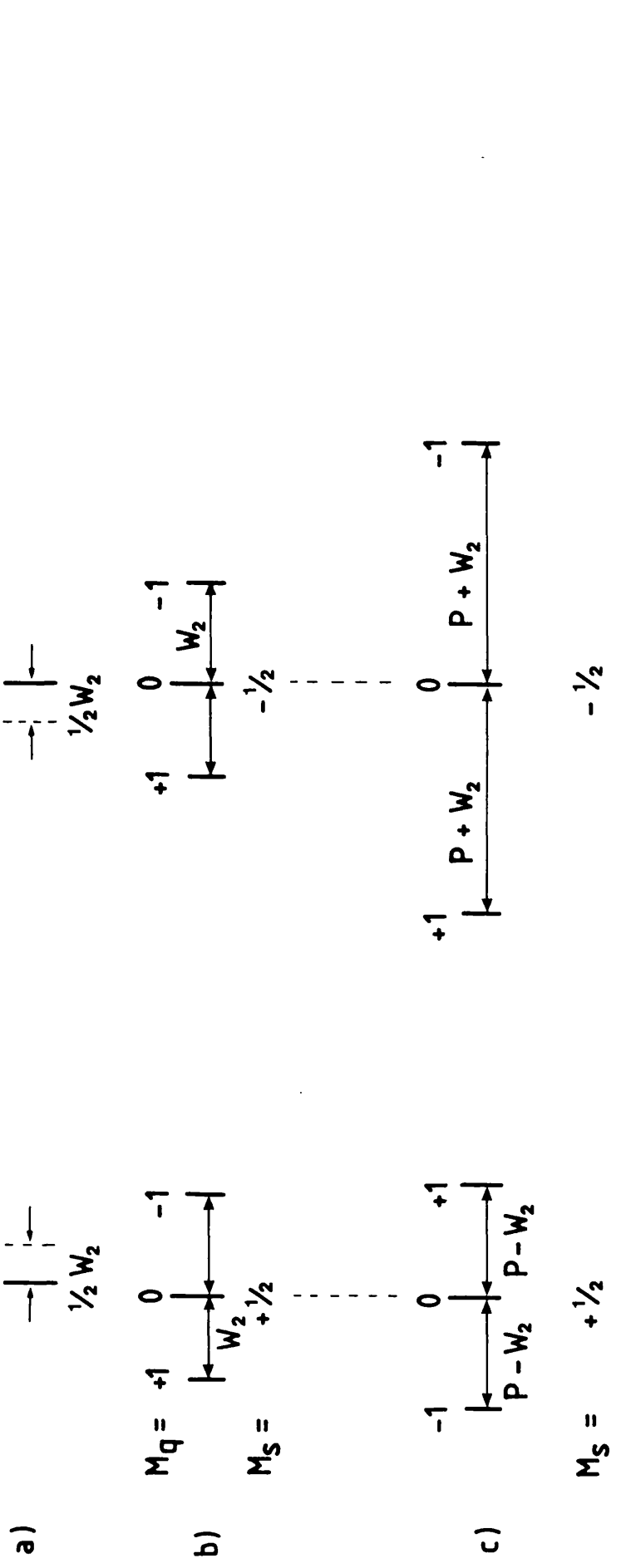

FIGURE 10

Second order ENDOR transition frequencies for $A > 0$, $P > 0$, $A/h > 2\mu_N$ and (a) one nucleus with $I = ½$, (b) one nucleus with $I = 3/2$ and no quadrupole interaction, (c) one nucleus with $I = 3/2$ and a quadrupole interaction.

$$m_S W_2' [I(I+1) - m_I(m_I \pm 1)] \pm m_S W_2'' [I(I+1) - m_I(m_I \pm 1)] \qquad (27)$$

where $$W_2' = \frac{[a - b/2(3\cos^2\theta - 1) - b'/2 \sin^2\theta \cos 2\theta]^2}{2 g_e \mu_B B_0}$$

and $$W_2'' = \frac{\sin^4\theta (3/2 b + 1/2 b' \cos 2\phi)^2 + b'^2 \sin^2 2\phi \cos^2\theta}{2 g_e \mu_B B_0}$$

In eqn 26, the second term is replaced by

$$-m_q (W_2' + W_2'') \mp \tfrac{1}{2}(W_2' - W_2'') \qquad (28)$$

When equivalent nuclei are present, indirect spin-spin coupling through the electron spin can occur. This results in a further splitting of the ENDOR spectrum. If there is no quadrupole interaction, the energy levels and ENDOR transition frequencies can be calculated by replacing m_I with the total nuclear spin $I_1 + I_2 + \ldots + I_N$, as for the ESR spectrum. The spin-spin splittings for two equivalent nuclei with spin 3/2 and no quadrupole interaction are shown in Figure 11a. As for quadrupole splittings, the m_I components of the saturated ESR line determine which second order lines are observed in the ENDOR spectrum.

If a quadrupole interaction is present, the Breit-Rabi effect causes the quadrupole lines for a single nucleus to shift, but not to split. The energy levels and transition energies in eqns 25 and 26 become

$$E = g_\theta \mu_B B_0 m_S + a m_S m_I + m_S W_2 [I(I+1) - m_I(m_I \pm 1)]$$
$$+ \tfrac{1}{2} P_\theta [m_I^2 - \tfrac{1}{3} I(I+1)] - g_N \mu_N B_0 m_I \qquad (29)$$

$$\Delta E(\pm)_{ENDOR} = \tfrac{1}{2}a \mp \tfrac{1}{2}W_2 \pm m_q (P_\theta \mp W_2) \mp h\nu_N$$

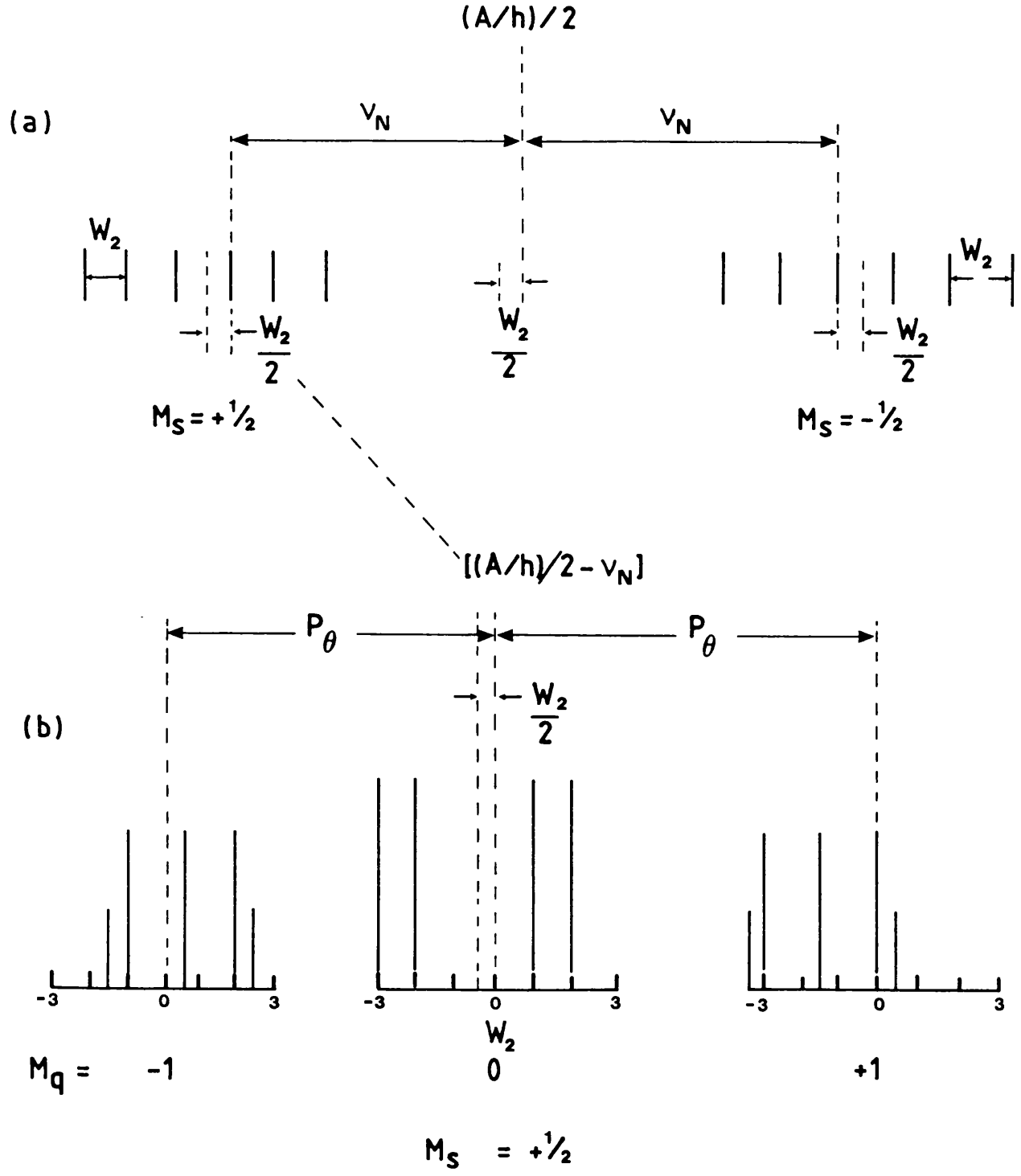

FIGURE 11

Second order ENDOR transition frequencies for two equivalent nuclei with $I = 3/2$, $A > 0$, $(A/h)/2 > \nu_N$ and (a) no quadrupole interaction, (b) quadrupole interaction with $P \gg W_2$, for which only the $M_s = +1/2$ manifold is shown.

These quadrupole effects would not be apparent in the second order shifts of the ESR lines. The second order ENDOR transition frequencies for a single nucleus with spin 3/2 and a quadrupole splitting are shown in Figure 10c.

If both a quadrupole interaction and equivalent nuclei are present, the quadrupole interaction lifts the degeneracy of the $m_I = m_1 + \ldots + m_N$ states, and the second order effects can no longer be calculated by using the total nuclear spin in eqns 25 and 26. In this case, the ENDOR spectrum obtained depends very much on the relative magnitude of the second order effect, W_2, and the quadrupole interaction, P_θ. A complete treatment has been given by Feuchtang[8] and by Schoemaker.[9] For two equivalent Cl ligands, with $q \gg W_2$, isotropic a and $\vec{B}_o$ aligned along the z-axis, the energy levels are given to second order by

$$E = g_\theta \mu_B B_0 m_S + (a m_S - g_N \mu_N B_0)(m_{I_1} + m_{I_2}) + q[3(m_{I_1}^2 + m_{I_2}^2) - 2I(I+1)] \qquad (30)$$

There are 16 eigenvalues and 20 allowed transitions, some of which are degenerate at this orientation. Thus, each m_s component is split into 14 lines, as shown in Figure 11b. Each m_s component is centered at the same frequency as the second order ENDOR transitions for a single nucleus. Figure 12 shows the ENDOR spectrum for two equivalent $^{35}Cl^-$ ligands in the complex $(RhCl_6)^{4-}$ in NaCl. As predicted by eqn 30, the largest second order splitting ($3W_2$) occurs on the $m_q = 0$ lines, and is just resolved in this spectrum.

The distinction between magnetically equivalent and geometrically equivalent nuclei should be noted. Magnetically equivalent nuclei occur in pairs in complexes with an inver-

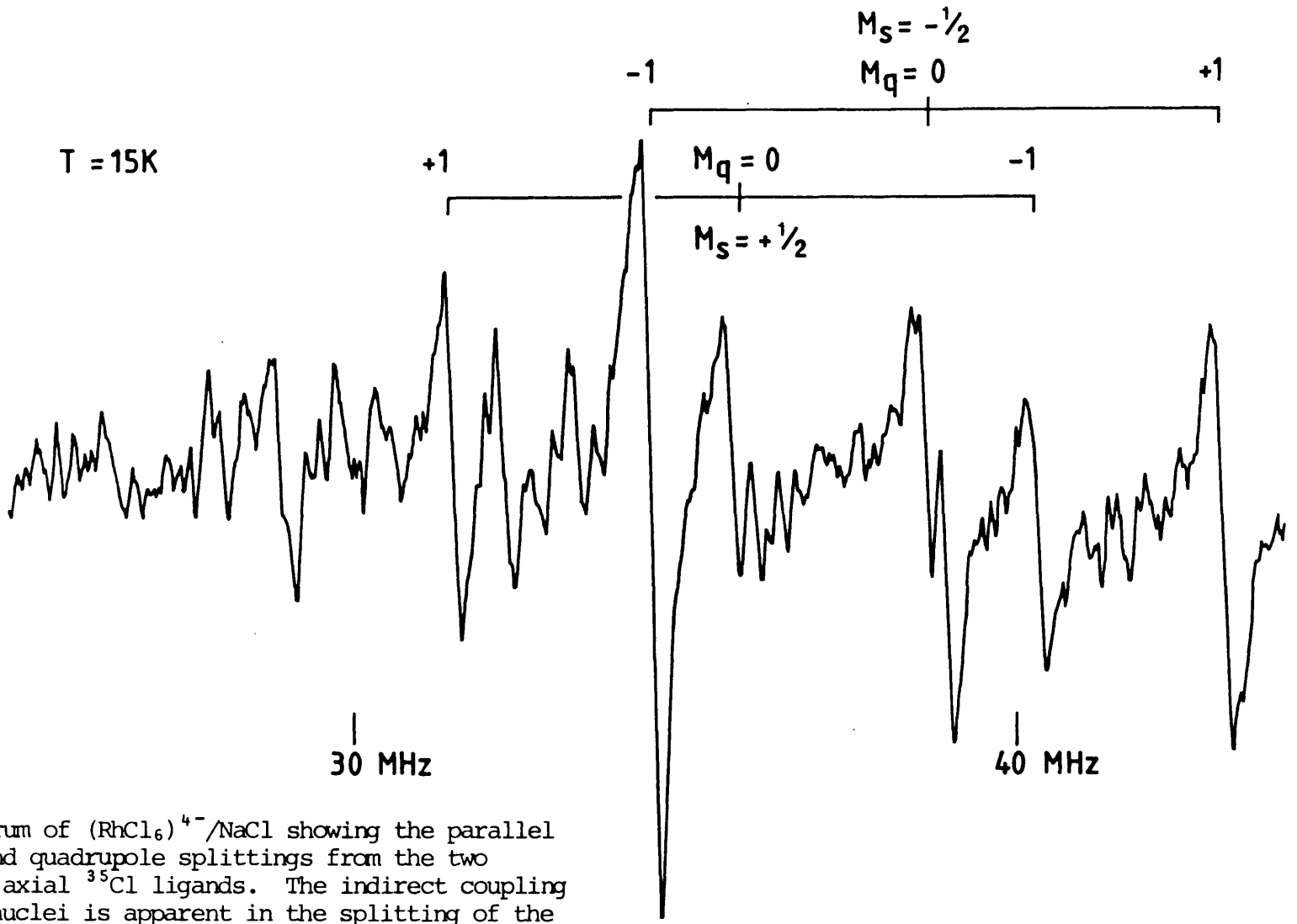

FIGURE 12

ENDOR spectrum of $(RhCl_6)^{4-}/NaCl$ showing the parallel hyperfine and quadrupole splittings from the two equivalent, axial ^{35}Cl ligands. The indirect coupling of the two nuclei is apparent in the splitting of the $M_q = 0$ lines. Some ^{37}Cl lines are also present.

sion centre. Goemetrically equivalent nuclei will only be equivalent along selected symmetry directions.

The coupling of inequivalent nuclei, which includes different isotopes of the same element, has a much smaller effect on the ENDOR spectrum than the coupling of equivalent nuclei. It is of the order of $\frac{a^2}{2g_\theta^2 \mu_B^2 B_0^2}$. If the hyperfine splittings from both nuclei are resolved in the ESR spectrum, so that each m_I component can be saturated separately, then a shift of the ENDOR lines is observed. A splitting is observed if several m_I components are saturated simultaneously. These effects have been observed in the ENDOR spectra of Cu- and Ag-containing organic complexes, which have a large hyperfine interaction of the central metal nucleus, and account for the very broad ENDOR lines sometimes observed for transition metal complexes.[10]

The presence of strongly anisotropic interactions in the effective spin Hamiltonian has a number of direct and indirect effects on the ENDOR spectrum that have so far been ignored.

The nuclear Hamiltonian of eqn 16 can be written as

$$\underset{\wedge}{\mathcal{H}}_N = (a m_S - g_N \mu_N B_0) \underset{\wedge}{\vec{I}}_z + (m_S \hat{e}_z) \tilde{B} \vec{I} + \underset{\wedge}{\vec{I}} \tilde{Q} \underset{\wedge}{\vec{I}} \qquad (31)$$

$\hat{e}_z$ is the unit vector in the z-direction. This can be rewritten as

$$\mathcal{H}_N = \vec{B}_{eff} \underset{\wedge}{\vec{I}}_z + (m_S \hat{e}_z) \tilde{B} \vec{I} + \underset{\wedge}{\vec{I}} \tilde{Q} \underset{\wedge}{\vec{I}} \qquad (32)$$

where $\vec{B}_{eff} = |B_0 - m_S a/g_N \mu_N| \hat{e}_z$

For a hyperfine interaction with small anisotropy, the effective field is along the applied field direction. Its magnitude is inversely proportional to the nuclear frequency, ν_N, and is therefore enhanced for nuclei with small ν_N (eqn 32). A related enhancement of the oscillating rf field occurs. This

is fortunate, since the rf field strength necessary for the observation of an ENDOR signal is inversely proportional to ν_N (eqn 8). For a large anisotropic hyperfine interaction, the effective field is no longer along the applied magnetic field direction. The magnitude and direction are now defined by the equations

$$\begin{aligned} |B_{eff}| &= |B_0 - m_S(a+\tilde{B})/g_N\mu_N| \\ &= [(B_{eff})_x^2 + (B_{eff})_y^2 + (B_{eff})_z^2]^{\frac{1}{2}} \\ \tan\epsilon &= \frac{[(B_{eff})_x^2 + (B_{eff})_y^2]^{\frac{1}{2}}}{(B_{eff})_z} \end{aligned} \tag{33}$$

ϵ is the angle between the effective field and the xy plane of the laboratory axis system. For axial symmetry, eqns 33 become

$$\begin{aligned} B_{eff} &= {}^1/g_N\mu_N\left\{m_S a + b(3\cos^2\theta - 1) - g_N\mu_N B_0{}^2] + g_\theta m_S^2 b^2 \sin^2\theta\cos^2\theta\right\}^{\frac{1}{2}} \\ &\approx {}^1/g_N\mu_N|\, m_S[a + b(3\cos^2\theta - 1) - g_N\mu_N B_0]\,| \\ \tan\epsilon &= \frac{3b\sin\theta\cos\theta}{a + b(3\cos^2\theta - 1) - g_N\mu_N B_0/m_S} \end{aligned} \tag{34}$$

The first order solutions given by eqns 20 and 21 only hold when the magnetic field is aligned along a principal axis. At all other orientations, $\vec{B}_o$ must be replaced by $\vec{B}_{eff}$. Thus, eqn 22 becomes

$$\begin{aligned} \nu(\pm) &= |\,({}^{A\theta}/h)m_S - g_N\mu_N B_{eff} - m_q P_\theta\,| \\ P_\theta &= 3[q(3\cos^2\theta''_{eff} - 1) + q^2\sin^2\theta''_{eff}\cos 2\phi''_{eff}] \end{aligned} \tag{35}$$

where $\theta''_{eff} = \theta'' - \epsilon$. An example of the deviations from eqn 22 at off-axis orientations, due to a large anisotropic hyperfine interaction is shown in Figure 13. This shows the angular

FIGURE 13

Angular rotation plot of ENDOR lines from the two axial Cl^- ligands in $(RhCl_6)^{4-}/AgCl$, showing the crossing angle, as influenced by B_{eff}, of the quadrupole lines. [See eqns. 34 and 35]

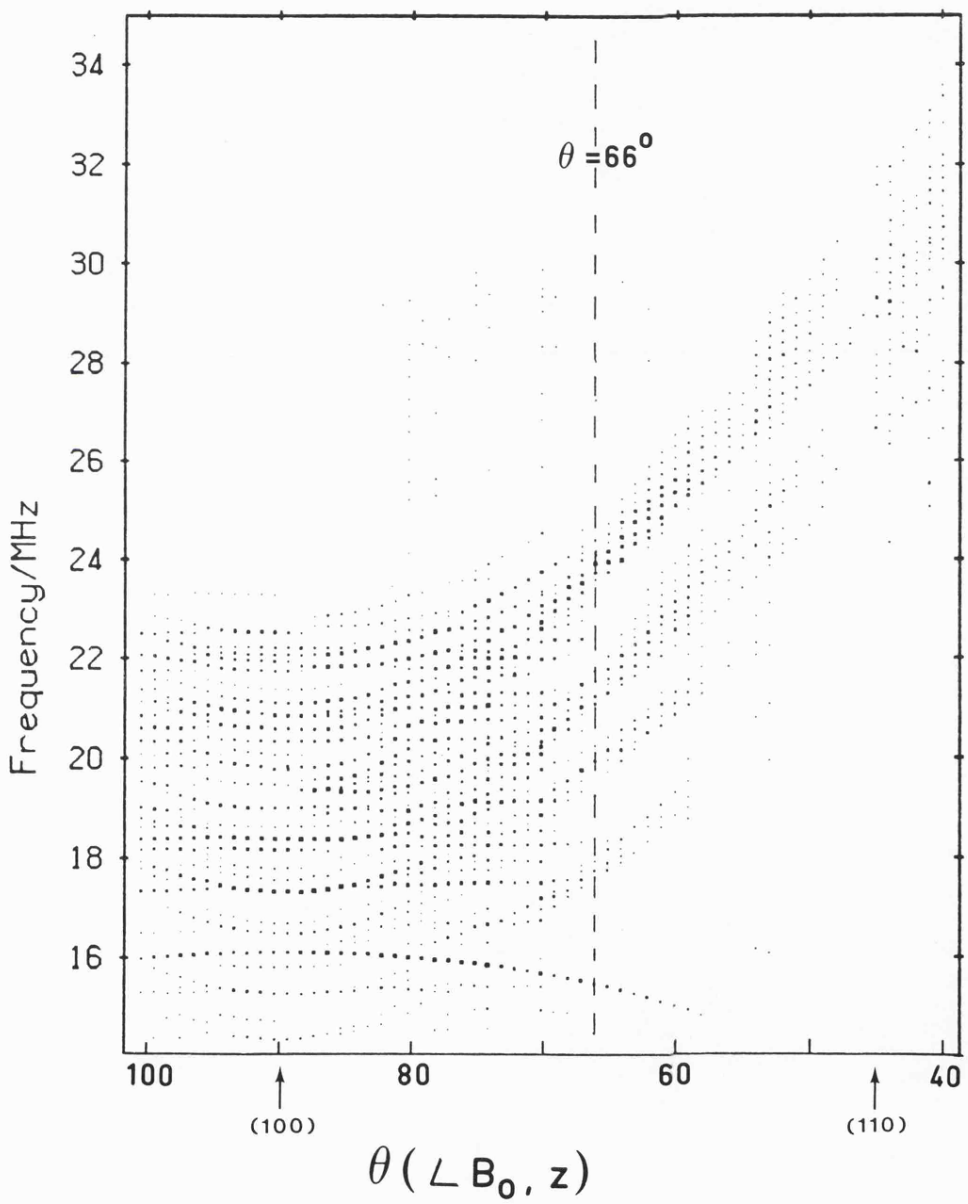

dependence of the six ENDOR lines from the two axial chlorines of the $(RhCl_6)^{4-}$ complex in AgCl. The quadropole splittings collapse to a pair of lines at $\theta = 66^\circ$ instead of at 54.4°, as predicted by equation 22. Thus, the angle that the effective field makes with respect to the normal of the applied field is 11.6°.

As discussed above, strongly anisotropic hyperfine interactions lead to a breakdown of the high field approximation, which is essentially the assumption that the electron spin is quantized along the direction of B_{eff}. This assumption is also violated when other strongly anisotropic interaction tensors are present in the spin Hamiltonian. Thus, an anisotropic g-tensor can affect the principal values and direction cosines of the hyperfine interaction, causing a deviation from the cosine law dependence given by equation 17. This is shown schematically in Figure 14. Except for extremely anisotropic g-or fine structure-tensors, this effect can usually be ignored.

As a result of the field dependence of ν_N and W_2, an anisotropic ESR spectrum has a direct effect on the ENDOR transition frequencies (eqns 12, 22, 26 and 35). It is helpful in the analysis of the ENDOR spectra to subtract out this strong Larmor frequency dependence.

The anisotropy of an ESR spectrum often results in the spectral separation of absorptions arising from complexes in inequivalent orientations. In such an instance, the ENDOR spectrum will be only from those orientations responsible for the saturated ESR line. If resolved fine structure features are present in the ESR spectrum, ENDOR spectra due to each m_s state can be obtained separately.

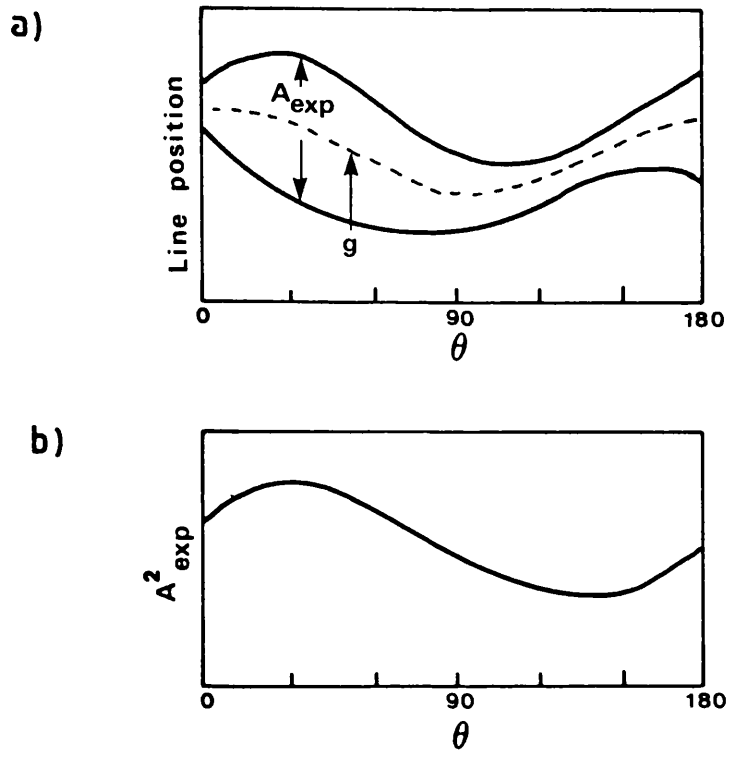

FIGURE 14

Isofrequency plot, for a four level system, of the (a) experimental ESR data and (b) hyperfine splitting, showing the effect of g-tensor anisotropy on the hyperfine interaction. From reference 2.

When all of the interactions in the nuclear Hamiltonian are of the same order of magnitude, the second order approximations discussed above are not very good, and higher perturbation solutions converge very slowly. In these circumstances, an exact diagonalization of the Hamiltonian is necessary. It should be noted that second and higher order corrections to the ENDOR transition frequencies become necessary when first order solutions are still sufficient to explain the ESR transition energies.

5.3.4 Matrix ENDOR

In the ENDOR spectra of solids, particularly disordered solids, the dominant feature is usually a single line at the nuclear free frequency. This is called the matrix ENDOR line and is the result of a T_{1e} ENDOR mechanism. It results from a purely dipolar interaction of the unpaired electron with nuclei up to 5-6 Å distant. Closer nuclei give rise to a doublet spectrum due to both contact and dipolar interactions, as described above. In liquids, rapid tumbling of the paramagnetic complex averages the dipolar interactions to zero and no matrix line is observed.

The lineshape of the matrix ENDOR line is dependent upon the lineshape function, $g(\nu - \nu_0)$, of the NMR spin packet. This is centred at the resonant frequency, ν_0, and the frequency dependence of $g(\nu - \nu_0)$ is determined by nuclear relaxation processes involving T_{1N} and T_x. If these processes are independent of angle, then ν is given by the expression:
$\sum_i g_e \mu_B g_N \mu_N (3\cos^2\theta - 1) m_s I_{z_i} r_i^{-3}$ summed over i nuclei at distance r. The resulting spectrum is a doublet with a line corresponding to each m_s manifold, as discussed above

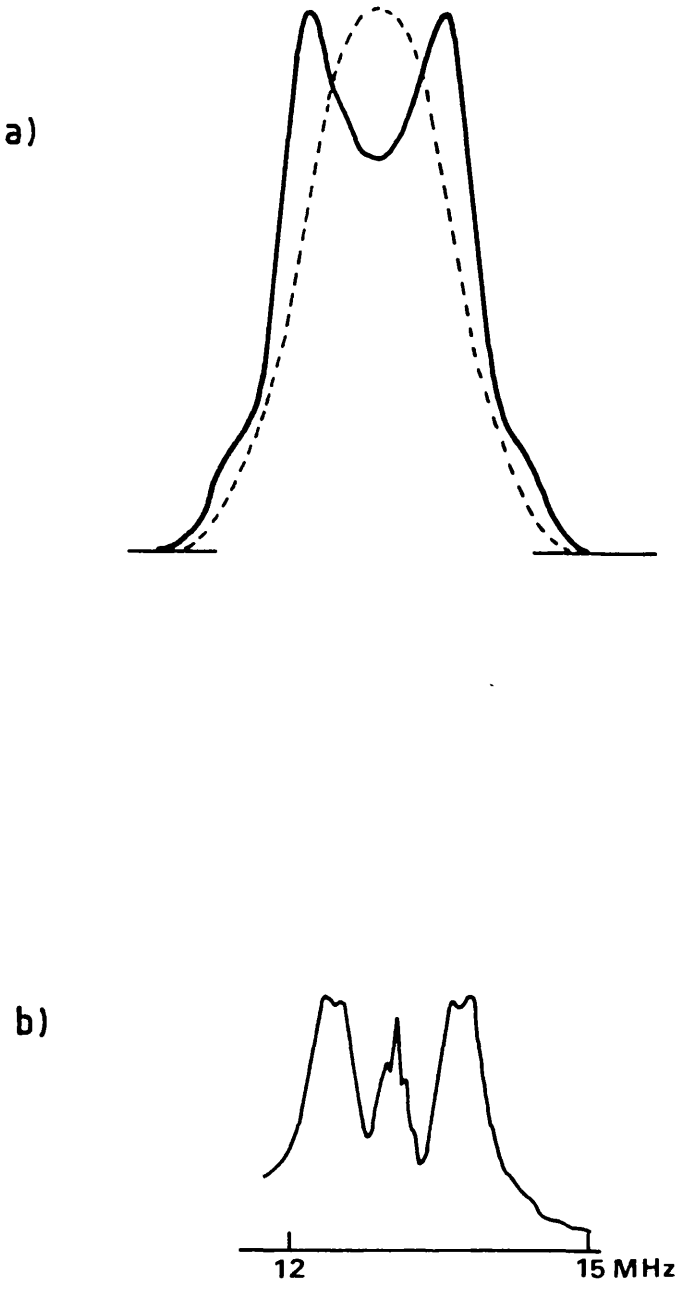

FIGURE 15

(a) Matrix ENDOR lineshapes simulated with (----) and without (——) angularly dependent nuclear relaxation processes. From reference 6.

(b) Experimental matrix ENDOR line of trapped H atoms in NH_4 Y-type zeolite. Motional relaxation processes give rise to shoulders on the central line. From reference 16.

(Figure 15a). If an angular dependence of the relaxation processes is assumed, such as is observed for the electron-nuclear dipolar (END) mechanism discussed in reference 6, then a single matrix line results. The latter case is almost always observed experimentally. Depending on the exact nature of the END mechanism, one or two shoulders are sometimes observed on either side of the matrix line (Figure 15b). This can occur when either the matrix nuclei or the paramagnetic species undergo rapid motion so that motional relaxation processes are much more efficient than END relaxation processes.[6,16] In such cases, chemical or physical arguments must be used to distinguish between shoulder matrix lines and small isotropic hyperfine splittings.

5.4 The Assignment of ENDOR Lines

5.4.1 Directly from the ENDOR data

If an ENDOR spectrum is comprised of transitions from several types of nuclei, some with more than one isotope or symmetry poition, and from a number of complexes, the assignment of ENDOR lines to a particular complex and nucleus becomes difficult. In this section, several data analysis methods and experimental techniques are presented which aid ENDOR spectral assignment.

As discussed above, to first order, the pair of ENDOR lines resulting from a given hyperfine interaction are either centred at or separated by $2\nu_N$. Thus, if ENDOR lines can be associated in pairs, the type of nucleus involved in the hyperfine interaction is unequivocally identified. However, in complex spectra, it is sometimes difficult to pick out pairs of lines. If the nucleus in question has several naturally

abundant isotopes, then the associated ENDOR lines will have a characteristic pattern which should aid assignment of transitions. The ENDOR pairs from each isotope N will either be centered at $A_N/2$ or separated by A_N where $A_{N_i}/A_{N_k} = \nu_{N_i}/\nu_{N_k}$. The intensities of the ENDOR lines from an isotope N will be proportional to its natural abundance.

The frequency shift of an ENDOR line as a function of a small change in the static magnetic field position is given by

$$\Delta\nu = \frac{g_N \mu_N}{h} \quad (\Delta B_o) \tag{36}$$

Thus, a measurement of line position as a function of magnetic field can aid the assignment of an ENDOR line to a particular type of nucleus. This approach can also be used to determine if an ENDOR line is one of a pair centered at ν_N or centred at A/2, since an increase in field causes different shifts for the two cases (Figure 16.)

Once an ENDOR spectrum is resolved into pairs of lines that can be assigned to a type of nucleus, these splittings must be assigned to a particular complex and site. If the sample is a single crystal, an angular rotation study provides information about the site symmetry of each nucleus. This very often pinpoints the nucleus' position in the complex. If the sample is a powder or liquid, one must use chemical techniques, such as isotopic substitution, as well as "chemical intuition" to assign the splittings. In some cases, as discussed in the next chapter, a type of angular rotation ENDOR study is possible for powder samples.

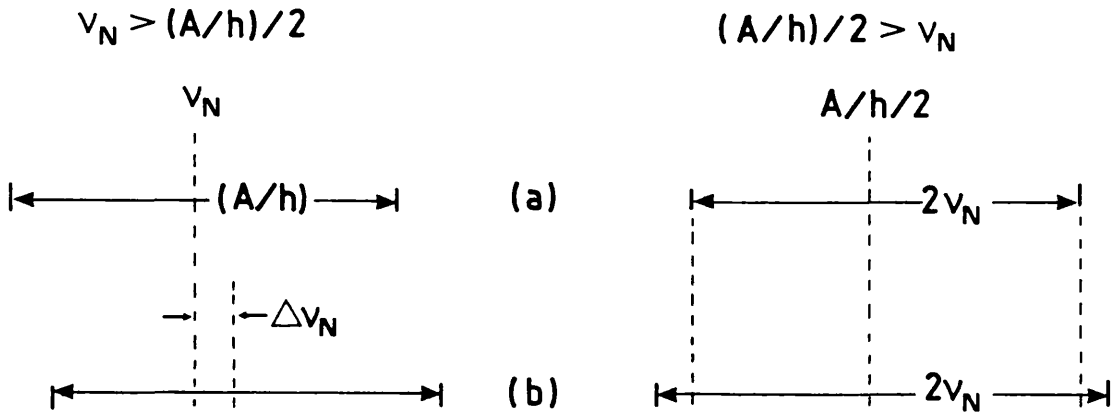

FIGURE 16

ENDOR line shifts as a function of magnetic field.
(a) $B_0 = B_1$, (b) $B_0 = B_2$. $B_2 > B_1$.

5.4.2 From TRIPLE ENDOR experiments

A double ENDOR experiment, called TRIPLE ENDOR, can be used to unravel overlapping ENDOR spectra from different complexes. The TRIPLE ENDOR experiment consists of first obtaining an ordinary ENDOR spectrum by sweeping the rf field. An ENDOR line, at frequency ν_i, is selected and saturated by irradiating the system with a second strong rf field at ν_i. Meanwhile, the first rf field is swept again, and changes induced by the second pumping field are noted.

The nature of these changes can be deduced from Figures 17 and 18. An experimental example considered in the next chapter is ditertiary butyl nitroxide in toluene. The ENDOR spectrum consists of a pair of lines at $(A_N/2) \pm \nu_N$ from the nitrogen nucleus, and a pair of lines at $\nu_N \pm (A_H/2)$ from the 18 equivalent methyl protons. A simplified six level energy diagram for this system, considering only one proton and one nitrogen, and assuming that ν_N and A_H are both positive is shown in Figure 18a. The ENDOR line intensity will be proportional to the population difference between the levels involved in the NMR transition following saturation of the ESR transition. As discussed above, and shown in Figure 18 b, for the transient ENDOR mechanism, this difference is $\epsilon/2$, for each of the four ENDOR transitions. If a saturating rf field is applied between levels 7 and 8, that is, the low frequency proton line is saturated, levels 6, 7, and 8 will be equalized in population (Figure 18b). The population difference will decrease for ENDOR transitions 7 to 8 and 7 to 9, and increase for 5 to 6 and 4 to 6. The resulting change in the ENDOR spectrum is shown in Figure 17. In general, it can be shown that transitions in the same electronic manifold as the saturated

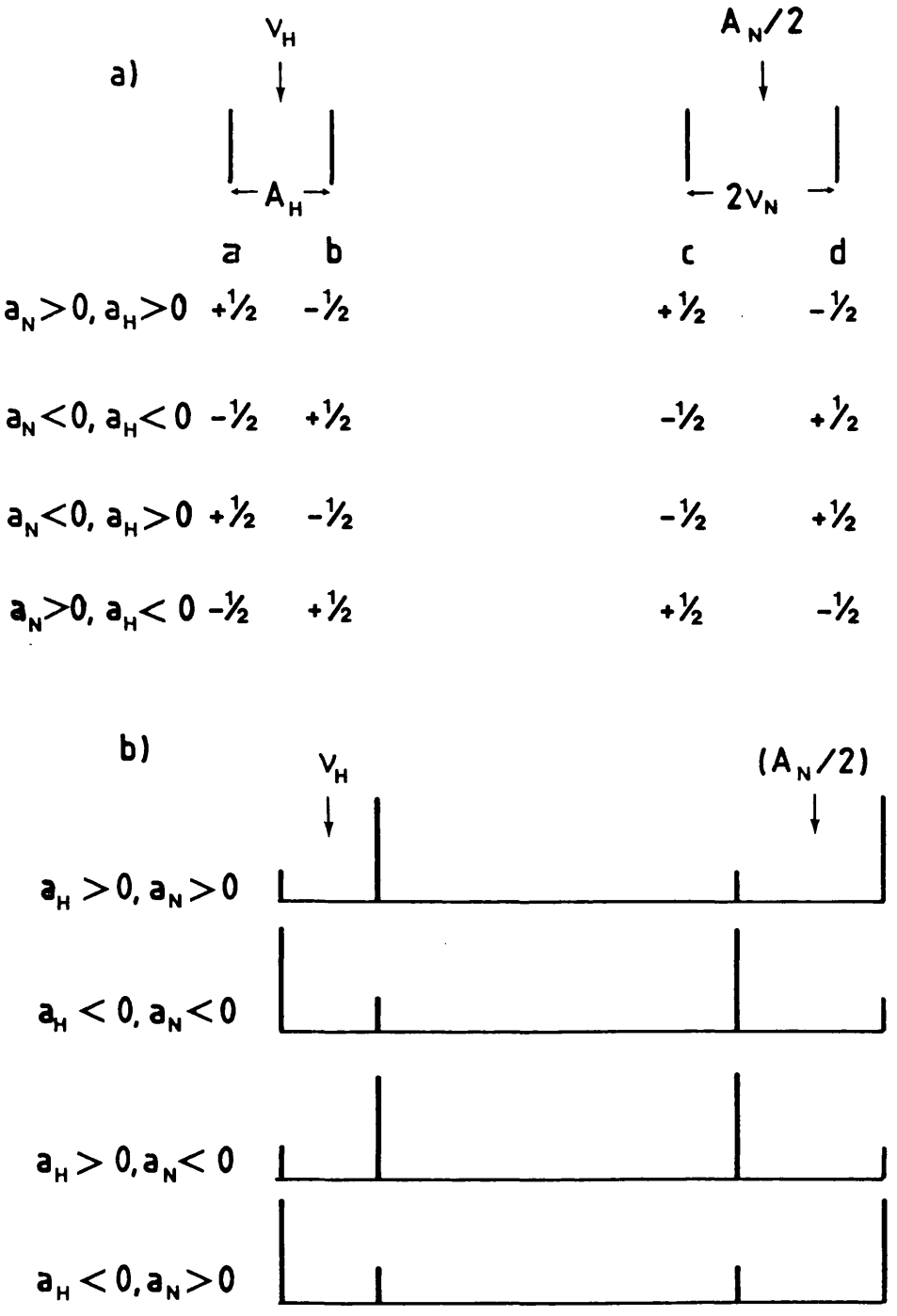

FIGURE 17

Schematic ENDOR (a) and TRIPLE ENDOR (b) spectra for an interaction with one proton and one nitrogen nucleus, showing the intensity changes observed as a result of pumping the $M_S = +½$ nitrogen (or proton) ENDOR line for all possible sign combinations of a_N and a_H.

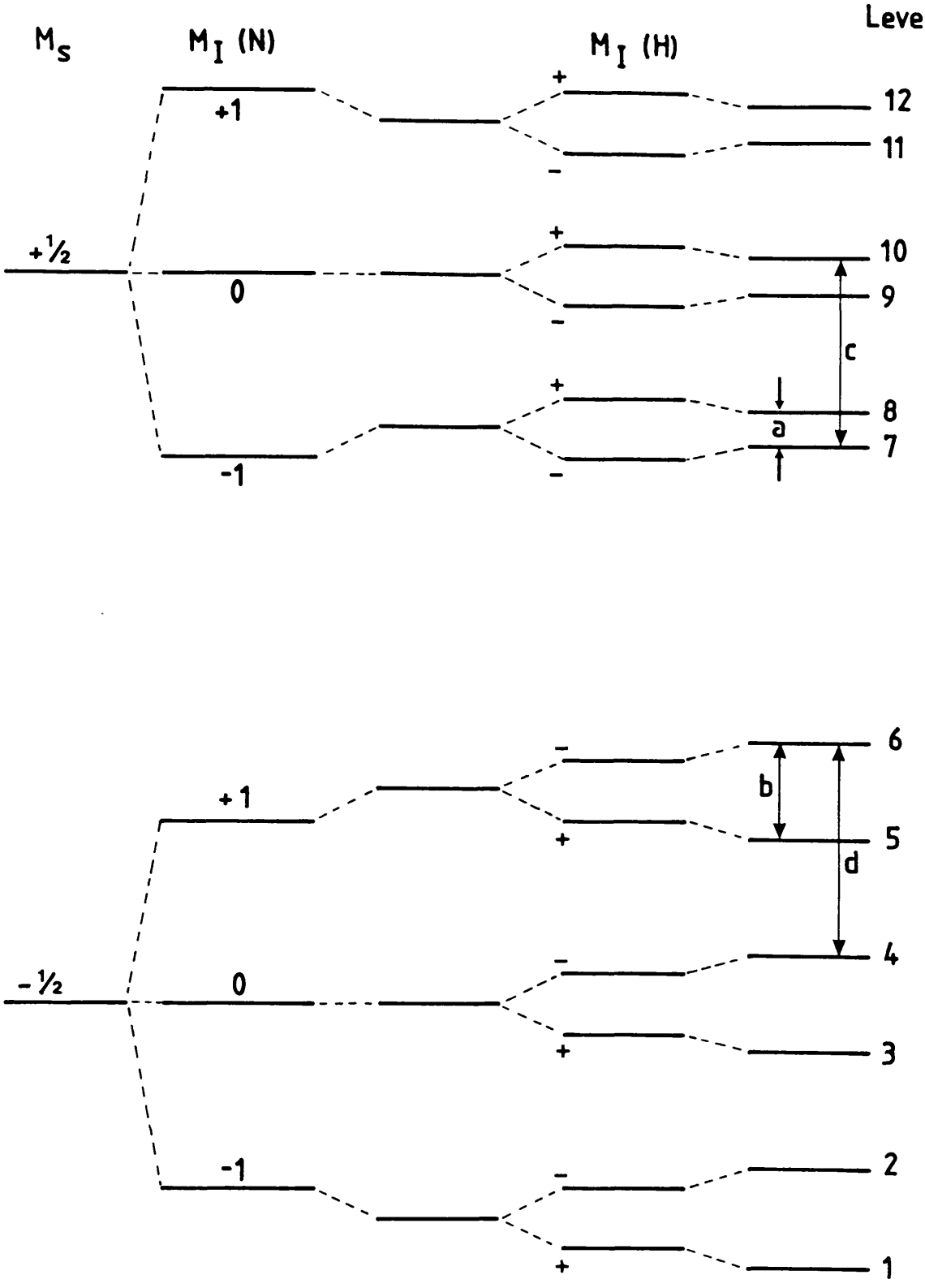

FIGURE 18(a)

Energy level diagram for an interaction for one nitrogen and one hydrogen nucleus showing ENDOR transitions labelled a, b, c and d in Fig. 17. A_H, $A_N > 0$.

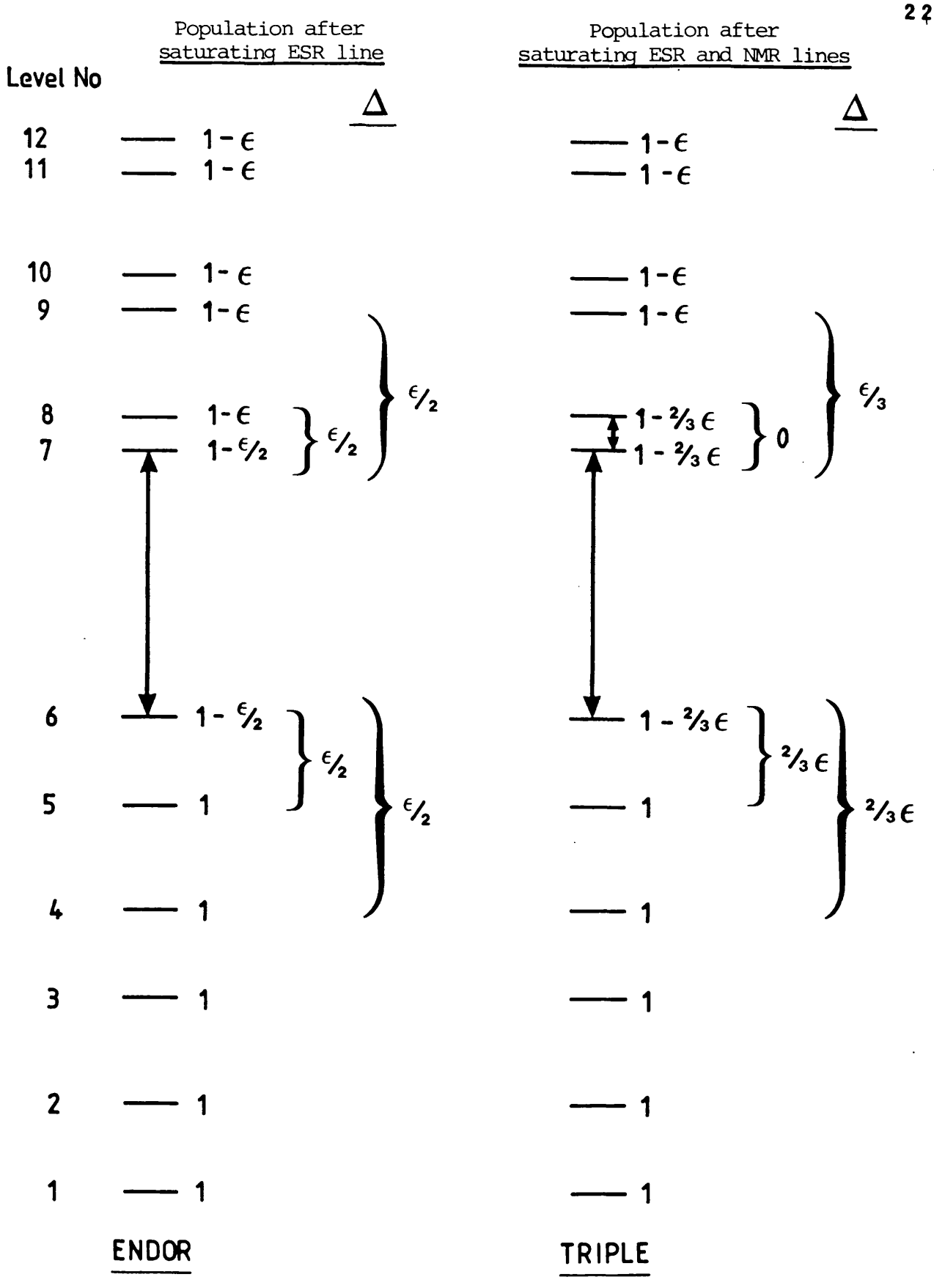

FIGURE 18(b)

Energy level populations and differences (Δ) for an ENDOR and a TRIPLE experiment for the system described in Fig. 18(a).

NMR transition will decrease in intensity, and those in the other electronic manifold will increase in intensity. If an ENDOR spectrum is a composite of several different complexes, a TRIPLE experiment on an ENDOR line from one of the complexes will distinguish the component spectra. Only ENDOR lines from that complex will change in intensity.

TRIPLE ENDOR can also sometimes be used to deduce the relative signs of hyperfine couplings. The four possible sign combinations and the corresponding TRIPLE responses for the DTBN radical are shown in Figure 17. If A_N and A_H have the same sign, alternate lines increase in intensity. If the hyperfine signs are dissimilar, neighbouring lines increase or decrease in intensity. It is not possible to establish the absolute hyperfine signs from the TRIPLE ENDOR experiment alone. In order for this experiment to work, the ENDOR mechanism must have at least a small transient component.

The TRIPLE ENDOR technique just described is referred to as general TRIPLE. A variation of this technique, special TRIPLE, used to enhance weak spectra, is discussed in Chapter 6.

5.4.3 From ENDOR-induced ESR

The technique of ENDOR-induced ESR can also be used to distinguish ENDOR lines arising from different complexes. In doing so, it becomes possible to separate overlapping ESR spectra.

As described above, an ENDOR response is observed when an ESR transition is saturated by a strong microwave field fulfilling the resonance condition $h\upsilon_e = g_\theta \mu_B B_o$, and an rf field is frequency swept until it fulfills the resonance condition $h\upsilon_N = g_N \mu_N B_o$, inducing an NMR transition.

The NMR transition causes a detectable change in the signal intensity of the saturated ESR line. The NMR transition can equally well be detected by first choosing the rf field frequency to fulfill the NMR resonance condition and then sweeping the static magnetic field until the ESR resonance condition is fulfilled. As with the usual ENDOR experiment, the intensity change in the ESR signal is detected, but here, as a function of static magnetic field. Thus, an ESR spectrum is obtained which includes only ESR transitions belonging to the same complex as the induced NMR transition. This is the ENDOR-induced ESR spectrum. An example of such a separation of ESR spectra is shown in Figure 19 for F centers in BaFCl.

The ENDOR-induced ESR spectrum will include only those ESR transitions whose m_I components are among those involved in the induced NMR transition. Thus, if quadrupole or second order splitting, which remove the degeneracy of different m_I levels, are resolved in the ENDOR spectrum, the ENDOR-induced ESR spectrum will depend on which ENDOR line is stimulated.

As an example, consider the ENDOR-induced ESR spectra of $(RhCl_6)^{4-}$ in AgCl in Figure 20. The normal ESR spectrum, with $\vec{B}_o$ along the symmetry axis of the complex, consists of seven lines due to the hyperfine interaction of a single unpaired electron with two equivalent chloride ligands. The ENDOR-induced ESR spectrum obtained when the $m_s = -\frac{1}{2}$, $m_q = -1$ quadrupole line is stimulated consists of only the five high field ESR lines. The low field transitions, which involve m_I components +3/2 and +1/2, are not observed since complexes with these m_I components are not involved in the $m_q = -1$ quadrupole transition. If, however, there was efficient relaxation between nuclear spin states, or strong T_{x2} relaxation processes, all

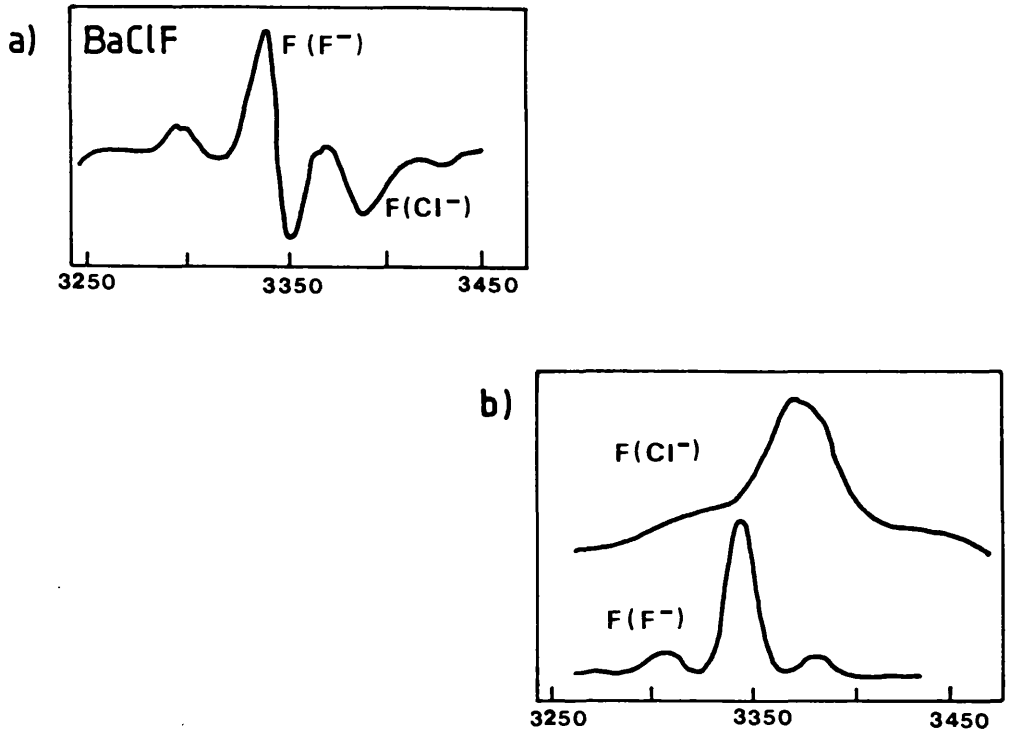

FIGURE 19

(a) ESR spectrum and (b) ENDOR-induced ESR spectra of an electron trapped at a Cl^- or F^- vacancy in BaFCl [$F(Cl^-)$ or $F(F^-)$]. The ENDOR-induced ESR spectra were obtained by pumping the well-separated ENDOR transitions of either the $F(Cl^-)$ or the $F(F^-)$ center. From reference 11.

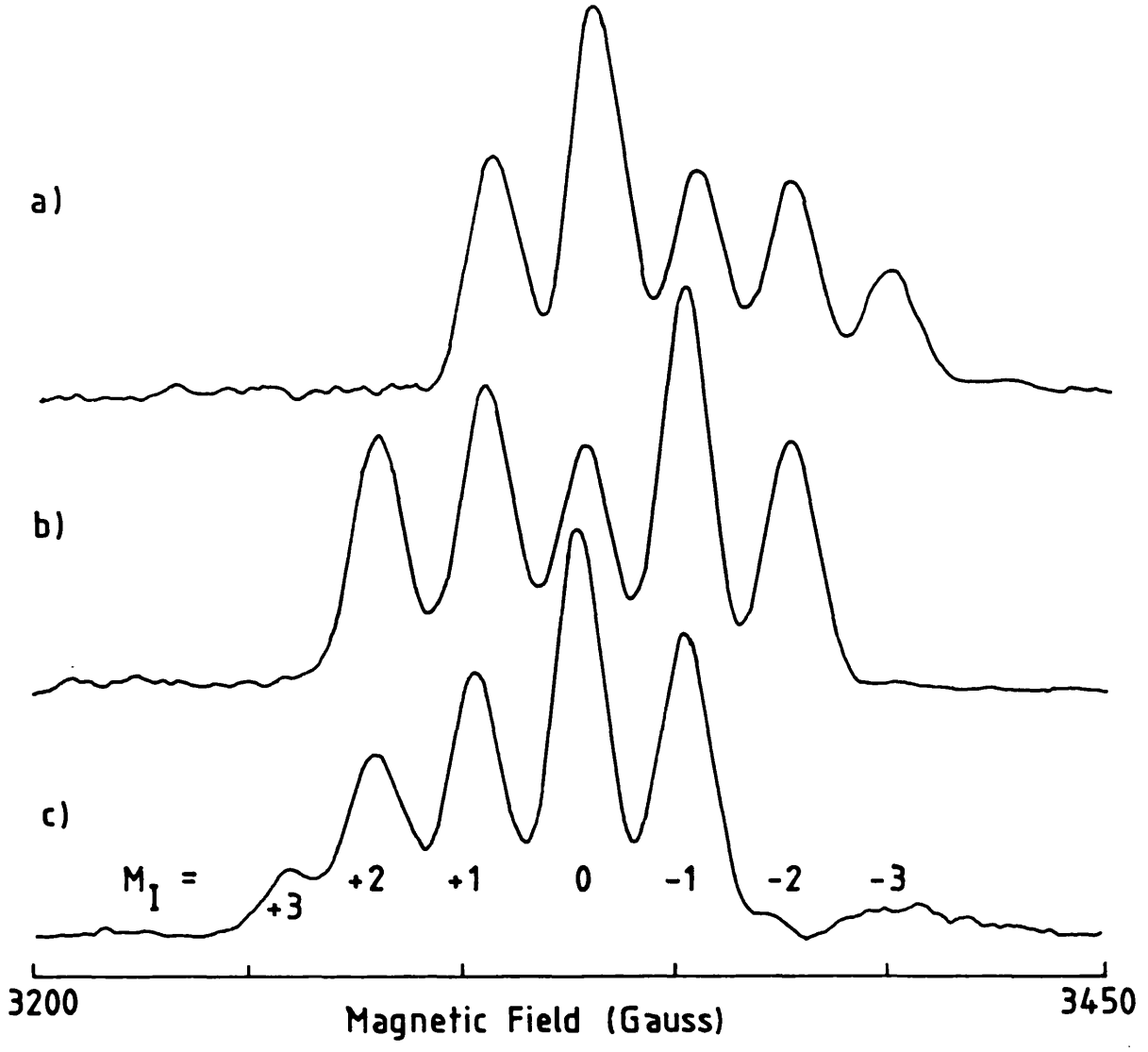

FIGURE 20

ENDOR-induced ESR spectra of $(RhCl_6)^{4-}/AgCl$, B_o 11 Z, measured while exciting one of the (a) $M_q = -1$, (b) $M_q = 0$ and (c) $M_q = +1$ ENDOR transitions in Figure 9.

quadrupole lines would be observed. A complete discussion of such effects is given by Niklas and Spaeth.[11]

A number of other variations of the basic ENDOR experiment have been developed which are helpful in unravelling complex spectra. These are summarized in references 10 and 12.

5.5 The Quadrupole Interaction

A quadrupole splitting is observed when the nuclear electric quadrupole constant is nonzero, that is, for $I > \frac{1}{2}$, and for a nonzero electric field gradient. A nonzero electric field gradient at a nucleus can arise as a result of the electron distribution of the nucleus' electrons. In the example of $(RhCl_6)^{4-}$, if the host lattice is essentially ionic, then the Cl ion has a closed valence shell; the electrons have a spherical distribution, and there is no electric field gradient at Cl^- due to chlorine. Likewise, if the Cl ion is surrounded by a distribution of ionic charges with cubic symmetry, as in an undisturbed AgCl lattice, this charge distribution has zero field gradient and thus gives no quadrupole splitting. However, an electric field gradient can arise as a result of electron density in the Cl^---Rh^{2+}--Cl^- bond. The quadrupole interaction is sensitive to <u>total</u> electron density, not just unpaired electron density, in a bond and thus provides information about the degree of covalency in bonding. The quadrupole interaction also sometimes yield information about sp hybridization, since s-electron density does not contribute to the quadrupole splitting. Even if the bonding in the $(RhCl_6)^{4-}$ complex is purely ionic, the electric field gradient at the ligands will be nonzero if the ionic charge of Rh^{2+} is nonzero with respect to the host lattice. If the bonding is

purely ionic and the metal nucleus is treated as a point with an overall charge q, then the electric field gradient along the z-axis is

$$(\partial^2 V/\partial z^2) = 2q / r^3 \qquad (37)$$

r is the distance between the chlorine ligand and the central metal ion. Ideally, one could determine the charge on the central metal ion using equation (37). However the interpretation of the calculated electric field gradient must take into account the antishielding effect. If a nucleus is charged, the closed shell electrons close to the nucleus are distorted; this leads to a huge correction to the electric field gradient. The correction is a function of r_n, the distance from the nucleus, but to a good approximation, inside the charge distribution the correction is small, and outside, it rapidly approaches a finite value. The correction is

$$\frac{\partial^2 V}{\partial z^2} = \left(\frac{\partial^2 V}{\partial z^2}\right)^0 \left[1 - \gamma(r_n)\right] \qquad (38)$$

$\gamma(r_n)$ is the Sternheimer antishielding factor.
For Cl, $\gamma(\infty) = 48$.[15]

References

1. H. Seidel, Habilitationsschrift, Technischen Hochshule Stuttgart (1966).

2. C.P.Poole, Jr. and H.A. Farach, The Theory of Magnetic Resonance (Wiley-Interscience, New York, 1972).

3. M.C.R. Symons, Chemical and Biochemical Aspects of Electron-Spin Resonance Spectroscopy (Van Nostrand Reinhold, New York, 1978).

4. J.E. Wertz and J.R. Bolton, Electron Spin Resonance: Elementary Theory and Practical Applications (McGraw - Hill, New York, 1972).

5. C.P. Poole, Jr., Electron Spin Resonance: A Comprehensive Treatise on Experimental Techniques, 2nd ed. (John Wiley & Sons, New York, 1983).

6. L. Kevan and L.D. Kispert, Electron Spin Double Resonance Spectroscopy (Wiley & Sons, New York, 1976).

7. M.M. Dorio and J.H. Freed, Multiple Electron Resonance Spectroscopy (Plenum Press, New York, 1979).

8. T.E. Feuchtang, Phys. Rev. 126, 1628 (1962).

9. D. Shoemaker, Phys. Rev. 174, 1060 (1968).

10. A. Schweiger, Habilitationsschrift, ETH-Zentrum, Zurich (1983).

11. J.R. Niklas and J.M. Spaeth, phys. stat. sol. (b) 101; 221 (1980).

12. A. Schweiger and Hs. H. Günthard, J. Mag. Res. 57, 65 (1984).

13. G. Breit and I.I. Rabi, Phys. Rev. 38, 2028L (1931).

14. J.M. Baker, E.R. Davies and T. Rs. Reddy, Contemp. Phys. 13, 45 (1972).

15. C.P. Slichter, Principles of Magnetic Resonance (Springer-Verlag, New York, 1980).

16. J.C. Vedrine, J.S. Hyde and D.S. Leniart, J. Phys. Chem. 76, 2087 (1972).

C H A P T E R S I X

EXPERIMENTAL ASPECTS OF ENDOR SPECTROSCOPY

CHAPTER SIX

Experimental Aspects of ENDOR Spectroscopy

6.1 Obtaining an ENDOR Spectrum

The ENDOR sensitivity which is attainable in practice is reduced from the ESR sensitivity by a factor of 100; thus, the optimization of instrumental and sample parameters is especially important. These parameters are material-dependent and can have a narrow optimum range so that an empirical approach can be rather "hit-or-miss". Therefore, those experimental factors affecting sensitivity and relative line intensities are outlined below. A description is given of the two ENDOR spectrometers used for the studies discussed in this thesis, along with an evaluation of their applicability to various systems. Several model studies of disordered materials and of liquids are discussed.

6.1.1 General Requirements

A general set of conditions which must be fulfilled in order to obtain an ENDOR spectrum are[1]

$$T_E \gg (T_{1e}\, T_{2e})^{\frac{1}{2}} \geq (\gamma_e\, H_1)^{-1} \approx (\gamma_N\, H_2)^{-1}$$

$$(T_{1N}\, T_{2N})^{\frac{1}{2}} \geq (\gamma_N\, H_2)^{-1} \qquad (1)$$

T_E is the electron exchange time and can correspond to a spin exchange time, T_{ss}, a spin diffusion time, or a cross relaxation time, T_x; T_{1e} and T_{2e} are the electron spin lattice and electron spin-spin relaxation times; T_{1N} and T_{2N} are the nuclear spin lattice and nuclear spin-spin relaxation times; γ_e and γ_N are the electron and nuclear magnetogyric ratios; and H_1

and H_2 are the amplitudes of the microwave and radiofrequency fields reapectively. The terms $(\gamma_e H_1)^{-1}$ and $(\gamma_N H_2)^{-1}$ can be regarded as the times to achieve an electronic or nuclear transition. $(T_1 T_2)^{\frac{1}{2}}$ is the characteristic time for an electron or nucleus to return to thermal equilibrium.

The first condition, $T_E \gg (T_{1e} T_{2e})^{\frac{1}{2}}$, requires that the ESR line is inhomogenously broadened, that is, that the microwave energy is dissipated to the lattice faster than to the spin system. If T_E is very short, saturation of the ESR line may not be possible or the ENDOR lines may be broadened beyond detection. If T_{ss} is short, the saturation of one ESR transition will be transferred to other transitions in the same spin system. If all the T_{1e} processes are saturated, then no ENDOR effect can occur. Thus, the spin concentration, which partially determines T_{ss}, is more critical for obtaining ENDOR spectra than for obtaining ESR spectra. In liquids, the spin diffusion time, as affected by temperature and solvent viscosity, is also critical. T_x, a rather invariant parameter of the system, is usually longer than $(T_{1e} T_{2e})^{\frac{1}{2}}$.

The conditions $(T_{1e} T_{2e})^{\frac{1}{2}} \geq (\gamma_e H_1)^{-1}$ and $(T_{1N} T_{2N})^{\frac{1}{2}} \geq (\gamma_N H_2)^{-1}$ simply state that the characteristic electron relaxation time must be long enough (or H_1 strong enough) for the ESR transition to be saturated, and the characteristic nuclear relaxation time must be long enough (or H_2 strong enough) for the NMR transition to desaturate the ESR transition. In solids, both characteristic relaxation times generally decrease with temperature. In liquids, the nuclear and electronic relaxation times may go through a maximum as the temperature is reduced. These can occur at different temperatures and the optimum

ENDOR signal is obtained when the two relaxation times are equal.In solids, the lowest attainable temperature does not necessarily produce the optimum ENDOR signal, since at low T° $(T_1T_2)^{\frac{1}{2}}$ may become smaller than T_x. Note that for nuclei with small nuclear frequencies, a stronger rf field is required to obtain an ENDOR spectrum. As mentioned in Chapter 5, this effect is somewhat counterbalanced by the enhancement of the field at the nucleus by the hyperfine interaction, which is larger for small γ_N. Similarly, if the electronic g-tensor is very anisotropic, one might expect higher microwave powers to be required for the saturation of low field signals ($\gamma_e = g\beta/\hbar$).

The final condition, $(\gamma_e H_1)^{-1} \approx (\gamma_N H_2)^{-1}$, implies that the nuclear transition time is comparable to all competing relaxation times, so that the NMR transition affects the saturation behaviour of the ESR signal.

As can be seen from Table 5.1, one can expect the % ENDOR enhancement to be about 10% of the ESR signal intensity. The ESR signal intensity measured in an ENDOR cavity is approximately $^1/10$ the intensity obtainable in an ESR cavity. Thus, the ENDOR sensitivity is at least two orders of magnitude lower than the optimum ESR sensitivity, and it is necessary to enhance the ENDOR S/N ratio by the use of single or double modulation, phase sensitive detection schemes. Double modulation schemes involve modulation of the rf field and of the static magnetic field. One side effect of Zeeman field modulation can be broadening of the ENDOR lines. This can be particularly severe in disordered solids (see below), and can be avoided by using microwave resonance-signal phase modulation in place of field modulation.[2] Magnetic field modulation, without phase sensitive detection, can sometimes effect the % ENDOR

enhancement.[3] Signal enhancements of 10x have been reported for F-centres in KCl[4]. One reason proposed for this enhancement is that more of the spin packets of the inhomogenously broadened line are brought into resonance at large modulation amplitudes. The effects of Zeeman field modulation on the ENDOR signal intensity are discussed further in reference 3. The designs of modern ENDOR instruments have improved such that those commercial instruments available today use only a single phase sensitive detection system, modulating the rf field.

The choice of rf modulation frequency is less critical than the operating factors discussed above; however, if it is fast enough to be comparable to T_{1N}^{-1} (or T_{1e}^{-1}, which is less likely) then it effectively increases the relaxation rate. This then results in the distortion and/or broadening of the ENDOR lines and the necessity of higher rf powers (and microwave powers) to obtain an ENDOR signal.[5] These considerations only become important in most systems at liquid helium temperatures.

6.1.2 ENDOR Signal Intensities

i) As a function of H_1 and H_2

The results of a straightforward, phenomenological treatment of the ENDOR signal intensity, provided by Seidel,[6] are presented below. A more rigorous, but more complex approach, using a density matrix method, has been taken by Freed and coworkers, and is reviewed in reference 7.

Seidel took the ESR signal amplitude as given by[8]:

$$A = \frac{\pi \gamma_e \chi_o H_1 H_o}{2(1 + \frac{1}{4}\gamma_e^2 H_1^2 T_{1e}^2)^{\frac{1}{2}}} \cdot g(\omega - \omega_o) \qquad (2)$$

where χ_o is the static magnetic susceptibility, $g(\omega - \omega_o)$ is a lineshape function, and $T_1 = T_2$. Following the application of the radiofrequency field, H_2, the amplitude changes to A^*, with T_1 in eqn 2 replaced by T_1^*. The ENDOR signal amplitude is then proportional to the induced change in the ESR signal:

$$A_{ENDOR} = \frac{A^* - A}{A} \qquad (3)$$

Assuming that the relaxation processes are those shown in Figure 5.3 and that $T_N \gg T_x$, T_1^* is given by:

$$T_1^* = (\frac{1}{T_{1e}} + \frac{1}{T_N})^{-1} \qquad (4)$$

The ENDOR signal intensity is determined by the efficiency of the applied field in changing the level populations associated with the saturated ESR line. This, in turn, is dependent on the NMR transition probability, P, which is given by[9]

$$P = \frac{\pi^2}{2H_o^2} [\, r_m^2 \upsilon_{\pm}^2 H_2^2 T_{2N} \,] \qquad (5)$$

where $r_m^2 = (I + m_I)(I - m_I + 1)$ and $\upsilon_{\pm}$ is the transition frequency of the ENDOR line, $|\upsilon_N \pm (A/h)/2|$. From eqns 2,4 and 5, the ENDOR signal amplitude can be written in the form

$$A_{ENDOR} = (\frac{2}{2I + 1})(1 - \alpha_{\pm}) \cdot \frac{x^3}{(1+x^2)^{3/2}} \cdot \frac{y^2}{(1+y^2)} \qquad (6a)$$

x and y are functions of H_1 and H_2, respectively:

$$x = \tfrac{1}{2}\gamma_e H_1 T_{1N}, \quad y = \frac{\pi}{H_o} \upsilon_{\pm} r_m H_2 (T_{2N} T_x)^{\frac{1}{2}} \qquad (6b)$$

The factor $2I/(2I+1)$ is included because the ENDOR transition affects only 2 of the $(2I+1)$ spin levels in each m_s manifold. α is a relaxation parameter and is a function of all of the transition probabilities involved in the relevant relaxation pathways. Thus, at low rf powers, the ENDOR signal intensity increases linearly with rf power. For low microwave powers, the signal intensity increases as $P_\mu^{3/2}$. At high rf or microwave powers, the signal intensity is expected to reach a maximum and become independant of power. This behaviour has been observed for F-centres in alkali halides and in the Rh/AgCl system described in Chapter 7. It should be noted that the exact nature of the ENDOR signal intensity-rf power dependence will be a function of the operative relaxation pathways. However, for T_{1e} mechanisms the dependence will generally be as just discussed.[10] At high rf powers, the ENDOR lines may broaden and split due to coherence effects. This is discussed further in reference 3.

If the ESR derivative signal amplitude of a homogeneous line, from the steady state solution to the Bloch equations, is used in place of eqn.2, a slightly different H_1 dependence is obtained.[10,11] The signal amplitude is then given by

$$A' = \frac{2\chi_o H_o \gamma_e^3 H_1 (H_o - H)}{(1 + \gamma_e^2 T_{2e}^2 (H_o - H)^2 + \gamma_e^2 H_1^2 T_{1e} T_{2e})^2} \qquad (8)$$

Setting $A'=0$ and solving for H, the intensity at the derivative maximum is

$$A'_{max} = \pm \frac{3\sqrt{3}}{8} \left[\frac{\chi_o H_o \gamma_e^2 H_1 T_{2e}^2}{(1 + \gamma_e^2 H_1^2 T_{1e} T_{2e})^{3/2}} \right] \qquad (9)$$

Assuming a T_{1e} ENDOR mechanism, the ENDOR signal amplitude at this field is

$$A'_{ENDOR} = d(A'_{max}) = \pm \frac{9\sqrt{3}}{16} \cdot \frac{\chi_o H_o \gamma_e^4 T_{2e}^3 H_1^3}{(1 + \gamma_e^2 H_1^2 T_{1e} T_{2e})^{5/2}} \cdot \Delta T_{1e} \quad (10)$$

where ΔT_{1e} is the change in the effective relaxation time brought about by the rf field. A'_{ENDOR} reaches a maximum at $\gamma_e^2 H_1^2 T_{1e} T_{2e} = \frac{3}{2}$ and then decreases in intensity at higher microwave powers. Thus, for a homogenous line, the optimum microwave power level for ENDOR is three times that which gives the maximum ESR intensity. This power dependence behaviour was observed for the silver olefin complexes described in Chapter 8.

ii) As a function of ENDOR transition frequency

Since y is proportional to the ENDOR transition frequency (eqn 6b), equation 6a predicts that the ENDOR line intensities will increase quadratically with frequency at low rf powers and be independent of frequency at high rf powers. A more complicated dependence will occur at intermediate powers. Thus, the relative intensities of the ENDOR lines will change with rf power and the low frequency line of each ENDOR line will usually be weakest. This qualitative rule is sufficient for the understanding of many ENDOR spectra. For the interpretation and simulation of ENDOR powder spectra a more quantitative approach, as described in section 6.4 is required.[12]

iii) As a function of orientation

The ENDOR line intensity frequency dependence described by eqn 6 only holds if the hyperfine interaction is isotropic.

In general, $y^2 = 2P(\upsilon_{\pm}) T_{1N}$ where P, the ENDOR transition probability, is angularly dependent:[12]

$$P_{m \leftrightarrow m-1} = \left(\frac{2\pi}{\hbar^2}\right) \left| \langle m-1 \left| \mathcal{H}_N \right| m \rangle \right|^2 g(\omega) \qquad (11)$$

$\mathcal{H}_N$ is the nuclear Hamiltonian given in eqn 5.16. The transition probabilities represented by the relaxation parameter can also be angularly dependent. Angular dependences of ENDOR line intensities become important in the interpretation and simulation of powder ENDOR spectra.

iv) As a function of number of nuclei

Relative intensities of ENDOR lines do not ordinarily reflect the number of equivalent nuclei involved in each ENDOR transition. Inequivalent nuclei in a molecule with different relaxation processes have different ENDOR % enhancements (Table 5.1). The ENDOR line intensities also depend on the magnitude of the hyperfine interaction for small couplings. This results from the simultaneous saturation of overlapping ESR hyperfine lines so that only a small population difference between NMR levels can be obtained. In an extreme example using the four level spin system in Figure 5.3, if both transitions $1 \Rightarrow 4$ and $2 \Rightarrow 3$ are saturated at the same time no ENDOR response will be possible. This effect can be taken into account for homogeneously broadened ESR lines by the equation[10]

$$I = I_{max} \cdot \frac{T_{2e}^2 \Delta\omega^2}{T_{2e}^2 \Delta\omega^2 + 2.5} \qquad (12)$$

where $\Delta\omega = A(Hz) \times 2\pi$. If the nuclei are similar, i.e. protons in aromatic radicals, I_{max} can be taken as a constant and the

corrected ENDOR intensities will reflect the number of equivalent nuclei associated with each transition. Some estimates of T_{2e} are given in reference 10.

In special TRIPLE experiments, the rf frequency is swept in both directions simultaneously, starting at the free nuclear frequency of interest. Thus, both υ_+ and υ_- ENDOR transitions are simultaneously irradiated (as long as $\upsilon_N > \frac{A}{2}$) and the ENDOR intensity dependence on T_{1N} is eliminated. In most cases, then, the resulting spectrum, connected with eqn 12, should reflect the number of equivalent nuclei.

6.2 Experimental

6.2.1 ENDOR instrumentation

The general block diagram of an ENDOR spectrometer is shown in Figure 1. It consists of an ESR spectrometer with the modifications necessary to allow the introduction of a sweeping radio frequency field at the sample. Thus, the components unique to the ENDOR spectrometer are the probehead (A), made up of the microwave cavity, the radiofrequency coils and the low temperature cryostat, and the radiofrequency circuit (B). The radiofrequency circuit consists of a scan generator, an audio oscillator, which normally supplies the Zeeman modulation in ESR experiments, an rf signal generator, a broad band rf power amplifier and a 50Ω dummy load. The radiofrequencies are synthesized by the rf signal generator, usually capable of a range of 1-220 MHz. The frequency output of the rf signal generator is controlled by the output voltage of the scan generator, enabling the frequency to be swept up or down, or, using a triangular waveform, simultaneously in

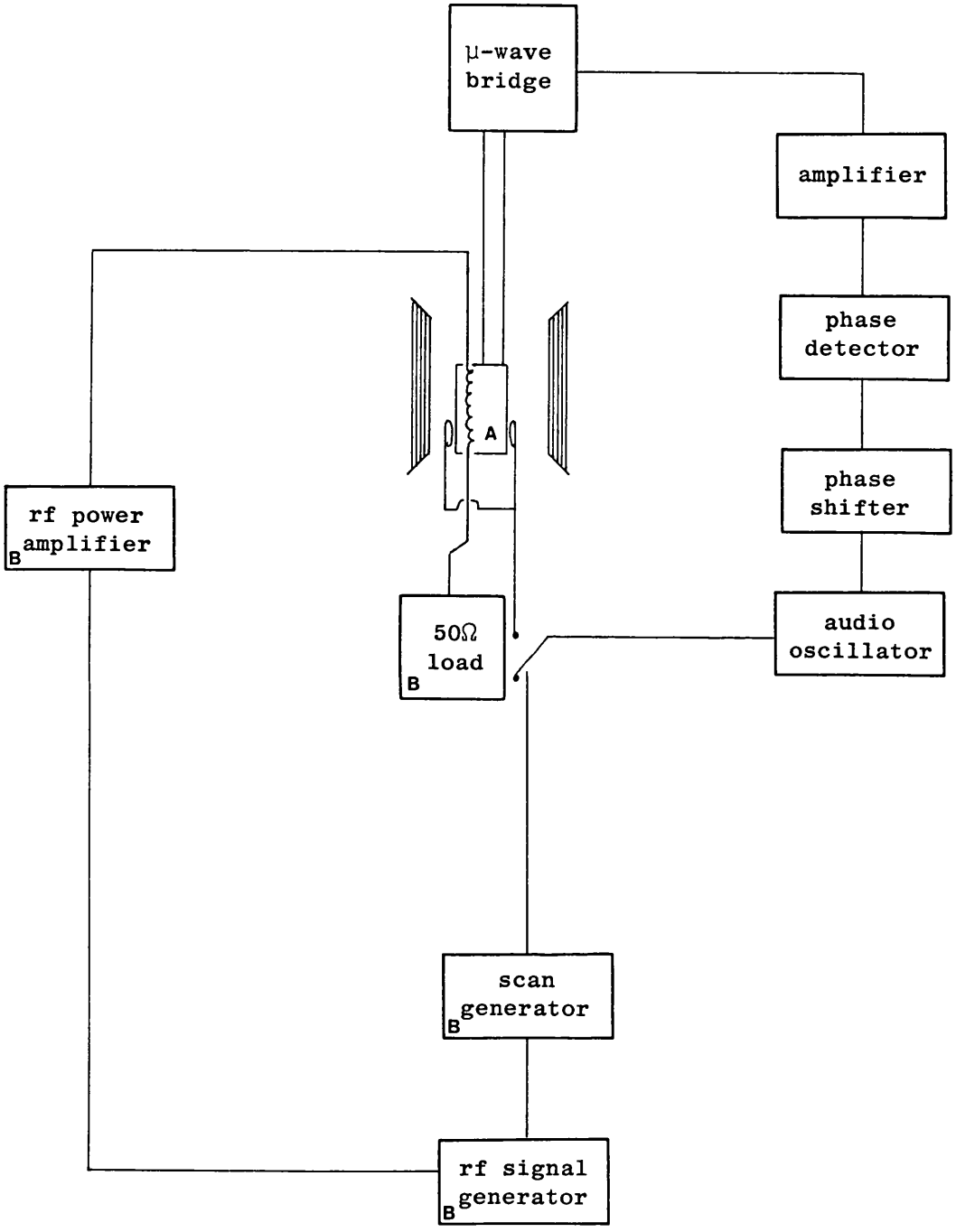

FIGURE 1

General block diagram of an ESR/ENDOR Spectrometer. Components marked A and B. A is the ENDOR probehead.

both directions. The scan generator also controls the starting frequency and scan range. In both instruments described here, the scan generator was based on a digital clock and software controlled. As pictured in Figure 1, both ENDOR instruments used a single rf modulation, phase sensitive detection scheme. The audio oscillator supplies the FM modulation signal to the scan generator and a reference signal, through a phase shifter, to the phase sensitive detector. It is useful to have the option of converting this signal to FM or AM modulation of the frequency output of the rf synthesizer. The output of the rf synthesizer is amplified by a broadband amplifier, usually with an output power of 50 - 300 W. The output impedance of the rf amplifier is about 50Ω and is frequency dependent. Thus, the current through the ENDOR coils and the amplitude of the radiofrequency field in the coils (H_2) are also frequency dependent due to the mismatch of the amplifier output impedance and the impedance of the ENDOR coils. Impedance matching is provided by the use of a 50Ω line, a thickness of coil wire such that the impedance across the coils is 50Ω, and a 50Ω load, matched to the approximate output impedance of the rf amplifier. The 50Ω load also provides a heat sink for the rf power, so that it is not dissipated in the coils. With the high rf powers employed in modern ENDOR spectrometers, this crude form of matching is adequate. More detailed general discussions of ENDOR intrumentation, along with descriptions of a number of different instruments, are given by Poole[14] and Leniart.[3]

i) University of Paderborn ENDOR Spectrometer

Some of the ENDOR experiments described in Chapter 7 were carried out in the Experimental Physics Department of the University of Paderborn, West Germany, under the supervision of Professor J.M. Spaeth and Dr. J.R. Niklas. The ENDOR spectrometer used was a noncommercial X-band homodyne system that worked fully on-line with a Hewlett Packard 21MXE computer.

The bridge design incorporated two notable aspects. The first of these was the use of a solid state microwave oscillator (Narda Microline 601 A) in place of a conventional Klystron. This provided several advantages. The frequency range of the solid state oscillator (8.2 - 12.4 GHz) was larger than that of an X-band Klystron (9 - 10 GHz), and the solid state oscillator ran at a lower voltage (~50V) than an X-band Klystron (300 - 450 V). The lower voltage was easier to stabilize; however, the lower current through the oscillator had to be carefully controlled. In general, a more stable frequency could be obtained with the solid state oscillator than with a Klystron.

The second notable feature of the Paderborn bridge was the introduction of two GaAs FET microwave peamplifiers (Narda 6244 S-24) prior to the detector diode.[5] These increased the signal-to-noise ratio, $^{S}/N$, by a factor of 10 at the low modulation frequencies (<1 KHz) and microwave powers (<20 mW) generally used with this system.

A single modulation phase sensitive detection scheme, as shown in Figure 1, was employed. The rf field could be modulated at any frequency between 1 Hz and 100 KHz. Double modulation schemes involving Zeeman field modulation were avoided because of possible line broadening effects. For the

same reason, the rf field was AM (square wave) modulated. This allowed large modulation depths (usually 100%) to be employed without the line broadening that would accompany FM field modulation. However, with AM modulation the signal was very susceptible to rf leakage. This became particularly critical when low modulation frequencies were used as a result of interference from lights, elevators, etc. For this reason, the microwave circulation port, the two preamplifiers, and the detector diode were in a well-shielded box.

One of two ENI power amplifiers were used (A-300 W, 55 dB, 0.3-35 MHz, and 550L, 50 W linear, 50 dB, 1.5-400 MHz). The 50 W amplifier was used for frequencies greater than 30 MHz.

All of the ENDOR signals obtained with the Paderborn instrument were superimposed on a large background signal, which resulted in part from the use of AM modulation. The background signal had a $^{1}/f$ dependence, as shown in Figure 2 and the sample signal intensity and the background signal intensity were inter-dependent. Thus, the sample signal could be optimized, even if it was very weak, by optimizing the background signal at some frequency less than 1 MHz. For ENDOR-induced EPR and TRIPLE experiments, it is necessary to excite an individual ENDOR transition independently. Unfortunately, because of coupling with the background signal, the pump rf energy was transferred throughout the spin system and all ENDOR transitions were pumped to some extent. Thus, a "jump-frequency" double modulation scheme was used for ENDOR-induced EPR and TRIPLE experiments. In this format, the stationery rf pumping frequency was jumped between a position

FIGURE 2

ENDOR spectra of Rh/AgCl a) as measured, b) after subtraction of the $^1/f$ background signal, c) after digital filtering and d) after deconvolution (100 iterations).

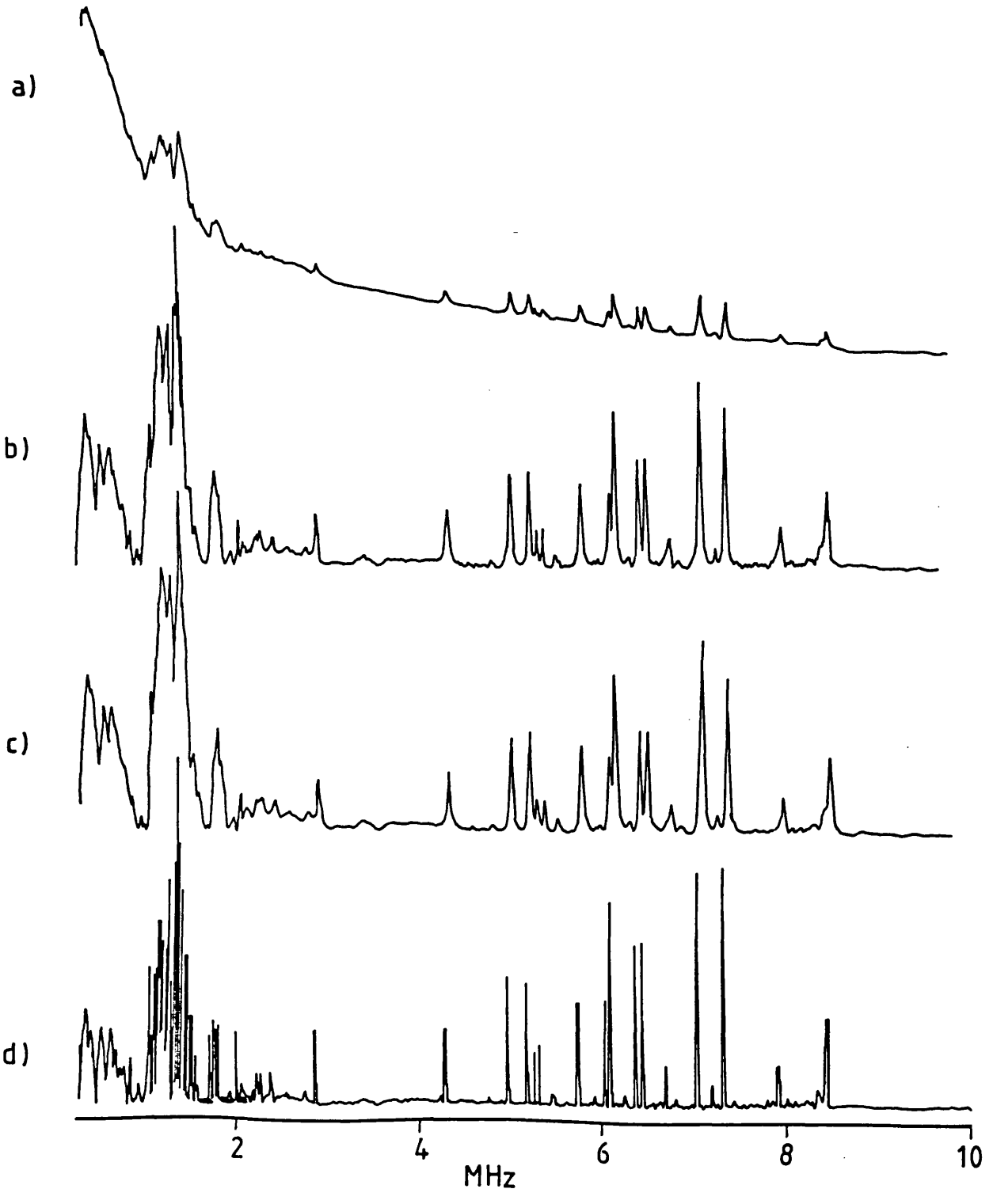

on the ENDOR line of interest and a selected off-line position, at a frequency ~1 KHz. The scanning rf field was modulated at a rate of 5 Hz. For such a double modulation scheme, the ratio of the two modulation frequencies must be greater than 1:10. The ENDOR signal was first phase sensitive detected at 5 Hz and then at 1 KHz. As a result, any background signal effects were subtracted out and only those changes due to pumping the single ENDOR line were observed. For TRIPLE experiments, a very convenient difference spectrum was obtained. Those signals which had increased in intensity due to the second rf pump gave positive absorption peaks and those signals that had decreased gave negative peaks.

The use of low rf modulation frequencies meant that lower microwave powers were required to saturate the ESR signal. At these lower power levels, the system was more susceptible to microwave leakage and reflection. To minimize this, aluminium wool was packed around the cavity and in the magnet pole gap to stop leakage. In order to avoid using optical-access gratings in the cavity, the sample was mounted on a cold finger which could be lowered, without affecting the crystal orientation, below the cavity and exposed through a window. An X-ray tube was mounted in the gap, below the cavity, which allowed in-situ X-irradiation of the lowered sample. Leakage from the top of the cavity was minimal because the cold finger stage fit snugly into the neck of the cavity.

The magnet, bridge and cooling system were mounted on a platform supported by inflatable shock absorbers to minimize vibrational interferences.

The probehead design, shown in Figure 3, allowed some flexibility in choice of cryostat, the use of a large sample,

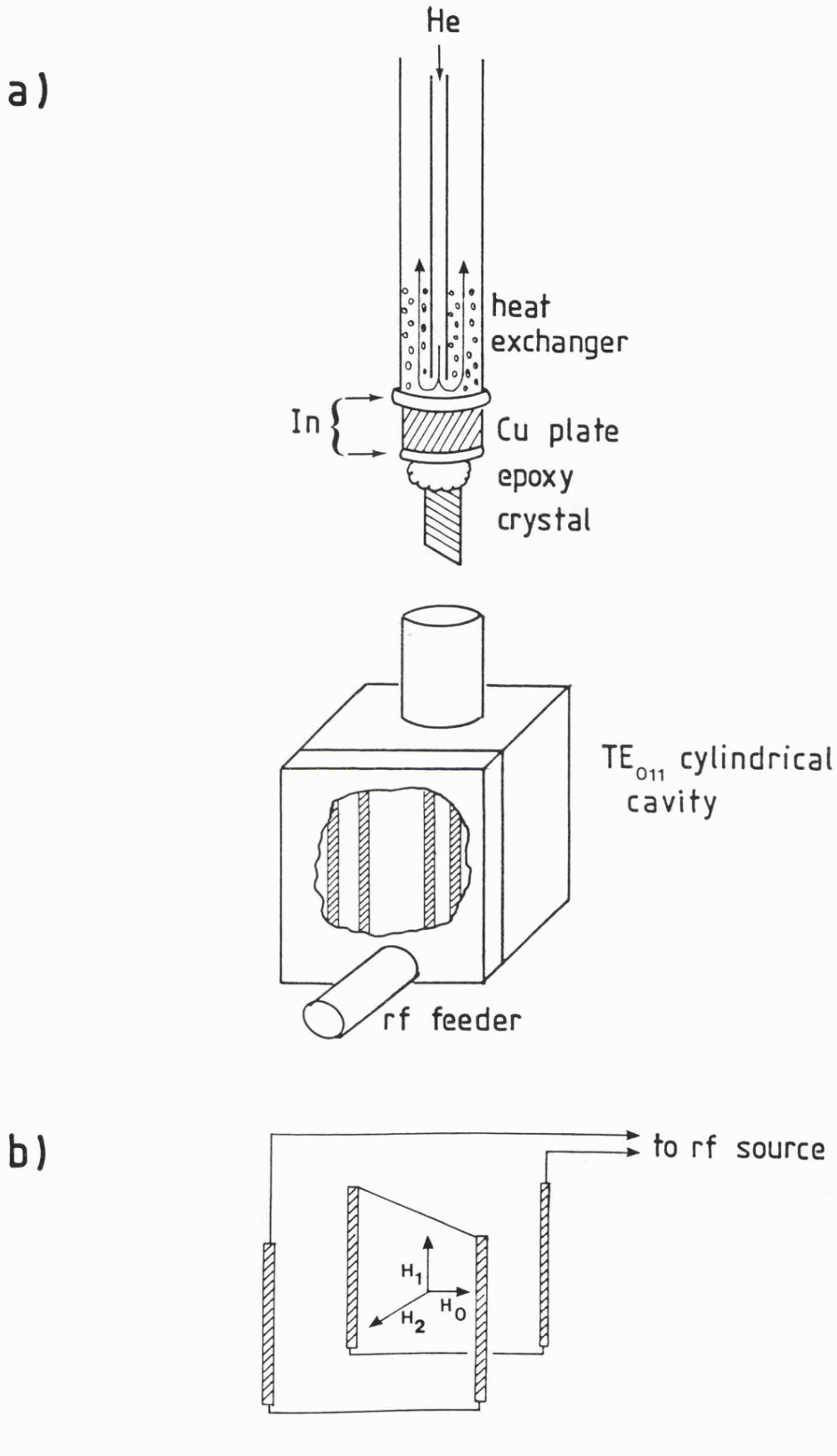

FIGURE 3

a) ENDOR probehead and b) expanded view of coils used with the University of Paderborn ENDOR spectrometer.

and automated sample rotation. A TE_{011} mode cylindrical cavity was used. Such a cavity has a relatively broad μ-wave magnetic field maximum, so that large samples (20 x 5 x 5 mm) could be accomodated, but was incompatible with the type of rf coils used in the Bruker instrument (Figure 6), which have a high rf power conversion factor. The single loop rf coil used consisted of four silver rods which provided an rf field mutually perpendicular to both the static and microwave magnetic fields. Based on the calibration of a similar Varian ENDOR probehead, this coil design was capable of producing an rf field at the sample of ~.5-1 G at 100 W of rf power.[3] Because of the lower rf power conversion factor of these coils, at high power (300 W), rf heating was sometimes a problem. The sample was mounted on a cold finger which was lowered until just the crystal, but not the cold finger were suspended in the cavity. A low temperature epoxy (Emerson and Cumming, Eccobond 286) ensured that the sample was ridgidly mounted. This cooling configuration had a minimum temperature of ~15 K at the sample. The liquid helium coolant was delivered via a transfer line (Oxford Instruments) at the top of the cavity (Figure 4).

An alternative cooling arrangement involved flowing cold gas through hollow ENDOR coils, which cooled a stationary gas in the cavity. This configuration was amenable to samples, such as powders, which could not be mounted on a cold finger. It also provided efficient cooling of the rf coils and lower sample temperatures could be attained.

As will become apparent in Chapter 7, ENDOR single crystal experiments often require a high degree of automation in order to extract the maximum amount of data in a reasonable length

FIGURE 4

University of Paderborn ENDOR spectrometer showing cooling and crystal rotation facilities.

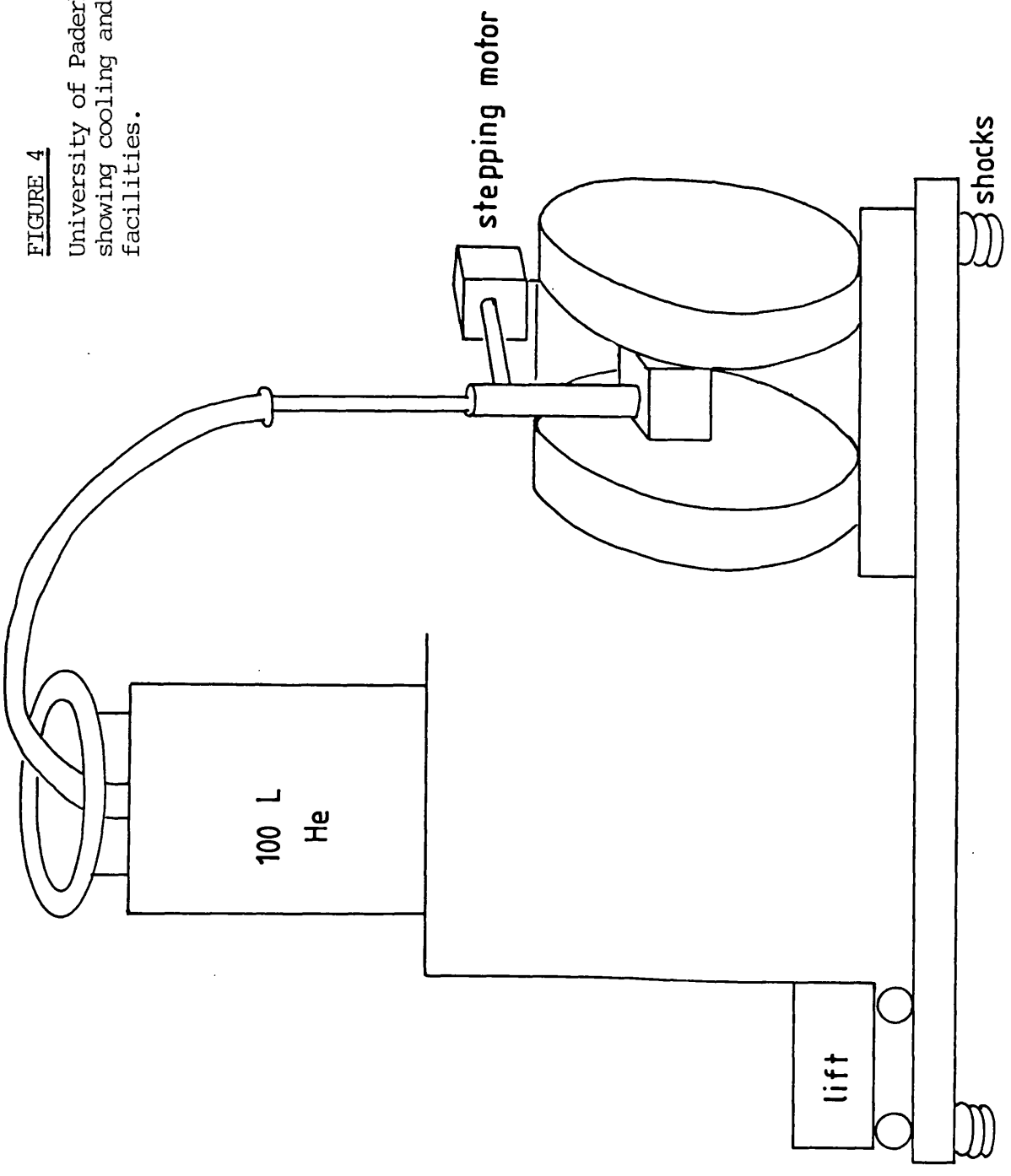

of time. Thus, once operating parameters such as power, temperature, modulation frequency and magnetic field position were optimized, data aquisition with the Paderborn instrument could be completely automated. A temperature control circuit maintained the temperature, as measured by a carbon thermistor, at a preset value, by controlling a heater located in the cold finger and the helium flow, via an electrically controlled needle valve. The needle valve was automatically adjusted to keep the heater current to a minimum so that helium consumption was low. The cold finger stage and crystal were rotated by a stepping motor (Figure 4) which was software controlled. Critical coupling of the cavity was maintained during the crystal rotation by an iris and automatic tuning circuit. The static magnetic field postition was software adjusted during the crystal rotation, according to the predetermined angular dependence of the ESR line. As described in Chapter 5, during ENDOR-induced EPR experiments, a stationary rf pumping frequency is applied to an ENDOR line as the magnetic field is swept. The shift of the ENDOR line with changing magnetic field was compensated for by automatic tuning of the signal generator to the frequency of the ENDOR line. Software provided for the preprogramming of any number of experimental sequences, and acquired data was stored for future analysis. In general, with 24 hours/day instrument running time possible, much more complete if perhaps less well optimized data could be obtained using the ENDOR automation options.

ii) Bruker ENDOR Instrumentation

The ENDOR spectrometer employed in studies carried out at the University of Leicester was a commercial Bruker instrument composed of an ER 220 D ESR spectrometer with an ER041-MR microwave bridge, an ER144 data system and an EN250 ENDOR accessory. The data system consisted of an Aspect 2000 microcomputer with the manufacturer-supplied EPR/ENDOR software. The ENDOR accessory included an ENDOR/TRIPLE cavity, two rf signal generators (Wavetek 3000-446, 1-220 MHz) and Programmed Test Sources 160,(.1-160 MHz), an ENI 100 W rf power amplifier and a Bruker computer interface. A complete description of this spectrometer can be found in the User's Manual.[13] Low temperature measurements above 77 K were made using a Bruker V-1000 variable temperature unit and specially adapted cryostat, and below 77 K using an adapted Oxford Instruments ESR-900 helium cryostat and control unit.

The spectrometer's block diagram was similar to that shown in Figure 1. A single modulation, phase sensitive detection scheme was used, and the ENDOR spectrometer was optimized for 12.5 KHz FM modulation of the rf field. A block diagram of the Bruker signal channel is shown in Figure 5a. The audio oscillator, used for Zeeman modulation in ESR experiments, produced an 800 KHz square wave signal, which was converted to one of four frequencies by a frequency selection network. Only the 12.5 KHz modulation frequency could be used for ENDOR measurements. Higher modulation frequencies would damage the Helmholtz modulation coils. The signal from the frequency selection network, divided in two, provided a reference signal through the phase shifter to the phase sensitive detector, and a signal to a modulation board. This was then passed through

FIGURE 5

a) Signal channel of Bruker ENDOR spectrometer for 12.5 KHz rf modulation,
b) signal channel for low frequency rf modulation (Brookdeal components).

a)

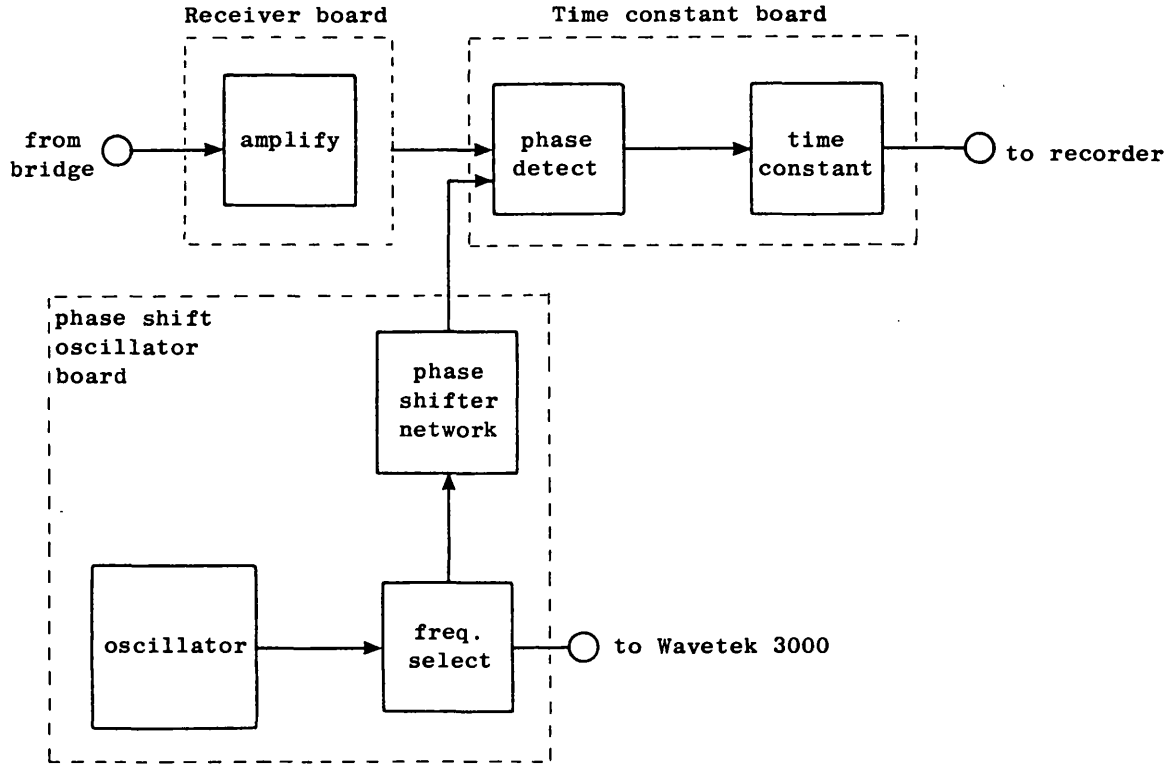

b)

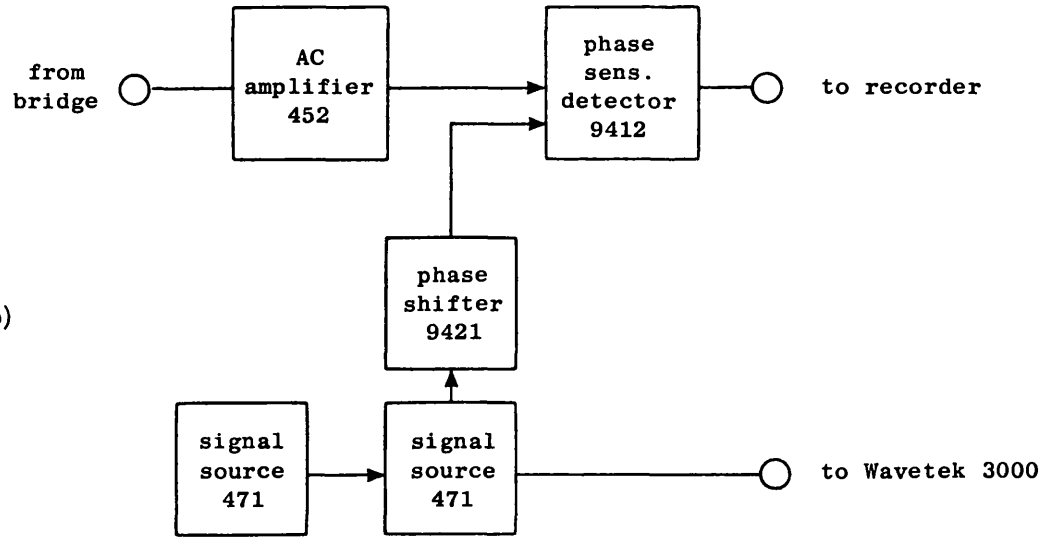

a 12.5 KHz narrow band pass filter which converted it to a sinewave signal, passed through awide band pass, low noise, low drift, high gain amplifier and applied to the rf signal generator through the computer interface. The modulation signal to the Helmholtz coils was disabled during the ENDOR experiment. The modulation depth was software controlled. An alternative signal channel was constructed which allowed the use of modulation frequencies lower than 12.5 KHz, from 1 Hz to 12.5 KHz, for ENDOR experiments (Figure 5b). This consisted of a Brookdeal Type 471 signal source, a Brookdeal 9421 phase shifter, a Brookdeal precision 452 AC amplifier and a Brookdeal 9412 phase sensitive detector. Band pass filters appropriate to the modulation frequency used could be selected on the phase shifter and amplifier. The modulation signal from this signal channel was fed directly to the Wavetek rf signal generator, and thus, modulation depth was manually controlled. Calibration experiments found that a 1 V rms output of the signal generator corresponded to an FM modulation depth of approximately 100 KHz.

The rf scan generator was computer-based. The rf level was also computer controlled via a control voltage fed to the rf signal generator. The low power rf signal was then fed to a 100 W rf power amplifier, the gain of which was constant, and applied to the rf coils in the ENDOR/ESR microwave cavity. A 50 Ω load after the coils provided impedance matching and a heat sink for the rf power. The Wavetek signal generator was used as the scanning rf signal generator, and the PTS signal generator was used to synthesize the pump frequencies for general TRIPLE ENDOR experiments. The option of using AM

rather than FM rf modulation was available at the Wavetek signal generator. However, when AM modulation was used, baseline stability and the signal-to-noise ratio ($^{S}/N$) were extremely poor, and very large background signals were apparent. The low baseline stability and $^{S}/N$ were probably attributable to rf interferences as a result of poor shielding. The large background signals, as discussed below, were most likely the result of frequency dependent dielectric losses of the materials used to construct the probehead. The increased noise level and sloping baseline might also have resulted from the torque produced on the coils by switching of the r.f. power. At high power levels this can modulate the rf coils and thus the cavity frequency and Q.

The ENDOR probehead is illustrated in Figure 6. A TM_{110} cylindrical mode cavity was used. This mode was less sensitive than the TE_{011} mode used for the Paderborn probehead, to the insertion of large quantities of metal in the cavity. However the microwave magnetic field maximum was narrow (Figure 6b) so that precise positioning of sample and dewar was necessary for critical cavity coupling. With the ENDOR coils in place, the cavity was very sensitive to the insertion of dielectrics. Thus, the amount of quartz and high dielectric sample in the cavity had to be kept to a minimum. The liquid nitrogen and helium cryostats were constructed of unusually thin quartz. For high dielectric samples, coupling was achieved with the use of a slide screw tuner inserted in the waveguide between the bridge and the cavity. The rf coils were tightly wound on the outside flow system cryostats. Thus thermal contact with the sample was minimal. RF heating was low because most

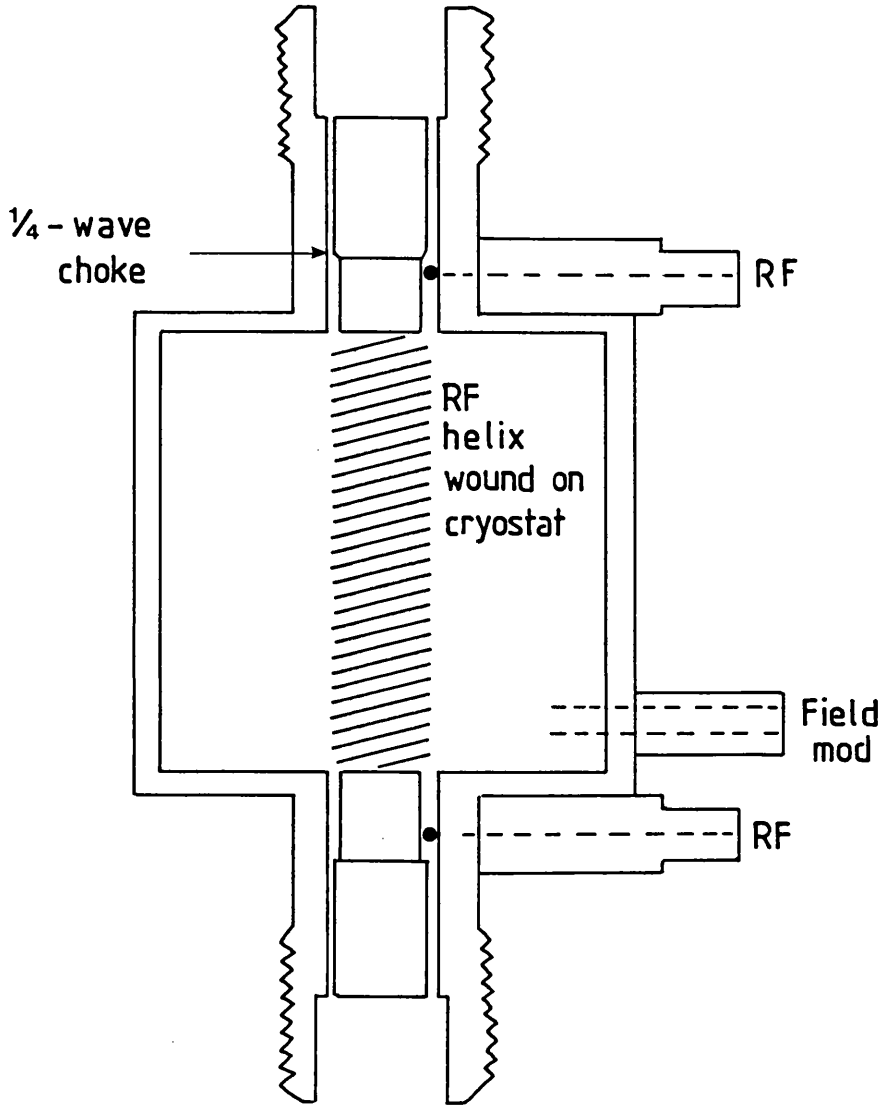

FIGURE 6(a)

Bruker ENDOR probehead - internal view.

b)

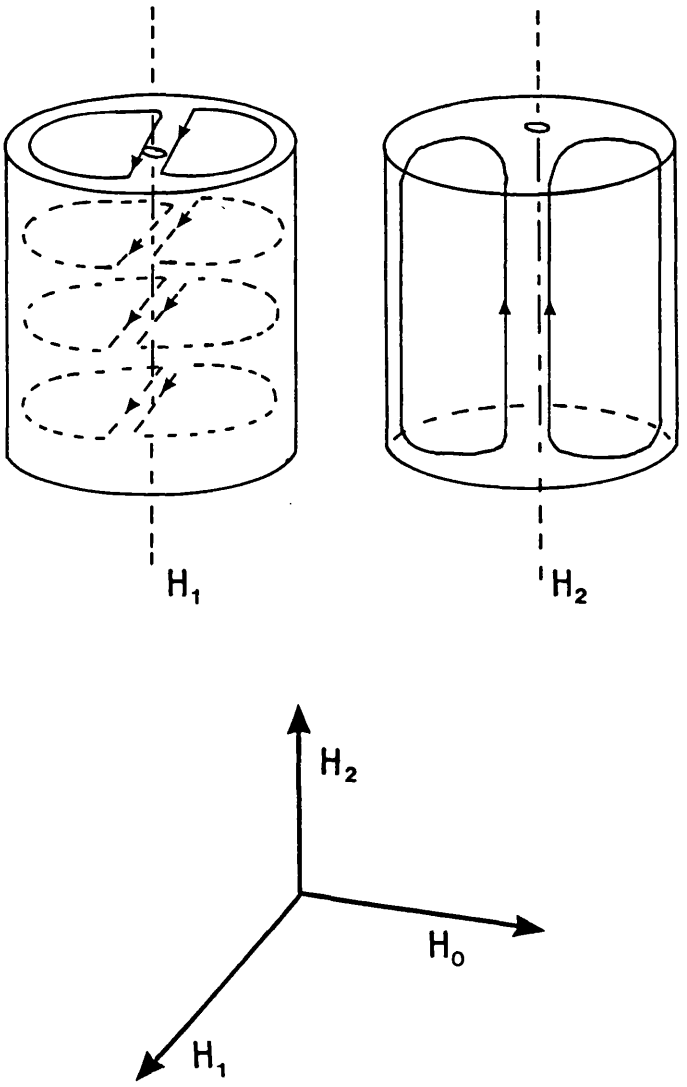

FIGURE 6(b)

Mode patterns for TM_{110} cylindrical cavity and for rf coils.

of the rf power was dissipated in the 50 Ω dummy load. Coil heating, as well as condensation in the cavity were reduced by flowing nitrogen gas through the cavity. It was found that a helium flow, ordinarily used during liquid helium ESR experiments, caused severe arcing across the rf coils due to the electrical discharge of the helium gas.[15] The rf power conversion factor of this probehead was very good. For a coil with 12 turns, an rf field at 14 MHz of ~6 gauss could be obtained at 14 MHz and 100 W rf power.[16] The conversion factor is given as $H_2 = .6032 \times \sqrt{P_{rf}(\text{watt})}$.[17] The power response was fairly broadband up to 60 MHz. The disadvantage of this probehead was that the quartz coil support and glue had significant dielectric losses which were nonlinearly dependent on rf frequency. This results in a background cavity ENDOR response even with FM rf modulation. In addition, the flowing cooling gas modulates the cavity's dielectric constant, causing low frequency microphonics. These effects were only a major problem when AM modulation or modulation frequencies less than ~10 KHz were used.

Single crystal rotations employed an Oxford instruments goniometer. The sample was mounted in a notched perspex rod. A perspex rather than quartz rod was used because of the lower dielectric losses of perspex.

The impedance matching of the rf coils to the rf circuit is frequency dependent and can be improved if coils of varying turns are used for different frequency ranges.[16] It was found, however, that over the frequency ranges employed in the studies described in this thesis (5 - 70 MHz), a single coil of 12 turns was adequate.

For ENDOR studies at 77 K, a finger dewar wound with an

rf coil was constructed. The quartz was etched with HF, and ground down until a good Q could be obtained when the dewar was inserted in the cavity. The exact centering of this dewar in the cavity was essential for critical coupling. Helium gas was bubbled through the liquid nitrogen to eliminate bumping. The rf coil was imbedded in heat shrinkable tubing and could be easily slipped on and off the dewar. The tubing had an ESR signal at free spin and, ideally, heat shrinkable Teflon tubing should have been used.[16]

Calibration experiments carried out as described in reference 13 found that low and high power ESR $^{S}/N$ ratios measured with a conventional TE_{102} ESR cavity with 100 KHz Zeeman modulation were the same as those obtainable with other state-of-the-art homodyne ESR spectrometers (i.e. a Varian E9 Century series spectrometer). Power and modulation amplitudes were calibrated prior to comparison of the two instruments. The klystron noise increased by a factor of 2 between 1 and 100 mW for the Varian bridge and by a factor of 1.5 for the Bruker bridge. The $^{S}/N$ ratio of the Varian instrument was proportional to log (modulation frequency = f) between .27 and 100 KHz; over the same range log N was inversely proportional to log f. $^{S}/N$ and N were frequency independent between 100KHz and 12.5 KHz for the Bruker instrument. The $^{S}/N$ ratio of the Bruker ENDOR signal decreased by a factor of 2 on going from 12.5 to 1 KHz which is similar to the decrease observed in the ESR sensitivity over the same range for the Varian instrument. Thus, the noise figure, $F = (^{S}/N)_{IN} / (^{S}/N)_{OUT}$, of the Bruker detector diode had a low frequency corner (where F becomes dependent on $^{1}/f$) of ~10 KHz.

Although the ENDOR S/N loss of 2 on going from 12.5 KHz to 1 KHz was not large, ENDOR measurements using the low frequency modulation unit described above, in either an AM or FM mode, were not practical. This was because at low modulation frequencies the phase-sensitive detector was overloaded by huge background signals, presumably due to interference effects. The use of a microwave preamlifier prior to the crystal detector, as in the Paderborn instrument, would improve sensitivity to some extent. The preamplifier essentially lowers the low frequency corner of F of the detector circuit. It has been reported that following the installation of preamplifiers in an older Bruker bridge, sensitivity was limited by excessive klystron noise.[5] However, the calibration experiments described above indicate that the klystron noise levels in the modern Bruker bridges are low.

Comparison of ENDOR measurements made on the Rh/AgCl system at 12.5 KHz and .8 KHz indicate that the higher modulation frequency did not give rise to line broadening. Similarly, the use of AM or FM modulation did not affect linewidths. Better resolution was obtained in the ENDOR spectra of Ag-cyclohexene complexes at the lower, 1 KHz, modulation frequency.

The S/N ratio of the ENDOR cavity was found to be reduced from that of the ESR cavity by a factor of 10. This was the result of the lower cavity Q.

The commercial ENDOR software did not provide for ENDOR-induced EPR experiments. In particular, no provision was made for tuning the ENDOR pumping frequency as the magnetic field was scanned. However, if the ENDOR line was fairly broad and small ESR scan widths were used, EI- EPR spectra could be obtained by setting the ENDOR starting frequency to the desired

pump frequency, killing the rf scan facility (computer command-"Kill Trace") and running a computer-controlled or manual ESR spectrum. EI-EPR spectra of a standard ditertiary butyl nitroxide(DTBN)/toluene sample are shown in Figure 7. These were obtained sitting on a methyl proton ENDOR line at υ = 14.378 MHz. Figure 7 illustrates some of the problems that must be corrected if the Bruker spectrometer is to be used for EI-EPR. Figure 7a was obtained with some rf FM modulation at a frequency of 12.5 KHz and at 50 KHz modulation depth. The lines marked with * are modulation sidebands at 12.5 KHz. A more intense signal was obtained with AM modulation (modulation depth = 20%) as shown in Figure 7b. An absorption signal should be obtained using AM modulation and a derivative signal using FM modulation. It is clear from Figures 7a and 7b that dispersion mode signals were detected. This is a result of the cavity modulation produced by the flowing nitrogen coolant gas. Figures 7c and 7d show that a weaker ESR signal could be obtained on an off-ENDOR line position. This is a result of the $^{1}/f$ background signal and was more pronounced for AM modulation. Thus, to optimize the Bruker as an EI-EPR spectrometer, lower modulation frequencies are required to eliminate sidebands and either a cold finger stage or cold finger dewar system must be used. For AM modulation better rf shielding is required. Stabilization of the ENDOR coils in Teflon shrinkable tubing might reduce coil vibrations during AM modulation. Tuning of the rf frequency as the field is changed could be provided by software or by a simple analog method.[18]

FIGURE 7

ENDOR-induced EPR of DTBN/toluene measured using 12.5 KHz rf modulation, a) FM modulation, pumping frequency (p.f.) on CH_3 ENDOR line, b) AM modulation, p.f. on CH_3 ENDOR line, c) FM modulation and p.f. off ENDOR line, and d) AM modulation and p.f. off ENDOR line. [The lines marked * are instrumental artifacts]

c) Gain = 4×10^4
FM mod. - 50 KHz depth
ν = 10 MHz (off-line)

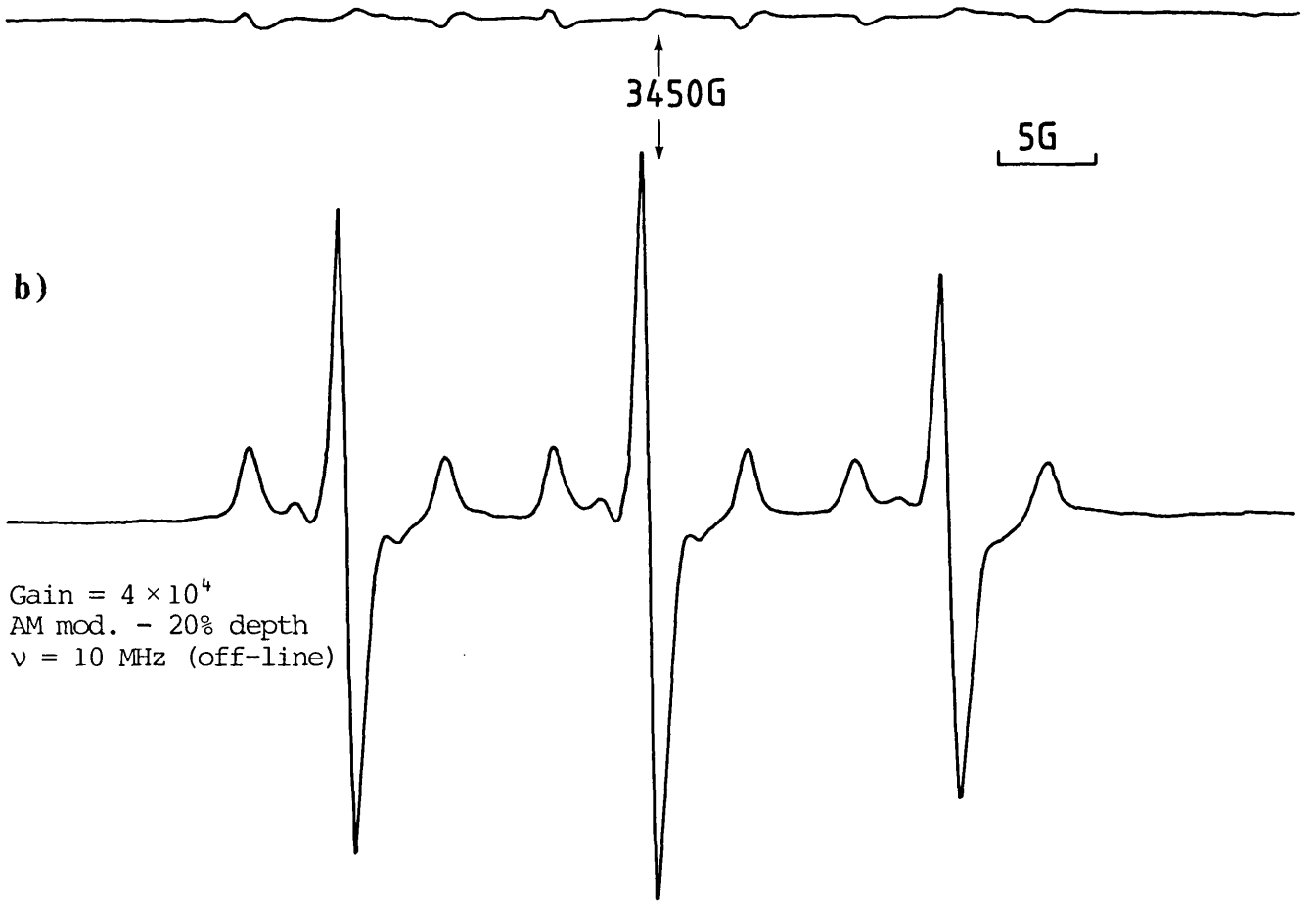

6.2.2 Computer analysis of ENDOR data

For work carried out at the University of Paderborn, use was made of the available computer programs for data enhancement and data analysis. The data enhancement program included a background correction option, a digital smoothing filter and deconvolution routine. A Savitzky-Golay smoothing filter with fast algorithm was used.[19] This acted as a low pass flat band-pass analog filter. The deconvolution routine was a standard Van Cittert-Jansson resolution enhancement program.[20] However, special nonlinear algorithms were used which prevented the buildup of noise and spurious signals, a problem ordinarily encountered after several iterations. Figure 2 illustrates these data enhancement programs for a Rh/AgCl ENDOR spectrum.

Spectra could be processed in blocks, using previously optimized enhancement parameters. Following deconvolution of spectra, a peak search and plot program could be employed. Angular dependence plots, with dot size a chosen function of intensity, could then be plotted. Data from these plots or from spectra could be directly used as input for a Hamiltonian diagonalization and fitting program.

The Bruker software included a noise reduction program which applied a Fourier transform and exponential filter to spectra. Hamiltionian diagonalization and fitting of ENDOR data was accomplished using the program ESR64, kindly donated by Dr. C.P. Keijzers of the University of Nijmegen, The Netherlands and a NAG-library E04 5BF minimization routine.

6.2.3 Conclusions

Parallel single crystal studies of Rh-doped AgCl indicated that the Bruker and University of Paderborn ENDOR spectrometers had approximately equivalent sensitivities. However, the sensitivity of the Paderborn instrument could be effectively increased by the use of larger samples and data enhancement programs. Also, the availability of computer automated techniques for data acquisition and data handling greatly increased the information that could be practicably obtained from an ENDOR single crystal study.

The sensitivity of the Bruker ENDOR spectrometer could be improved with the use of 12.5 KHz AM modulation with 100% modulation depth. This would require improved rf shielding and coil stabilization. For some samples, increased sensitivity could be obtained with the use of low frequency AM modulation. In addition to improved shielding this would require the installation of microwave preamplifiers and the use of a cold finger stage or dewar cooling system. The greatest improvement in "sensitivity" would result from the use of more efficient data handling techniques.

6.3 Sample Considerations

ENDOR studies can be classed as either single crystal studies, studies of disordered solids, or liquid studies. Each class requires different experimental techniques and interpretative methods. General techniques and methods, which are sufficient for single crystal studies, have been discussed so far in this Chapter and in Chapter 5. Examples of some single crystal ENDOR studies are given in Chapter 7. This

section is concerned with the interpretation of ENDOR spectra from disordered solids. In addition, the optimization of liquid ENDOR spectra is briefly reviewed and several examples are given.

6.3.1 Disordered Solids

Often, single crystals of a material are unobtainable and the only feasible sample formed is a powder or frozen glass. These latter are generally easier to prepare and a great deal of information can be gained from ESR studies of disordered materials.[21,22]

There are two major problems associated with ENDOR studies of powder samples. In principle, the same two difficulties are associated with powder ESR studies, that is, a loss in sensitivity and an increase in spectral complexity. It is useful, therefore, to begin this discussion of powder ENDOR spectral patterns with a brief review of the origin of ESR spectral patterns.

In a powder, all orientations of the crystallite with respect to the magnetic field direction, H_o, are equally probable. If one considers a paramagnetic species with $S = \frac{1}{2}$, $I = 0$ and an anisotropic g-tensor, and assumes that the g-tensor is uniquely oriented with respect to the crystal axes, then the orientation of a crystallite with respect to H_o is defined by the direction cosines (l_x, l_y, l_z) between H_o and the principal axes of the g-tensor. For this crystallite, a resonance line will be observed at $H_o = H_r$ where H_r is given by:

$$H_r = \left(\frac{l_x^2}{H_x^2} + \frac{l_y^2}{H_y^2} + \frac{l_z^2}{H_z^2} \right)^{-\frac{1}{2}} \qquad (13)$$

If $g_z < g_y < g_x$, H_r will range from H_x to H_z. It is obvious that a number of different orientations can result in a resonance at H_r. For example, assuming axial symmetry, the set of all allowed values of H_r form a prolate spheroid, as shown in Figure 8. Curves of constant H_r are circles in planes perpindicular to z. Figure 8 illustrates that there are more orientations "almost perpendicular" to z, resulting in a resonance at $H_r = H_2$, than are orientations "almost parallel" resulting in a resonance at $H_r = H_1$. This qualitatively explains why, despite the random nature of the distribution of crystallite orientations, there is a buildup of intensity at characteristic fields in the ESR absorption spectrum of a powder, enabling one to extract the principal values of the relevant interaction tensors (Figure 9a and 9b). The characteristic features in the first-derivative ESR spectum of a powder are the so-called "turning points", corresponding to relative maxima and minima of the absorption spectrum. For the case considered above, these turning points correspond to H_x, H_y and H_z.

If g is isotropic and A is anisotropic, a powder pattern similar to that just described is observed for each of the $N = (2I + 1)$ m_I- components (Figure 10c). These components may overlap, leading to somewhat more complex powder patterns. Anisotropies in H_r may also arise from spin-spin interactions. In the most general case, the spin Hamiltonian will contain a number of interaction tensors with anisotropies large enough to be resolved in the ESR spectrum, and these tensors will not all have coincident principal axes. While the principal

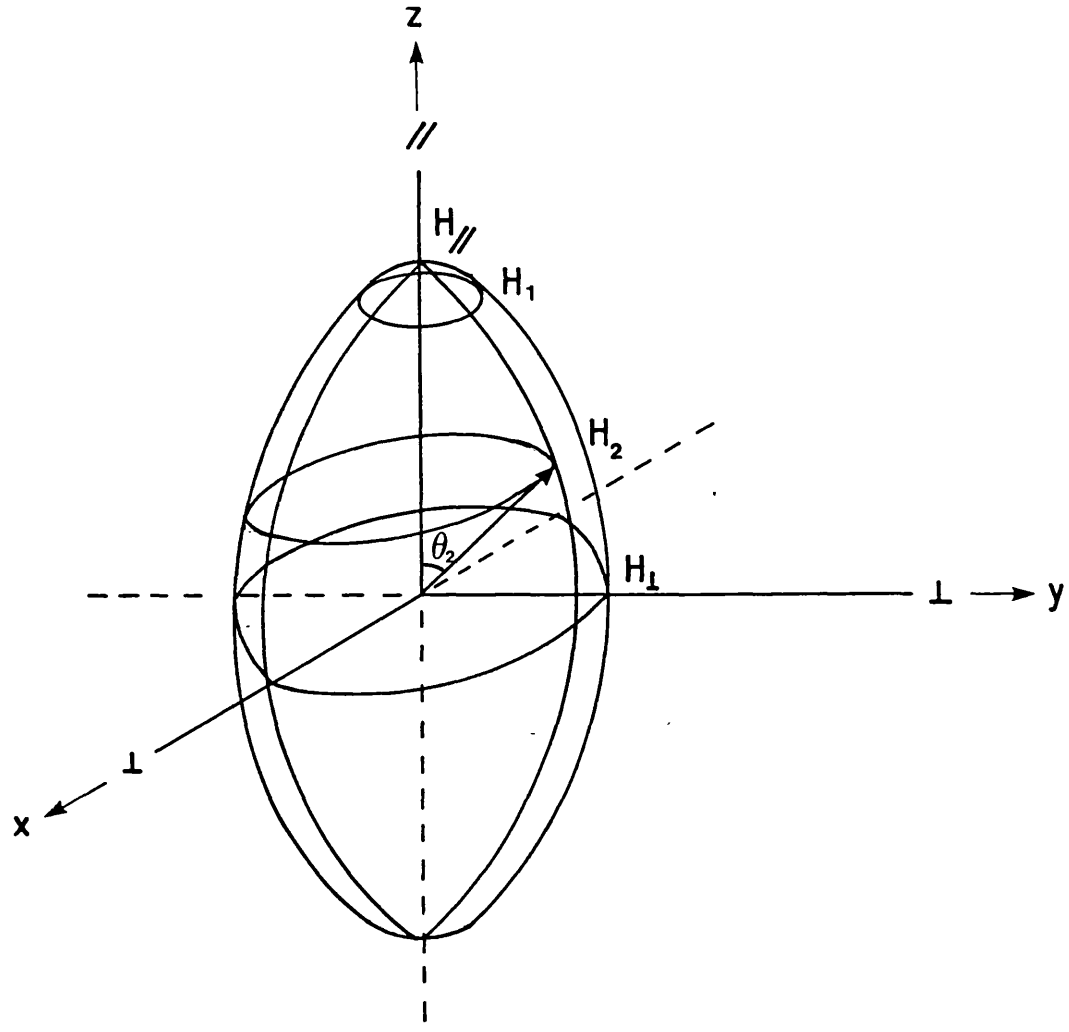

FIGURE 8

Prolate spheroid formed by allowed g-values of an axial system, showing circles of constant g.

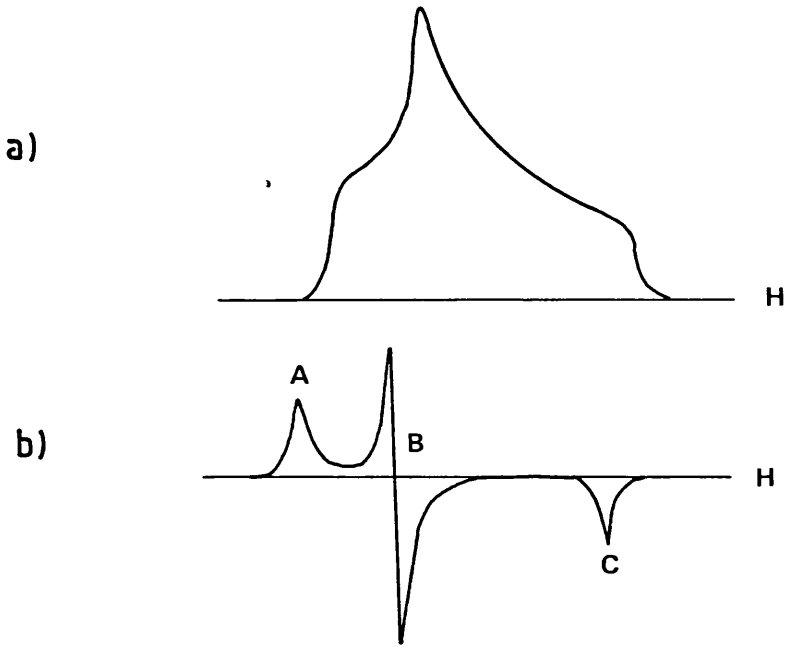

FIGURE 9

Absorption (a) and derivative (b) ESR powder spectra of a system with an orthorhombic g-tensor.

values of the interaction tensors can be determined from the ESR spectrum, the relative orientations cannot. Interpretation can also be complicated if intense "forbidden transitions" are present.

Quantitatively, the intensity at a particular field is calculated by summing the contributions from all possible orientations, according to the equation[14]

$$I(H) = \int_0^{2\pi} \int_0^{\pi} P(\theta,\phi)\, y\left[\frac{H - H_r(\theta-\phi)}{\Delta H(\theta,\phi)}\right] \sin\theta\, d\theta\, d\phi \qquad (14)$$

θ and ϕ are spherical coordinates, replacing the direction cosines in equation 13. $P(\theta,\phi)$ is the transition probability, which can depend on orientation as can the linewidth $\Delta H(\theta,\phi)$. $H_r(\theta,\phi)$ is calculated from the appropriate spin Hamiltonian. I(H) can be calculated over a range of fields, and such computer simulations can be invaluable in interpreting powder ESR spectra, particularly for low symmetry complexes or if $S>\frac{1}{2}$. Even if P and H are assumed to be independent of orientation, assumptions which are usually adequate in all but the most anisotropic cases, equation (14) is not easy to integrate and computer simulations can be quite time consuming.

An example of the sensitivity loss that results when going from a single crystal format to a powder format is shown in Figure 10. Figure 10a is the ESR spectrum of a substitutional $Rh^{2+}(d^7)$ ion in a NaCl crystal, with the magnetic field aligned parallel to (100). Figure 10b shows the corresponding powder spectrum where signal intensity has decreased by a factor of 50 in the perpendicular region due to the decreased number of crystallites with resonances at $H_\perp$. This sensitivity loss is almost compensated for by the larger powder sample

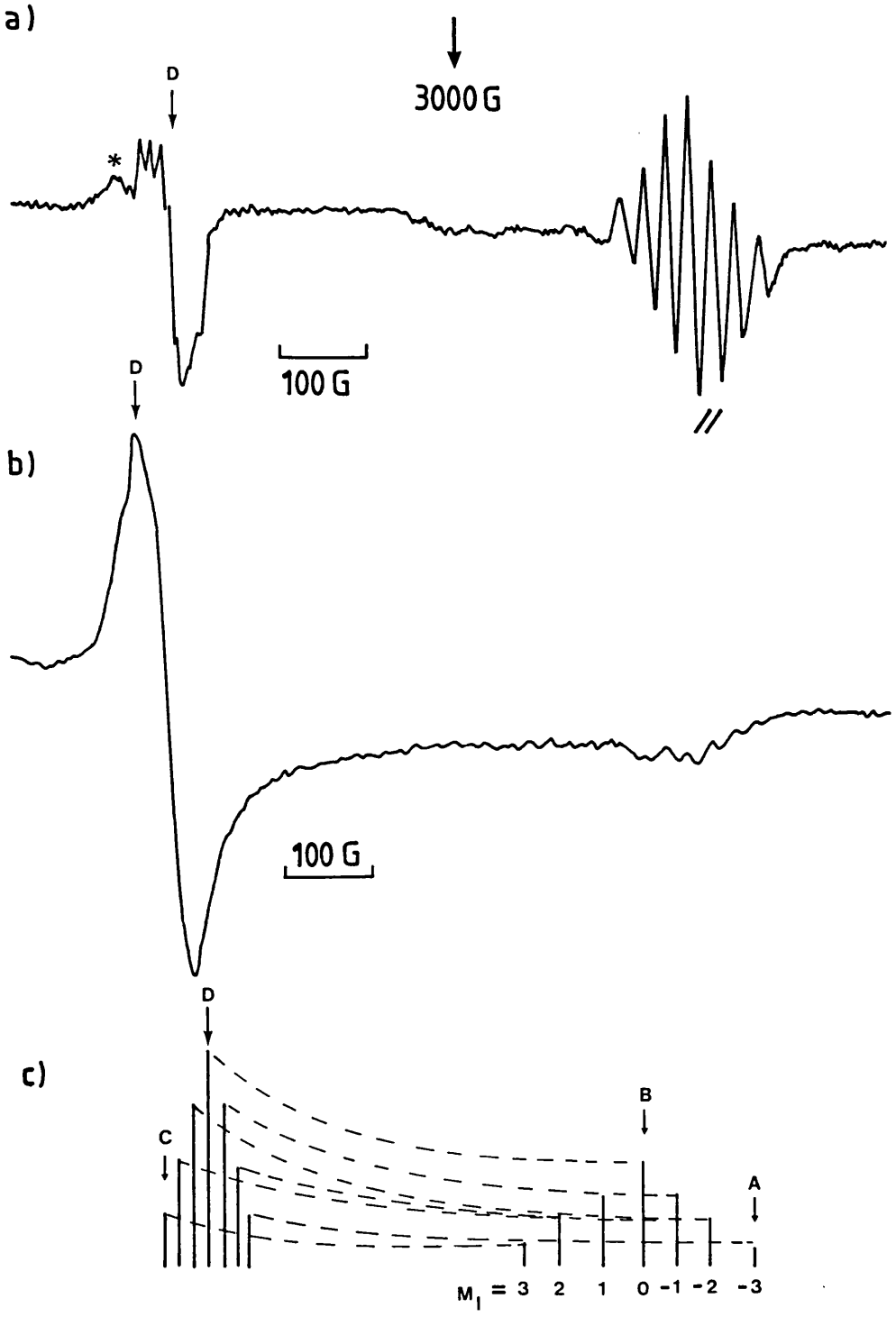

FIGURE 10

a) Single crystal ESR spectrum of the axial $(RhCl_6)^{4-}$ center in NaCl;
b) powder ESR spectrum of $(RhCl_6)^{4-}$/NaCl; and
c) stick diagram of the $(RhCl_6)^{4-}$ ESR powder spectrum resolved into M_I-components. Single-crystal-like ENDOR spectra would be obtained at A and C. Four different orientations of crystallite occur at B and at D.

size that can be used; however, an intensity loss of a factor of 10 in the parallel region of the spectrum still remains. The loss of sensitivity will, of course, be proportional to the degree of anisotropy present in the spectrum.

ENDOR powder spectra can be classified into two types. The first type is the exact analog of the ESR powder spectra just discussed, that is, the ENDOR spectrum is a composite due to all possible orientations of crystallites. In the second type only selected orientations contribute to the ENDOR spectrum. Such is the case if, with regard to Figure 10b, the saturating microwave field is positioned at point A in the parallel region of the Rh^{2+} powder spectrum. Only those $(RhCl_6)^{4-}$ complexes with g_z parallel to the external field contribute to the ENDOR spectrum. Here, the g-tensor is what Hyde refers to as a "separating vector", separating out select orientations.[23] Separating vectors occur in an ESR spectrum if one type of interaction is markedly more anisotropic than any other. They also occur if several tensors are equally anisotropic but have parallel axes, as in the case of the g-tensor and chlorine hyperfine tensor for $(RhCl_6)^{4-}$/NaCl.

i) Powder-Type ENDOR Powder Spectra

The first type of spectrum, which will be referred to as a powder-type ENDOR spectrum, is obtained if the observed ENDOR spectrum is independ nt of the position of the saturating microwave field on the powder ESR spectrum. This occurs if there are no separating vectors and an example is the single, inhomogenously broadened ESR resonance of the F-centre in an alkali halide lattice. Powder-type ENDOR spectra are also observed when coupling between individual spin packets

transfers the energy of the microwave field throughout the spin system faster than it is transferred to the lattice; that is, $T_{xx}^{-1} \gg T_{1e}^{-1}$. Such a condition is favoured at low temperatures, where T_{1e} is long, and in molecular crystals, where coupling to the lattice is weak. An example of the latter case are the x-irradiated aliphatic and alicyclic diacids studies by Dalton and Kwiram.[12] For a series of irradiated organic acids and polymers, they found that at 4.2 K, T_x^{-1} was in the range of 10^3 to 10^4 sec^{-1} and T_{1e}^{-1} was in the range of 10^{-2} to 10^2 sec^{-1}. Their approach to the simulation of powder-type ENDOR spectra illustrates some of the effects of temperature, modulation conditions and scan rate on the ENDOR powder lineshapes, and is outlined briefly below.

Dalton and Kwiram's approach consisted of calculating the transition probability "exactly", using equation 11, which allows for the angular dependence of P, but treating the effect of relaxation pathways on the ENDOR lineshape empirically, assuming α was independent of orientation. If it is assumed that the ENDOR experiment is performed with a strong saturating microwave field, and for simplicity, that $m_I = \frac{1}{2}$, equation 6a becomes

$$A_{ENDOR} = \frac{y^2}{(1+y^2)} \quad (1 - \alpha_{\pm}) \tag{15}$$

where, as before, $y^2 = P(\upsilon_{\pm})T_{1N}$. The transition probability $P(\upsilon_{\pm})$ is given by eqn 12 in reference 12. Using this, eqn 15 can be rewritten as

$$A_{ENDOR} = \frac{S'[1 \mp B'(\theta,\phi)/2\upsilon_N]^2 R}{1 + S'[1 \mp B'(\theta,\phi)/2\upsilon_N]^2} \tag{16}$$

B', defined in reference 12, is related to the hyperfine coupling at (θ,ϕ). For an axial system with H_o aligned $\perp$ to z, $B' = A_{||}$. Equation 16 must be applied separately to each different type of proton since A_{ENDOR} is the relative amplitude for resonances arising from a particular hyperfine interaction. R incorporates the relaxation parameter, $R = 0.5(1 - \alpha_+)$, and S', the NMR saturation parameter, is given by $\frac{1}{4}(\gamma_N^2 \bar{H}_2^2 T_{2N} T_{1N})$. It is assumed that S' and R are independent of orientation. An experimentally-derived lineshape function was used since the observed ENDOR lineshapes were neither Gaussian nor Lorentzian, but depended in a complex way on scan rate and modulation conditions. This dependence was particularly pronounced at 4.2 K, where the electron and nuclear spin lattice relaxation times were of the order of several seconds. It was assumed that the lineshape function was isotropic. The simulated powder spectrum for β-protons in x-irradiated glutaric acid, that results from this approach agrees well with experiment, as shown in Figure 11. A value of S' of about 0.1 was found to give the best fit for all the diacids investigated and this was consistent with the H_2 field used and the approximate relaxation times in such solids. If the spectrum was simulated for x-irradiated glutaric acid assuming that P was independent of orientation, the line intensities did not fit well with experiment, in particular the parallel features are much stronger than actually observed.

One notes that, due to the frequency dependence of A_{ENDOR}, α and β protons each have characteristic powder ENDOR lineshapes. For α protons, the lineshapes observed in the overlap region, between the highest frequency lines of pairs centred at υ_N, (υ_+), and the lowest frequency lines from pairs centred at

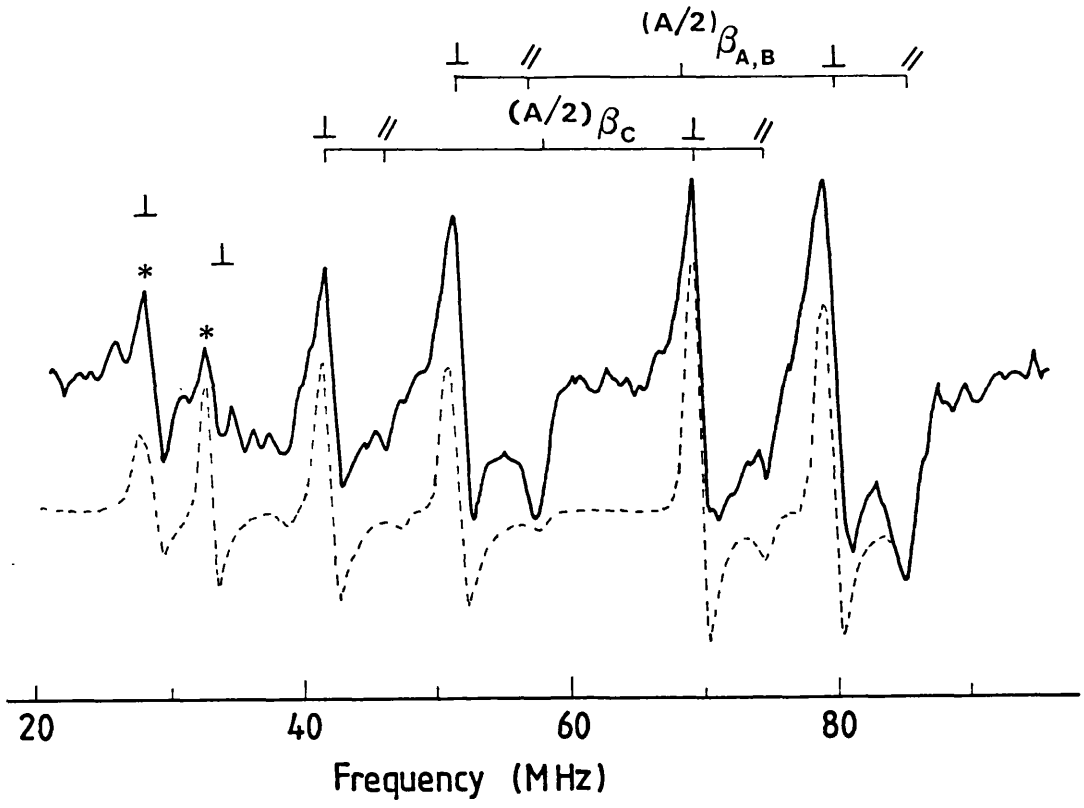

FIGURE 11

Experimental and simulated (---) powder-type ENDOR spectrum of β-protons in glutaric acid.
A, B and C refer to different molecular orientations.
*-lines are from unidentified β protons.
From reference 12.

A/2, (υ_-), are very dependent on and useful in characterising S′. At low values of S′ only the υ_+ lines are observed in this region. Also, the υ_- lines of resonances centered at υ_N are not observed at low values of S′ (Figure 12).

Figures 12 and 13 show the effect of S′ on the simulated ENDOR spectra of α and β protons, respectively. Experimentally, S′ will depend on temperature, so one expects that ENDOR lineshapes and intensities to vary markedly with temperature. As S′ increases, the intensity dependence on frequency changes from quadratic at low S′ to linear to frequency independent at very large S′.

Thus, in powder-type ENDOR spectra, as in powder ESR spectra, a sensitivity loss occurs because of the line broadening and spectral spread resulting from the hyperfine anisotropy. However, because the spectral resolution is greater in an ENDOR experiment, the sensitivity loss for a given degree of anisotropy is greater for ENDOR than for ESR. The increased resolution also allows one to detect the angular dependence of the transition probability, and this causes further intensity loss at certain regions of the powder spectrum, notably the parallel features. Finally, ENDOR lines arising from the most anisotropic hyperfine interactions are often completely submerged by those due to the least anisotropic interactions. For example, the α proton resonances are often not detectable when resonances from β protons are also present.

On the positive side, ENDOR powder-type spectra are generally easier to simulate and to interpret than are ESR powder spectra. Individual hyperfine interactions can be considered separately and there are no forbidden transtions to be

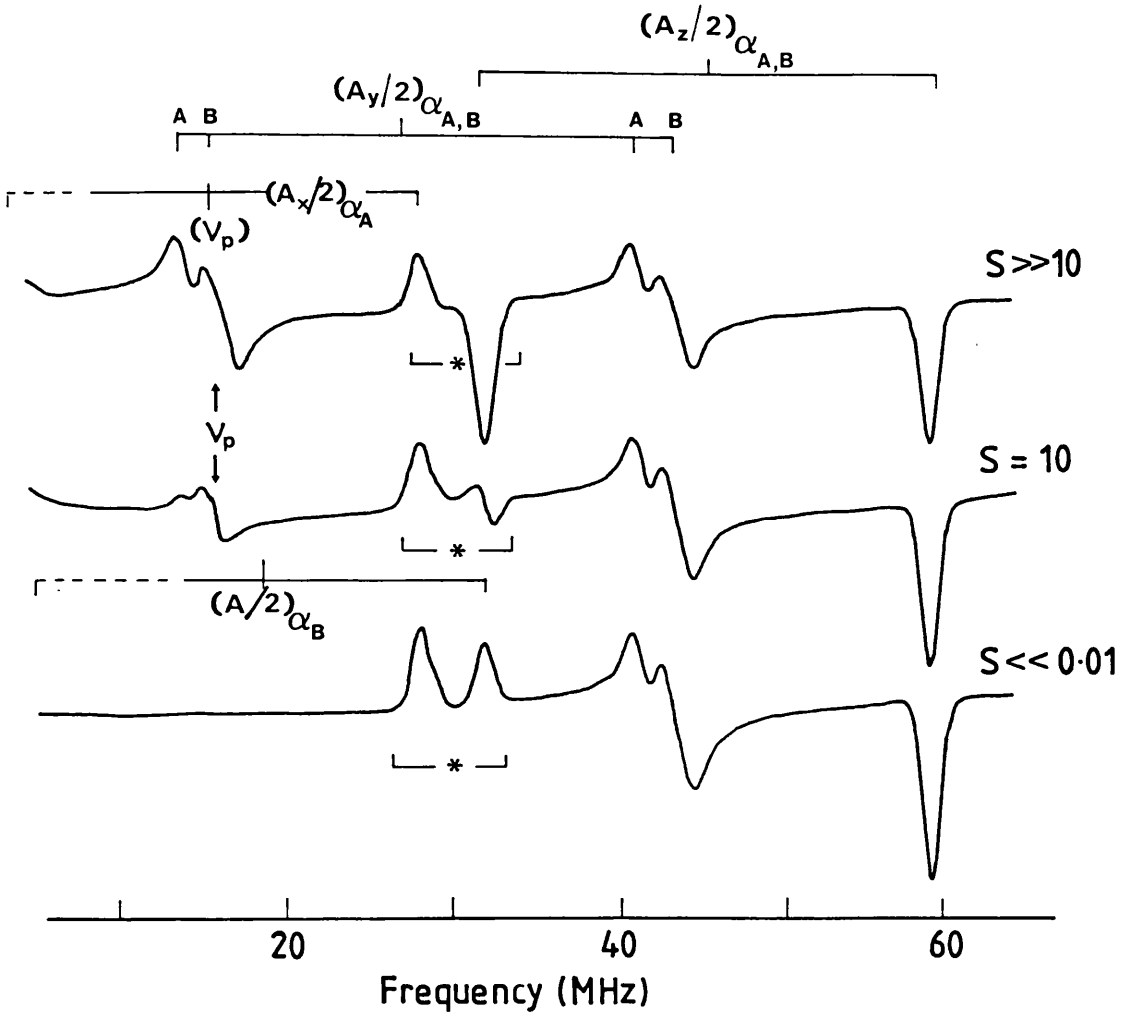

FIGURE 12

Computer simulations of the powder-type ENDOR spectra of malonic acid, showing the A_x, A_y and A_z couplings of α protons in configurations A and B. The overlap region of ν_+ lines centered at ν_p, and ν_- lines centered at A/2, is marked *. The effect of varying the saturation parameter, S′, is shown. From reference 12.

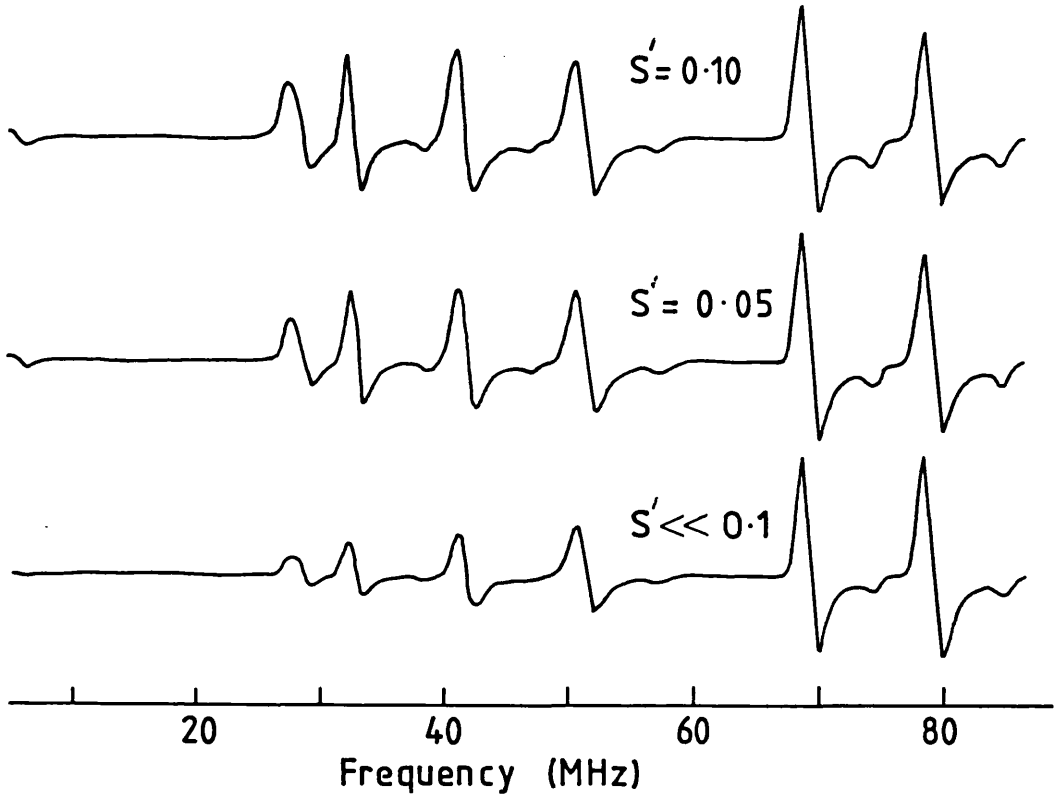

FIGURE 13

Computer simulations of the powder-type ENDOR spectrum of glutaric acid, showing the effect on β-proton line intensities of varying the saturation parameter, S'.

considered. The kind of nucleus giving rise to each hyperfine interaction can be unequivocally assigned. The major difficulty arises in assigning the various hyperfine components to the appropriate hyperfine tensors and this is sometimes compounded if some of the components are not detected because of large anisotropies. As with ESR powder patterns, chemical intuition must be used to assign the tensor orientations and to assign each tensor to a nucleus within the molecule. This can be difficult for the ENDOR spectra because of the large number of hyperfine interactions resolved.

In conclusion, the major difficulty for powder-type ENDOR studies is sensitivity, whereas the major difficulty in ESR powder studies is usually one of interpretation.

ii) "Single-Crystal like" and "Two-dimensional" ENDOR Powder Spectra

The second type of ENDOR powder spectrum occurs when the crystallite orientations which contribute to the ENDOR spectrum are determined by the magnetic field position, H_o. The necessary condition for this is $T_{1e}^{-1} \gg T_x^{-1}$. The concept of a separating vector is useful in considering how the position of H_o determines the ENDOR powder spectrum. Consider a complex with an axial g-tensor and a hyperfine interaction that is unresolved in the ESR spectrum; then the separating vector is $g_\parallel$. The ENDOR spectrum at $H_\parallel$ will be due only to those crystallites with $g_\parallel$ parallel to H_o and is referred to as a "single-crystal like" ENDOR powder spectrum. The observed hyperfine splittings will be

$$A_a^2 = A_{xx}^2 \, l_{xz'}^2 + A_{yy}^2 \, l_{yz'}^2 + A_{zz}^2 \, l_{zz'}^2 \qquad (16)$$

where ($l_{xz'}$, $l_{yz'}$, $l_{zz'}$) are the direction cosines between the separating vector and the principal axes of the hyperfine tensor (Figure 14a). When H is positioned at $H_{\perp}$, perpendicular to the separating vector, a "two-dimensional" ENDOR spectrum is observed, resulting from those crystallites with $g_{\parallel}$ perpendicular to H_o (Figure 14b). Turning points will be observed at

$$A_{b1}^2 = A_{xx}^2 l_{xx'}^2 + A_{yy}^2 l_{xy'}^2 + A_{zz}^2 l_{xz'}^2 \qquad (17)$$

$$A_{b2}^2 = A_{xx}^2 l_{yx'}^2 + A_{yy}^2 l_{yy'}^2 + A_{zz}^2 l_{yz'}^2$$

At any field between $H_{\parallel}$ and $H_{\perp}$, the ENDOR spectrum will result from a cone of orientations as shown in Figure 8. If the hyperfine tensor and the tensor containing the separating vector have coincident axes and the hyperfine tensor is axial, then the cone of orientations collapses to a single line, and one can essentially perform a single crystal rotation by shifting the position of the magnetic field between the parallel and perpendicular turning points. $A_{\parallel}$ can then be measured from the single-crystal-like spectrum and $A_{\perp}$ from the two-dimensional spectrum.

Usually, more than one anisotropic tensor is resolved in the ESR spectrum. The ESR powder spectrum will then consist of the superimposed axial or orthorhombic powder patterns of several spin states (Figure 10c). In this more general case there are only a few field positions where simple single-crystal-like or two dimensional spectra can be obtained. In Figure 10c, $H_{\parallel}$ (position B) selects four cones of orientations in the ENDOR spectrum. The situation is further complicated by the fact that each cone corresponds to a different m_I transition which will excite only certain quadrupole transitions in the

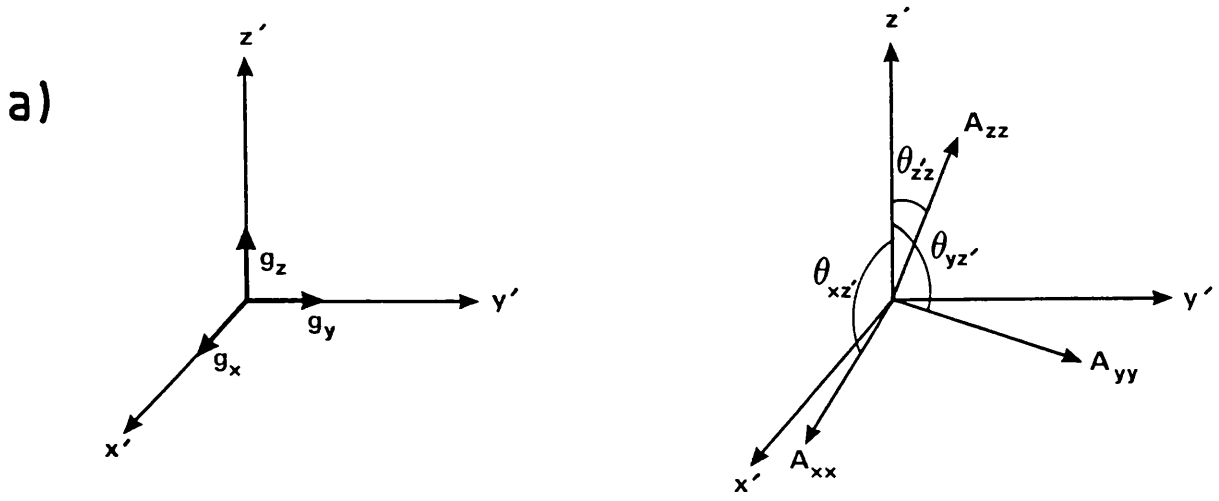

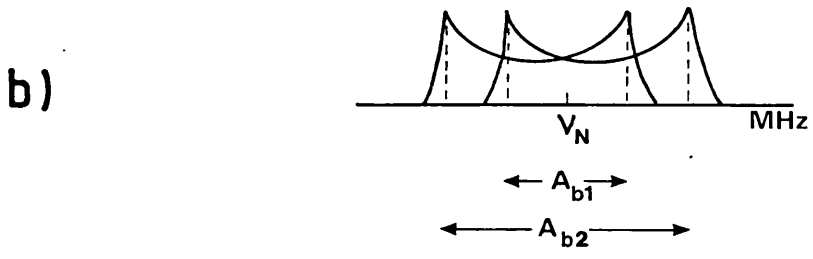

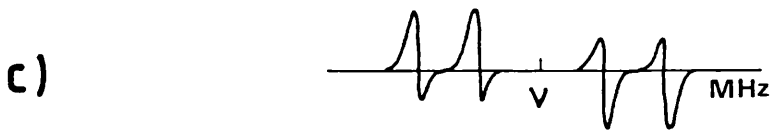

FIGURE 14

a) Relative orientations of g- and A-tensors;
b) absorption and c) derivative two-dimensional ENDOR powder spectra obtained with H_o in the x′-y′ plane. A_{b1} and A_{b2} are given by eqn. 17. $2\nu_N > A_{b1}, A_{b2}$.

ENDOR spectrum. Except at points A and C, this case would be difficult to interpret without computer simulation. In addition difficulties arise when singularities are observed which do not correspond to true turning points. These are also observed in some ESR spectra.[22]

Temperature might be expected to have a large effect on ENDOR linewidths since, as it is lowered, T_{1e}^{-1} approaches T_x^{-1}. In some instances it should be possible to change from single-crystal-like or two-dimensional ENDOR powder spectra to powder-type ENDOR powder spectra simply by lowering the temperature.

The sensitivity in single-crystal-like or two-dimensional ENDOR spectra will decrease, relative to single crystal spectra, by at least as much as the ESR sensitivity at the field where the ENDOR spectrum is taken. This decrease, of course, is a result of the reduced number of spins giving a resonance at this point. In the Rh/NaCl powder, sample packing has restored ESR and ENDOR sensitivity in the perpendicular region; however, the intensity of the simplest two-dimensional ENDOR powder spectrum, which is obtained at position C (Figure 10b) will be reduced by a factor of 10 as described above and by a further factor of 4, since the $m_I = -3$ ESR line rather than the $m_I = 0$ ESR line is being saturated. The ENDOR powder lines might be expected to be broader than in crystals since H_1 excites spin packets in a range ΔH which corresponds to a solid angle $\Delta\theta$. This effect is noticeable in the Rh/NaCl $\perp$ ENDOR powder spectrum (Figure 15). Such line broadening would be more pronounced if double modulation schemes employing Zeeman modulation were used. The difference in line intensities between the single crystal and powder ENDOR spectra in

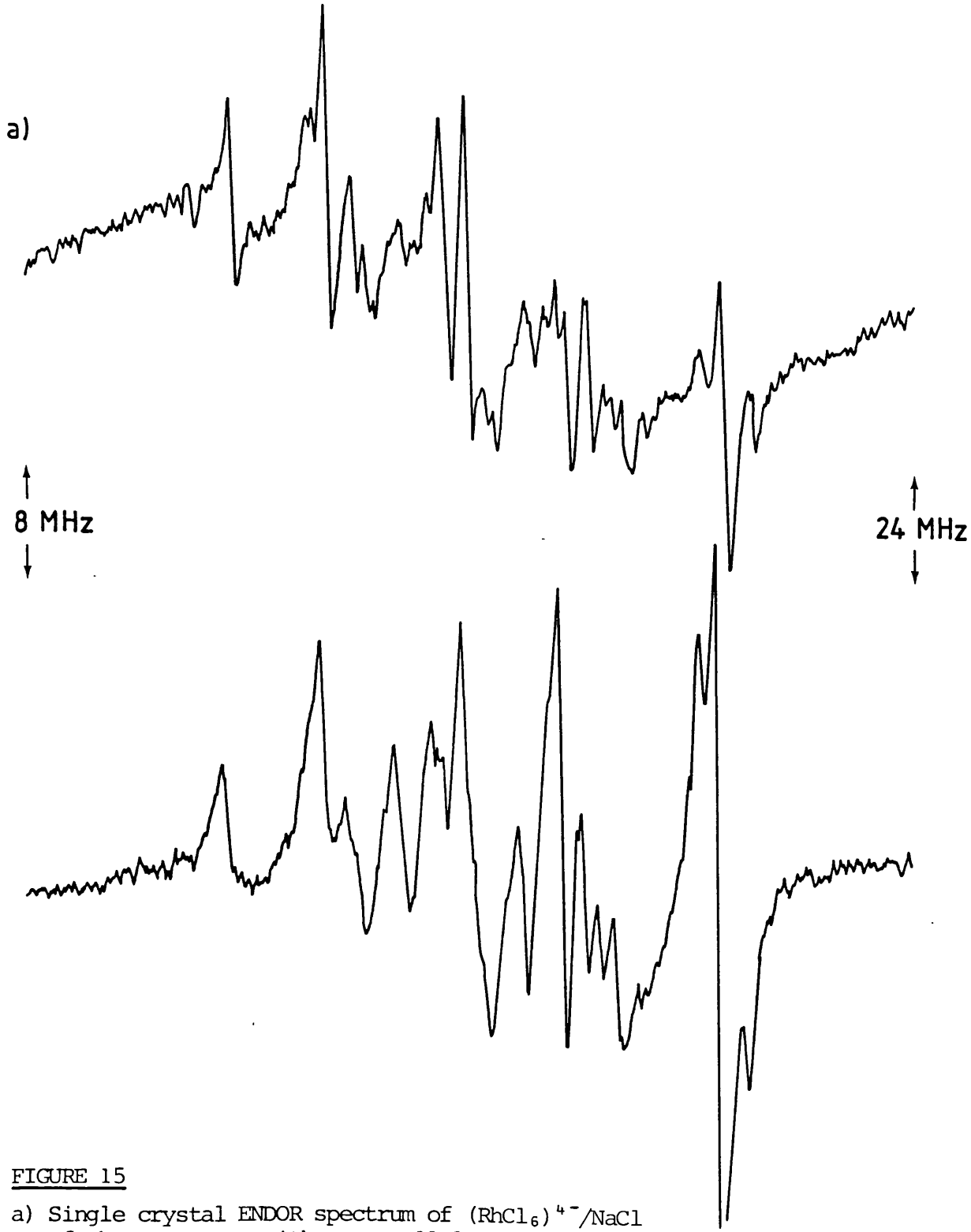

FIGURE 15

a) Single crystal ENDOR spectrum of $(RhCl_6)^{4-}$/NaCl of those centers with $g_\perp$ parallel to H_o, (position D in Figure 10a).
b) ENDOR powder spectrum of a $(RhCl_6)^{4-}$/NaCl powder with H_o at position D in Figure 10b.

Figure 15 is attributable to the different m_I components being excited at field position B.

iii) Frozen glasses

All of the considerations discussed above are applicable to frozen glasses. There is only one difference between powders and frozen glasses that need be considered in the interpretation and simulation of the ENDOR spectra of frozen glasses. This is that, in addition to having a random distribution of orientations, in glasses, the paramagnetic complexes are randomly distributed over a range of enviroments. In the simulation of the ESR spectra of frozen glasses, this is usually treated by assuming that for each given enviroment there is a random distribution of orientations, and conversely that for each orientation there is a random distribution of enviroments. The range of enviroments effectively results in a spread of Hamiltonian parameters. The structure of the glass might be such that this spread is smaller for a particular interaction component, resulting for instance in an ESR spectrum with the $g_{\parallel}$ feature larger than the $g_{\perp}$ feature.[14] Thus, due to the additional spread of Hamiltonian parameters, the ESR spectra from frozen glasses will generally be broader than from powder spectra. For all of the same reasons as discussed for powders,

this leads to additional line broadening and sensitivity loss in the ENDOR spectra of glasses.

iv) Sodium Formate Powder ENDOR

γ-irradiated sodium formate has often been used as a standard ENDOR sample since the CO_2^- radical observed is stable at room temperature and exhibits strong resonances over a large temperature range.[24] For these same reasons, it was chosen as a suitable system for a study of the information that can be obtained from powder ENDOR.

Sodium formate crystals are monoclinic. There are four sodium formate molecules per unit cell;[25] their relative positions and the dimensions of the unit cell are indicated in Figure 16. The sodium, carbon and hydrogen atoms form chains parallel to the b-axis, and these are arranged in layers parallel to the ab plane. In a given layer, like atoms in neighbouring chains are parallel, and like atoms in neighbouring chains in adjacent layers are staggered. The C-O bond distance is 1.27 Å and the bond angle is 124°.[25] The crystals used in this study were grown from aqueous solution and, as noted by Zachariasen,[25] were elongated along the c-axis and cleaved easily parallel to the ab plane.

The CO_2^- radical was produced by γ-irradiation at 77 K or room temperature. The ESR spectrum consisted of four lines of equal intensity due to an interaction with a single sodium ion. The principal g-values and hyperfine components are listed in Table I. Since the principal interest was not in the CO_2^- radical, but in ENDOR powder spectra, a single crystal rotation study was not done. Instead, the single crystal ESR study by Ovenall and Whiffen[26] was used as reference and

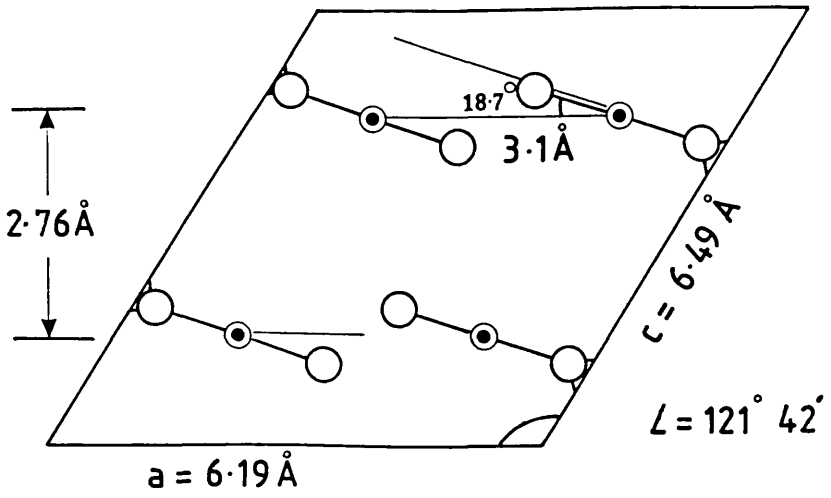

FIGURE 16

Crystal structure of sodium formate.[24]
Subscripts refer to hyperfine splittings in Table I.
$H_{(2)}$ and $Na_{(2)}$ are in parallel chains in the ab plane.

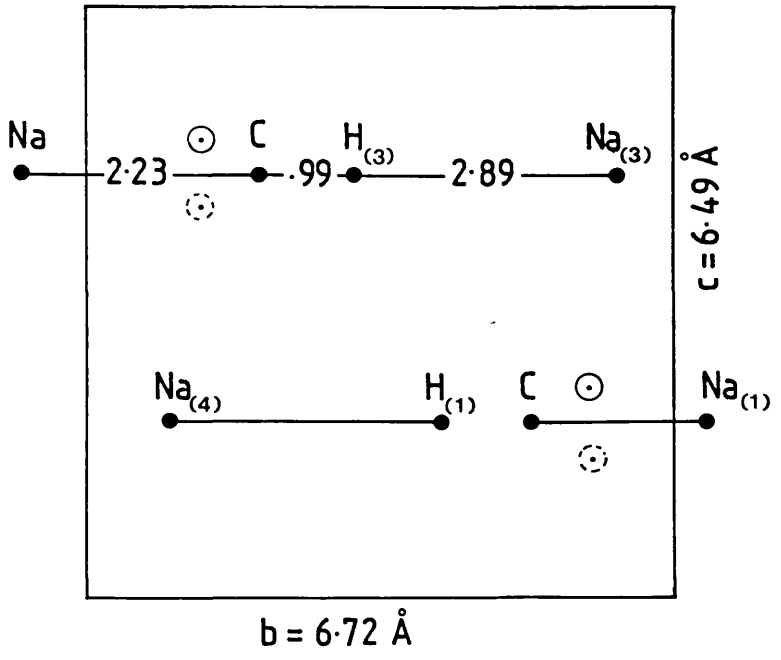

Table I - Hyperfine and Quadrupole Parameters from Sodium Formate Single Crystal

Nucleus	$A_{\parallel}$ b $Wq_{\parallel}$ b	$A_{\perp}$ formate plane $Wq_{\perp}$ formate plane	$A_{\parallel}$ a $Wq_{\parallel}$ a
	(MHz)		
Na_1	27.13 −.81	22.30 .27	20.46 −.78
$Na_{B(3)}$	.99 —	1.76 .18	
$Na_{C(4)}$	.35 ~.06	— —	— —
$Na_{D(2)}$	.64	.37	.96 .18
$H_{A(3)}$	1.85($\sim_{\parallel}$)	2.60($\sim_{\parallel}$)	1.30($\sim_{\perp}$)
$H_{B(2)}$	1.18($\sim_{\perp}$)	1.35($\sim_{\perp}$)	1.50($\sim_{\parallel}$)
$H_{C(1)}$	1.50($_{\parallel}$)	.48($_{\perp}$)	.43($_{\perp}$)
H_{D-F}	.83 .26	.43 .12	.80 .35 .23
g-values*	g_y=2.0014	g_x=2.0032	g_z=1.9975
ΔH_{pp}*	9.8	10.6	5.5

* = from reference 26.

ESR and ENDOR spectra were measured at selected angles. Ovenall and Whiffen found that the principal axes of the g-tensor and of the Na^{23} and C^{13} hyperfine tensors were parallel to b, perpendicular to b and parallel to the formate plane, and perpendicular to the formate plane. The $A_{\|}$ components for both Na^{23} and C^{13} were parallel to b. CO_2^- was shown to be bent, with a bond angle of $\sim 136^{\circ}$, occupying the same position as the parent ion. The unpaired electron is in a pseudo π antibonding orbital ($4a_1$) projecting along the external bisector of the $O\hat{C}O$ angle. There is 2.6% spin density on the sodium ion responsible for the four line splitting in the ESR spectrum, which is either Na_1 or Na_4 in Figure 16.

Single Crystal Measurements

ENDOR measurements were made with H_o parallel to b, parallel to a, and perpendicular to the formate plane. The hyperfine parameters obtained are listed in Table I. It should be noted that these directions are not necessarily the principal axes for each of the nuclei observed. Optimum ENDOR signals were obtained at temperatures between 50 and 120 K.

Quadrupole splittings for several sodium neighbours are also listed in Table I. For the principal sodium ion, Na_1 on the b-axis, either two or four of the six possible quadrupole transitions were observed, depending on whether one of the outer or inner two ESR lines was saturated. This allowed the determination of the relative signs of the hyperfine and the quadrupole coupling constants. It is reasonable to assume that $A_{\|}$ is positive.[26] If the high field, $I = {}^{-3}/_{2}$, ESR transition is saturated, an rf field will excite only those NMR transitions involving the Na_1 spin state $I = {}^{-3}/_{2}$. For these transitions,

$m_q = -1$. When H_o was parallel to b and the I = $^{-3}/2$ line was saturated, the outer two quadrupole lines were observed. For the highest frequency ENDOR line ($m_s = -\frac{1}{2}$), the observed ENDOR transition frequency is given, according to eqn 5.21, by:

$$h\upsilon = \left| -\tfrac{1}{2}A_{\|} - m_q P_{\|} - h\upsilon_{Na} \right| \qquad (18)$$

Since this is the highest frequency transition, the term $m_q P_{\|}$ must be positive. For this transition $m_q = -1$, so the sign of $P_{\|}$ must be negative. $P_{\|}$, the quadrupole splittings measured with H_o parallel to $A_{\|}$, is related to the quadrupole coupling constant q by equation 5.20: $P_\theta = 3\left[q(3\cos^2\theta'' - 1) + q' \sin^2\theta'' \cos\phi''\right]$. q and q′ are the components of the quadrupole interaction tensor $\tilde{Q}$ (eqn 5.14). The quadropole splittings measured along the principal axes were approximately -.8 MHz and -.8 MHz in the formate plane and +.3 MHz perpendicular to the plane. Therefore, q = -.14 MHz and q = -.10 MHz. The quadrupole tensor components are proportional to the electric field gradient along each principal axis (eqn 5.13). From the sign of q and q′, it can be deduced that there is a negative charge density uniformly distributed in the formate plane at some distance from Na_1 and a very small positive charge density perpendicular to the plane.

The observed major sodium hyperfine splittings indicate that the hyperfine interaction is with a sodium ion on the b-axis. CNDO calculations[27] indicate that the CO_2^- radical forms a tight ion pair with the Na_1 ion (Figure 16). Hyperfine splittings from two or three types of more distant sodium atoms and up to six different types of protons were also observed. The assignments of these splittings to the appropriate nuclei remain speculative without the aid of a crystal rotation.

However, for the purposes of interpreting the powder spectrum we have made tentative assignments by assuming the hyperfine interactions are largely dipolar and that the symmetry direction of the largest hyperfine component from each tensor will be along the line connecting the carbon atom in the CO_2^- radical and the nucleus concerned. The distances from the carbon atom to the nucleus were also considered; these are shown in Table III. The most likely assignments for the hyperfine components are listed in Table I, the numbered nuclei are shown in Figure 16. Of course, the measured hyperfine components in Table I are not all along principal directions. It is indicated in parenthesis whether the measured components are along approximately parallel or perpendicular axes, based on the nuclear assignment. There are two of each type of numbered nucleus, one on either side of the CO_2^- radical.

The largest dipolar coupling to sodium was 1.76 MHz, measured when H_o was perpendicular to the formate plane; this has been assigned to $Na_{(3)}$. As the spectrum in Figure 19c shows, there are more than the six expected quadropole lines centered at υ_{Na} at this orientation. This might be due to a slight inequivalency in the pair of $Na_{(3)}$ ions. Proton splittings H_{D-F} might be due to dipolar couplings with very distant protons or might be components of tensors for protons 1-4 where the proton pairs are slightly inequivalent.

Powder ENDOR Measurements

The powder ESR spectrum measured for CO_2^- is shown in Figure 17. ENDOR spectra were taken with H_o at positions A and B, and are shown in Figures 18b, 18d, 19b, and 19d. Clearly,

Table II - Hyperfine and Quadrupole Parameters from Sodium Formate powder

Nucleus	Position A ($H_o \perp$ b, $\parallel$ to formate plane)	Position B ($H_o \perp$ to formate plane)
	MHz	
Na_1	21.74	21.68
	.83	.35
		25.2
		.35
Na_{B-D}	.96	1.98
	—	—
	1.6	
H_{A-F}	1.6	3.5
	.93	1.6 - 1.7
	.48	.88
	.23	.40
		.23

Table III - Distances to ions from C*

	A
$H_{(1)}$	.99
$H_{(2)}$	2.9
$H_{(3)}$	3.3
$H_{(4)}$	5.7
$Na_{(1)}$	2.2
$Na_{(2)}$	3.6
$Na_{(3)}$	2.83
$Na_{(4)}$	3.22

* from reference 24

FIGURE 17

Powder ESR spectrum of CO_2^- radical in sodium formate at 96 K.

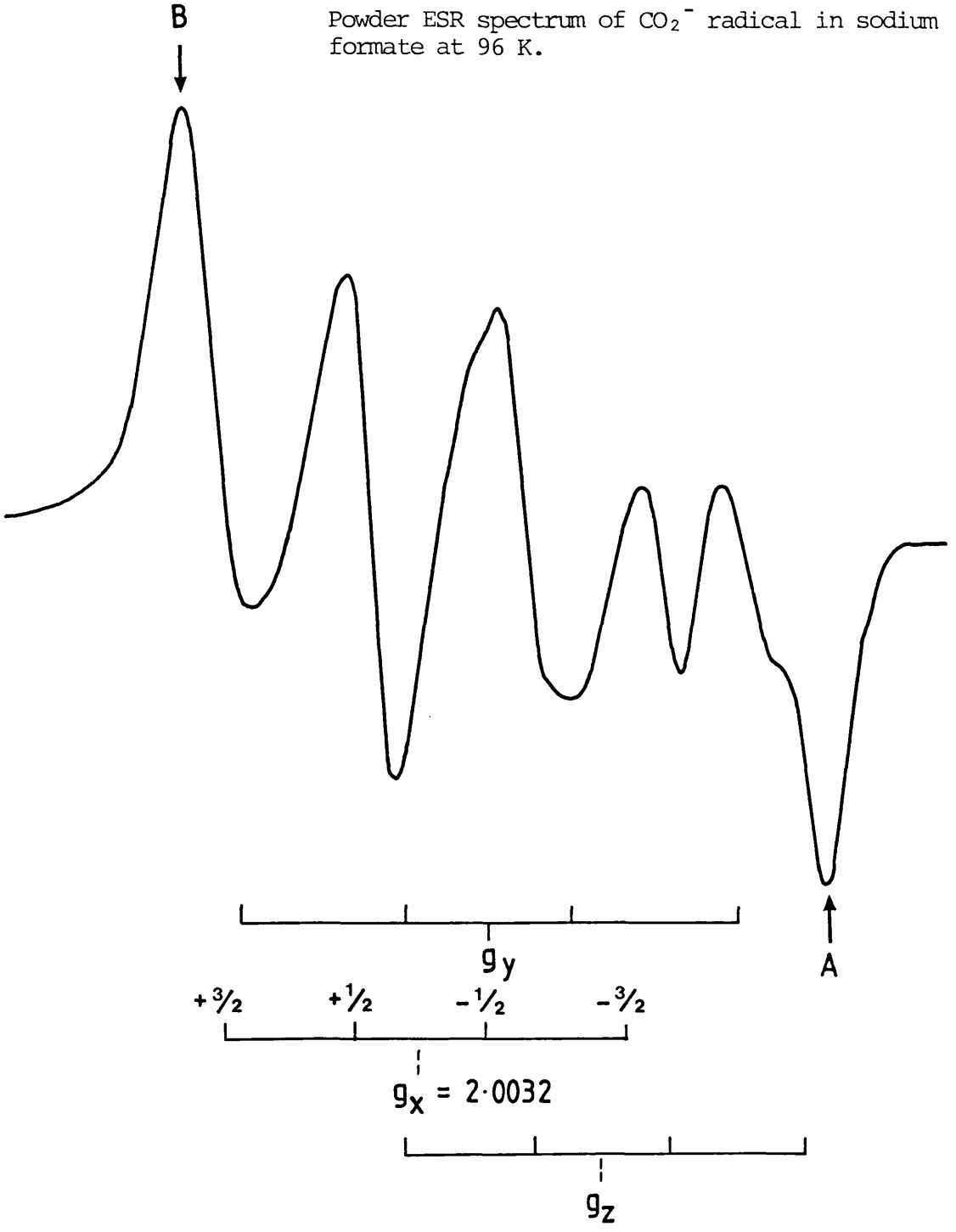

FIGURE 18

Single crystal (a, c) and powder (b, d) ENDOR spectra of CO_2^- in sodium formate at 96°K. Single crystal spectra were measured with H_o 11 a; powder spectra with H_o at A in Fig. 17.

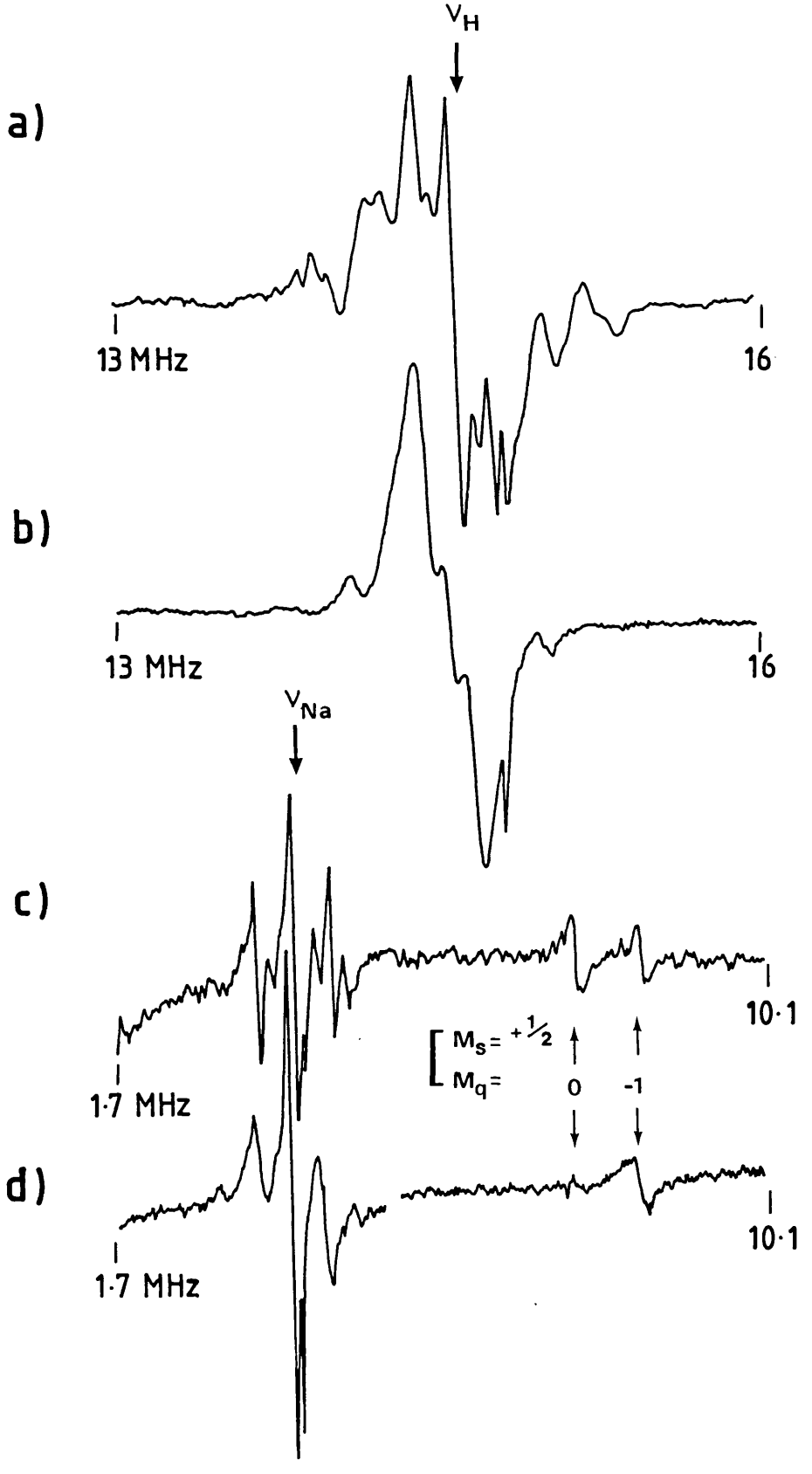

FIGURE 19

Single crystal (a, c) and powder (b, d) ENDOR spectra of CO_2^- in sodium formate at 96 K. Single crystal spectra were measured with $H_o \perp$ formate plane; powder spectra with H_o at B in Fig. 17.

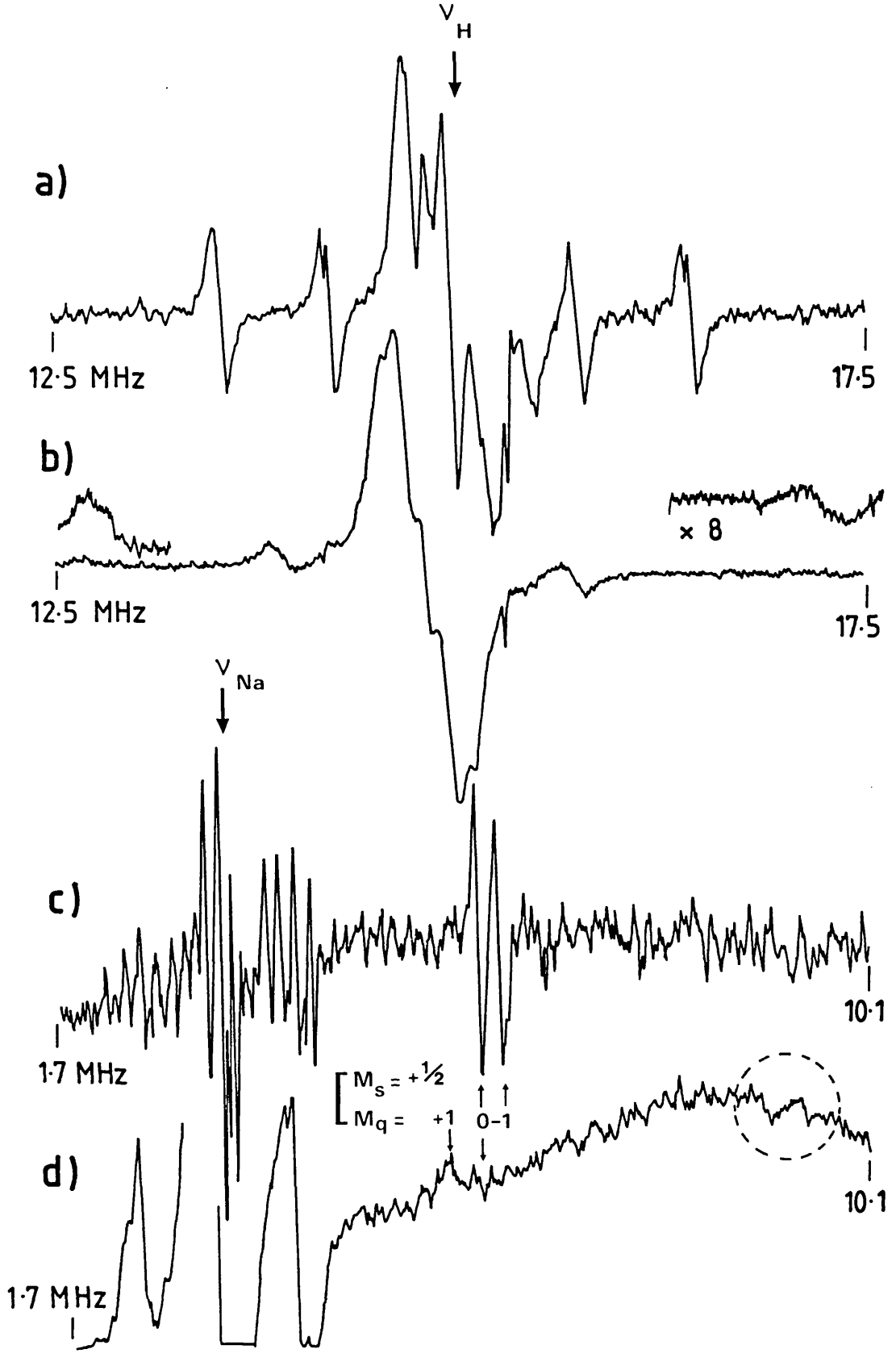

the ENDOR spectra depend on the position of the saturating microwave field, so these are the second type of ENDOR powder spectra defined by the condition that $T_{1e}^{-1} \gg T_x^{-1}$. The separating vector is g_z. Thus, position A will select out orientations parallel to the formate plane and perpendicular to b. Position B will select orientations perpendicular to the formate plane, and some or possibly all orientations in the plane containing this axis and the b-axis, depending on the overlap of the $^{+3}/2(x)$ and $^{+3}/2(y)$ ESR lines. Since this plane contains $A_\perp$ and $A_\parallel$ Na_1 hyperfine components, it is expected that the Na_1 lines at position B will be broad, and that a two-dimensional ENDOR spectrum might be observed. Only the two inner Na_1 quadrupole transitions will be observed at position A. At position B, excitations of $^{+3}/2(x)$ ESR lines will result in the observation of the outer two quadrupole lines and excitation of $^{+3}/2(y)$ lines will allow observation of the two inner lines.

For equivalent amounts of material the intensity of the single crystal and powder ESR signals were approximately the same, while the powder ENDOR signal intensity of lines due to small dipolar couplings was decreased by a factor of 10. This loss was restored however by using a powder sample twenty times larger than the single crystal sample.

Figure 18 compares single crystal ENDOR spectra taken with H_o parallel to a and powder spectra obtained at position A. For the purposes of this study, the orientation $H_o \parallel a$ will be considered equivalent to the orientation parallel to the formate plane and perpendicular to b (position A). Figure 19 compares single crystal ENDOR spectra taken with H_o perpendicular to the formate plane with powder spectra measured

at position B.

For position A, in the proton region (Figure 18b), the largest splitting is 1.6 MHz and is just discernible. It probably corresponds to the 1.3 and 1.5 MHz splittings in the single crystal spectrum. The smaller splittings are approximately the same as in the single crystal with slight differences probably arising from orientation differences. In the powder, lines from small couplings are relatively much more intense than in the single crystal. The sodium lines (Figure 18d) are approximately twice as broad in the powder, which results in the loss of quadropolar information for small sodium couplings. The hyperfine splitting for the Na_1 ion agrees well with single crystal results. There is a weak $m_q = 0$ line, which implies that a range of orientations, corresponding to a range of field positions $H_o \pm \Delta H$, including some $m_I = -\frac{1}{2}$ transitions, were excited. An additional small sodium coupling of 1.6 MHz was detected in the powder.

At position B an essentially two dimensional powder spectrum was observed from crystallites with their $A_{\parallel}(Na_1)$ direction in the plane perpendicular to the formate plane through the b-axis. For Na_1 interactions, turning points should occur at $A_{\perp}$ (outer quadrupole lines) and $A_{\parallel}$ (inner quadrupole lines). Only the $A_{\perp}$ turning point was observed and the lines were very broad and weak (Figure 19d). This suggests that there is not complete overlap of the g_x and g_y components and only orientations in the g_x-g_y plane and within an angle $\Delta\theta$ of the g_x direction were observed. The broad baseline drift at higher frequency could be due to other orientations in the plane. Some unexplained lines, at too high a frequency for $A_{\parallel}(Na_1)$ lines, were also observed. The dipolar Na splittings broadened

into a single splitting of 1.96 MHz centered at υ_{Na} which is consistent with the 1.76 MHz splitting observed in the single crystal.

The proton region at position B is much the same as at position A (Figure 19b). Approximately the same small couplings as in the single crystal were observed. The two largest proton splittings, of 3.5 and 1.6 MHz, were extremely weak. These probably correspond to $A_{\parallel}$ for proton 3 and an intermediate hyperfine splitting value for proton 2. Comparision of Figures 19 a and 19b indicate that in the powder, $I \propto {}^{1}/A^{2}$.

The principle values for $A_{\perp}$ (Na_1) obtained from powder measurements and $A_{\parallel}$ (Na_1) obtained from single crystal measurements agree well with those measured by Ovenall and Whiffen.[2] The spread of proton splittings measured in the g_x, g_y and g_z-directions are consistent with the observed ESR linewidths (Table I).

ENDOR measurements were made at 4 K in an attempt to obtain powder-type ENDOR spectra, characterized by the condition $T_{xx}^{-1} \gg T_{1e}^{-1}$. However, spectra could not be obtained below 30 K and at this temperature T_x was still larger than T_{1e}.

In conclusion, the ENDOR signal intensity was generally down by a factor of 10 in the sodium formate powder, but this could be restored by using larger powder samples. With the improved sample packing, at well separated orientations (A), the intensity of Na lines were approximately the same intensity as in single crystals, but about twice as broad. As more orientations were saturated, the Na_1 lines quickly broadened beyond detection (B), while the small dipolar couplings broadened, but remained intense. The small proton dipolar resonances were the dominant proton feature. The proton signal intensity

was approximately inversely proportional to the square of the hyperfine splitting. In this sample, however, the ESR signal was sufficiently intense to allow measurements of the more interesting larger hyperfine splittings. The data was less complete than in single crystals, but interpretable. For an example of a powder-type ENDOR powder study where ($T_{xx}^{-1} > T_{le}^{-1}$) see Chapter 8.

v) An ENDOR Study Of DTBN In Frozen Glasses

Frozen solutions of the ditertiary butyl nitroxide (DTBN) radical were used as a model system to determine the ENDOR sensitivity losses and line intensities that might be expected to occur in a glassy medium. The very intense ESR spectra obtained for DTBN in toluene provided a good starting point for such a study.

The ESR spectrum of a degassed, $\sim 1 \times 10^{-4}$ solution of DTBN in toluene is shown in Figure 20a. The isotropic nitrogen hyperfine splitting was 15.4 gauss. Well-resolved, intense liquid ENDOR spectrum could be obtained from such a sample, as discussed further in section 6.3.2 i (Figure 21). The ESR spectrum obtained from a frozen DTBN/toluene glass is shown in Figure 20b. The spectral breadth increased by a factor of ~ 2.5 as the $A_{//}$ (N) hyperfine splittings of 35 gauss became resolved. $A_{\perp}$(N) was less than 5 gauss. In order to obtain an ENDOR spectrum of the DTBN glass it was necessary to increase the DTBN concentration by a factor of 10 - to the point where significant spin exchange line broadening was observed in the ESR solution spectrum.

ENDOR measurements, obtained at the optimum temperature of 20 K, with the ER200D Bruker spectrometer, were taken at the maximum and minimum of the outer $A_{//}$(N) ESR features, and

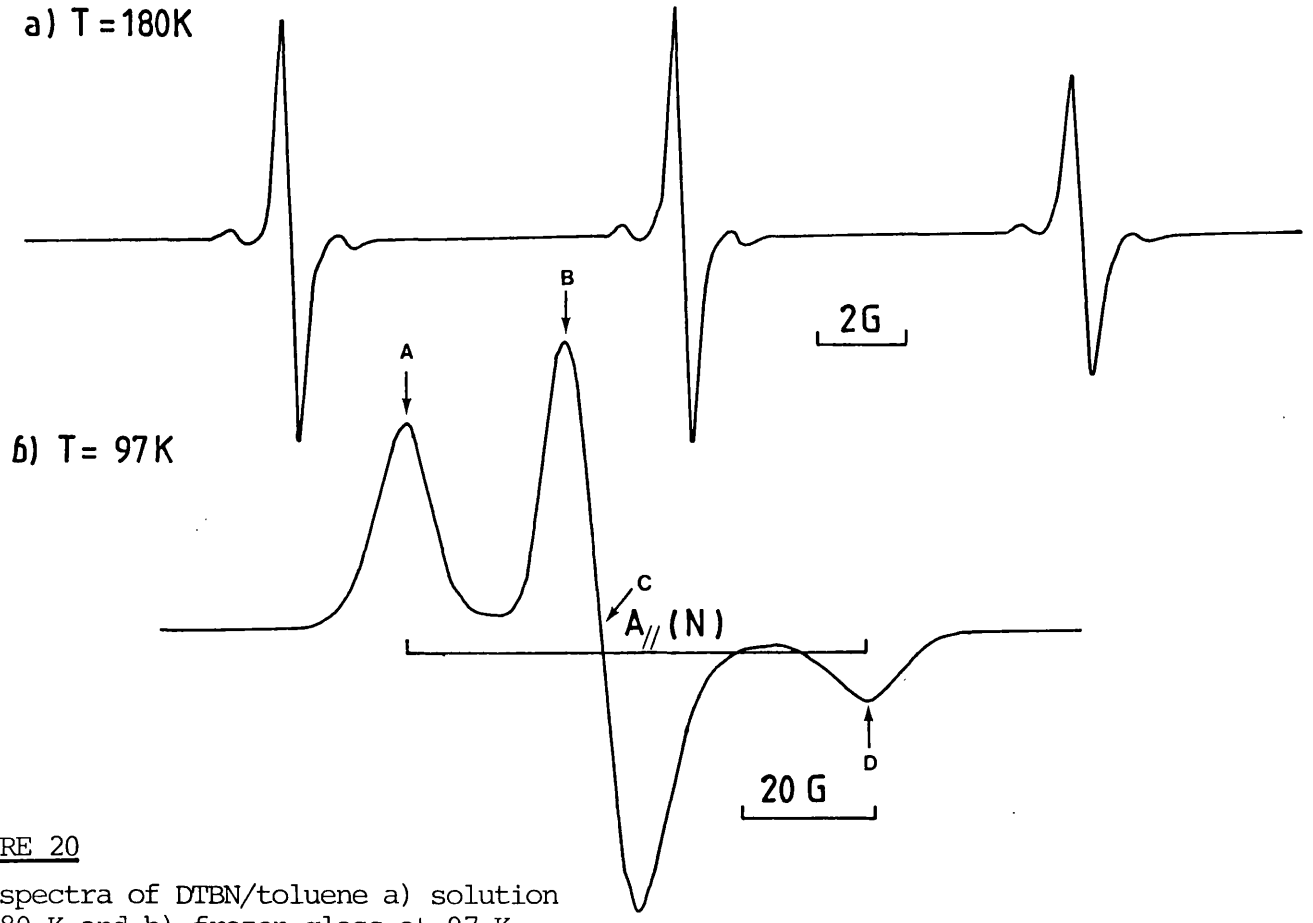

FIGURE 20

ESR spectra of DTBN/toluene a) solution at 180 K and b) frozen glass at 97 K.

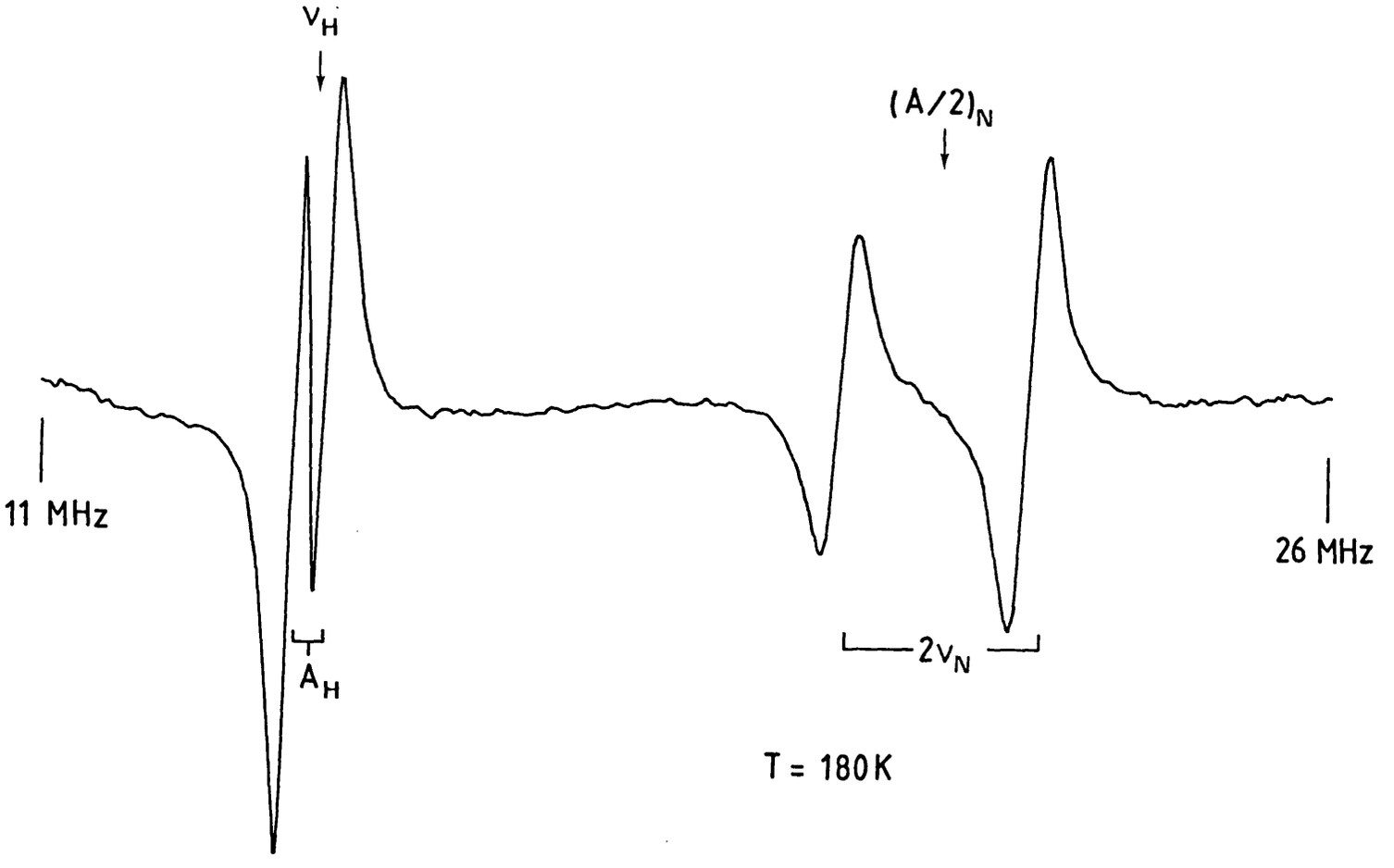

FIGURE 21

ENDOR spectrum of a DTBN/toluene solution at 180°K, showing N and methyl proton splittings.

at the crossover point and maximum of the $A_{\perp}(N)$ feature, points A, D, B and C respectively in Figure 20b. The spectra so obtained were very similar but not identical, indicating that they were single-crystal-like and two-dimensional powder spectra.

Those spectra obtained with H_o at point A are shown in Figure 22. The measured hyperfine splittings taken at points A(=D), B and C are given in Table IV. Two large hyperfine splittings of 5.76 and 7.2 MHz were resolved; the remaining smaller splittings were superimposed on a large proton matrix line and were identical at all three field positions. The smaller splittings could be divided into two groups. Those less than 2 MHz have been attributed to purely dipolar couplings with near matrix protons. This was based on an ENDOR study of DTBN in a trifluoromethylsulfonic acid glass (CF_3SO_3H). As discussed below, in this glass three hyperfine splittings were observed which correspond closely to the 2.61, 3.36 and 3.98 MHz splittings measured in toluene (Table IV). The smaller splittings were absent. Thus, those splittings of less than 2 MHz observed in the DTBN/ toluene glass have been assigned to toluene matrix protons. Because the splittings close to 2.61, 3.36 and 4.55 MHz were observed in both matrices, it is assumed that these arise from the DTBN radical. Also, the splittings of 5.76 and 7.20 MHz observed in the toluene glass have been assigned to DTBN splittings, as they are too large to arise from matrix protons. All of the splittings of less than 2 MHz probably arise from purely dipolar coupling to near matrix protons. The alternative is that some of them are shoulders on the matrix line, as discussed in Chapter 5. However, it seems unlikely that the motional relaxation processes

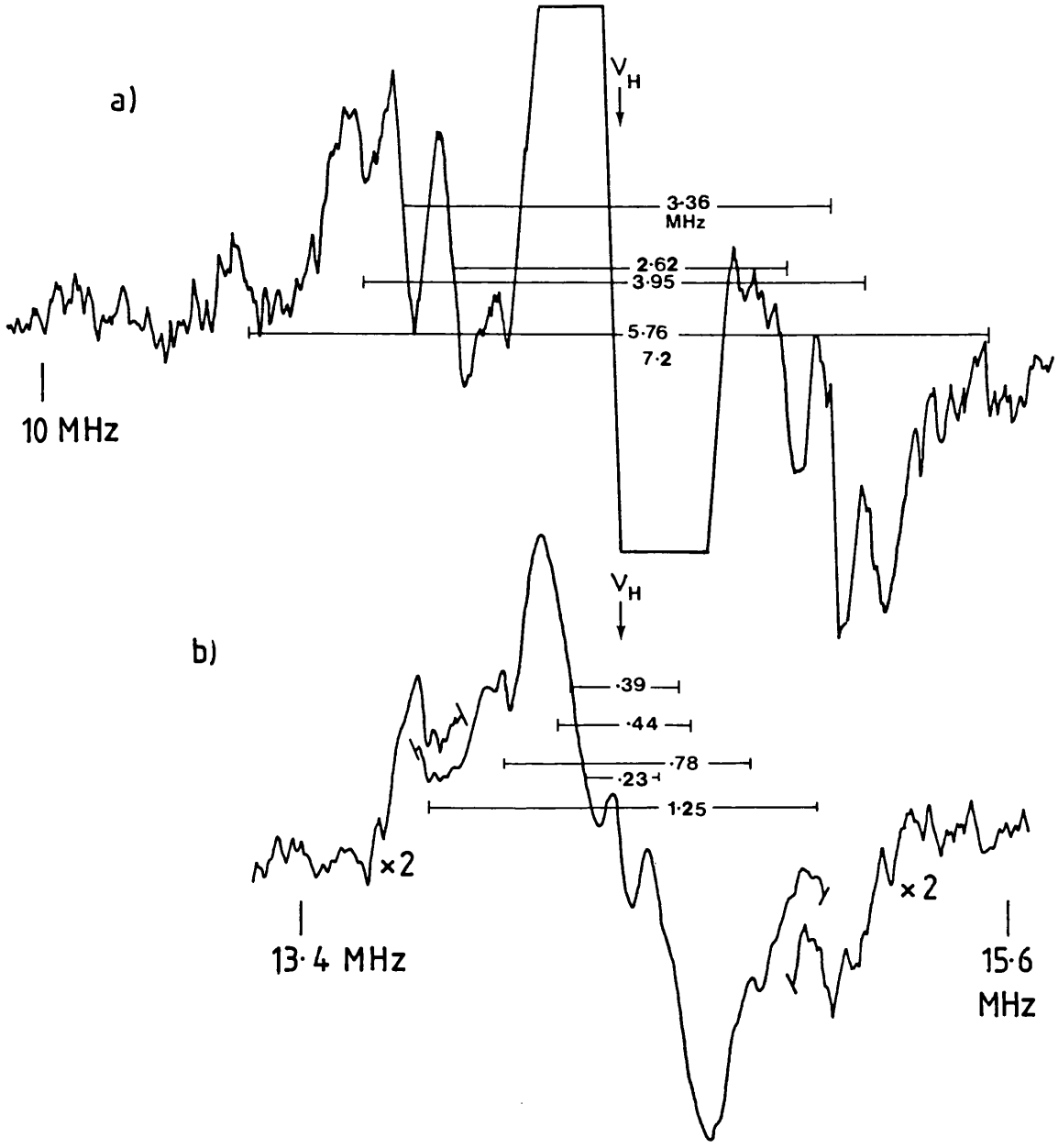

FIGURE 22

ENDOR spectrum of DTBN/toluene frozen glass at 20 K, taken with H_o at position A in Figure 20b, showing a) couplings to methyl protons, b) dipolar couplings to matrix protons superimposed on matrix line.

Table IV - Hyperfine Splittings Measured in DTBN/toluene and DTBN /CF_3SO_3H Solutions and Glasses

	DTBN/toluene	DTBN/CF_3SO_3H
$A_{\parallel}(N)$	35 G	47.5 G
$A_{\perp}(N)$	<5 G	8.8 G
$A_{iso}(N)$	15.4 G	21.7 G
$A_{iso}(CH_3)$	-.84G	<1.3 G
$A_{iso}(H)$	——	3.3 G

Hyperfine Splittings from ENDOR studies of Frozen Glasses of DTBN/toluene and DTBN/CF_3SO_3H measured at positions in Figures 20b and 23c.

	DTBN/toluene			DTBN/CF_3SO_3H	
	A(MHz)			A(MHz)	
Position:	A	B	C	A	B
$A_{dipolar}$- toluene matrix protons	.23	.22	.2		
	.39	.34	.3		
	.44	.43	.4		
	.78	.77	.78		
	1.25	1.08	1.25		
	2.61	2.58	2.60	2.3	
	3.36	3.34	3.35	3.5	3.5
	3.95	3.80	3.90	4.6	4.6
	5.76		5.74		
	7.20		7.20		

at 20 K would be sufficient to give rise to such shoulders.

The 5.76 and 7.2 MHz splittings were observed in ENDOR spectra taken at positions A and C, but not at postion B. It is expected that ENDOR resonances from complexes with their nitrogen hyperfine z-principal axis parallel to the field direction, that is with H_o perpendicular to the plane containing the nitroxide radical, would be strongest at points A and C. Those resonances from complexes with their z-axis $\perp$ to H_o would be strongest at B. Thus, the 5.76 and 7.2 MHz splittings are assigned to protons in complexes with $A_{\parallel}(N)$ parallel to H_o. Since the proton and nitrogen hyperfine tensors are not likely to have coincident principal axes, these are probably not $A_{\parallel}(H)$ splittings. If they are "almost" $A_{\parallel}(H)$ splittings, then $A_{\perp}(H)$ splittings would be expected at 3.2 and 2.4 MHz assuming that $A_{\parallel}(H)$ is negative. These could be buried with the 2.61-3.95 MHz splittings. If they are "almost" $A_{\perp}(H)$ splittings, then the much larger $A_{\parallel}(H)$ splittings, which should be observed with H_o at position B, were too weak to be detected. The 2.61, 3.36 and 3.95 MHz splittings, which were observed at positions A, B, C and D, could be due to three fairly isotropic proton interactions, or could result from a larger number of anisotropic splittings which superimpose to give a less well-resolved isotropic spectrum.

Neither parallel nor perpendicular nitrogen splittings could be detected.

Generally the same results were observed in DTBN/CF_3SO_3H glasses. In the ESR solution spectrum, an isotropic proton splitting of 3.3 gauss (~9.2 MHz), resulting from the protonation of the nitroxide radical, was observed on each of the

three nitrogen hyperfine lines (Figure 23a). At intermediate temperatures, 135 K$<$T$<$200 K, a good glass was formed and a parallel proton splitting of ~6 gauss was resolved (Figure 23b). The perpendicular proton splitting was unresolved, and thus less than 2.5 gauss. With a further reduction in temperature, T$<$135 K, the glass remained clear but the ESR lines broadened until $A_{\parallel}(H)$ was no longer resolved (Figure 23c), presumably due to the onset of a phase transition or phase separation. The ENDOR spectra obtained at 95 K are shown in Figure 24. Very similar spectra were observed with H_o at point A and point B in Figure 23c. These consisted of two structureless matrix lines from F and H nuclei and three "isotropic" splittings of 2.3, 3.5 and 4.6 MHz, similar to those observed in the toluene glass. No parallel hyperfine splittings from the acid protons were observed. The perpendicular interaction could correspond to the 2.3 MHz splitting if $A_{\perp}$ and $A_{//}$ are both positive or both negative. No nitrogen hyperfine splittings were detected. It was hoped that narrower ENDOR lines might be obtained at higher temperatures, where the ESR spectra were better resolved, but no ENDOR resonances could be detected above 120 K.

Thus, the same trends in sensitivity loss were observed in a glassy matrix as in powders, with a greater overall loss in sensitivity.

Spectral simulation programs, as described above would allow one to extract more data from ENDOR studies of disordered systems.

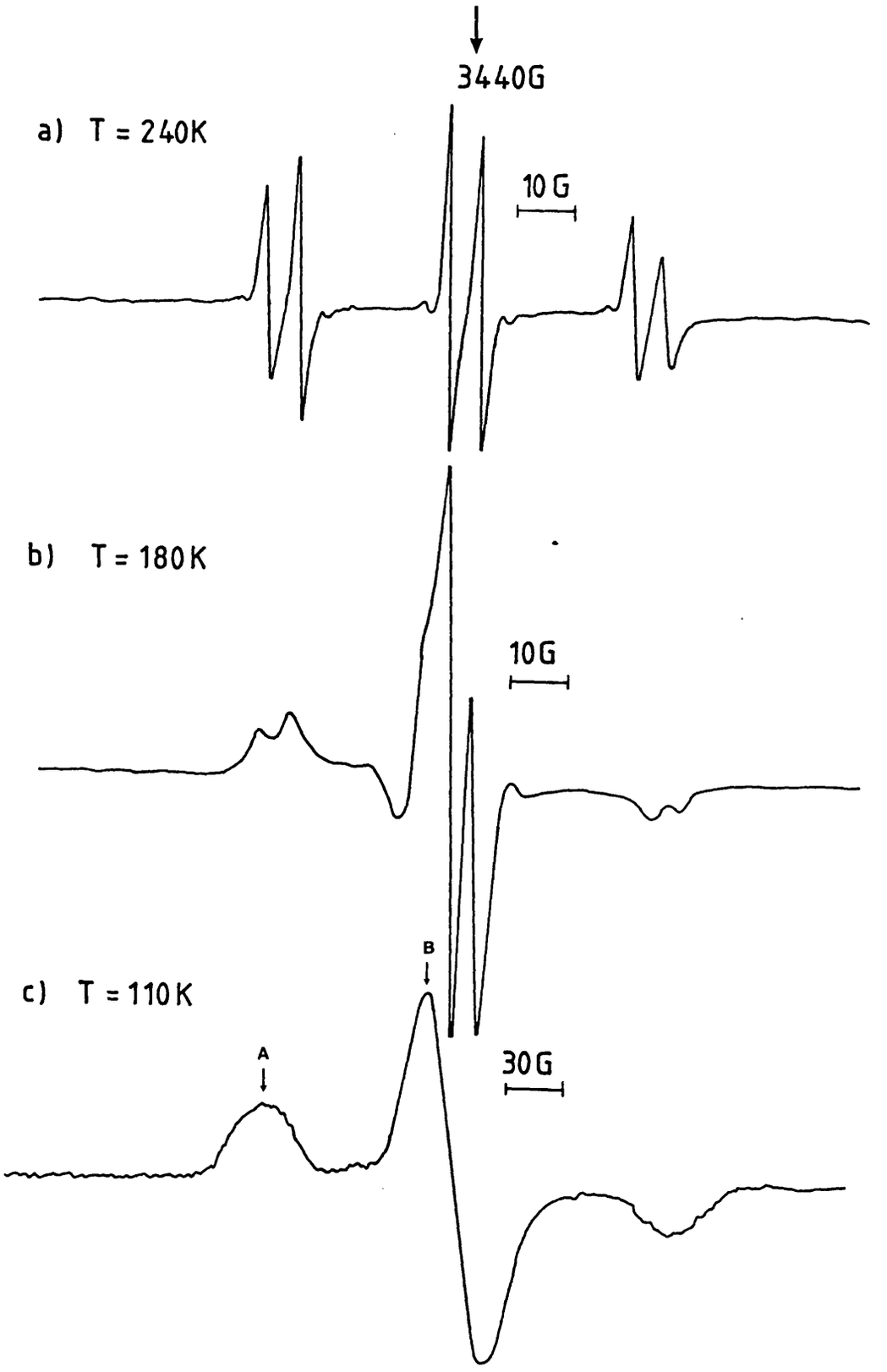

FIGURE 23

ESR spectra of a DTBN/CF_3SO_3H acid a) solution at 240 K and of frozen glasses at b) 180 K, and c) 110 K.

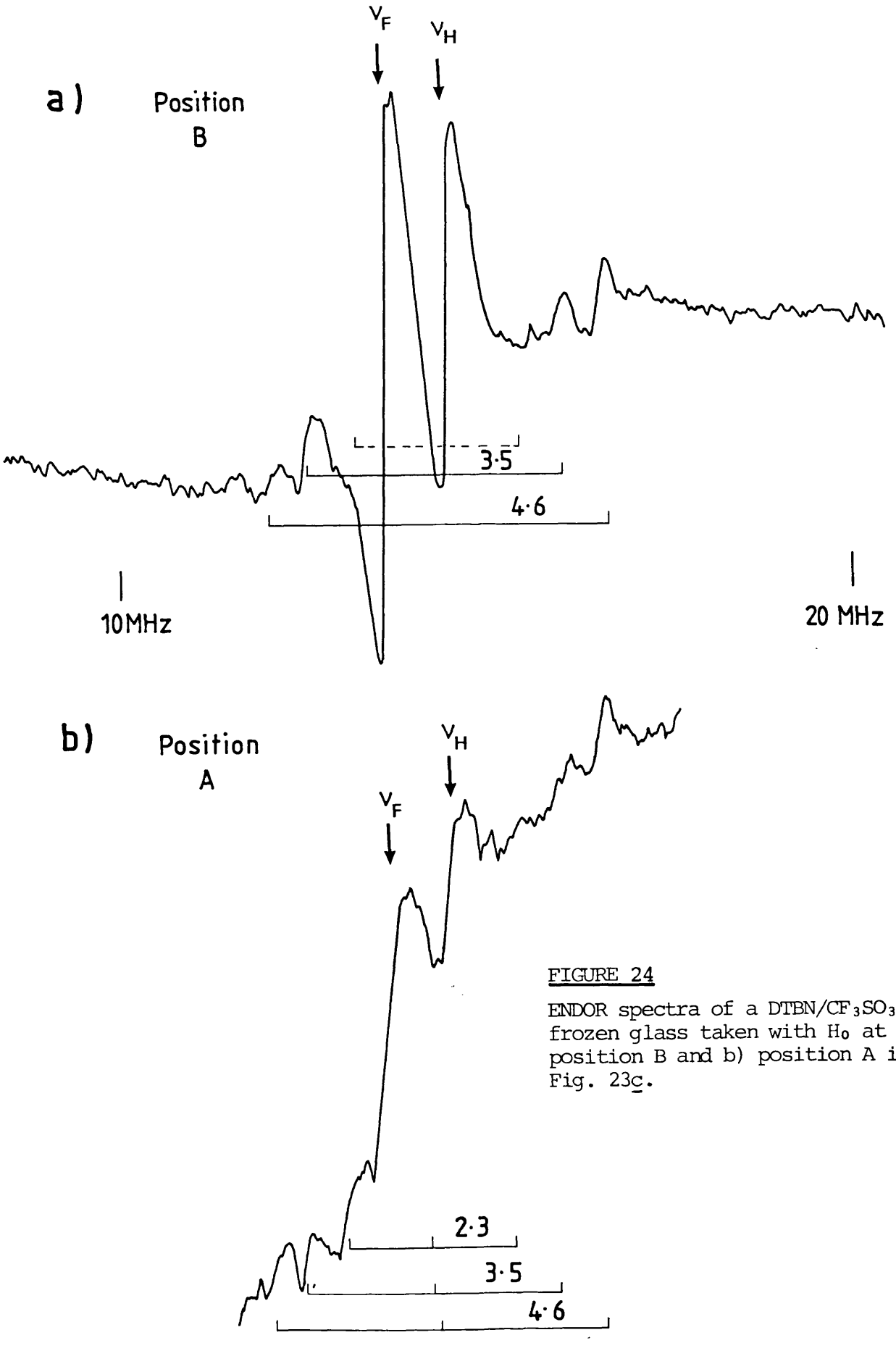

FIGURE 24

ENDOR spectra of a DTBN/CF_3SO_3H frozen glass taken with H_o at a) position B and b) position A in Fig. 23c.

6.3.2 Liquids

Some aspects of liquid ENDOR are discussed here for the sake of completeness. A good overview of this subject can be obtained from references 28 and 29.

Generally, liquid ENDOR spectra, once obtained, are less complex than the corresponding ESR spectra (see Figure 5.1) and interpretation is straightforward, using the equations and methods discussed in Chapter 5. However, finding the optimum experimental conditions can be more difficult than for most solid state ENDOR studies. The experimental considerations unique to liquid ENDOR studies can be deduced from eqn. 1. In liquids, the solvent viscosity, and spin concentration, as well as temperature must be fully optimized so that the spin exchange time fulfills the condition $T_E \gg (T_1\ T_2)^{\frac{1}{2}}$. In addition, solvents must be dry and thoroughly degassed. Very narrow operating temperature ranges sometimes occur, since nuclear and electron relaxation rates generally reach a minimum at different temperatures as T is reduced.

Nuclei in a molecule with differing relaxation times, will undergo optimum ENDOR conditions at different temperatures, and microwave and rf power levels.

Spin relaxation times in liquids can be of the order 10^{-5} to 10^{-6}s, so that fields of up to 100 gauss, or up to ~1000 W of rf power can be required.

Thus, an empirical approach to the optimization of solvent, temperature, radical concentration, H_1 and H_2 can lead to a rather low success rate in obtaining ENDOR spectra. A rigorous approach to this problem has been taken by Möbius[29] using the density matrix method developed by Freed.[7] ENDOR

amplitudes are computer optimized as a function of H_1, H_2, temperature, spin concentration and modulation conditions. Line distortion and coherence effects are correctly predicted. Input parameters included the number, spin, nuclear frequencies and isotropic coupling constants of nuclei, and parameters which determine the relaxation processes such as viscosity, temperature, tumbling volume and the r_{ne}, the electron nuclear distance.

i) A Solution ENDOR Study Of DTBN

Some aspects of liquid ENDOR are illustrated by the ENDOR study of some DTBN solutions described below. The original intent of this study was to determine the sign of the isotropic methyl proton hyperfine coupling in acidic media using TRIPLE resonance spectroscopy. In toluene, $A_{iso}(CH_3)$ is 0.3 MHz, as measured by ENDOR (Figure 21). As the spin density on nitrogen, and thus $A_{iso}(N)$ is increased through a range of solvents, ESR lines become narrower as $A_{iso}(CH_3)$ decreases. In very acidic media, with large spin density on nitrogen, the ESR linewidths begin to increase again. If the linear decrease of $A_{iso}(CH_3)$ with increasing $A_{iso}(N)$ is to be maintained, then $A_{iso}(CH_3)$ would have to change sign. Thus, attempts were made to determine the sign of $A_{iso}(CH_3)$ in trifluoromethylsulfonic acid (CF_3SO_3H).

CF_3SO_3H has a high dielectric constant, so capillary tubes were used for ENDOR measurements. DTBN is fairly unstable in acidic media. Thus, solutions of DTBN in CF_3SO_3H were prepared by immersing a glass thread in DTBN and touching this to a frozen solution of CF_3SO_3H in a capillary tube. This was then placed in an X-band ESR tube, evacuated and very

slowly thawed. If any decompostion of the DTBN occurred, the solution coloured a blue-green, and was discarded. After thawing, the solution was freeze-thaw degassed. Solutions of DTBN in CF_3SO_3H/phosphoric acid mixtures and in concentrated sulfuric acid were prepared in an attempt to obtain more viscous solutions for ENDOR measurements. However, DTBN decomposed in phosphoric acid solutions and was not stable enough in sulfuric acid to give ESR signals intense enough for ENDOR measurements.

The ESR solution spectrum of DTBN/CF_3SO_3H is shown in Figure 23 and the ENDOR spectrum in Figure 25. The latter was quite weak because of the lowering of the cavity Q by the high dielectric solvent, the small sample size and the low stability of DTBN in CF_3SO_3H. The ENDOR signal intensity was optimum at the lowest possible solution temperature, and at the highest available microwave power (200 mW) and rf power (100 W). Thus, the unsuccessful attempts to decrease relaxation rates by increasing solvent viscosity were made. Isotropic methyl proton splittings were not resolved and were taken to be less than 0.4 MHz. ENDOR signal intensities were insufficient for TRIPLE resonance measurements. As mentioned in section 6.3.1v, the information obtained from frozen glasses of CF_3SO_3H was not complete enough to allow the determination of the sign of $A_{iso}(CH_3)$ based on $A_{\parallel}(CH_3)$ and $A_{\perp}(CH_3)$ values.

ENDOR measurements of DTBN/toluene solutions were more successful. The ENDOR spectrum is shown in Figure 21. This was also optimum at the lowest liquid temperature and highest available rf power. A microwave power of 100 mW was used.

General TRIPLE ENDOR measurements were carried out in order to determine the relative signs of $A_{iso}(N)$ and $A_{iso}(CH_3)$.

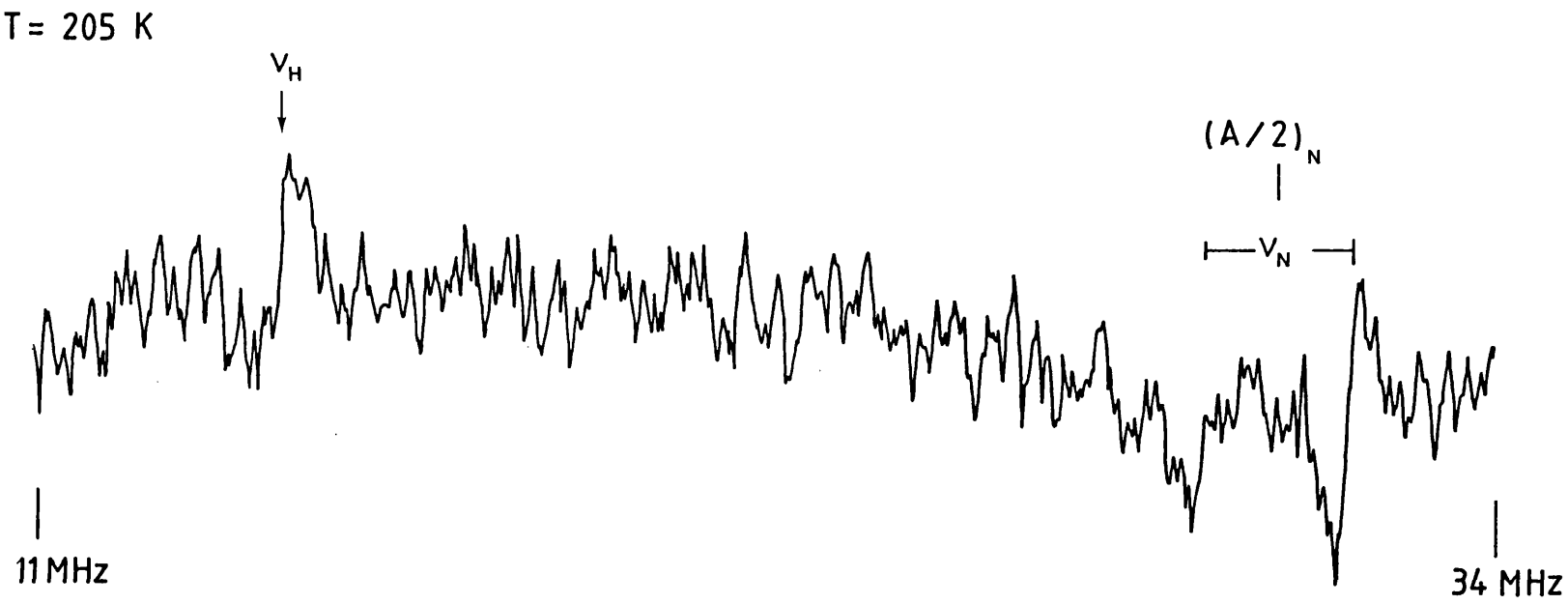

FIGURE 25

ENDOR spectrum of a DTBN/CF_3SO_3H solution at 205 K.

If the high frequency N ENDOR line was pumped, the low frequency N line and the high frequency proton line both increased in intensity. As explained in Chapter 5, with an energy level diagram appropriate to this system (Figure 5.18), these changes imply that $A_{iso}(N)$ and $A_{iso}(CH_3)$ have opposite signs (Figure 5.19). Since $A_{iso}(N)$ must be positive, this implies that $A_{iso}(CH_3)$ is negative.

Finally, $A_{iso}(N)$ was large enough for the measured coupling to require the second order correction given in eqn. 5.26. However, second order effects were not large enough to give a second order splitting when the $m_I = 0$ N ESR transition was saturated. More precise ENDOR measurements of $A_{iso}(N)$ of nitroxides have shown that the nitrogen transition frequencies were not adequately explained by a Breit-Rabi correction. A dynamic frequency shift, proportional to the mean square fluctuation of the resonance frequency had also to be taken into account.[28]

Further liquid ENDOR studies would require more powerful rf amplifiers and would benefit from the rigorous optimization of parameters using the software described above.

References

1. J.S. Hyde in Magnetic Resonance in Biological Systems, eds. A. Ehrenberg, B.G. Malmstrom, T. Vanngard (Pergamon Press, Oxford, 1967).

2. J.S. Hyde, Rev. Sci. Instr. 41, 1598 (1970).

3. D.S. Leniart in Multiple Electron Resonance Spectroscopy, eds. M.M. Dorio and J.H. Freed (Plenum Press, New York, 1979).

4. A.B. Wolbarst, Solid St. Comm. 18, 1193 (1976).

5. Ch. Hoentzsch, J.R. Niklas and J.M. Spaeth, Rev. Sci. Instrum. 49, 1100 (1978).

6. H. Seidel, Z. Physik 165, 239 (1961).

7. J.H. Freed in reference 3.

8. A.M. Portis, Phys. Rev. 91, 1071 (1953).

9. N. Bloemberger, R.V. Pound and E.M. Purcell, Phys. Rev. 71, 466 (1947).

10. L. Kevan and L.D. Kispert, Electron Spin Double Resonance Spectroscopy (John Wiley & Sons, New York, 1976).

11. R. Allendoerfer and A.H. Maki, J. Magn. Res 3, 396 (1970).

12. L.R. Dalton and A.L. Kwiram, J. Chem. Phys. 57, 1132 (1972).

13. ER Series Users Manual, 1st ed., Bruker Analytishe Messtechnik GMBH, EPR Division (1983).

14. C.P. Poole, Jr., Electron Spin Resonance: A Comprehensive Treatise on Experimental Techniques (John Wiley & Sons, New York, 1983).

15. V. Macho, R. Kendrick and C.S. Yannoni, J. Mag. Res. 52, 450 (1983).

16. G. Hurst, K. Kraft, R. Schultz and R. Kreilick, J. Mag. Res. 49, 159 (1982).

17. R. Biehl, EPR Applications Note 79-2, Bruker Analytishe Messtechnik GMBH, EPR Division (1979).

18. A. Schweiger, M. Rudin and J. Forrer, Chem. Phys. Letters 80, 376 (1982).

19. A. Savitzky and M.J.E. Golay, Anal. Chem. 36, 1627 (1964); M.U.A. Bromba and H. Ziegler, Anal. Chem. 53, 1583 (1981).

20. P.A. Jansson, R.H. Hunt and E.K. Plyler, J. Opt. Soc. Am. 60, 597 (1970).

21. M.C.R. Symons, Chemical and Biochemical Aspects of Electron-Spin Resonance Spectroscopy (Van Nostrand Reinhold Company, New York, 1978).

22. P.C. Taylor, J.F. Baugher and H.M. Kriz, Chem. Rev. 75, 203 (1975).

23. G.H. Rist and J.S. Hyde, J. Chem. Phys. 52, 4633 (1970).

24. R.J. Cook, J. Sci. Instr. 43, 548 (1966).

25. W.H. Zachariasen, J.A.C.S. 62, 1011 (1940).

26. D.W. Ovenall and D.H. Whiffen, Mol. Phys. 4, 135 (1951).

27. J.M. Park, Ph.D Thesis, Univ. of British Columbia, Canada (1977).

28. N.M. Atherton in reference 3.

29. K. Möbius, M. Plato, W. Lubitz, Phys. Rev. 87, 171 (1982).

CHAPTER SEVEN

ESR AND ENDOR STUDIES OF RHODIUM-DOPED SILVER CHLORIDE

CHAPTER SEVEN

ESR and ENDOR Studies of Rhodium-Doped AgCl

7.1 Introduction

Trivalent transition metal ions can be incorporated into silver halide melt-grown single crystals by addition to the melt, or into powders and emulsions by co-precipitation from aqueous solution. The majority of such addenda occupy substitutional positions on the cation sub-lattice and act as deep electron traps.[1-7] They can have a significant effect on the photographic degradation of the silver halide lattice and are used to control the sensitometric properties of photographic materials. In commercial products, transition metal ion addenda convert the silver halide system from the negative-working format ordinarily used for black and white and color print films to the positive-working system used for transparencies. In graphic arts products, dopants are used to increase contrast and reduce high intensity reprocity failure.

The photographic effect of a transition metal ion is determined by its trapping cross-section and by the lifetime of the trapped species, as well as by the trapping parameters of the photoproduct. These in turn are a function of the attractive potential of the impurity ion and of the mechanism of relaxation of the impurity ion and surrounding lattice following a trapping event. The attractive potential of trapping states can be considered to be made up of two components.[8] For distances $r > r_c$ from the ion, the potential is Coulombic and can be treated by the effective mass approximation described in Chapter 2. For $r < r_c$, the potential is a core potential which depends on the electronic structure as well as on the charge of the impurity ion. For shallow traps, such as the divalent cations discussed in Chapter 4, the trapped electron has a Bohr radius greater than r_c, so that the trapping behaviours of these impurities are determined entirely by the Coulombic potential. Likewise, the ESR spectrum can be predicted by the effective mass approxima-

tion and is principally a function of the properties of the host lattice. For deep traps, many properties of interest, such as optical and phonon properties, are determined mainly by the Coulombic potential.[9] To first order, many aspects of the trapping behaviour of deep traps are also determined by the Coulombic potential. However, the myriad of trapping behaviours exhibited by trivalent metal ion addenda indicates that the core potential and the lattice structure in the core region must be considered in any detailed explanation of trapping mechanisms. Since the orbital radii of the impurity valence electrons are less than r_c, where r_c is of the order of the nearest neighbour distance, the ESR spectrum of deep impurites is determined by the core potential and by the immediate environment of the impurity ion. Thus, ESR spectroscopy has been widely used to study the electronic wavefunctions in the core regions of deep traps.[1-7]

In the silver halides, aliovalent impurity cations are generally associated with charge-compensating silver ion vacancies. It has been found experimentally that the trapping behaviour of impurity-defect complexes is very sensitive to the number and arrangement of vacancies, and to the relaxation mechanism of the impurity-defect moiety once trapping occurs.[1-7] While ESR spectroscopy has proved a valuable tool in studying such structures in the silver halides, the resonances observed are always broadened by hyperfine interaction with the many surrounding magnetic nuclei. Hyperfine data is usually only resolved for either axial or equatorial first shell halide ions, so that the structure of the impurity-vacancy complex must be inferred from the symmetry of the g-tensor. The study of these complexes should benefit from the greater resolution provided by ENDOR spectroscopy

Only one ENDOR study of metal ion-vacancy complexes in the silver halides has been reported.[10] In this study, of the interstitial Fe^{3+} ion in silver chloride single crystals, only the hyperfine data from four equivalent Cl^- ions in the first ion shell could be analyzed. In the work described

below, it was possible, with the aid of digitally controlled ENDOR instrumentation and data handling facilities, to analyze the hyperfine data from all chlorines in the first ion shell, as well as the small couplings from more distant shells. Rh^{3+}-doped AgCl single crystals were chosen as a model system for these initial exploratory ENDOR studies since it had been reported that a strong Rh^{2+} ESR signal, from a single type of $(RhCl_6)^{4-}$ defect site, with an apparently simple structure, could be produced by methods other than photolysis.[5, 11, 12]

Earlier studies have shown that the rhodium dopant is incorporated into silver halide crystals grown in a nonoxidizing environment as the d^7 ion, Rh^{2+}.[5, 11] Crystals grown under halogen contain the diamagnetic ion, Rh^{3+}.[5] In both AgBr[5] and AgCl[13], the trivalent rhodium acts as a deep electron trap. The Rh^{2+} species produced by photolysis has an infinitely long lifetime at room temperature. The same species can also be produced by annealing Rh^{3+}-doped crystals in air or vacuo above 300°C.[5, 11] This procedure injects electrons,[7] which can then be trapped at Rh^{3+} sites.

Because of its properties as a long-lived electron trap, rhodium (III) is used as a dopant in some photographic products to increase contrast. The contrast increase is a result of the exponential relation between the developed optical density of the silver halide film (D) and the level of exposure (E). If x Rh^{3+} traps are added to a film that ordinarily requires n photoelectrons to attain maximum density, the number of electrons required by the doped system increases to (n + x). This shifts and compresses the s-shaped D-log E curve along the abscissa, so that the slope of the exposure-dependent region of the curve increases.[14] The slope of the D-log E sensitometric curve is a measure of the contrast response of the film. Of course, the shift of the D-log E curve also represents a loss in the sensitivity of the film.

In the initial ESR studies of rhodium-doped silver halides, some confusion arose as to the valence state of the paramagnetic rhodium species.

This stemmed from uncertainty as to the valence state of rhodium as incorporated in the melt (Rh^{1+} or Rh^{3+} in oxidizing environments, and Rh^{o} or Rh^{2+} in non-oxidizing environments) and from the difficulty of distinguishing d^7 and d^9 ions by ESR. The observation of a rhodium-associated ESR signal was first reported by Wilkens, et. al.,[15] in Rh/AgCl single crystals grown in vacuo. At temperatures less than 110 K, an axially symmetric spectrum was observed, with $g_{//} < g_{\perp}$, and hyperfine splittings from two equivalent chloride ions. Between 160 and 300 K, this reversibly converted to a spectrum with $g_{\perp} < g_{//}$, showing no hyperfine interactions. Finally, at temperatures above 200 K, a broad, single, isotropic line began to appear at the isotropic g-value of the two low temperature species. These signals were assigned to the d^9 Rh^{o} ion, in a d_{z2} ground state undergoing a static Jahn-Teller contraction below 110 K, in a d_{x2-y2} ground state undergoing a static Jahn-Teller elongation between 160 and 300 K, and finally undergoing a dynamic Jahn-Teller distortion at high temperatures. No explanation for the change in ground state was put forward. This assignment was called into question when a similar species in Rh^{3+}-doped AgBr was assigned to Rh^{2+}, in an elongated d_{z2} ground state at low temperatures, and in a contracted d_{x2-y2} ground state at higher temperatures, on the basis of ESR, optical absorption and microwave photoconductivity measurements.[5] A later study of Rh/AgCl crystals grown in vacuo, γ-irradiated Rh^{3+}doped aqueous grown NaCl single crystals and γ-irradiated $Na_3RhCl_6 \cdot 6H_2O$ powders provided further evidence that the paramagnetic species observed in Rh/AgCl were Rh^{2+} complexes.[11]

No direct evidence for vacancy compensation could be obtained from the Rh^{2+} ESR spectrum. If it was assumed that compensation did occur, the axial symmetry of the ESR spectrum indicated that the compensating silver ion vacancy was located along the distortion axis.[5] It was hoped that in the present ENDOR study more direct information about the nature of vacancy compensation could be obtained.

In addition to single crystal studies, exploratory ENDOR studies of rhodium-doped powders were carried out. Such preliminary studies are required before ENDOR investigations can be extended to any practical photographic systems.

7.2 Experimental

Rhodium-doped single crystals were grown from ultrapure AgCl, prepared as described in Chapter 4, and from the dopant salt $Na_3RhCl_6 \cdot 6H_2O$ (Atomergic Chemetals, Plainview, N.Y.). Crystals were grown under chlorine by the Bridgeman method, aligned by the standard x-ray back reflection technique, and cut into cubes with either a (100) or (110) axis parallel to the cube faces. Crystals with nominal dopant levels of 50, 200, and 1000 mppm were studied. The crystals ranged in color from light orange to dark red. Crystals from the latter boule are referred to below as heavily-doped, and from the 50 and 200 mppm boules, as lightly doped. The paramagnetic rhodium-associated species were produced by annealing the crystals at 300°C in air. In this way, a stronger ESR signal was produced than could be obtained by photolysis. In situ photolysis with the ENDOR cavity had to be accomplished by using the crystal mounting rod as a light pipe, and was not very efficient.

Rh^{3+}-doped NaCl crystals were grown from saturated aqueous solution saturated with ultrapure NaCl (Puratronic, Ventron, Karlsruhe) and doped with the salt $Na_3RhCl_6 \cdot 6H_2O$. Dopant levels of 1000 mppm were used. The resulting crystals were pink and cubic with the dimensions 4x4x1 mm. The large faces were (100) planes. Paramagnetic rhodium centers were produced by γ-irradiation (as in Chapter 3) at room temperature for a period of twelve hours. The crystals were subsequently annealed for several hours at 100°C to destroy the V_k center ESR signal.[11] ENDOR studies of rhodium-doped NaCl crystals were used as an aid to the interpretation of ENDOR data from rhodium-doped AgCl crystals.

X-band ESR measurements were carried out on a standard Century series Varian E-109 spectrometer using an Oxford Instruments helium cryostat for measurements made below 77 K. Q-band measurements were made with a Varian E-12 spectrometer with a Q-band bridge.

ENDOR measurements were obtained using the University of Paderborn ENDOR spectrometer and the commercial Bruker ENDOR spectrometer which were described in detail in Chapter 6. The absorption ENDOR spectra shown in the figures in this chapter were measured on the former instrument at ~30 K, using .8 KHz pulsed AM modulation, 20 mW of microwave power, and an rf field of .5 - 2 G at the sample. The derivative spectra shown here were measured with the commercial Bruker instrument at ~30 K, using 12.5 KHz FM modulation with a 25 - 50 KHz modulation depth, 40 mW of microwave power and a ~5 G rf field at the sample. No line broadening was observed as a result of FM modulation of the rf carrier as long as the modulation depth was less than 50 KHz. The sensitivities of the two instruments were comparable; however, the sensitivity of the Paderborn spectrometer was effectively increased by the use of digital filtering and deconvolution programs and of automated peak searching and plotting facilities. Thus, most of the ENDOR angular rotational studies and all of those shown here were carried out on the Paderborn spectrometer. The programs used for data fitting and analysis are described in Chapter 6. All of the absorption ENDOR spectra shown below have been digitally filtered and deconvoluted.

7.3 Results

7.3.1 ESR Measurements

Intense ESR spectra were obtained from both lightly-doped and heavily-doped Rh^{3+}/AgCl single crystals, which had been heat-treated as described above. Signals from a primary and a secondary species were observed. The primary species was essentially the same as that reported previously,[11, 15] giving rise to a different ESR spectrum in each of the three temperature ranges

4 - 85 K, 85 K - RT, and > RT. The predominant form of the primary species in each of these temperature ranges is referred to below as the low temperature species, the high temperature species, and the isotropic species, respectively. These signals could be reversibly interconverted by varying the temperature. ESR signals from the secondary species were more pronounced in lightly-doped crystals and are marked with an asterisk in Figures 1 - 4.

The ESR spectrum of the low temperature species, measured with H_o // (100), is shown in Figure 1a. Angular rotation studies in the (100) and (110) planes indicated that the symmetry of the low temperature species departed slightly from axial (Figures 5 and 6). The principal axes of the g-tensor were parallel to the cubic axes, indicative of a symmetry which could only result from a substitutional site. The orthorhombic nature of the site was confirmed by angular rotation measurements made at Q-band frequencies. The parallel region of the spectrum, at g = 2.013 ± .002, was composed of a septet of lines in the intensity ration of 1:2:3:4:3:2:1. The ENDOR studies described below confirmed that the septet resulted from a hyperfine interaction with two equivalent chlorines along the z-axis; thus, A_z was parallel to g_z. The perpendicular region of the spectrum was the superposition of the g_x component, made up of a poorly resolved septet, and the g_y component, made up of a much weaker multiplet. Again, ENDOR measurements confirmed that the septet arose from a hyperfine interaction with the two chlorines perpendicular to the (100) plane containing H_o, along the z-axis. The ESR spectrum of the low temperature species, measured with H_o // (110), is shown in Figure 1b. The $\frac{1}{2}(g_x^2 + g_z^2)$ and $\frac{1}{2}(g_y^2 + g_z^2)$ features overlapped to give an eight line spectrum at this orientation while a septet was observed at $\frac{1}{2}(g_x^2 + g_y^2)$ from those complexes oriented such that H_o was along a (110) axis perpendicular to the z-axis. The x and y g-values obtained by fitting the angular rotation data were 2.432 ± .002 and 2.397 ± .002.

The spectrum shown in Figure 1a could be measured up to approximately

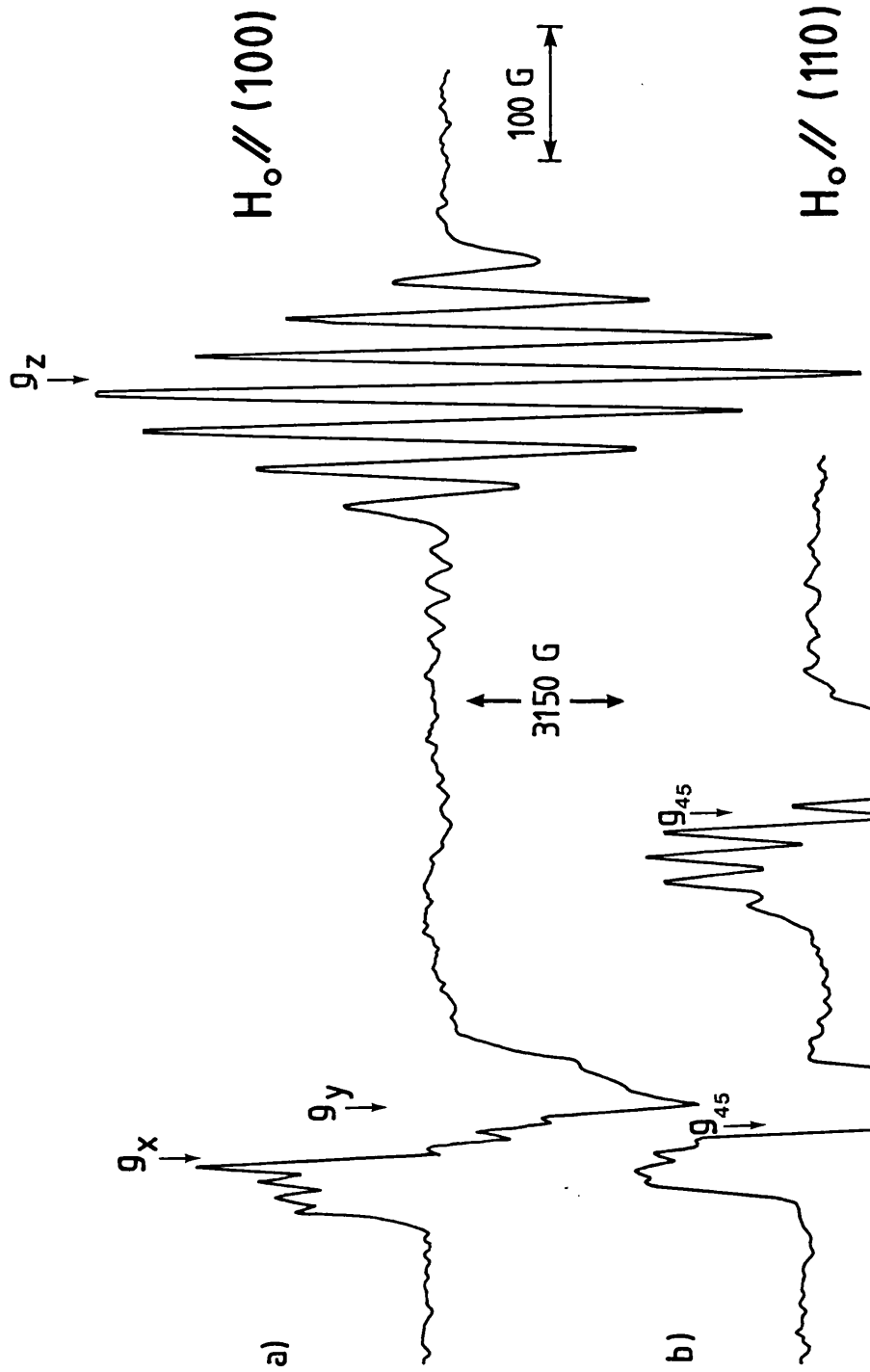

FIGURE 1

ESR spectrum of the $(RhCl_6)^{4-}$ complex in a heavily-doped AgCl single crystal with a) H_0 // (100) and b) H_0 // (110). T = 20 K.

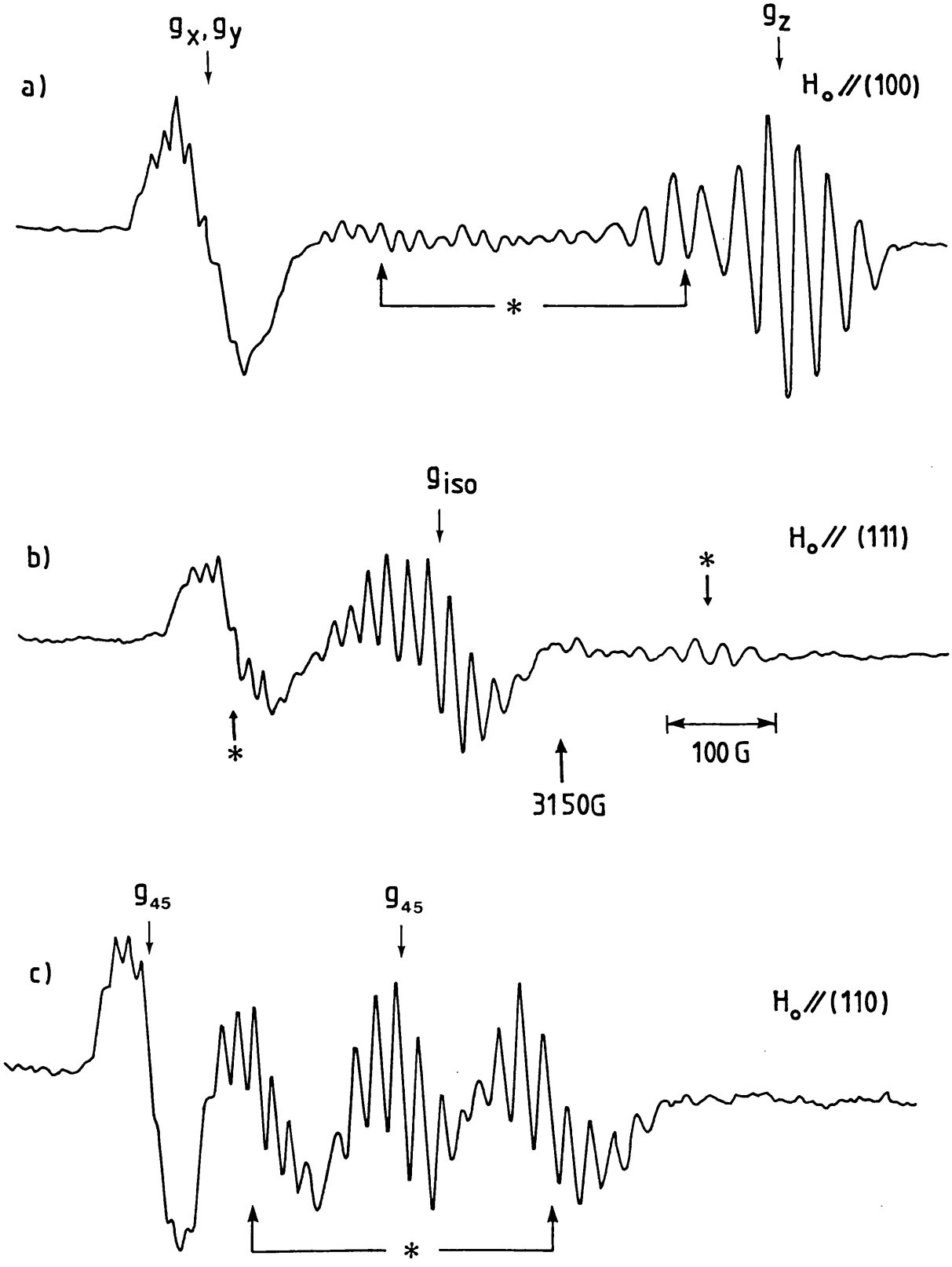

FIGURE 2

ESR spectrum of the $(RhCl_6)^{4-}$ complex in a lightly-doped AgCl single crystal with a) H_o // (100), b) H_o // (111) and c) H_o // (110). The * marks the secondary paramagnetic species. T = 20 K.

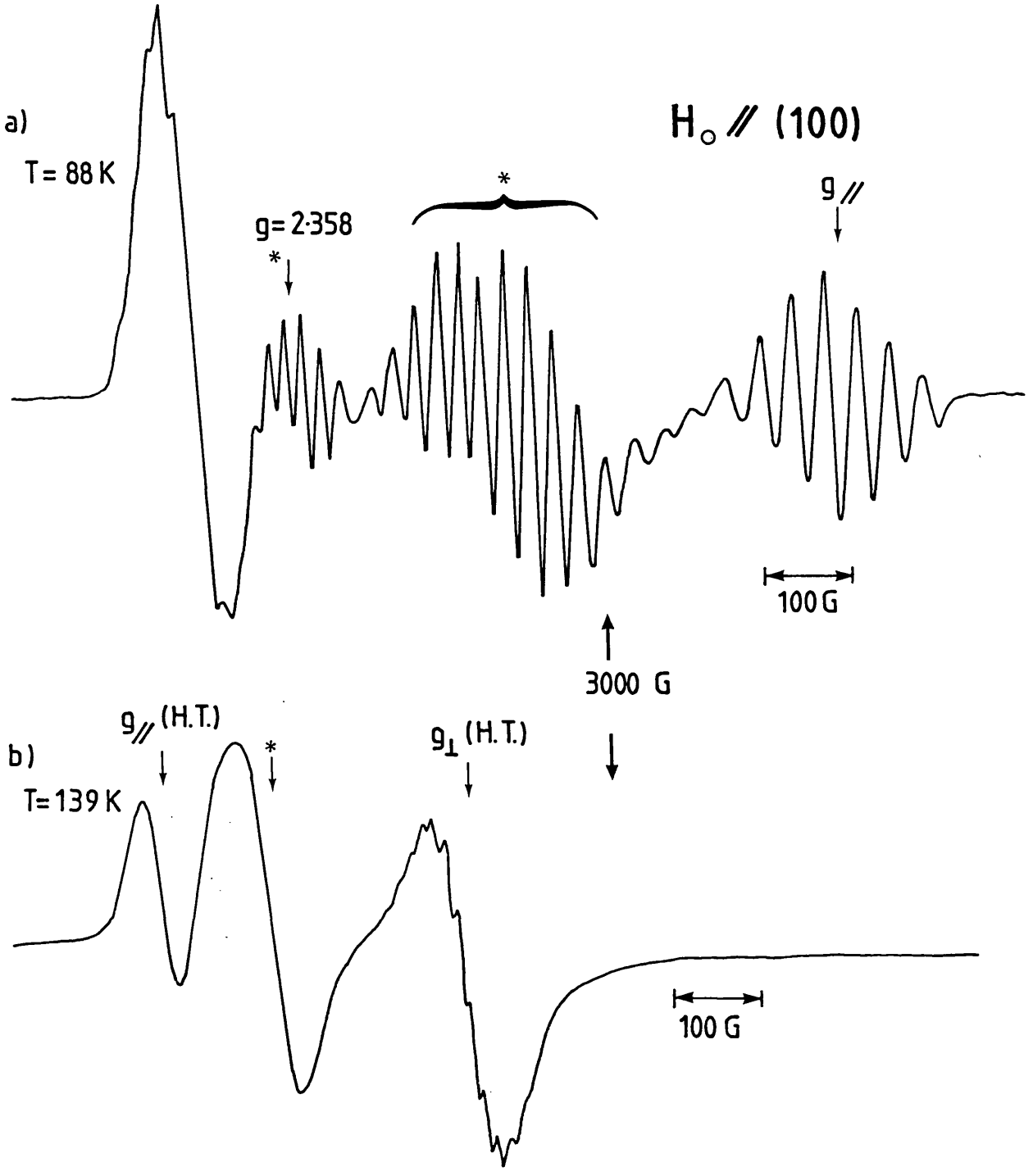

FIGURE 3

ESR spectrum of the $(RhCl_6)^{4-}$ complex in a lightly-doped AgCl single crystal with H_o // (100) showing the growth of the high temperature species. The * marks the secondary paramagnetic species.

FIGURE 4

ESR spectrum of $(RhCl_6)^{4-}$ in a heavily-doped AgCl single crystal with H_o // (100), showing a) the high temperature $(RhCl_6)^{4-}$ signal and b,c) the growth of the isotropic signal (g = 2.289) with increasing temperature.

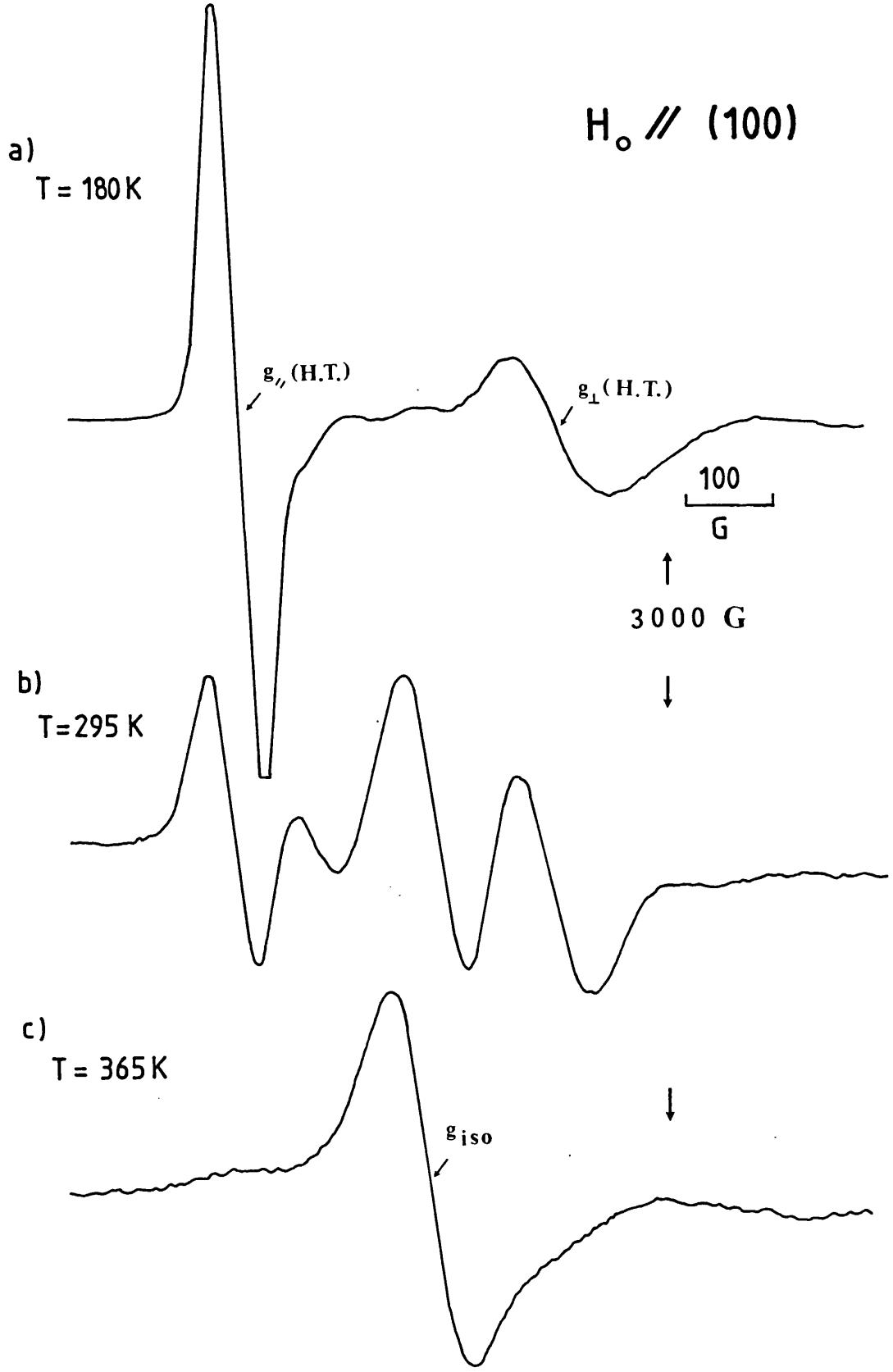

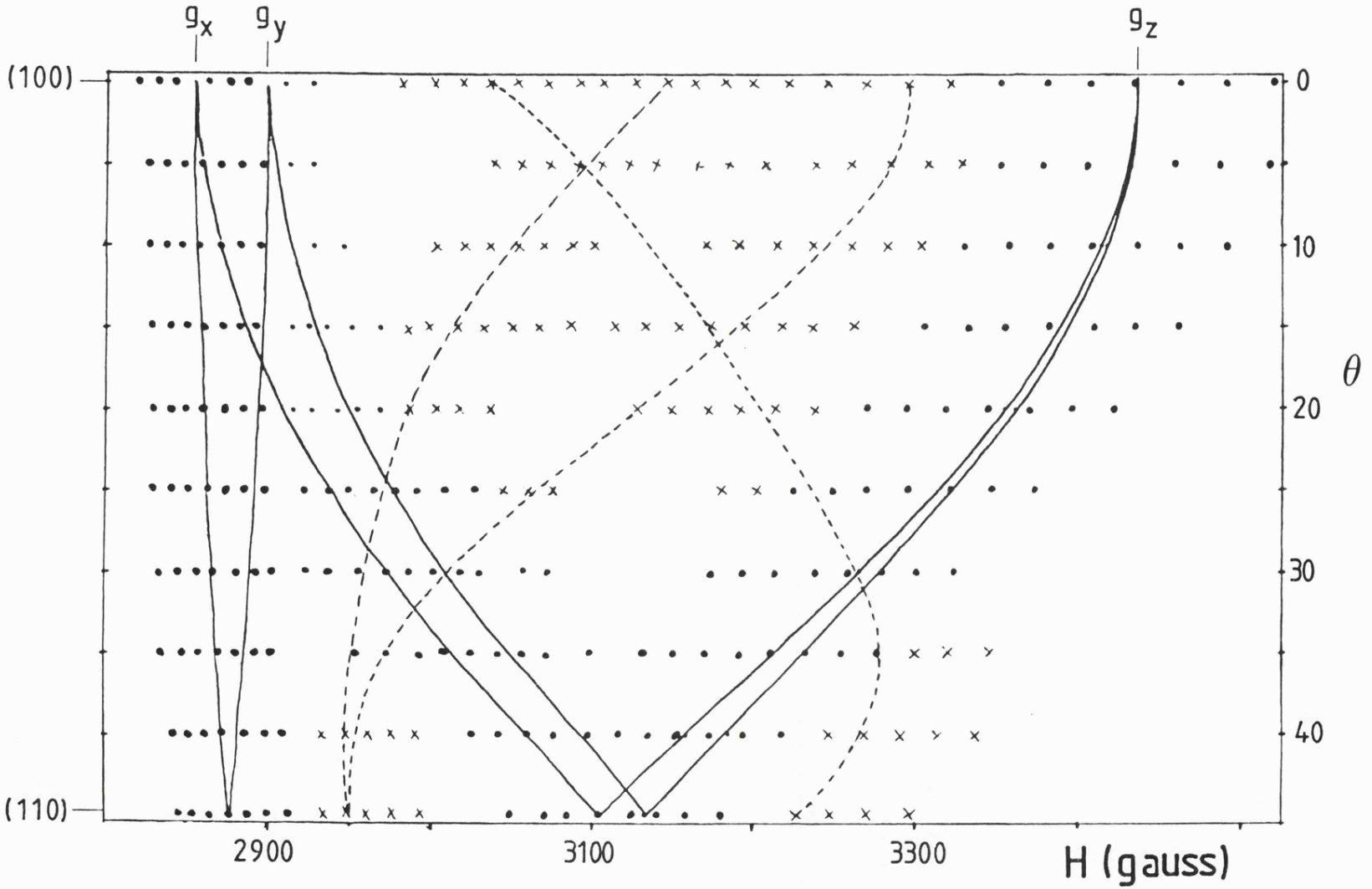

FIGURE 5

Isofrequency plot in the (100) plane of the $(RhCl_6)^{4-}$ ESR signals (——) and secondary signals (---) in a heavily-doped AgCl crystal. The solid lines are the calculated field positions. T = 20 K.

FIGURE 6

Isofrequency plot in the (110) plane of the $(RhCl_6)^{4-}$ ESR signals and secondary ESR signals at 77 K. The lines marked P and g_x, g_y, g_z are the calculated curves for $(RhCl_6)^{4-}$.

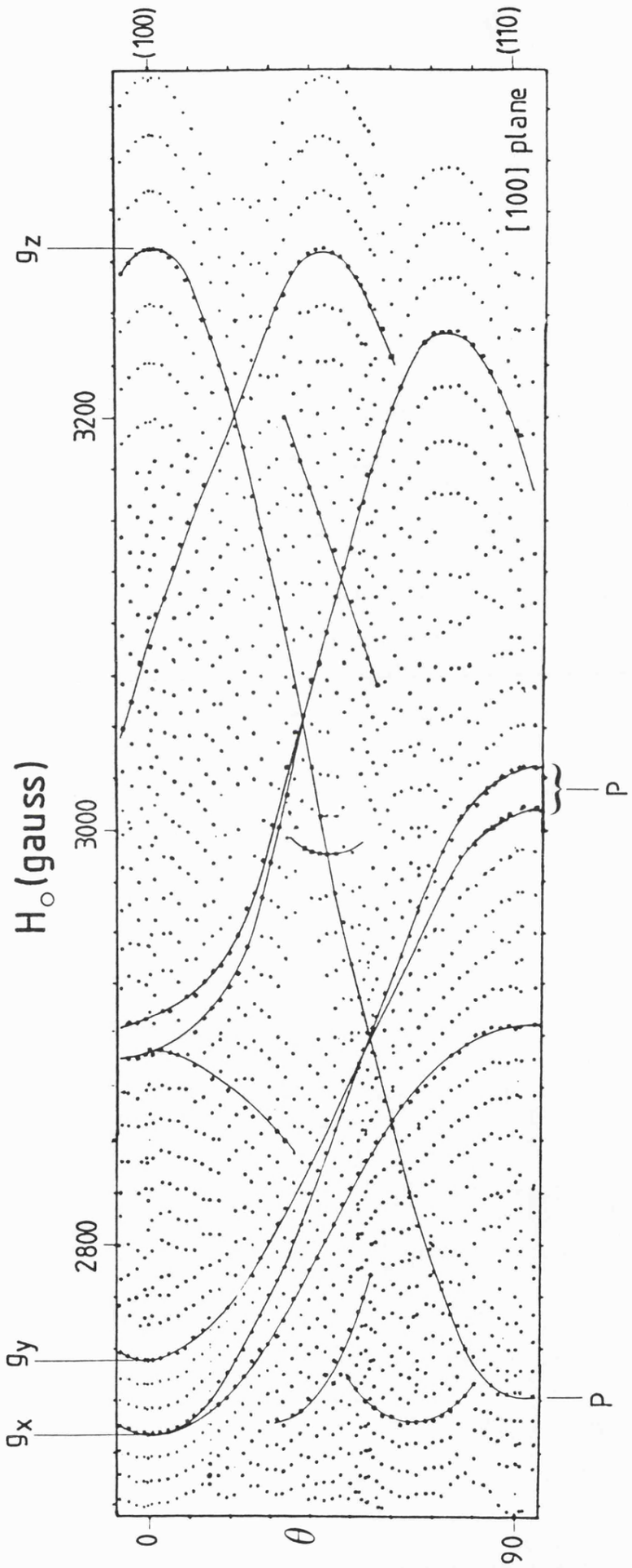

80 K. Between 80 and 90 K, the parallel region of the spectrum became progressively weaker relative to the perpendicular region (Figure 3a). By ~110 K, the hyperfine splittings of the parallel feature were poorly resolved, being superimposed on a broad background signal. At the same temperature that the parallel feature disappeared (~125 K), a signal grew in at g = 2.216. In lightly-doped crystals, this feature rapidly increased in intensity until, at that temperature at which the parallel feature disappeared, it was 1 - 2 times the intensity of the g_x feature. At this point, the g = 2.216 feature was composed of a 14 line multiplet with a splitting of ~10 G. In heavily-doped crystals, the g = 2.216 feature was very weak at that temperature at which the parallel feature disappeared, exhibited no hyperfine structure, and approached the intensity of the g_x feature at a temperature ~80 K higher than in lightly-doped crystals. Considering now the temperature dependence of the perpendicular components of the low temperature species, these broadened and hyperfine resolution was lost, as the temperature was raised above 80 K. As the temperature was raised further, the linewidths of the g_x and g_y components began to narrow until, at 110 K, the envelopes of the two g-values could be clearly distinguished. The g_y component disappeared at the same temperature as the parallel feature, leaving a spectrum composed of a symmetric g_x feature and the g = 2.216 line (apart from lines associated with the secondary species). This spectrum was that of the high temperature species and is shown in Figures 3b, 4a and 4b. Rotation studies showed that the g_x feature rotated as a parallel component and that the g = 2.216 feature behaved as a perpendicular component. The principal g tensor components were parallel to the cubic axes.

At approximately 210 K, an isotropic ESR signal appeared at g = 2.289. As the temperature was raised, this line grew in intensity, while the parallel and perpendicular features of the high temperature species broadened and moved in towards the isotropic line. By 300 K, the isotropic signal was

the dominant signal. At 365 K, the highest temperature attainable with the ESR cavity used, the isotropic species was the only resolved line present, with a very small amount of spectral anisotropy apparent in the wings (Figure 4c).

The g-values of the low temperature species, the high temperature species, and the isotropic species are listed in Table I. The following points, apparent from this tabulation, are noteworthy: i) $g_{\perp}$ of the high temperature species was the same, within experimental error, as the averaged g-values of the y and z components of the low temperature species, ii) $g_{//}$ of the high temperature species was identical to g_x of the low temperature form. These points suggest that the low temperature form of the primary species was converted to the high temperature form via motional processes which averaged spin interactions in the yz plane. Such averaging would make the x direction a parallel axis and the yz plane a pseudo-perpendicular plane of the axially symmetric high temperature species. The nature of the spectral changes which accompanied the conversion between the low temperature and high temperature forms confirmed that an averaging interaction occurred in the yz plane of the primary complex as the temperature was raised.[15] Of the spectral features which were averaged, those spread over the smallest field range averaged at the lowest temperatures. Thus, with H_o // (110), spectral averaging was apparent at lower temperatures than with H_o // (100). The origin of the averaging processes became clear upon completion of the ENDOR study of the primary species, and is discussed further below.

It is also apparent from Table I, that the g-value of the isotropic species was the same as the isotropic g-value of both the low temperature and high temperature species. Once again, the spectral changes which accompanied the conversion of the high temperature species to the isotropic species were indicative of a motional process, which in this case averaged the spin interactions along the x, y and z directions of the primary species.

TABLE I

G-Values of the Low Temperature, High Temperature and Isotropic Forms of the Primary Rh^{2+} Species in AgCl

Type of Distortion	g-tensor components[a]		
	x	y	z
static elongation (low temperature form)	2.432	2.397	2.013
Dynamic two-dimensional (high temperature form)	2.216	2.216	2.432
Dynamic three-dimensional (isotropic form)	2.289	2.289	2.289

[a] ±.002

TABLE II

Natural Abundances, Nuclear Spins and Nuclear Frequencies for Selected Isotopes

Isotope	Natural Abundance	Spin	ν_N in 3500 G Field
^{23}Na	100	3/2	3.9416
^{35}Cl	75.53	3/2	1.4601
^{37}Cl	24.47	3/2	1.2152
^{103}Rh	100	1/2	.4690
^{107}Ag	51.82	1/2	.6030
^{109}Ag	48.18	1/2	.6932

Resonances from a secondary species were observed in all crystals cut from the three Rh/AgCl boules studies, as well as in heat-treated, powdered crystals. These signals, which are just visible in the ESR spectrum of the heavily-doped crystal in Figure 1a, are more clearly shown in Figure 2, where they are marked with asterisks. The secondary signals were relatively more intense in lightly-doped crystals, with intensities ~30% of those of the primary species in crystals containing 50 mppm rhodium. The observation of secondary signals in powders ruled out the possibility that they arose from misaligned primary species in twinned crystals. The secondary species were not observed in pure AgCl crystals; thus, they were associated in some way with rhodium doping. The signals were not the result of impurities introduced with the rhodium dopant salt, since their intensities, relative to those of the primary signals, were inversely proportional to the rhodium dopant concentration. For the same reason, they probably did not result from rhodium ion aggregates. Therefore, the secondary species could arise in one of three ways: i) the center is a rhodium-defect complex with a configuration favored by the intrinsic defect equilibrium existing at low aliovalent dopant levels, ii) the center is a rhodium-impurity complex, with a concentration limited by the impurity content of the undoped crystal, or iii) the center results from hole-trapping, either by rhodium or by impurities, and is only stable if a deep, long-lived electron trap is present to prevent recombination at the hole trap. The latter possibility does not seem likely since it is generally assumed that the annealing treatment used to produce the Rh^{2+} centers only injects electrons.[5, 7]

The overlap of the ESR signals from the primary and secondary species made analysis of the secondary signals difficult. The latter appeared to be composed of septets of lines, with maximum and minimum turning points in the (100) and (110) planes occurring at less extreme field values than for the primary species. Partial rotation plots are shown in Figures 5 and 6. The

unlabelled dashed and solid lines in these figures are not theoretical curves, but are meant to show the general angular dependences of the secondary signals. These rotations indicated that the center had principal axes which were nearly parallel to the (111), (1$\bar{1}$0) and ($\bar{1}\bar{1}$2) directions. The seven line hyperfine pattern, exhibited clearly at turning points, suggests interactions with two equivalent chlorine nuclei. Such an interaction is most likely to occur for a substitutional site. If the secondary species is a rhodium center, one would expect it to prefer the octahedral coordination provided by a substitutional position.[16]

As the temperature was raised, resolution of hyperfine splittings on the secondary signals was lost, at somewhat higher temperatures than for the primary species (Figure 3b). Overlap with the primary species signals made analysis of the temperature behaviour difficult. The further evaluation of the nature of the secondary species is left for future studies.

In summary, ESR measurements identified a substitutional, orthorhombic primary species in AgCl crystals which was produced by rhodium doping and subsequent heat treatment. Hyperfine interactions, most likely from two chlorines along the z-axis of the complex, were observed. Motional processes which averaged spin interactions in the yz plane of the complex occurred as the temperature was raised. At room temperature and above, motional processes averaged interactions along all three principal directions. A secondary species, also introduced by rhodium doping, was observed. This had principal axes approximately along (111), (1$\bar{1}$0) and ($\bar{1}\bar{1}$2). It appeared to be a substitutional center and exhibited hyperfine interactions most likely arising from two equivalent chlorine nuclei.

7.3.2 ENDOR Measurements

All ENDOR measurements were carried out on the heavily-doped AgCl crystal at approximately 30 K, and thus, only the low temperature form of

the primary species was examined. Angular rotations were carried out in the (100) plane. These were performed by locating the saturating microwave field on a component of the ESR signal and moving the field to follow this line as the crystal was rotated. ENDOR measurements were then taken every two degrees over a fifty degree interval. The ENDOR spectra obtained were greatly simplified by the fact that the g_x and g_y features of the primary species were well separated from g_z. Thus, data could be obtained independently from those complexes oriented with their z-axes parallel and perpendicular to the magnetic field. As a result, the angular plots obtained were of three types: those measure while saturating the parallel component of the ESR spectrum as the crystal was rotated to make it a perpendicular component, those measured while saturating the perpendicular region and following the component which moved towards the parallel region as the crystal was rotated, and those measured while saturating the nearly isotropic component of the perpendicular region as the crystal was rotated. The first two types of plots gave information about those primary species oriented with either their x or y axes perpendicular to the plane of rotation, while the third type pertained to those complexes oriented with their z-axes perpendicular to the plane of rotation. Because of the overlap of the x and y components of the ESR signal, ENDOR data could not be obtained separately from each component. The various plots are referred to below as those measured in the plane containing z, from H_o // z towards H_o $\perp$ z (// $\rightarrow \perp$); those measured in the plane containing z, from H_o $\perp$ z towards H_o // z ($\perp \rightarrow$ //); and those measured in the plane perpendicular to z ($x \Leftrightarrow y$).

The ENDOR spectra described below arose from hyperfine interactions with a central Rh^{2+} nucleus, with first shell axial and equatorial chlorines, and with second and fourth shell silvers. For convenience, the nuclear spins and nuclear free frequencies of the isotopes relevant to this study are listed in Table II. The conventional numbering scheme used to refer to the ion shells

is shown below:

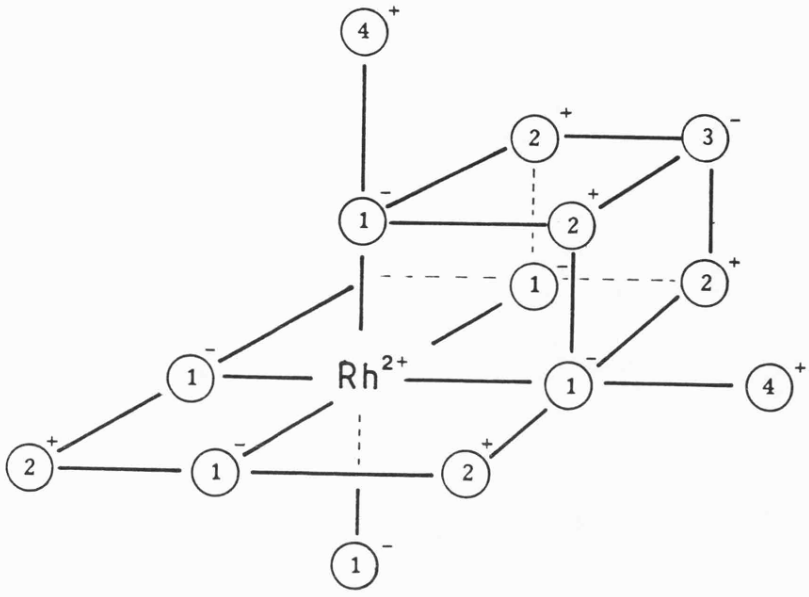

The following scheme was used for numbering the first shell chloride ions:

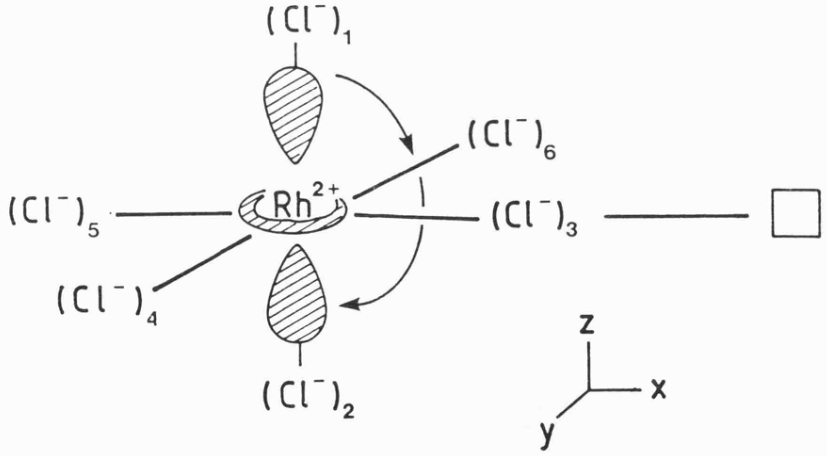

Thus, the axial chlorine ions will be referred to as $(Cl^-)_{1,2}$.

ENDOR spectra, measured with H_o // z and in the frequency range where the large hyperfine splittings observed in the ESR spectrum might be expected to occur, are shown in Figures 7 and 9a. When the m_I = 0 ESR line was saturated, eleven ENDOR lines were observed with relative positions and intensities

consistent with their assignment to ^{37}Cl and ^{35}Cl hyperfine lines, split by a quadrupole interaction. The ENDOR transitions have been labelled accordingly in Figures 7 and 9a. The assumption has been made that the signs of the chlorine hyperfine tensor components are positive.[11] The EI-EPR and ENDOR-vs.-field position experiments, described in Chapter 5 (Figures 5.20 and 5.7-5.9 respectively) each established that the quadrupole splittings had a sign opposite to that of the hyperfine splittings. At this orientation, the ^{37}Cl, $m_s = -\frac{1}{2}$, $m_q = +1$ and the ^{35}Cl, $m_s = +\frac{1}{2}$, $m_q = +1$ lines overlapped, reducing the number of lines observed from the expected twelve to eleven.

The angular rotation plot for these large hyperfine interactions, measured in the (100) planes containing z, from $H_o \parallel z$ towards $H_o \perp z$, is shown in Figure 7. The $m_q = -1$ lines are missing from the first 25^o of the plot because, for these measurements, the field was not centered on the $m_I = 0$ ESR line. It is evident from the ENDOR spectra and from the angular rotation plot that the ^{35}Cl ENDOR lines were split into multiplets with $H_o \parallel z$ and that the number of splittings increased as the crystal was rotated off axis. The splittings observed with $H_o \parallel z$ are shown clearly in the expanded spectrum in Figure 8. The splittings at this orientation disappeared on all but the $m_q = 0$ ENDOR lines if the $m_I = 0$ ESR line was saturated (Figure 9a). Such behaviour, as well as the fact that only the ^{35}Cl ENDOR transitions were split, is characteristic of second order effects due to indirect spin-spin coupling of two equivalent nuclei. The isotopic pairs ^{35}Cl-^{35}Cl, ^{35}Cl-^{37}Cl, and ^{37}Cl-^{37}Cl occur in the population ratios of 9:3:1. Thus, the strongest ^{35}Cl ENDOR signals are from equivalent isotope pairs, which will exhibit a second order splitting, while the strongest ^{37}Cl ENDOR signals are from inequivalent isotope pairs where second order effects are negligible. As discussed in Chapter 5 (eqn 5.30), the largest second order splitting, of $3W_2$, is expected to occur on the $m_q = 0$ ^{35}Cl ENDOR line. This was qualitatively observed, as shown in Figure 9a. The small central feature of the $m_q = 0$

FIGURE 7

ENDOR spectrum, measured with H_o // z, of $(Cl^-)_{1,2}$ in $(RhCl_6)^{4-}$ and corresponding angular rotation plot, measured in the plane containing z, from H_o // z towards H_o ⊥ z. Line marked * is expanded in Fig. 8.

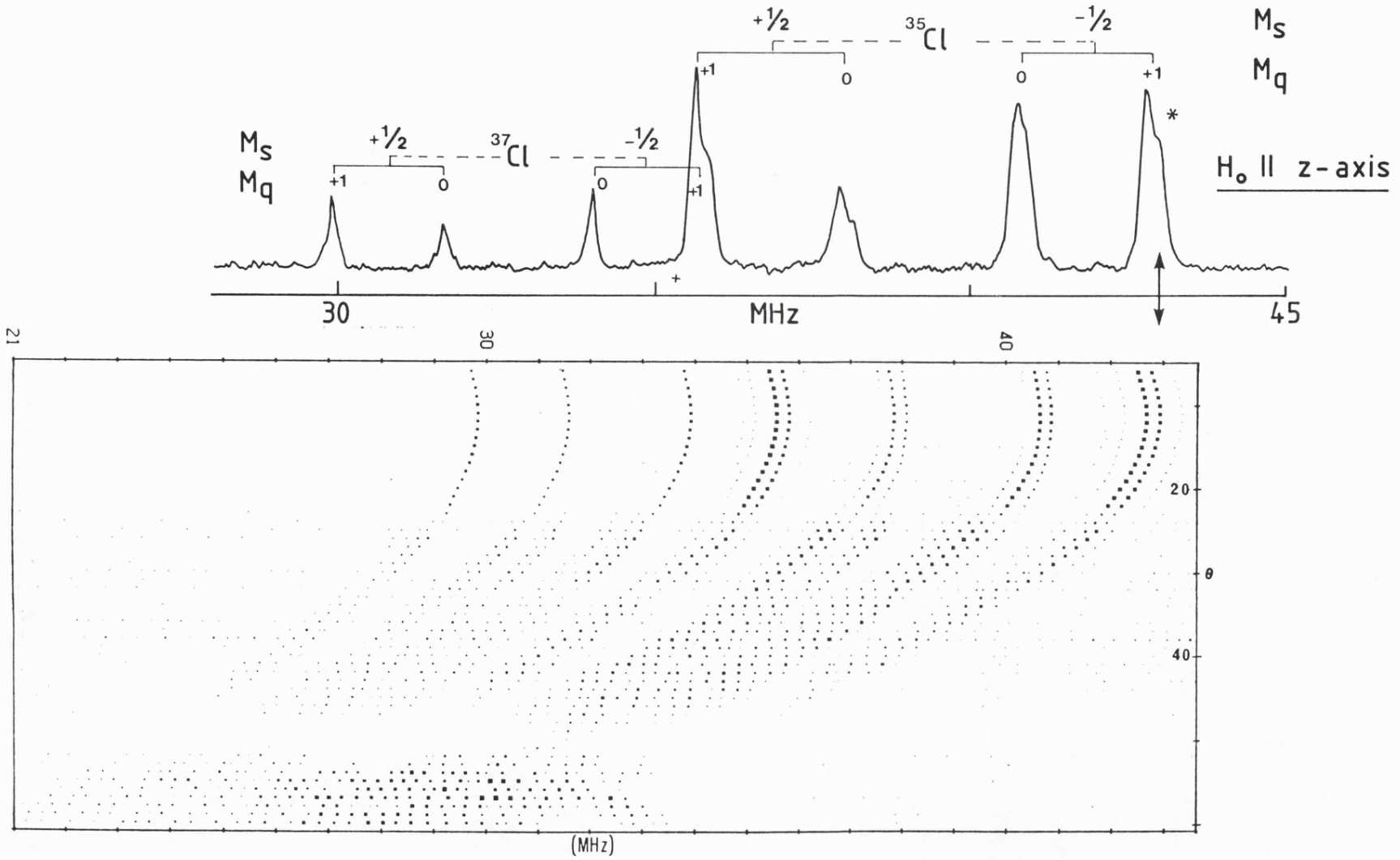

FIGURE 8

Expansion of the $M_S = -\frac{1}{2}$, $M_q = +1$ $(^{35}Cl^-)_{1,2}$ ENDOR line, measured with H_o // z and sitting on the $M_I = +2$ ESR line. The second order splittings are shown a) as measured and b) after filtering and deconvolution.

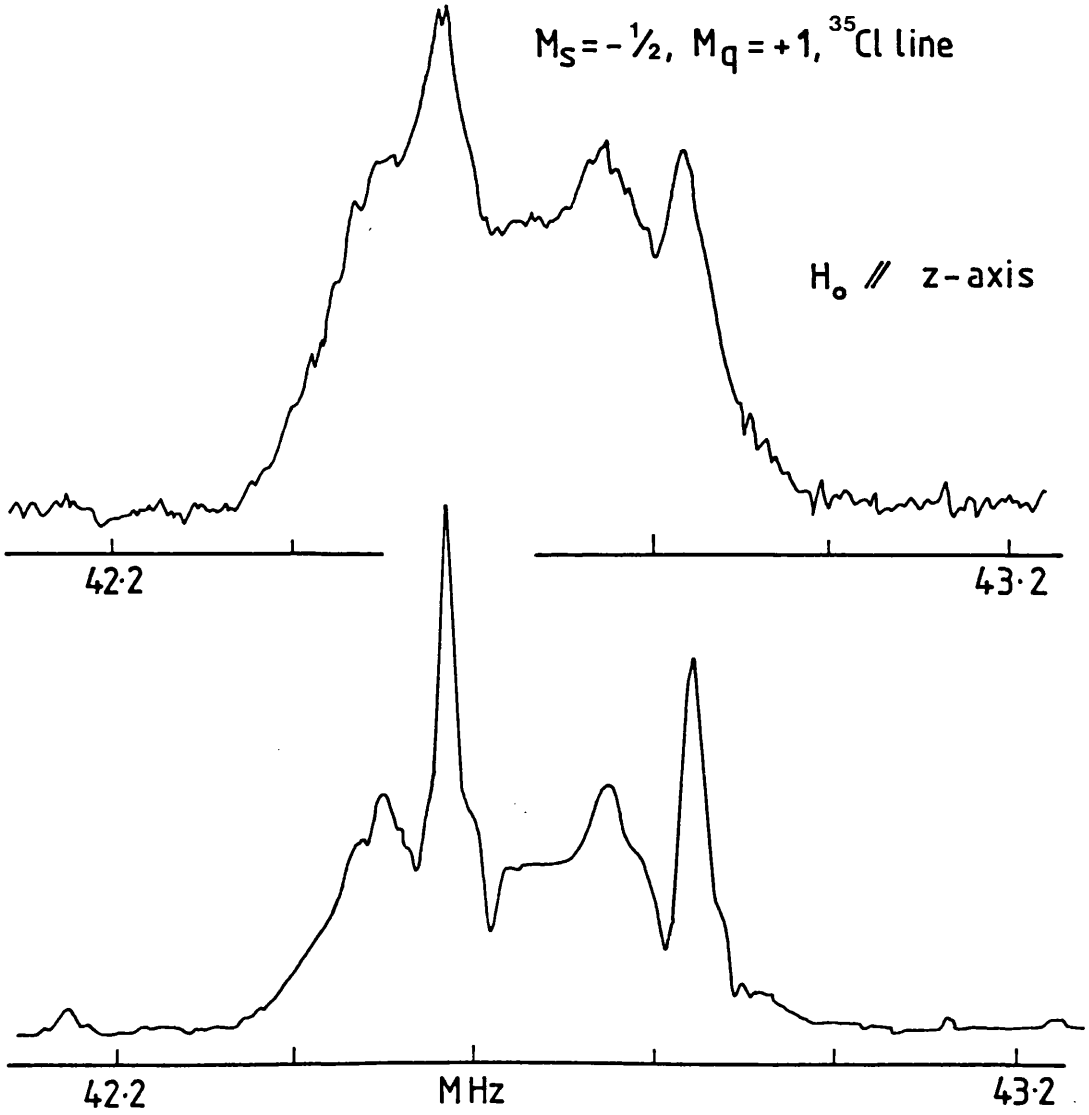

FIGURE 9

Spectra of $(Cl^-)_{1,2}$ showing a) the simplified second order splittings and b,c) the orthorhombic splittings of the ENDOR lines, measured with (a,c) H_o on the $M_I = 0$ ESR line and (b) H_o on the $M_I = +2$ ESR line. Rotation in (100) plane.

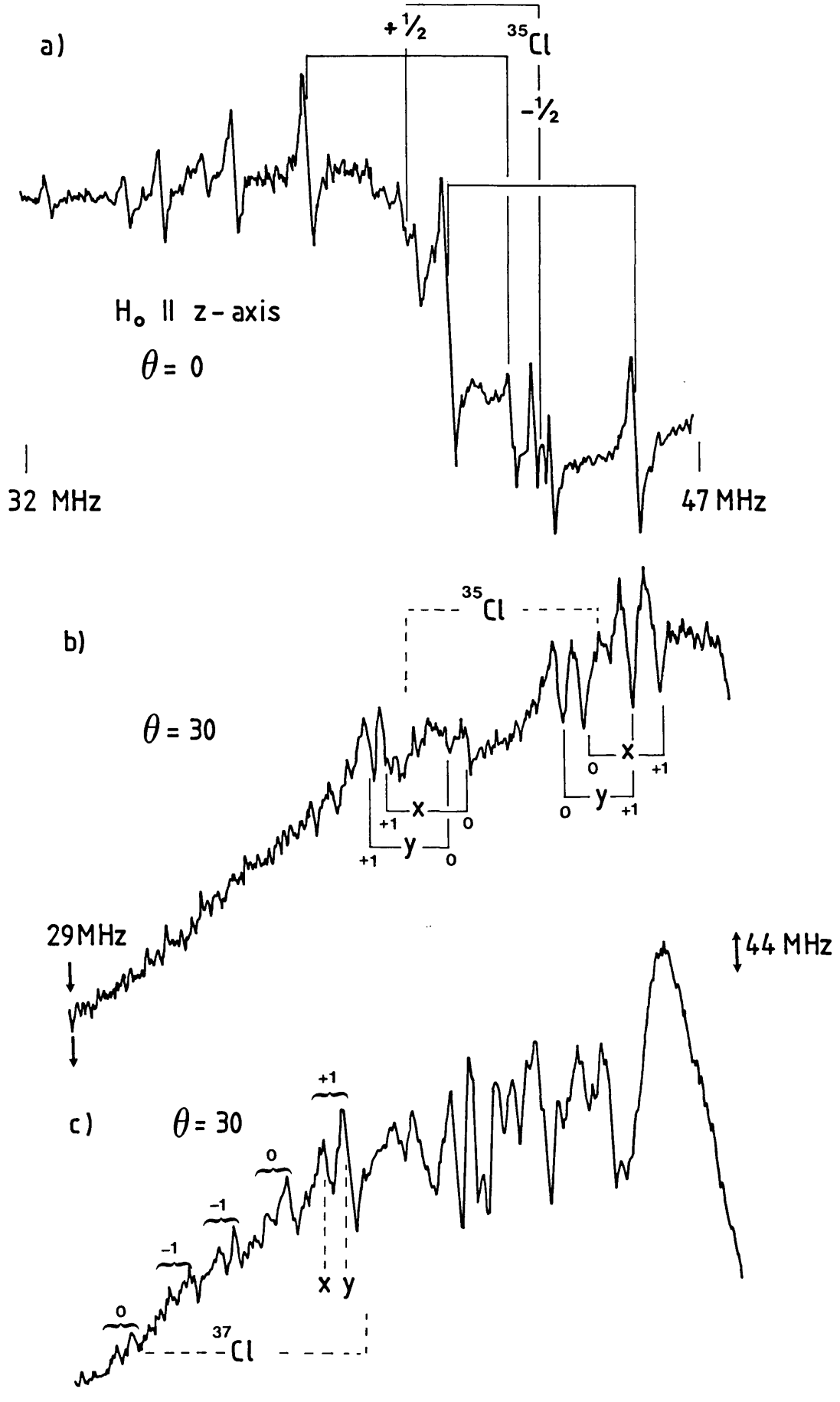

line is probably due to ^{35}Cl nuclei in ^{35}Cl-^{37}Cl pairs. However, eqn 5.30 could not be used to quantitatively calculate second order transition frequencies because the second order interaction energy and the quadrupole interaction energy were of the same order of magnitude, that is, $W_2 \cong P$. Under these conditions, the mixing of quadrupole terms must be considered, and the more involved treatments of Feuchtang[17] and Shoemaker[18] must be used. As a result of the mixing of quadrupole terms, the patterns of ENDOR transitions observed at all crystal orientations other than H_o // z were quite complex and the lines could not readily be assigned to m_q = +1, 0 and -1 groups. Indeed, as can be seen from Figure 7, as a result of the complexity introduced by the second order splittings, an orthorhombic hyperfine tensor and an asymmetric quadrupole tensor, it was not possible to follow the course of individual transitions past $\theta = 25^o$. This difficulty was overcome by supplementary rotations measured while stimulating the m_I = +2 or +3 ESR lines. This reduced the number of observed quadrupole transitions, and also simplified second order couplings (Figure 9b). Fitting of the ENDOR data was also simplified by following the ^{37}Cl ENDOR lines, although these tended to be quite weak at off axis positions (Figure 9c). The ENDOR spectra shown in Figures 9b and 9c confirm the orthorhombic nature of the axial chlorine hyperfine tensor. In this way, it was possible to establish that the // → ⊥ chlorine transitions in Figure 7 were associated with those lines observed when H_o was perpendicular to the z axis and parallel to (100) in the 14 - 24 MHz range, which moved to higher frequency in the course of the ⊥ → // rotation (Figure 10), as well as with those lines in the same frequency range which were nearly isotropic in the x ⇔ y rotation (Figure 11). These resonances were in the frequency range expected from the perpendicular ESR spectrum. Although, as mentioned above, it was difficult to assign individual lines at off-axis positions, it is clearly shown in Figures 7 and 10, that the ENDOR lines from the large chlorine hyperfine splittings moved in four groups which could be assigned to $m_s = \pm\frac{1}{2}$

FIGURE 10

Angular rotation plot in the (100) planes containing z, showing all the ENDOR resonances from the corresponding $(RhCl_6)^{4-}$ complexes. [The * marks resonances from ions outside shell one.]

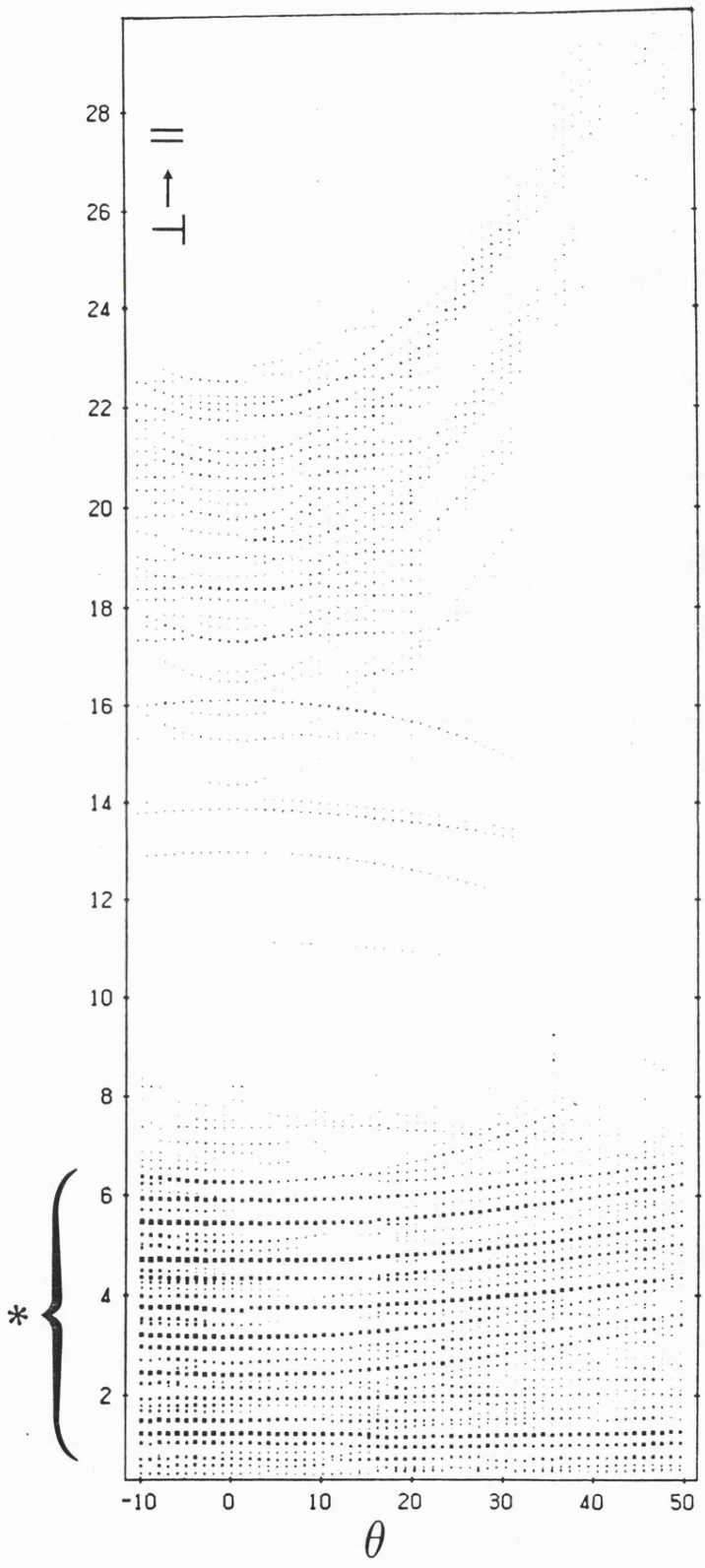

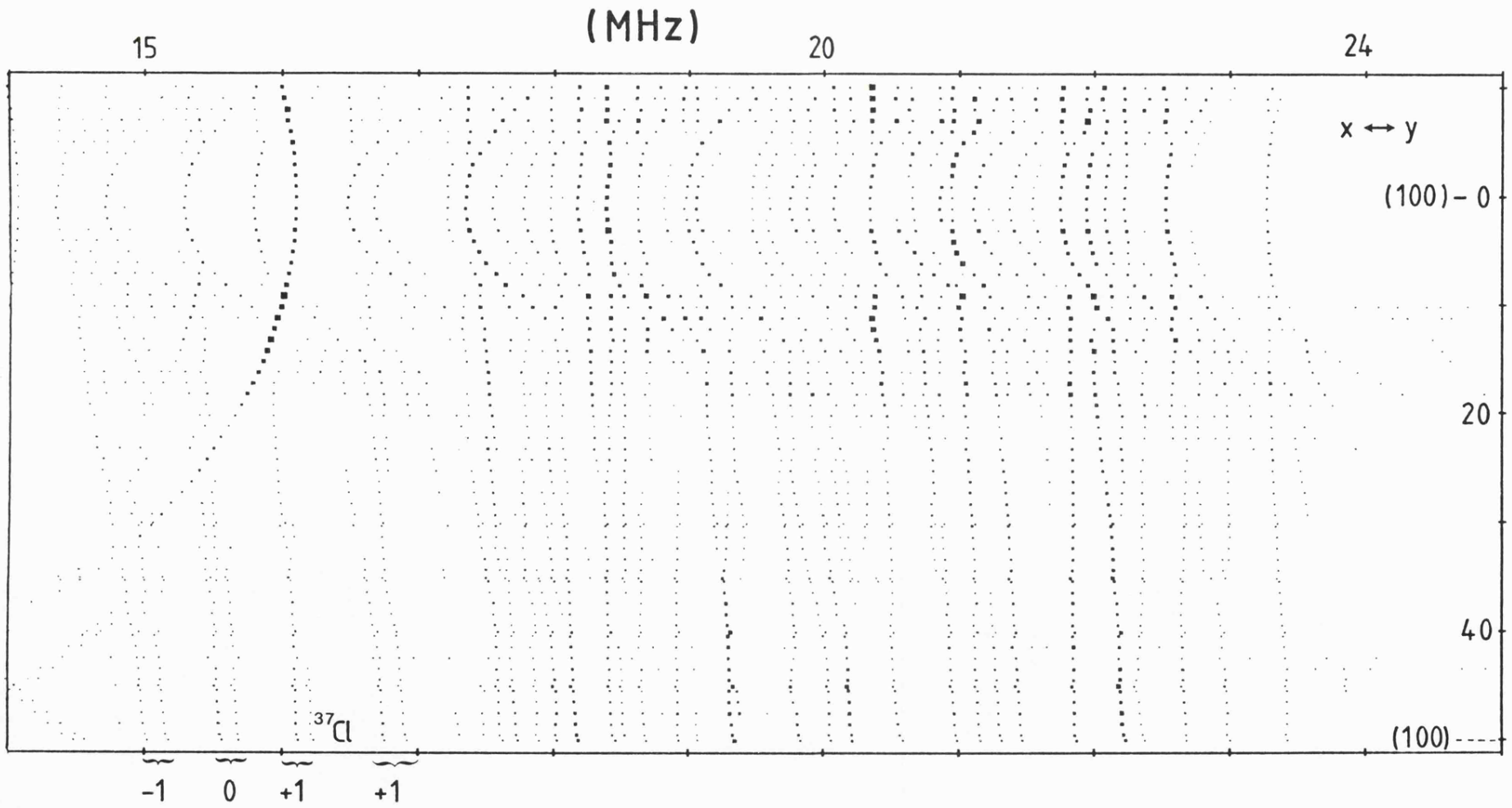

FIGURE 11

Angular rotation plot of ENDOR resonances from $(Cl^-)_{1,2}$ in the (100) plane perpendicular to z. The $(^{37}Cl^-)_{1,2}$ lines are marked.

components from ^{37}Cl and ^{35}Cl isotopes. In the x $\Leftrightarrow$ y rotation plot, the anqularly dependent curves of the $\perp \rightarrow$ // rotation were observed for $\theta = -10^{\circ}$-20°, as there was some overlap of ESR signals from the x $\Leftrightarrow$ y component and the $\perp \rightarrow$ // component at these orientations. It should be noted that the curves originating at 16, 14 and 13 MHz in Figures 10 and 11, and moving from high to low frequency as θ was moved from 0° to 50°, quite clearly originate from nuclei with a symmetry different from those chlorines with the largest hyperfine splittings.

The orthorhombic nature of the hyperfine tensor associated with the large chlorine ENDOR splittings is not immediately obvious from the x $\Leftrightarrow$ y isofrequency plot (Figure 11). While the $A_x \rightarrow A_y$ rotational curves are apparent, only a few of the $A_y \rightarrow A_x$ curves were resolved. This was because the overlap of the g_x and g_y ESR components was such that at any given saturating field position, different x- and y- component quadrupole transitions were excited. The orthorhombic character of the hyperfine tensor can be seen clearly by comparing the ENDOR spectra shown in Figures 12a and 12b, which were measured with H_o in the plane perpendicular to z and oriented parallel to (100) and (110) respectively. The ^{37}Cl A_x and A_y components are marked. These components coalesced at H_o // (110) and thus the ^{37}Cl transitions were easily assigned at this orientation. It is useful to compare these spectra with those measured for the complex $(RhCl_6)^{4-}$ in NaCl, which had an axial g-tensor (Figure 6.15). In this system, identical ENDOR spectra from the axial chlorines were obtained with H_o in the plane perpendicular to z, oriented parallel to (100) and oriented parallel to (110). The assignments of the ^{37}Cl lines shown in Figure 12 were consistent with the results of TRIPLE ENDOR experiments,which extablished the parent m_s manifold of each line.

The ^{37}Cl transitions, marked in the angular rotation plot of Figure 11, are clearly doublets. As discussed above, doublets of equal intensity can not be attributed to second order effects for ^{37}Cl transitions. Neither can the

FIGURE 12

ENDOR spectra of $(Cl^-)_{1,2}$ in $(RhCl_6)^{4-}$ measured with H_o in the plane perpendicular to z and with a) H_o // (100) and b) H_o // (110). A_x and A_y coalesce to give a simpler spectrum in (b), where the $^{37}Cl^-$ lines are marked.

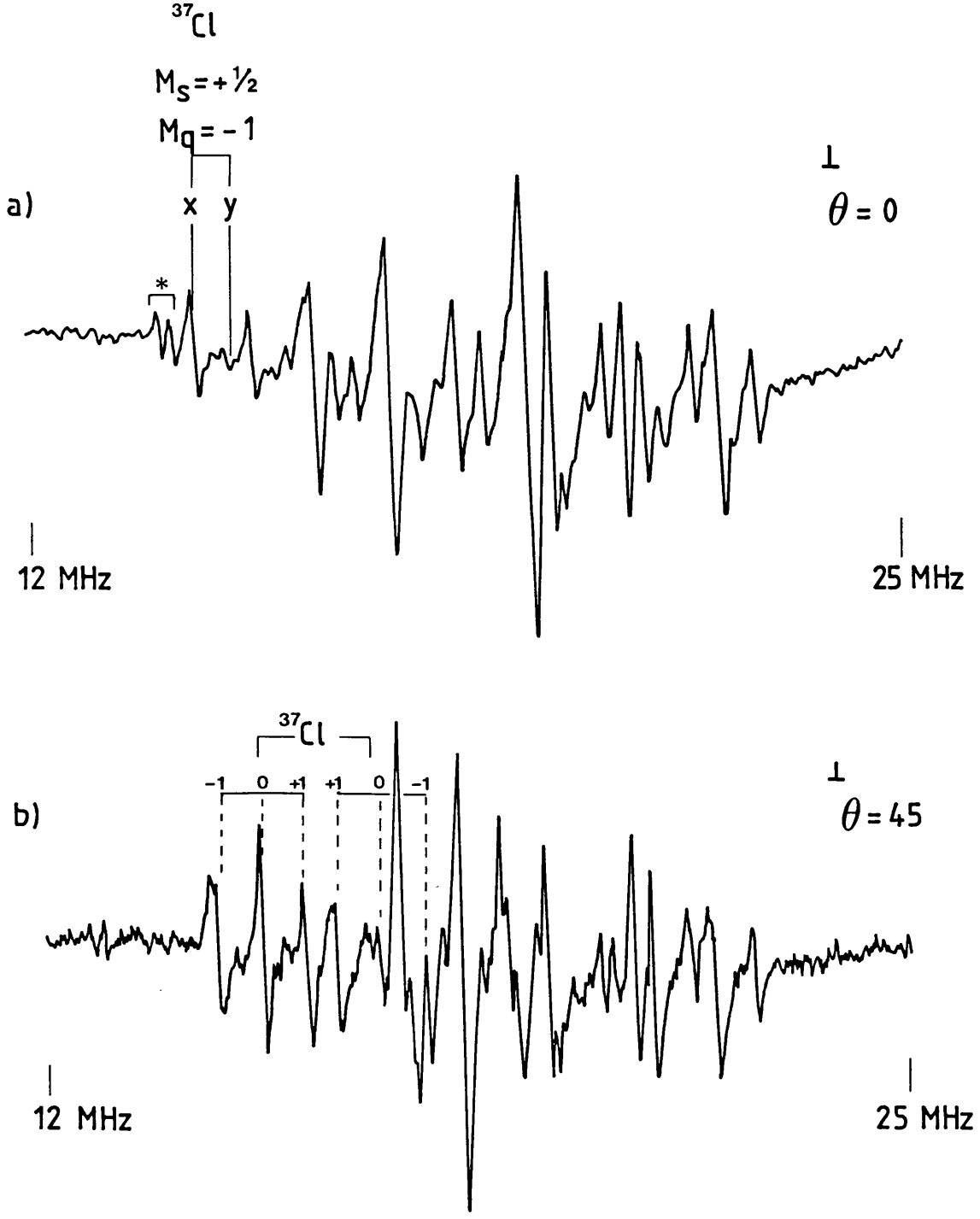

splittings be attributed to crystal misalignment, since the lines did not cross during rotation, and no splitting was observed with H_o parallel to z. Thus, the most likely assignment for the doublets is that they result from twinned crystals, with a small relative misalignment of the two crystallites about a screw axis parallel to the (100) axis in the plane of rotation. Screw dislocations are commonly observed in heavily-doped silver halide crystals, and would be most likely to occur in the large crystals used for the majority of the angular rotation measurements. Initially, it was thought that the large number of lines observed in the 14 - 24 MHz region of the ENDOR spectrum measured with $H_o \perp z$ indicated the presence of more than one type of complex. However, the complexity was considerably reduced in the absence of twinning (Figure 12). The remaining multiplicity, which was greater than the 24 lines expected to first order for overlapping A_x and A_y components, could be attributed to second order splittings of the ^{35}Cl lines. This was confirmed by TRIPLE and ENDOR-vs.-field position experiments. In the latter, as the position of the saturating microwave field was moved from low field to high field across the perpendicular ESR signal, the quadrupolar transitions were excited in the sequence m_q = (+1), (+1, 0), (0, -1), (-1) in a manner which encompassed all of the lines in the 14 - 24 MHz region, and which illustrated the mixing of quadrupole terms by second interactions (Figure 13). The interpretation of these experiments for the ^{37}Cl lines was straightforward, as it had been for both ^{37}Cl and ^{35}Cl lines when H_o was parallel to z (Figures 5.7 - 5.9). In the TRIPLE ENDOR experiments, if any of the ^{35}Cl transitions were saturated, changes were observed in all of the ^{35}Cl lines, but in none of the ^{37}Cl lines. Conversely, if any of the ^{37}Cl transitions were excited, responses were observed from all of the ^{37}Cl lines as well as from some ^{35}Cl lines, which had been very weak in the normal ENDOR spectrum. This behaviour confirmed the fact that the major part of the ^{35}Cl line intensities originated from ^{35}Cl-^{35}Cl pairs, while the major part of the ^{37}Cl line intensities

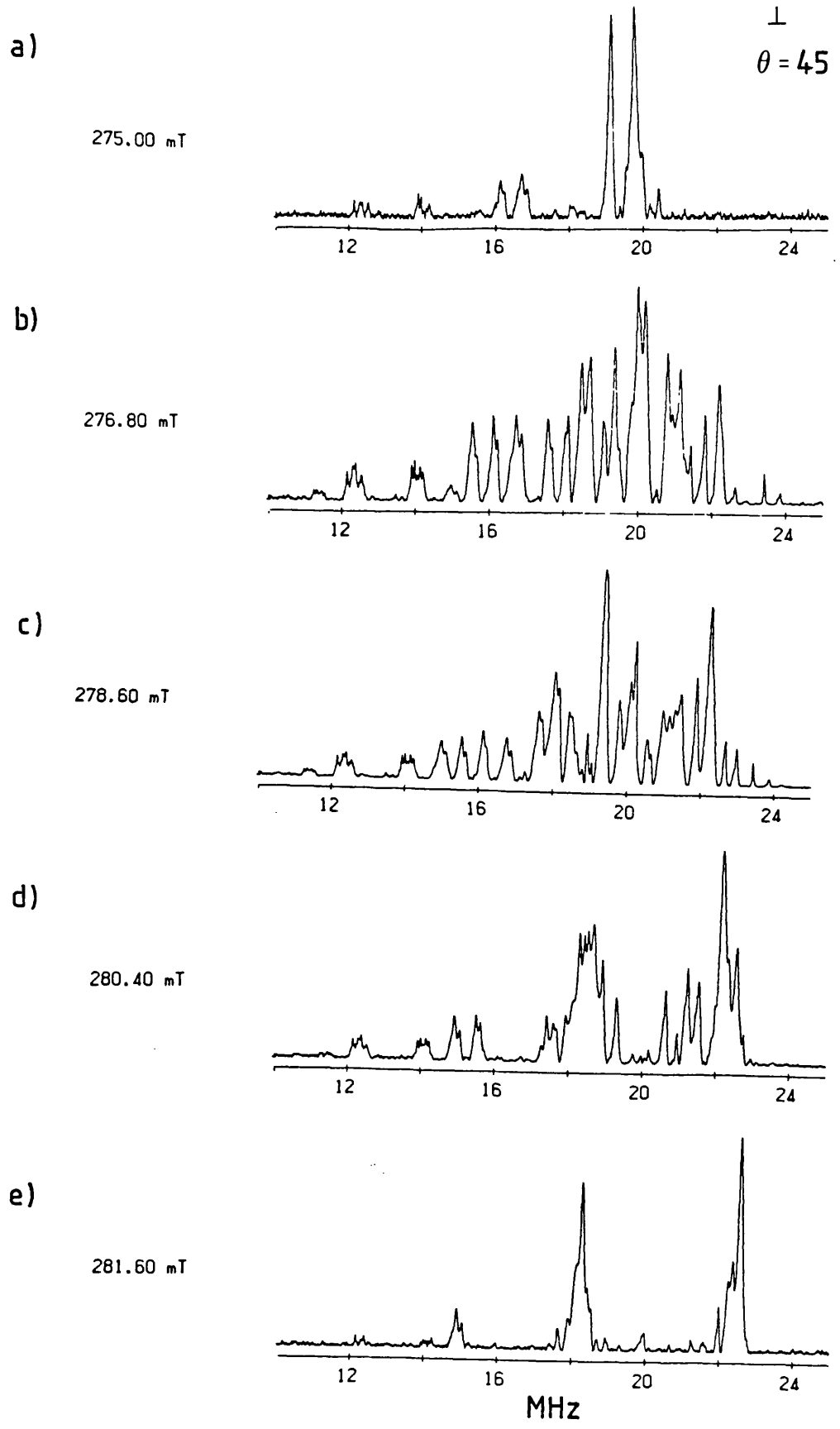

FIGURE 13

ENDOR spectra of $(Cl^-)_{1,2}$ measured with H_o in the plane perpendicular to z and with H_o // (110). H_o was moved from the $M_I = +3$ to the $M_I = -3$ ESR line in (a)-(e). Signals from equatorial chlorines are marked e and e'.

originated from ^{35}Cl-^{37}Cl pairs. The TRIPLE experiments also confirmed that all of the resonances in the 14 - 24 MHz range arose from the same type of complex. The results of the TRIPLE experiments were consistent with the suggestion that the ^{37}Cl doublets originated from twinning. If one line of a doublet was excited, only one line of all the other doublets responded (Figure 14). One puzzling aspect of the TRIPLE experiments is apparent from Figures 14a - 14d. Ordinarily, all quadrupole transitions from all m_s manifolds respond to the TRIPLE experiment by an increase or decrease in intensity, with all changes being of the same order of magnitude. However, in the present experiments, if a particular quadrupolar transition of the ^{37}Cl nucleus in a ^{37}Cl-^{35}Cl pair was stimulated, a major change was only observed for the same m_q transition in the opposite manifold for the ^{37}Cl nucleus, and for the dissimilar m_q transitions in the same m_s manifold for the ^{35}Cl nucleus. At present, this phenomenon is not understood.

The symmetry of the angular rotation curves for the large chlorine hyperfine splittings indicated that the chloride ions were aligned along the z-axis of a substitutional complex with orthorhombic symmetry (Figures 7, 10 and 11). Thus, these splittings were assigned to the first shell axial chlorines of the primary species. As evidenced by second order splittings, the sites of $(Cl^-)_1$ and $(Cl^-)_2$ were geometrically equivalent. The components of the hyperfine and quadrupolar tensors were obtained by fitting the angular rotation data and well-aligned spectra at selected orientations, as described above. These parameters are collated in Table III. The hyperfine parameters are consistent with the less precise values measured from the parallel and perpendicular septets of the ESR spectrum.

After the axial Cl^- hyperfine splittings, one might expect that the largest hyperfine splittings would be those from the equatorial chlorines measured parallel to the x and/or y complex axes. These splittings would be expected to give rise to ENDOR lines which moved from low to high

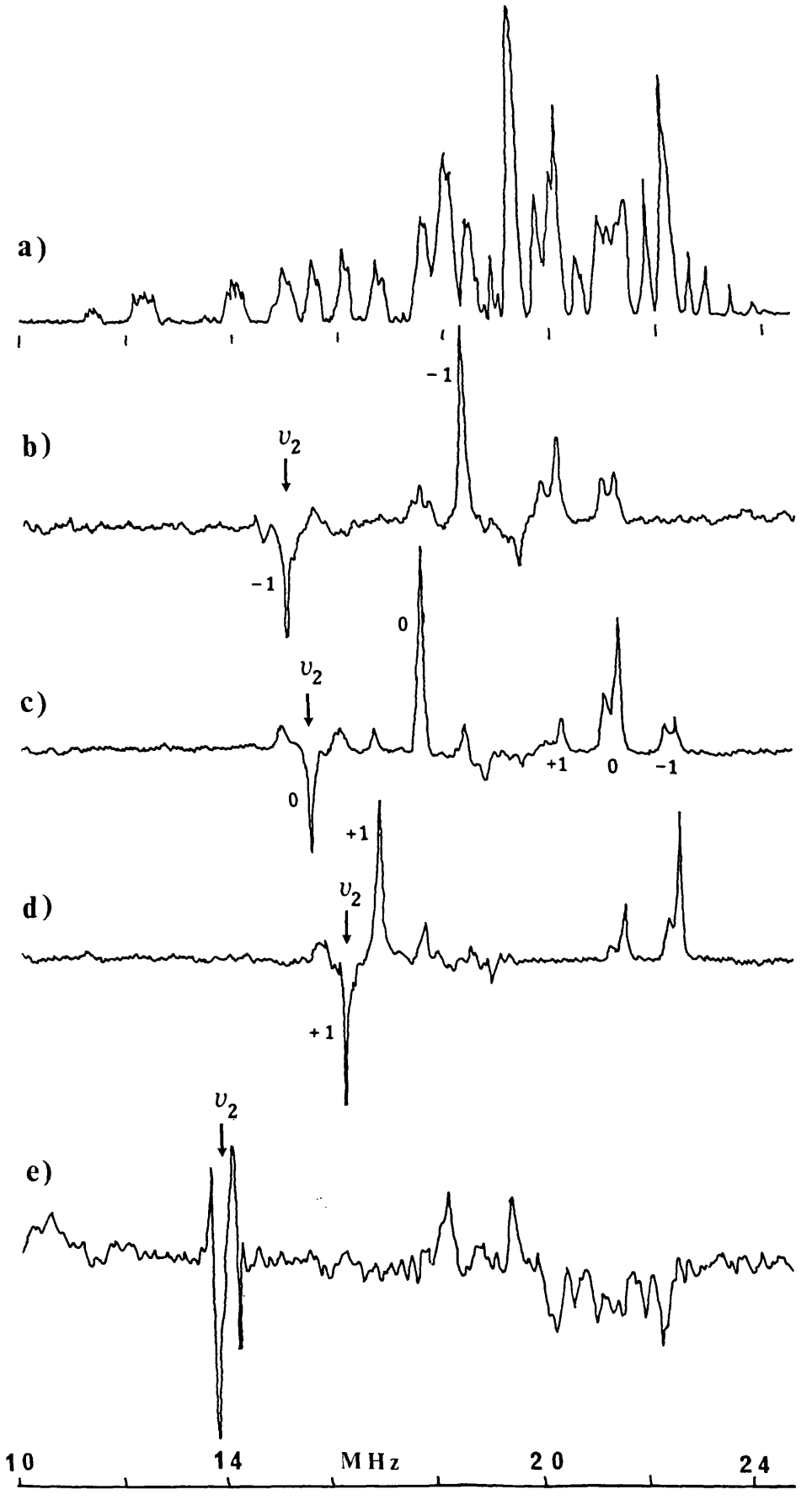

FIGURE 14

TRIPLE ENDOR spectra of Rh^{2+}/AgCl, measured with H_o // (110) and perpendicular to z, pumping (a - d) the axial $^{37}Cl^-$ transitions and (e) an equatorial $^{35}Cl^-$ transition.

frequencies in a $// \rightarrow \perp$ rotation, and from high to low frequencies in a $\perp \rightarrow //$ rotation, in opposition to the movement of the axial chlorine lines. Resonances fulfilling these conditions are shown in the expanded rotation plots of Figures 15a and 15b. The $x \Leftrightarrow y$ angular rotation plot of these lines, shown in Figure 15c, can be seen to be composed of a superposition of the $// \rightarrow \perp$ and of the $\perp \rightarrow //$ plots. This indicates that the relevant hyperfine tensors were axial. The relative line positions were consistent with assignment to two different types of ^{35}Cl nuclei; lines from the two kinds of nuclei are marked e and e' in Figure 15. The e resonances clearly exhibited a quadrupole splitting, with all three quadrupole transitions observable for each m_s component at some point in the rotation plot. The e' resonances were each split into doublets. These doublets have also been assigned as quadrupole splittings, with the assumption that one transition was undetected. This assignment is less definite than that of e lines since twinning could also give rise to a doublet splitting. However, no twinning was observed for the more anisotropic e lines. Thus, it seems likely that the doublets associated with the e' transitions resulted from quadrupole effects.

The angular rotation curves arising from lines in the perpendicular region of the e and e' ENDOR spectra were not resolved. The hyperfine splittings obtained from fitting the rotation data, listed in Table III, are therefore approximate. TRIPLE experiments confirmed that the e and e' lines were associated with the same complex as the axial chlorines (Figure 14e). These experiments also indicated that the e and e' originated from chlorine nuclei in ^{35}Cl-^{35}Cl pairs. ^{37}Cl resonances were apparently too weak to be detected.

The ENDOR transition from small hyperfine interactions, measured with H_o // z, are shown in Figure 16. TRIPLE ENDOR experiments confirmed that these lines were associated with the same complex as the axial chlorine lines. The relation of these transitions to the axial chlorine transitions is demonstrated in the $\perp \rightarrow //$ rotation plot of Figure 10, where the small hyperfine

a) ∥ → ⊥

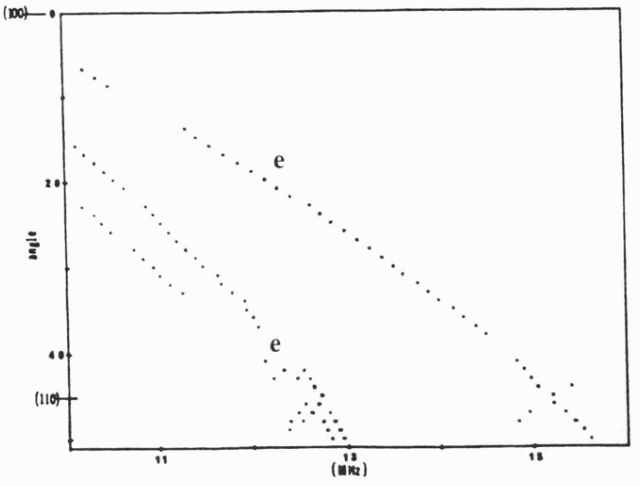

b) ⊥ → ∥

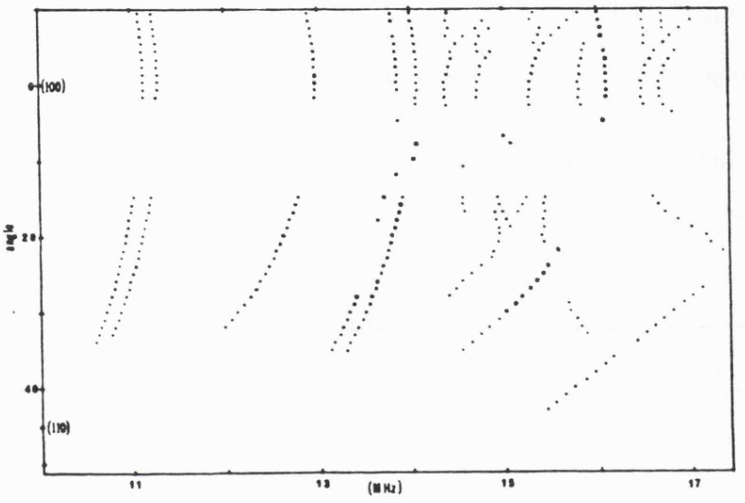

c) x ↔ y

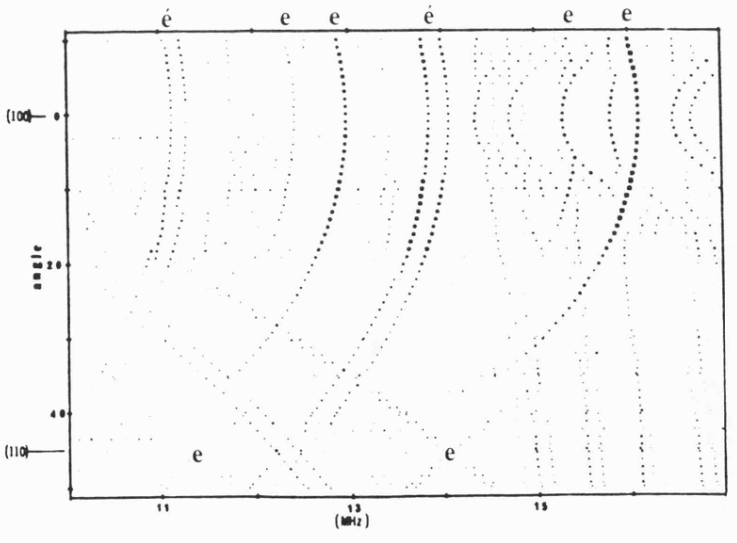

FIGURE 15

Angular rotation plots of the ENDOR lines from equatorial chlorines of $(RhCl_6)^{4-}$. The rotations were a,b) in the (100) planes containing z a) from H_o // z towards H_o ⊥ z, b) from H_o ⊥ z towards H_o // z, and c) in the (100) plane perpendicular to z.

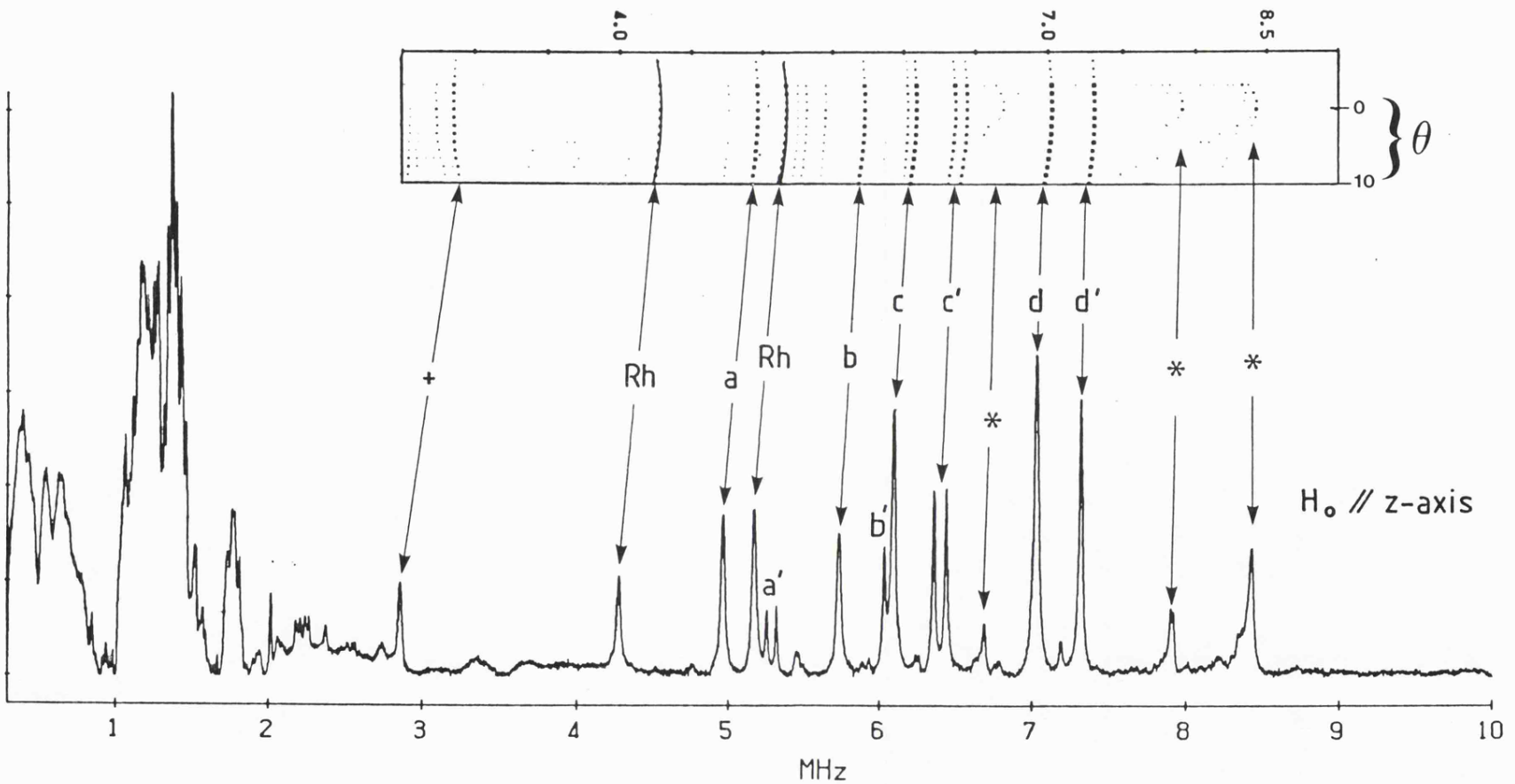

FIGURE 16

ENDOR spectrum, measured with H_o // z, showing the relative intensities of lines from Rh^{2+}, 4th. shell silvers (a-d) and other outer shell ions (a'-d', *) and indicating the corresponding curves in the rotation plot of Fig. 17.

transitions are marked with an asterisk. This frequency range is expanded in Figure 17. The corresponding rotations in the planes containing z, from H_o // z towards $H_o \perp$ z, and in the plane perpendicular to z, are shown in Figures 18 and 19.

The angular dependences of the lines labelled Rh in Figure 16 indicated that the corresponding hyperfine tensor had principal axes which coincided with those of the g-tensor and of the hyperfine tensor of the axial chlorines. The angular dependences of these transitions are marked by solid lines in the rotation plots of Figures 17 - 19. The orthorhombic character of the Rh hyperfine tensor is obvious from Figure 19. The observed symmetry behaviour indicated that these transitions originate from nuclei on the z-axis of the primary species. The lines had separations characteristic of transitions form the nucleus ^{103}Rh and were assigned accordingly. The principal components of the rhodium hyperfine tensor, calculated by fitting the rotation data, are listed in Table III.

The lines labelled a - d in Figure 16 also arose from nuclei on the z-axis of the primary complex. The rotational curves corresponding to these transitions are annotated in Figures 18 and 19, and are represented by solid lines in Figure 20. Figure 20 is a superposition of the // $\rightarrow \perp$ and $\perp \rightarrow$ // rotational data. The relative positions and intensities of the lines were indicative of an interaction with ^{107}Ag and ^{109}Ag nuclei. As can be seen from Figure 20, the hyperfine tensor for this interaction was axial. Components are given in Table III. It is assigned to the two axial 4^{th} shell silver ions.

Similarly, the lines labelled a' - d' in Figure 16 had separations and intensities characteristic of silver resonances. TRIPLE measurements confirmed that these lines were associated with the primary complex. In the // $\rightarrow \perp$ and $\perp \rightarrow$ // rotations, the lines had angular dependences very similar to those of the a - d transitions. However, in the x $\Leftrightarrow$ y rotation plot, no isotropic lines, as would result from axial symmetry, could be associated with the

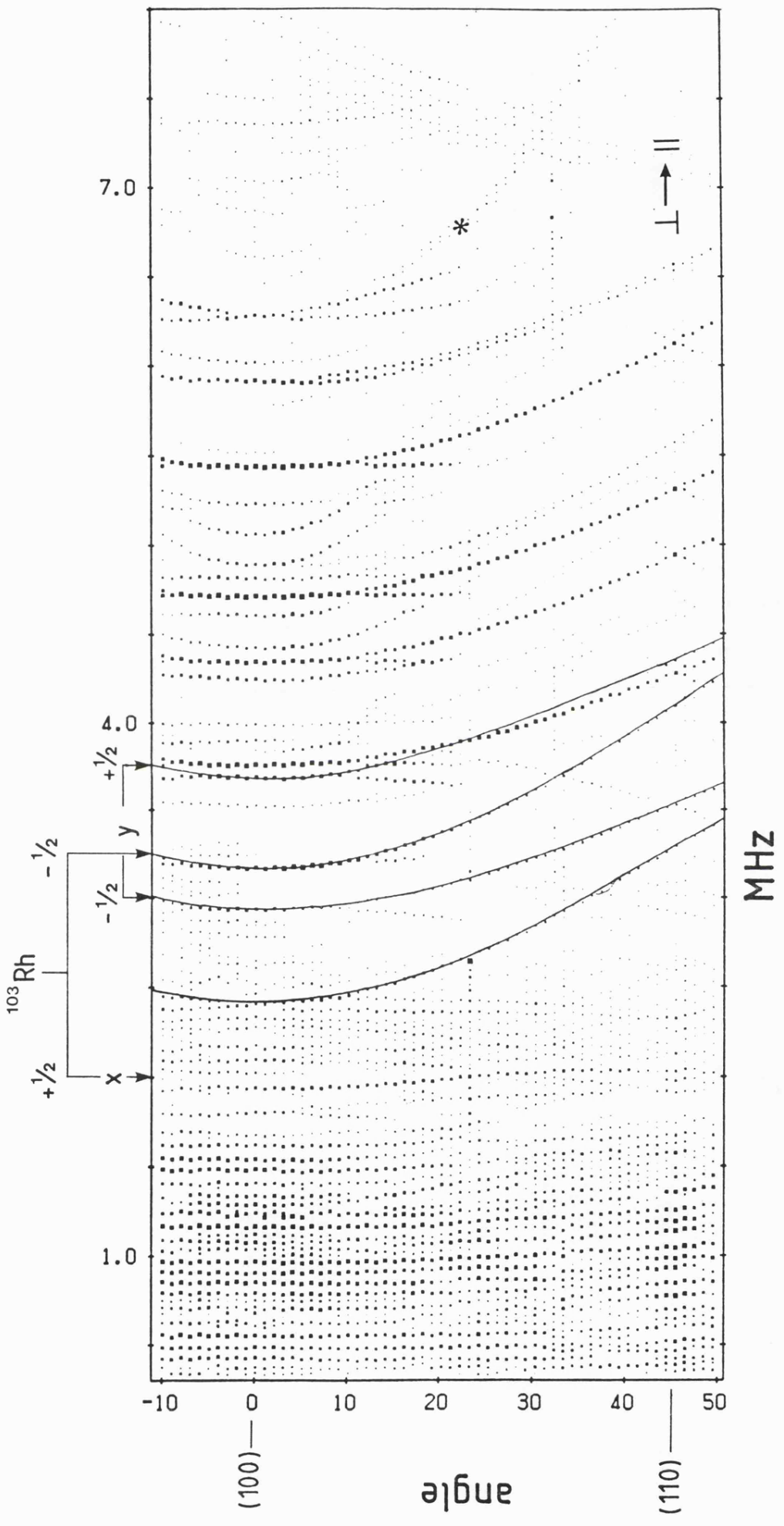

FIGURE 17

Angular rotation plots of Rh^{2+} and outer shell hyperfine data in the (100) plane containing z, from $H_o \perp z$ towards $H_o \parallel z$.

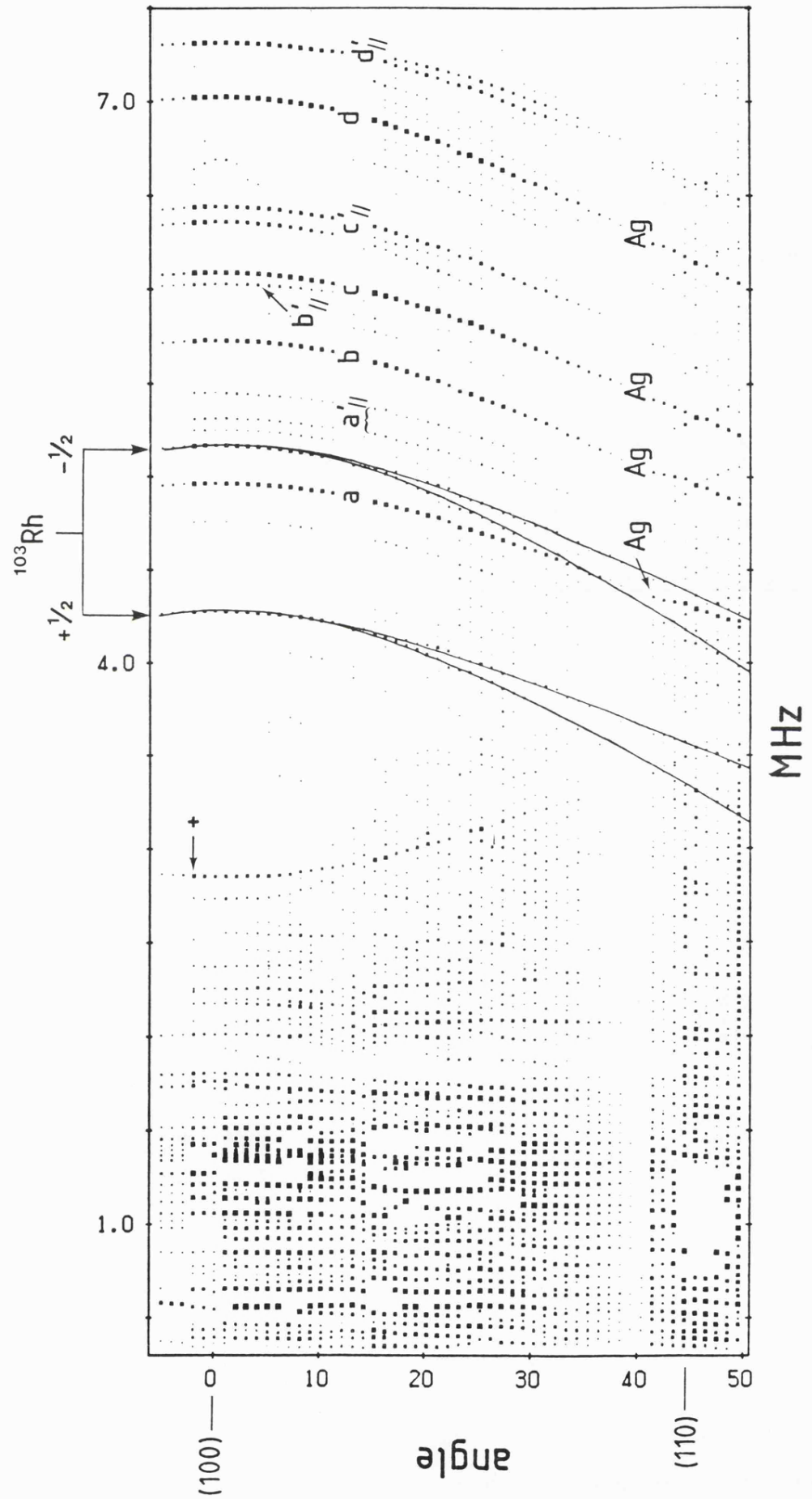

FIGURE 18

Angular rotation plot in the (100) planes containing z from H_o // z towards H_o ⊥ z.
Lines a-d are from 4th. shell silvers; lines $a'_{//}$ - $d'_{//}$ are discussed in the text.

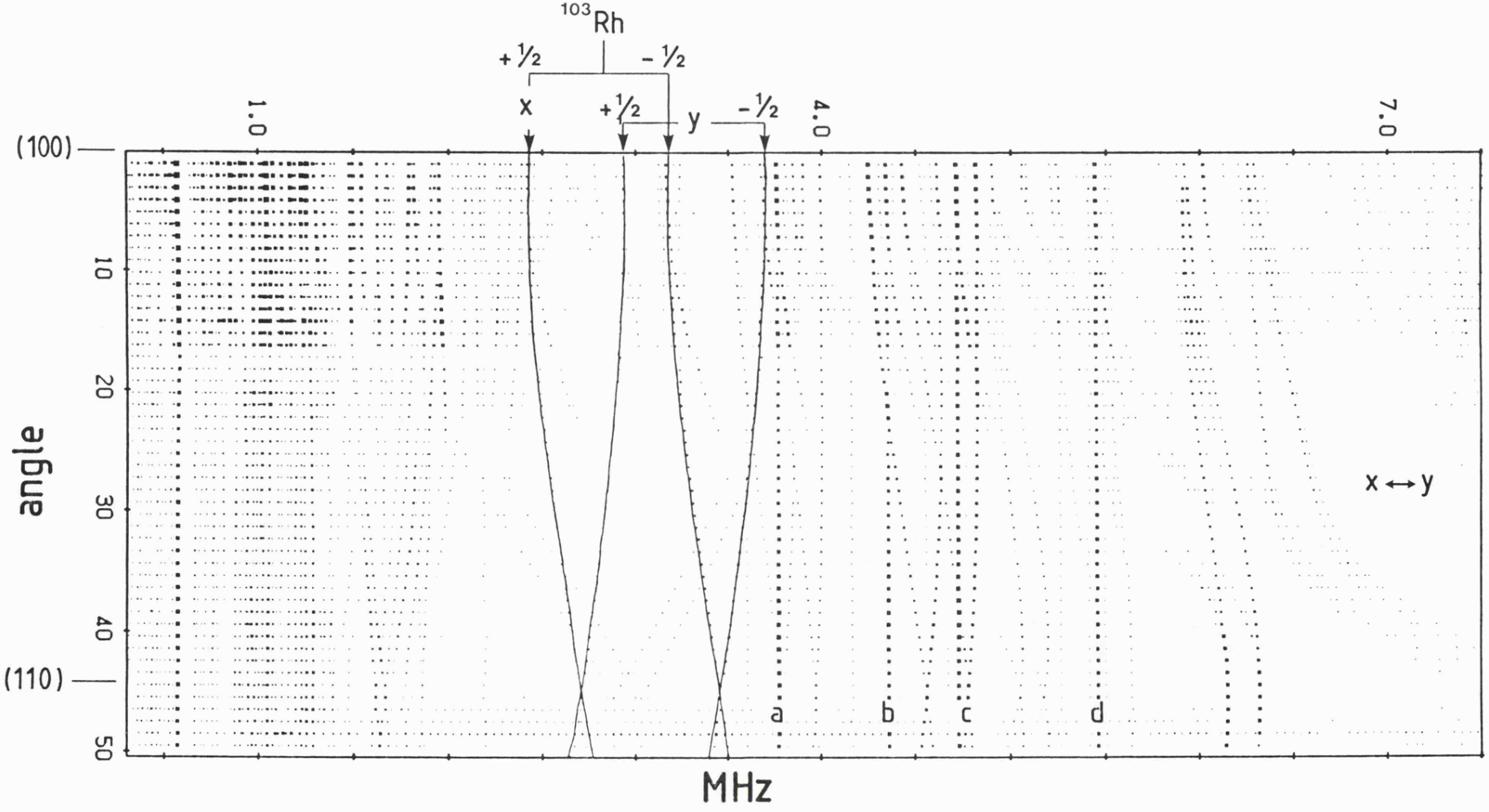

FIGURE 19

Angular rotation plot of Rh^{2+} and outer shell hyperfine data in the (100) plane perpendicular to z.

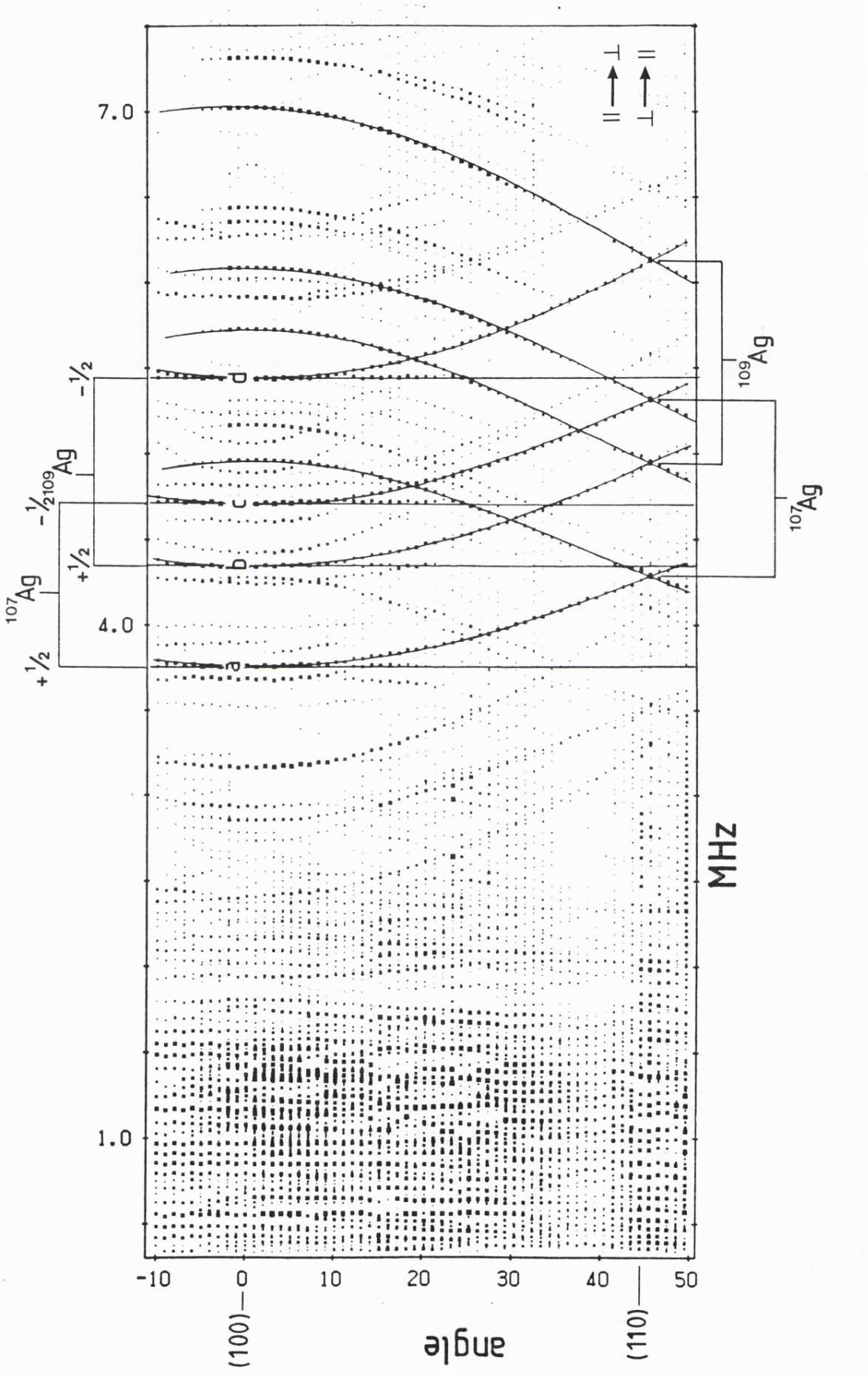

FIGURE 20

Combined plots of // to ⊥ and ⊥ to // rotations in the (100) planes containing z. The solid lines are the fitted curves for the 4th. shell silver splittings.

a' - d' transitions. Rather, a number of weak, angularly dependent curves were observed, which originated at frequencies close to the $a'_{//}$ - $d'_{//}$ and $a'_{\perp}$ - $d'_{\perp}$ line positions. These positions are marked in the x ⇔ y rotation plot shown in Figure 21. In this figure, the angularly dependent lines were emphasized by plotting only those lines with intensities below a given value. The intensities of the angularly dependent lines relative to the axial 4^{th} shell silver ion lines can be seen in the ENDOR spectrum measured with H_o // (110) in the plane perpendicular to z shown in Figure 21. Since the axial chlorines were equivalent, the two axial 4^{th} shell silvers must also be equivalent. Thus, lines a' - d' cannot be assigned to one of the 4^{th} shell silvers. The most likely assignment for lines a' - d', and for the weak angularly dependent lines in Figure 20 is to the eight 2^{nd} shell silver ions in the (100) planes containing the z-axis. Further analysis of the angular rotation data is required to confirm this interpretation.

A large number of lines, from interactions with more distant shells, were observed below 2 MHz. Although some angularly dependent patterns were visible, the spectral density was too high to allow interpretation. A number of weak lines at higher frequencies also remain unassigned. These include the lines marked with an asterisk in Figures 16 and 17, and those marked with a cross in Figures 18 and 21. The lines in Figure 21 could arise from equatorial chlorine 3, as discussed further below, with the doublet splitting resulting from a partially resolved quadrupole interaction. If these lines belong to the $m_s = -\frac{1}{2}$ component of a ^{35}Cl interaction then the corresponding axial hyperfine tensor components are ~5 and ~1.5 MHz. If the lines arise from the $m_s = +\frac{1}{2}$ component, the corresponding splittings are ~8.8 and ~6.4 MHz. Some of the very weak lines observed, such as those marked with brackets in Figure 22, could be associated with the secondary species.

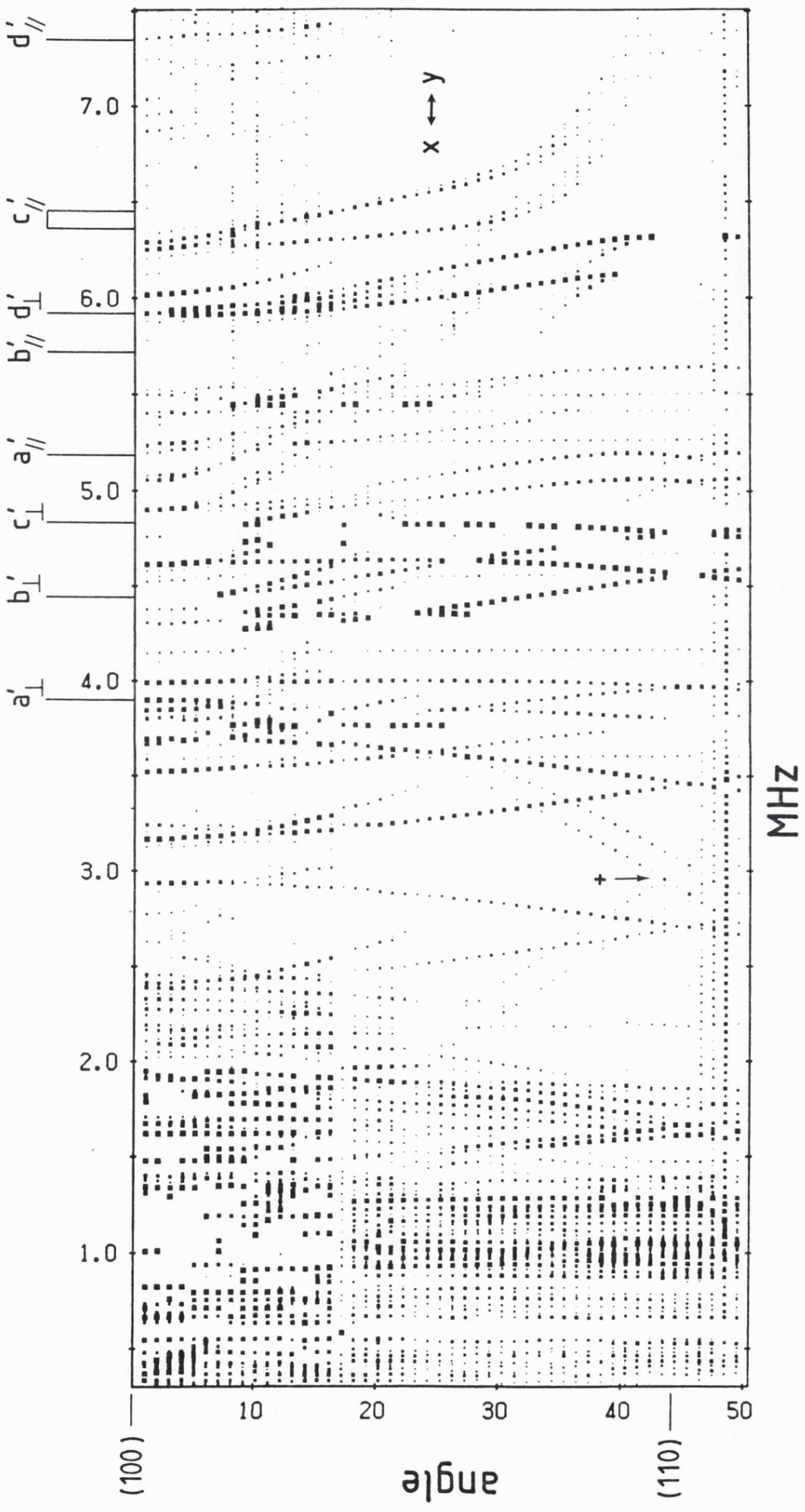

FIGURE 21

Angular rotation plot as in Fig. 18, but plotted so as to enhance curves from weak resonances and to suppress curves from strong resonances.

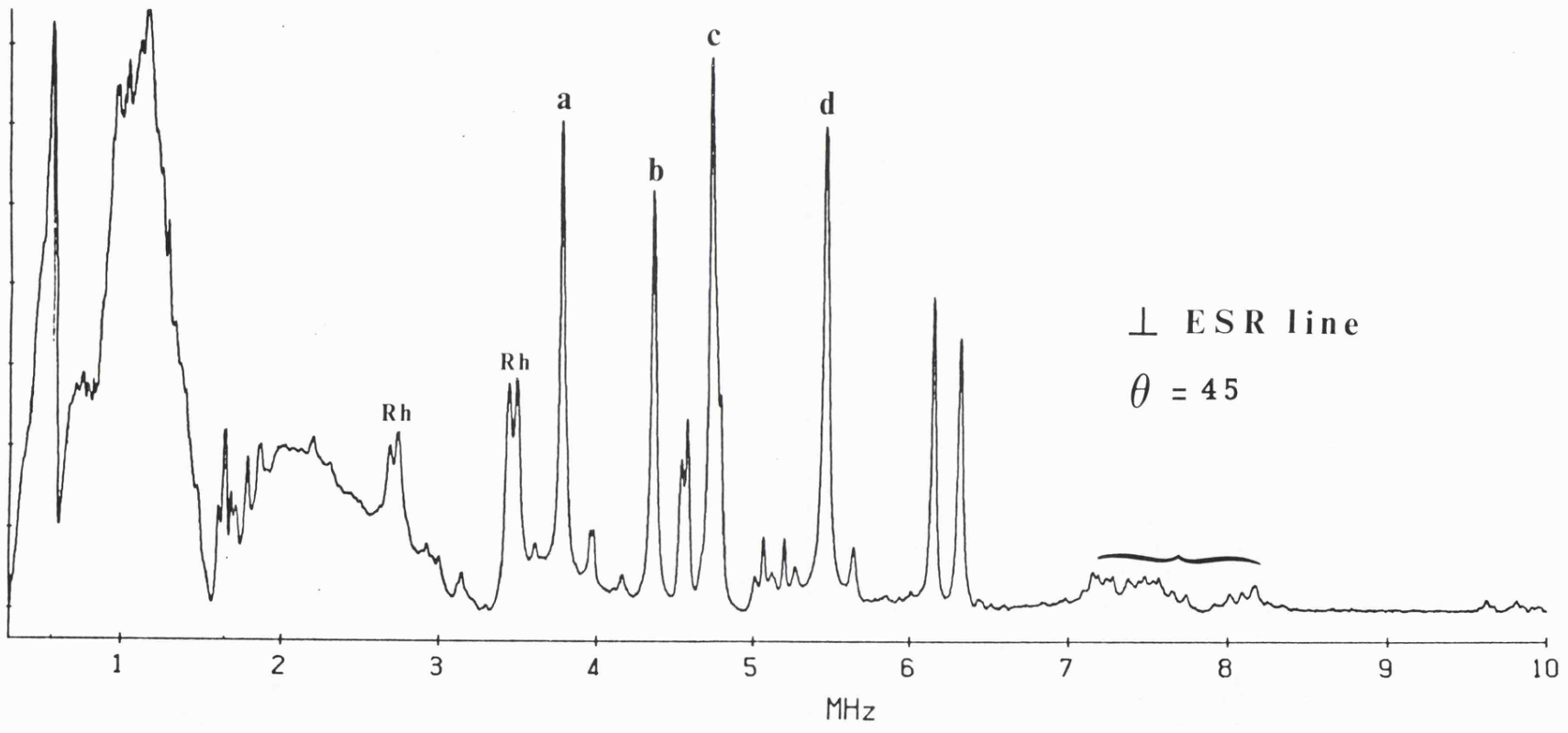

FIGURE 22

ENDOR spectrum measured with $H_o \perp z$ and $\parallel (110)$, showing the relative intensities of the weak lines plotted in Fig. 21.

No ENDOR signals could be obtained from rhodium-doped AgCl powders. As shown in Figure 6.15, powder ENDOR spectra were observed in rhodium-doped NaCl when saturating the perpendicular ESR region. The Rh^{2+} ESR signal in NaCl was 2 - 5 times stronger than in AgCl. Thus, the failure to observe powder ENDOR in AgCl resulted from the usual low sensitivity encountered in powder studies with an additional loss in sensitivity due to the orthorhombic Rh^{2+}/AgCl site symmetry.

Finally, in preliminary studies of Ag^{2+} in Rh^{2+}/AgCl, produced by x-irradiation at 30 K, and of Ru^{3+} (low spin d^5) in AgCl and AgBr, detailed ENDOR spectra were obtained. Thus, the general applicability of ENDOR spectroscopy of the study of defect centers in the silver halides has been demonstrated.

7.4 Discussion

The ENDOR results described above confirm that the primary species in the Rh/AgCl system was a rhodium complex. The sign of the quadrupole coupling constant of the axial chlorines can now be used to deduce the charge of the rhodium nucleus relative to the AgCl lattice. If it is assumed that the signs of the components of the axial chlorine hyperfine tensor are positive, then the TRIPLE experiments described above indicate that the signs of the components of the quadrupole tensor were negative. The quadrupole interaction energy, measured with H_o // z is given by (Chapter 5):

$$P_{//} = \left[\frac{6\ e\ Q}{4\ I\ (2I - 1)}\right] \frac{2\ q\ (1 - \gamma_\infty)}{r^3} \qquad (1)$$

where q is the point charge on the rhodium nucleus, which is a distance r from the axial chlorine nucleus. For ^{35}Cl, Q, the nuclear electric quadrupole constant, is negative, with a value of $-.0797 \times 10^{-24}$ cm^2, and the Sternheimer antishielding factor, $(1 - \gamma_\infty)$ is positive, with a value of 57.6.[19] Thus, eqn 1 becomes

$$P_{//}\ (\text{MHz}) = -1081\ \frac{q}{r^3\ (\text{a.u.}^3)} \qquad (2)$$

Since P is negative, the sign of q, the charge on the rhodium nucleus relative to the AgCl lattice must be positive. Thus, it is confirmed that the primary species is a Rh^{2+} complex rather than a Rh^{o} complex.

Assuming a positive charge of 1 at the rhodium nucleus, and replacing r by the cation-anion distance for the undisturbed AgCl lattice, the calculated value of P is -7.5 MHz. The measured value was -1.8 MHz. The discrepancy is not surprising given the assumptions used to obtain eqn 2. Large errors are introduced as a result of neglecting covalency effects and lattice distortions that may be induced by the Rh^{2+} ion. Errors also arise from the uncertainty in the antishielding correction factor. However, these errors should be approximately the same for quadrupole interactions calculated for other substitutional impurity complexes in the alkali chlorides. Thus, by comparing the ratio of measured to calculated quadrupole interaction for the rhodium complex in AgCl with those for compensated and uncompensated aliovalent impurities in the alkali chlorides, it should be possible to determine if the Rh^{2+} ion is charge compensated. This is done in Table IV. It can be seen that for uncompensated substitutional Ag^{o} centers in KCl and NaCl, the measured quadrupole coupling constant is ~45% of that calculated assuming a -1 charge at the silver nucleus. For a substitutional hydrogen atom in KCl, compensated by a Sr^{2+} ion in a nnn position, the measured quadrupole coupling constant for the chlorine ions perpendicular to the H^{o}--Sr^{2+} axis was 23% of the value calculated assuming a -1 point charge at H^{o}. The measured-to-calculated ratio of the quadrupole constant for Rh^{2+} in AgCl is very close to that for H^{o}--Sr^{2+} in KCl. This suggests that a charge compensating silver ion vacancy is associated with the Rh^{2+} ion in plane perpendicular to the axial chlorine--Rh^{2+} axis.

The presence of a charge compensating silver ion vacancy along the x or y axis of the primary species is supported by the observation of an orthorhombic g-tensor and orthorhombic $(Cl^-)_{1,2}$ and Rh^{2+} hyperfine tensors. It is also consistent with the second order splittings of the $(Cl^-)_{1,2}$ ENDOR lines which implied that the two axial chlorines as well as the two axial 4^{th} shell silvers were in completely equivalent sites.

The observations of large hyperfine interactions with the two axial chlorines and of a $g_{//}$ value which was less than $g_{\perp}$ indicate that the unpaired antibonding electron of the Rh^{2+} d^7 ion was in a ground state with a large d_{z^2} orbital contribution. The energy of the d_{z^2} orbital was lowered relative to the $d_{x^2-y^2}$ orbital via an elongation of the Rh^{2+} complex along the z-axis. The effective contraction of the Rh^{2+} complex in the plane containing the silver ion vacancy and perpendicular to z has the effect of reducing the total electron density in the vicinity of the vacancy, which is negatively charge relative to the lattice. This observation is consistent with the fact that for the low spin d^5 ions Ru^{3+} and Re^{2+}, association with a nnn vacancy caused a contraction along the vacancy axis.[1, 3] For this electronic configuration, such a distortion also minimizes the total electron density in the vicinity of the vacancy.

The Rh^{2+}-vacancy configuration described above suggests an explanation for the temperature dependence of the primary complex ESR spectrum. The averaging of interactions in the yz plane most likely results from a hopping of the elongation axis between the (100) axes perpendicular to the Rh^{2+}-vacancy axis. Such a pinned two-dimensional dynamic distortion would result in a ground state resembling a contracted $d_{x^2-y^2}$ complex, which is consistent with the experimental magnetic resonance parameters. The possibility of motional averaging occurring via vacancy motion can be ruled out since ionic motion was frozen at the temperatures at which the averaging began to occur. Thus, since averaging occurred in the yz plane, the vacancy can be assigned a nnn position along the x-axis. A similar type of "propellor motion"

has been observed in ESR studies of the Sn^{2+}-nnn vacancy complex in KCl.[20]

The motional processes which gave rise to the isotropic ESR line could result from a three-dimensional dynamic distortion of the Rh^{2+} complex, from diffusion of the vacancy away from Rh^{2+}, or from a combination of these mechanisms. The observation of an isotropic signal and of broadened, coalescing $(g_{//})_{H.T.}$ and $(g_{\perp})_{H.T.}$ signals simultaneously might indicate that both mechanisms are taking place.

It should be possible to calculate the energy barrier between the distortion minima along the x, y, and z axes, as well as the energy of association of the nnn vacancy, from the temperature behaviour of the ESR signal.[21] However, because the temperature behaviour was a function of rhodium concentration, such calculations necessitate further ESR studies.

It is not possible to assign the A_x and A_y components of the $(Cl^-)_{1,2}$ or Rh^{2+} hyperfine tensor to the x or y axes of the Rh^{2+} complex on the basis of the ENDOR measurements; however, it is reasonable to expect that the greatest electron density will be away from the vacancy, that is, along the y-axis. Thus, the principal axes of the $(Cl^-)_{1,2}$ and the Rh^{2+} hyperfine tensors should coincide with those of the g-tensor.

For the model of the Rh^{2+}-vacancy complex proposed, the $(Cl^-)_{4,6}$ ions should be equivalent, giving rise to a relatively large parallel hyperfine splitting. The $(Cl^-)_3$ ion would be expected to have a small parallel splitting and the $(Cl^-)_5$ ion a somewhat larger coupling. The perpendicular region of the ESR spectrum could be simulated by assuming an orthorhombic g-tensor and the $(Cl^-)_{1,2}$ hyperfine splittings given in Table III, a splitting of ~8 gauss along the x axis due to one chlorine, and a splitting of ~8 gauss along the y axis due to two chlorines. Poor fits were obtained if either zero or two 8 gauss splittings were considered for the x axis. Thus, the parallel equatorial chlorine splittings of 29.1 and 25.1 MHz can be assumed to arise from two equivalent $(Cl^-)_{4,6}$ and from one $(Cl^-)_5$ nucleus. Because of the

presence of two chlorine isotopes and numerous small hyperfine interactions, the ESR simulations were not precise enough to determine which equatorial chlorine splitting could be associated with the $(Cl^-)_{4,6}$ nuclei. The largest quadrupole splitting occurred for the 29.1 MHz splitting. This might reasonalbly be assigned to the $(Cl^-)_5$ nucleus since, on a point charge model, the electric field gradient is expected to be larger at this position than at $(Cl^-)_{4,6}$.

The observation of hyperfine interactions with the axial 4^{th} shell and possibly 2^{nd} shell silver ions is consistent with the elongated d_{z^2} charge distribution of the Rh^{2+} complex.

The optical properties and ESR parameters of substitutional transition metal ions in the silver halides have been successfully explained by a molecular orbital treatment of the complex $(MX_6)^{n-}$.[1-7, 22] Thus, the ground state wavefunction of the unpaired electron in an antibonding orbital would ordinarily be represented as[23]

$$\psi(a_{1g}^*) = N\left\{\beta|3z^2 - r^2\rangle + \beta'|5s\rangle - \frac{C}{\sqrt{12}}(2\bar{\sigma}_1 + 2\bar{\sigma}_2 - \bar{\sigma}_3 - \bar{\sigma}_4 - \bar{\sigma}_5 - \bar{\sigma}_6)\right\} \qquad (3)$$

where $\sigma_i = n|4p_z\rangle^i \pm (1 - n^2)^{\frac{1}{2}}|4s\rangle$.

Such a treatment would only apply in first order to the primary Rh^{2+} complex under consideration since spin density on the 2^{nd} and 4^{th} shell silver ions was detected and the equatorial ligands were inequivalent. Molecular orbital calculations which consider these points are in progress; however, approximate spin density calculations are presented here.

Assuming an axial rhodium hyperfine tensor, the components are given by

$$A_{//} = B_{//} + A_{iso}^{exptl}$$
$$A_{\perp} = B_{\perp} + A_{iso}^{exptl} \qquad (4)$$

For a d^7 ion with an unpaired electron in the $4d_{z^2}$ orbital, $A_{//}$ and $A_{\perp}$ can be related to the $4d_{z^2}$ orbital electron density ($N^2\beta^2$) by [23]

$$A_{//} = A_{iso}^{exptl} + \frac{4}{7} m^2 P - \frac{1}{7}\Delta g_{\perp} P$$
$$A_{\perp} = A_{iso}^{exptl} - \frac{2}{7} m^2 P + \frac{15}{14}\Delta g_{\perp} P \qquad (5)$$

where $P = g_e g_N \beta_e \beta_N \langle r^{-3} \rangle_{4d}$ and $m^2 = N^2\beta^2$.

The signs of $A_{//}$ and $A_{\perp}$ could not be determined experimentally; however, using a value of P one-half that of the free Rh^{2+} ion (1.6×10^{-4} cm^{-1}),[24] m was calculated for all sign combinations. Only the combinations of $+A_{//}$, $+A_{\perp}$ and $-A_{//}$, $+A_{\perp}$ gave values of m less than one. The former combination yielded m = .78, A_{iso}^{exptl} = -9.6 MHz, and the latter m = .44, A_{iso}^{exptl} = -18.3 MHz. A_{iso}^{exptl} is made up of a positive contribution from direct s electron contribution to $\psi(a_{1g}^*)$ and of a negative contribution from inner s shell polarization by the unpaired 4d electron. It was not possible to separate these two components, but since A_{iso}^{exptl} was large and negative, the s contribution was not significant.

It is reasonable to assume that $A_{//}$ and $A_{\perp}$ for the axial chlorines were both positive. Assuming once more an axial hyperfine tensor, the spin densities in the $|3s\rangle$ and $|3p\rangle$ orbitals were calculated according to the equations

$$f_s = \frac{A_{iso}^{exptl}}{A_{iso}^{o}} \qquad f_p = \frac{B_{//}}{2B^{o}} \qquad (6)$$

using values for A_{iso}^{o} and $2B^{o}$ given by Froese.[25, 26] f_s and f_p were determined to be .01 and .10 respectively, giving 22% total spin density on the axial ligands.

Similar calculations for the equatorial ligands resulted in the spin densities listed in Table V. Thus, the total spin density on the $(Ag^+)_4$,

$(Cl^-)_{4,6}$, $(Cl^-)_5$, and $(Cl^-)_{1,2}$ nuclei was approximately 33%. The spin density on $(Cl^-)_3$ and the second shell silvers would be expected to be less than 5%. Thus, if the spin density in the $|5s\rangle$ orbital is negligible, the most reasonable sign combination of $A_{//}$ (Rh), $A_{\perp}$ (Rh) would be both positive, giving a spin density on Rh of 78% and a total spin density of 116%. However, if there is some spin density in the Rh $|5s\rangle$ orbital, then the alternative of 44% spin density in d_{z^2} and ~18% in $|5s\rangle$ would be possible.

For the d^5 ions Re^{2+}, Ru^{3+} and Os^{3+}, three to five different substitutional metal ion--vacancy complexes were observed in AgCl and AgBr.[1, 2, 3] The failure of ESR to detect more than one site for the d^7 ions Ir^{2+} and Rh^{2+} has led to the speculation that the d^7 ions are not as sensitive a probe as the d^5 ions of their immediate environment. This was not the case for the primary rhodium species in AgCl. Both ESR and ENDOR studies showed that the primary species consisted of a single well-defined rhodium--vacancy configuration. Thus, the differences between the d^5 and d^7 ions appear to be real. Cross-over studies comparing the heat-treated and photo-produced Rh^{2+} centers, and studies of Rh^{2+} photolytically generated at temeratures where ionic motion is frozen would further clarify this question.

7.5 Conclusions

ESR and ENDOR studies confirmed that the primary species in heat-treated Rh^{3+} doped AgCl single crystals was a substitutional Rh^{2+} complex. Contrary to previous studies, this was found to have orthorhombic symmetry. This was the result of a vacancy in the nnn position and a complex elongation along a (100) axis perpendicular to the rhodium--vacancy axis. The unpaired electron was in essentially $5d_{z^2}$ orbital ground state. A pinned, two-dimensional dynamic distortion about the vacancy axis occurred as the temperature was raised.

A secondary species was also observed, with principal symmetry axes

approximately parallel to (111), ($1\bar{1}0$) and ($\bar{1}\bar{1}2$).

It was shown that modern ENDOR instrumentation can be fruitfully applied to the study of transition metal defect sites in silver halide single crystals. Studies of powders will probably be limited to a few axial or isotropic centers.

TABLE III

Hyperfine and Quadrupole Parameters for the Primary Rh^{2+} Species in AgCl

Nucleus	Hyperfine Tensor (MHz)			Quadrupole Tensor (MHz)		
	A_x	A_y	A_z	Q_{xx}	Q_{yy}	Q_{zz}
$(^{35}Cl^-)_{1,2}$	+35.4	+38.2	+73.5	.66	.33	1.8
^{103}Rh	5.4	6.0	8.9			
^{109}Ag - 4^{th} shell	9.5	9.5	12.7			
$(^{35}Cl^-)_5$	~ 20	~ 20	29.1			.20
$(^{35}Cl^-)_{4,6}$	~ 15	~15	25.1			.06
$(^{35}Cl^-)_3$	~1.5 ~6.4	~ 1.5 or ~ 6.4	~ 5 ~8.3			.06

TABLE IV

Measured and Calculated Quadrupole Coupling Constants for Several Systems

System	q/h (MHz) Measured	Calculated	$\frac{\text{measured}}{\text{calculated}}$ %
$H^{o}_{Sr^{2+}\text{-vac}}/KCl$	+.195[27]	+.86	23 %
Ag^{o}/KCl	+.39[28]	+.86	45 %
$Ag^{o}/NaCl$	+.52[28]	+1.19	44 %
$Rh^{2+}_{vac}/AgCl$	_.30	-1.25	24 %

TABLE V

Calculated Spin Densities for the Primary Rh^{2+} Species in AgCl

^{103}Rh		Total Spin Density on Nuclei
$A_{//}$ +	$a = -9.6$ MHz	78 %
$A_{\perp}$ +	$m^2 = .78$	$\|5s\rangle$
$A_{\perp}$ +	$a = -18.3$ MHz	44 %
$A_{//}$ -	$m^2 = .44$	$\|5s\rangle$
$(Cl^-)_{4,6}$	$f_s = .004$ $f_p = .007$	2.2%
$(Cl^-)_5$	$f_s = .004$ $f_p = .013$	1.7 %
$(Ag^+)_4$	$f_s = .007$ $f_p = .026$	6.6 %
$(Cl^-)_{1,2}$	$f_s = .01$ $f_p = .10$	22 %

REFERENCES

1. J.R. Buntaine and R.S. Eachus, Conf. Soc. Phot. Sci. and Eng., Boston (1980).

2. R.S. Eachus and M.T. Olm, rad. eff. 73, 69 (1983).

3. D.A. Corrigan, R.S. Eachus, R.E. Graves and M.T. Olm, J. Chem. Phys. 70, 5676 (1979).

4. R.S. Eachus and R.E. Graves, J. Chem. Phys. 65, 1530 (1976).

5. R.S. Eachus and R.E. Graves, J. Chem. Phys. 61, 2860 (1974).

6. R.S. Eachus and R.E. Graves, J. Chem. Phys. 63, 83 (1975); R.S. Eachus, R.E. Graves and M.T. Olm, J. Chem. Phys. 69, 4580 (1978).

7. R.S. Eachus and R.E. Graves, J. Chem. Phys. 65, 5445 (1976); R.S. Eachus, R.E. Graves and M.T. Olm, phys. stat. sol. (a) 57, 429 (1980).

8. A.G. Milnes, Deep Impurities in Semiconductors (John Wiley & Sons, New York, 1973).

9. H.B. Bebb and R.A. Chapman in Theory of Deep Impurity Centers in Semiconductors, Proceedings of the 3rd International Conference on Photoconductivity, 1969 ed. E.M. Pell (Pergamon Press, New York, 1971) p 245.

10. J.C. Garth, Phys. Rev. 140, A656 (1965).

11. J.R. Shock and M.T. Rogers, J. Chem. Phys. 62, 2640 (1975).

12. W. John and W. Windsch, phys. stat. sol. b 55, K39 (1973).

13. R.S. Eachus, unpublished results.

14. L. Kellogg, unpublished results.

15. J.E. Wertz and J.R. Bolton, Electron Spin Resonance: Elementary Theory and Practical Applications (McGraw Hill, New York, 1972) p 198.

16. S.E. Livingstone in Comprehensive Inorganic Chemistry, Vol 3 ed. A.F. Trotman-Dichenson (Pergamon Press, Oxford, 1973) p 1163.

17. T.E. Feuchtang, Phys. Rev. 126, 1628 (1962).

18. D. Schoemaker, Phys. Rev. 174, 1060 (1968).

19. C.P. Slichter, Principles of Magnetic Resonance, 2nd ed. (Springer-Verlag, Berlin, 1980).

20. C.J. Delbecq, R. Hartford, D. Schoemaker, and P.H. Yuster, Phys. Rev. 13, 3631 (1976).

21. S.U. Cheema and M.J.A. Smith, J. Phys. C 4, 1231 (1971).

22. J.A. Aramburu and M. Moreno, J. Chem. Phys. 79, 4996 (1983).

23. A. Abragam and B. Bleaney, Electron Paramagnetic Resonance of Transition Ions (Clarendon, Oxford, 1970).

24. A.H. Maki, N. Edelstein, A. Davison and R.H. Holm, J.A.C.S. 86, 4580 (1964).

25. C. Froese, J. Chem. Phys. 45, 1417 (1966).

26. M. Symons, Chemical and Biochemical Aspects of Electron Spin Resonance Spectroscopy (Van Nostrand-Reinhold Co., New York, 1978).

27. P. Studzinski, J.R. Niklas, and J.M. Spaeth, phys. stat. sol. b 44, 671 (1980).

28. G.E. Holmberg, W.P.Unruh and R.J. Friauf, Phys. Rev. B 13, 983 (1976).

C H A P T E R E I G H T

ESR AND ENDOR STUDIES

OF THE

SILVER:CYCLOHEXENYL RADICAL

CHAPTER 8

ESR and ENDOR Studies of the Silver:Cyclohexenyl Radical

8.1 Introduction

The formation of stable complexes between the noble metals and olefinic compounds is well known.[1] It is likely that such complexes form at the silver halide grain surface in photographic emulsions as a result of interactions with gelatin, sensitizing dyes, and other organic addenda. Thus, the bonding in these complexes is of practical as well as of fundamental interest.

The stability of metal:olefinic complexes is a function of steric factors and of the basicity of the olefin[2,3] and, in metal:diolefin complexes, of the degree of conjugation.[4] For 1:1 complexes, bonding consists of a σ-type bond resulting from the donation of π-2p bonding electrons of the olefin into the silver 5s orbital, and of a π-type bond resulting from the back donation of silver 4d electrons into vacant π^*- 2p antibonding orbitals of the olefin.[5,6] Diligand complexes between Cu^o or Ag^o and acetylene or ethylene have been detected in rare gas matrices by ESR spectroscopy.[7,8] In this instance, bonding occurs between a Ag p-orbital and the π^* antibonding orbitals of two flanking acetylene or ethylene molecules.

Stable silver:olefin radicals can be produced by γ-irradiation of many of the silver:olefin complexes.[4,7-11] ESR spectroscopy has proved a useful tool in studying the structure and bonding in these radicals and, by extrapolation, the structure and bonding of the parent complexes.[4,7-11] However, the ESR spectra of many of the silver:olefin radicals, particularly the larger cyclic olefins consist of a single,

uninformative, inhomogenously broadened line.[4] Only a few silver:cyclic diolefin complexes have been fruitfully studied by ESR.[4,10] For those radicals exhibiting inhomogenously broadened lines, ENDOR spectroscopy should be the ideal tool for extracting hyperfine splittings.

The difficulty or impossibility of growing single crystals of silver:olefin complexes has meant that all ESR studies have been on powders. No ENDOR powder studies of these complexes have been reported. Thus, in the work described below, the silver:cyclohexenyl radical was chosen as a model system for the ENDOR powder studies of metal:olefin complexes. The silver: cyclohexenyl radical is one of a series of radicals, formed by γ-irradiation of silver:cyclopentene - silver:cycloheptene powders, which have been studied previously by ESR.[9] The larger cyclic olefin complexes gave only broad uninterpretable lines on γ-irradiation.

8.2 Experimental

The Ag:cyclohexene powder complex was prepared in powder form by the method of Comyns and Lucas[12] using reagent grade cyclohexene and silver perchlorate (Alpha Products). Samples were dried in dim light under a stream of nitrogen gas and stored in the dark at $0^{\circ}C$.

Samples were γ-irradiated at 77K and at room temperature using ^{60}Co Vickrad source with a dose rate of about 1 Mrad h^{-1}.

ESR and ENDOR measurements were made with the Bruker spectrometer and with the cryostats described in Chapter 6. A superheterodyne ESR spectrometer was utilized for Q-band measurements. Some X-band ESR measurements were carried out on a Varian E-109 spectrometer system.

8.3 Results and Discussion

The X-band ESR spectrum shown in Figure 1b was obtained from a silver:cyclohexene powder which had been γ-irradiated at room temperature. This is essentially the same as that obtained by Gee, et. al.[9] The spectra shown in Figures 1a and 1b were measured at room temperature. As the temperature was lowered, resolution of the hyperfine structure was lost and the overall envelope of the line broadened (Figures 1c-d).

The g-value of the silver:cyclohexene radical was 2.0030 $\pm$ .0005, differing somewhat from the value of 2.0017 $\pm$ .0002 previously reported.[9] Q-band measurements indicated that the g-tensor was slightly anisotropic. The overall spectral width at room temperature, measured between the outermost peaks, increased from 135 - 139 G at X-band, to 165 - 175 G at Q-band. Thus, the anisotropic spread of the g-tensor was 0.004 - 0.006.

ENDOR spectra could be obtained from silver:cyclohexene powders from 4 K to 200 K, with a broad optimum temperature range of 60 K to 150 K. Resolution and sensitivity were not improved by helium temperature measurements. A typical ENDOR spectrum is shown in Figure 2 with expanded sections shown in Figures 3 and 4. These were "powder-type" ENDOR powder spectra (Chapter 5), that is, the same spectrum was obtained regardless of the position of the saturating magnetic field. This was either the result of the absence of a "separating" vector", or the fulfillment of the condition required for the transfer of microwave energy throughout the spin system, $T_{xx}^{-1} \gg T_{le}^{-1}$.

All of the ENDOR lines observed arose from proton hyperfine couplings. The lines could be paired into $m_s = +\frac{1}{2}$ and $m_s = -\frac{1}{2}$ components, as shown in Figures 2 and 3. Pairs 1 through 17 were centred at the free proton nuclear frequency

FIGURE 1

ESR spectra of silver:cyclohexene powders which were γ-irradiated 24 hours at room temperature and measured at a) Q-band frequency and room temperature, b) X-band frequency and room temperature, c) 155 K and d) 40 K.

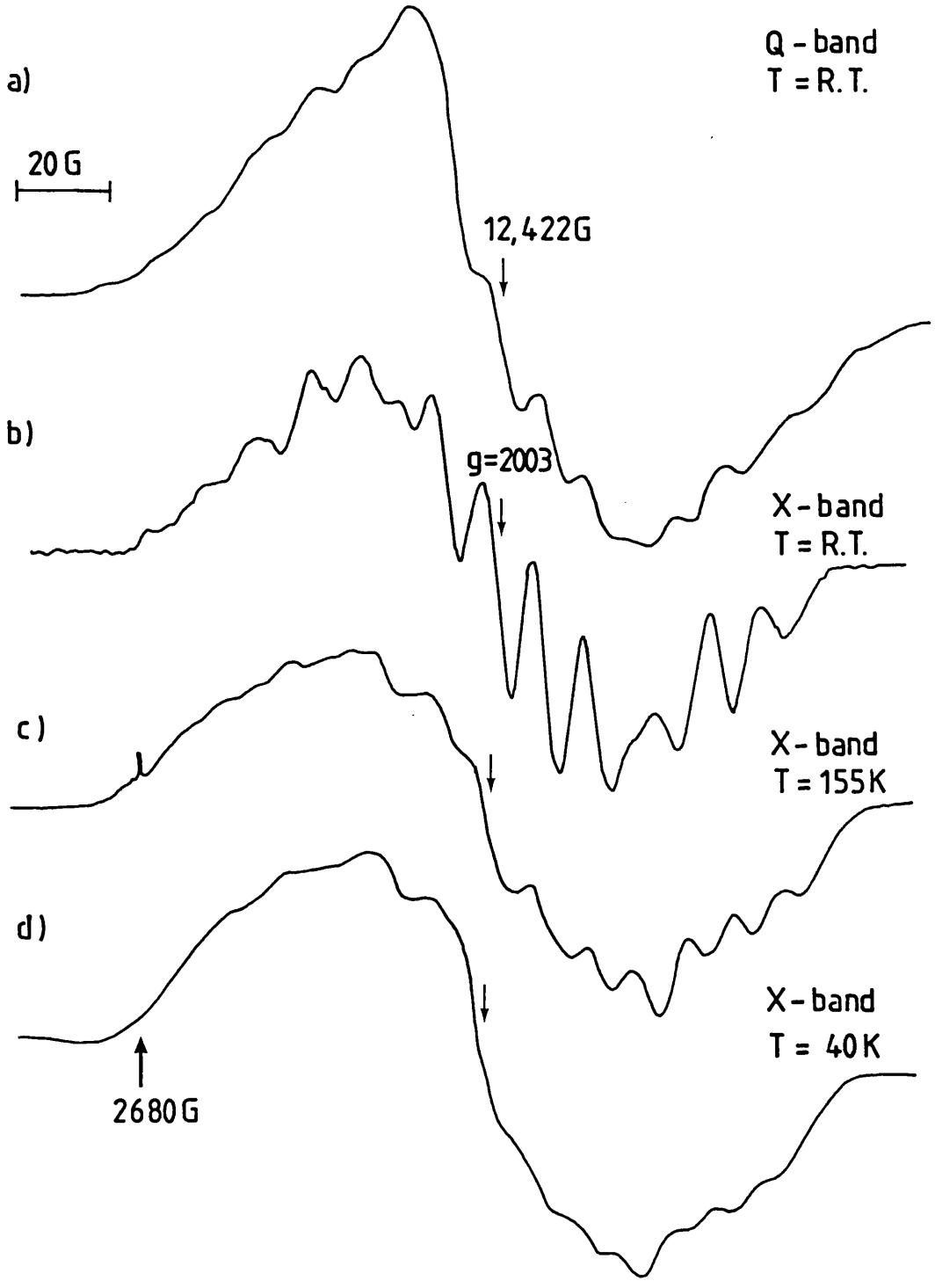

FIGURE 2

ENDOR spectrum of a silver:cyclohexene powder which was γ-irradiated 24 hours at room temperature measured at 155 K.
[The lines marked with * are expanded in Figures 3 and 4. For spectral assignments see Table IV.]

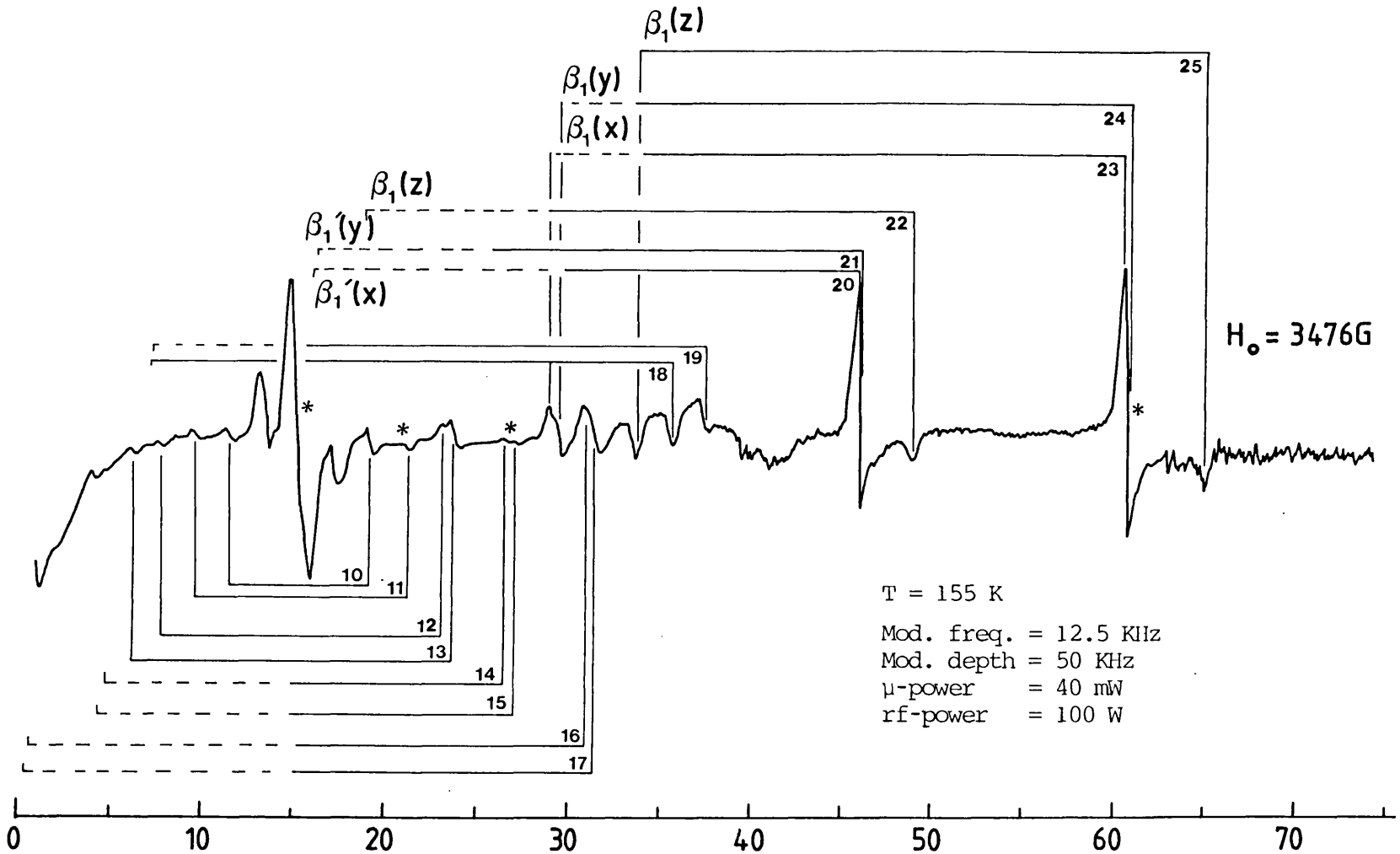

FIGURE 3

Expanded ENDOR powder spectrum of the silver:cyclohexene radical showing small hyperfine couplings.

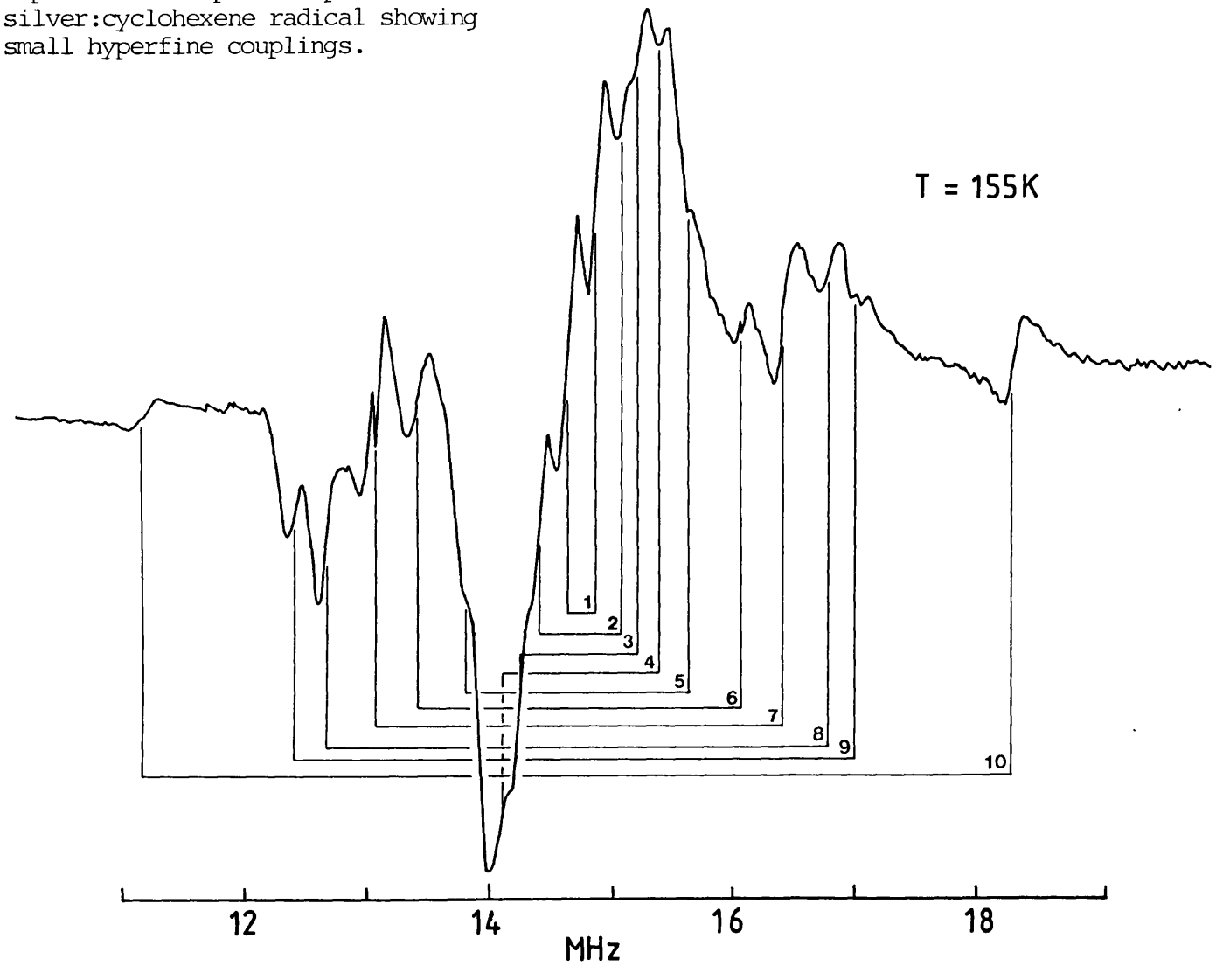

FIGURE 4

Expanded ENDOR powder spectra of silver:cyclohexene complex showing doublet structure, T = 155 K.

and pairs 18 - 25 were separated by the free proton nuclear frequency and centred at a/2. As expected from equations 6.15 and 6.16, the low frequency line of each pair was the weakest and in some cases (18,19) not detectable. Sensitivity was instrument limited below 4 MHz; thus, the low frequency lines of pairs 14 - 17 were not detected. The low frequency lines of pairs 20 - 22 were obscured by the high frequency lines of small, less anisotropic hyperfine couplings.

In GENERAL TRIPLE ENDOR experiments, pumping any one of the lines in Figure 2 resulted in an intensity change in all of the others, suggesting that all of the lines in Figure 2 arose from the same complex. This conclusion must be qualified by the observation that for overlapping lines it can be difficult either to "pump" only one component or to independently attribute resulting intensity changes to one or the other component. Thus, considering the central small hyperfine couplings shown in Figure 3, as long as some of the overlapping hyperfine couplings (pairs 1 - 9) arose from the silver: cyclohexene radical (or surrounding matrix protons), it was not possible to establish that all of the small couplings were associated with such a radical. Many of the ENDOR lines shown in Figure 2 were composed of doublets. On the basis of TRIPLE experiments, it can only be said at least one component of each doublet was associated with at least one component of every other line in the ENDOR spectrum. However, the TRIPLE ENDOR experiments were able to establish the significant fact that the two large β-proton splittings (Pairs 20 - 22 and 23 - 25 as assigned below) arose from the same silver:cyclohexene complex. Figure 5 shows that pumping the high frequency $(\beta_1)_\perp$ line (pairs 23,24) caused a decrease in the intensity of the

FIGURE 5

a) ENDOR and b) TRIPLE ENDOR powder spectra silver:cyclohexene radical showing the effect of pumping the high frequency line from the large β proton splitting. [The low frequency line of this splitting is marked *]

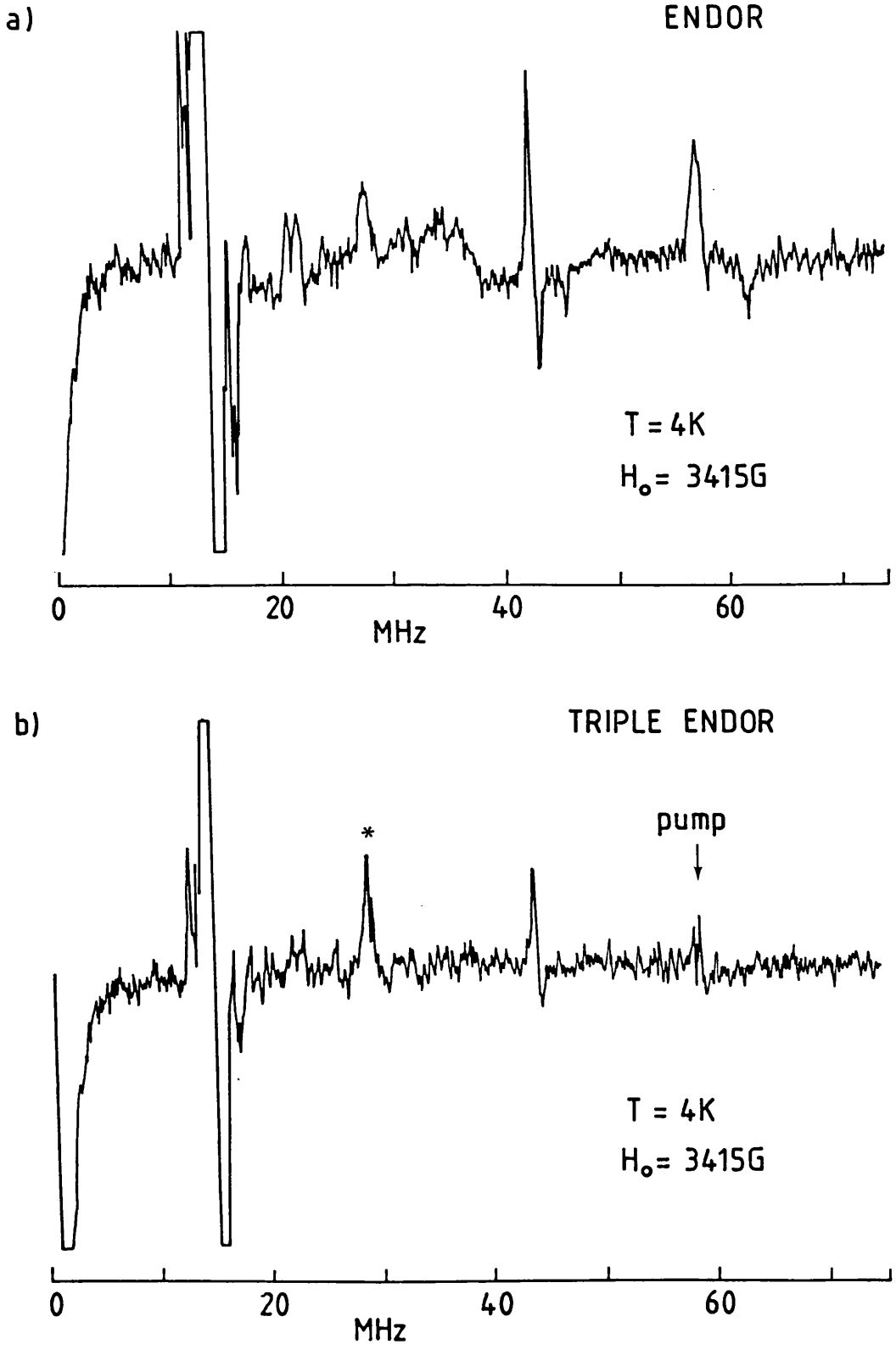

high frequency (β'_1) lines (pairs 20 - 22). Also, as expected, pumping the high frequency ($\beta_1)_\perp$ line caused it to decrease in intensity while the low frequency ($\beta_1)_\perp$ line, marked with an asterisk in Figure 5, increased in intensity.

A helium cryostat insert was used for the measurements of the ENDOR spectra shown in Figures 5 and 6, and, as a result, the position of the saturating magnetic field was 60 gauss lower than that used to obtain the spectra in Figures 2 - 4. This had a significant effect in the "overlap region" of the spectrum, causing the low frequency lines of pairs 23 and 24 and the high frequency lines of pairs 16 and 17 to coalesce to the single line marked with an asterisk in Figures 5 and 6. The nature of the line movements as a function of the static magnetic field confirmed the line pairing assignments made in Figure 2. (See Figure 5.16).

Many of the ENDOR lines were split into doublets. Splittings were best resolved at low rf powers and therefore did not result from rf coherence effects.[13] As discussed below, the splittings reflected either the slight orthorhombic character of the hyperfine tensor (23-24, 20-21, 16-17, 12-13) or the slight inequivalence of two protons (14-15).

The ENDOR lines could all be consistently assigned to the model of the silver:cyclohexenyl radical shown below:

FIGURE 6

ENDOR powder spectra of the silver:cyclohexene radical at a) 40 K and b) 4 K. [The * marks the overlap region of the high frequency lines of pairs 16-17 and the low frequency lines of pairs 23-24.]

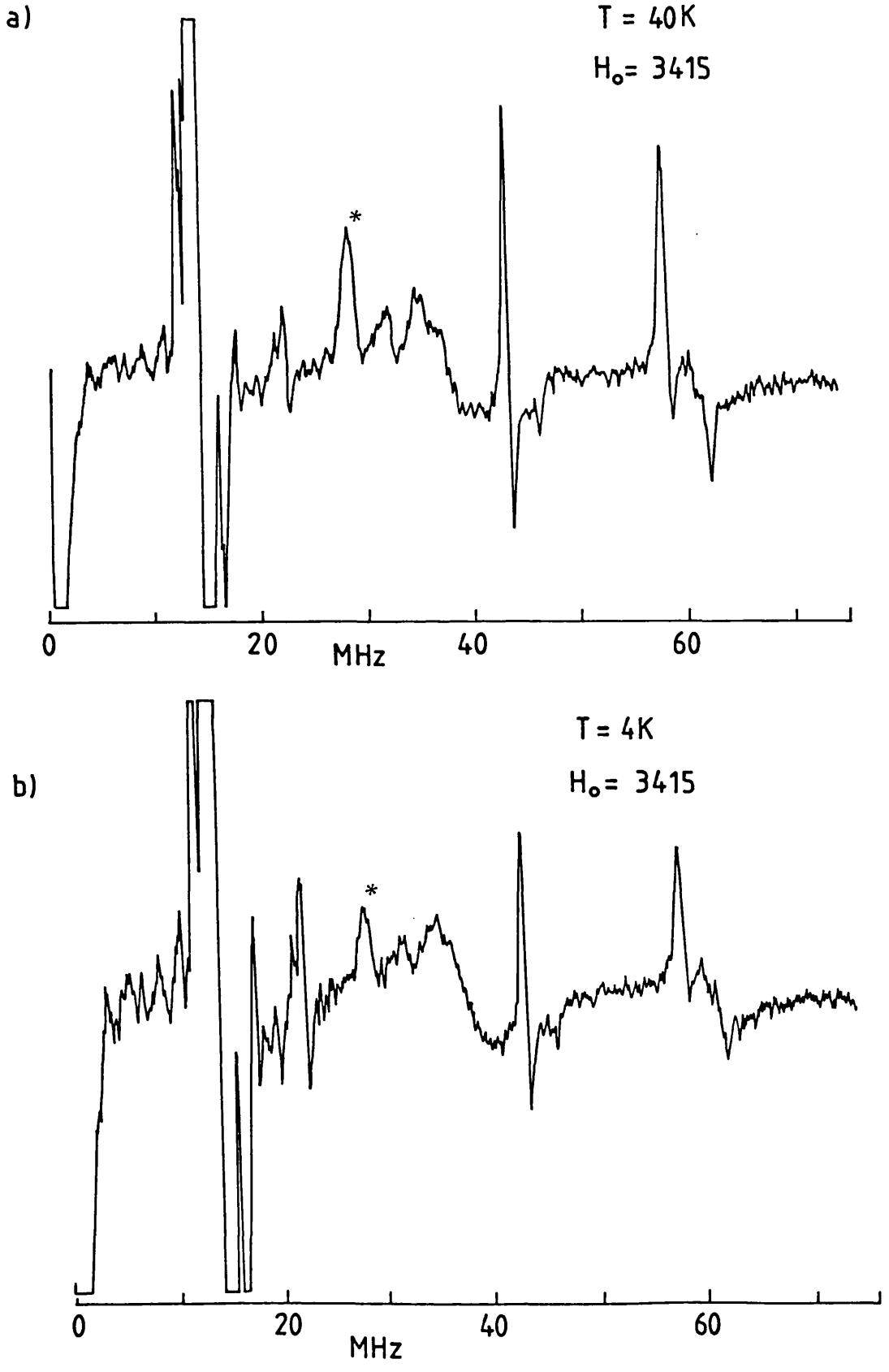

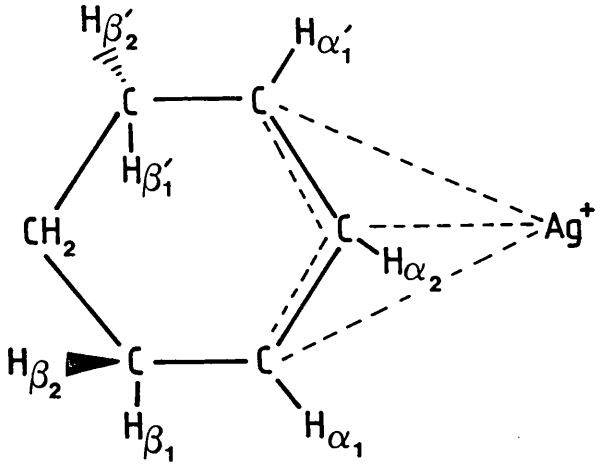

Assignments of hyperfine splittings to individual nuclei were made by analogy with the observed splittings in similar radicals such as the allyl[14] and hexadienyl radical.[15] Thus, the largest hyperfine splittings (23-25 and 20-22) were assigned as components of the slightly orthorhombic hyperfine tensors of two β protons (Tables I and II). The ENDOR powder patterns are typical of those observed for β protons.[16] The small anisotropy of the hyperfine tensors is also typical of β protons and leads to the ENDOR powder spectrum being dominated by β proton resonances.

The largest degree of σ-π delocalization, and thus the maximum β proton hyperfine splitting is attained when the proton - carbon bond is perpendicular to the nodal plane of the π electron system. Thus, the isotropic hyperfine splittings for β_1 and β_2 protons are predicted by the relationships[14]

$$\begin{aligned} a\,(\beta_1) &= A_{max}\cos^2\theta \\ a\,(\beta_2) &= A_{max}\cos^2(120+\theta) \end{aligned} \qquad (1)$$

For equal spin density on two sets of β protons (β and β'), $A_{max} \cong 23$ gauss. If, for the cyclohexenyl radical, it is

assumed the spin densities on the β and β' protons are unequal, and A_{max} for the β_1 proton is allowed to be 31 gauss (Table II), then according to eqn 1, this proton is perpendicular to the π nodal plane. The β'_1 proton has too large a splitting to be on the same carbon as the β_1 proton. However, the pairs of lines 12 and 13 have a typical β proton lineshape and have been assigned as the x and y components of the β_2 proton hyperfine tensor. The $(\beta_2)_z$ splittings were not observed; but, assuming ~10% anisotropy, as for the β_1 proton hyperfine tensor, the isotropic hyperfine splitting for β_2 was 5.6 gauss. This is consistent with the value predicted by eqn 1. The pairs of lines 16 - 18 also have a characteristic β proton shape and were assigned as components of the β'_2 hyperfine tensor. The isotropic hyperfine splittings for β'_1 and β'_2 of 21.3 and 11.8 gauss are consistent with eqn 1.

The isotropic splittings of the α protons are expected to be of the order of 13 G, with the anisotropic part of the hyperfine tensor being of the form (+B, 0, -B).[14] A large degree of anisotropy is anticipated. Thus, pairs of lines 14 and 15, corresponding to splittings of 7.55 and 7.88 gauss, can reasonably be assigned to x hyperfine components of inequivalent α_1 and α'_1 protons. The lines are much weaker than the β proton resonances, as expected for α protons.[16] Line 19, corresponding to a hyperfine coupling of 14.76 gauss, has the correct shape for the a_y component. Thus, the α hyperfine tensor has the principal components (7.7, 14.8, ~ 21.8) and the a_z splittings are buried beneath the β proton resonances 20 - 22.

Pairs of lines 10 and 11 are of the correct shape and intensity to be assigned to the y and z hyperfine lines of

the α_2 proton. The corresponding splittings of 2.51 and 4.02 gauss are too large to arise from dipolar couplings with matrix protons or from the γ proton. The a_x component cannot be inequivocally assigned to a particular one of the smaller hyperfine splittings; however, pairs of lines 8 and 9 correspond to splittings of the correct order of magnitude. Thus, the principal hyperfine tensor components for the α_2 proton are ($\sim$1.5, 2.5, 4.0).

The γ protons will probably be inequivalent with splittings of the order of one gauss.[17] Without deuteration experiments, it is not possible to distinguish these from the dipolar matrix couplings, which are of the same order of magnitude.

Lines arising from silver hyperfine splittings would be expected to be quite characteristic as a result of the presence of two silver isotopes. However, no silver splittings were observed even at helium temperatures. This can be understood by remembering that the silver resonances are expected to be relatively weak ($\nu_H/\nu_{Ag} = 10$) and to occur in the vicinity of the β proton resonances (Table II). Thus, the silver ENDOR lines were probably obscured by the β proton resonances. A silver splitting of 17 G was calculated from the measured proton splittings and the ESR spectral width.

The relative ENDOR line intensities were approximately those predicted by the treatment of Dalton and Kwiram (eqn 6.16), assuming an anisotropic and frequency dependent transition probability.[16] Based on this treatment, a useful qualitative observation is that the parallel features of all protons with a similar saturation parameter, S, are of equal intensity regardless of the transition frequency. This was

observed for the β_1, β'_1 and β'_2 parallel resonances, as shown in Table III. The calculated line intensities, using eqn 6.16, and assuming R = 1, for several values of S, are also shown in Table III. The best fit for the β_1 and β_2 protons were obtained with a value of S of 0.003 and for the β'_1 and β'_2 with $S \approx 0.043$. However, the calculated line intensities were not particularly sensitive to S, and the agreement between experimental and calculated intensities not good enough to use the fitted value of S to calculate relaxation times. The weak small line intensities observed for α protons indicate that for these protons, S was less than 0.003.

The line intensities in Table III were calculated assuming that there was one of each type of β-proton and that the ENDOR line intensities were not affected by overlap of the ESR hyperfine components. The latter assumption can be shown to be justified using the measured β proton splittings and a reasonable estimate of 1×10^{-7} sec for T_{2e} in eqn 6.12.[18] The validity of the first assumption could not be tested because of the inaccuracies in fitting S for each type of proton.

As the temperature was lowered, some of the ENDOR lines broadened and some splittings changed slightly (Figure 6). This can probably be attributed to packing effects. The relative line intensities, and thus the various S-values, did not change significantly on cooling.

8.4 Conclusions

The hyperfine splittings measured by ENDOR in γ-irradiated silver:cyclohexene powders were assigned to the silver:cyclohexenyl radical. The observation of two large β proton

splittings indicated the inequivalence of the β and β' protons at temperatures less than 200 K. The inequivalence can be attributed to a skew conformation of the cyclohexene molecule and/or the off-centre placement of the silver ion. The average of the isotropic splittings calculated from the ENDOR data (Table II) for the β_1 and β'_1 protons was similar to the isotropic splitting which was fitted to the room temperature ESR spectrum assuming equivalent β_1 protons.[9] The same was true for the β_2 protons. The calculated isotropic splittings for the α protons were also close to those fitted to the room temperature spectrum (Table II). Thus, the greater spectral resolution of room temperature ESR spectra may be due to motional averaging of the β and β' proton inequivalence.

This study showed that ENDOR powder spectroscopy can be successfully applied to the study of bonding in silver:olefin complexes. Deuteration experiments would allow the unequivocal assignment of small hyperfine splittings. In most cases, the Ag hyperfine splittings would have to be deduced from fitting the proton splittings derived by ENDOR to the ESR spectrum. K - band or Q - band ENDOR experiments might also allow the derivation of the Ag hyperfine splittings.

Table I: Hyperfine Splittings and ENDOR Line Positions Measured In γ-irradiated Ag:Cyclohexene Powders At 155 K

Pair no.	Line Position ($\nu_{\pm}$ - MHz)	Hyperfine Splitting (MHz/gauss)
1	14.58 14.79	.21/.075
2	14.34 15.01	.66/.24
3	14.22 15.11	.89/.32
4	14.05 15.29	1.24/.44
5	13.78 15.54	1.76/.63
6	13.74 15.99	2.62/.94
7	13.00 16.37	3.37/1.20
8	12.63 16.73	4.10/1.46
9	12.37 17.05	4.68/1.67
10	11.17 18.21	7.04/2.51
11	9.15(9.08) [a] 20.32	11.26/4.02
12	7.45(7.36) 22.02	14.66/5.23
13	6.09(6.76) 22.62	15.86/5.66
14	(4.11) 25.27	21.16/7.55
15	(3.64) 25.74	22.10/7.88
16	(.32) 29.75	30.07/10.73

Table I (Cont.): Hyperfine Splittings and ENDOR Line Positions Measured In γ-irradiated Ag:Cyclohexene Powders At 155 K

Pair no.	Line Position ($\nu_{\pm}$ - MHz)	Hyperfine Splitting (MHz/gauss)
17	(.57) 30.00	30.57/10.90
18	(4.51) 33.97	38.48/13.73
19	(5.95) 35.42	41.37/14.76
20	(13.95) 43.52	57.44/20.49
21	(14.16) 43.71	57.87/20.64
22	(17.16) 46.75	63.91/22.80
23	27.77(27.74) 57.50	85.24/30.41
24	28.22(28.32) 58.08	86.39/30.82
25	32.34(32.13) 61.97	94.21/33.61

[a] The figures in parenthesis are calculated line positions. A second order correction (eqn 5.26) was applied to pairs 16 - 25.

Table II: Assignments of Nuclei to Hyperfine Splittings for the Ag:Cyclohexenyl Radical

Nucleus	Pair no.	$a_{iso}^{a,c}$ (155 K)	a_{iso}^{b} (RT)
β_1	23,24,25	31.61	28.5
β'_1	20,21,22	21.31	
β_2	12,13 -	(5.6)	8.5
β'_2	16,17,18	11.79	
α_1	14,19,-	(14.8)	11.0
α'_1	15,19,-	(14.8)	
α_2	-,10,11,	(2.7)	3.8
Ag	-	17[d]	22.5

a From averaged a values of ENDOR measurements

b From a values fitted to RT ESR spectrum[9]

c Figures in parenthesis are estimates, as discussed in text

d Calculated from measured proton splittings and the ESR spectral width

Table III: Experimental and Calculated Line Intensities

Nucleus	Pair no.	Line Positions[a] (MHz)	Exp. Int.	Calculated Intensity S=.003	S=.043	S=.23
$(\beta_1)_\perp$	23,24	28.22	6	5.9	10.3	2.9
		57.8	21	21	26.0	21.0
$(\beta_1)_{\prime\prime}$	25	32.24	2.5	1.3	2.5	4.9
		61.97	3.5	1.3	2.5	4.9
$(\beta_2)_\perp$	12,13	(6.8)	-			
		22.32	3.8	2.9	5.5	9.1
$(\beta'_1)_\perp$	20,21	(14.0)	-	1.7	3.3	6.2
		43.6	18.3	12.2	18.2	18.3
$(\beta'_1)_{\prime\prime}$	22	17.16	-	1.3	2.5	4.9
		46.75	2.5	1.3	2.5	4.9
$(\beta'_2)_\perp$	16,17	(.4)	-			
		29.85	6.2	5.1	9.1	12.7
$(\beta'_2)_{\prime\prime}$	18	(5.2)	-	1.3	2.5	4.9
		34.7	2	1.3	2.5	4.9

[a] Lines in parenthesis were not observed.

References

1. L.J. Andrews and R.M. Keefer, Molecular Complexes in Organic Chemistry (Holden-Day, Inc., San Francisco, 1964).

2. M.A. Muhs and F.T. Weiss, J.A.C.S. 84, 4697 (1962).

3. J.G. Traynham and J.R. Olechowski, J.A.C.S. 81, 571 (1959).

4. D.R. Gee and J.K.S. Wan, Can. J. Chem. 49, 160 (1971).

5. M.J.S. Dewar, Bull. Soc. Chim. Fr. 18, C79 (1951).

6. H. Hosoya and S. Nagakura, Bull. Chem. Soc. Jpn. 37, 249 (1964).

7. P.H. Kasai, D. McLeod Jr. and T. Watanabe, J.A.C.S. 102, 179 (1979).

8. P.H. Kasai, J. Phys. Chem. 86, 3684 (1982).

9. D.R. Gee, K.E. Russell and J.K.S. Wan, Can. J. Chem. 48, 2740 (1970).

10. D.R. Gee, K.E. Russell and J.K.S. Wan, J. Chem. Phys. 53, 847 (1970).

11. C. Alesbury, Ph.d. thesis, Leicester University (1975).

12. A.E. Comyns and H.J. Lucas, J.A.C.S. 79, 4339 (1957).

13. D.S. Leniart in Multiple Electron Resonance Spectroscopy, eds. M.M. Dorio and J.H. Freed (Plenum Press, New York, 1979).

14. M.C.R. Symons, Chemical and Biochemical Aspects of Electron Spin Resonance Spectroscopy (Van Nostrand Reinhold Company, New York, 1978).

15. R.W. Fessenden and R.H. Schuler, J. Chem. Phys. 39, 2147 (1963).

16. L.R. Dalton and A.L. Kwiram, J. Chem. Phys. 57, 1132 (1972).

17. R.W. Fessenden and R.H. Schuler, J. Chem. Phys. 38, 773 (1963).

18. L. Kevan and L.D. Kispert, Electron Spin Double Resonance Spectroscopy (John Wiley & Sons, New York, 1976).

ABSTRACT

MAGNETIC RESONANCE STUDIES OF SOME SILVER HALIDE-BASED MODEL IMAGING SYSTEMS

Myra Toffolon Olm

Band gap excitation of silver halides produces charge carriers which are subsequently localized at hydrogenic or deep traps. These intrinsic or extrinsic defects control the photographic behaviour of practical silver halide systems. This thesis describes the use of magnetic resonance techniques to study the structure of such traps in model systems.

The lifetime of photoproduced conduction electrons can be greatly extended in silver-halide based materials designed to encourage the partitioning of free electrons and holes. Conduction Electron Spin Resonance was used to study the conduction processes of shallowly trapped and free carriers in several such materials, including Pb^{2+}-doped AgCl, AgBr/AgCl, AgI/AgCl and AgCl/NaCl single crystals and powders. Mechanisms for the extension of the free electron lifetime are proposed, and the temperature and microwave power dependences of the CESR g-value and lineshape are discussed. In addition to studying the band structure and conduction processes as a function of silver concentration and Fermi level in AgCl/NaCl alloys, magnetic resonance studies were used to probe the microcrystalline structure and phase separation processes in these materials.

Transition metal impurities, often associated with lattice defects, act as deep traps in the silver halides. The structure of the metal ion-defect site affects its trap cross-section and lifetime. The enhanced resolution provided by Electron Nuclear Double Resonance techniques was used to determine the structure of Rh^{2+}-silver ion vacancy complexes in Rh^{3+}-doped AgCl and NaCl single crystals and powders. The primary site in AgCl exhibited a static Jahn-Teller distortion at low temperature, which gave way to a two-dimensional and finally to a three-dimensional dynamic distortion as the temperature was raised.

The application of ENDOR to glasses and powders was explored via studies of the DTBN radical in glassy matrices and of γ-irradiated sodium formate and silver:cyclohexene powders. The latter two studies provided, respectively, examples of "single-crystal-like" and "powder-type" ENDOR powder spectra.